

Dynamic Balancing of Reciprocating Machinery  
With Application to Weaving Machines

Dynamisch Balanceren van Machines die  
Heen-en-Weer Gaande Bewegingen Uitvoeren met  
Toepassing op Weefmachines

Bram Demeulenaere  
Ph.D. thesis  
Katholieke Universiteit Leuven, Belgium

May 2004

© Katholieke Universiteit Leuven  
Faculteit Toegepaste Wetenschappen  
Kasteelpark Arenberg 1, B-3001 Leuven (Heverlee), Belgium

Alle rechten voorbehouden. Niets uit deze uitgave mag worden verveelvoudigd en/of openbaar gemaakt worden door middel van druk, fotokopie, microfilm, elektronisch of op welke andere wijze ook zonder voorafgaandelijke schriftelijke toestemming van de uitgever.

All rights reserved. No part of this publication may be reproduced in any form, by print, photoprint, microfilm or any other means without written permission from the publisher.

D/2004/7515/28  
ISBN 90-5682-490-2  
UDC 677.054

# Voorwoord

*Wie doet wat hij kan,  
is een eerlijk man.*

Op het einde van het doctoraatsparcours, is een steeds terugkerende vraag, vooral op recepties van gelukkigen die net gepromoveerd zijn: ‘...en wanneer is het jouw beurt?’ Een al even clichématige vraag moest ik tot vervelens toe beantwoorden in de zomer van 1998, net voor het aanvatten van mijn laatste ingenieursjaar: ‘...en wat ga jij doen als je afgestudeerd bent?’ Wat dat betreft, had ik toen een wel heel duidelijke mening: ‘Ik weet het nog niet, maar ik weet wel wat ik zeker niet ga doen: doctoreren.’

Nu, een kleine zes jaar later, ligt voor u, beste lezer, de neerslag van viereneenhalf jaar onderzoekswerk, onder de vorm van 10 hoofdstukken en Q bijlagen. Wat mij bezielt heeft om zo’n monster van 431 bladzijden te produceren, is mij nog niet helemaal duidelijk. Wat ik wel weet, is waarom ik er in oktober 1999 aan begonnen ben: omdat ik graag het waarom van dingen uitzoek en graag in Matlab programmeer.

Dat was namelijk waar ik veel plezier aan beleefd had tijdens de eerste, lesvrije maand (september 1998) van mijn eindwerk. In al mijn naïviteit dacht ik dat doctoreren niet anders was dan dat, en zo kwam het dat ik, een klein jaar en een geslaagde beursaanvraag later, op de stoel van Herman Van de Straete zat, in een bureau met Vincent (Lampaert) en Jan (Swevers), onder het motto<sup>1</sup>: ‘Science is the best way to satisfy your own curiosity for the governmental account’.

Dit voorwoord bestaat uit twee delen. Omdat ik mij levendig herinner dat het mij in 1999 een raadsel leek hoe een doctoraat tot stand komt, geeft het eerste deel een (historisch helemaal niet correct, en zwaar gekleurd) overzicht van hoe het in mijn geval gelopen is. In het tweede deel probeer ik niemand te vergeten van de vele mensen die een grote of kleine bijdrage aan dit werk geleverd hebben.

---

<sup>1</sup>Lev Artsimovich (1909-1973), Russisch fysicus.

## La petite histoire . . .

De aanvankelijke bedoeling van dit werk was voortbouwen op een onderzoeklijn die Joris (De Schutter) al een aantal jaar daarvoor opgestart had, maar door allerlei omstandigheden wat in het slop zat: identificatie en optimalisatie van meervoudige nokkensystemen. Aanvankelijk kwam dit vooral neer op verder werken op de identificatiemethode die Vincent en ik in ons eindwerk ontwikkeld hadden. D.w.z., proberen de bereikte simulatieresultaten in de praktijk om te zetten, en, aangemoedigd door Jan en Joris, publiceren over die resultaten: Nationaal Mechanica Congres 2000, Benelux conferentie 2000 en ISMA 2000. Mijn eerste ISMA heb ik doorgebracht op een Turks strand, maar mijn eerste Benelux was een schot in de roos (conferentiecentrum met bowlingbaan en tropisch zwembad, en een bende jonge PMA-honden daarin losgelaten).

Echt vaart in het onderzoek kwam er na een suggestie van Joris om een paper van Herman Van de Straete eens wat grondiger door te nemen. In combinatie met wat ik van Pascal (Degezelle) geleerd had over energie in nokkensystemen, bleek plots, ergens in maart/april 2000, dat één van randwaardeproblemen van Herman ook via een gewone algebraïsche vergelijking kon opgelost worden. De inertiael gecompenseerde nokken waren geboren (en mijn krullen ondertussen verdwenen). Heel de zomer van 2000 werd besteed aan een verslag over die nokken, dat de basis werd voor mijn eerste 'echte' internationale conferentie (AIM2001 in Como, Italië), en mijn eerste journal publicatie, die na een editoriale lijdensweg van bijna twee jaar, in september 2003 dan toch verschenen is.

Ondertussen waren de inertiael gecompenseerde nokken ook een deel van een IWT-projectvoorstel geworden, met PMA, Picanol N.V. en het WTCM als partners. Het project had als (onmogelijke) titel *'Ontwikkelen van methodes en technieken om het afgestraalde geluid en de trillingen van machines, met mechanismen die oscillerende bewegingen uitvoeren, te verminderen'*. Het 'Picanol-project' startte daadwerkelijk in de herfst van 2000. Ik was er aanvankelijk maar matig enthousiast over, vooral toen vrij snel bleek dat inertiael gecompenseerde nokken geen goede oplossing waren voor de dynamische problemen in weefmachines.

Toen alles wat vast leek te lopen, kwam echter een tweede grote stimulans: koppelcompensatie. Als alternatief voor inertiael gecompenseerde nokken, stelde Philip Cornelissen, toenmalig projectleider bij Picanol, een koppelcompenserend mechanisme voor. Omwille van een vervelende differentiaalvergelijking kwam dit mechanisme op mijn bureau terecht. Na een uitgebreide literatuurstudie, die mij tot in de archieven van de Heverleese Jezuïten en een flink eind terug in de tijd bracht, bleek dat er nog geen (correcte) methode bestond om dit zgn. geïnverteerd nokkenmechanisme te ontwerpen. Het was dus de moeite er zelf een te ontwikkelen, hetgeen mij een publicatie opleverde voor de 'Biennial Mechanisms and Robotics Conference' tijdens DETC2002 in Montréal. Ik keerde met een pak motivatie terug uit Canada, niet in het

minst door een aantal coryfeeën uit het nok- en mechanismenontwerp te ontmoeten: Jorge Angeles, Richard Berkof en Bob Norton (Joris herinnert zich vast nog de enthousiaste verslagen die ik toen elke avond naar België mailde).

Toen bleek dat er technologische problemen verbonden waren met de constructie van het geïnverteerde nokkenmechanisme, kwam Philip Cornelissen met een ander compenserend mechanisme op de proppen: de nokgebaseerde centrifugaalslinger. Ook hier bleek weer geen ontwerpmethodologie voor handen in de literatuur, en dus werd ook voor dit mechanisme een ontwerpmethodologie ontwikkeld. Aangezien ik ondertussen een expert was (volgens de definitie van Niels Bohr: iemand die alle fouten heeft gemaakt, die überhaupt gemaakt kunnen worden in een heel nauw domein), ging dit een stuk sneller, mede door het feit dat Pieter (Spaepen) als projectmedewerker heel wat werk verzette.

Er werden plannen gemaakt om een prototype van de centrifugaalslinger te bouwen, en zo werd beslist een weefmachine à blanc aan te kopen en in het labo O&J Peters te installeren. Het ontwerp van het prototype, en het aan de praat krijgen van de proefopstelling was het werk van Pieter, en toen hij vertrok, had ik een werkende opstelling, een hoop technische tekeningen, maar nog geen prototype. Daarvoor zorgde Stephan Masselis, en na de vakantie van 2003 had ik, al druk schrijvend aan dit boek, dus ook een werkend prototype. Toen moest het ergste nog komen: het aan de praat krijgen van alle sensoren. Ik was in die tijd een veel (en op de duur waarschijnlijk ook minder graag) geziene en vaak vloekende gast in de werkplaats en de dienst elektronica. Met veel hulp van onze technische diensten had ik begin november 2003 echter ook een werkende meetopstelling. En dank zij Paul (Bielen) en Gregory (Pinte) werd er op 3 en 5 november 2003, telkens 's avonds, ook daadwerkelijk gemeten. Het resultaat hiervan is in Hoofdstuk 7 terecht gekomen: op het 'detail' van een onvoorziene torsieresonantie na, bleek mijn 'ballerina' goed te functioneren, en het dynamisch gedrag van de proefopstelling significant te verbeteren. Drie-Werf hoera!

Niet alles wat ik in de voorbije viereneenhalf jaar gedaan heb, heeft echter direct met het Picanol-project te maken. Een belangrijk aspect van mijn eindwerk was optimalisatie. Optimalisatie was, en is nog altijd, een groot hiaat in de opleiding tot werktuigkundig ingenieur. Toen in het begin van ons onderzoek bleek dat niet alleen ikzelf, maar ook Vincent, Tine (Lefebvre), Walter (Verdonck), Wim (Symens),... wel optimalisatietechnieken gebruikten, maar er ten gronde weinig van af wisten, kwam er op initiatief van Jan een ontmoeting met de mensen uit de groep rond Bart De Moor. Bart startte de vergadering met Rockafellar's uitspraak: 'Het grote onderscheid in optimalisatie is niet tussen lineair en niet-lineair, maar tussen convex en niet-convex.'

Van die vergadering is, bij mijn weten, achteraf nog weinig gekomen, maar ik was zo wel gefascineerd geraakt door het werk van Stephen Boyd en Lieven Vandenberghen i.v.m. toepassing van convexe optimalisatie op ingenieursproblemen. Ik begon bijgevolg nogal onstuimig te zoeken naar een convexe herformulering van het optimale identificatieprobleem uit mijn eindwerk. Een obstakel hierbij was dat er eigenlijk geen behoorlijk referentiemateriaal bestond,

behalve de beknopte cursusnota's van Boyd en Vandenberghe. Aangezien Jan, Lieven Vandenberghe echter nog kende uit een ver en verdrongen ESAT verleden, werd deze laatste binnen het kader van ICCoS uit Los Angeles gehaald, om in juni 2001 gedurende een week een graduate school te geven in Auditorium A van ESAT. Tot en met de derde les kon ik volgen, en dat vormt nog altijd de kern van het weinige dat ik weet over convexe optimalisatie.

Met de toen verworven kennis raakte ik echter nog altijd niet vooruit met het optimale identificatieprobleem. En ook het oplossen (met eindige differenties) van de eerder vermelde niet-lineaire differentiaalvergelijking bleek, ondanks dagenlange kopbrekens, niet convex te krijgen. Gelukkig was onder-tussen een ander, interessant kandidaat-probleem opgedoken: balanceren met tegengewichten. Ik had die techniek leren kennen tijdens mijn literatuurstudie over koppelcompensatie, aangezien beide vakgebieden nauw verwant zijn. Tijdens die literatuurstudie was ik op (Haines, 1981) gestoten, een nogal hermetische paper, die mij echter intrigeerde om twee redenen: (i) er stonden figuren in met elliptische, dus duidelijk convexe, contourlijnen en (ii) er werd gewezen op de superpositie-eigenschappen van een alternatieve massaparameterisatie. Uiteindelijk bleek het meer dan de moeite om dit werk uit te spitten: het vormt de basis van de convexe herformulering van het balanceringsprobleem (Hoofdstuk 8 en 9).

Als het in Hoofdstuk 9 ontwikkelde convexe framework verre van af is, en bijvoorbeeld nog niet toegepast op complexe mechanismen (ondanks het feit dat de methode dit soort mechanismen inherent aan kan), heeft dit veel te maken met het feit dat ik er enkel 'tussen de soep en de patatten', d.w.z. tussen het werk i.v.m. koppelcompensatie door, aan gewerkt heb. Ik geloof echter rotsvast in het potentieel van de methode, en dat van convexe optimalisatie in (bio)mechanische toepassingen in het algemeen. Dit is voor mij dan ook de grootste motivatie om hier als postdoc op verder te werken, er een nieuw industrieel project rond op te zetten en (hopelijk) in oktober 2004 naar UCLA te vertrekken, om mij verder in convexe optimalisatie in te werken onder de hoede van Lieven Vandenberghe.

## Dankjewel!

Tot dit werk hebben heel veel mensen een grote of kleine (puur of helemaal niet technische) bijdrage geleverd. Via deze weg wil ik hen daarvoor danken.

Eerst en vooral gaat mijn oprechte dank naar mijn promotoren, Prof. Joris De Schutter en Prof. Jan Swevers.

Jans wetenschappelijke bijdrage aan dit werk heeft vooral te maken met zijn doorgedreven kennis van periodische signalen (de meeste ideeën rond simulatie en controle van reciprocerende machines zijn een (on)rechtstreekse spin-off hiervan) en zijn rijke meetervaring. Ik moet Jan danken voor zijn hulp bij mijn eindwerk, voor het naar Leuven halen van Lieven Vandenbergh, en het feit dat hij steeds klaar stond om mee te helpen nadenken over zowel heel praktische (Matlab- en meet-), als meer theoretische (identificatie-, controle- en andere lineaire algebra) problemen. Zoals Vincent het in zijn dankwoord verwoordt, konden wij, als bureaugenoten, bij Jan (en Annemie) echter terecht voor veel meer dan alleen technische en doctoraatsgebonden problemen. Hierbij neem ik vooral een voorbeeld aan de manier waarop Jan werk en alle, veel belangrijker dingen daarbuiten, probeert te combineren: ikzelf heb wat dat betreft nog een lange weg af te leggen.

Als Joris zegt dat zijn voornaamste bijdrage tot mijn onderzoek het stellen van de 10 mei-deadline is, onderschat hij zichzelf. Hij heeft voor mij het perfecte kader geschapen, door het aantrekken van het Picanol-project, het aanmoedigen tot publiceren en bijwonen van conferenties, en het geven van vooral heel veel vrijheid, zonder hierbij in de val van onverschilligheid te trappen. Hij heeft mij meer dan eens verrast met een originele interpretatie van resultaten en de toepasbaarheid ervan. Het was bovendien fijn te ervaren dat ook hij in de toepasbaarheid van de convexe optimalisatietechnieken gelooft, toen ik aangemoedigd werd er een SBO en FWO projectaanvraag rond te formuleren. Ik heb van Joris ook een aantal 'attitudes' overgenomen: het gebruik van eenvoudige modellen, het intuïtief proberen te interpreteren van resultaten en de aandacht voor mondelinge en schriftelijke rapportering.

Waar het contact aanvankelijk eerder zakelijk was, hebben wij elkaar, vooral na Joris' sabbatjaar, ook als mens heel wat beter leren kennen, hetgeen ik sterk apprecieer. Ik moet Joris ook danken voor zijn begrip, toen bleek dat ik mijn aanvankelijke deadline van december 2003 niet ging halen, en het feit dat ik nu een jaar 'op zijn (GOA/99/04) kosten' onderzoek kan doen.

Ik moet mijn beide assessoren, Prof. Bart De Moor en Prof. Hendrik Van Brussel danken voor de niet-onaanzienlijke inspanning om dit lijvige werk op (te) korte tijd door te nemen, en er nuttige commentaar bij te geven. Het doet plezier te zien dat Prof. Van Brussel met externe bezoekers vaak mijn proefopstelling aandoet. Van hem heb ik ook het citaat waarmee dit werk begint. Zoals al aangehaald, heeft Bart De Moor mij de absolute essentie van optimalisatie bijgebracht. Ik hoop hem als 'wederdienst' ook iets over mechanica geleerd te hebben. Als hem nu gevraagd wordt: 'Hoe bouw je een compenserend mechanisme?' kan hij dus hopelijk: 'Zo!' als antwoord geven.

I would like to thank Prof. Jorge Angeles for accepting to be a member of my jury, for making the long trip across the Atlantic and for being a referee for the FWO-project concerning convex optimization. Prof. Lieven Vandenberghe dien ik om dezelfde redenen te bedanken. Zijn werk heeft een grote invloed gehad op het mijne, en ik ben dan ook vereerd met zijn aanwezigheid in deze jury. Ik wil hem ook danken voor zijn bereidwillige medewerking aan mijn FWO postdoc-aanvraag, en het eventueel daarmee verbonden verblijf aan UCLA. Prof. Berlamont wil ik danken om het voorzitterschap van deze jury op zich te nemen.

Prof. Wim Desmet dank ik voor het aanvaarden van het lidmaatschap van deze jury, en de belangstelling die hij, vanuit een totaal andere invalshoek dan de mijne, voor dit onderzoek heeft getoond. Als dat tot een aantal stevige discussies geleid heeft, is dat de kwaliteit van dit werk alleen maar ten goede gekomen. Ik wil hem ook bedanken voor het vooraf doornemen van Hoofdstuk 7, en de terechte commentaar die hij daarbij gemaakt heeft. Mocht het aan Wims retorische talenten liggen, was blauw-zwart elk jaar kampioen.

Ook ir. Kristof Roelstraete wil ik danken om tot deze jury te willen behoren. De samenwerking met Picanol N.V. is tot nu toe steeds in een sfeer van goede verstandhouding en wederzijds respect verlopen. Dit apprecieer ik in sterke mate, evenals het feit dat mijn publicaties rond het Picanol-project steeds zonder problemen vrijgegeven zijn.

Twee niet-proffen verdienen bijzondere dank bij het tot stand komen van dit werk. Eerst en vooral Vincent Lampaert. Gedurende een kleine acht jaar heb ik met hem, eerst als 'duopartner', en later als collega-assistent en bureaugenoot, op een heel fijne manier samengewerkt. Ik heb Vincents visie op de technische problemen waar ik mee worstelde, steeds sterk geapprecieerd, evenals de avondlijke Alma-bezoeken die meer en meer voorvielen naarmate zijn doctoraatsdeadline dichterbij kwam. Vincent: het is nu duidelijk experimenteel bewezen dat het net-(niet)-halen-van-de-deadline fenomeen mijn schuld is. Ik wens je een mooie toekomst met Ine, en veel plezier met de nokken en mechanismen die nu je pad lijken te kruisen.

Pieter Spaepen heeft een belangrijke (wetenschappelijke en praktische) bijdrage geleverd in het Picanol-project, door de opstelling operationeel te maken en het prototype van de centrifugaalslinger te ontwerpen. Ook toen Pieter al lang niet meer betaald werd op het Picanol-project, kwam hij regelmatig een kijkje nemen, en bijspringen indien nodig. Hij heeft mij ook op weg gezet naar de veelbelovende biomechanische toepassing van het in dit werk ontwikkelde convexe optimalisatieframework. Ik wil Pieter echter vooral ook danken voor het fijne persoonlijke contact, en wens hem alle succes in zijn eigen onderzoek.

Toen Jan uit de 01.027 verdween, werd zijn plaats ingenomen door Kris Smolders. Ik moet Kris danken voor het prettig samenwerken en 'samenhokken' tot nu toe.

René Boonen wil ik danken voor de vele keren dat zowel Pieter als ikzelf bij hem zijn langs geweest om een beroep te doen op zijn kritische oordeel.

Van hem heb ik geleerd dat je eerst de rigid-body dynamica van een machine in orde moet krijgen, daarna de eerste resonantie in rekening moet brengen, en dat je dan al op een behoorlijke machine uitkomt. De hier gepresenteerde experimentele resultaten zijn daar een mooie illustratie van. Ook Gregory Pinte moet ik van harte bedanken voor de hulp bij het (na de werkuren) uitvoeren, en achteraf interpreteren van de geluidsmetingen.

In het Picanol-project heb ik met veel uitstekende ingenieurs mogen samenwerken, en veel van hen geleerd. Ik wil er twee van hen in het bijzonder bedanken. Eerst en vooral Philip Cornelissen: hij heeft mij, een in 1999 onervaren, pas afgestudeerde Matlab-nerd, heel wat bijgebracht over machinedynamica in het algemeen, en weefmachines in het bijzonder. Zonder zijn input zou dit werk een heel andere aanschijn gekregen hebben. Ook Jan Hemelsoen, mijn oud-klasgenoot uit het Ieperse college, die Philip als projectverantwoordelijke opvolgde na diens vertrek naar China, wil ik van harte bedanken voor de bijzonder vlotte en aangename samenwerking, en de belangstelling die hij in het algemeen voor mijn werk getoond heeft. In het Picanol-project was ook het WTCM, in de persoon van Stephan Masselis, nauw betrokken. Ik wil hem van harte danken voor de fijne samenwerking, die resulteerde in het prototype van de centrifugaalslinger.

Pascal Degezelle en Raf Dequeker wil ik bedanken voor de kansen die ze mij geboden hebben om te proeven van de praktijk van een competitief ingenieursbureau. Pascal moet ik ook bedanken voor de vele zaken, niet in het minst i.v.m. nokken, die ik van hem geleerd heb tijdens mijn vierdejaars industrieel project en mijn eindwerk. Hij zal met plezier vaststellen dat ik voortdurend over 'energie' spreek.

Een aantal PMA-professoren verdienen ook hun plaats in dit dankwoord. Met Farid Al-Bender heb ik nauw samengewerkt voor mijn DETC2002-paper, en daarbij heel wat geleerd over differentiaalvergelijkingen en andere obscure zaken, die je alleen in, uit het Russisch vertaalde, vergeten wiskunde-monografieën van MIR-publishers vindt. Paul Vanherck heeft mij meermaals waardevolle suggesties gegeven, die ik in al mijn koppigheid even vaak ook weer naast mij neergelegd heb. Ik heb echter steeds, zowel in het labo, als in ALMA III, met plezier met hem gediscussieerd en gefilosofeerd. Herman 'advocaat van de duivel' Bruyninckx heeft mij vaak uit mijn kot gelokt, en gedwongen diep na te denken, met zijn uitdagende meningen over allerlei zaken. Hij was ook steeds een enthousiast 'meedenker' in de OSA's die ik gegeven heb, hetgeen onder andere geleid heeft tot een andere, en betere implementatie van de gemiddelde snelheidsberekening in Average Speed Control. Herman is, samen met Klaas 'smiley' Gadeyne ook mijn  $\text{\LaTeX}$ , euh, goeroe. Ik moet Klaas hierbij bedanken voor de hartelijke en adequate manier waarop hij mijn altijd dringende (want zich steeds net voor een deadline voordoende) problemen wist op te lossen. Ik zal nog heel wat wafels moeten kopen om mijn schuld af te lossen.

Naar aanleiding van de 'biomechanische suggestie' van Pieter, heb ik het plezier gehad te mogen samenwerken met dr. Ilse Jonckers. Ik heb met haar

een aantal lange, zeer open en steeds bijzonder vruchtbare discussies gevoerd om biomechanische en kinesiologicalische problemen te reduceren tot een niveau waarop ik ze kon vatten. Het was mij ook een raadsel hoe zij er, met drie kinderen en een echtgenoot, steeds in slaagde om haar bijdrages voor het SBO en andere FWO-projecten steeds mooi op tijd klaar te krijgen. Binnen dit kader wil ik ook (toekomstig ir.) Goele Pipeleers bedanken. Als jobstudente heeft zij heel wat nuttig werk verricht in verband met balanceren met tegengewichten, en als thesisstudente het potentieel van convexe optimalisatie voor musculo-skeletale analyse aangetoond. Ik hoop dat wij, als collega's dan, nog lange tijd op dezelfde aangename manier kunnen samenwerken.

Ik dank het Fonds voor Wetenschappelijk Onderzoek-Vlaanderen voor de vierjarige aspirant-beurs die dit onderzoek mogelijk heeft gemaakt, en de steeds vlotte afhandeling van de (tot een absoluut minimum beperkte) hiermee verbonden administratieve plichtplegingen.

De mensen van de technische en ondersteunende diensten verdienen allemaal meer dan één woord van dank, voor hun vlotte, en vaak bijzonder hartelijke 'service': Jan en Ronny, Eddy, Dirk en Viggo, Paul, Luc, Karin, Lieve, Ann en Carine, Luc, Raymond, Polleke, Jean-Pierre en Firmin: dankjewel! Sommigen van jullie hebben mij ook heel wat geleerd over niet-technische zaken: ook daarvoor hartelijke dank.

Werken op PMA biedt twee grote 'extralegale' voordelen. Een ongebreidelde vrijheid om je eigen weg te zoeken, maar ook, en vooral, een goed uitgebouwd sociaal leven. Toen ik begon, bestond dat ruwweg uit de wekelijkse voetbal, het PMA-weekend<sup>2</sup>, de jaarlijkse barbecue, het bezoek van de Sint/Kerstman en het Kerstdiner. Ik heb het aantal activiteiten zien 'exploderen': ondertussen wordt er ook gesquasht, is er een nieuwelingenreceptie<sup>3</sup>, een wekelijks Happy Hour, een jaarlijkse kroegentocht, een voetbal- en een wielpronostiek en ga zo maar door. Het Social Events Team (SET, ook gekend als bert'S Events Team) heeft mooi werk verricht. Ik was er graag bij, en heb er, net als tijdens de koffiepauzes en frequente Alma-bezoeken, veel aangename momenten beleefd en veel collega's op een 'andere' manier leren kennen. Dank daarvoor!

Ik moet mijn vrienden en mijn zussen Bieke, Saartje en Lore danken voor de vele keren dat ze, na mij weeral een hele tijd niet meer gezien te hebben, toch voor mij klaar stonden. Dat heb ik vooral mogen ondervinden toen het in de eerste helft van 2003 helemaal niet zo goed met mij ging. Dankjewel!

Tot slot, en heel in het bijzonder, wil ik mijn ouders danken voor de vele kansen die ze mij geboden hebben, en hun onvoorwaardelijke steun. Ik denk dat zij, meer dan wie ook, blij zijn dat het er *eindelijk* op zit.

bram, 3 mei 2004

---

<sup>2</sup>Mijn eerste PMA-weekend heb ik, net als al mijn jaargenoten, behalve Benny dan, gebrost—we hebben het geweten!

<sup>3</sup>Door ons ingevoerd ter compensatie van het brossen van ons eerste PMA-weekend.

# Abstract

This work aims at reducing vibration in reciprocating machinery. This is machinery in which the rotary movement of the driving actuator is mechanically converted, through mechanisms, into the oscillation motion of one or more machine parts. The adopted approach is to intervene at the level of vibration excitation, by reducing or eliminating the forces and torques (dynamic reactions) associated with the mechanical motion conversion. This approach is termed dynamic balancing and requires distinct implementations for cam-follower mechanisms and linkages.

In machines with cam-follower mechanisms, such as weaving machines, a cause of vibration is that the drive speed is not perfectly constant, as supposed during the cam design. Consequently, the cam-follower motions are distorted, resulting in increased follower vibration. A first solution is taking the drive speed fluctuation into account during the cam design. Such compensated cams offer a cheap and generic solution, but are very sensitive to the highly variable configurations of weaving machines. Therefore, a second solution is proposed, that is, forcing the drive speed to be constant through addition of an auxiliary input torque balancing mechanism (an 'intelligent flywheel'). Two such mechanisms are designed and optimized, one of which has actually been built. Experimental validation of this mechanism on an airjet weaving machine à blanc shows that it functions as predicted and reduces the vibration level of the up-and-down moving frames by half.

Secondary results from this part of the research are the development, for reciprocating machinery, of novel strategies for (i) simulating the forward dynamics and (ii) controlling the average drive speed of the driving motor.

For machines with linkages, the dynamic reactions are reduced by adding counterweights to the mechanism links. Determining the counterweight location and size constitutes a nonlinear optimization problem. This problem is reformulated as a convex optimization problem, resulting in a method which is fast, applies to planar mechanisms of arbitrary complexity and yields the global optimum. This constitutes a major breakthrough compared to current methods, which require long computational times, are restricted to four-bar mechanisms and suffer from local minima.



# Beknopte Samenvatting

Het doel van dit werk is het reduceren van trillingen in machines die heen-en-weer gaande bewegingen uitvoeren. In dit soort machines wordt de rotatieve beweging van de aandrijvende actuator mechanisch omgezet, door mechanismen, in de oscillerende beweging van één of meer machineonderdelen. De gevolgde aanpak is het aanpakken van de trillingen bij de bron: alle ontwikkelde methodes hebben tot doel de krachten en momenten te verminderen die verbonden zijn met de mechanische bewegingsconversie (de zogenaamde dynamische reacties). Deze aanpak wordt dynamisch balanceren genoemd en heeft verschillende implementaties voor nok-volgermechanismen en stangenmechanismen.

In het geval van machines met nok-volgermechanismen, zoals weefmachines, zijn trillingen o.a. het gevolg van het feit dat de aandrijfsnelheid niet perfect constant is, zoals verondersteld tijdens het nokontwerp. Hierdoor wordt de beweging van de nokvolgers vervormd, wat resulteert in grotere volgertrillingen. Een eerste mogelijke oplossing is de snelheidsfluctuatie in rekening te brengen tijdens het nokontwerp. Dergelijke gecompenseerde nokken vormen een nieuwe, generische en goedkope oplossing, maar zijn zeer gevoelig voor de sterk wisselende instellingen van weefmachines. Daarom wordt een tweede oplossing voorgesteld, nl. het opleggen van een constante aandrijfsnelheid door het toevoegen van een koppelcompenserend mechanisme. Dit kan beschouwd worden als een 'intelligent vliegwiel'. Twee dergelijke mechanismen worden ontworpen en geoptimaliseerd, waarvan er één daadwerkelijk geconstrueerd is. De experimentele validatie van dit mechanisme op een luchtstraal-weefmachine à blanc toont aan dat het mechanisme functioneert zoals voorspeld en het de trillingsniveaus van de op-en-neer bewegende kaders halveert.

Secundaire resultaten van dit deel van het onderzoek zijn het ontwikkelen, voor de beschouwde klasse van machines, van nieuwe strategieën voor (i) het simuleren van de voorwaartse dynamica en (ii) het controleren van de gemiddelde snelheid van de aandrijvende motor.

Voor machines met stangenmechanismen worden de dynamische reacties gereduceerd door het toevoegen van tegengewichten aan de stangen van het mechanisme. Het bepalen van de grootte en locatie van deze tegengewichten

is een niet-lineair optimalisatieprobleem. De bijdrage van dit werk is het herformuleren van dit probleem als een convex optimalisatieprobleem. De resulterende methode is snel en levert een globaal optimum op voor vlakke mechanismen van een willekeurige complexiteit. Dit betekent een belangrijke doorbraak t.o.v. de huidige methodes, die af te rekenen hebben met lange rekestijden, beperkt zijn tot vierstangenmechanismen en lokale optima opleveren.

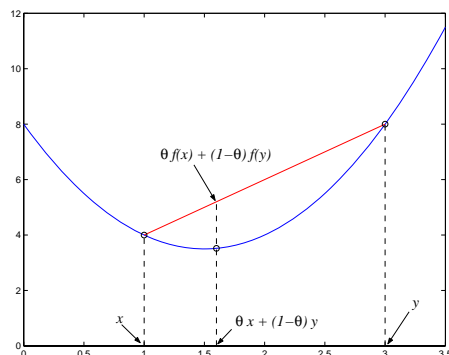
# Nederlandse Samenvatting

## Dynamisch balanceren van machines die heen-en-weer gaande bewegingen uitvoeren met toepassing op weefmachines

### 1 Inleiding

Dit werk legt de nadruk op optimalisatie van *mechanisch* ontwerp als een basisvereiste voor het bouwen van performante machines, meer bepaald, *reciprocerende* machines. Dit zijn machines waarin de rotatieve beweging van een aandrijfmotor mechanisch omgezet wordt, met behulp van een *mechanisme*, in de reciprocerende, d.w.z., heen-en-weer gaande beweging van één of meerdere machineonderdelen.

Het bouwen van performante machines vereist het beperken van trillingen en de daarmee verbonden problemen zoals vermoeiing, lawaai en slijtage. De hier gekozen aanpak bestaat erin de trillingen aan de bron aan te pakken, via het reduceren van de krachten en momenten die de trillingen veroorzaken. In een reciprocerende machine zijn deze krachten en momenten verbonden met de mechanische bewegingsomzetting, en worden ze kortweg *dynamische reacties* genoemd. Vandaar de algemene benaming voor de gekozen aanpak: *dynamisch* balanceren. De ontwikkelde methodes worden toegepast op een belangrijk industrieel voorbeeld van reciprocerende machines: *weefmachines*.



FIGUUR 1: Geometrische interpretatie van (1) voor een convexe functie.

## 2 Methodiek

### 2.1 Optimalisatieaanpak

Een wijdverspreid misverstand betreffende optimalisatie is dat enkel lineaire problemen (d.w.z., problemen met een doelfunctie en beperkingen die lineair zijn in de optimalisatieparameters) gemakkelijk op te lossen zijn. Dit is niet correct: er bestaat een klasse van niet-lineaire problemen, *convexe* problemen genaamd, die *ook* snel en met garantie op een globaal optimum kunnen opgelost worden.

Het rechttoe, rechtaan opstellen van een optimalisatieprobleem resulteert doorgaans in een niet-convex probleem. Om een convex probleem te verkrijgen, dient de ontwerper andere formuleringen en parameterisaties van het probleem uit te proberen, totdat zowel de doelfunctie, als de functies die de beperkingen beschrijven, convex zijn. Een functie is convex als zijn domein  $\mathbf{dom} f$  convex is en  $\forall x, y \in \mathbf{dom} f$  en  $\theta \in [0, 1]$ , geldt:

$$f(\theta x + (1 - \theta)y) \leq \theta f(x) + (1 - \theta)f(y). \quad (1)$$

Een domein is convex als elk lijnstuk tussen twee punten van het domein volledig binnen het domein ligt. Figuur 1 interpreteert de definitie van een convexe functie geometrisch: de koorde die  $(x, f(x))$  verbindt met  $(y, f(y))$  moet boven de grafiek van de functie  $f(x)$  liggen.

Dit werk toont aan dat het dynamisch balanceren van stangenmechanismen met behulp van tegengewichten een convex optimalisatieprobleem is. Dit betekent dat dit probleem, dat tot nu toe als moeilijk oplosbaar beschouwd werd, zeer snel, en met garantie op een globaal optimum opgelost kan worden.

## 2.2 Modelleringsaanpak

Het bepalen van de dynamische reacties van een mechanisme gebeurt op basis van een model. Twee belangrijke veronderstellingen beheersen het opstellen van modellen in dit werk: (i) het mechanisme bestaat uit een kinematische ketting van stijve lichamen en (ii) inertiaële krachten zijn dominant.

De eerste veronderstelling impliceert dat abstractie gemaakt wordt van elastische vervorming van de lichamen en dat de gewrichten van het mechanisme spelingsvrij zijn. De tweede veronderstelling houdt het verwaarlozen van gravitatie, veerkrachten en externe krachten in.

Deze veronderstellingen lijken op het eerste gezicht vrij strikt, maar zijn klassiek in de literatuur over hogesnelheidsmechanismen (Berkof, 1979). Bovendien volstaan ze om de aandrijfdynamica van een weefmachine te modelleren: in de aandrijftrein van een weefmachine komen geen veren voor, o.w.v. het gebruik van vormgesloten nokkenmechanismen. Zwaartekracht is verwaarloosbaar door de hoge toerentallen, terwijl externe krachten afwezig zijn.

## 2.3 Voorwaartse of Inverse Dynamische Aanpak

Het bepalen van de dynamische reacties van een mechanisme, op basis van het opgestelde model, gebeurt via een voorwaartse of een inverse dynamische analyse. Een inverse dynamische analyse impliceert dat aan alle vrijheidsgraden van het mechanisme een gekend traject opgelegd wordt door de aandrijvende actuator(en). Hierdoor is de kinematica van het mechanisme volledig bepaald, en volgen de dynamische reacties uit een eenvoudige matrixinversie.

Bij een voorwaartse dynamische analyse daarentegen, worden de actuatoren expliciet mee gemodelleerd, en volgen de resulterende trajecten van de verschillende vrijheidsgraden uit het integreren van een differentiaalvergelijking.

Bij het ontwerpen van mechanismen is telkens voor een inverse dynamische aanpak gekozen; voor het simuleren van het dynamisch gedrag van weefmachines telkens voor een voorwaartse dynamische aanpak. Voor het simuleren van de voorwaartse dynamica van reciprocerende machines in het algemeen, is een dubbele bijdrage geleverd (Sectie 3): (i) het ontwikkelen van een frequentiedomein-gebaseerde methode voor het bepalen van de voorwaartse dynamica en (ii) het uitbreiden van het (in de Duitse literatuur bekende) concept van eigenbeweging, geldig voor machines zonder energiedissipatie, tot machines met energieverlies. Binnen deze context is ook een nieuw en eenvoudig regelalgoritme ontwikkeld (Sectie 5.6) voor het aansturen van reciprocerende machines.

## 2.4 Aanpak voor Nokken- en Stangenmechanismen

**Nokkenmechanismen** Bij nokkenmechanismen, zoals die voorkomen in weefmachines, is een belangrijke trillingsoorzaak het fluctueren van de aandrijsnelheid van de nokkenas. Deze fluctuatie is een gevolg van de wisselende belasting op de as en leidt tot vervormde nokvolgerbewegingen, aangezien nokontwerp klassiek aanneemt dat de aandrijsnelheid constant is. Een symptoom van de bewegingsvervorming is het voorkomen van significante, ongewenste hogere harmonischen in het versnellingspectrum van de volger. De overeenkomstige inertiaële krachten kunnen resonanties van de nokvolger exciteren, zoals experimenteel waargenomen in weefmachines.

Om de nokvolgerbewegingen nauwkeuriger te realiseren, en bijgevolg de ongewenste hogere harmonischen te reduceren, worden twee methodes voorgesteld. Een eerste methode bestaat erin de fluctuatie van de aandrijsnelheid a-priori te berekenen en die in rekening te brengen in het nokontwerp. Dit geeft aanleiding tot zgn. *inertieel gecompenseerde nokken* (Sectie 4). Deze oplossing is goedkoop en efficiënt, maar zeer gevoelig voor de sterk wisselende instellingen van weefmachines.

Daarom wordt een tweede oplossing voorgesteld, nl. het gebruik van klassieke nokken, in combinatie met het onderdrukken van de fluctuatie van de aandrijsnelheid. Dit kan door het gebruik van een groot vliegwiel of een motorregelaar met hoge bandbreedte. Deze oplossingen leiden echter tot een verslechterd aanloopgedrag, respectievelijk een hoger energieverbruik. Het toevoegen van een koppelcompenserend mechanisme heeft deze nadelen in veel beperktere mate (Sectie 5). Een koppelcompenserend mechanisme is een hulpmechanisme dat op de aandrijf-as een koppel uitoefent, dat tegengesteld is aan het koppel van het oorspronkelijke (nokken)mechanisme. Bijgevolg is het netto koppel op de aandrijf-as theoretisch nul, hetgeen resulteert in een perfect constante aandrijsnelheid. In dit werk zijn twee koppelcompenserende mechanismen ontworpen en geoptimaliseerd, waarvan er één ook daadwerkelijk gebouwd en experimenteel gevalideerd is. Dit mechanisme blijkt correct te werken, en het trillingsniveau van de kaders van een weefmachine te halveren.

**Stangenmechanismen** Bij stangenmechanismen vormen de reactiekrachten en -momenten, door het mechanisme uitgeoefend op het ondersteunende frame, een belangrijke oorzaak van frametrillingen. Een welbekende manier om deze problemen aan te pakken, is het toevoegen van tegengewichten aan de stangen van het mechanisme. Het bepalen van de locatie en de grootte van de tegengewichten is een optimalisatieprobleem, dat tot nu toe als niet-lineair en dus moeilijk op te lossen beschouwd werd. Sectie 6 toont aan dat dit niet-lineaire optimalisatieprobleem herformuleerbaar is als een convex probleem. De ontwikkelde methodiek is algemeen, toepasbaar voor vlakke mechanismen van een willekeurige complexiteit, en uitbreidbaar naar ruimtelijke mechanismen.

### 3 Eigenbeweging van Reciprocerende Machines

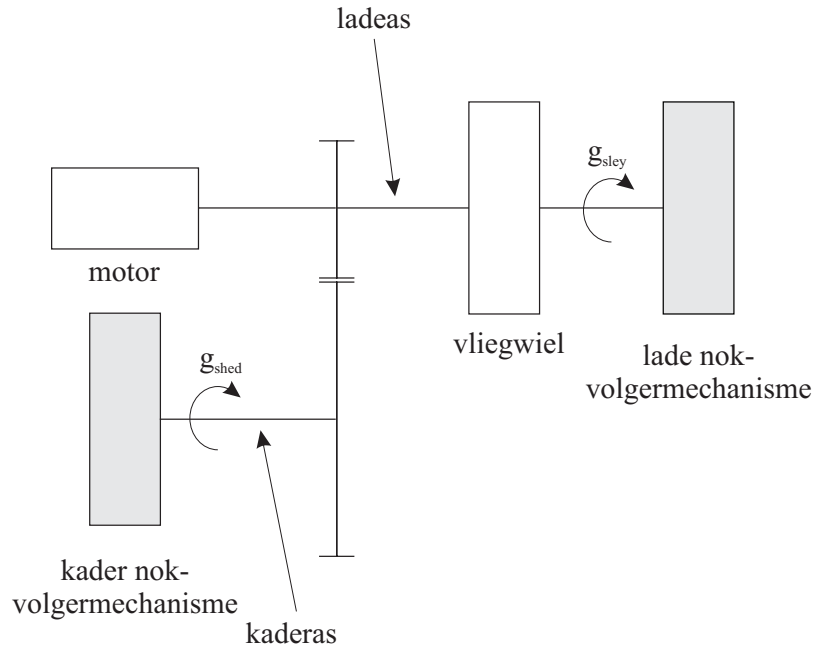
*Eigenbeweging* is een belangrijk concept in dit werk voor het simuleren van de voorwaartse dynamica van reciprocerende machines, en is welbekend in de Duitse literatuur. Het wordt hier formeel gedefinieerd als *de regimebeweging van een reciprocerende machine, waarin geen energiedissipatie, noch externe arbeidskrachten aanwezig zijn en waarin de aandrijfmotor een nul-koppel uitoefent*. Voor machines waarin wel energiedissipatie aanwezig is, wordt in dit werk het concept *gedempte eigenbeweging* gedefinieerd, en wel als *de regimebeweging van een machine met energiedissipatie, waarbij de motor een constant koppel  $M_{\text{mot}}$  [N-m] uitoefent, zodanig dat een bepaalde gewenste gemiddelde aandrijfsnelheid  $\Omega$  [rad/s] gerealiseerd wordt*.

Eigenbeweging en gedempte eigenbeweging zijn relevant voor het karakteriseren van het regimegedrag van machines, waarvan de motor een regelaar met lage bandbreedte heeft. Hoe lager de bandbreedte, hoe kleiner de fluctuatie van het motorkoppel rond zijn gemiddelde waarde  $M_{\text{mot}}$ , en hoe meer het regimegedrag bijgevolg de gedempte eigenbeweging benadert. Als bovendien de energiedissipatie klein is, is het verschil tussen de eigenbeweging en de gedempte eigenbeweging klein. Eigenbeweging vormt dan een goede benadering voor het regimegedrag van de machine.

Picanol weefmachines zijn voorzien van zo'n lage-bandbreedte regelaar, en dit om het energieverbruik van de motor te reduceren. Bijgevolg levert (gedempte) eigenbeweging een goede benadering van het regimegedrag. Dit heeft als voordeel dat vrijwel geen informatie over de aandrijvende motor of zijn regelsysteem vereist is: enkel de motorinertie moet bekend zijn.

Het berekenen van de (gedempte) eigenbeweging wordt beheerst door een differentiaalvergelijking, die klassiek via tijdsintegratie opgelost wordt. Dit werk stelt een nieuwe, frequentiedomein-gebaseerde techniek voor. Deze techniek is gebaseerd op (i) het herformuleren van de differentiaalvergelijking als een randwaardeprobleem; (ii) het parameteriseren van de oplossing van dit probleem als een eindige Fourierreeks en (iii) het bepalen van de onbekende coëfficiënten van de Fourierreeks via een niet-lineair kleinste-kwadratenprobleem. Deze techniek is nieuw, en algemeen toepasbaar voor het berekenen van het regimegedrag van een reciprocerende machine, ook indien de motor geen constant koppel uitoefent, of het machinemodel niet enkel uit stijve lichamen bestaat. Dergelijke uitbreidingen verhogen echter de orde van de differentiaalvergelijking, en bijgevolg ook de vereiste rekentijd.

Toepassing op een vereenvoudigd model van een luchtstraalweefmachine illustreert de ontwikkelde techniek. Dit model, getoond in Fig.2, bestaat uit de aandrijvende motor, twee gekoppelde nok-volgermechanismen (het *laden* en het *kader*mechanisme), een vliegwiel en een 1:2 tandwielreductie. Dit is het meest eenvoudige model van een weefmachine dat toch toelaat de essentie van de aandrijfdynamica te vatten. Het regime van dit model is periodisch, met periode  $T$  [s], gelijk aan  $2\pi/\Omega$ , waarbij  $\Omega$  [rad/s] de gemiddelde snelheid van de kaderas voorstelt.



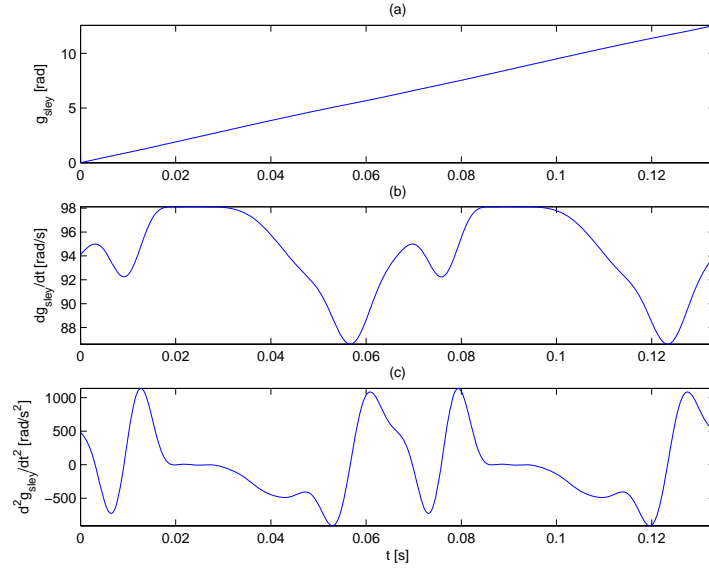
FIGUUR 2: Vereenvoudigd model van een luchtstraalweefmachine.

Figuur 3(b) toont het resulterende traject, tijdens eigenbeweging, van de aandrijfsnelheid van de ladeas voor  $\Omega = 450 \text{ rpm}^{(4)}$  en illustreert de substantiële snelheidsfluctuatie (12.2%). Dit is een gevolg van het feit dat het vliegwiel in deze machine klein is, om te garanderen dat de machine voldoende snel aanloopt.

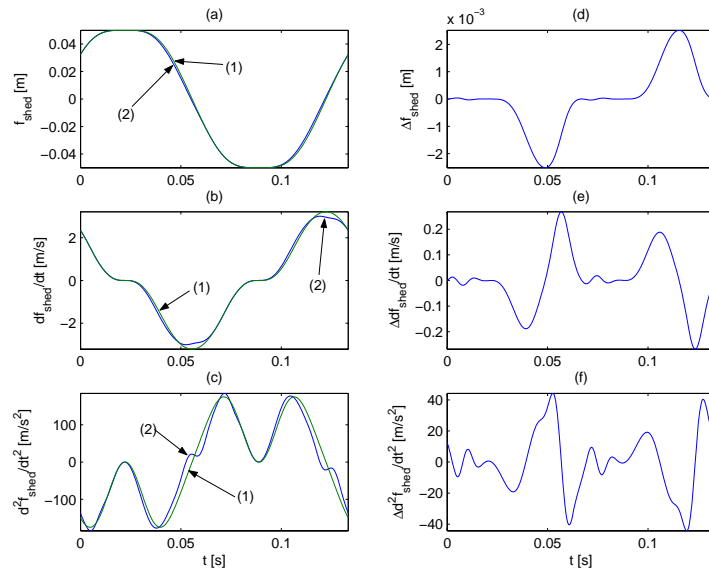
De snelheidsfluctuatie resulteert in vervormde volgerbewegingen. Figuur 4 illustreert dit voor het geval van de kadervolger, aangezien het vooral voor de kadervolger is dat zich dynamische problemen voordoen. Als gevolg van de vervorming verschijnen significante, ongewenste<sup>5</sup>, hogere harmonischen  $k = \{7, 9, \dots\}$  in het versnellingspectrum van de kadervolger, tijdens eigenbeweging (Fig.5). Deze hogere harmonischen stoten resonanties aan en veroorzaken op die manier dynamische problemen.

<sup>4</sup>Dit komt overeen met  $47.2 \text{ rad/s}$ , zodat de gemiddelde snelheid van de ladeas  $2 \times 47.2 = 94.4 \text{ rad/s}$  is.

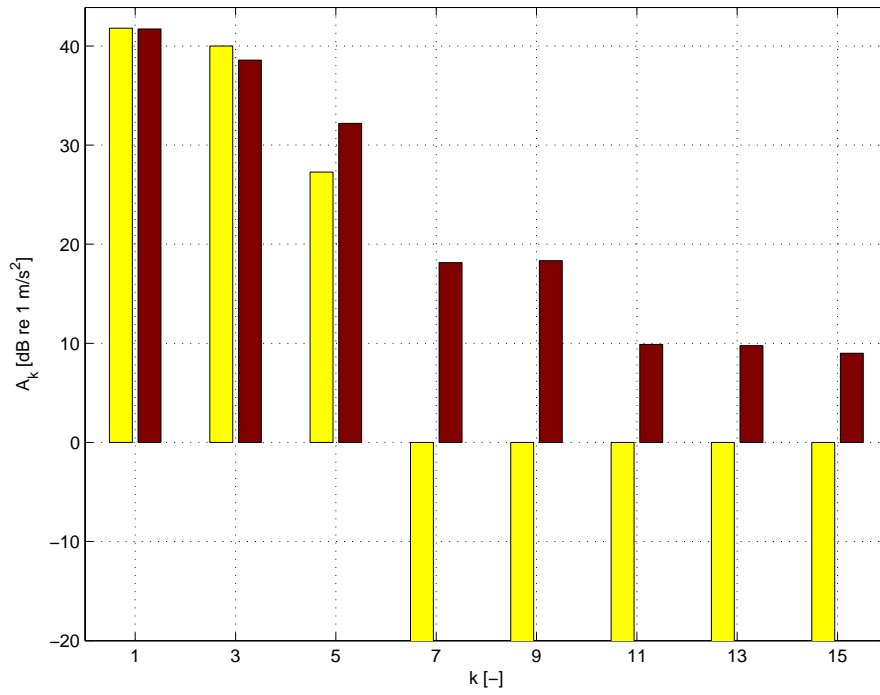
<sup>5</sup>Gewenst zijn enkel de harmonischen  $k = \{1, 3, 5\}$ .



FIGUUR 3: Eigenbeweging van een luchtstraalweefmachine: één machineperiode van de rotatiehoek (a), -snelheid (b) en -versnelling (c) van de ladeas.



FIGUUR 4: Eigenbeweging van een luchtstraalweefmachine, resultaten voor de kadervolger: één machineperiode van de gewenste (1) en werkelijk generaliseerde (2) positie (a), snelheid (b) en versnelling (c), en het verschil tussen beide (d – e – f).



FIGUUR 5: Eigenbeweging van een luchtstraalweefmachine, resultaten voor de kadervolger: spectrum [dB re 1 m/s<sup>2</sup>] van de gewenste (linker balk) en werkelijk gerealiseerde (rechter balk) versnelling. Waarden van -20 [dB re 1 m/s<sup>2</sup>] geven  $A_k = 0$  waarden aan. Enkel oneven harmonischen worden getoond: de even harmonischen zijn te klein om relevant te zijn.

## 4 Inertieel Gecompenseerde Nokken

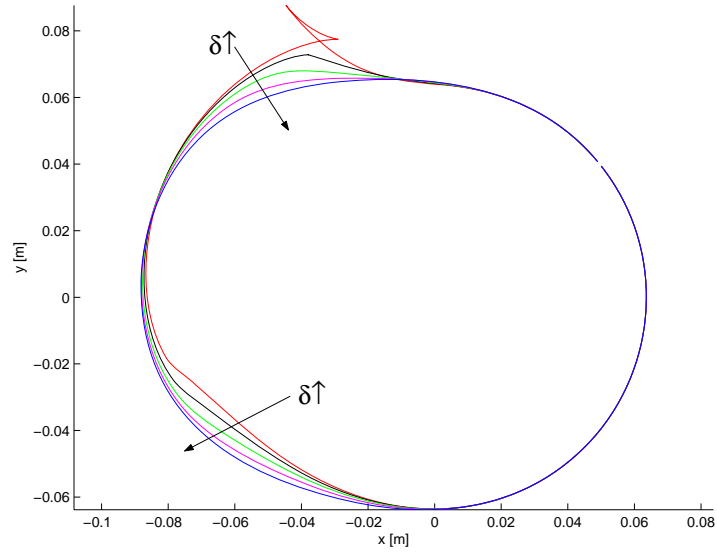
Zoals besproken in Sectie 2.4, is een eerste mogelijke oplossing voor het verminderen, in nok-volgersystemen, van de bewegingsvervorming t.g.v. snelheidsfluctuaties, het aanpassen van het nokontwerp aan de snelheidsfluctuatie. De resulterende *inertieel gecompenseerde nokken* vormen een subklasse van *dynamisch gecompenseerde nokken*. Dit is een algemene naam voor nokken die dynamica van het nok-volgermechanisme compenseren in hun ontwerp. Klassiek is dit de dynamica van de volger. Hier wordt echter de dynamica van het aandrijfsysteem gecompenseerd.

**Ontwerpprocedure** De ontwerpprocedure is gebaseerd op de veronderstelling dat de machine wrijvingsloos en puur inertiael is, vandaar de naam *inertieel gecompenseerde nokken*. Het bepalen van de hefwet van de gecompenseerde nokken, is gebaseerd op een dimensieloze, algebraïsche vergelijking, afhankelijk van één ontwerpparameter  $\delta$ . Dit is de verhouding tussen de minimale en maximale nokkenassnelheid tijdens eigenbeweging ( $0 \leq \delta \leq 1$ ). De gekozen  $\delta$ -waarde is een compromis tussen het verkrijgen van een kleine vliegwielinertie en het verkrijgen van voldoende zacht verlopen nokprofielen.

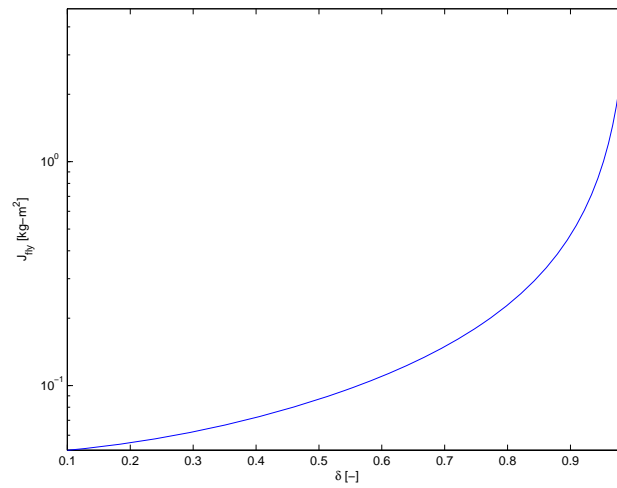
Figuur 6 en 7 illustreren dit voor een academisch voorbeeld, bestaande uit twee nok-volgermechanismen, gemonteerd op een gemeenschappelijke aandrijfas. Voor het eerste nok-volgermechanisme toont Fig.6 het nokprofiel i.f.v.  $\delta$ : voor kleine waarden van  $\delta$  vertoont het nokprofiel ondersnijding en is het dus waardeloos, terwijl het voor grotere waarden voldoende zacht is om industrieel toepasbaar te zijn. Grotere waarden van  $\delta$  resulteren echter in grotere vliegwielinerties, zoals geïllustreerd in Fig.7.

**Robuustheid t.o.v. Energiedissipatie** De ontwerpprocedure veronderstelt dat de machine wrijvingsloos is, en volgens haar eigenbeweging beweegt. In de aanwezigheid van energiedissipatie (en dus een motor), neemt de machine een regimegedrag aan dat verschillend is van de eigenbeweging. Het correct functioneren van de gecompenseerde nokken vereist dat de resulterende regimebeweging zo goed mogelijk op de eigenbeweging lijkt.

Dit is zo als aan twee voorwaarden voldaan is: (i) de aandrijvende motor moet uitgerust zijn met een lage-bandbreedte regelaar, zodat de machine beweegt volgens haar gedempte eigenbeweging; (ii) de wrijvingsverliezen mogen niet te groot zijn, zodat de gedempte eigenbeweging niet te veel afwijkt van de eigenbeweging. Simulatie van de gedempte eigenbeweging van het bovenvermelde academische voorbeeld, toont aan dat het opleggen van deze voorwaarden volstaat voor een goede werking (d.w.z., nauwkeurig gerealiseerde volgerbewegingen) van de gecompenseerde nokken. Ter illustratie: indien het wrijvingsverlies 5% of 20% bedraagt, zijn de ongewenste harmonischen van de versnelling van de eerste nokvolger tenminste een factor 18, respectievelijk 4.5 kleiner dan wanneer klassiek ontworpen nokken gemonteerd zijn.



FIGUUR 6: Academisch voorbeeld inertiael gecompenseerde nokken: nokprofiel van eerste nok-volgermechanisme i.f.v.  $\delta = \{0.1, 0.3, 0.5, 0.7, 0.9\}$ . De pijlen geven toenemende  $\delta$ -waarden aan. Voor  $\delta = 0.1$ , vertoont het bovendeel van de nok ondersnijding.



FIGUUR 7: Academisch voorbeeld inertiael gecompenseerde nokken: vliegwielinertie i.f.v.  $\delta$ .

**Toepassing op Luchtstraalweefmachines** De bovenvermelde ontwerp-procedure neemt aan dat alle nokken in een machine inertiael gecompenseerd zijn. Indien één of meerdere nokken niet herontworpen worden, dient ze aangepast te worden. Deze laatste situatie doet zich voor in een luchtstraalweefmachine, waarin het enkel zinvol is de kadernokken te herontwerpen. De aanpassingen zorgen ervoor dat de hefzet van de gecompenseerde nokken niet langer op een algebraïsche, maar op een differentiaalvergelijking gebaseerd is.

Simulaties van de gedempte eigenbeweging van een luchtstraalweefmachine tonen aan dat ook in dit geval wrijving de werking van de nokken niet compromitteert: indien het wrijvingsverlies 5% of 20% bedraagt, zijn de ongewenste harmonischen van de kaderversnelling tenminste een factor 18, respectievelijk 6 kleiner dan wanneer klassiek ontworpen kadernokken gemonteerd zijn.

Een bijzonder aspect van weefmachines is de variabiliteit (i.f.v. het te maken weefsel) van de synchronisatie tussen het lade- en het kadermechanisme. De correcte werking van inertiael gecompenseerde nokken is hier jammer genoeg zeer gevoelig voor, en gaat volledig verloren als de synchronisatiewijzigingen groter dan vijf machinegraden zijn. Bijgevolg heeft het geen zin dergelijke nokken te gebruiken in een industriële weefmachine, en is een andere oplossing vereist voor de vervorming van de kaderbeweging: koppelcompensatie.

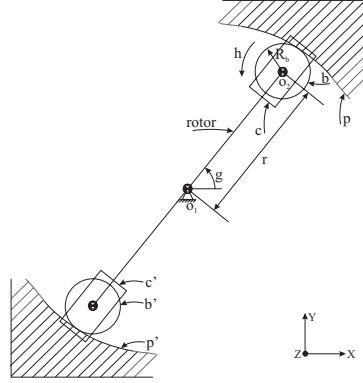
## 5 Koppelcompensatie

In dit werk zijn twee koppelcompenserende mechanismen ontworpen en geoptimaliseerd. Beide zijn *intelligente vliegwielen* waarvan de gewenste inertiaeverandering opgelegd wordt door interne nokprofielen. Figuur 8 en 9 tonen beide mechanismen.

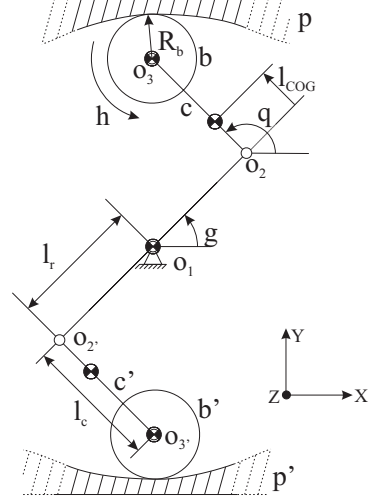
Het *geïnverteerde nokkenmechanisme* (Inverted Cam Mechanism, ICM) van Fig.8 bestaat uit een rond  $\hat{o}_1$  draaiende rotor, waarop twee glijstukken  $c$  en  $c'$  glijden. Elk van die glijstukken is via een scharniergewricht verbonden met een looprol  $b$  of  $b'$  die over een inwendig nokprofiel loopt. In de *nokgebaseerde centrifugaalslinger* (Cam-Based Centrifugal Pendulum, CBCP) van Fig.9 vervangen een scharniergewricht in het punt  $\hat{o}_2$  en een koppelstang  $c$  het glijstuk.

In beide mechanismen garandeert de centrifugaalkracht het contact tussen de looprollen en het inwendig nokprofiel. De symmetrie t.o.v.  $\hat{o}_1$  maakt deze mechanismen krachtgebalanceerd. Er worden echter wel buigmomenten (rond de  $X$  en  $Y$ -as) uitgeoefend op de aandrijvende as en het ondersteunende frame, evenals een schudmoment (rond de  $Z$ -as) op het ondersteunende frame.

De kinematische schema's van deze beide mechanismen zijn bekend in de literatuur. Voor zover onze kennis strekt, bestaan er in de open literatuur echter geen ontwerpmethodologieën voor (CBCP), of zijn ze verkeerd (ICM).



FIGUUR 8: Geïnverteerd nokken-



FIGUUR 9: Nokgebaseerde centrifugaalslinger: kinematisch schema.

## 5.1 Ontwerp van de Nokprofielen

De vorm van de nokken is zo dat het mechanisme, bij constante aandrijsnelheid  $2\pi/T$  [rad/s] van de rotor, een aandrijskoppel vraagt dat tegengesteld is aan het aandrijskoppel  $M_o(t)$  van een bepaald, te compenseren mechanisme. Onderstaande vergelijkingen drukken deze voorwaarde uit:

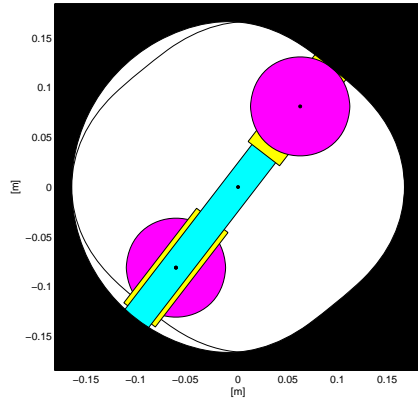
$$M_o(t) + \frac{1}{2\pi} \cdot m^* \cdot \left( \dot{r} \cdot \ddot{r} + \left( \frac{2\pi}{T} \right)^2 \cdot r \cdot \dot{r} \right) = 0; \text{ (ICM)} \quad (2)$$

$$M_o(t) + \frac{1}{2\pi} \cdot J_2^* \cdot \dot{q} \cdot \ddot{q} + J_3^* \cdot s = 0. \text{ (CBCP)} \quad (3)$$

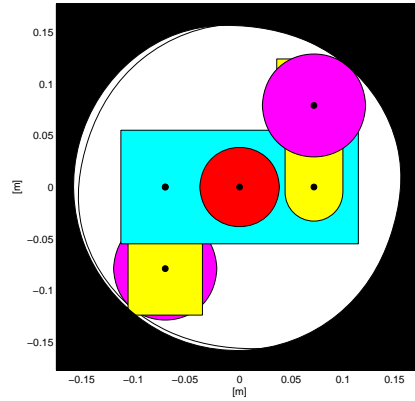
Aangezien

$$s(t) = \ddot{q} \cdot \cos \left( \frac{2\pi}{T} \cdot t - q \right) - \dot{q} \cdot \sin \left( \frac{2\pi}{T} \cdot t - q \right) \cdot \left( \frac{2\pi}{T} - \dot{q} \right),$$

en  $J_i^*$  en  $m^*$  veralgemeende massa's en inerties voorstellen, zijn (2) en (3) tweede-orde, niet-lineaire differentiaalvergelijkingen in  $r(t)$  en  $q(t)$  respectievelijk. Hierbij is  $r(t)$  de afstand tussen  $\hat{o}_1$  en  $\hat{o}_2$  (Fig.8) en  $q(t)$  de hoek tussen de koppelstang  $c$  en de positieve  $X$ -as (Fig.9). Beide differentiaalvergelijkingen worden opgelost door de oplossing te parameteriseren als een eindige Fourierreeks en de onbekende Fouriercoëfficiënten te bepalen met niet-lineaire kleinste-kwadratentechnieken.



FIGUUR 10: Geoptimaliseerde ICM-configuratie.



FIGUUR 11: Geoptimaliseerde CBCP-configuratie.

## 5.2 Optimalisatie van Kinematische en Dynamische Parameters

Voor beide mechanismen is een procedure ontwikkeld voor het optimaliseren van de dynamische (d.w.z., massa-) en kinematische parameters. De doel-functie van deze optimalisatie is het minimaliseren van de equivalente inertie  $J_{eq}$  [kg-m<sup>2</sup>] van het gecombineerde systeem, bestaande uit het oorspronkelijke en het koppelcompenserende mechanisme. De equivalente inertie drukt de constante kinetische energie van het gecombineerde systeem uit als de inertie [kg-m<sup>2</sup>] van een vliegwiel dat draait met snelheid  $\Omega = 2\pi/T$ . Hoe kleiner deze inertie, hoe beter het aanloopgedrag.

De beperkingen van het optimalisatieprobleem zijn, o.a., minimale contactkracht tussen de looprollen en de nokprofielen, beperkte Hertziaanse spanningen in de nokprofielen, minimum levensduur van de looprollen en het vermijden van botsingen tussen de bewegende onderdelen. Om deze beperkingen te kunnen implementeren wordt de vorm van de verschillende onderdelen geparameteriseerd, waarbij de vormparameters rechtstreeks als optimalisatievariabelen gebruikt worden.

Om dit niet-convexe optimalisatieprobleem beheersbaar te houden, worden de te optimaliseren vormparameters opgedeeld in een beperkt aantal te optimaliseren hoofdvariabelen (twee voor het ICM, vier voor de CBCP), en nevenvariabelen met een vaste, goed gekozen waarde. In het geval van het ICM wordt het optimalisatieprobleem opgelost door exhaustief alle combinaties van de twee optimalisatievariabelen door te rekenen. In het geval van de CBCP wordt een SQP algoritme gebruikt. In beide gevallen wordt een compact mechanisme verkregen. Figuur 10 en 11 tonen het resultaat, wanneer het lademechanisme van een luchtstraalweefmachine gecompenseerd wordt.

### 5.3 Praktische Implementatie

Qua praktische haalbaarheid is de nokgebaseerde centrifugaalslinger in het voordeel t.o.v. het geïnverteerde nokkenmechanisme. Dit is een gevolg van het feit dat het glijstuk  $c$  met grote snelheden en versnellingen een beweging met beperkte slag uitvoert. Standaard rolgeleidingen kunnen dit niet aan, terwijl glijgeleidingen technologische onzekerheid introduceren i.v.m. hun smering en levensduur. Daarom is de centrifugaalslinger gebouwd, aangezien die enkel scharniergewrichten bevat.

Figuur 12 toont de CBCP voor en na montage. Figuur 13 toont de opstelling waaraan het mechanisme aangebouwd is. Dit is een luchtstraalweefmachine *à blanc*, d.w.z., een luchtstraalweefmachine gereduceerd tot zijn essentiële onderdelen: het lade- en kadermechanisme, de motor en het ondersteunende frame. Alle onderdelen die te maken hebben met het afwikkelen van het gevormde weefsel, de luchtinsertie, . . . zijn verwijderd. Het testen van een machine *à blanc* is een typische stap in het karakteriseren van het dynamisch gedrag van een weefmachine, alvorens over te gaan tot het testen van een volledige machine.

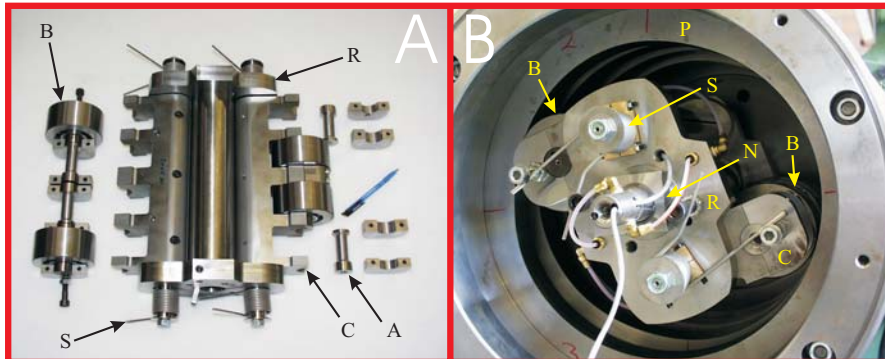
De CBCP compenseert enkel het lademechanisme, en niet het kadermechanisme. Indien dit wel zo zou zijn, zou iedere significant verschillende synchronisatie tussen de lade en de kaders vervanging van de interne nokken vereisen. Dit is praktisch niet haalbaar. Bovendien is het zo dat vooral de kaderbeweging last heeft van de invloed van de lade, en niet omgekeerd.

### 5.4 Experimentele Resultaten: CBCP-Koppel

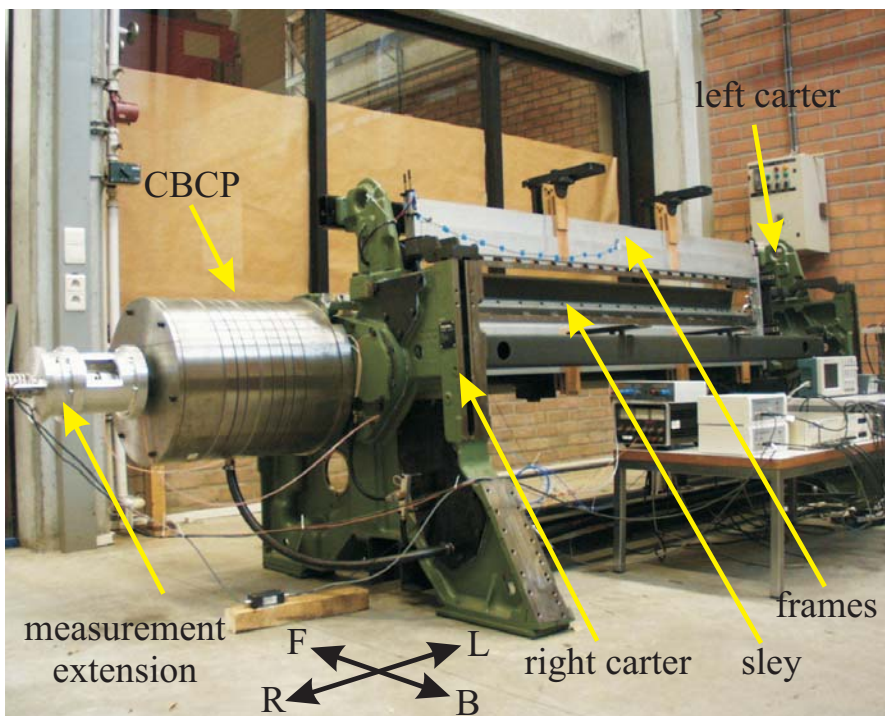
Een eerste doel van de uitgevoerde metingen is nagaan of het ontworpen mechanisme correct functioneert, door het CBCP-koppel m.b.v. rekstrookjes op te meten voor een reeks toerentallen  $\Omega$ . Toerentallen worden hier uitgedrukt t.o.v. de kaderas.  $\Omega = 400$  rpm betekent dus dat de ladeas aan 800 toeren per minuut draait. Figuur 14 toont één periode van het gemeten en het theoretische CBCP-koppel voor  $\Omega = \{200, 250, 300, 413.5\}$  rpm.

Voor  $\Omega = \{200, 250\}$  rpm is de overeenkomst tussen de experimentele en theoretische resultaten goed, behalve in de zone van theoretisch nul-koppel. Deze afwijking is het gevolg van een combinatie van de fluctuatie van de aandrijfsnelheid, wrijving en onvolkomenheden in de constructie.

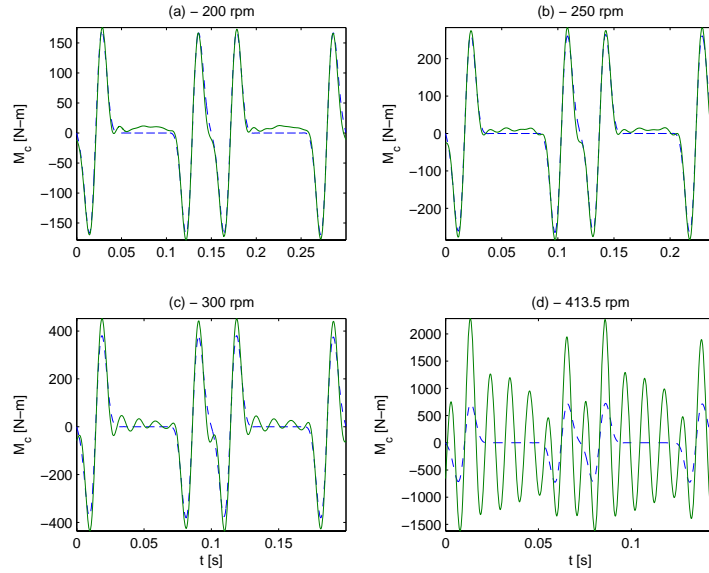
Bij 413.5 rpm domineert een resonantiefenomeen de respons (piekamplitude van 2280 N-m!). Deze resonantie is een gevolg van de beperkte torsiestijfheid van de ladeas. Simulatieresultaten van een torsiemodel (verkregen door uitbreiding van het rigid-body model van Fig.2 met een torsievrijheidsgraad die de stijfheid van de ladeas modelleert) bevestigen deze hypothese. Analyse van het spectrum van het gemeten CBCP-koppel, toont aan dat de resonantie rond 96-97 Hz ligt en geëxciteerd wordt door de veertiende (koppel)harmonische van  $413.5/60=6.9$  Hz voor  $\Omega = 413.5$  rpm.



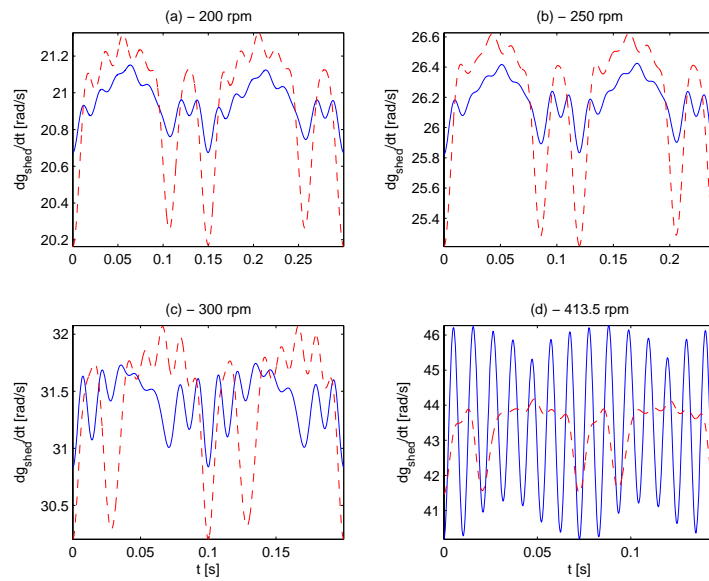
FIGUUR 12: CBCP-constructie: (a) overzicht van alle onderdelen; (b) CBCP na montage en toevoegen van de interne nokprofielen. (A) extra massa; (B) looprol; (C) koppelstang; (N) moer; (P) inwendige nok; (R) rotor; (S) veer.



FIGUUR 13: Achteraanzicht van de opstelling. De stalen ton aan de rechterzijde bevat de CBCP. Links (L), rechts (R), voor (F) en achter (B) worden gedefinieerd door de pijlen.



FIGUUR 14: Eén periode van het gemeten CBCP-koppel  $M_{c,exp}$  (volle lijn) en het theoretische CBCP-koppel  $M_{c,the}$  (streeplijn) voor  $\Omega = \{200, 250, 300, 413.5\}$  rpm.



FIGUUR 15: Eén periode van de kaderasnelheid  $\dot{g}_{shed}$  [rad/s] in de CBCP-configuratie (volle lijn) en de FLY-configuratie (streeplijn) voor  $\Omega = \{200, 250, 300, 413.5\}$  rpm.

## 5.5 Experimentele Resultaten: Machinegedrag

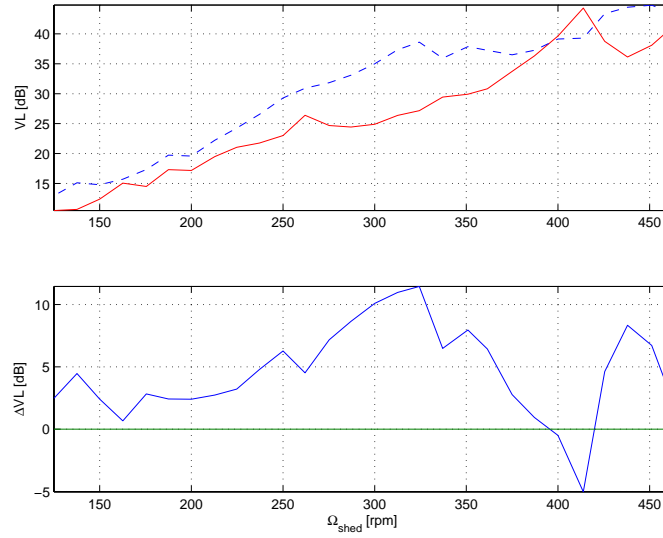
Een tweede doel van de uitgevoerde metingen is het nagaan van de invloed van de CBCP op het dynamisch gedrag van de luchtstraalweefmachine. Daartoe wordt, voor de opgemeten toerentallen, het dynamisch gedrag van twee verschillende configuraties van de luchtstraalweefmachine opgemeten: (i) in de CBCP-configuratie is de CBCP actief; (ii) in de FLY-configuratie zijn de bewegende onderdelen van de CBCP opgespannen met een opklemgereedschap, en gedraagt de CBCP zich als een vliegwiel. Het vergelijken van de CBCP-configuratie en de FLY-configuratie is de meest eerlijke manier om het effect van de CBCP in te schatten, aangezien massa-effecten (door de toevoeging aan het frame van de stalen ton (zie Fig.13), en de toevoeging aan de ladeas van de rotatieve CBCP-inertie) geen van beide configuraties bevoordeelt t.o.v. de andere.

Figuur 15 toont één periode van de kaderas-snelheid  $\dot{j}_{\text{shed}}$  [rad/s] in de CBCP-configuratie en de FLY-configuratie voor  $\Omega = \{200, 250, 300, 413.5\}$  rpm. Voor  $\Omega = 413.5$  rpm, is de torsieresonantie van de CBCP-configuratie terug duidelijk aanwezig onder de vorm van een hevig fluctuerende aandrijfsnelheid. Voor  $\Omega = \{200, 250, 300\}$  rpm anderzijds, is de snelheidsfluctuatie in de CBCP-configuratie een factor 2.5 kleiner dan in de FLY-configuratie. Het valt op dat de scherpe, neerwaartse pieken, aanwezig in de FLY-configuratie, veel kleiner zijn in de CBCP-configuratie. Dit is logisch, aangezien die pieken verbonden zijn met de ladebeweging, en deze laatste door de CBCP gecompenseerd wordt.

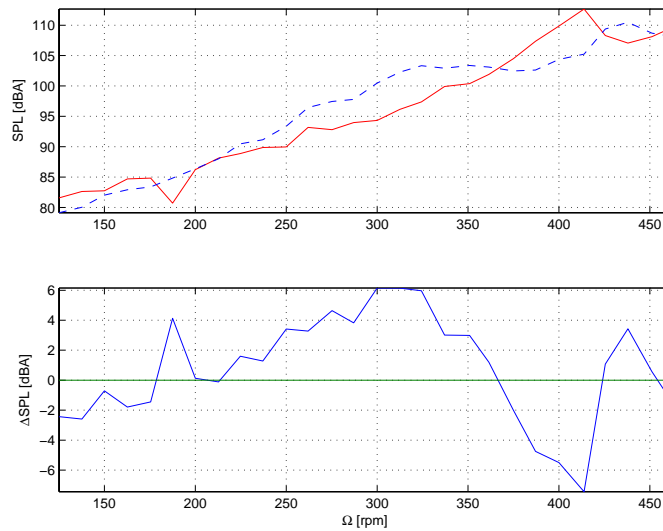
Het verminderen van de snelheidsfluctuatie zorgt ervoor dat de vervorming van de kaderbeweging kleiner is, en bijgevolg ook de ongewenste, hogere harmonischen in het versnellingspectrum. Dit resulteert in lagere excitatie van de resonanties van de kaders en een overeenkomstige daling van de kadertrillingen. Figuur 16 illustreert dit door het trillingsniveau te tonen van de kaderversnelling, i.f.v.  $\Omega$  en voor beide configuraties van de opstelling. Het trillingsniveau  $VL$  [dB re  $b$ ] van een versnellingssignaal  $\ddot{y}$  is de rms-waarde van het ongewenste deel  $\ddot{y} - \ddot{y}_{\text{des}}$  van de versnelling:

$$VL = 20 \cdot \log_{10} \left( \frac{\text{rms}(\ddot{y} - \ddot{y}_{\text{des}})}{b} \right),$$

waarbij  $\ddot{y}_{\text{des}}$  de gewenste versnelling (zoals de sinusoidale versnelling van de kaders) van het beschouwde machineonderdeel voorstelt. De waarden van  $\Delta VL = VL_{\text{FLY}} - VL_{\text{CBCP}}$  in Fig.16(b) tonen aan dat het trillingsniveau tot 10 dB (een factor 3) lager ligt in de CBCP-configuratie, behalve rond  $\Omega = 413.5$  rpm, waar de torsieresonantie domineert. In het snelheidsbereik waarin de CBCP correct functioneert (d.w.z., beneden 350 rpm) is de trillingsreductie significant: gemiddeld gezien 5.2 dB, d.w.z., een factor 2. Dit betekent dat voor dit snelheidsbereik, het toevoegen van de CBCP het trillingsniveau van de kaders *halveert*.



FIGUUR 16: (a) Trillingsniveau  $VL$  [dB re  $1 \text{ m/s}^2$ ] van de kaderversnelling i.f.v.  $\Omega$  [rpm] in de FLY-configuratie (streeplijn) en de CBCP-configuratie (volle lijn); (b)  $\Delta VL = VL_{FLY} - VL_{CBCP}$  [dB] i.f.v.  $\Omega$ .



FIGUUR 17: (a) A-gewogen geluidsdrumniveau  $SPL$  [dB(A)] i.f.v.  $\Omega$  [rpm] in de FLY-configuratie (streeplijn) en de CBCP-configuratie (volle lijn); (b)  $\Delta SPL = SPL_{FLY} - SPL_{CBCP}$  [dB(A)] i.f.v.  $\Omega$ .

Het verlagen van het trillingsniveau van de kaders, zorgt ook voor een verminderde geluidsproductie. Figuur 17 toont het A-gewogen geluidsdrukniveau  $SPL$ , opgemeten door een microfoon, geplaatst op 1 meter afstand van de kaders. Voor  $\Omega$  tussen 250 en 375 rpm, is de geluidsdrukreductie in de CBCP-configuratie (d.w.z.,  $\Delta SPL = SPL_{FLY} - SPL_{CBCP} \geq 0$ ) significant, want groter dan 3 dB(A). Voor lagere toerentallen is er geen reductie, maar een toename t.g.v. het rolgeluid van de looprollen in de CBCP. Voor hogere toerentallen is het opnieuw de torsieresonantie die zorgt voor een toename, i.p.v. een afname van het geluidsdrukniveau.

De hier gepresenteerde resultaten zijn geldig voor een machine à blanc. Hoe groot de trillings- en lawaai-reductie in een volledige weefmachine is, is niet voorspelbaar op basis van de uitgevoerde metingen. Daarom is het nodig de CBCP effectief aan een volledige machine aan te bouwen en te testen, na het nemen van maatregelen om de hinderlijke torsieresonantie te verschuiven naar hogere frequenties.

## 5.6 Gemiddelde Snelheidscontrole

Voor het aansturen van de proefopstelling is een nieuw, eenvoudig controlealgoritme ontwikkeld, *gemiddelde snelheidscontrole* (Average Speed Control, ASC). Dit algoritme zorgt ervoor dat de aandrijvende motor in regime een constant koppel uitoefent om de machine op toerental te houden. Wegens de definitie van gedempte eigenbeweging, volgt hieruit dat ASC gedempte eigenbeweging oplegt aan een machine.

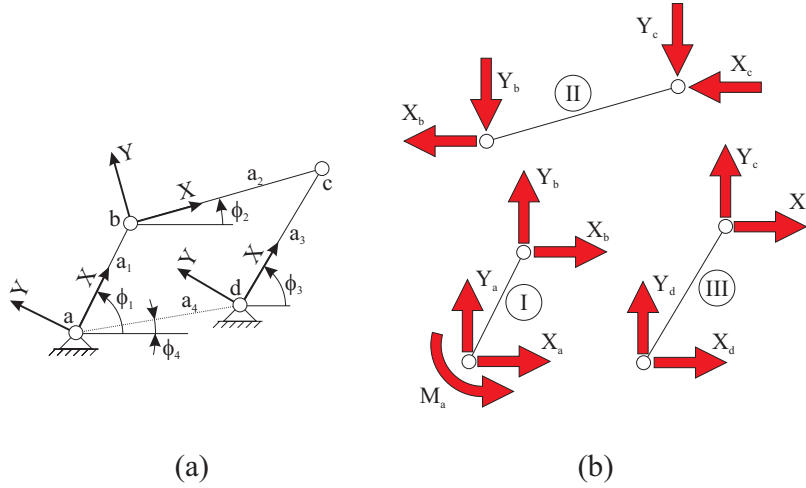
Het basisidee achter ASC is zeer eenvoudig: de fout  $e(t)$  [rad/s], op basis waarvan een proportioneel-integrerende regelaar het controlesignaal  $u$  [V] voor de motor berekent, wordt bepaald als het verschil tussen de gewenste *gemiddelde* snelheid  $2\pi/T$  [rad/s] en de werkelijke *gemiddelde* snelheid  $\dot{j}_{avg}(t)$  [rad/s].  $\dot{j}_{avg}$  wordt berekend als een voortschrijdend gemiddelde over één machineperiode.

ASC werkt uitstekend, zowel op simulatie als in de praktijk, en is gemakkelijk robuust in te stellen. Een belangrijk bijkomend voordeel van ASC is dat het toelaat om het gemiddelde toerental van een machine zeer nauwkeurig te regelen, en het dus mogelijk maakt meetsignalen op een betrouwbare manier in het tijdsdomein uit te middelen.

# 6 Balanceren met Tegengewichten

## 6.1 Originele Formulering (Vierstangenmechanisme)

Balanceren met tegengewichten vertrekt van het kinematisch ontwerp van een mechanisme, en zoekt de optimale dynamische (d.w.z., massa-) parameters voor het reduceren of elimineren van de dynamische reacties. De dynamische parameters kunnen aangepast worden door het veranderen van de algemene



FIGUUR 18: Kinematisch schema (a) en vrijgemaakte stangen (b) van een vierstangenmechanisme.

vorm van de stangen, of door het toevoegen van tegengewichten. Het basisidee van de methode wordt uitgelegd op basis van Fig.18.

Figuur 18(a) toont het kinematische schema van een vierstangenmechanisme. Stang I, de kruk, draait op constante snelheid. Stang II, de koppelstang, verbindt de kruk met stang III, de gedreven stang. Deze laatste voert een heen-en-weer gaande beweging uit. Figuur 18(b) toont de vrijgemaakte stangen, op basis waarvan de dynamische reacties gedefinieerd zijn. De  $X$  en  $Y$ -component van de schudkracht  $F_{\text{shak}}$  [N], en het schudmoment  $M_{\text{shak}}$  [N-m] (t.o.v. het punt  $\hat{a}$ ) zijn gelijk aan:

$$\begin{aligned} F_{\text{shak},x} &= -(X_a + X_d); \\ F_{\text{shak},y} &= -(Y_a + Y_d); \\ M_{\text{shak}} &= -(M_a + Y_d \cdot a_4 \cdot \cos \phi_4 - X_d \cdot a_4 \cdot \sin \phi_4). \end{aligned}$$

$M_a$  [N-m] is het aandrijfkoppel.  $X_i$  en  $Y_i$  [N],  $i = \{a, b, c, d\}$  zijn de verbindingskrachten.

Balanceren met tegengewichten is een oud en welbekend principe in het ontwerp van mechanismen en is een typisch optimalisatieprobleem, met als doelcriterium het minimaliseren van de schudkracht, het schudmoment, het inputkoppel en de verbindingskrachten. In het geval van het vierstangenmechanisme van Fig.18 zijn er 12 optimalisatievariabelen, vier voor elke stang: de massa  $m_i$  [kg], het inertiemoment  $J_i$  [kg-m<sup>2</sup>] (t.o.v. het massacentrum) en de coördinaten van het massacentrum  $X_i$  [m] en  $Y_i$  [m], t.o.v. een lokaal assenkruis, vastgemaakt aan elk van de stangen.

Om een afweging te maken tussen de verschillende dynamische reacties, wordt in dit werk het onderstaande optimalisatieprobleem opgelost (verbindingskrachten worden niet beschouwd):

$$\begin{array}{ll} \text{minimaliseer} & \alpha_{\text{msh}}, \\ \text{onderworpen aan} & \alpha_{\text{fsh}} \leq \alpha_{\text{fsh}}^{\text{M}}, \\ & \alpha_{\text{drv}} \leq \alpha_{\text{drv}}^{\text{M}}, \end{array}$$

waarbij de *balanceer effect index*  $\alpha_i$  [-] gedefinieerd is als (Lowen et al., 1974) de verhouding van de rms-waarde van de geoptimaliseerde dynamische reactie  $d(t)$  t.o.v. de rms-waarde van de dynamische reactie  $d^o(t)$  in het niet-gebalanceerde mechanisme:

$$\alpha = \frac{d_{\text{rms}}}{d_{\text{rms}}^o}.$$

De subscripten {fsh,msh,drv} wijzen respectievelijk op een eigenschap van de schudkracht, het schudmoment en het aandrijfkoppel. Het superscript M duidt een bovengrens aan.

In de hier gepresenteerde formulering is dit probleem niet-convex, o.a. omwille van een impliciet, niet-lineair verband tussen de indices  $\alpha_i$  en de optimalisatievariabelen.

## 6.2 Convexe Herformulering (Vierstangenmechanisme)

Deze sectie bespreekt de drie belangrijkste ingrediënten van de convexe herformulering van het optimalisatieprobleem. Voor een volledig bewijs wordt de lezer naar Hoofdstuk 9 van dit werk verwezen.

**Ingrediënt 1:  $\mu$ -parameters** Een eerste ingrediënt van de herformulering is het gebruik van onderstaande massaparameters, i.p.v. de klassieke massaparameters:

$$\begin{aligned} \mu_{1i} &= m_i; \\ \mu_{2i} &= m_i \cdot X_i; \\ \mu_{3i} &= m_i \cdot Y_i; \\ \mu_{4i} &= J_i + m_i \cdot (X_i^2 + Y_i^2). \end{aligned}$$

Deze alternatieve massaparameters zijn niet nieuw, en vinden algemene toepassing in robotidentificatie. Wat dan wel weer weinig geweten is, is het feit dat deze massaparameters superponeerbaar zijn (Haines, 1981): als  $\mu_{ij}^o$  een eigenschap is van de oorspronkelijke stang, en  $\mu_{ij}^*$  een eigenschap van het toegevoegde tegengewicht, dan heeft de gebalanceerde stang  $\mu_{ij} = \mu_{ij}^o + \mu_{ij}^*$  als massaparameter. Deze superpositie-eigenschap vormt het fundament van de convexe herformulering.

**Ingrediënt 2: Lineair Onafhankelijke Vectoren** De dynamische reacties  $d(t)$  die volgen uit de inverse dynamische analyse van een puur inertiaal mechanisme, kunnen algemeen geschreven worden als (Berkof and Lowen, 1969; Atkeson et al., 1986)

$$d(t) = \mathbf{e}^T(t) \cdot \mathbf{p} = \sum_{i=1}^n e_i(t) \cdot p_i. \quad (4)$$

Hierbij is  $\mathbf{e} \in \mathbb{R}^n$  een vector met  $n$  lineair onafhankelijke tijdsfuncties  $e_i(t)$ , die enkel afhangen van de kinematica van het mechanisme.  $\mathbf{p} \in \mathbb{R}^n$  is een vector van  $n$  constanten  $p_i$ , die een lineaire combinatie zijn van de bovenvermelde  $\mu$ -parameters. Dergelijke uitdrukkingen worden LIV (Linearly Independent Vector) uitdrukkingen genoemd in dit werk. Via dit soort uitdrukkingen is het mogelijk een expliciet, lineair verband op te stellen tussen de optimalisatievariabelen  $\mu$  en de beschouwde dynamische reacties.

**Ingrediënt 3: Algemene Massabeperkingen** Alhoewel sommige balanceringsmethodes, bijvoorbeeld (Haines, 1981), de  $\mu$ -parameters en LIV-uitdrukkingen tegelijkertijd gebruiken, leveren ze toch geen convex optimalisatieprobleem op. Naast het feit dat deze auteurs niet op de hoogte zijn van convexe optimalisatie in het algemeen, is dit vooral een gevolg van de aanname (gemaakt om praktisch realiseerbare tegengewichten te verkrijgen) dat de tegengewichten cirkelvormig zijn. Dit impliceert dat de locatie, straal en dikte van deze circulaire tegengewichten de optimalisatievariabelen zijn, hetgeen resulteert in een niet-convex optimalisatieprobleem.

Wat dit aspect betreft, is de aanpak in dit werk totaal verschillend. Geen enkele aanname wordt gemaakt betreffende de vorm van de tegengewichten: de beperkingen om tot praktisch haalbare tegengewichten te komen, worden uitgedrukt in hun meest algemene vorm, d.w.z., in functie van de  $\mu$ -parameters. Dit soort beperkingen is nieuw in de literatuur.

Drie soorten beperkingen komen aan bod: ultieme, praktische en praktische<sup>+</sup> beperkingen. Ultieme beperkingen leggen enkel op dat de massa en de inertie van een tegengewicht positief moeten zijn. Praktische beperkingen leggen als extra beperking op dat de dikte van het tegengewicht niet groter mag zijn dan een bepaald maximum  $t^M$  [m]. Praktische<sup>+</sup> beperkingen voegen hier nog aan toe dat het tegengewicht vast met de stang verbonden moet zijn (niet mag 'zweven' t.o.v. de stang). De wiskundige uitdrukking van deze voorwaarden volgt hierna, zonder afleiding:

### Ultieme Beperkingen

$$\begin{aligned} \mu_{1i}^* &\geq 0; \\ \mu_{1i}^* \cdot \mu_{4i}^* &\geq (\mu_{2i}^*)^2 + (\mu_{3i}^*)^2; \\ \mu_{4i}^* &\geq 0; \end{aligned}$$

	$i = 1$	$i = 2$	$i = 3$
$a_i$ [m]	0.0508	0.1524	0.0762
$m_i$ [kg]	0.0894	0.2394	0.1215
$X_i$ [m]	0.0254	0.0762	0.0381
$Y_i$ [m]	0	0.102	0
$J_i$ [ $10^{-3}$ kg-m <sup>2</sup> ]	0.0198	0.6792	0.2198

TABEL 1: Vierstangenmechanisme: numerieke parameters van stang 1, stang 2 en stang 3.  $a_4 = 0.1397$  m en  $\phi_4 = 0$ .

### Praktische Beperkingen

$$\mu_{4i}^* \geq \frac{(\mu_{1i}^*)^2}{2 \cdot \pi \cdot t^M \cdot \rho} + \frac{(\mu_{2i}^*)^2}{\mu_{1i}^*} + \frac{(\mu_{3i}^*)^2}{\mu_{1i}^*};$$

$$\mu_{1i}^* \geq 0;$$

$$\mu_{4i}^* \geq 0;$$

### Praktische<sup>+</sup> Beperkingen

$$\mu_{1i}^* \cdot \mu_{4i}^* \geq \frac{3}{2} \cdot [(\mu_{2i}^*)^2 + (\mu_{3i}^*)^2];$$

$$\mu_{2i}^* \leq 0;$$

$$\mu_{4i}^* \geq \frac{(\mu_{1i}^*)^2}{2 \cdot \pi \cdot t^M \cdot \rho} + \frac{(\mu_{2i}^*)^2}{\mu_{1i}^*} + \frac{(\mu_{3i}^*)^2}{\mu_{1i}^*};$$

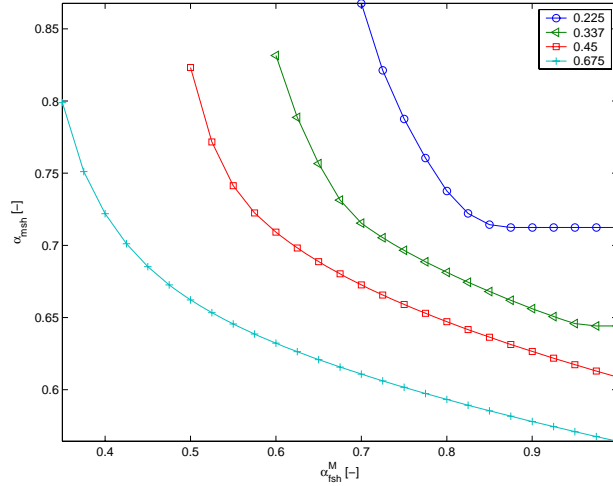
$$\mu_{1i}^* \geq 0;$$

$$\mu_{4i}^* \geq 0.$$

Sommige van deze beperkingen zijn niet-lineair in de  $\mu$ -parameters. Alle niet-lineaire beperkingen zijn echter convex, wat resulteert in convexe optimalisatieproblemen.

## 6.3 Numerieke Resultaten (Vierstangenmechanisme)

Gebruik makende van de praktische<sup>+</sup> beperkingen, worden hier numerieke resultaten gegenereerd voor een vierstangenmechanisme, waarvan Tabel 1 de numerieke parameters geeft (Tricamo and Lowen, 1983b; Lee and Cheng, 1984). De kruk draait met een constante aandrijfsnelheid van 500 rpm.

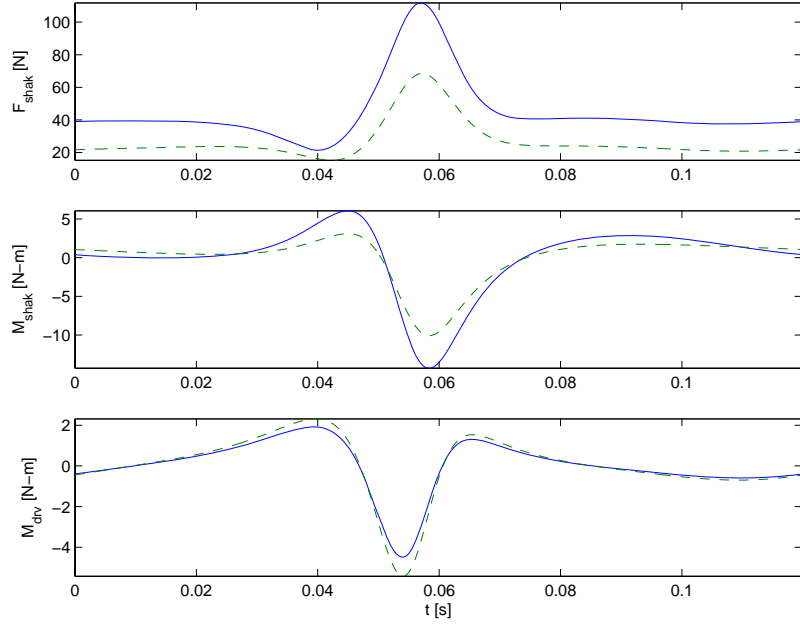


FIGUUR 19:  $\alpha_{msh} [-]$  in functie van  $\alpha_{fsh}^M [-]$  voor  $\alpha_{drv}^M = 1.2 [-]$  en  $m_{tot}^M = \{0.225, 0.338, 0.450, 0.675\}$  kg.

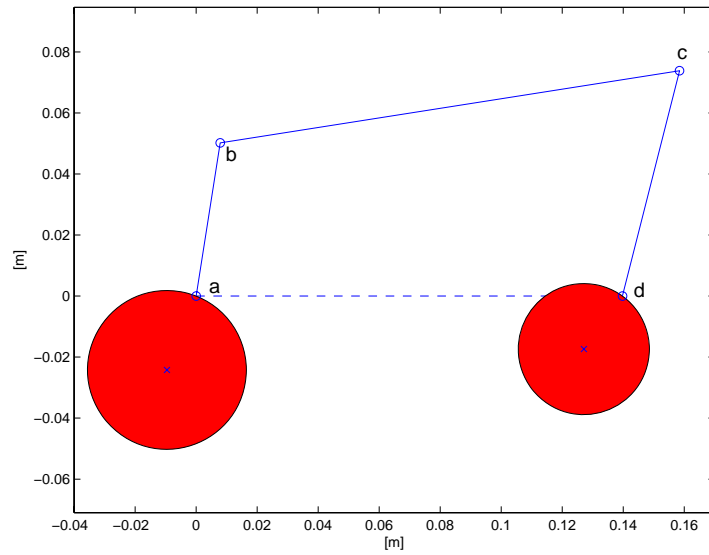
De som van de massa's van de tegengewichten is beperkt tot  $m_{tot}^M = \{0.225, 0.338, 0.450, 0.675\}$  kg, hetgeen respectievelijk  $\{50, 75, 100, 150\}$ % van de massa van het oorspronkelijke mechanisme vertegenwoordigt.

Figuur 19 toont  $\alpha_{msh}$  i.f.v.  $\alpha_{fsh}^M$  wanneer  $\alpha_{drv}^M = 1.2$ . Dit betekent dat de ontwerper toelaat dat de rms-waarde van het aandrieffkoppel met 20% toeneemt, om tot een reductie van de rms-waarde van het schudmoment te komen. De vier curven voor  $m_{tot}^M = \{0.225, 0.338, 0.450, 0.675\}$  kg tonen dat de schudkracht en het schudmoment gelijktijdig gereduceerd kunnen worden tot ongeveer  $\{0.76, 0.71, 0.68, 0.63\}$  keer hun oorspronkelijke rms-waarde. Het blijkt dat balanceren met tegengewichten geen magische oplossing is: de schudkracht en schudmoment dalen, maar dit ten koste van een toegenomen aandrieffkoppel en significante massatoevoeging.

Figuur 20 en 21 illustreren de bekomen resultaten voor het geval  $\alpha_{fsh}^M = 0.6$ ,  $\alpha_{drv}^M = 1.2$ ,  $m_{tot}^M = 0.450$  kg, waarbij de tegengewichten een dikte hebben die het dubbel is van die in Figuur 19. Figuur 20 toont één periode van de dynamische reacties van het originele en geoptimaliseerde mechanisme, terwijl Fig.21 het gebalanceerde mechanisme toont. Het mechanisme blijft vrij compact, maar dit ten koste van een dikte van de tegengewichten die vijf keer die is van de stangen. Het gebruik van een materiaal met een grotere dichtheid, zoals lood, laat toe de dikte te reduceren.



FIGUUR 20: Eén periode van de dynamische reacties van het originele (volle lijn) en geoptimaliseerde (streeplijn) mechanisme [ $\alpha_{\text{fsh}}^M = 0.6$ ,  $\alpha_{\text{drv}}^M = 1.2$ ,  $m_{\text{tot}}^M = 0.450$  kg].



FIGUUR 21: Vooraanzicht van het geoptimaliseerde mechanisme [ $\alpha_{\text{fsh}}^M = 0.6$ ,  $\alpha_{\text{drv}}^M = 1.2$ ,  $m_{\text{tot}}^M = 0.450$  kg].

## 6.4 Uitbreiding naar Mechanismen met $N$ Stangen

De ontwikkelde methodiek is generiek en uitbreidbaar tot mechanismen met  $N$  stangen. Daartoe is het nodig om op eenvoudige wijze LIV-uitdrukkingen als (4) op te stellen. In het geval van een vierstangenmechanisme kan dit op een analytische manier, door symbolische manipulatie. Voor mechanismen van een grotere complexiteit onttaardt dit echter snel in een zeer uitgebreide en tijdrovende oefening.

Om dit probleem te omzeilen is in dit werk een methodiek ontwikkeld om LIV-uitdrukkingen op te stellen op basis van (i) numerieke simulatie van het mechanisme in een simulatiepakket, en (ii) het toepassen van de singuliere waardenontbinding. Dit maakt symbolische manipulatie overbodig en laat toe mechanismen van een willekeurige complexiteit, ook ruimtelijke, te beschouwen. De kern van deze methodiek is een superpositieprincipe dat hieronder kort aan bod komt.

Beschouw een willekeurige stang  $i$  van een puur inertiael mechanisme, dat beweegt volgens een voorgeschreven beweging (inverse dynamische analyse). Beschouw drie verschillende massaverdelingen voor deze stang:

$$\begin{aligned}\mathbf{p}\mu_i^T &= [{}^p\mu_{1i} \ {}^p\mu_{2i} \ {}^p\mu_{3i} \ {}^p\mu_{4i}]; \\ \mathbf{q}\mu_i^T &= [{}^q\mu_{1i} \ {}^q\mu_{2i} \ {}^q\mu_{3i} \ {}^q\mu_{4i}]; \\ \mathbf{r}\mu_i^T &= [{}^r\mu_{1i} \ {}^r\mu_{2i} \ {}^r\mu_{3i} \ {}^r\mu_{4i}].\end{aligned}$$

Laat nu  $\{{}^p d_j(t)\}$ ,  $\{{}^q d_j(t)\}$  en  $\{{}^r d_j(t)\}$ ,  $j = 1 \dots J$  de set van  $J$  krachten en momenten zijn die werken op de stang, overeenkomstig de massaverdelingen  $\mathbf{p}\mu_i^T$ ,  $\mathbf{q}\mu_i^T$  en  $\mathbf{r}\mu_i^T \in \mathbb{R}^4$ . Als geldt dat

$$\mathbf{r}\mu_i = v \cdot (\mathbf{p}\mu_i) + w \cdot (\mathbf{q}\mu_i),$$

met  $v, w, \in \mathbb{R}$ , dan

$${}^r d_j(t) = v \cdot ({}^p d_j(t)) + w \cdot ({}^q d_j(t)), j = 1 \dots J.$$

Appendix Q geeft een bewijs voor dit superpositiebeginsel. De ontwikkelde methode levert niet alleen LIV-uitdrukkingen op zonder symbolische manipulatie, maar laat ook toe op eenvoudige manier LIV-uitdrukkingen te bepalen voor de verbindingskrachten. Bestaande methodes kunnen dit niet.

Een tweede aspect van de uitbreiding van de ontwikkelde methodiek naar mechanismen met  $N$  stangen, betreft de praktische<sup>+</sup> beperkingen (voor de ultieme en de praktische beperkingen is er geen enkel conceptueel verschil tussen vierstangen of meer ingewikkelde stangenmechanismen). De wiskundige afleiding van deze beperkingen veronderstelt immers dat het lokale assenkruis voor het bepalen van de coördinaten van de tegengewichten, zo gekozen is dat het tegengewicht een negatieve  $X$ -coördinaat heeft. Dit impliceert dat de lokale assenkruisen 'goed' of 'slecht' gekozen kunnen zijn. Voor vierstangenmechanismen is het een eenvoudige zaak de assenkruisen 'goed' te kiezen. Voor meer

complexe mechanismen wordt hier gesteld dat het mogelijk is een 'goede' keuze te maken, op basis van de ligging van de tegengewichten die volgen uit het gebruik van de ultieme of praktische beperkingen. Deze claim dient echter nog bevestigd te worden door het effectief toepassen van de ontwikkelde methode op complexe mechanismen.

## 7 Voornaamste Bijdrages

**Simulatie van Reciprocerende Machines** Het begrip *eigenbeweging* is uitgebreid, voor machines met energiedissipatie, tot *gedempte eigenbeweging*. Voor het berekenen van (gedempte) eigenbeweging is een frequentiedomein-gebaseerde techniek ontworpen.

**Ontwerp van Dynamisch Gecompenseerde Nokken** Inertieel gecompenseerde nokken integreren puur inertiaële aandrijfdynamica in hun ontwerp, en slagen erin volgerbewegingen nauwkeurig te realiseren, zelfs indien de energiedissipatie vrij groot is.

**Koppelcompensatie** Twee koppelcompenserende mechanismen zijn ontworpen en geoptimaliseerd. De nokgebaseerde centrifugaalslinger is daadwerkelijk gebouwd, en levert het gewenste koppel voor toerentallen beneden 350 rpm. Voor die toerentallen halveert het trillingsniveau van de kaders in de beschouwde weefmachine à blanc.

**Controle van Reciprocerende Machines** Gemiddelde snelheidscontrole is een nieuwe, eenvoudige techniek om gedempte eigenbeweging in de praktijk op te leggen. Dit regelschema is robuust, effectief (zowel op simulatie als experimenteel) en laat toe op een betrouwbare manier metingen in het tijdsdomein uit te middelen.

**Balanceren met Tegengewichten** Het optimaliseren van de massaparameters van tegengewichten is geherformuleerd als een convex optimalisatieprobleem. De resulterende methode is snel en levert een globaal optimum op voor vierstangenmechanismen. De methode is geldig voor vlakke mechanismen van een willekeurige complexiteit, en ruimtelijke mechanismen, indien de ultieme en praktische beperkingen gebruikt worden. Voor de praktische<sup>+</sup> beperkingen is de uitbreiding minder vanzelfsprekend, en dienen de voorgestelde oplossingen gevalideerd te worden door ze effectief toe te passen op complexe mechanismen. De hier ontwikkelde methodiek betekent een belangrijke doorbraak t.o.v. de huidige methodes, die af te rekenen hebben met lange rekentijden, beperkt zijn tot vierstangenmechanismen en lokale optima opleveren.



# List of Symbols

## General Symbols

$a$	: scalar (lower case character)
$\mathbf{a}$	: vector (lower case, bold character)
$\mathbf{A}$	: matrix (upper case, bold character)
$\odot$	: point
$\vec{\cdot}$	: vector
$ \cdot $	: absolute value
$\ \cdot\ $	: $L2$ -norm: $\ x\  = \sqrt{x^T \cdot x}$
$(\cdot)^M, (\cdot)^m$	: upper and lower bound on $(\cdot)$
$t$	: time [s]
$\dot{(\cdot)}$	: first derivative w.r.t. time $t$
$\ddot{(\cdot)}$	: second derivative w.r.t. time $t$
$(\cdot)_0$	: value at time instant $t = 0$
$(\cdot)_{\text{avg}}$	: average value
$(\cdot)_{\text{max}}$	: maximum value
$(\cdot)_{\text{min}}$	: minimum value
$\Omega$	: average drive speed [rad/s] or [rpm]
$T$	: period of motion [s]
$T_s$	: sample period [s]
$f_s$	: sample frequency [Hz]
$a_{\text{grav}}$	: gravity acceleration [9.81 m/s <sup>2</sup> ]
$T_{(\cdot)}(t)$	: kinetic energy [J]
$\vec{L}(t)$	: linear momentum [N-s]
$L_x(t)$	: $X$ -component of linear momentum [N-s]
$L_y(t)$	: $Y$ -component of linear momentum [N-s]
$A_{(\cdot)}(t)$	: angular momentum [N-m-s]

$F_{\text{shak},x}(t)$	: $X$ -component of shaking force [N]
$F_{\text{shak},y}(t)$	: $Y$ -component of shaking force [N]
$F_{\text{shak}}(t)$	: magnitude of shaking force [N]
$M_{\text{shak}}(t)$	: shaking moment [N-m]
$M_{(\cdot)}(t)$	: input torque [N-m]
$M_{\text{mot}}$	: (constant) motor torque during damped eigenmotion [N-m]

**Simulation of Reciprocating Machinery**

$K$	: number of harmonics [-]
$L$	: number of samples during one period of motion [-]
$T$	: machine period [s]
$\Omega$	: average drive speed of slowest turning axis to which a mechanism is attached [rad/s] or [rpm]
$\kappa$	: coefficient of drive speed fluctuation [%], see (2.17)
$A_k$	: amplitude of $k$ -th harmonic of periodic function
$T_{\text{tot}}(t)$	: total kinetic energy of reciprocating machine [J]
$T_{\text{tot,avg}}$	: average (over one period) total kinetic energy [J]
$E_{\text{loss}}(t)$	: total energy dissipated during one period [J]
$\eta$	: nondimensionalized coefficient of energy dissipation [-]
$M_{\text{mot}}$	: constant motor torque during damped eigenmotion [N-m]
$\hat{(\cdot)}$	: approximation (due to Fourier series truncation)
$\mathbf{z}$	: $2K$ or $2K + 1$ -vector of unknown coefficients
$d(t, \mathbf{z})$	: residual function

**Weaving Machines**

$g_{\text{sley}}(t)$	: sley axis angle [rad]
$g_{\text{shed}}(t)$	: shed axis angle [rad]
$g_{\text{cross}}$	: crossing angle [rad]
$\Omega_{\text{sley}}$	: average sley axis speed [rad/s] or [rpm]
$\Omega_{\text{shed}}$	: average shed axis speed [rad/s] or [rpm]
$F_{\text{sley}}(g_{\text{sley}})$	: sley motion law [rad]
$F_{\text{shed}}(g_{\text{shed}})$	: shed motion law [m]
$f_{\text{sley}}(t)$	: actually realized sley displacement [rad]
$f_{\text{shed}}(t)$	: actually realized shed follower displacement [m]
$f_{\text{sley}}^*(t)$	: desired sley displacement [rad], see (2.3a)

---

$f_{\text{shed}}^*(t)$	: desired shed follower displacement [m], see (2.6a)
$\Delta f_{\text{sley}}(t)$	: $f_{\text{sley}}(t) - f_{\text{sley}}^*(t)$ [rad]
$\Delta f_{\text{shed}}(t)$	: $f_{\text{shed}}(t) - f_{\text{shed}}^*(t)$ [m]
$(\cdot)'$	: first derivative w.r.t. $g_{\text{sley}}$ OR $g_{\text{shed}}$
$(\cdot)''$	: second derivative w.r.t. $g_{\text{sley}}$ OR $g_{\text{shed}}$
$N_{\text{shed}}$	: number of sheds in motion [-]
$J_{\text{sley}}$	: sley inertia [kg-m <sup>2</sup> ]
$J_{\text{shed}}$	: shed follower (equivalent) inertia [kg]
$J_{\text{fly}}$	: flywheel inertia [kg-m <sup>2</sup> ]
$T_{\text{sley}}(t)$	: sley kinetic energy [J]
$T_{\text{shed}}(t)$	: shed follower kinetic energy [J]
$T_{\text{fly}}(t)$	: flywheel kinetic energy [J]
$P_i(t)$	: power [W]: $dT_i(t)/dt$ ( $i = \{\text{tot}, \text{sley}, \text{shed}, \text{fly}\}$ )
$M_{\text{coul}, \text{sley}}$	: sley Coulomb-friction torque [N-m]
$M_{\text{coul}, \text{shed}}$	: shed Coulomb-friction force [N]
$M_{\text{coul}}$	: $M_{\text{coul}} = M_{\text{coul}, \text{sley}} = M_{\text{coul}, \text{shed}}$ [N] or [N-m]

### Inertially Compensated Cams

$g(t)$	: cam angle [rad]
$\Delta \dot{g}(t)$	: difference between desired and actually realized $\dot{g}(t)$ [rad/s]
$F_i(g)$	: $i$ -th follower motion law [rad] or [m]
$f_i^*(t)$	: desired $i$ -th follower displacement [rad] or [m]
$f_i(t)$	: actually realized $i$ -th follower displacement [rad] or [m]
$\Theta_i$	: desired $i$ -th follower displacement amplitude [rad] or [m]
$\Theta_{\text{ref}}$	: reference displacement [ $2\pi$ rad]
$N$	: number of cam-follower mechanisms [-]
$J_i$	: $i$ -th follower inertia [kg-m <sup>2</sup> ] or [kg]
$J_{\text{fly}}$	: flywheel inertia [kg-m <sup>2</sup> ]
$J_{\text{ref}}$	: reference inertia [1 kg-m <sup>2</sup> ]
$T_{\text{tot}}(t)$	: total kinetic energy of multi-follower cam-follower system [J]
$\tau$	: nondimensionalized time [-]
$(\cdot)'$	: first derivative w.r.t. $\tau$ or $g$
$(\cdot)''$	: second derivative w.r.t. $\tau$ or $g$
$\theta_i(\tau)$	: nondimensionalized desired $i$ -th follower displacement [-]
$\psi(\tau)$	: nondimensionalized camshaft displacement [-], see (3.4)

$\phi(\tau)$	: nondimensionalized camshaft displacement [-], see (3.5)
$\delta$	: coefficient of drive speed fluctuation [-], see (3.13)
$\zeta_i$	: nondimensionalized coefficient [-], see (3.8)
$\epsilon_{\text{tot}}(\tau)$	: nondimensionalized total kinetic energy [-]
$\epsilon_{\text{fly}}(\tau)$	: nondimensionalized flywheel kinetic energy [-]
$\epsilon_{\text{fol}}(\tau)$	: nondimensionalized follower kinetic energy [-]
$R_{\text{b,max}}$	: maximum allowable roller follower radius [m]
$R_{\text{C,max}}$	: maximum allowable cutter radius [m]
$\rho$	: (pitch profile) radius of curvature [m]
$\rho_{\text{min,+}}$	: minimum of all positive $\rho$ -values [m]
$\rho_{\text{min,-}}$	: minimum absolute value of all negative $\rho$ -values [m]

**Input Torque Balancing (General)**

$m$	: order of disturbing torque [-]
$E_o(t)$	: energy function of original system [J]
$T_c(t)$	: kinetic energy of ITB mechanism [J]
$T_o(t)$	: kinetic energy of original system [J]
$J_{\text{eq,o}}(t)$	: equivalent inertia of original system [kg-m <sup>2</sup> ]
$J_{\text{eq}}$	: equivalent inertia of combined system [kg-m <sup>2</sup> ]
$A_o(t)$	: angular momentum of original system [N-m-s]
$A_c(t)$	: angular momentum of ITB mechanism [N-m-s]
$A(t)$	: angular momentum of combined system [N-m-s]
$M_o(t)$	: input torque of original system [N-m]
$M_c(t)$	: input torque of ITB mechanism [N-m]
$M_{\text{shak,o}}(t)$	: shaking moment of original system [N-m]
$M_{\text{shak,c}}(t)$	: shaking moment of ITB mechanism [N-m]
$M_{\text{shak}}(t)$	: shaking moment of combined system [N-m]
$M_{\text{shak,NW}}(t)$	: shaking moment component due to $N(t)$ and $W(t)$ [N-m].
$g(t)$	: rotor rotation angle w.r.t. positive X-axis [rad]
$m_r, J_r$	: rotor mass [kg] and centroidal moment of inertia [kg-m <sup>2</sup> ]
$\rho_r$	: rotor mass density [kg/m <sup>3</sup> ]
$m_b, J_b$	: roller follower mass [kg], centroidal moment of inertia [kg-m <sup>2</sup> ]
$R_b$	: roller follower radius [m]
$h(t)$	: roller follower rotation angle [rad]
$N(t)$	: contact force exerted by internal cam on roller follower [N]
$W(t)$	: friction force exerted by internal cam on roller follower [N]

---

$\mathbf{p}_b \in \mathbb{R}^3$	: roller follower secondary parameter vector
$L_{\text{roll}}$	: roller follower bearing lifetime [h]
$C$	: dynamic load carrying capacity of roller follower bearing [N]
$F_{\text{roll}}(t)$	: force transmitted by roller follower bearing [N]
$P_{\text{roll}}$	: equivalent dynamic load on roller follower bearing [N]
$\omega_{\text{roll}}(t)$	: angular speed of roller follower bearing [rad/s]
$\ \vec{v}_i\ $	: absolute velocity of $\hat{o}_i$ [m/s]
$(o_{ix}, o_{iy})$	: coordinates of $\hat{o}_i$ [m]
$(v_{ix}, v_{iy})$	: coordinates of $d\hat{o}_i/dt$ [m/s]
$(a_{ix}, a_{iy})$	: coordinates of $d^2\hat{o}_i/dt^2$ [m/s <sup>2</sup> ]
$X_i(t), Y_i(t)$	: revolute joint reaction forces in $\hat{o}_i$ [N]
$r_p$	: radius of internal cam profile [m]
$\rho$	: radius of curvature of internal cam pitch profile [m]
$\rho_{\text{min},+}$	: minimum of all positive $\rho$ -values [m]
$\rho_{\text{min},-}$	: minimum absolute value of all negative $\rho$ -values [m]
$R_C$	: cutter or grinding stone radius [m]
$p_{\text{max}}$	: maximum Hertzian pressure [MPa]
$R_{p0,2}$	: yield strength [MPa]
$\Delta$	: safety tolerance for collision constraint [m]
$d(\cdot, \cdot)$	: distance between two points [m]
$i_1, i_2$	: collision flags [m]

### Input Torque Balancing (ICM)

$r(t)$	: ICM pitch radius [m]
$\hat{o}_i$	: points defined in Fig.5.6 ( $i = \{1, 2\}$ )
$m_c, J_c$	: carriage mass [kg] and centroidal moment of inertia [kg-m <sup>2</sup> ]
$m^*$	: generalized mass [kg]
$J^*$	: generalized moment of inertia [kg-m <sup>2</sup> ]
$n_{\text{ICM}}$	: number of ICMs [-]
$M_2(t), T_2(t)$	: prismatic joint reaction torque [N-m] and force [N]
$d_M(t, \mathbf{z})$	: torque residual function [N-m]
$d_E(t, \mathbf{z})$	: energy residual function [J]
$\hat{r}_M(t, \mathbf{z})$	: approximate solution for $r$ based on torque residual [m]
$\hat{r}_E(t, \mathbf{z})$	: approximate solution for $r$ based on energy residual [m]

$(l_r, d_r, t_r)$	: length, width and thickness of rotor rectangular prism [m]
$(l_c, d_c, t^*)$	: length, width and thickness of carriage rectangular prism [m]
$(R_c, t_c)$	: radius and thickness of inner ring of roller follower bearing [m]
$R$	: drive shaft radius [m]
$a$	: rotor length safety factor [-]
$\rho_c$	: carriage mass density [kg/m <sup>3</sup> ]
$\mathbf{p}_c \in \mathbb{R}^4$	: carriage secondary parameter vector
$\mathbf{p}_r \in \mathbb{R}^3$	: rotor secondary parameter vector
$\mathbf{p}_i \in \mathbb{R}^2$	: vector of optimization variables ( $i = \{1, 2, 3\}$ )
$\tau$	: nondimensionalized time [-]
$(\ )'$	: first derivative w.r.t. $\tau$
$(\ )''$	: second derivative w.r.t. $\tau$
$\Theta$	: motion amplitude [rad]
$\theta(\tau)$	: nondimensionalized desired follower displacement [-]
$\xi(\tau)$	: nondimensionalized pitch radius [-]
$\hat{\xi}_M(\tau)$	: approximate solution for $\xi(\tau)$ [-]

**Input Torque Balancing (CBCP)**

$q(t)$	: coupler rotation angle w.r.t. positive X-axis [rad]
$\hat{q}(t, \mathbf{z})$	: approximate solution for $q$ [rad]
$s(t)$	: help function defined by (6.13) [rad/s <sup>2</sup> ]
$\hat{o}_i$	: points defined in Fig.6.5 ( $i = \{1, 2, c, 3\}$ )
$\hat{o}_i$	: points defined in Fig.6.11 ( $i = \{2a, 2b, 3a, 3b, 3c, 3d\}$ )
$l_r$	: half of rotor length [m]
$l_c$	: coupler length [m]
$l_{\text{COG}}$	: length determining coupler COG [m], see Fig.6.1
$m_c, J_c$	: coupler mass [kg] and centroidal moment of inertia [kg-m <sup>2</sup> ]
$m^*$	: generalized mass [kg]
$J_i^*$	: generalized moments of inertia [kg-m <sup>2</sup> ] ( $i = \{1, 2, 3\}$ )
$n_b$	: number of roller followers [-]
$L_{\text{osc}}$	: oscillating bearing lifetime [h]
$C_0$	: static load carrying capacity of oscillating bearing [N]
$F_{\text{osc}}(t)$	: force transmitted by oscillating bearing [N]
$P_{\text{osc}}$	: equivalent static load on oscillating bearing [N]
$R^*$	: radius of additional mass, attached to coupler [m], see Fig.6.10

---

$R_1, R_3$	: radii defined in Fig.6.10 and Fig.6.11 [m]
$\rho_c$	: coupler mass density [kg/m <sup>3</sup> ]
$\mathbf{p}_c \in \mathbb{R}^{15}$	: coupler secondary parameter vector
$\mathbf{p}_r \in \mathbb{R}^5$	: rotor secondary parameter vector
$\mathbf{p}_i \in \mathbb{R}^4$	: vector of optimization variables ( $i = \{1, 2, 3, 4, 5\}$ )

### Experimental Results (General)

$F_{\text{sword}}(g_{\text{shed}})$	: sword motion law [rad]
$f_{\text{sword}}(t)$	: sword displacement [rad]
$f_{\text{frame}}(t)$	: up-and-down frame displacement [m]
$h_{\text{frame}}(t)$	: out-of-plane frame displacement [m]
$J_{\text{CBCP}}$	: flywheel inertia of clamped CBCP [kg-m <sup>2</sup> ]
$(\cdot)_1$	: $(\cdot)_{\text{sley}}$
$(\cdot)_2$	: $(\cdot)_{\text{shed}}$
$M_{c,\text{exp}}(t)$	: experimentally measured CBCP torque [N-m]
$M_{c,\text{the}}(t)$	: theoretical CBCP torque [N-m]

### Experimental Results (ASC)

$s$	: Laplace variable [1/s]
$C(s)$	: Laplace transform of control law
$U(s)$	: Laplace transform of control signal $u(t)$
$E(s)$	: Laplace transform of error signal $e(t)$
$u(t)$	: control signal (torque demand) [V]
$e(t)$	: error signal [rad/s]
$e_{\text{inst}}(t)$	: error signal (instantaneous drive speed measurement) [rad/s]
$e_{\text{avg}}(t)$	: error signal (average drive speed measurement) [rad/s]
$g_2^{\text{enc}}(t)$	: $g_2$ with finite resolution of encoder [rad]
$\dot{g}_{\text{des}}(t)$	: desired instantaneous drive speed [rad/s]
$\dot{g}(t)$	: actually realized instantaneous drive speed [rad/s]
$\dot{g}_{\text{avg}}(t)$	: actually realized average drive speed [rad/s]
$n_{\text{inst}}(t)$	: instantaneous shed axis speed [rpm]
$n_{\text{avg}}(t)$	: average shed axis speed [rpm]
$M_{\text{SR}}(t)$	: torque delivered by SR motor [N-m]
$M_{\text{SR,max}}(\dot{g}_1)$	: maximum torque that SR motor can deliver [N-m]
$M_{\text{dist}}(t)$	: disturbance torque [N-m]

$M_{\text{tot}}(t)$	: total torque applied to setup [N-m]
$T_w$	: time window for average drive speed calculation [s]
$L$	: (integer) number of periods $T$ contained in $T_w$ [-]
$P$	: (integer) number of samples contained in $T_w$ [-]
$K_p$	: gain of proportional part of PI-controller [V/(rad/s)]
$K_i$	: gain of integrating part of PI-controller [V/rad]

**Experimental Results (Torsional Model)**

$K_t$	: sley axis torsional stiffness [N-m/rad]
$C_t$	: sley axis torsional damping [N-m-s/rad]
$\zeta$	: sley axis damping ratio [-]
$M_{\text{mot}}$	: constant damped eigenmotion torque [N-m]
$M_{\text{tors}}(t)$	: torque transmitted by sley axis [N-m]
$g_{\text{sley}}(t)$	: rotation angle of left part of sley axis [rad]
$g_{\text{CBCP}}(t)$	: rotation angle of right part of sley axis [rad]
$f_{\text{sley,r}}(t)$	: displacement of right sley part [rad]
$f_{\text{sley,l}}(t)$	: displacement of left sley part [rad]
$T_{\text{tot,r}}(t)$	: kinetic energy of right setup side [J]
$T_{\text{tot,l}}(t)$	: kinetic energy of left setup side [J]
$P_{\text{loss,r}}(t)$	: power dissipated in right setup side [W]
$P_{\text{loss,l}}(t)$	: power dissipated in left setup side [W]

**Counterweight Balancing (General)**

$N$	: number of mechanism links [-]
$K$	: number of samples during one period of motion [-]
$n_i$	: number of LIV functions [-] ( $i = \{\text{fsh,msh,dry}\}$ )
$m_i$	: $i$ -th link mass [kg]
$X_i$	: $i$ -th link COG $X$ -coordinate [m] ( $i = 1, 2, \dots$ ) $X_i$ and $Y_i$ also denote the $X$ and $Y$ -component of the reaction force in joint $i$ ( $i = a, b, \dots$ ). Because of different subscripts, no confusion is possible.
$Y_i$	: $i$ -th link COG $Y$ -coordinate [m] ( $i = 1, 2, \dots$ )
$J_i$	: $i$ -th link centroidal inertia [kg-m <sup>2</sup> ]
$t_i$	: $i$ -th link thickness [m]
$\mu_{1i}$	: $m_i$ [kg]
$\mu_{2i}$	: $m_i \cdot X_i$ [kg-m]

---

$\mu_{3i}$	: $m_i \cdot Y_i$ [kg-m]
$\mu_{4i}$	: $J_i + m_i \cdot (X_i^2 + Y_i^2)$ [kg-m <sup>2</sup> ]
$(\cdot)^*$	: counterweight property
$(\cdot)^\circ$	: property of unbalanced link
$R_i^*$	: $i$ -th counterweight radius [m]
$t_i^*$	: $i$ -th counterweight thickness [m]
$m_{\text{tot}}$	: total counterweight mass [kg]
$a_i$	: $i$ -th link length [m]
$\phi_i(t)$	: $i$ -th link angular displacement [rad] ( $i = 1, 2, \dots$ )
$\phi_1(t)$	: input crank angle [rad] (angular displacement of link 1)
$\vec{r}_i(t)$	: $i$ -th link COG location [m]
$\vec{v}_i(t)$	: $i$ -th link COG velocity [m/s]
$\vec{r}_S(t)$	: linkage center of gravity location [m]
$S$	: overall center of gravity of linkage
$\vec{L}(t)$	: linear momentum [N-s]
$L_x(t)$	: $X$ -component of linear momentum [N-s]
$L_y(t)$	: $Y$ -component of linear momentum [N-s]
$A_{(\cdot)}(t)$	: angular momentum [N-m-s]
$T_i(t)$	: $i$ -th link kinetic energy [J]
$T_{\text{tot}}(t)$	: total kinetic energy [J]
$d(t)$	: general dynamic reaction
$F_{\text{shak},x}(t)$	: $X$ -component of shaking force [N]
$F_{\text{shak},y}(t)$	: $Y$ -component of shaking force [N]
$F_{\text{shak}}(t)$	: magnitude of shaking force [N]
$M_{\text{shak}}(t)$	: shaking moment [N-m]
$M_{\text{drv}}(t)$	: input torque [N-m]
$X_i(t)$	: $X$ -component of reaction force in joint $i$ [N] ( $i = a, b, \dots$ ) $X_i$ and $Y_i$ also denote the $i$ -th link COG $X$ and $Y$ -coordinate ( $i = 1, 2, \dots$ ). Because of different subscripts, no confusion is possible.
$Y_i(t)$	: $Y$ -component of reaction force in joint $i$ [N] ( $i = a, b, \dots$ )
$F_i(t)$	: magnitude of reaction force in joint $i$ [N] ( $i = a, b, \dots$ )
$(\cdot)_{\text{fsh}}$	: property of shaking force magnitude
$(\cdot)_{\text{fshx}}$	: property of shaking force $X$ -component
$(\cdot)_{\text{fshy}}$	: property of shaking force $Y$ -component
$(\cdot)_{\text{msh}}$	: property of shaking moment
$(\cdot)_{\text{drv}}$	: property of driving (input) torque

$q$	: auxiliary variable
$p_i$	: LIV constant
$e_i(t)$	: LIV function
$\mathbf{p}$	: $n$ -vector of $p_i$ , $i = 1 \dots n$
$\mathbf{e}(t)$	: $n$ -vector of $e_i(t)$ , $i = 1 \dots n$
$\mathbf{d}$	: $K$ -vector of $d(t_k)$ , $k = 1 \dots K$
$\mathbf{z}$	: $n$ -vector, defined by (9.36)
$\mathbf{E}$	: $K \times n$ matrix of $\mathbf{e}_i(t_k)$ , $i = 1 \dots n$ , $k = 1 \dots K$
$\mathbf{D}$	: $K \times s$ -vector of $^j \mathbf{d}$ , $j = 1 \dots s$
$\mathbf{U}$	: $n \times n$ matrix of singular vectors, defined by (9.35)
$\mathbf{C}$	: $n \times 12$ matrix, defined by (9.33)
$\mathbf{\Psi}$	: $n \times n$ matrix, defined by (9.36)
$\text{diag}(\sigma_1, \dots)$	: $n \times n$ diagonal matrix with diagonal elements $\sigma_1, \dots$
$\alpha$	: (rms) balancing effect index [-] ( $i = \{\text{fsh, msh, drv, a, b, c, d}\}$ )
$\beta$	: (max) balancing effect index [-] ( $i = \{\text{fsh, msh, drv, a, b, c, d}\}$ )
$\gamma$	: link thickness ratio [-]
$\eta$	: balancing efficiency index [%]
$\sigma$	: singular value

**Counterweight Balancing (Section 9.5)**

$^p(\cdot)$	: property of link/mechanism that has $p$ -th mass distribution (but same kinematic parameters)
$s$	: number of link mass parameters in $N$ -bar (planar) mechanism
$\mu_{ij}$	: $i$ -th link mass parameter ( $j = 1 \dots 4$ )
$\mu_i$	: 4-vector, $i$ -th link mass distribution
$\mu$	: $s$ -vector, linkage mass distribution
$\mathbf{s}$	: $s$ -vector, coordinates of linkage mass distribution in basis $\mathbf{M}$
$\mathbf{M}$	: $s \times s$ matrix of $^p \mu$ , $p = 1 \dots s$
$\mathbf{C}$	: $n \times s$ matrix: $\mathbf{p} = \mathbf{C} \cdot \mu$
$\mathbf{U}$	: $K \times K$ matrix of left singular vectors, defined by (9.53)
$\mathbf{V}$	: $s \times s$ matrix of right singular vectors, defined by (9.53)
$\mathbf{U}_r$	: $K \times r$ matrix (first $r$ columns of $\mathbf{U}$ )
$\mathbf{V}_r$	: $s \times r$ matrix (first $r$ columns of $\mathbf{V}$ )

# List of Abbreviations

## Standard Abbreviations

1D, 2D, 3D	: 1-, 2-, or 3-dimensional
4R four-bar	: four-bar mechanism with four revolute joints
AC	: Alternating Current
BVP	: Boundary Value Problem
CAD	: Computer Aided Design
COG	: Center Of Gravity
CP	: Convex Program
DC	: Direct Current
DFT	: Discrete Fourier Transform
LCS	: Local Coordinate System
LMI	: Linear Matrix Inequality
LP	: Linear Program
MIC	: Microphone
NVH	: Noise, Vibration and Harshness
ODE	: Ordinary Differential Equation
QP	: Quadratic Program
rms	: Root Mean Square
rpm	: Revolutions Per Minute
SDP	: Semidefinite Program
SOCP	: Second-Order Cone Program
SPL	: Sound Pressure Level

SQP	: Sequential Quadratic Programming
SR	: Switched Reluctance
SVD	: Singular Value Decomposition
VDI	: Verein Deutscher Ingenieure

### Dedicated Abbreviations

ASC	: Average Speed Control
CBCP	: Cam-Based Centrifugal Pendulum
CBCP-(·)	: setup configuration with clamped CBCP (Section 6.6, 7.3–7.4)
CON-(·)	: system with conventional cams (Section 3.3–3.4)
CPVA	: Centrifugal Pendulum Vibration Absorber
CWB	: Counterweight Balancing
ERI	: Experimental Robot Identification
FLY-(·)	: setup configuration with active CBCP (Section 6.6, 7.3–7.4)
ICM	: Inverted Cam Mechanism
ITB	: Input Torque Balancing
LDV	: Linearly Dependent Vector
LIV	: Linearly Independent Vector
TPVA	: Torsional Pendulum Vibration Absorber
TUVA	: Translational Undamped dynamic Vibration Absorber
VAR-(·)	: system with inertially compensated cams (Section 3.3–3.4)
VL	: Vibration Level

# Glossary

**airjet weaving machine** Weaving machine in which an airflow produces the insertion of the insertion yarn in the opening between the chain yarns.

**Average Speed Control** Control system approach, such that a motor, operated in torque mode, acts as a constant torque source. In this way, damped eigenmotion can be implemented on a practical set-up.

**binary link** Link with two pivot points, that is, two connection points with neighboring links.

**conjugate cam-follower mechanism** Form-closed cam-follower mechanism (see Fig.1.1).

**constraint function** Function defining an equality or an inequality constraint of a mathematical program, according to (9.1).

**convex function** A function  $f : \mathbb{R}^n \rightarrow \mathbb{R}$  is convex if its domain  $\mathbf{dom} f$  is a convex set and  $f(\theta x + (1-\theta)y) \leq \theta f(x) + (1-\theta)f(y)$ , for all  $x, y \in \mathbf{dom} f$  and  $\theta \in [0, 1]$ .

**convex program** Optimization problem with a convex goal function, convex inequality constraint functions and affine (that is, linear plus a translation) equality constraint functions.

**convex set** A set  $S \subseteq \mathbb{R}^n$  is convex if the line segment between any two points in  $C$  lies in  $C$ .

**counterweight balancing** Dynamic balancing method that optimizes a mechanism's link mass parameters, in order to reduce or eliminate the dynamic reactions. The link mass parameters are adapted by modifying the link shape or by counterweight addition.

**crank-rocker** see *Grashoff criteria*.

**crossing angle** Setting of a weaving machine that determines the synchronization between the sley and the shed follower motion.

**damped eigenmotion** Regime motion of a reciprocating machine in which energy dissipation is present, and in which the motor exerts a constant torque  $M_{\text{mot}}$  [N-m] to realize some desired average drive speed  $\Omega$  [rad/s].

**double crank** see *Grashoff criteria*.

**dyad** Two-link mechanism.

**dynamically compensated cams** Cams of which the cam profile is adapted such that some desired motion is imposed, despite the machine dynamics (for instance, flexibility of the follower).

**dynamic balancing** In this thesis, dynamic balancing is understood, in a broad sense<sup>6</sup>, as the action of reducing or eliminating the dynamic reactions in *reciprocating machinery*. For reference, it should be mentioned here that in the area of *rotating machinery*, dynamic balancing has a different meaning. That is, it is considered to be an extension of static balancing, if the considered rotating machine is long (compared to the radial direction) in the axial direction (see Section 8.5).

**dynamic reactions** Forces and torques, associated with the mechanical motion conversion in reciprocating machinery. These include the shaking force, shaking moment, input torque and joint forces.

**eigenmotion** Regime motion of a reciprocating machine in which no energy dissipation nor external work forces are present, and in which the motor exerts a zero torque.

**force-balanced mechanism** Mechanism that exerts no shaking force on its supporting frame.

**form/force-closed cam-follower mechanism** In a force-closed mechanism, a spring ensures the contact between the cam and its follower, see Fig.1.1(a). In a form-closed mechanism, contact is ensured by the geometry of the mechanism, see Fig.1.1(b).

**forward dynamic approach** Approach for determining the dynamic behavior of a mechanism, whereby (as opposed to the inverse dynamic approach) no input crank speed trajectory is given. Determining the mechanism kinematics (including the input crank speed trajectory) and the resulting forces requires time integration of a differential equation that is based on a model of the machine *and* its driving actuator.

**Grashoff criteria** The Grashoff criteria allow determining, based on the link lengths, whether a four-bar mechanism operates as a crank-rocker, a

---

<sup>6</sup>As opposed to its sometimes used, more inclusive meaning, that is, a synonym for counterweight balancing.

double crank or a double rocker. In a crank-rocker, link I (see Fig.1.2) rotates completely and link III oscillates. In a double crank, both link I and link III rotate completely, while both links oscillate for a double rocker. Expressions for the Grashoff criteria can for instance be found on p.24–26 of (Mabie and Reinholtz, 1987).

**ground bearing force** A (joint) force, acting on a mechanism link through a ground bearing. In Fig.1.2,  $X_a$ ,  $X_d$ ,  $Y_a$  and  $Y_d$  are ground bearing forces.

**inertially compensated cams** Cams that impose some desired follower motion, despite the drive speed fluctuation occurring during eigenmotion of the dominantly inertial machine to which they belong. Inertially compensated cams are an example of dynamically compensated cams.

**inertia counterweight** Rotary inertia, rotating or oscillating with the opposite angular velocity of its corresponding link, and driven by it, for instance through gears or a figure-eight timing belt or chain. See also *minimum inertia counterweight*.

**inline** A mechanism is inline if all of its links are inline. An inline link is a link of which the center of gravity lies on the line connecting the pivots. This line may extend beyond the pivots.

**input crank (angle)** (rotation angle of) the driven link in a mechanism with one degree of freedom.

**input (or driving) torque** Torque required for driving a mechanism with some prescribed (often constant) drive speed.

**input torque balancing** Taking measures that aim at smoothing the input torque, required for imposing a constant input crank speed to a mechanism.

**input torque balancing mechanism** Auxiliary mechanism that requires an input torque that partly or completely eliminates the input torque of some original mechanism.

**inverse dynamic approach** Approach for determining the dynamic behavior of a mechanism, whereby some input crank speed trajectory is assumed. As a result, the complete mechanism kinematics are determined<sup>7</sup>, and the dynamic reactions result from a simple matrix inversion.

**joint forces** Forces with which a mechanism's joints are loaded in order to transmit motion from one link to another.

---

<sup>7</sup>This is true provided that the mechanism has a single degree of freedom; if not, kinematic trajectories for the additional degrees of freedom are required for doing an inverse dynamic analysis.

**linear matrix inequality** A linear matrix inequality in  $x$  is a constraint of the general form  $A(x) \succeq 0$ , that is,  $A_0 + x_1 A_1 + \dots + x_n A_n \succeq 0$ , where  $A_i \in \mathbb{R}^{n \times n}$  are symmetric matrices. The inequality sign in  $A(x) \succeq 0$  means that  $A(x)$  is positive definite, i.e.,  $z^T A(x) z \geq 0$  for all  $z \in \mathbb{R}^n$ .

**linear program** Optimization problem with a goal function and constraint functions that are linear in the optimization variables.

**machine** Mechanism or collection of mechanisms which transmit force from the source of power to the resistance to be overcome (Mabie and Reinholtz, 1987).

**mathematical program** Synonym for optimization problem.

**mechanism** Combination of rigid or resistant bodies so formed and connected that they move upon each other with definite relative motion (Mabie and Reinholtz, 1987).

**minimum inertia counterweight** Counterweight that is circular and tangent to a link pivot. Do not confuse 'minimum inertia counterweights' with 'inertia counterweights': the former are masses (of a particular shape), rigidly attached to their corresponding link, while the latter rotate w.r.t. their corresponding link, and are driven by it through for instance a gear pair.

**motion law** Function that gives a cam-follower mechanism's follower displacement as a function of the cam angle.

**reciprocating machinery** Machines in which the rotary movement of the driving actuator is mechanically converted, through a mechanism, into the reciprocating (rocking, oscillating) movement of one or more machine parts.

**second-order cone constraint** Constraint of the general form  $\|A \cdot x + b\| \leq c^T x + d$ , where  $\|\cdot\|$  denotes the  $L2$ -norm:  $\|x\| = \sqrt{x^T \cdot x}$ .

**second-order cone program** Mathematical program in which a linear goal function is minimized, subject to linear equality constraints, linear inequality constraints and second-order cone constraints.

**semidefinite program** Mathematical program in which a linear goal function is minimized, subject to linear equality constraints, linear inequality constraints, second-order cone constraints and linear matrix inequalities.

**shaking force** Total force, transmitted to the machine frame, by a mechanism.

**shaking moment** Total moment (taken w.r.t. some arbitrary point), transmitted to the machine frame, by a mechanism.

- shed (cam-follower) mechanism** The shed mechanism is a cam-linkage mechanism that drives the up-and-down movement of the frames, in order to create an opening (called the shed) between the chain yarns. It is simplified in this thesis to a conjugate cam-follower mechanism with a translating follower (that is, the ensemble of the frames).
- single-degree-of-freedom mechanism** Mechanism in which (for given link lengths) the position, velocity and acceleration of all links are determined by the position, velocity and acceleration of one, driven link.
- sley (cam-follower) mechanism** After insertion of an insertion yarn in the opening between the chain yarns, the sley (driven by a conjugate cam-follower mechanism) beats up the insertion yarn to the already woven fabric.
- static balancing** A rotating link with a fixed pivot is *statically balanced* if its center of gravity coincides with its fixed pivot.
- sword** In the context of a weaving machine, the swords (link I in Fig 7.4) are the oscillating followers of the shed cams.
- torque mode** A motor operated in torque mode, interprets the analogue voltage signal, applied to its control input, as some desired motor torque.
- undercutting** In the context of cams, this term denotes the degenerate cam profile that results if, during cam manufacture, the cutter undercuts or removes material needed for cam contours in different locations.
- weaving machine à blanc** Stripped version of a complete machine. This implies that the machine is reduced to its essential parts: (i) the driving motor, (ii) the conjugate cam-follower mechanisms that drive the sley and (iii) the cam-linkage mechanisms that impose the frame motion. All other parts associated with the air insertion of the insertion threads, the handling of the yarn threads, and the transport of the woven fabric are removed.



# Table of Contents

<b>Voorwoord</b>	<b>i</b>
<b>Abstract</b>	<b>ix</b>
<b>Beknopte Samenvatting</b>	<b>xi</b>
<b>Nederlandse Samenvatting</b>	<b>xiii</b>
1 Inleiding . . . . .	xiii
2 Methodiek . . . . .	xiv
2.1 Optimalisatieaanpak . . . . .	xiv
2.2 Modelleringsaanpak . . . . .	xv
2.3 Voorwaartse of Inverse Dynamische Aanpak . . . . .	xv
2.4 Aanpak voor Nokken- en Stangenmechanismen . . . . .	xvi
3 Eigenbeweging van Reciprocerende Machines . . . . .	xvii
4 Inertieel Gecompenseerde Nokken . . . . .	xxi
5 Koppelcompensatie . . . . .	xxiii
5.1 Ontwerp van de Nokprofielen . . . . .	xxiv
5.2 Optimalisatie . . . . .	xxv
5.3 Praktische Implementatie . . . . .	xxvi
5.4 Experimentele Resultaten: CBCP-Koppel . . . . .	xxvi
5.5 Experimentele Resultaten: Machinegedrag . . . . .	xxix
5.6 Gemiddelde Snelheidscontrole . . . . .	xxxix
6 Balanceren met Tegengewichten . . . . .	xxxix
6.1 Originele Formulering (Vierstangenmechanisme) . . . . .	xxxix
6.2 Convexe Herformulering (Vierstangenmechanisme) . . . . .	xxxiii
6.3 Numerieke Resultaten (Vierstangenmechanisme) . . . . .	xxxv
6.4 Uitbreiding naar Mechanismen met $N$ Stangen . . . . .	xxxviii
7 Voornaamste Bijdrages . . . . .	xxxix
<b>List of Symbols</b>	<b>xli</b>
<b>List of Abbreviations</b>	<b>li</b>

<b>Glossary</b>	<b>liii</b>
<b>Table of Contents</b>	<b>lix</b>
<b>1 Introduction</b>	<b>1</b>
1.1 Motivation . . . . .	2
1.2 Approach . . . . .	3
1.2.1 Optimization Approach . . . . .	4
1.2.2 Modelling Approach . . . . .	6
1.2.3 Inverse or Forward Dynamic Approach . . . . .	9
1.2.4 Dynamic Balancing of Cam-Follower Mechanisms . . . . .	9
1.2.5 Dynamic Balancing of Linkages . . . . .	11
1.3 Relevance . . . . .	12
1.4 Main Contributions . . . . .	13
1.5 Outline . . . . .	15
1.6 Notation . . . . .	17
<b>2 Eigenmotion of Reciprocating Machinery</b>	<b>19</b>
2.1 A Weaving Machine Primer . . . . .	20
2.1.1 Shed Mechanism . . . . .	20
2.1.2 Batten (Sley) Mechanism . . . . .	22
2.1.3 Insertion Mechanism . . . . .	22
2.1.4 Specific Issues . . . . .	23
2.2 Simplified Airjet Weaving Machine Model . . . . .	23
2.2.1 Sley Cam-Follower Mechanism . . . . .	24
2.2.2 Shed Cam-Follower Mechanism . . . . .	25
2.2.3 Crossing Angle . . . . .	26
2.3 Eigenmotion of Reciprocating Machinery . . . . .	26
2.4 Frequency-Domain Eigenmotion Determination . . . . .	29
2.4.1 Derivation of Boundary Value Problem . . . . .	30
2.4.2 Solution of Boundary Value Problem . . . . .	31
2.5 Eigenmotion of an Airjet Weaving Machine . . . . .	32
2.6 Frequency-Domain Damped Eigenmotion Determination . . . . .	37
2.6.1 Energy Dissipation Mechanism . . . . .	37
2.6.2 Derivation of Boundary Value Problem . . . . .	38
2.7 Damped Eigenmotion of an Airjet Weaving Machine . . . . .	39
2.8 Conclusion . . . . .	42
<b>3 Inertially Compensated Cams</b>	<b>45</b>
3.1 State-of-the-Art of Integrated Kinematic-Dynamic Design . . . . .	46
3.1.1 Fully Integrated Kinematic-Dynamic Design . . . . .	47
3.1.2 Kinematic Design with Dynamic Considerations . . . . .	48
3.1.3 Drive Speed Fluctuation Design . . . . .	49
3.2 Design of Inertially Compensated Cams . . . . .	50
3.2.1 Nondimensionalization . . . . .	51

3.2.2	Choice of the Initial Camshaft Speed . . . . .	53
3.2.3	Calculation of the Equivalent Camshaft Inertia . . . . .	54
3.2.4	Calculation of the Cam Motion Law . . . . .	54
3.3	Application to an Academic Example . . . . .	55
3.3.1	Cam Design Procedure . . . . .	55
3.3.2	Influence of $\delta$ . . . . .	57
3.3.3	Sensitivity w.r.t. Energy Dissipation . . . . .	60
3.4	Application to an Airjet Weaving Machine . . . . .	62
3.4.1	Design Procedure . . . . .	63
3.4.2	Sensitivity w.r.t. Energy Dissipation . . . . .	64
3.4.3	Sensitivity w.r.t. Variable Machine Settings . . . . .	65
3.5	Conclusion . . . . .	66
<b>4</b>	<b>Input Torque Balancing: State-of-the-Art</b>	<b>69</b>
4.1	Survey of Input Torque Balancing Methods . . . . .	70
4.2	Auxiliary Input Torque Balancing Devices . . . . .	71
4.2.1	Torsional Vibration Absorbers . . . . .	72
4.2.2	Cam-Based Mechanisms . . . . .	75
4.2.3	Noncircular Gear Pair Based Mechanisms . . . . .	78
4.2.4	Mechanisms Providing Partial Balance . . . . .	79
4.3	Centrifugal Pendulum Vibration Absorber . . . . .	80
4.4	Cam-Follower Mechanism as ITB Device . . . . .	81
4.4.1	A Historical Note . . . . .	81
4.4.2	Recent Work . . . . .	83
4.5	Benefits of Input Torque Balancing . . . . .	84
4.6	Conclusion . . . . .	85
<b>5</b>	<b>Input Torque Balancing: Inverted Cam Mechanism</b>	<b>87</b>
5.1	Derivation of the Describing Equation . . . . .	88
5.1.1	Nomenclature . . . . .	88
5.1.2	Describing Equation: General Form . . . . .	89
5.1.3	Describing Equation: Differential Equation Form . . . . .	90
5.2	Solution of the Describing Equation . . . . .	92
5.2.1	Parameterization of the Solution . . . . .	92
5.2.2	Nonlinear Least Squares Problem . . . . .	93
5.3	Design Example . . . . .	93
5.3.1	Mechanism to be Balanced . . . . .	94
5.3.2	Kinematic and Inverse Dynamic Analysis . . . . .	97
5.3.3	Technological Analysis . . . . .	101
5.4	Design Optimization . . . . .	103
5.4.1	Optimization Variables . . . . .	103
5.4.2	Goal Function . . . . .	104
5.4.3	Constraints . . . . .	106
5.4.4	Design Procedure . . . . .	107
5.4.5	Design Chart . . . . .	108

5.5	Nondimensionalized Analysis . . . . .	108
5.5.1	Nondimensionalized Trajectories . . . . .	108
5.5.2	Nondimensionalized Design Procedure . . . . .	109
5.5.3	Nondimensionalized Design Chart . . . . .	110
5.5.4	Prismatic Joint Implementation . . . . .	112
5.5.5	Peak Phenomenon . . . . .	113
5.6	Conclusion . . . . .	116
<b>6</b>	<b>Input Torque Balancing: Cam-Based Centrifugal Pendulum</b>	<b>117</b>
6.1	Derivation of the Describing Equation . . . . .	118
6.1.1	Nomenclature . . . . .	118
6.1.2	Describing Equation: General Form . . . . .	119
6.1.3	Describing Equation: Differential Equation Form . . . . .	120
6.2	Solution of the Describing Equation . . . . .	122
6.3	Design Example . . . . .	122
6.3.1	Mechanism to be Balanced . . . . .	123
6.3.2	Kinematic and Inverse Dynamic Analysis . . . . .	125
6.3.3	Technological Analysis . . . . .	128
6.4	Design Optimization . . . . .	129
6.4.1	Optimization Variables . . . . .	130
6.4.2	Goal Function . . . . .	131
6.4.3	Constraints . . . . .	132
6.4.4	Optimization Algorithm . . . . .	136
6.4.5	Optimization Results . . . . .	136
6.5	Design Chart . . . . .	138
6.5.1	Parameter Choice for Design Example and Prototype . . . . .	139
6.6	Application to an Airjet Weaving Machine . . . . .	140
6.7	Conclusion . . . . .	147
<b>7</b>	<b>Input Torque Balancing: Experimental Validation</b>	<b>149</b>
7.1	Experimental Setup . . . . .	150
7.1.1	Airjet Weaving Machine . . . . .	150
7.1.2	CBCP Design and Construction . . . . .	154
7.1.3	Measurement and Control Systems . . . . .	157
7.1.4	Measurement Sensors . . . . .	157
7.1.5	Signal Processing . . . . .	158
7.2	Average Speed Control . . . . .	160
7.2.1	Basic Idea . . . . .	160
7.2.2	Simulation Results . . . . .	162
7.2.3	Conclusion . . . . .	166
7.3	Experimental Measurement Campaign . . . . .	166
7.3.1	ASC Performance . . . . .	168
7.3.2	CBCP Torque . . . . .	170
7.3.3	Shed Axis Speed and Acceleration . . . . .	172

7.3.4	Low-Frequency Sword and Frame Acceleration Spectrum . . . . .	176
7.3.5	Vibration Level . . . . .	176
7.3.6	Noise Level . . . . .	178
7.4	Torsional Vibration . . . . .	182
7.4.1	Derivation of Torsional Setup Model . . . . .	182
7.4.2	Simulation of Torsional Setup Model . . . . .	183
7.4.3	Simulation Results . . . . .	184
7.5	Conclusion . . . . .	186
<b>8</b>	<b>Counterweight Balancing: State-of-the-Art</b>	<b>189</b>
8.1	Basic Definitions . . . . .	191
8.2	Linearly Independent Vectors . . . . .	193
8.2.1	Purpose of LIV Expressions . . . . .	194
8.2.2	Basic Berkof-Lowen Method . . . . .	196
8.2.3	Extensions of Berkof-Lowen Method . . . . .	198
8.3	Main Theoretical Results . . . . .	200
8.3.1	Shaking Force Balancing of Planar Linkages . . . . .	200
8.3.2	Shaking Moment Balancing of Planar Linkages . . . . .	202
8.4	Optimization Approaches . . . . .	204
8.4.1	Full Force Balance Approaches . . . . .	205
8.4.2	Partial Force Balance Approaches . . . . .	208
8.5	Conclusion . . . . .	212
<b>9</b>	<b>Counterweight Balancing: A Convex Optimization Framework</b>	<b>215</b>
9.1	A Convex Optimization Primer . . . . .	216
9.2	4R Four-Bar: Constraint-Based Optimization Approach . . . . .	220
9.2.1	Optimization Variables . . . . .	220
9.2.2	Goal Function—Handling the Trade-Off . . . . .	220
9.2.3	Constraints—Counterweight Implementation . . . . .	221
9.2.3.1	Ultimate Constraints . . . . .	222
9.2.3.2	Practical Constraints . . . . .	222
9.2.3.3	Practical <sup>+</sup> Constraints . . . . .	223
9.2.3.4	Additional constraints . . . . .	226
9.2.4	Resulting Optimization Problems . . . . .	226
9.3	4R Four-Bar: Convex Reformulation . . . . .	226
9.3.1	Mass Parameterization . . . . .	227
9.3.2	LIV Expressions . . . . .	229
9.3.3	Resulting Convex Programs . . . . .	232
9.3.4	Discussion . . . . .	234
9.4	Numerical Results . . . . .	234
9.4.1	Practical <sup>+</sup> Constraints . . . . .	235
9.4.2	Relation with Ultimate and Practical Constraints . . . . .	239
9.5	Extension to $N$ -bar planar mechanisms . . . . .	245

9.5.1	Problem Statement . . . . .	245
9.5.2	Force Superposition Principle . . . . .	245
9.5.3	Automated LIV Procedure . . . . .	246
9.5.4	Discussion . . . . .	248
9.6	Conclusion . . . . .	248
<b>10</b>	<b>Conclusions and Future Work</b>	<b>253</b>
10.1	Conclusions . . . . .	253
10.2	Limitations and Future Work . . . . .	257
	<b>Bibliography</b>	<b>261</b>
	<b>Curriculum Vitae</b>	<b>277</b>
	<b>List of Publications</b>	<b>279</b>
<b>A</b>	<b>ICM: Kinematic Analysis</b>	<b>281</b>
A.1	Position, Velocity and Acceleration of $\hat{o}_i, i = \{1, 2\}$ . . . . .	282
A.2	Kinematics of the Roller Follower . . . . .	283
A.3	Cam Profile . . . . .	284
<b>B</b>	<b>ICM: Inverse Dynamic Analysis</b>	<b>285</b>
B.1	Validity of the Results: Input Torque . . . . .	286
B.2	Validity of the Results: Shaking Moment . . . . .	287
<b>C</b>	<b>CBCP: Kinematic Analysis</b>	<b>289</b>
C.1	Position, Velocity and Acceleration of $\hat{o}_i, i = \{1, 2, c, 3\}$ . . . . .	290
C.2	Kinematics of the Roller Follower . . . . .	292
C.3	Cam Profile . . . . .	293
<b>D</b>	<b>CBCP: Inverse Dynamic Analysis</b>	<b>295</b>
D.1	Validity of the Results: Input Torque . . . . .	297
D.2	Validity of the Results: Shaking Moment . . . . .	297
<b>E</b>	<b>CBCP: Mass Parameterization</b>	<b>301</b>
E.1	Parameterization . . . . .	301
E.2	Mass Properties . . . . .	301
E.3	Parameter Values . . . . .	304
<b>F</b>	<b>CBCP: Collision Constraints</b>	<b>307</b>
F.1	Intersection of/Distance Between a Circle and a Line Segment . . . . .	307
F.2	Coordinates of Coupler Points . . . . .	308

<b>G Technological Analysis of Cams: Radius of Curvature</b>	<b>311</b>
G.1 Determination of the Radius of Curvature . . . . .	311
G.2 Undercutting and Other Geometrical Problems . . . . .	313
G.2.1 Undercutting . . . . .	315
G.2.2 Underrolling . . . . .	315
G.2.3 Feasibility Problems . . . . .	316
<b>H Technological Analysis of Cams: Allowable Stresses</b>	<b>317</b>
H.1 Contact Pressure in General Contacts . . . . .	317
H.2 Avoiding Yield in Cam Profiles . . . . .	319
H.3 Limiting Surface Fatigue in Cam Profiles . . . . .	320
H.4 Example: CBCP Prototype . . . . .	321
<b>I Technological Analysis of Cams: Bearing Lifetime</b>	<b>325</b>
I.1 Roller Followers . . . . .	325
I.2 Oscillating bearings . . . . .	326
<b>J Modelling of Shed Mechanism</b>	<b>329</b>
J.1 Kinematic Modelling . . . . .	330
J.2 Dynamic Modelling . . . . .	331
<b>K Measurement Equipment Specifications</b>	<b>333</b>
<b>L Measurement Averaging in Reciprocating Machinery</b>	<b>337</b>
<b>M Average Speed Control: Moving Average Properties</b>	<b>343</b>
M.1 Amplitude and Phase Characteristic . . . . .	344
M.2 Interpretation . . . . .	344
<b>N Proof of Mass Superposition Principle</b>	<b>345</b>
N.1 Link in Plane Motion . . . . .	345
N.2 Link in Spatial Motion . . . . .	346
<b>O 4R Four-Bar: Linearly Independent Vector Expressions</b>	<b>349</b>
<b>P LMI Derivation and Conversion</b>	<b>351</b>
P.1 The Schur Complement . . . . .	351
P.2 LMI Derivation . . . . .	352
P.3 LMI Conversion . . . . .	353
<b>Q Proof of Force Superposition Principle</b>	<b>355</b>
Q.1 Notation and Basic Facts . . . . .	356
Q.2 Force Superposition . . . . .	357
Q.3 Moment Superposition . . . . .	358
<b>Index</b>	<b>361</b>



# Chapter 1

## Introduction

*Whatever the power of control engineering and informatics,  
even today one cannot turn poor mechanics,  
into a good machine.*

H. Van Brussel (1996)

IN the past two decades, the (r)evolution in microelectronics, control engineering and computer science has dramatically affected machine design, the traditional playground of the mechanical engineer. As indicated in (Van Brussel, 1996), the hype created around these new technologies has resulted in the misconception that smart control may solve every problem, even inadequate mechanics.

With this in mind, this thesis focuses on optimization of *mechanical* design as a basic prerequisite for building high-performance machinery, more specifically, *reciprocating* machinery. Essentially, these are machines in which the rotary movement of the driving actuator is mechanically converted, through a *mechanism*, into the reciprocating (rocking, oscillating) movement of one or more machine parts. Mabie and Reinholtz (1987) define a mechanism to be a combination of rigid or resistant bodies, so formed and connected that they move upon each other with definite relative motion.

Building high-performance machinery requires limiting machine vibration and the associated dynamic problems, such as fatigue, noise and wear. A number of methods exists for doing so. The approach adopted in this work is to intervene at the level of vibration excitation, by reducing or eliminating the forces and torques associated with the mechanical motion conversion, the so-called *dynamic reactions*. This approach is denoted here as *dynamic balancing*. The developed methods are applied to an important, industrial example of reciprocating machinery: *weaving machines*.

This chapter firstly discusses the threefold motivation for this research (Section 1.1), followed by an overview of the adopted approach (Section 1.2). Section 1.3 and 1.4 respectively assess the relevance and main contributions. In Section 1.5, a chapter-by-chapter overview is given. Finally, Section 1.6 discusses the used notation.

## 1.1 Motivation

While long, sweeping and very abstract statements can be made about the motivation of a particular research project, everyday practice learns that the motivation for most PhD research is somewhat more down-to-earth. This definitely holds for this research, as shown hereafter. The terms in italics are clarified in Section 1.2.

The PMA<sup>1</sup> division of K.U.Leuven's mechanical engineering department has known a long tradition of dynamic optimization of machinery. Within this tradition, and prior to this work, research had been done on the design of dynamically compensated cams and experimental cam dynamics identification. The initial motivation was to build upon and generalize these ideas. One of the first results was the extension of some results of Van de Straete and De Schutter (1999) for point-to-point motions, to the periodical motions generated by cam-follower mechanisms. This gave rise to the design of *inertially compensated cams*.

A second motivation was a three-year industrial project, which officially started in April 2000 (six months after the start of this research), and brought together three partners: (i) Picanol N.V., one of the world's leading weaving machine manufacturers<sup>2</sup>, (ii) PMA and (iii) WTCM<sup>3</sup>, a research institute closely related to Agoria<sup>4</sup>, the Belgian multisector federation for the technology industry. The overall purpose of this project was the development of methodologies to reduce vibration and noise in reciprocating machinery, more specifically, in weaving machines.

For the moment, it suffices to think of a weaving machine as consisting of two cam-follower mechanisms (the *sley* and *shed* cam-follower mechanisms, which are discussed in detail in Chapter 2), mounted on the same drive shaft. The main problem that has developed in its functioning, is excessive vibration of the shed cam-follower mechanism, resulting in premature failure and increased noise production.

Firstly inertially compensated cams were applied to solve these problems. However, the variable synchronization between the shed and sley cam-follower

---

<sup>1</sup>PMA stands for Production engineering, Machine design and Automation, and is a division of K.U.Leuven's mechanical engineering department.

<sup>2</sup>[www.picanol.be](http://www.picanol.be)

<sup>3</sup>Wetenschappelijk en Technisch Centrum van de Metaalverwerkende Nijverheid (Center for Scientific and Technical Research in Metal Manufacturing, [www.wtcm.be](http://www.wtcm.be)).

<sup>4</sup>[www.agoria.be](http://www.agoria.be)

mechanism renders this methodology infeasible for weaving machines. *Input torque balancing mechanisms* do not suffer from this problem and therefore, two such mechanisms have been designed, one of which has been experimentally tested. Secondary results of this project are the development of novel methods to (i) simulate the forward dynamics of reciprocating machinery and (ii) control the actuator driving the reciprocating machine.

A third motivation is the work of Boyd and Vandenberghe<sup>5</sup> on application of *convex optimization techniques* to engineering problems. Literature on input torque balancing and *counterweight balancing* of rigid-body linkages are very much interrelated, and reveals that counterweight balancing is a nonlinear, difficult optimization problem. Therefore, attempts were made to reformulate counterweight balancing as a convex optimization problem, in order to benefit from the computational power and theoretical elegance of the convex optimization framework. Inspired by ideas developed in the seminal paper (Berkof and Lowen, 1969) and the rather unknown, but equally important paper (Haines, 1981), these attempts resulted in the development of a convex optimization framework for counterweight balancing of planar, rigid-body linkages.

## 1.2 Approach

*Dynamic balancing* is used here as a term to denote all methods that optimize a mechanism's design in order to reduce its *dynamic reactions*. Four kinds of dynamic reactions are distinguished here. (i) The *shaking force* exerted by a mechanism, is the total force, transmitted to the machine frame, by the mechanism. (ii) The *shaking moment* exerted by a mechanism, is the total moment, transmitted to the machine frame, by the mechanism. (iii) The *input torque* (or *driving torque*) is the torque required for driving the mechanism with a prescribed (often constant) drive speed. (iv) The *joint forces* are the forces with which the mechanism's joints are loaded in order to transmit motion from one link to another. These formal definitions are illustrated for the case of a four-bar mechanism in Section 1.2.5.

Two important modelling assumptions govern the determination of the dynamic reactions: (i) the mechanism is a kinematic chain of rigid bodies and (ii) inertial dynamics dominate the dynamic response. These assumptions are discussed and justified in Section 1.2.2. Furthermore, in determining the dynamic reactions, a choice has to be made between performing an *inverse* or a *forward* dynamic analysis. Both analysis approaches are adopted in this work and are discussed in Section 1.2.3.

---

<sup>5</sup>Stephen P. Boyd is Professor at the Electrical Engineering Department of Stanford University ([www.stanford.edu/~boyd](http://www.stanford.edu/~boyd)); Lieven Vandenberghe is Associate Professor at the Electrical Engineering Department of the University of California in Los Angeles ([www.ee.ucla.edu/~vandenbe](http://www.ee.ucla.edu/~vandenbe)).

Two kinds of mechanisms are considered in this thesis: cam-follower mechanisms and linkages. For both kinds of mechanisms, the considered dynamic reactions, and therefore the resulting dynamic balancing approaches, are different. In the case of cam-follower mechanisms, the main focus lies on the input torque, and its effect on the dynamic behavior (for instance, the resulting drive speed fluctuation) of the cam-follower mechanism. The adopted dynamic balancing approach is discussed in Section 1.2.4.

In the case of linkages, it is assumed that the driving actuator imposes a constant drive speed. Here, the main focus lies on the shaking force and shaking moment. The adopted dynamic balancing approach is the subject of Section 1.2.5 and is based on optimizing a mechanism's *inertial* design (that is, its link mass parameters), by modifying the link shape or through counterweight addition. This method is well-known, and is termed *counterweight balancing* in this thesis. In literature, dynamic balancing is sometimes used, in a more inclusive sense, as a synonym of counterweight balancing.

Optimization plays an important role in this work. An optimization problem is often called *a mathematical program*, a term that is somewhat confusing because it suggests the writing of computer programs with a mathematical orientation<sup>6</sup>. The adopted optimization approach is explained hereafter. It is assumed that the reader is familiar with elementary optimization concepts as goal function, constraint, local and global optimum, . . . If not, a comprehensive introduction is found in Chapter 1 of the excellent treatise on numerical optimization, given by Nocedal and Wright (1999).

### 1.2.1 Optimization Approach

*In fact the great watershed in optimization  
isn't between linearity and nonlinearity,  
but convexity and nonconvexity*

R.T. Rockafellar (1993)

The first part of the above citation expresses a common misconception among engineers: if either the goal function or the constraints of an optimization problem are nonlinear, the problem is difficult to solve. Indeed, *linear programs*, that is, optimization problems with a goal function and constraints that are linear in the optimization variables, have nice properties: effective algorithms exist that can reliably solve (that is: determine the *global* optimum) even large problems, with hundreds or thousands of variables and constraints. However, many engineers consider 'linear' and 'easy' on the one hand, and

---

<sup>6</sup>As explained in (Nocedal and Wright, 1999), this term was coined in the 1940s, before the word 'programming' became inextricably linked with computer software. The original meaning of this word (and the intended one in the context of optimization) was more inclusive, with connotations of problem formulation and algorithm design and analysis.

'nonlinear' and 'difficult' on the other hand, as being synonyms, at least in the area of optimization.

This is not quite correct, as suggested by the second part of Rockafellar's citation: *convex programs* are *nonlinear* optimization problems for which very effective algorithms exist that can reliably and efficiently determine the *global* optimum, even for large problems. The mathematical properties of convex programs are briefly discussed in Chapter 9. As with linear programs, it can be said, with only a bit of exaggeration, that, if a problem can be formulated as a convex program, the original problem has been solved (Boyd and Vandenberghe, 2004). Formulating an optimization problem as a convex program, therefore, has great advantages.

Unfortunately, recognizing convex optimization problems, or those that can be transformed into convex optimization problems, may be quite challenging. In this respect, Boyd and Vandenberghe (2004) make an interesting comparison between local<sup>7</sup> optimization methods for nonlinear programming<sup>8</sup> and convex optimization: 'Since differentiability of the objective and constraint functions is the only requirement for most local optimization methods, formulating a practical problem as a nonlinear optimization problem is relatively straightforward. The art in local optimization is in solving the problem (in the weakened sense of finding a *locally optimal* point), once it is formulated. In convex optimization these are reversed: the art and challenge is in problem formulation; once a problem is formulated as a convex optimization problem, it is relatively straightforward to solve it.'

Most research in the area of mechanism optimization focuses on the art of *solving* optimization problems. This art involves testing different optimization algorithms, tuning the parameters of the chosen optimization algorithm (this can itself be an optimization problem), developing a methodology to find a good enough initial guess (when one instance is to be solved) or a method for producing a good enough initial guess (when a family of problems is to be solved),...

Conversely, this work focuses on the art of *formulating* optimization problems: for all optimization problems arising, considerable effort has been invested in their formulation, so as to obtain programs with favorable structure. As a result, counterweight balancing of linkages has been reformulated as a

<sup>7</sup>Boyd and Vandenberghe (2004) make the following distinction between *local* and *global* optimization methods for nonlinear programs: local optimization methods (such as Sequential Quadratic Programming) generate a local optimum, while global optimization methods are guaranteed to generate the true global optimum. The compromise is efficiency: the worst-case complexity of global methods grows exponentially with the problem size. Therefore, these methods are only suited for problems with a small number of variables, where computing time is not critical, and the value of finding the true global solution is very high. In this strict sense, stochastic methods, such as genetic and evolutionary algorithms, are local methods as they cannot guarantee a global optimum.

<sup>8</sup>Nonlinear optimization (or nonlinear programming) is the term used by Boyd and Vandenberghe (2004) to describe an optimization problem that is not linear and not known to be convex.

convex optimization problem. If convexity could not be proven (as in the case of the design optimization of the input torque balancing mechanisms), it was attempted to keep the optimization problem tractable by reducing the number of optimization variables to a few significant ones.

### 1.2.2 Modelling Approach

*The best model of a cat, is a cat—preferably the same cat.*

N. Wiener (1894-1964),  
US mathematician

#### From Rigid Body Dynamics ...

Considering a mechanism to be a kinematic chain of rigid bodies, implies that its dynamic behavior can be determined based on its *rigid-body dynamics*. This constitutes a significant simplification of reality, as it makes abstraction of two important dynamic effects: (i) elastic deformation of the mechanism links and (ii) joint clearance.

As Wiener's citation suggests, the validity of such simple models is limited. (VDI2149, 1999), the VDI<sup>9</sup> norm covering dynamic balancing, states that the lowest mechanism eigenfrequency should be at least tenfold the mechanism's average drive speed  $\Omega$  [rad/s], for elastic deformation to be negligible. In a weaving machine for instance, this condition is not fulfilled. Furthermore, joint clearance can dramatically affect a mechanism's dynamic behavior. Clearly, if one wants to accurately *simulate* the full dynamic behavior of a mechanism, a rigid-body model does not suffice.

Why then using rigid-body models at all? *Firstly*, for *design optimization* purposes, a rigid-body model is very attractive, due to its simplicity. Therefore, rigid-body models are widely used for design purposes. Moreover, it makes good sense to first optimize the rigid-body dynamic behavior of a mechanism, before proceeding to optimizing its elastic dynamic behavior. In theory, the suboptimality induced by this step-by-step approach, is overcome by simultaneous optimization of the rigid-body and elastic dynamic behavior. In practice however, the increased computational complexity (due to the increased number of optimization variables) may result in only marginally better mechanism designs, despite much longer computational times.

*Secondly*, also for *simulation*, rigid-body models are useful: it is for example a common assumption when simulating flexible mechanisms, that elastic deformation is small (Yuan and Rastegar, 2002). Consequently, although the full dynamic behavior cannot be captured, a rigid-body model still predicts at least a basic part of the dynamic response.

---

<sup>9</sup>Verein Deutscher Ingenieure, the Association of German Engineers ([www.vdi.de](http://www.vdi.de)).

Machine type	$\Omega$ [rpm]	$a_{\max}/a_{\text{grav}}$ [-]
Cutters, presses	30 ... 50	0.3 ... 1.2
Rolling mills	100 ... 350	10 ... 35
Weaving machines	200 ... 1000	1 ... 15
Knitting machines	1500 ... 3000	15 ... 40
Marine diesel engines	400 ... 500	70 ... 80
Domestic sewing machines	1000 ... 2000	50 ... 100
Industrial sewing machines	5000 ... 10000	300 ... 800

TABLE 1.1: Usual values of average drive speed  $\Omega$  [rpm] and acceleration ratio  $a_{\max}/a_{\text{grav}}$  [-] for some classes of reciprocating machinery.  $a_{\text{grav}}$  represents the gravity acceleration (9.81 m/s<sup>2</sup>). Reproduced from (VDI2149, 1999).

### ... to Inertial Dynamics

In addition to the assumption of rigid-body dynamic behavior, all mechanisms considered here are assumed to be *dominantly inertial*. Firstly, this implies that gravity is negligible w.r.t. inertial forces. This can be assessed by considering the ratio  $a_{\max}/a_{\text{grav}}$  of the maximum acceleration of a mechanism's output link<sup>10</sup>, to the gravity acceleration  $a_{\text{grav}}$ . (VDI2149, 1999) gives a table (see Table 1.1) of this ratio for some classes of reciprocating machinery, but does not clearly define a dominantly inertial system. Here, it is assumed that for  $a_{\max}/a_{\text{grav}} \geq 10$ , a system behaves as such.

Secondly, spring forces must be negligible w.r.t. inertial forces. This excludes so-called *force-closed* cam-follower mechanisms, see Fig.1.1(a), in which a spring ensures the contact between the cam and its follower. On the other hand, *form-closed* or *conjugate* cam-follower mechanisms, see Fig.1.1(b), behave dominantly inertially.

Thirdly, external work (such as gas forces in combustion engines and compressors, or plastic deformation work in presses) must be small w.r.t. inertial forces. Fourthly, energy dissipation due to e.g. joint friction may not dominate the dynamic response.

Although these assumptions may seem rather restrictive, they are classical in the design of high-speed cam-follower mechanisms and linkages (Berkof, 1979; Lowen et al., 1983). Furthermore, they are valid for modelling the drive system dynamics of a weaving machine: with drive speeds up to 1200

<sup>10</sup>For instance, the follower of a cam-follower mechanism, or the oscillating output link ('rocker') of a crank-rocker four-bar mechanism.

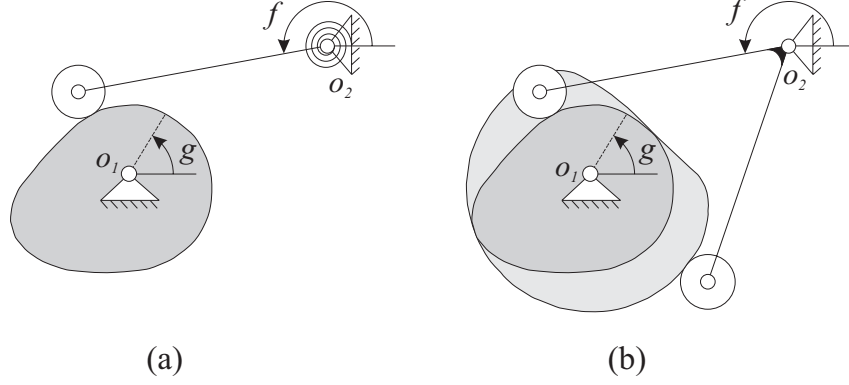


FIGURE 1.1: Force-closed (a) and conjugate or form-closed (b) cam-follower mechanism with rotating cam and oscillating roller follower. Rotation of the cam imposes an oscillating motion  $f$  to the follower. A torsional spring ensures the contact between the cam and its follower in the force-closed system.

rpm,  $a_{\max}/a_{\text{grav}}$  is sufficiently high for gravity to be neglected (see Table 1.1); conjugate cam-follower mechanisms are used, so no springs are present; there is no external work and friction losses are moderate.

In his survey on the input torque of linkages, Berkof (1979) reviews the various principles (such as virtual work, Lagrange's equation and classical force analysis based on free-body diagrams and equilibrium equations) for obtaining an analytic expression for the input torque of purely inertial, single-degree-of-freedom mechanisms<sup>11</sup>. He identifies the simplest formulation to be a concise kinetic energy derivative:

$$M = \frac{1}{\dot{\phi}_1} \cdot \frac{dT_{\text{tot}}}{dt} = \frac{1}{\dot{\phi}_1} \cdot \frac{d\left(\sum_{i=1}^{N-1} T_i\right)}{dt}, \quad (1.1)$$

where all variables are functions of time  $t$  [s].  $M$  [N-m] and  $T_{\text{tot}}$  [J] respectively denote the mechanism's input torque (applied to the input crank) and total kinetic energy.  $\dot{\phi}_1$  [rad/s] is the angular speed of the input crank.  $T_{\text{tot}}$  is the sum of the kinetic energies  $T_i$  [J] of the  $N$  mechanism links<sup>12</sup>. The kinetic energy  $T_i$  [J] of any rigid link  $i$  is the sum of its translational and rotational kinetic energy:

$$T_i = \frac{m_i \cdot \|\vec{v}_i\|^2}{2} + \frac{J_i \cdot \dot{\phi}_i^2}{2}, \quad (1.2)$$

<sup>11</sup>In single-degree-of-freedom mechanisms, the position, velocity and acceleration of all links are determined (for given link lengths) by the position, velocity and acceleration of one, driven link. This link is termed the *input crank*.

<sup>12</sup>Conventionally, link 0 is the fixed ground, which has no kinetic energy.

where  $m_i$  [kg] and  $J_i$  [kg·m<sup>2</sup>] respectively denote the link's mass and centroidal moment of inertia;  $\bar{v}_i$  [m/s] is the velocity of the center of gravity, while  $\dot{\phi}_i$  [rad/s] denotes the link's angular velocity.  $\|\cdot\|$  denotes the  $L2$ -norm:  $\|x\| = \sqrt{x^T \cdot x}$ . If a rotating link with a fixed pivot is *statically balanced*, that is, if its center of gravity coincides with its fixed pivot, the first term of (1.2) drops.

### 1.2.3 Inverse or Forward Dynamic Approach

Given the mechanism's model, determining the dynamic reactions is done based on either an inverse or a forward dynamic approach. In the *inverse dynamic approach* (also called *kinetostatic* approach), some input crank speed trajectory is assumed<sup>13</sup>. As a result, the complete mechanism kinematics are determined<sup>14</sup>, and the dynamic reactions are calculated based on a matrix inversion. No model of the driving actuator is required. This is the analysis approach adopted in Chapter 5–6 and Chapter 8–9.

In the *forward dynamic approach* on the other hand, no input crank speed trajectory is given. In that case, determining the mechanism kinematics (including the input crank speed trajectory) and the resulting forces requires time integration of a differential equation, which is based on a model of the machine *and* its driving actuator. This is the analysis approach adopted in Chapter 2–3, Section 6.6 and Chapter 7.

A forward dynamic approach is for instance required for determining the *eigenmotion* of a mechanism/machine. Eigenmotion is a concept well-known in German literature and is formally defined here as *the regime motion of a reciprocating machine in which no energy dissipation nor external work forces are present, and in which the motor exerts a zero torque*. Eigenmotion is a useful tool for studying the regime behavior of reciprocating machines that are driven by a motor with a *low-bandwidth* controller (see Chapter 2). Eigenmotion is also an important concept in the design of inertially compensated cams (see Chapter 3).

### 1.2.4 Dynamic Balancing of Cam-Follower Mechanisms

**Dynamic Problems in Weaving Machines** In a simplifying manner, Picanol weaving machines can be modelled as two cam-follower mechanisms, the sley and shed cam-follower mechanism, mounted on the same drive shaft. The fluctuating input torque of these mechanisms causes the drive speed to fluctuate as well. The drive speed fluctuation is substantial (greater than 10%), due to the limited flywheel size. As cams are designed with a constant

<sup>13</sup>If the mechanism's *regime* behavior is under study, the input crank speed trajectory is often assumed to be constant.

<sup>14</sup>This is true provided that the mechanism has a single degree of freedom; if not, kinematic trajectories for the additional degrees of freedom are required for performing an inverse dynamic analysis.

drive speed in mind, the drive speed fluctuation results in distorted follower motions. One of the consequences of the motion distortion is the presence of undesired harmonics in the followers' acceleration spectrum. The corresponding inertial forces excite follower resonances, causing vibration, wear, premature failure, noise, . . . These problems have mainly developed for the shed cam-follower mechanism.

**Possible Solutions** An obvious solution for solving these problems is reducing the drive speed fluctuation by (i) increasing the flywheel size or (ii) equipping the motor with an advanced, high-bandwidth control system. However, for reasons explained in Chapter 2, these solutions are rejected here, and another approach has to be sought.

A first approach is based on the conviction that reducing drive speed fluctuations may not be an aim *an sich*: the dynamic problems result from the follower motion distortion, not from the drive speed fluctuation itself. If the cam design was adapted such that the desired follower motion is realized without distortion, despite the fluctuating drive speed, the dynamic problems would be solved. *Inertially compensated cams* comply with this requirement, provided that inertial dynamics are dominant. This novel way of designing cams is cheap and effective for solving the aforementioned dynamic problems. Unfortunately, it is not applicable to weaving machines, due to its sensitivity for the typical synchronization changes between the sley and shed cam-follower mechanism.

Therefore, another approach is proposed, that is, addition of an *input torque balancing (ITB) mechanism*. This is an auxiliary mechanism, which requires an input torque that (partly or completely) eliminates out the input torque of the original mechanism. Consequently, the net torque on the drive shaft, and hence the drive speed fluctuation, are either substantially reduced or made zero. Two simple, cam-based ITB mechanisms, providing quasi complete input torque balance, are designed and optimized in this work: the inverted cam mechanism (ICM) and the cam-based centrifugal pendulum (CBCP). The CBCP is experimentally tested on a weaving machine.

### **Shaking Force and Shaking Moment in Cam-Follower Mechanisms**

The above discussion is only concerned with the input torque requirements of cam-follower mechanisms. But what with the other dynamic reactions? Complete shaking force elimination is easily achieved in cam-follower mechanisms with an oscillating follower, by statically balancing the cam and the follower. On the other hand, shaking force reduction in cam-follower mechanisms with a translating follower is not so trivial. And although the shaking moment exerted by cam-follower mechanisms may be huge (see Section 5.3.2), to the author's knowledge, measures for reducing it are not described in open literature.

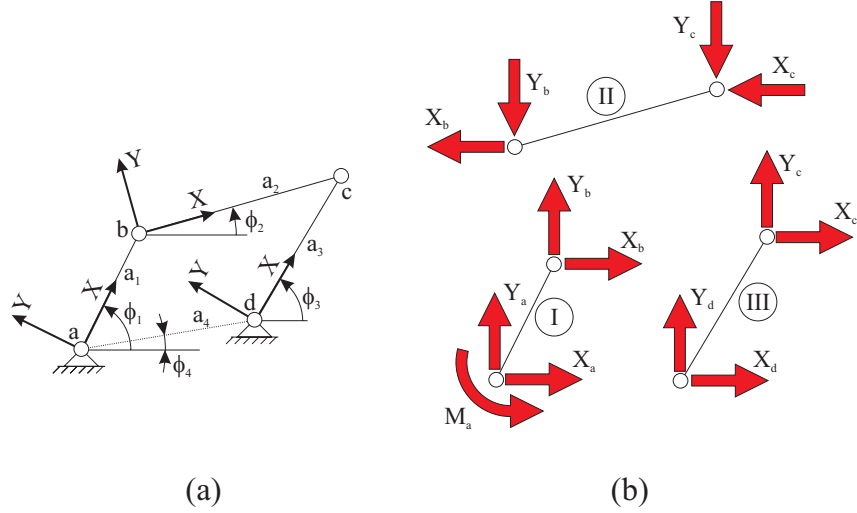


FIGURE 1.2: Kinematic scheme (a) and free-body diagram of a crank-rocker four-bar mechanism.

### 1.2.5 Dynamic Balancing of Linkages

The method adopted in this work for dynamic balancing of linkages is *counterweight balancing* (CWB). Counterweight balancing starts from a given *kinematic* mechanism design, and optimizes the *inertial* design, that is, the link mass parameters, in order to reduce or eliminate the dynamic reactions. The link mass parameters are adapted by modifying the link shape or by counterweight addition. The basic idea of counterweight balancing is explained based on Fig.1.2.

Figure 1.2(a) shows the kinematic scheme of a crank-rocker four-bar mechanism. Link I, the crank, is assumed to rotate at constant speed. Link II, the coupler, connects the crank with link III, the rocker. The latter performs an oscillating (rocking) motion. Figure 1.2(b) shows a free-body diagram, based on which the dynamic reactions are defined. The  $X$  and  $Y$ -component of the shaking force  $F_{\text{shak}}$  [N], and the shaking moment  $M_{\text{shak}}$  [N-m] (w.r.t. the point  $\hat{a}$ ) equal:

$$\begin{aligned} F_{\text{shak},x} &= -(X_a + X_d); \\ F_{\text{shak},y} &= -(Y_a + Y_d); \\ M_{\text{shak}} &= -(M_a + Y_d \cdot a_4 \cdot \cos \phi_4 - X_d \cdot a_4 \cdot \sin \phi_4). \end{aligned}$$

$M_a$  [N-m] is the input torque,  $X_i$  and  $Y_i$  [N],  $i = \{a, b, c, d\}$  the joint forces.

Counterweight balancing is an old and well-known principle in mechanism design and inherently constitutes an optimization problem. Generally

in CWB, one seeks to minimize a combination of the root-mean-square values of the shaking force, shaking moment, input torque and joint forces. The optimization variables are the link mass parameters. In the case of a crank-rocker four-bar, there are hence twelve optimization variables, that is, four for each link: the mass  $m_i$  [kg], centroidal moment of inertia  $J_i$  [kg-m<sup>2</sup>] and center of gravity coordinates  $X_i$  [m] and  $Y_i$  [m] w.r.t. to some local coordinate system, fixed to the link. The basic constraints are nonnegativity constraints on  $m_i$  and  $J_i$ .

The particular contribution of the present work is the reformulation of this optimization problem as a *convex optimization* problem. A two-step approach is adopted: first, it is shown that counterweight balancing of a planar, purely inertial four-bar mechanism is a convex optimization problem; secondly, this approach is generalized to planar, purely inertial  $N$ -bar mechanisms. The main motivation for choosing the CWB approach is that, for a dominantly inertial linkage, its results are valid for any mean drive speed, as opposed to methods based on spring addition.

### 1.3 Relevance

Despite the growing use of servomotors for motion generation, cam mechanisms and linkages are still widely employed in *high-speed*, industrial applications: 'Cams are the first choice of many designers for motion control where high precision, repeatability, and long life are required. All automotive engines depend on cams for their proper valve function. Most automated production machinery uses cams extensively ...' (Norton, 2002). Weaving and packaging machines, agricultural machinery, combustion engines, reciprocating compressors and pumps: mechanisms are omnipresent.

Dynamic balancing, as an approach for optimizing the dynamic behavior of such machinery, is old and widespread. Lowen and Berkof (1968) cite a total of 119 references in their 1968 survey paper on the dynamic balancing of linkages. 158 additional references are presented in the 1983 update of the state-of-the-art by the same authors (Lowen et al., 1983).

The main driving force for further developing dynamic balancing methods is the ever growing drive speed of machinery, with the associated (quadratic) increase of inertial forces. As an example: (VDI2149, 1999) recommends to take dynamic balancing measures if the previously defined ratio  $a_{\max}/a_{\text{grav}}$  exceeds one. Table 1.1 shows that dynamic balancing is hence relevant for quite a lot of machines.

Moreover, the legislator is imposing increasingly stern demands. For instance, the European Directive 89/39/EEC of June 12th, 1989, concerning the conditions that have to be satisfied in the work environment, has led to a regulation to limit workers' exposure to *physical agents*, in particular vibrations and noise. This was one of the direct motivations for the definition of the Picanol project.

In marked contrast with the practical relevance of mechanisms in general, and dynamic balancing in particular, is the seemingly dwindling academic interest. It cannot be denied that the number of scientific journals and conferences related to mechanism design is very small compared to, let's say, the ones related to robotics. This needs not necessarily be a disadvantage, but still illustrates that mechanism design is not a 'hot' academic topic (anymore). This might be explained by the already mentioned hype created around smart control. However, as every (normal) dynamic system eventually settles somewhere in between, and in view of the increasing importance of *mechatronics* as a design paradigm, a renewed academic interest in mechanical design may be anticipated. It is hoped that the present work contributes to this.

## 1.4 Main Contributions

Below, a list is given of the main contributions, in an order corresponding to the ordering of the different chapters.

**Simulation of Reciprocating Machinery** Two novel concepts concerning the *forward* dynamic analysis of reciprocating machinery are developed. Firstly, the concept of eigenmotion is generalized to mechanisms in which energy is dissipated. This generalization is termed *damped eigenmotion*. Secondly, instead of directly integrating the governing differential equation, the forward dynamic analysis problem is solved by formulating a boundary value problem and applying (well-known) nonlinear least-squares techniques to it. This computational scheme is introduced in mechanism literature for the first time.

**Dynamically Compensated Cam Design** *Dynamically compensated cams* are designed so as to impose some desired motion, despite the machine dynamics. Classically, only *follower* system dynamics (such as flexibility of the follower) are taken into account, assuming that the drive speed is constant. The present work, by contrast, integrates the *drive* system dynamics in the cam design, through the design of inertially compensated cams. Such cams accurately realize follower motions, despite the presence of significant drive speed fluctuation, provided that the machine in which they are mounted, behaves dominantly inertially.

The academic and industrial relevance of employing inertially compensated cams stems from the fact that it is cheap (as opposed to mounting an auxiliary input torque balancing mechanism), energy efficient (as opposed to imposing a constant drive speed through the motor) and does not compromise a machine's start/stop behavior (as opposed to a large flywheel). The main disadvantage of these cams is that they are very sensitive for the synchronization changes occurring in weaving machines.

**Input Torque Balancing** ITB is an old and well-known principle, and both the ICM and CBCP are described<sup>15</sup> in literature. The contributions made here are (i) a literature survey that bridges the gap between the literature on ITB mechanisms and that on torsional vibration absorbers; (ii) the formulation of boundary value problems for determining the internal cams in the ICM and the CBCP, and the application of nonlinear least-squares techniques for solving them; (iii) the integration of collision and technological constraints into the ICM and CBCP design optimization process; (iv) the development of design charts to speed up the design optimization; (v) the actual construction of the CBCP and the experimental verification that it delivers the designed torque; (vi) the experimental verification of the beneficial effect of ITB on the dynamic behavior of an industrial machine, that is, an *airjet* weaving machine *à blanc*. One of the main aspects of this beneficial effect is that the vibration level of the up-and-down moving frames is halved.

**Control of Reciprocating Machinery** A novel type of low-bandwidth controller for reciprocating machine is proposed: *Average Speed Control*. An average speed controlled, reciprocating machine moves according to its damped eigenmotion, which is one of the requirements for inertially compensated cams to function properly. Average Speed Control is easily implementable and robust. It additionally results in reliable time-domain averaging of measurement signals in reciprocating machinery.

**Counterweight Balancing** A first contribution is the literature survey given here, which, as opposed to existing, more encyclopedic literature surveys on the topic, can serve as a gentle introduction for the newcomer in the field. Secondly, the literature survey reveals the resemblance between the *linearly independent vector expressions*, common in CWB literature, and the *minimal*, linear models used in experimental robot identification.

The main contribution is the development of a convex optimization framework for optimizing the counterweight mass parameters of planar, purely inertial  $N$ -bar mechanisms. This framework is inherently superior to all existing counterweight balancing methods, due to its flexibility, efficiency and the guarantee to obtain a global optimum. The development of this framework should serve as a basis for turning CWB from an academic into an industrially relevant method.

---

<sup>15</sup>That is, their configurations are well-known; however, design methodologies are erroneous (ICM) or nonexistent (CBCP).

## 1.5 Outline

**Chapter 2** formally defines eigenmotion and introduces the concept of damped eigenmotion for mechanisms in which energy dissipation is present. Furthermore, it shows how to formulate (damped) eigenmotion determination as a boundary value problem (BVP) and how to apply nonlinear least-squares techniques for solving this BVP. These concepts are subsequently applied to a simplified model of an airjet weaving machine. The obtained simulation results illustrate the drive speed fluctuation and the resulting follower motion distortion. The simplified model is derived after a discussion of the basic layout of a weaving machine. Based on this discussion, requirements are formulated with which methods for reducing the follower motion distortion should comply, in order to be applicable to weaving machinery.

**Chapter 3** discusses the design of inertially compensated cams, which are an example of integrated mechanism design that simultaneously considers kinematic and dynamic design aspects. First, a literature survey of comparable design methodologies is given, followed by the development of a methodology for designing inertially compensated cams, which is applied to an academic example. Application to an airjet weaving machine shows that these cams are capable of significantly reducing the undesired shed follower acceleration harmonics, even in the presence of a moderate amount of friction. However, they fail miserably to do so if significant synchronization changes are present.

**Chapter 4** firstly reviews the state-of-the-art of classical input torque balancing methods. This leads to the conclusion that the classical method, complying best with the specific requirements of a weaving machine, is the addition of a compact, cam-based, input torque balancing mechanism. Two promising candidate mechanisms are identified: the inverted cam mechanism (ICM) and the cam-based centrifugal pendulum (CBCP). They are compact and have a simpler construction than other cam-based mechanisms. Moreover, design procedures for them are either erroneous, too rough an approximation or simply nonexistent.

**Chapter 5** shows how to design and optimize the ICM. The ICM is technologically feasible, but a considerable amount of technological risk is associated with its practical realization, due to the presence of a prismatic joint, imposing small displacements, but with high speeds and accelerations.

**Chapter 6** therefore focuses on the design and optimization of the CBCP, in which all joints are revolute. The CBCP is shown to be technologically feasible, and to result in significant reduction of the undesired shed follower acceleration harmonics. Therefore, it was decided to actually build this mechanism in order to test its practicality.

**Chapter 7** discusses the experimental validation of the CBCP on an airjet weaving machine, and the development of Average Speed Control. Average Speed Control is shown to work well and to result in reliable time-domain averaging of measurement signals. Furthermore, the CBCP is shown to function properly, and to enhance the dynamic machine behavior, provided that the machine turns at a speed below some critical drive speed. Above that speed, an unexpected torsional resonance phenomenon starts to dominate the dynamic response. A torsional simulation model is developed in order to explain the observed experimental behavior.

**Chapter 8** gives an overview of the state-of-the-art of counterweight balancing. This literature survey has a threefold purpose. It is firstly meant as a gentle introduction to the subject for the newcomer in the field. Secondly, it introduces the idea of *linearly independent vector* expressions, a fundamental concept in counterweight balancing, and illustrates the resemblance between these expressions and the minimal, linear models used in experimental robot identification. Thirdly, an overview is given of the various known *formulations* of counterweight balancing as an optimization problem.

**Chapter 9** develops a general convex optimization framework for counterweight balancing of planar, purely inertial  $N$ -bar mechanisms. After giving a brief introduction to the mathematics of convex optimization, the basic flavor of the convex optimization framework is illustrated by developing it for a planar, purely inertial four-bar mechanism. Numerical results are provided in order to reveal the potential of counterweight balancing. After that, the framework is generalized to  $N$ -bar mechanisms.

**Chapter 10** repeats the main conclusions of this work, identifies its limitations and gives suggestions for future work.

**Reading Trajectories** The following reading trajectories are proposed, depending on the reader's interest:

- simulation of reciprocating machinery: Chapter 2;
- dynamically compensated cam design: Chapter 2-3;
- input torque balancing: Chapter 2, 4-7;
- control of reciprocating machinery: Chapter 2, Section 7.2;
- counterweight balancing: Chapter 8-9.

In order to facilitate the reading process, the main definitions and concepts are summarized in a *glossary*. Also an *index* is provided.

## 1.6 Notation

Three particular aspects of the adopted notation are clarified here: (i) the way angular displacements are denoted, (ii) the use of Greek symbols and (iii) the use of the symbols  $T$  and  $\Omega$ .

In dealing with linkages, the angular displacement of the  $i$ -th mechanism link is denoted as  $\phi_i$ , which is the notation conventionally used in literature on counterweight balancing of four-bar mechanisms. If the mechanism has one degree of freedom,  $\phi_1$  and  $\dot{\phi}_1$  respectively denote the angular displacement (rotation angle) and velocity of the driven link or *input crank*, and are respectively termed the *input crank angle* and *input crank speed*. Figure 1.2, and equations (1.1–1.2) are consistent with this notation, which is used in Chapter 8–9.

On the other hand, in dealing with cam-follower mechanisms and the input torque balancing mechanisms of Chapter 5–6, the angular displacement of mechanism links is denoted using lower case characters such as  $f, g, \dots$ . The symbol  $g$  [rad] is consistently used<sup>16</sup> to denote the input crank angle of these (one-degree-of-freedom) mechanisms, that is, the cam angle of a cam-follower mechanism (Fig.1.1) and the rotor angle of the input torque balancing mechanisms (Fig.5.1 and 6.1). Based on this notation, used throughout Chapter 2–7, (1.1–1.2) are rewritten as:

$$M = \frac{1}{\dot{g}} \cdot \frac{dT_{\text{tot}}}{dt}; \quad (1.3)$$

$$T_i = \frac{m_i \cdot \|\vec{v}_i\|^2}{2} + \frac{J_i \cdot \dot{e}_i^2}{2}, \quad (1.4)$$

where  $\dot{e}_i$  [rad/s] denotes the  $i$ -th link's angular velocity.

The different angular displacement notations are motivated by the fact that nondimensionalization is an important aspect in Chapter 2–7. In this context, lower case Latin and lower case Greek characters are used to distinguish between dimensionalized and nondimensionalized<sup>17</sup> quantities respectively. For instance:  $\phi$  denotes the nondimensionalized counterpart of  $g$ . On the other hand, nondimensionalization is not used in Chapter 8–9, and therefore  $\phi_i$ , the conventional notation for link angular displacements in counterweight balancing literature, is used.

A final note concerns the symbols  $T$  and  $\Omega$ . If no subscript is present,  $T$  denotes a mechanism's period of motion [s].  $T_s$  denotes a sample period [s]. If any other subscript is present,  $T_{(\cdot)}$  is used as a symbol for kinetic energy

<sup>16</sup>This definition of  $g$  overrules the conventional use of  $g$  as the symbol of gravity acceleration. In order to avoid any possible confusion, the gravity acceleration is denoted as  $a_{\text{grav}} = 9.81 \text{ m/s}^2$ .

<sup>17</sup>Two symbols constitute an exception to this general rule, that is, (i)  $\rho$  [kg/m<sup>3</sup>] or [m], the generally accepted symbol for respectively denoting mass density or a curve's radius of curvature and (ii) the  $\mu$ -parameters that denote the alternative mass parameterization used in Chapter 8–9, defined by (8.20a–8.20d).

[J]. The average drive speed  $\Omega$  is expressed either in [rad/s] or in [rpm]. In Chapter 2–7,  $\Omega$  [rad/s] is the average value of  $\dot{g}$ , while it is the average value of  $\dot{\phi}_1$  in Chapter 8–9.

## Chapter 2

# Eigenmotion of Reciprocating Machinery

*Bei sich selbst überlassenen Mechanismen stellt sich eine sogenannte Eigenbewegung mit stellungsabhängiger veränderlicher Drehgeschwindigkeit ein.*

H. Dresig (2001)

WITH this citation<sup>1</sup>, the concept of *eigenmotion* is introduced on page 320 of (Dresig, 2001), a monograph on vibration in mechanical drive systems. Eigenmotion is an important notion in this work, since the regime motion of Picanol weaving machines is quite similar to their (damped) eigenmotion. Also the design of inertially compensated cams is closely related to eigenmotion.

This chapter formally defines eigenmotion and introduces the concept of damped eigenmotion for mechanisms in which energy dissipation is present (Section 2.3). A *frequency-domain approach* is developed for calculating both machine regimes. It is based on (i) formulating (damped) eigenmotion determination as a boundary value problem and (ii) solving this boundary value problem using nonlinear least-squares techniques.

The frequency-domain approach is illustrated by applying it to a simplified model of an airjet weaving machine, both for eigenmotion (Section 2.4) and damped eigenmotion (Section 2.6). The corresponding numerical simulation results are discussed in Section 2.5 and 2.7 respectively, and illustrate (i) the shed and sley follower motion distortion due to the drive speed fluctuation

---

<sup>1</sup>Mechanisms, left to themselves, exhibit a so-called Eigenmotion with position-dependent drive speed.

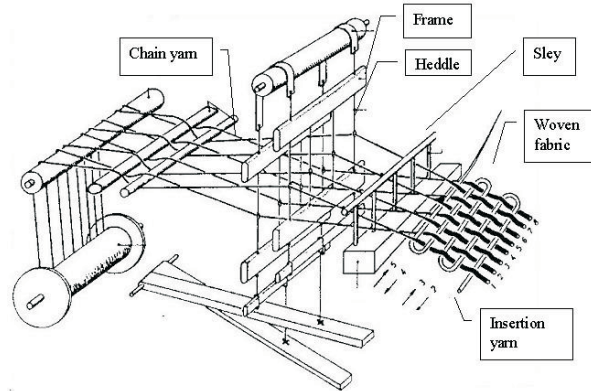


FIGURE 2.1: Working principle of a (manual) weaving machine. (Courtesy of Picanol N.V.)

and (ii) the close resemblance between eigenmotion and damped eigenmotion if friction losses are moderate.

Section 2.8 clarifies the term 'frequency-domain approach' and discusses the general applicability of the developed methodology. Furthermore, requirements are formulated, with which methods for reducing the follower motion distortion in weaving machines should comply.

The simplified airjet weaving machine model is derived in Section 2.2. In order to do so, it is necessary to elaborate on the principle of weaving and the basic structure of a weaving machine, which are the subjects of the following section.

## 2.1 A Weaving Machine Primer

A woven fabric is formed by interlacing two systems of yarns, perpendicular to each other: *insertion* yarns along the machine (fabric) width and *chain* yarns in the direction perpendicular to it, as shown in Fig.2.1. In order to interlace the yarn system, a weaving machine consists of several mechanisms, which impose synchronized, reciprocating movements. These mechanisms are driven by one main motor and are discussed hereafter.

### 2.1.1 Shed Mechanism

In order to insert a yarn in the fabric, an opening (called the *shed*) has to be created between the chain yarns, using either a *frame* system, as in Fig.2.1, or a *jacquard* system. The former system consists of frames, each of which

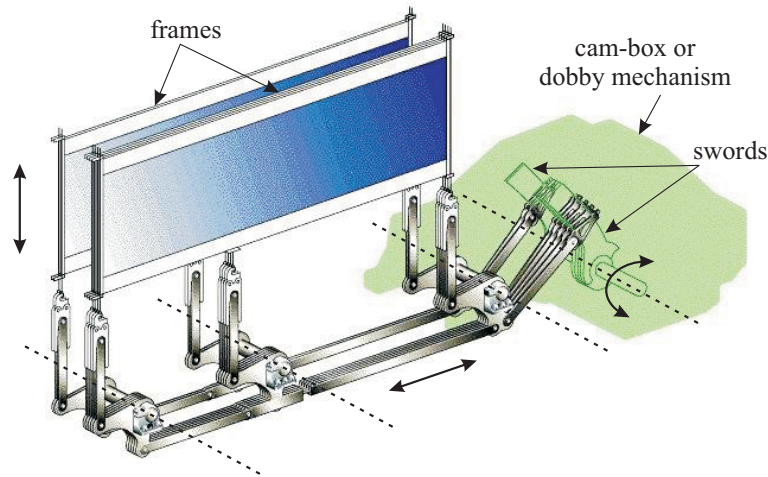


FIGURE 2.2: Linkage that transmits the motion from the cam-box or dobbie mechanism to the frames. Joint axes indicated with a dashed line constitute a connection between the linkage and the supporting machine frame. The frames are connected to the machine frame by a prismatic joint (not shown in the figure). (Courtesy of Picanol N.V.)

commands some part of the chain yarns. Each yarn passes through an eye, connected to the frame with a *heddle*. By moving the frames up and down, the required opening between the chain yarns is created. In the jacquard system, on the other hand, every single chain yarn is driven separately, which makes it possible to make fabrics with complex patterns. Jacquard machines are not considered in this work.

Several systems exist for creating the up-and-down frame motion. For simple weave fabrics, crank-slider mechanisms are used. Slightly more complex patterns can be created by driving the frames with a *cam-box mechanism*. Each frame is then driven by a separate conjugate cam (with an oscillating follower, called the *sword*), designed so as to create optimal weaving conditions. A linkage system, as shown in Fig.2.2, transforms the oscillating movement of the sword into the up-and-down frame movement. This linkage is further discussed in Chapter 7.

A disadvantage of the cam-box mechanism is the laborious rebuilding if another kind of fabric is woven. The *dobby system* overcomes this disadvantage. This system is equipped with an electronic selection system, driven by the weaving machine's microprocessor, which decides upon the number of swords (frames), moving during a weaving cycle. Again, the linkage of Fig.2.2 transforms the sword motion into the frame motion. The dobbie system is more expensive and is more limited in speed.

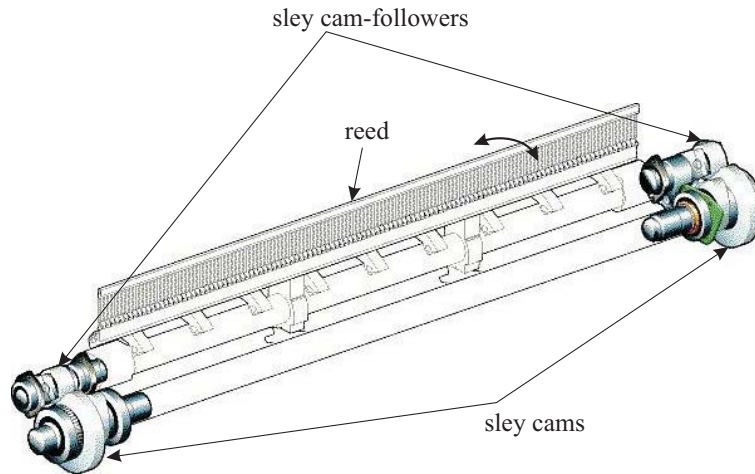


FIGURE 2.3: Sley (including reed), driven by two rotating, conjugate cams and their oscillating followers. (Courtesy of Picanol N.V.)

### 2.1.2 Batten (Sley) Mechanism

Each time an insertion yarn is inserted, the *sley* (with the *reed* mounted on it) beats the yarn up to the already woven fabric. The sley can be driven by a four or six-bar linkage, or by a cam-follower mechanism with oscillating follower. Nowadays, Picanol uses conjugate cam-follower mechanisms, as shown in Fig.2.3, because of their superior mechanical performance, and the possibility to optimize the sley's motion for air insertion. The sley is driven at one or at two machine sides, depending on its allowed torsional deformation.

### 2.1.3 Insertion Mechanism

Picanol uses *airjet* and *gripper insertion* for insertion of the insertion yarn. In an *airjet weaving machine*, an airflow produces the insertion: the main nozzle on the (left) side of the machine gives a certain initial speed to the insertion yarn. Additional nozzles maintain the airflow during insertion, by blowing in the insertion canal of the reed, at specific, synchronized time instants.

In a *rapier machine*, a gripper grips the insertion yarn, carries it into the middle of the fabric and passes it through to another gripper, which pulls the yarn out of the fabric. Both grippers are attached to a flexible tape that slides along a support connected to the sley. This tape is driven by the *rapier wheel*. The rapier wheel's oscillating motion can be realized by for instance a 3D-linkage system (as used by Picanol) or a cam system.

### 2.1.4 Specific Issues

A major dynamic issue in a weaving machine is its **start/stop behavior**. A weaving machine needs to be at nominal speed at the end of the first machine cycle, in order to avoid faults in the fabric. A classical AC-motor cannot yield the required start-up torque and necessitates the use of a flywheel, connected to the machine via an electromagnetic coupling. The motor starts up the flywheel, which is subsequently connected to the machine. The transfer of kinetic energy from the flywheel to the machine results in sufficiently fast start-up.

Thanks to the development of a powerful, switched-reluctance (SR) motor, Picanol weaving machines no longer require a start-up flywheel, since the SR motor produces enough torque to bring the machine to nominal speed in one machine cycle. As a result, Picanol machines are characterized by a **small flywheel** and a compact drive system.

Besides the start-stop behavior, a second important issue in a weaving machine is its **variability**. For example, different fabrics require different synchronizations between the shed and the sley mechanism. Furthermore, the number of moving frames is also variable. Moreover, weaving machines are driven at a multitude of speeds. Robustness for variable configurations and variable drive speeds is therefore an important issue when developing methods for enhancing the dynamic behavior of a weaving machine.

**Energy efficiency** is an important sales argument for weaving machinery. In this respect, the compactness of Picanol's direct drive system is beneficial. Moreover, in order to further limit the motor's energy consumption, it is controlled by a low-bandwidth controller.

## 2.2 Simplified Airjet Weaving Machine Model

In this work, *airjet* weaving machines are considered, for which a simplified model is shown in Fig.2.4. An electrical SR motor directly<sup>2</sup> drives the sley axis, on which a flywheel of inertia  $J_{\text{fly}} = 0.7385 \text{ kg}\cdot\text{m}^2$  and the sley cam-follower mechanism (Section 2.2.1) are mounted.  $J_{\text{fly}}$  represents the rotational inertia, reduced to the sley axis, of all rotating parts (motor inertia, cams, gears, ...). Via a 1:2 reduction, the motor drives the shed axis, on which the shed cam-follower mechanism (Section 2.2.2) is mounted.

The grey boxes schematically indicate the cam-follower mechanisms: for instance, the upper grey box contains a conjugate cam-follower mechanism, as the one shown in Fig.1.1(b). The synchronization between the cam-follower mechanisms is variable (Section 2.2.3).

---

<sup>2</sup>In reality, the motor drives the sley axis via a 1:2 reduction, which is omitted from the model for reasons of simplicity. The 1:2 reduction is taken into account when reducing the motor inertia to the sley axis.

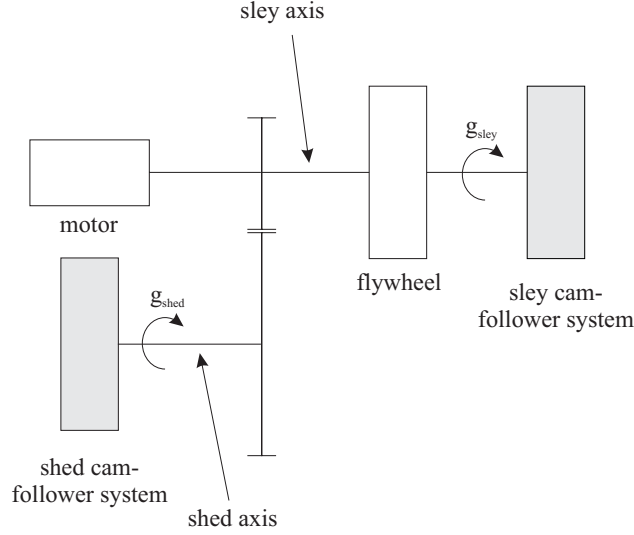


FIGURE 2.4: Simplified airjet weaving machine model.

$g_{\text{sley}}$  and  $g_{\text{shed}}$  [rad] denote the rotation angle of the sley and shed axis respectively. The shed axis turns at half<sup>3</sup> the speed of the sley axis:  $\dot{g}_{\text{shed}} = \dot{g}_{\text{sley}}/2$ . As a result, the shed mechanism's period  $2\pi/\Omega_{\text{shed}}$  [s] is double the sley mechanism's period  $2\pi/\Omega_{\text{sley}}$  [s], where  $\Omega_{\text{shed}}$  and  $\Omega_{\text{sley}}$  [rad/s] respectively denote the mean drive speed of the shed and the sley axis. In reciprocating machinery, the period of motion is determined by the slowest turning axis to which a mechanism is attached. For the model of Fig.2.4, the machine period  $T$  [s] hence equals  $T = 2\pi/\Omega_{\text{shed}} = 4\pi/\Omega_{\text{sley}}$ .

### 2.2.1 Sley Cam-Follower Mechanism

The sley constitutes the oscillating follower of the sley cam-follower mechanism. It is statically balanced and has a centroidal moment of inertia  $J_{\text{sley}}$  of  $0.766 \text{ kg}\cdot\text{m}^2$ .  $F_{\text{sley}}$  [rad] denotes the sley *motion law*, that is, the function that gives the sley's displacement as a function of the sley axis angle  $g_{\text{sley}}$ . It is synthesized as a finite Fourier series with six harmonics:

$$F_{\text{sley}}(g_{\text{sley}}) = a_0 + \sum_{k=1}^6 a_k \cdot \cos(k \cdot g_{\text{sley}}) + b_k \cdot \sin(k \cdot g_{\text{sley}}). \quad (2.1)$$

<sup>3</sup>Depending on the fabric to be woven, the shed axis turns at half, one third, one fourth,... of the sley axis speed. Here, the shed axis speed is half the sley axis speed, since this is the speed at which the shed axis turns in the experimental setup, discussed in Chapter 7.

In order to obtain  $f_{\text{sley}}(t)$  [rad], that is, the sley's displacement as a function of time,  $F_{\text{sley}}(g_{\text{sley}})$  has to be evaluated for some time trajectory of  $g_{\text{sley}}(t)$ . The corresponding velocity and acceleration time trajectories are found by applying the chain rule for differentiation (a dot ( $\dot{\phantom{x}}$ ) denotes a time-derivative, whereas a prime ( $\prime$ ) denotes a derivative with respect to  $g_{\text{sley}}$ ):

$$f_{\text{sley}}(t) = F_{\text{sley}}(g_{\text{sley}}); \quad (2.2a)$$

$$\dot{f}_{\text{sley}}(t) = F'_{\text{sley}}(g_{\text{sley}}) \cdot \dot{g}_{\text{sley}}; \quad (2.2b)$$

$$\ddot{f}_{\text{sley}}(t) = F''_{\text{sley}}(g_{\text{sley}}) \cdot \dot{g}_{\text{sley}}^2 + F'_{\text{sley}}(g_{\text{sley}}) \cdot \ddot{g}_{\text{sley}}. \quad (2.2c)$$

As cams are designed for a constant input speed, the sley's *desired* displacement, velocity, and acceleration as a function of time (for a given period of motion  $2\pi/\Omega_{\text{sley}}$ ) are obtained by choosing  $g_{\text{sley}} = \Omega_{\text{sley}} \cdot t$  as the input trajectory and applying (2.2a–2.2c):

$$f_{\text{sley}}^*(t) = F_{\text{sley}}(\Omega_{\text{sley}} \cdot t); \quad (2.3a)$$

$$\dot{f}_{\text{sley}}^*(t) = F'_{\text{sley}}(\Omega_{\text{sley}} \cdot t) \cdot \Omega_{\text{sley}}; \quad (2.3b)$$

$$\ddot{f}_{\text{sley}}^*(t) = F''_{\text{sley}}(\Omega_{\text{sley}} \cdot t) \cdot \Omega_{\text{sley}}^2. \quad (2.3c)$$

Figure 2.5 shows one sley period  $2\pi/\Omega_{\text{sley}} = 0.0666$  s of  $f_{\text{sley}}^*$  [rad] and its time-derivatives for a constant drive speed  $\Omega_{\text{sley}}$  of 900 rpm.

### 2.2.2 Shed Cam-Follower Mechanism

The shed cam-follower mechanism is a simplified representation of the (group of) cam-linkage mechanism(s), shown in Fig.2.2. It consists of a rotating, conjugate cam with a translating follower (that is, the ensemble of the frames). This simplification is justified, from a kinematic and dynamic point of view, in Section 7.1.1 and Appendix J.

The translating follower represents the ensemble of the frames. The number of frames in motion depends on the fabric to be woven and is denoted by  $N_{\text{shed}}$ . Each frame is assumed to have an equivalent mass of 13 kg. Hence, the mass of the shed follower equals  $J_{\text{shed}} = N_{\text{shed}} \cdot 13$  kg.

$F_{\text{shed}}$  [m] denotes the shed follower's motion law. It is synthesized as a finite Fourier series with a first, third and fifth harmonic:

$$F_{\text{shed}}(g_{\text{shed}}) = a_0 + \sum_{k=1,3,5} c_k \cdot \cos(k \cdot g_{\text{shed}}) + d_k \cdot \sin(k \cdot g_{\text{shed}}). \quad (2.4)$$

The displacement, velocity and acceleration trajectories as a function of time are determined in a similar fashion as for the sley motion (a dot ( $\dot{\phantom{x}}$ ) denotes a time-derivative, whereas a prime ( $\prime$ ) denotes a derivative with respect to

$g_{\text{shed}}$ ):

$$f_{\text{shed}}(t) = F_{\text{shed}}(g_{\text{shed}}); \quad (2.5a)$$

$$\dot{f}_{\text{shed}}(t) = F'_{\text{shed}}(g_{\text{shed}}) \cdot \dot{g}_{\text{shed}}; \quad (2.5b)$$

$$\ddot{f}_{\text{shed}}(t) = F''_{\text{shed}}(g_{\text{shed}}) \cdot \dot{g}_{\text{shed}}^2 + F'_{\text{shed}}(g_{\text{shed}}) \cdot \ddot{g}_{\text{shed}}. \quad (2.5c)$$

The desired displacement, velocity and acceleration as a function of time are obtained by choosing  $g_{\text{shed}} = \Omega_{\text{shed}} \cdot t$  as the input trajectory and applying (2.5a–2.5c):

$$f_{\text{shed}}^*(t) = F_{\text{shed}}(\Omega_{\text{shed}} \cdot t); \quad (2.6a)$$

$$\dot{f}_{\text{shed}}^*(t) = F'_{\text{shed}}(\Omega_{\text{shed}} \cdot t) \cdot \Omega_{\text{shed}}; \quad (2.6b)$$

$$\ddot{f}_{\text{shed}}^*(t) = F''_{\text{shed}}(\Omega_{\text{shed}} \cdot t) \cdot \Omega_{\text{shed}}^2. \quad (2.6c)$$

Figure 2.6 shows one period  $2\pi/\Omega_{\text{shed}} = 0.1333$  s of  $f_{\text{shed}}^*$  [m] and its time-derivatives for a constant drive speed  $\Omega_{\text{shed}}$  of  $900/2=450$  rpm.

### 2.2.3 Crossing Angle

Besides  $N_{\text{shed}}$ , another important setting of a weaving machine is the so-called *crossing angle*  $g_{\text{cross}}$  [rad], which determines the synchronization between the sley and the shed follower motion. It was previously stated that  $\dot{g}_{\text{shed}} = \dot{g}_{\text{sley}}/2$ , suggesting that  $g_{\text{shed}} = g_{\text{sley}}/2$ . In fact, the following is true:

$$g_{\text{shed}} = \frac{g_{\text{sley}} - g_{\text{cross}}}{2}. \quad (2.7)$$

$g_{\text{cross}}$  can assume any value between 280 and 360 degrees and is interpreted as follows. Since the shed axis turns at half the speed of the sley axis, one shed period takes 720 sley axis degrees.  $g_{\text{cross}} = 360$  degrees means that the shed follower passes through its zero position after 360 sley axis degrees. In Fig.2.6, the shed follower passes through its zero position at  $t = 0.0555$  s. The period being 0.1333 s, this implies that the crossing angle equals

$$\frac{0.0555}{0.1333} \cdot 720 = 300^\circ.$$

$g_{\text{cross}} = 280$  or  $360$  degrees corresponds to an 'extremely early' or an 'extremely late' crossing respectively.

## 2.3 Eigenmotion of Reciprocating Machinery

**Forward Dynamic Approach: Motor Models** As explained in Section 1.2.3, a forward dynamic approach for determining the dynamic reactions

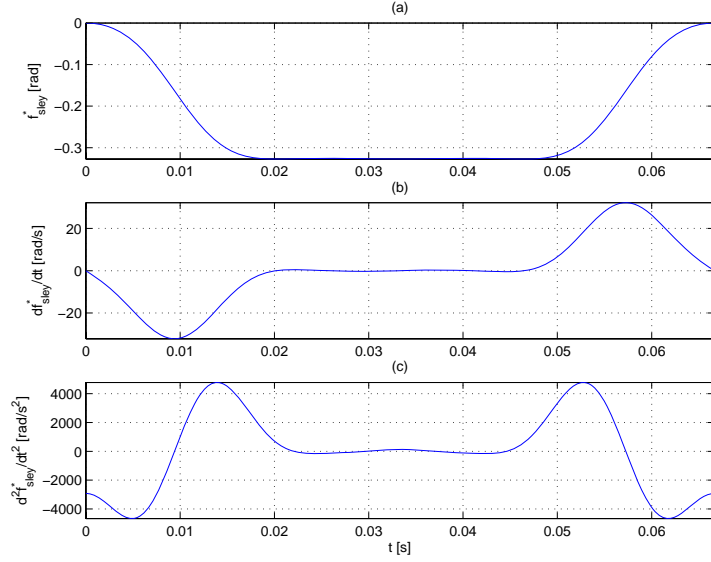


FIGURE 2.5: One period of the desired position (a), velocity (b) and acceleration (c) of the sley, as a function of time ( $\Omega_{\text{sley}} = 900$  rpm).

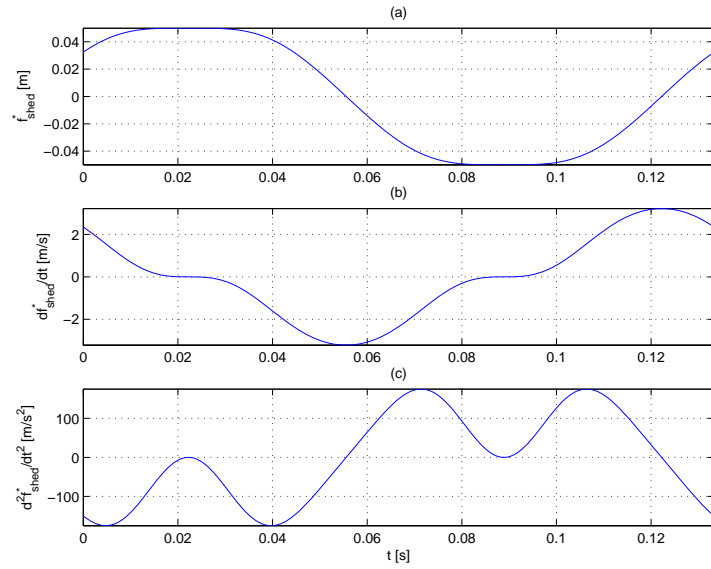


FIGURE 2.6: One period of the desired position (a), velocity (b) and acceleration (c) of the shed follower, as a function of time ( $\Omega_{\text{shed}} = 450$  rpm,  $g_{\text{cross}} = 300^\circ$ ).

requires a model of both the mechanism/machine *and* its driving actuator. Three kinds of actuator models are distinguished here (in decreasing order of complexity): (i) a complete dynamic model of the driving actuator, including its control system (Sadler et al., 1980; Mayne et al., 1980; Myklebust, 1982; Liou et al., 1991); (ii) a torque-speed model that models the motor as some torque-speed relationship, such as a motor torque that varies linearly with drive speed (Kulitzscher, 1970), or a quadratic relationship (Liniecki, 1969; Wiederrich, 1982; Taşcan, 1985, 1988) and (iii) a source of constant torque  $M_{\text{mot}}$  [N-m] in series with the motor's rotor inertia.

In the latter model, the constant motor torque  $M_{\text{mot}}$  is such that some desired average drive speed  $\Omega$  is realized, despite the present energy dissipation. Since the amount of energy dissipation depends on  $\Omega$ , there is a one-to-one relation between the desired  $\Omega$  and the applied  $M_{\text{mot}}$ : if  $M_{\text{mot}}$  is too small, the energy dissipation causes the machine to slow down to standstill. Conversely, if it is too large, the machine accelerates to an infinite average drive speed. If no energy dissipation, nor external work forces are present,  $M_{\text{mot}}$  is zero. Such a machine is *conservative*, that is, the sum of its potential and kinetic energy is constant as a function of time. This constant energy level determines the resulting average drive speed  $\Omega$ .

**(Damped) Eigenmotion: Formal Definition** Based on this third kind of actuator model, the concepts of eigenmotion and damped eigenmotion are introduced. *Eigenmotion* is formally defined as *the regime motion of a reciprocating machine in which no energy dissipation nor external work forces are present, and in which the motor exerts a zero torque*. This is not the same as the regime motion that would occur in a reciprocating machine without energy dissipation and external work forces, from which the motor is *decoupled*. In that case, the motor's rotor inertia is no longer present, and a different periodic motion results.

*Damped Eigenmotion* is defined as *the regime motion of a reciprocating machine in which energy dissipation is present, and in which the motor exerts a constant torque  $M_{\text{mot}}$  to realize some desired average drive speed  $\Omega$* .

(Damped) eigenmotion is a useful tool for studying the regime behavior of reciprocating machines that are driven by a motor with a *low-bandwidth* controller. Due to the low bandwidth of the controller, the resulting regime motor torque is varying with a *small* amplitude around some average value  $M_{\text{mot}}$ , which depends on the desired average drive speed  $\Omega$  and the amount of energy dissipation in the machine. Based on the definition of damped eigenmotion, it follows that damped eigenmotion provides a good approximation of the regime behavior of such a machine, the approximation being better if the motor torque fluctuation is smaller (that is, if the controller bandwidth is lower). If additionally, friction losses are small, damped eigenmotion and eigenmotion are virtually identical, and eigenmotion itself yields a good approximation of the machine's regime behavior.

Picanol weaving machines are an example of reciprocating machines with a low-bandwidth controller<sup>4</sup>. As a result, damped eigenmotion is a useful concept for approximating their regime motion. The main advantage of this approach is that no detailed information concerning the motor or its control system is required: only the motor's rotor inertia needs to be known.

**State-of-the-Art and Contributions** Eigenmotion is a literal translation of the German term *Eigenbewegung*, and is a well-known concept in German literature: general expressions for the resulting differential equation, are given in e.g. (VDI2149, 1999; Dresig, 2001). In Anglo-Saxon literature, on the other hand, only Sherwood (1968) determines a mechanism's forward dynamic regime behavior by considering it to be conservative.

While eigenmotion itself is well-known, the idea of applying a constant motor torque in order to overcome friction losses, that is, damped eigenmotion, is new in literature. The main rationale for applying a constant motor torque is obtaining a machine motion that is very similar to the 'true' eigenmotion, despite the presence of energy dissipation. Obtaining an eigenmotion-like behavior in the presence of friction is a basic prerequisite for inertially compensated cams to function properly (Section 3.5).

Calculating (damped) eigenmotion is done here by formulating boundary value problems and solving them using (well-known) nonlinear least-squares techniques. This is a novel concept, compared to all other forward dynamic approaches known in literature, which are based on direct time integration of the governing differential equation.

Another novel concept is the development of *Average Speed Control* (ASC) in Section 7.2. This is a simple control technique, designed such that a motor, operated in torque mode<sup>5</sup>, acts as a constant torque source. In this way, damped eigenmotion can be implemented on a practical setup.

## 2.4 Frequency-Domain Eigenmotion Determination

This section develops a frequency-domain approach for calculating the eigenmotion of a reciprocating machine. First, eigenmotion determination is formulated as a boundary value problem (Section 2.4.1). After that, a nonlinear least-squares approach is proposed for solving this boundary value problem (Section 2.4.2). The method is developed by applying it to the simplified airjet weaving machine model of Fig.2.4.

---

<sup>4</sup>The motivation for using such a controller is to avoid high motor torques and the corresponding high motor currents. As a result, energy losses due to the finite motor efficiency are reduced.

<sup>5</sup>Torque mode implies that the analogue voltage, applied to the motor's control input, is interpreted as some desired motor torque.

### 2.4.1 Derivation of Boundary Value Problem

The definition of eigenmotion implies that the reciprocating machine is *conservative*, that is, the sum of its potential and kinetic energy is constant as a function of time. For a purely inertial machine, such as the simplified airjet weaving machine model of Fig.2.4, conservation of energy reduces to conservation of kinetic energy:

$$T_{\text{tot}}(t) = T_{\text{tot}}(0), \forall t \in [0, T], \quad (2.8)$$

where  $T$  [s] represents the machine period. The first step in the derivation of the boundary value problem (BVP) is therefore determining an expression for the total kinetic energy  $T_{\text{tot}}$  [J] of the reciprocating machine. For the model of Fig.2.4,  $T_{\text{tot}}$  is the sum of the kinetic energy of the flywheel, the sley and the shed follower:

$$T_{\text{tot}}(t) = T_{\text{fly}}(t) + T_{\text{sley}}(t) + T_{\text{shed}}(t). \quad (2.9)$$

Based on (1.4), it follows that:

$$T_{\text{tot}}(t) = \frac{J_{\text{fly}} \cdot \dot{g}_{\text{sley}}^2}{2} + \frac{J_{\text{sley}} \cdot \dot{f}_{\text{sley}}^2}{2} + \frac{J_{\text{shed}} \cdot \dot{f}_{\text{shed}}^2}{2}. \quad (2.10)$$

Combining (2.8) with (2.2b), (2.5b), (2.7) and (2.10) shows that eigenmotion is governed by a first-order differential equation in  $g_{\text{sley}}$ . Without loss of generality, the initial condition  $g_{\text{sley}}(0) = 0$  is imposed.

Two approaches are possible for solving (2.8). Application of standard numerical integration techniques, that is, solving it as an *ordinary differential equation*, requires that also an initial value of  $\dot{g}_{\text{sley}}(t)$  be chosen, in order to determine  $T_{\text{tot}}(0)$ . A periodical response results, its period depending on the adopted value of  $\dot{g}_{\text{sley}}(0)$ . The value  $\dot{g}_{\text{sley}}(0)$ , giving rise to some prescribed period of motion, can be determined by trial-and-error. Another approach is considering (2.8) as a *boundary value problem*, by imposing:

$$\begin{cases} T_{\text{tot}}(t) &= T_{\text{tot}}(0), \forall t \in [0, T]; \\ g_{\text{sley}}(0) &= 0; \\ g_{\text{sley}}(T) &= g_{\text{sley}}(0) + 4\pi. \end{cases} \quad (2.11)$$

This guarantees the resulting response to have the correct periodicity  $T$ <sup>(6)</sup>. Several techniques exist for solving this kind of problems. Finite difference techniques, for instance, are well-developed (Ascher et al., 1988). Here however, a nonlinear least-squares approach is adopted, based on parameterizing the solution  $g_{\text{sley}}$  as a finite Fourier series. This is the subject of the next section.

<sup>6</sup>The periodicity of the machine is the length of the time interval in which the shed axis makes one complete revolution. Hence, during one machine period, the sley axis makes two complete revolutions, such that  $g_{\text{sley}}(T) = g_{\text{sley}}(0) + 4\pi$  needs to be imposed.

### 2.4.2 Solution of Boundary Value Problem

The requirement that  $g_{\text{sley}}(T) = g_{\text{sley}}(0) + 4\pi$ , is met automatically if  $\dot{g}_{\text{sley}}(t)$  is parameterized as a Fourier series with average value  $4\pi/T$  and period  $T$ :

$$\dot{g}_{\text{sley}}(t) = \frac{4\pi}{T} + \sum_{k=1}^{\infty} a_k \cdot \cos(k\Omega t) + b_k \cdot \sin(k\Omega t),$$

where  $\Omega = 2\pi/T = \Omega_{\text{shed}}$ . Solving (2.11) is equivalent to determining the unknown amplitudes  $a_k$  and  $b_k$ ,  $k = 1 \dots \infty$ . In order to limit the number of unknown parameters, the Fourier series is truncated after  $K$  harmonics:

$$\dot{g}_{\text{sley}}(t) = \frac{4\pi}{T} + \sum_{k=1}^K a_k \cdot \cos(k\Omega t) + b_k \cdot \sin(k\Omega t). \quad (2.12)$$

Hence  $\hat{g}_{\text{sley}}(t)$  and its second derivative  $\ddot{\hat{g}}_{\text{sley}}(t)$  are given by:

$$\hat{g}_{\text{sley}}(t) = C + \frac{4\pi}{T} \cdot t + \sum_{k=1}^K a_k \cdot \frac{1}{k\Omega} \cdot \cos\left(k\Omega t - \frac{\pi}{2}\right) + b_k \cdot \frac{1}{k\Omega} \cdot \sin\left(k\Omega t - \frac{\pi}{2}\right); \quad (2.13)$$

$$\ddot{\hat{g}}_{\text{sley}}(t) = \sum_{k=1}^K a_k \cdot k\Omega \cdot \cos\left(k\Omega t + \frac{\pi}{2}\right) + b_k \cdot k\Omega \cdot \sin\left(k\Omega t + \frac{\pi}{2}\right). \quad (2.14)$$

$C$  denotes an integration constant. The hats ( $\hat{\cdot}$ ) are introduced since, due to the truncation of the Fourier series, not the exact solution  $g_{\text{sley}}$  is calculated, but an approximation  $\hat{g}_{\text{sley}}$  of it. The value of  $K$  is a compromise between obtaining an accurate solution and limiting the number ( $2K$ ) of unknown parameters (and hence the required computational time). For the simulations of this chapter,  $K = 20$  results in a good compromise between these conflicting demands. The unknown parameters are grouped into the parameter vector  $\mathbf{z} \in \mathbb{R}^{2K}$ :

$$\mathbf{z} = [ a_1 \quad b_1 \quad \dots \quad a_K \quad b_K ]^T. \quad (2.15)$$

The integration constant  $C$  is not part of  $\mathbf{z}$  since its value is determined by the initial condition  $\hat{g}_{\text{sley}}(0) = 0$ . Because of the parameterization,  $\hat{g}_{\text{sley}}$  and its derivatives are denoted as  $\hat{g}_{\text{sley}}(t, \mathbf{z})$ ,  $\dot{\hat{g}}_{\text{sley}}(t, \mathbf{z})$  and  $\ddot{\hat{g}}_{\text{sley}}(t, \mathbf{z})$ . The unknown parameter vector  $\mathbf{z}$  is determined via the following unconstrained optimization problem:

$$\mathbf{z} = \min_{\mathbf{z} \in \mathbb{R}^{2K}} \int_0^T d^2(t, \mathbf{z}) dt,$$

in which the residual function  $d(t)$  is defined, based on (2.8), as:

$$d(t, \mathbf{z}) = T_{\text{tot}}(t, \mathbf{z}) - T_{\text{tot}}(0, \mathbf{z}), t \in [0, T].$$

In order to numerically solve this *nonlinear least-squares problem*, it is approximated by

$$\mathbf{z} = \min_{\mathbf{z} \in \mathbb{R}^{2K}} T_s \cdot \sum_{l=1}^L d^2((l-1) \cdot T_s, \mathbf{z}), \quad (2.16)$$

where  $f_s = 1/T_s$  is the rate at which  $d(t, \mathbf{z})$  is sampled and  $T_s = T/L$ .  $L \in \mathbb{Z}$  denotes the number of sampling points within one period of motion. Although this problem can be solved using a general purpose unconstrained optimization technique, it is more efficient to apply a dedicated nonlinear least-squares technique such as the Levenberg-Marquardt algorithm. This algorithm exploits the special structure of the gradient and Hessian matrix, and hence results in faster convergence (Nocedal and Wright, 1999). It is implemented in the `lsqnonlin` algorithm of the MATLAB OPTIMIZATION TOOLBOX which is used to solve (2.16). The algorithm always converges to a physically meaningful solution, which is verified by inspection of the resulting residual  $d(t, \mathbf{z})$ . Once  $\mathbf{z}$  is calculated,  $\hat{g}_{\text{sley}}$  and its time-derivatives follow from (2.13), (2.12) and (2.14).

## 2.5 Eigenmotion of an Airjet Weaving Machine

Using the techniques developed in the previous section, the eigenmotion of the simplified airjet weaving machine model is calculated here. Section 2.2 provides all model data. It is assumed that the crossing angle  $g_{\text{cross}}$  equals  $300^\circ$  and that  $N_{\text{shed}} = 8$  frames are moving.  $\Omega_{\text{sley}}$  equals 900 rpm.

**Drive Speed Fluctuation** Figure 2.7 shows the resulting rotation angle, velocity and acceleration of the sley axis if the machine period  $T$  equals 0.1333 s ( $\Omega_{\text{sley}} = 900$  rpm). The coefficient of drive speed fluctuation  $\kappa$  [%], defined as:

$$\kappa = 100 \cdot \frac{\dot{g}_{\text{sley,max}} - \dot{g}_{\text{sley,min}}}{\dot{g}_{\text{sley,avg}}} = 100 \cdot \frac{\dot{g}_{\text{sley,max}} - \dot{g}_{\text{sley,min}}}{\Omega_{\text{sley}}}, \quad (2.17)$$

equals 12.2%, and is hence substantial. The drive speed fluctuation is due to the exchange of kinetic energy between the cam mechanisms and the flywheel, as shown in Fig.2.8. Clearly, the sum of the kinetic energies of the sley and shed follower mechanism is heavily fluctuating (Fig.2.8(a)), between zero (when both followers stand still) and a maximum of 784 J. As a consequence, the flywheel kinetic energy  $T_{\text{fly}}$  (Fig.2.8(b)) must fluctuate with the same amplitude, in order to keep the total kinetic energy  $T_{\text{tot}}$  constant (Fig.2.8(c)). Due to the limited flywheel size, the aforementioned significant drive speed fluctuation of 12.2% results.

Figure 2.8(c) shows the effect of the truncation of the Fourier series to  $K = 20$  harmonics: the total kinetic energy is not perfectly constant, but exhibits

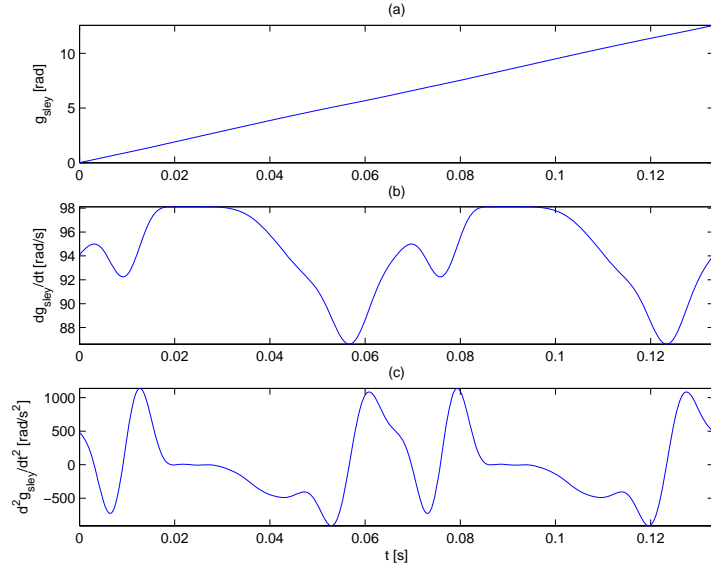


FIGURE 2.7: Eigenmotion of an airjet weaving machine: one machine period of the rotation angle (a), velocity (b) and acceleration (c) of the sley axis.

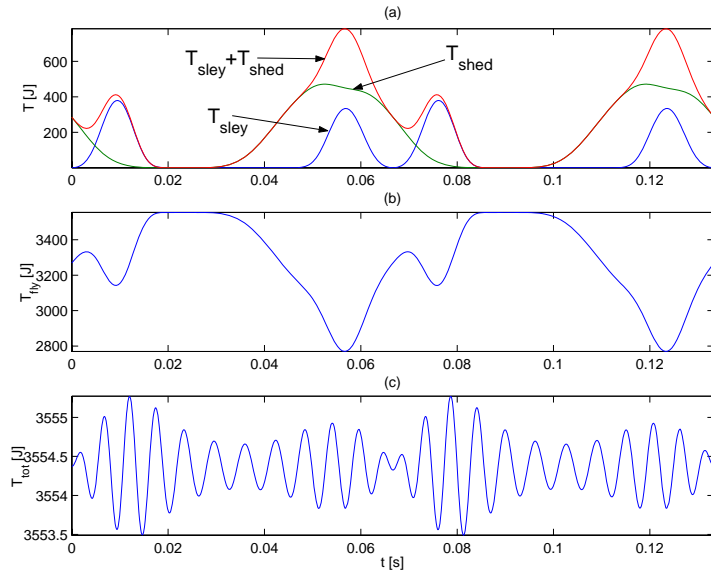


FIGURE 2.8: Eigenmotion of an airjet weaving machine: one machine period of the kinetic energy of the sley and the shed mechanism (a), kinetic energy of the flywheel (b) and total kinetic energy (c).

some jitter with a dominant 21st/22nd harmonic. The jitter amplitude of approximately 2 J is negligible, compared to the amplitude of the energy signals, plotted in Fig.2.8(a – b).

**Follower Motion Distortion (time domain)** Cams are classically designed with a constant drive speed in mind. Drive speed fluctuations as large as the ones shown in Fig.2.7(b) therefore cause significant motion distortion. This is illustrated in Fig.2.9–2.10, which show the desired and actually realized position, velocity and acceleration, and their difference, for the case of the sley and the shed follower respectively. The distortion of the accelerations is significant.

**Follower Motion Distortion (frequency domain)** The motion distortion gives rise to significant undesired harmonics in the acceleration spectrum of both the sley and the shed follower.

Figure 2.12 compares the desired and the actually realized *shed* follower acceleration in the frequency domain, by showing the amplitude  $A_k$  [dB re 1 m/s<sup>2</sup>]<sup>(7)</sup> of the harmonics  $k = \{1, 3, \dots, 15\}$  of  $\Omega_{\text{shed}}$  [rad/s]. As expressed by (2.4), the desired shed follower acceleration has a first, third and fifth harmonic of  $\Omega_{\text{shed}}$  [rad/s]. These desired harmonics are slightly distorted in the actually realized shed follower acceleration. More importantly however, significant undesired harmonics  $k = \{7, 9, 11, 13, \dots\}$  pop up: the seventh and ninth harmonic, for instance, are only 9 dB<sup>(8)</sup> (that is, a factor 3) lower than the desired, fifth harmonic. The inertial forces, corresponding to these undesired acceleration harmonics, excite frame resonances.

Although dynamic problems have mainly developed for the frames, undesired harmonics  $k = \{7, 8, 9, \dots\}$ <sup>(9)</sup> of  $\Omega_{\text{sley}}$  are also present in the *sley* acceleration spectrum, as shown by Fig.2.11. If they are not so harmful, this can mainly be attributed to the fact that the sley follower is a massive part, as opposed to the lightweight and therefore flexible frames.

---

<sup>7</sup>Throughout this thesis,  $A_k$  is defined as follows, for a signal  $y(t)$  [b] with period  $T$ :

$$y(t) = A_0 + \sum_{k=1}^{\infty} A_k \cdot \cos(k\Omega t + \zeta_k),$$

where  $\Omega = 2\pi/T$ . ( $A_k, \zeta_k$ ) are numerically determined using the Discrete Fourier Transform (DFT) algorithm. The amplitudes  $A_k$  [b] are graphically depicted on a [dB re b] scale, which is defined as follows:

$$A_k \text{ [dB re } b] = 20 \cdot \log_{10} \left( \frac{A_k}{b} \right).$$

<sup>8</sup>In comparing two signals expressed on a [dB re b] scale, the resulting dB-value is independent of the used reference  $b$ . Hence, '9 dB' is written here, instead of '9 [dB re 1m/s<sup>2</sup>]'.

<sup>9</sup>As expressed by (2.1), the sley acceleration is supposed to contain only the first six harmonics of  $\Omega_{\text{sley}}$  [rad/s].

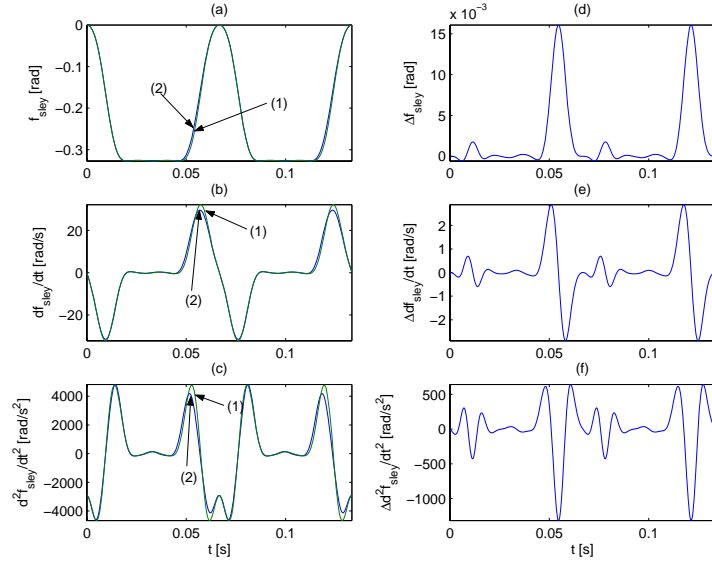


FIGURE 2.9: Sley motion during eigenmotion of an airjet weaving machine: one machine period of the desired (1) and actually realized (2) position (a), velocity (b) and acceleration (c), and their difference (d – e – f).

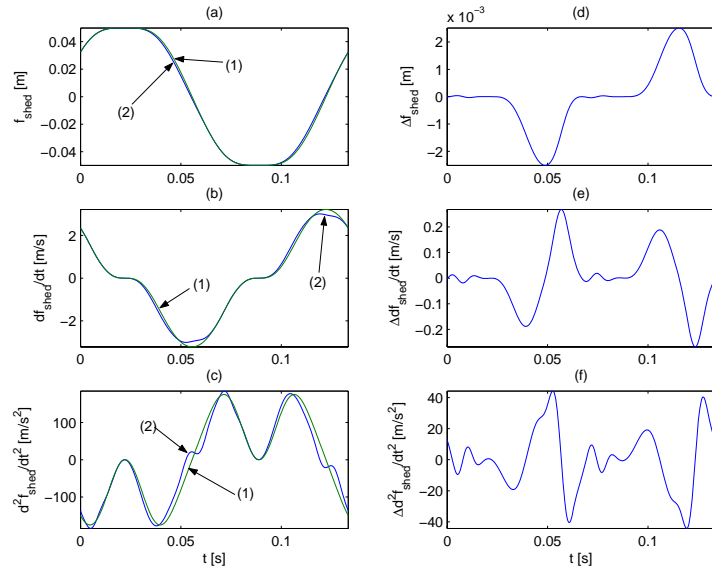


FIGURE 2.10: Shed follower motion during eigenmotion of an airjet weaving machine: one machine period of the desired (1) and actually realized (2) position (a), velocity (b) and acceleration (c), and their difference (d – e – f).

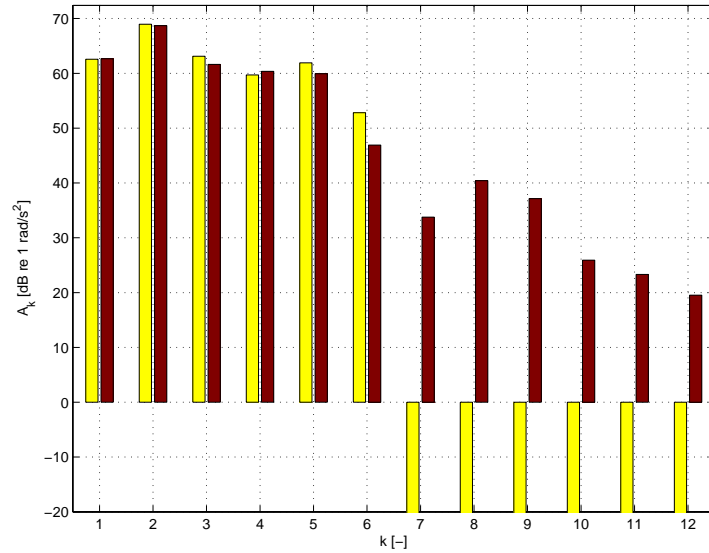


FIGURE 2.11: Eigenmotion of an airjet weaving machine: spectrum [dB re 1 rad/s<sup>2</sup>] of the desired (left bar) and actually realized (right bar) sley acceleration. Values of -20 [dB re 1 rad/s<sup>2</sup>] are used to indicate  $A_k = 0$  values.

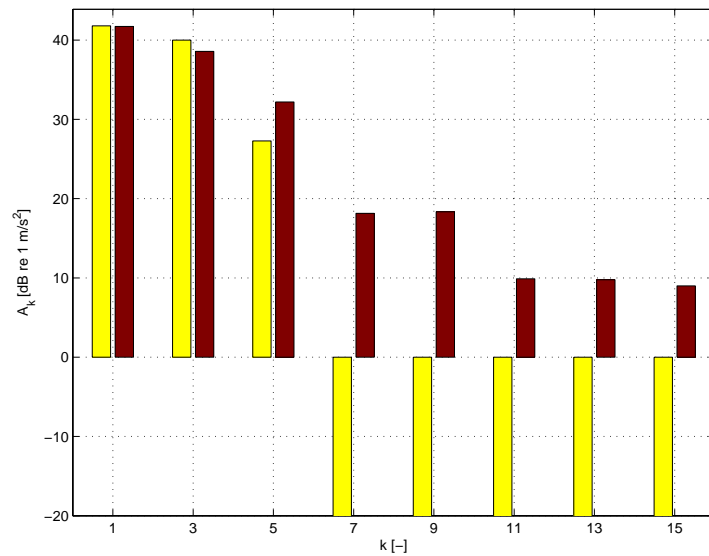


FIGURE 2.12: Eigenmotion of an airjet weaving machine: spectrum [dB re 1 m/s<sup>2</sup>] of the desired (left bar) and actually realized (right bar) shed follower acceleration. Values of -20 [dB re 1 m/s<sup>2</sup>] are used to indicate  $A_k = 0$  values. Only the uneven harmonics are relevant; the even harmonics have therefore been omitted from the figure.

## 2.6 Frequency-Domain Damped Eigenmotion Determination

This section develops the frequency-domain approach for calculating the damped eigenmotion of a reciprocating machine. First, the adopted energy dissipation mechanism is discussed. After that, the frequency-domain approach itself is briefly outlined.

### 2.6.1 Energy Dissipation Mechanism

Viscous friction is often used to model energy dissipation in cam-follower mechanisms. However, in the field of high-speed overhead cam mechanisms, formerly often used in automotive applications, Coulomb friction at the rocker pivot has been proven (Pisano and Freudenstein, 1983) to be the major source of energy dissipation. Subsequent efforts to model the dynamics of cam mechanisms have therefore emphasized the role of Coulomb friction (Pisano, 1984; Hanachi and Freudenstein, 1986; Ünlüsoy and Tümer, 1994).

For this reason, a counteracting Coulomb friction torque  $M_{\text{coul,sley}}$  [N-m] and a counteracting Coulomb friction force  $M_{\text{coul,shed}}$  [N] are assigned to the sley and shed follower respectively, in order to introduce energy dissipation in the model of Fig.2.4. For convenience, both are assumed to have equal numerical values (though different units: [N-m] for  $M_{\text{coul,sley}}$  and [N] for  $M_{\text{coul,shed}}$ ):  $M_{\text{coul,sley}} = M_{\text{coul,shed}} = M_{\text{coul}}$ . In order to make a well-founded choice of  $M_{\text{coul}}$ , the nondimensionalized coefficient of energy dissipation  $\eta$  [-] is introduced as

$$\eta = \frac{E_{\text{loss}}}{T_{\text{tot,avg}}}. \quad (2.18)$$

$T_{\text{tot,avg}}$  [J] denotes the average (over one period) total kinetic energy.  $E_{\text{loss}}$  [J] represents the energy dissipated during one period:

$$E_{\text{loss}} = \int_0^T P_{\text{loss}} \cdot dt,$$

where  $P_{\text{loss}}(t)$  [W] denotes the dissipated power as a function of time. Since the energy dissipation is modelled by Coulomb friction,  $E_{\text{loss}}$  is given by:

$$E_{\text{loss}} = \int_0^T \left( M_{\text{coul,sley}} \cdot |\dot{f}_{\text{sley}}| + M_{\text{coul,shed}} \cdot |\dot{f}_{\text{shed}}| \right) \cdot dt; \quad (2.19a)$$

$$E_{\text{loss}} = \int_0^T M_{\text{coul}} \cdot \left( |\dot{f}_{\text{sley}}| + |\dot{f}_{\text{shed}}| \right) \cdot dt. \quad (2.19b)$$

If a value of  $\eta$ , or conversely,  $E_{\text{loss}}$ , is specified beforehand, the corresponding  $M_{\text{coul}}$  can be calculated approximately by assuming that the actually realized

follower velocities coincide with the desired follower velocities<sup>10</sup>. Taking into account (2.18) and (2.19b), this results in:

$$M_{\text{coul}} \approx \frac{\eta \cdot T_{\text{tot,avg}}}{\int_0^T \left( |\dot{f}_{\text{sley}}^*| + |\dot{f}_{\text{shed}}^*| \right) \cdot dt}, \quad (2.20)$$

where  $T_{\text{tot,avg}}$  is determined based on (2.10).

$\eta = 0$  implies that there is no energy dissipation in the system, whereas  $\eta = 0.20$  implies that the system would almost come to standstill after approximately five periods of motion, in the absence of an external torque applied to the system. In Section 2.7, it is shown that  $\eta = 0.20$  slightly overestimates the energy dissipation in the weaving machine configuration used in this chapter (that is, an airjet weaving machine turning at 900 rpm with  $N_{\text{shed}} = 8$  moving frames).

### 2.6.2 Derivation of Boundary Value Problem

For reference, the definition of damped eigenmotion, given in Section 2.3 is repeated here: damped eigenmotion is the regime motion of a reciprocating machine in which energy dissipation is present, and in which the motor exerts a constant torque  $M_{\text{mot}}$  [N-m] to realize some desired average drive speed  $\Omega$  [rad/s]. Consequently, the reciprocating machine is no longer a conservative system, as in the case of eigenmotion. Therefore, in case of a purely inertial machine, such as the simplified airjet weaving machine model of Fig.2.4, (2.8) is replaced by the following energy balance:

$$T_{\text{tot}}(t) - T_{\text{tot}}(0) = \int_0^t M_{\text{mot}} \cdot \dot{g}_{\text{sley}} \cdot dt - \int_0^t M_{\text{coul}} \cdot \left( |\dot{f}_{\text{sley}}| + |\dot{f}_{\text{shed}}| \right) \cdot dt. \quad (2.21)$$

Combining (2.21) with (2.2b), (2.5b), (2.7) and (2.10) shows that the above expression is a first-order differential equation in  $g_{\text{sley}}$ . Without loss of generality, the initial condition  $g_{\text{sley}}(0) = 0$  is imposed.

Following a similar reasoning as in Section 2.4.2, this differential equation is transformed into a boundary value problem by imposing that  $g_{\text{sley}}(T) = g_{\text{sley}}(0) + 4\pi$ , in order to guarantee the correct periodicity. This boundary value problem is again solved using the nonlinear least-squares approach. For ease of numerical implementation, it is convenient to define the residual function  $d(t)$  based on the time-derivative of (2.21):

$$d(t) = dT_{\text{tot}}/dt - M_{\text{mot}} \cdot \dot{g}_{\text{sley}} + M_{\text{coul}} \cdot \left( |\dot{f}_{\text{sley}}| + |\dot{f}_{\text{shed}}| \right), t \in [0, T]. \quad (2.22)$$

As it is not known in advance what constant torque  $M_{\text{mot}}$  yields a regime response with the correct periodicity, the scalar  $M_{\text{mot}}$  is added to the vector  $\mathbf{z}$  of optimization variables, defined by (2.15).

<sup>10</sup>In other words, it is assumed that  $\dot{g}_{\text{sley}} \equiv \Omega_{\text{sley}}$ .

## 2.7 Damped Eigenmotion of an Airjet Weaving Machine

Using the techniques developed in the previous section, the damped eigenmotion of the simplified airjet weaving machine model is determined here. Except for the added Coulomb friction, the machine model is identical to that of Section 2.5. Comparison is made here between eigenmotion, that is,  $\eta = 0$ , and damped eigenmotion for  $\eta = \{0.10, 0.20\}$ . Based on the desired sley and shed follower motions, the average kinetic energy level  $T_{\text{tot,avg}}$  for  $\Omega_{\text{sley}} = 900$  rpm is determined:  $T_{\text{tot,avg}} = 3559$  J. The numerical values of  $E_{\text{loss}}$  and  $M_{\text{coul}}$  are determined based on (2.18) and (2.20) and given in Table 2.1.

Figure 2.13 compares the sley axis velocity and acceleration trajectories for  $\eta = \{0, 0.10, 0.20\}$ . These trajectories, as well as the  $\kappa$ -values given in Table 2.1, are only slightly dependent on  $\eta$ . As a result, also the sley and shed follower motions depend only slightly on  $\eta$ . This is illustrated by Fig.2.14, which compares the difference<sup>11</sup>  $\Delta \ddot{f}_{\text{shed}}$  [m/s<sup>2</sup>] between the actually realized shed follower acceleration  $\ddot{f}_{\text{shed}}$  and its desired value  $\ddot{f}_{\text{shed}}^*$  for  $\eta = \{0, 0.10, 0.20\}$ . Consequently, also the shed follower acceleration spectrum of Fig.2.15 shows little difference between the different friction regimes.

All these observations confirm the claim of Section 2.3 that, if friction losses are small ( $\eta \leq 0.10$ ), or moderate ( $\eta \leq 0.20$ ), applying a constant motor torque results in a motion (that is, damped eigenmotion) in the presence of energy dissipation, that is very similar to the 'true' eigenmotion. This result is important for the robustness w.r.t. friction of inertially compensated cams (Section 3.5).

The validity of the obtained damped eigenmotion results is proven by checking the different components of the power residual  $d(t)$ , defined by (2.22), for  $\eta = 0.20$ . Figure 2.16(a) shows the powers  $P_{\text{fly}} = dT_{\text{fly}}/dt$ ,

<sup>11</sup>This is the same quantity as shown in Fig.2.10(f).

	$\eta = 0$	$\eta = 0.10$	$\eta = 0.20$
$E_{\text{loss}}$ [J]	-	356	712
$M_{\text{coul}}$ [N-m] or [N]	-	234	468
$\kappa$ [%]	12.2	11.9	11.7
$M_{\text{mot}}$ [N-m]	-	28.3	56.6

TABLE 2.1: Comparison of eigenmotion and damped eigenmotion of an airjet weaving machine: numerical values of some drive system characteristics.

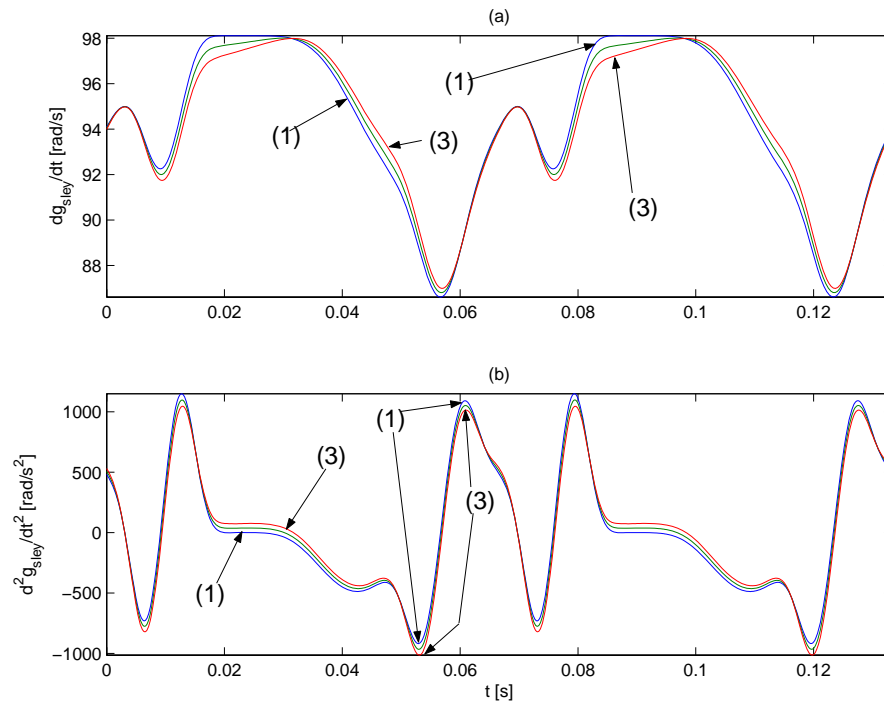


FIGURE 2.13: Comparison of sley axis velocity (a) and acceleration (b) for eigenmotion ( $\eta = 0$ ) and damped eigenmotion ( $\eta = \{0.10, 0.20\}$ ) of an airjet weaving machine. Line (1) gives the results for  $\eta = 0$ ; Line (3) gives the results for  $\eta = 0.20$ ; the line for  $\eta = 0.10$  always lies in between.

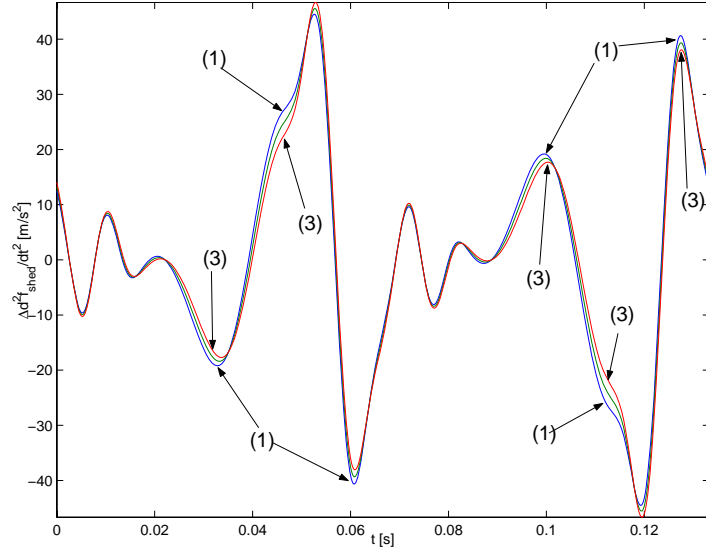


FIGURE 2.14: Comparison of shed follower acceleration difference  $\Delta \ddot{f}_{\text{shed}} = \ddot{f}_{\text{shed}} - \ddot{f}_{\text{shed}}^*$  [m/s<sup>2</sup>] for eigenmotion ( $\eta = 0$ ) and damped eigenmotion ( $\eta = \{0.10, 0.20\}$ ) of an airjet weaving machine. Line (1) gives the results for  $\eta = 0$ ; Line (3) gives the results for  $\eta = 0.20$ ; the line for  $\eta = 0.10$  always lies in between.

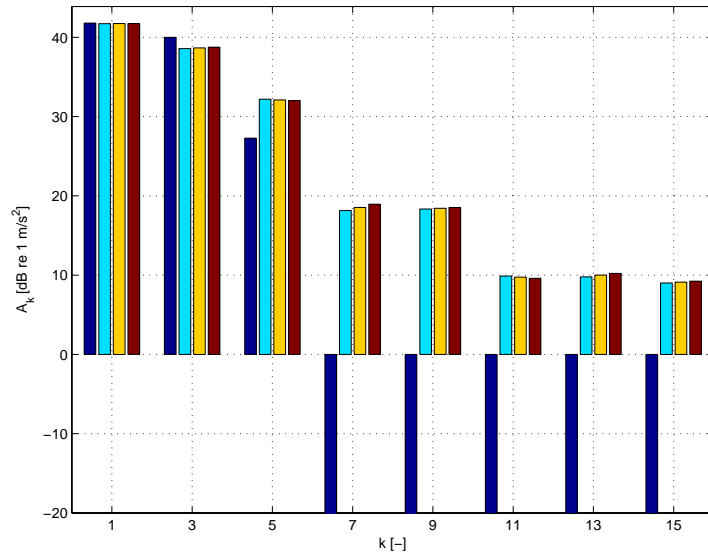


FIGURE 2.15: Desired, eigenmotion ( $\eta = 0$ ) and damped eigenmotion ( $\eta = \{0.10, 0.20\}$ ) spectrum (in that order) of shed follower acceleration [dB re 1 m/s<sup>2</sup>] of an airjet weaving machine. Values of -20 [dB re 1 m/s<sup>2</sup>] are used to indicate  $A_k = 0$  values.

$P_{\text{sley}} = dT_{\text{sley}}/dt$  and  $P_{\text{shed}} = dT_{\text{shed}}/dt$ , associated with respectively the flywheel, sley and shed follower motion. This results in the total (rigid-body motion associated) power  $dT_{\text{tot}}/dt$  of Fig.2.16(b). While substantial powers are exchanged between the flywheel, sley and shed follower, the resulting power fluctuation, visible to the motor, is one order of magnitude lower. This constitutes one of the main advantages of coupling all mechanisms to one drive shaft. On the other hand, it has the disadvantage of creating possibly problematic interactions, such as distortion of the follower motions.

The power  $P_{\text{loss}}$  [W], dissipated due to Coulomb friction, is shown in Fig.2.17(a). Obviously, it is always positive. It exhibits several sharp 'turning points', due to the discontinuity of the Coulomb friction force at velocity reversals. Figure 2.17(a) also shows the power  $P_{\text{mot}} = M_{\text{mot}} \cdot \dot{g}_{\text{sley}}$  injected by the motor. Despite the constant value of  $M_{\text{mot}}$ , it fluctuates due to the sley axis speed fluctuation. The average motor power is about 5.2 kW, which shows that  $\eta = 0.20$  slightly overestimates the real  $\eta$ , as an airjet weaving machine with the configuration used here, normally has a power consumption of about 4.5 kW.

Finally, Fig.2.17(b) shows the power residual  $d(t) = dT_{\text{tot}}/dt - P_{\text{mot}} + P_{\text{loss}}$ . Compared to the magnitudes of its components,  $d$  is virtually zero, except at time instances corresponding to sharp peaks of  $P_{\text{loss}}$ , associated with sley and shed follower velocity reversals. Augmenting the number of harmonics  $K$  could reduce these peaks further, at the expense of a longer computational time. In this case,  $K = 40$  harmonics are used.

## 2.8 Conclusion

**(Damped) Eigenmotion of Reciprocating Machinery** This chapter has formally defined eigenmotion and introduced the novel idea of damped eigenmotion. A method has been developed, based on formulating and solving boundary value problems, for simulating these motions. This method constitutes a *frequency-domain* approach since it directly determines the Fourier coefficients of the machine's regime drive speed. This approach is novel in mechanism literature: all references mentioned in Section 2.4 solve the governing differential equation by numerical integration techniques.

The main advantage of the frequency-domain approach is that the obtained solution inherently has the correct periodicity, without needing a trial-and-error approach. In addition, it is efficient: the regime behavior of the simplified weaving machine model is calculated in a few seconds' time on a laptop equipped with a PIII@600MHz processor.

The presented method has been developed for (damped) eigenmotion determination of a single-degree-of-freedom machine. It is however applicable to any (that is, with an arbitrary number of degrees of freedom) model of a reciprocating machine, using any type of motor model. The price to be paid is the number of unknown parameters contained in the vector  $\mathbf{z}$ , which increases

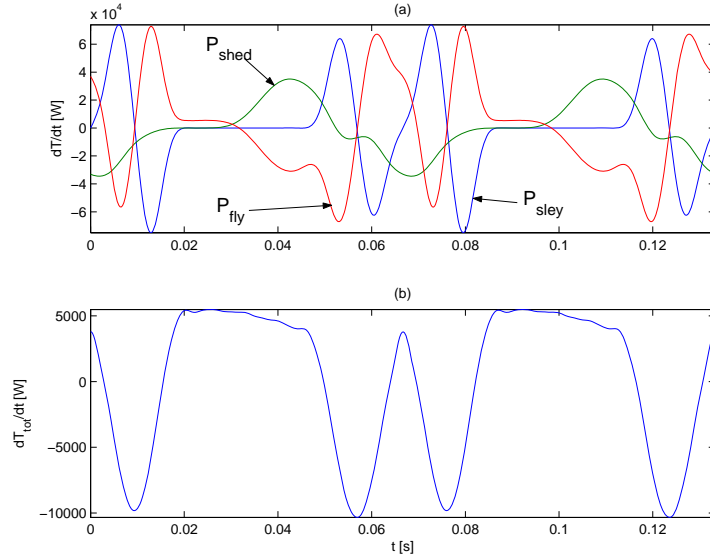


FIGURE 2.16: Power transmission in an airjet weaving machine ( $\eta = 0.20$ ): sley power  $P_{sley}$ , shed power  $P_{shed}$ , and flywheel power  $P_{fly}$  (a);  $dT_{tot}/dt = P_{sley} + P_{shed} + P_{fly}$  (b).

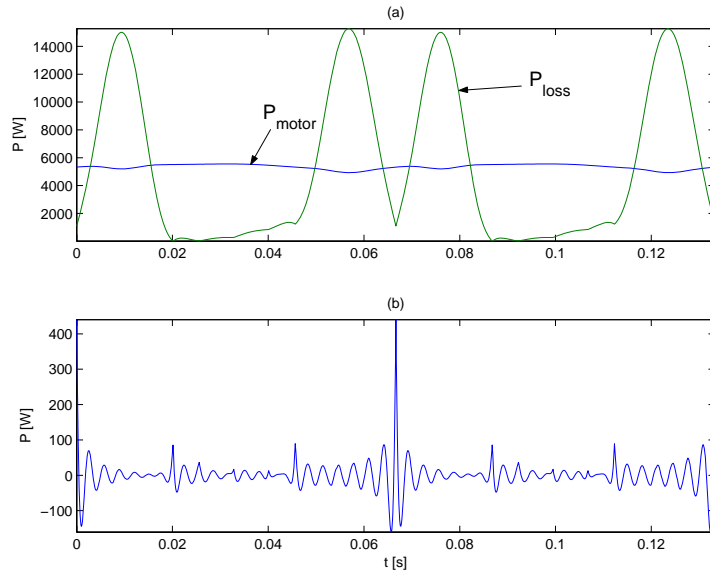


FIGURE 2.17: Power transmission in an airjet weaving machine ( $\eta = 0.20$ ): power loss  $P_{loss}$  due to Coulomb friction and power  $P_{mot}$  added by the motor (a); sum  $dT_{tot}/dt + P_{loss} + P_{mot}$  of all powers (b).

linearly with the number of states in the model and hence negatively affects the required computational time.

For instance, in Section 7.4.2, the approach is applied to damped eigenmotion determination of a weaving machine model that has *two* degrees of freedom, due to the presence of a torsional flexibility. As a result,  $\mathbf{z}$  contains  $4K + 1$  instead of  $2K + 1$  unknown parameters.

**(Damped) Eigenmotion of Airjet Weaving Machines** The basic layout of an airjet weaving machine has been introduced, based on which a simplified model has been derived. This model essentially consists of the sley and shed cam-follower mechanisms, connected via a 2:1 reduction and having a variable synchronization.

Eigenmotion simulation has shown that the drive speed fluctuation, which is substantial ( $\geq 10\%$ ) due to the limited flywheel size, distorts the follower motions. The discussion of Section 2.1.4 shows that, if solutions are to be found for the follower motion distortion, they should comply with the following requirements:

- R1** the machine's energy consumption may not be raised substantially;
- R2** the machine's start/stop behavior may not be compromised;
- R3** the method must be valid for any average drive speed of the machine;
- R4** the method must be robust for changing machine settings, that is, variable synchronization between the sley and shed cam-follower mechanisms, and variable shed follower inertia;
- R5** the method must be easy to integrate with the present machine and not substantially raise its cost.

Simulation of the damped eigenmotion confirms the claim that, if friction losses are small ( $\eta \leq 0.10$ ), or even moderate ( $\eta \leq 0.20$ , as in an airjet weaving machine), damped eigenmotion is very similar to 'true' eigenmotion. This result is important for the robustness w.r.t. friction of inertially compensated cams (Section 3.5).

## Chapter 3

# Inertially Compensated Cams

*Cam design and motion analysis have enjoyed considerable development; however, this development has been perpetuated on a false assumption. (...) We cannot keep adding new and more sophisticated profiles and not start considering time as the actual mechanism sees it.*

E.J. Sarring (1962)

**I**F a low-bandwidth controller is used, a reciprocating machine adopts a motion similar to its (damped) eigenmotion. As discussed in the previous chapter, the associated drive speed fluctuation distorts the follower motions in cam-follower mechanisms, a fact to which Sarring drew attention in his 1962 conference paper (Sarring, 1962). The motion distortion and the associated dynamic problems, can be tackled using two fundamentally different approaches: *the eigenmotion can be adapted to the cam design or cam design can be adapted to the eigenmotion.*

In the former approach, measures are taken for reducing the drive speed fluctuation during eigenmotion, such as increasing the flywheel size or adding an input torque balancing mechanism. A survey of these methods is given in Chapter 4. The latter approach is conceptually totally different, in that it allows the drive speed to fluctuate according to the eigenmotion, and adapts the cam profile such that the desired follower motion is realized, despite the nonconstant drive speed.

Cams designed according to this approach are termed *inertially compensated cams*, since their design procedure is based on the assumption of dom-

inating inertial forces. The fact that the drive speed fluctuation is taken into account, implies that inertially compensated cams incorporate the *drive system dynamics* (more specifically, the flywheel and motor inertia) of a machine into their design. This aspect distinguishes them from other types of dynamically compensated cams, which only compensate for the *follower system dynamics* (such as flexibility of the follower), under the assumption that the drive speed is constant.

Dynamically compensated cams in general, and inertially compensated cams in particular, are examples of *integrated design* in which kinematic and dynamic design aspects are considered simultaneously. Section 3.1 gives an overview of the state-of-the-art of such integrated methods. Section 3.2 develops the methodology for designing inertially compensated cams, which is subsequently applied to an academic example in Section 3.3. Section 3.4 and Section 3.5 respectively discuss the practical applicability of inertially compensated cams in airjet weaving machines in particular, and in reciprocating machinery in general.

### 3.1 State-of-the-Art of Integrated Kinematic–Dynamic Design

The idea of integrating kinematic and dynamic design considerations is not new. Three categories of methods are distinguished here, and discussed in the following sections.

*Fully integrated kinematic-dynamic design* accounts for (drive and/or follower) system dynamics during a mechanism’s kinematic synthesis. Mechanisms synthesized in this way realize some desired output motion correctly, despite for instance the occurring drive speed fluctuation or follower flexibility. Synthesis of inertially compensated cams belongs to this group of methods.

*Kinematic design with dynamic considerations* constitutes a second class of methods. These methods suppose the drive speed to be constant during the kinematic synthesis step. Based on the observation that sometimes not all kinematic parameters are fixed by the kinematic requirements, the subsequent redundancy is used to optimize some criterion associated with the dynamic behavior of the mechanism. The accuracy of the output motion depends on the steadiness of the drive speed.

*Drive speed fluctuation design* constitutes a third class of methods. Again, the drive speed is supposed to be constant during kinematic synthesis. However, afterwards, some fluctuating drive speed is designed that optimizes some dynamic characteristic of the mechanism. This inherently distorts the mechanism’s output motion, unless the mechanism’s kinematic parameters are adapted to the designed, fluctuating drive speed.

Although we are mainly concerned in this chapter with the design of cam-follower mechanisms, also references concerning linkages are included.

### 3.1.1 Fully Integrated Kinematic-Dynamic Design

Adapting a mechanism’s kinematic design to the dynamics of the drive system is introduced by Sherwood (1968) and Liniecki (1970), who both consider a slider-crank mechanism. Sherwood considers the coupler length as a variable parameter, and calculates it, so that during eigenmotion, the slider passes through prescribed positions, specified at three time instants. Liniecki determines the crank radius, coupler length and offset<sup>1</sup>, so as to obtain a desired slider velocity for three specified crank positions, if the mechanism is driven by an AC motor with a quadratic torque-speed characteristic.

Sherwood and Liniecki have the merit of apparently being the first ones completely integrating kinematic and dynamic design. Their iterative schemes (based on an initially constant drive speed, successive recalculations of its fluctuation and subsequent adaptations of the kinematic parameters) are however ad hoc solutions and could nowadays easily be robustified and generalized to more complex mechanisms, by formulating them as optimization problems.

Liu (1997) proposes a systematic, iterative procedure, using a finite element method, to synthesize and analyze a high-speed, cam-actuated, elastic slider-crank linkage with its actuator, a DC motor. The cam profile is synthesized such that a desired output motion is realized, despite the elastic deflections induced by the large inertia of the linkage and the fluctuating drive speed of the driving motor.

The method is general and well-developed. However, as shown in simulation, it is sensitive to differences between the assumed and actually applied mean drive speed and damping ratios. This is a general problem when designing dynamically compensated cams that compensate for follower dynamics. For example, the *polydyne* method (Stoddart, 1953) for compensating follower dynamics under the assumption of a constant drive speed, exhibits exactly the same problems. Consequently, considerable efforts have been made to render it more robust, see e.g. (Kanzaki and Itao, 1972; Srinivasan and Jeffrey Ge, 1998). These kinds of robustifications are also required for making Liu’s method industrially applicable, especially since damping ratios are usually hard to quantify or experimentally identify. Despite that, Liu’s contribution is significant, as he is the first one to consider both drive and follower system dynamics simultaneously.

All of the presented methods are inherently iterative, in that they are based on repeated kinematic synthesis–dynamic analysis steps, until convergence to some desired kinematic behavior of the output link is obtained. This constitutes a major difference with inertially compensated cams, which are designed based on a single calculation (governed by an algebraic equation in Section 3.3 or a boundary value problem in Section 3.4) of the drive speed fluctuation during eigenmotion.

---

<sup>1</sup>That is, the perpendicular distance between the line of action of the slider and the crank pivot.

### 3.1.2 Kinematic Design with Dynamic Considerations

Dizioğlu (1956) and Chen (1969) consider variants of the following classical problem in the kinematic synthesis of crank-rocker four-bar mechanisms: determine the link lengths, given the base length ( $a_4$  in Fig.1.2) and two requirements concerning the mechanism's dead center positions<sup>2</sup>. These two requirements are e.g. (Chen, 1969)  $\Delta_{\text{crank}}$  and  $\Delta_{\text{rocker}}$ , the angle between the two dead-center positions of respectively the crank and the rocker. In German, this problem is called *Totlagenkonstruktion*.

Given the base length, meeting the two dead-center requirements fixes all but one kinematic parameters. This freedom is exploited to optimize some criterion associated with the mechanism's dynamic behavior. Chen (1969) considers the transmission angle and the input torque fluctuation, and shows them to be conflicting demands. Dizioğlu (1956) looks for a compromise between the amount of drive speed fluctuation during eigenmotion and the mechanism's 'flywheel effect', and points out that the resulting compromise does not yield a minimum transmission angle.

Conte et al. (1975) develop a general, computer-aided, kinematic synthesis-dynamic analysis procedure for planar four-bar mechanisms. They give the example of a path generating four-bar mechanism with prescribed input crank speed and three precision points<sup>3</sup>. Satisfying these requirements leaves four kinematic parameters to be arbitrarily chosen. These parameters are the optimization variables of an optimization problem, aiming at minimizing the maximum shaking force, shaking moment, input torque or joint force<sup>4</sup>, exerted by the mechanism. Transmission angle limits, as well as the Grashoff criteria<sup>5</sup> for four-bar mechanisms, constitute the optimization constraints. In the optimization routine, the link mass parameters are automatically calculated, based on the assumption of a rectangular link cross-section, with a fixed thickness and a width equal to some fraction of the link length.

Not only do the optimization results show spectacular improvement of the dynamic reaction penalized by the goal function, but also the other dynamic reactions are substantially reduced. This constitutes a major advantage of kinematic optimization, as compared to counterweight balancing, since the latter method always results in a trade-off between the various dynamic reactions.

Taşcan reduces the drive speed fluctuation in cam-follower mechanisms,

---

<sup>2</sup>The mechanism's dead-center positions occur when the crank is in line with the coupler.

<sup>3</sup>These precision points lie on the path generated by a point on the coupler of a reference four-bar, described in (Berkof and Lowen, 1969). The dynamic reactions of the newly designed four-bar, passing through the precision points, are compared to the dynamic reactions of this reference four-bar.

<sup>4</sup>All forces and moments are determined based on an inverse dynamic analysis, in which a constant input crank speed is assumed.

<sup>5</sup>The Grashoff criteria allow determining, based on the link lengths, whether a four-bar mechanism operates as a crank-rocker, a double crank or a double rocker. More information is given in the Glossary.

driven by an AC motor with a quadratic torque-speed characteristic, through optimization of a kinematic parameter: the distance between the pivots of a rotating cam and its oscillating, flat-faced follower (Taşcan, 1985) or the eccentricity of a rotating cam with a translating, roller follower. Note, however, that the geometry of a cam-follower mechanism can only affect the drive speed fluctuation, provided that friction or external work forces that depend on the geometry are present. This is the case in both papers: Coulomb friction between the cam and its oscillating, flat-faced follower (Taşcan, 1985) and Coulomb friction between the translating, roller follower and its guideway (Taşcan, 1988). Both friction forces depend on the contact force between the follower and the cam, and are hence geometry-dependent. If, however, rotating cams with oscillating roller followers are considered, friction is negligible, and geometry optimization is useless for reducing drive speed fluctuations.

### 3.1.3 Drive Speed Fluctuation Design

Yan et al. (1996b) synthesize cams in the classical way, assuming a constant drive speed, but subsequently optimize a polynomially parameterized cam input speed in order to reduce the peak values of the follower velocity, acceleration, . . . Experimental results are given in (Yan et al., 1996a). The industrial relevance of this approach is however questionable. Firstly, the obtained reduction in peak velocity, acceleration or jerk is very limited. Moreover, the follower motion distortion due to the applied drive speed fluctuation is not taken into account, and may result in timing problems or undesired acceleration harmonics.

Hsu and Chen (1999) use a similar polynomial cam input speed in order to minimize the inertial part<sup>6</sup> of the input torque. Reductions of about 45% are obtained, whereas the inertially compensated cams designed hereafter require no input torque at all. Furthermore, the motion distortion due to application of a fluctuating drive speed to a cam designed for constant drive speed, is again not considered.

Yan and Soong (2001) elaborate on the work of Conte et al. (1975). They consider the same reference crank-rocker four-bar, but, instead of considering solely the link lengths as optimization variables, they simultaneously optimize: (i) the four link lengths, (ii) nine control points of a Bézier curve that parameterizes the fluctuating input speed of the crank and (iii) nine parameters defining the location and radius of circular counterweights (of a given thickness and attached to the crank, coupler and rocker). The goal function is a weighted combination of the *root-mean-square* (rms) values of the shaking force and the input torque.

The rms values of shaking force and input torque are reduced by 83% and 64% respectively. Despite the five times greater number of optimization variables (22 in total), these reductions are of the same order of magnitude as

<sup>6</sup>I.e., the part of the input torque for accelerating and decelerating the follower inertia.

the ones obtained by Conte et al. (1975), who merely use four kinematic optimization variables. In the latter paper, for instance, the *maximum* shaking force and input torque are reduced respectively by 71% and 74%.

Kochev (1990) shows that simultaneous elimination of the shaking moment and input torque in a planar mechanism is possible, provided that (i) some fluctuating drive speed is applied to the driving crank and (ii) an auxiliary flywheel, driven by a noncircular gear pair, is added. Application of the method to a force-balanced<sup>7</sup> four-bar however shows that it is more of academic than of practical importance. For instance, a shaking moment and input torque eliminating drive speed fluctuation with  $\kappa = 10\%$  requires a flywheel inertia that is 4.2 times bigger than the flywheel needed to obtain an eigenmotion with  $\kappa = 10\%$ . Furthermore, the motion distortion due to the fluctuating drive speed is not taken into consideration.

## 3.2 Design of Inertially Compensated Cams

This section develops the methodology for designing inertially compensated cams, that is, cams that impose some desired follower motion, despite the drive speed fluctuation occurring during eigenmotion of the dominantly inertial machine to which they belong.

The type of machine considered here is termed a *multi-follower cam-follower system* and is a purely inertial machine, consisting of a (rigid) drive shaft on which a motor, a flywheel and  $N$  cam-follower mechanisms are mounted. The rotation angle of the drive shaft is denoted as  $g(t)$  [rad], whereas  $f_i(t)$  [rad] or [m] describes the (angular or translational) displacement of the  $i$ -th follower as a function of time. The  $i$ -th follower inertia<sup>8</sup> is represented by  $J_i$ , whereas  $J_{\text{fly}}$  [kg-m<sup>2</sup>] denotes the summed rotational inertia of the cams, the flywheel and the motor's rotor.

Eigenmotion implies that the motor exerts no torque, and that no energy dissipation nor external work forces are present. As a result, conservation of energy applies, which reduces to conservation of kinetic energy for a multi-follower cam-follower system:

$$\frac{J_{\text{fly}} \cdot \dot{g}^2}{2} + \sum_{i=1}^N \frac{J_i \cdot \dot{f}_i^2}{2} = \frac{J_{\text{fly}} \cdot \dot{g}_0^2}{2} + \sum_{i=1}^N \frac{J_i \cdot \dot{f}_{i,0}^2}{2}. \quad (3.1)$$

The left part of (3.1) equals the system's total kinetic energy, equal to the sum of the kinetic energy of the flywheel and the  $N$  followers. The subscript 0 indicates initial values.

---

<sup>7</sup>A force-balanced mechanism exerts no shaking force on its supporting frame.

<sup>8</sup>That is, the mass of a translating follower or the centroidal moment of inertia of an oscillating follower. Throughout this thesis, oscillating followers are supposed to be statically balanced.

(3.1) is the basic equation that governs the design of inertially compensated cams. At first sight, there is no conceptual difference between this equation and the equations (2.8–2.10) for determining the eigenmotion of a reciprocating machine. A difference however arises from the fact that in the design of inertially compensated cams, the follower velocities  $\dot{f}_i$  in (3.1) are *not* determined based on their motion law and the applied camshaft velocity, as expressed by (2.2b) in Section 2.2, but by assuming that they are in fact equal to the *desired* follower velocities  $\dot{f}_i^*$ :

$$\frac{J_{\text{fly}} \cdot \dot{g}^2}{2} + \sum_{i=1}^N \frac{J_i \cdot \dot{f}_i^{*,2}}{2} = \frac{J_{\text{fly}} \cdot \dot{g}_0^2}{2} + \sum_{i=1}^N \frac{J_i \cdot \dot{f}_{i,0}^{*,2}}{2}. \quad (3.2)$$

This equation shows that, given the desired follower velocities  $\dot{f}_i^*(t)$  and the follower inertias  $J_i$ , determining  $\dot{g}(t)$  is governed by an algebraic equation, depending on the chosen initial value  $\dot{g}_0^2$  and flywheel size  $J_{\text{fly}}$ . The resulting  $\dot{g}(t)$  and the given  $\dot{f}_i^*(t)$  fix the motion law and hence the profile of the inertially compensated cams.

This basic idea is elaborated hereafter in a nondimensionalized way. Nondimensionalization of (3.2) in Section 3.2.1 shows that the nondimensionalized camshaft speed  $\phi'(\tau)$  is independent of  $J_{\text{fly}}$ , and hence only depends on the adopted initial value  $\phi'_0$ . Subsequently, Section 3.2.2 introduces the nondimensionalized coefficient  $\delta$  as a way of making a well-founded  $\phi'_0$  choice. Section 3.2.3 proves that  $\delta$  fixes the value of the flywheel inertia  $J_{\text{fly}}$ . Hence, whereas (3.2) suggests that  $\dot{g}_0$  and  $J_{\text{fly}}$  may be chosen independently, they are in fact coupled. Finally, Section 3.2.4 indicates how to calculate the cam motion laws.

### 3.2.1 Nondimensionalization

This section shows how to determine  $\dot{g}(t)$  from (3.2) in a nondimensionalized way. For cam-follower mechanisms, using nondimensionalized parameters is a standard technique (Angeles and López-Cajún, 1991; Chen, 1982) to decouple the follower motion shape from its amplitude  $\Theta_i$  and period of motion  $T$ :

$$f_i(t) = |\Theta_i| \cdot \theta_i(t \cdot \Omega) = |\Theta_i| \cdot \theta_i(\tau), \quad (3.3)$$

where  $\Omega = 2\pi/T$ .  $\Theta_i$  has the dimension of [m] in the case of a translating follower and [rad] in the case of an oscillating follower.  $\tau = t \cdot \Omega$  represents the nondimensionalized time. The periodicity of  $f_i(t)$  implies that  $\theta_i(\tau)$  is periodic with period  $2\pi$ .  $\theta_i(\tau) : [0, 2\pi] \rightarrow [0, 1]$  is the nondimensionalized follower displacement.

Nondimensionalization of the camshaft's rotation angle is less common. A possible approach consists of defining:

$$g(t) = 2\pi \cdot \psi(t \cdot \Omega) = 2\pi \cdot \psi(\tau). \quad (3.4)$$

As the camshaft makes one complete revolution during one period of motion,  $g$  ranges from 0 to  $2\pi$ , hence  $\psi$  ranges from 0 to 1.  $\psi(\tau) : [0, 2\pi] \rightarrow [0, 1]$  is the nondimensionalized camshaft displacement. This definition, though obvious, is less useful than (Van de Straete and De Schutter, 1999):

$$g(t) = \Theta_{\text{ref}} \cdot \sqrt{\frac{J_{\text{ref}}}{J_{\text{fly}}}} \cdot \phi(t \cdot \Omega) = \Theta_{\text{ref}} \cdot \sqrt{\frac{J_{\text{ref}}}{J_{\text{fly}}}} \cdot \phi(\tau). \quad (3.5)$$

$J_{\text{ref}}$  is a reference inertia equal to 1 kg-m<sup>2</sup>, whereas  $\Theta_{\text{ref}}$  is a reference displacement of  $2\pi$  rad.  $\phi(\tau) : [0, 2\pi] \rightarrow [0, \phi_{\text{max}}]$  is the nondimensionalized camshaft displacement. Applying the chain rule for differentiation to (3.3) and (3.5) yields the following proportional relations between the time-derivatives of  $f_i(t)$  and  $g(t)$  and the  $\tau$ -derivatives of  $\theta_i(\tau)$  and  $\phi(\tau)$  respectively:

$$\frac{d^n f_i(t)}{dt^n} = |\Theta_i| \cdot \Omega^n \cdot \theta_i^{(n)}(\tau); \quad (3.6)$$

$$\frac{d^n g(t)}{dt^n} = \Theta_{\text{ref}} \cdot \Omega^n \cdot \sqrt{\frac{J_{\text{ref}}}{J_{\text{fly}}}} \cdot \phi^{(n)}(\tau). \quad (3.7)$$

Applying (3.7) and (3.6) to (3.2), and substituting the nondimensionalized coefficients  $\zeta_i$ , defined as

$$\zeta_i = \frac{J_i}{J_{\text{ref}}} \cdot \frac{\Theta_i^2}{\Theta_{\text{ref}}^2}, \quad (3.8)$$

yields<sup>9</sup>:

$$\phi'^2(\tau) + \sum_{i=1}^N \zeta_i \cdot \theta_i'^2(\tau) = \phi_0'^2 + \sum_{i=1}^N \zeta_i \cdot \theta_{i,0}'^2, \quad (3.9)$$

which expresses the conservation of kinetic energy in a nondimensionalized way. The left part of (3.9) is the nondimensionalized total kinetic energy  $\epsilon_{\text{tot}}(\tau)$ :

$$\epsilon_{\text{tot}}(\tau) = \frac{T_{\text{tot}}(t \cdot \Omega)}{\frac{J_{\text{ref}} \cdot (\Theta_{\text{ref}} \cdot \Omega)^2}{2}} = \underbrace{\phi'^2(\tau)}_{\epsilon_{\text{fly}}(\tau)} + \underbrace{\sum_{i=1}^N \zeta_i \cdot \theta_i'^2(\tau)}_{\epsilon_{\text{fol}}(\tau)}. \quad (3.10)$$

$\epsilon_{\text{tot}}(\tau)$  equals the sum of  $\epsilon_{\text{fly}}(\tau)$ , the nondimensionalized flywheel kinetic energy and  $\epsilon_{\text{fol}}(\tau)$ , the nondimensionalized follower kinetic energy. (3.9) gives

---

<sup>9</sup> $\theta_i'$  should in fact be denoted as  $\theta_i^{* \prime}$ , to express that nondimensionalized versions of the *desired* trajectories  $f_i^*$  are considered. However, in order to alleviate notation, the asterisk is omitted.

rise to the following algebraic equation for calculating  $\phi'(\tau)$ :

$$\phi'(\tau) = \left( \phi_0'^2 + \sum_{i=1}^N \zeta_i \cdot \theta_{i,0}'^2 - \sum_{i=1}^N \zeta_i \cdot \theta_i'^2(\tau) \right)^{1/2} \quad (3.11)$$

$$= (\epsilon_{\text{fly},0} + \epsilon_{\text{fol},0} - \epsilon_{\text{fol}}(\tau))^{1/2}. \quad (3.12)$$

Equation (3.12) leads to a threefold conclusion:

- $\phi'(\tau)$  depends on  $\epsilon_{\text{fly},0}$ ,  $\epsilon_{\text{fol},0}$  and  $\epsilon_{\text{fol}}(\tau)$ . If  $\theta_i(\tau)$ ,  $\Theta_i$  and  $J_i$  (that is, the desired follower motions and the follower inertias) are given,  $\epsilon_{\text{fol}}(\tau)$  and  $\epsilon_{\text{fol},0}$  are entirely determined and one basic design choice remains to be made:  $\epsilon_{\text{fly},0} = \phi_0'^2$ .
- $\phi'(\tau)$  is independent of  $T$ , since  $\epsilon_{\text{fol}}(\tau)$  is independent of  $T$ .
- The frequency content of  $\theta_i'(\tau)$  and  $\phi'(\tau)$  are not equal because of the nonlinear square root operation.

### 3.2.2 Choice of the Initial Camshaft Speed

In order to make a well-founded choice of  $\phi_0'$ , the nondimensionalized coefficient of camshaft speed fluctuation  $\delta$  is introduced as:

$$\delta = \frac{\dot{g}_{\min}}{\dot{g}_{\max}} = \frac{\Theta_{\text{ref}} \cdot \Omega \cdot \sqrt{\frac{J_{\text{ref}}}{J_{\text{fly}}}} \cdot \phi'_{\min}}{\Theta_{\text{ref}} \cdot \Omega \cdot \sqrt{\frac{J_{\text{ref}}}{J_{\text{fly}}}} \cdot \phi'_{\max}} = \frac{\phi'_{\min}}{\phi'_{\max}}, \quad (3.13)$$

where  $\dot{g}_{\min}$  and  $\dot{g}_{\max}$  denote the minimum and maximum of  $\dot{g}(t)$  over  $[0, T]$ , and  $\phi'_{\min}$  and  $\phi'_{\max}$  the minimum and maximum of  $\phi'(\tau)$  over  $[0, 2\pi]$ . The relationship between  $\delta$  and  $\phi_0'$  is derived as follows. Substituting  $\epsilon_{\text{fly},0} = \phi_0'^2$  into (3.12) yields:

$$\phi'^2(\tau) = \phi_0'^2 + \epsilon_{\text{fol},0} - \epsilon_{\text{fol}}(\tau). \quad (3.14)$$

Consequently:

$$\phi_{\min}'^2 = \phi_0'^2 + \epsilon_{\text{fol},0} - \epsilon_{\text{fol},\max}; \quad (3.15)$$

$$\phi_{\max}'^2 = \phi_0'^2 + \epsilon_{\text{fol},0} - \epsilon_{\text{fol},\min}. \quad (3.16)$$

Substituting (3.15) and (3.16) into (3.13) and solving  $\phi_0'$  from the resulting equation, yields the following relationship between  $\phi_0'$  and  $\delta$ :

$$\phi_0'^2 = -\epsilon_{\text{fol},0} + \frac{\epsilon_{\text{fol},\max} - \delta^2 \cdot \epsilon_{\text{fol},\min}}{1 - \delta^2}. \quad (3.17)$$

This equation simplifies by choosing the time instant where the kinetic energy of the followers is a minimum, as the beginning of the motion cycle:

$\epsilon_{\text{fol},0} = \epsilon_{\text{fol},\min}$ . This convention<sup>10</sup> does not compromise the generality of the equations, and yields:

$$\phi_0'^2 = \frac{\epsilon_{\text{fol},\max} - \epsilon_{\text{fol},\min}}{1 - \delta^2}. \quad (3.18)$$

This equation shows that  $\phi_0'$  depends on: (i) the chosen value of  $\delta$  and (ii)  $\epsilon_{\text{fol}}(\tau)$ . Hence,  $\phi_0'$  is independent of  $T$ . As  $\epsilon_{\text{fol},\max}$  is greater than  $\epsilon_{\text{fol},\min}$ , and  $\delta$  is smaller than one, the right part of (3.18) is always positive, guaranteeing that  $\phi_0'$  is a real number.

### 3.2.3 Calculation of the Equivalent Camshaft Inertia

$J_{\text{fly}}$  cannot be chosen freely, as shown hereafter. Taking the average (over one period) of both sides of (3.5), for  $n = 1$ , results in

$$\dot{g}_{\text{avg}} = \Omega \cdot \sqrt{\frac{J_{\text{ref}}}{J_{\text{fly}}}} \cdot \phi'_{\text{avg}},$$

where

$$\begin{aligned} \dot{g}_{\text{avg}} &= \frac{1}{T} \int_0^T \dot{g}(t) \cdot dt; \\ \phi'_{\text{avg}} &= \frac{1}{2\pi} \int_0^{2\pi} \phi'(\tau) \cdot d\tau. \end{aligned}$$

Since the average camshaft speed  $\dot{g}_{\text{avg}}$  must equal  $\Omega$ , the following constraint is imposed on  $J_{\text{fly}}$ :

$$J_{\text{fly}} = J_{\text{ref}} \cdot \phi_0'^2, \quad (3.19)$$

which proves that  $J_{\text{fly}}$  does not depend on  $T$ , since  $\phi'(\tau)$  is independent of  $T$ .

### 3.2.4 Calculation of the Cam Motion Law

This section proves that not only  $J_{\text{fly}}$ , but the cams as well, are independent of  $T$ , by showing that the cam motion law  $F_i(g)$  is independent of  $T$ . The cam motion law  $F_i(g)$  gives the  $i$ -th follower displacement  $f_i$  as a function of the camshaft rotation angle  $g$ .  $F_i(g)$  is hence defined by the look-up table with  $g(t)$  as entries and  $f_i(t)$  as corresponding values. In order to prove that  $F_i(g)$  is independent of  $T$ , it suffices to prove that both the entries  $g(t)$  and the corresponding values  $f_i(t)$  of the look-up table are independent of  $T$ . We have that

$$g(t) = 2\pi \cdot \sqrt{\frac{J_{\text{ref}}}{J_{\text{fly}}}} \cdot \phi(\tau),$$

---

<sup>10</sup>For a system with one follower, this convention boils down to choosing the instant where the follower stands still, as the beginning of the motion cycle.

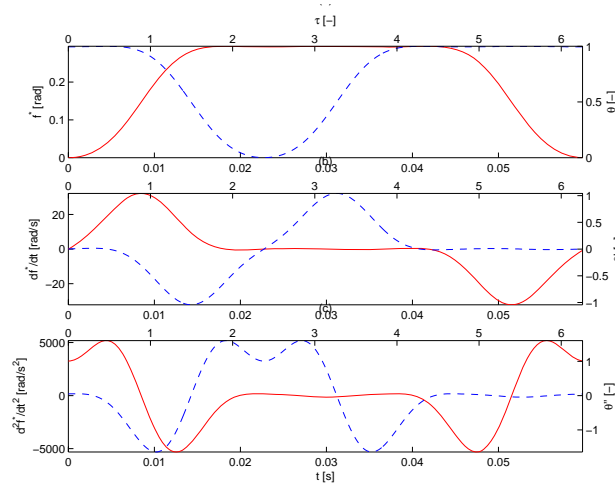


FIGURE 3.1: Desired position (a), velocity (b) and acceleration (c) of the  $N = 2$  followers of the design example ( $i = 1$ : solid line;  $i = 2$ : dashed line) in dimensionalized (left y-axis) and nondimensionalized (right y-axis) form.

with  $\phi(\tau)$  independent of  $T$ , as it is the integral of  $\phi'(\tau)$ , itself independent of  $T$ . Moreover, since also  $J_{\text{fly}}$  is independent of  $T$ , it is proven that the same goes for  $g(t)$ .  $f_i(t) = \Theta_i \cdot \theta_i(\tau)$  is independent of  $T$  by definition of  $\theta_i(\tau)$ .

The motion law  $F(g)$  itself does not contain any information about the drive speed, i.e. it gives for each value of  $g$  a corresponding displacement, without saying anything about the time trajectory of  $g(t)$ . Consequently, once the motion law  $F(g)$  is determined, the design procedures for a cam with constant drive speed and for a cam with variable drive speed are identical.

### 3.3 Application to an Academic Example

#### 3.3.1 Cam Design Procedure

As a summary of the previous section, a design procedure is formulated, starting from the following data:  $T$ , the  $N$  desired follower motions  $f_i^*(t)$  and the  $N$  follower inertias  $J_i$ . The procedure returns the cam profiles of the inertially compensated cams, and is applied to an academic multi-follower cam-follower system, consisting of two conjugate cam mechanisms, each with an oscillating, statically balanced follower with centroidal moment of inertia  $J_1 = J_2 = 0.9 \text{ kg}\cdot\text{m}^2$ . Figure 3.1(a) shows one period ( $T = 0.06 \text{ s}$ ) of the desired displacement  $f_i^*(t)$  of the first follower (solid line) and the second follower (dashed line) as a function of time. Both displacements are synthesized as a finite

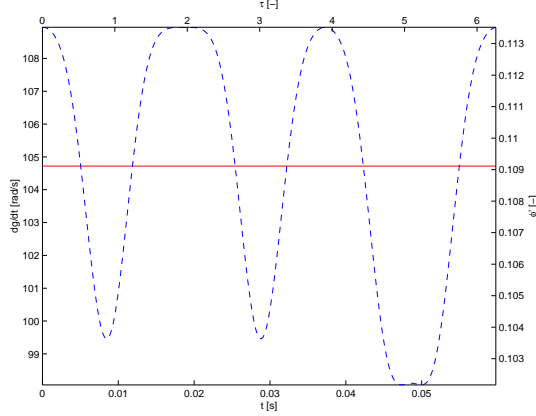


FIGURE 3.2: Fluctuating *design* camshaft speed for the inertially compensated cams of the academic example ( $\delta = 0.90$ ), in dimensionalized (left y-axis) and nondimensionalized (right y-axis) form (dashed line). The solid line indicates the average value  $\phi'_{\text{avg}} = 0.1091$ .

Fourier series with six harmonics, and are identical but shifted in time with respect to each other. The design procedure consists of seven steps:

1. Determine  $\Theta_i$  to calculate  $\theta'_i(\tau)$  using (3.6):  $\Theta_1 = \Theta_2 = 0.2945$  rad. Fig.3.1(b) shows  $\theta'_i(\tau)$ ,  $i = 1, 2$ .
2. Determine  $\zeta_i$  based on (3.8):  $\zeta_1 = \zeta_2 = 1.9772e-3$ . Calculate  $\epsilon_{\text{fol}}(\tau)$  and determine the value of  $\tau$  for which  $\epsilon_{\text{fol}}(\tau)$  is a minimum:  $\tau_{\text{min}} = 2.3807$ . Choose  $\tau_{\text{min}}$  as the beginning of the motion cycle.
3. Choose a value of  $\delta$ :  $\delta = 0.90$ . This choice fixes  $\phi'_0$  according to (3.18):  $\phi'_0 = ((0.0024485 - 0)/(1 - 0.9^2))^{0.5} = 0.1135$ .
4. Calculate  $\phi'(\tau)$  according to (3.12). Calculate  $\phi(\tau)$  by integrating  $\phi'(\tau)$ . Determine  $g(t)$  based on (3.5). Figure 3.2 shows  $\phi'(\tau)$  and its dimensionalized counterpart  $\dot{g}(t)$ .
5. Calculate  $J_{\text{fly}}$  using (3.19):  $J_{\text{fly}} = 1 \cdot (2\pi)^2 \cdot 0.1091^2 = 0.4700$  kg-m<sup>2</sup>.
6. Calculate the motion law  $F_i(g)$  as the look-up table with  $g(t)$  as entries and  $f_i(t)$  as corresponding values.
7. Determine the cam profiles based on  $F_i(g)$ , taking into account the type of cam-follower mechanism. Algorithms for calculating the cam profile, based on the knowledge of  $F_i(g)$  and the type of cam-follower mechanism, are given in e.g. (Chen, 1982; Norton, 2002).

For the same cam-follower system, cams can also be designed in the traditional way, that is, based on the assumption of a constant camshaft speed. The system with inertially compensated cams is termed the VAR-system while the system with conventional cams is the CON-system<sup>11</sup>. The value of  $J_{\text{fly}}$  in the CON-system is equal to the  $J_{\text{fly}}$ -value in the VAR-system:  $0.47 \text{ kg}\cdot\text{m}^2$ .

Figure 3.3 compares, for the first cam-follower mechanism ( $i = 1$ ), the cam motion law  $F_1(g)$  and its derivatives  $F_1'(g)$  and  $F_1''(g)$  w.r.t.  $g$ , for the VAR-system (dashed line) and the CON-system (solid line). The fluctuating camshaft speed in the VAR-system causes the cam motion law and its derivatives to be more pointed. This effect, slightly present in Figure 3.3, is much more pronounced for smaller values of  $\delta$ , and results in degeneration of the cam profile, as illustrated in Section 3.3.2.

### 3.3.2 Influence of $\delta$

This section investigates the influence of  $\delta$  on  $J_{\text{fly}}$  and the cams designed in Section 3.3.1. Figure 3.4 shows that  $J_{\text{fly}}$  increases rather slowly for  $\delta \leq 0.8$  but very rapidly for higher  $\delta$ -values. Obviously, an infinitely large flywheel would be necessary for  $\delta$  to be one (no speed fluctuation).

Figure 3.5 and 3.6 show, for the master<sup>12</sup> cam of the first cam-follower mechanism ( $i = 1$ ), the variation of the cam profile and the cam properties as a function of  $\delta$ . Figure 3.5 shows that the upper part of the cam profile degenerates for values of  $\delta$  smaller than 0.3. This is attributed to the fact that the cam motion law is very pointed for small values of  $\delta$ .

The degeneration of the cam profile is confirmed by the deterioration of the cam properties. Figure 3.6(a) focuses on the maximum pressure angle<sup>13</sup> and shows that it is too big (i.e., greater than  $30^\circ$ ) for  $\delta \in [0, 0.25]$ . Fig. 3.6(b) shows the maximum allowable roller follower radius  $R_{\text{b,max}}$  [m], in order to avoid undercutting of the cam profile. In Appendix G, it is shown that

$$R_{\text{b,max}} = \rho_{\text{min,+}},$$

that is, the minimum value (over of all convex<sup>14</sup> cam portions) of the radius of curvature  $\rho$  [m] of the cam's pitch profile. As the roller follower radius  $R_{\text{b}}$  equals 0.04 m, undercutting<sup>15</sup> occurs for  $\delta \leq 0.31$ .

<sup>11</sup>The terms VAR and CON are adopted since inertially compensated cams are designed for VARiable drive speed, while conventional cams are designed for CONstant drive speed.

<sup>12</sup>A conjugate cam-follower mechanism, as the one shown in Fig.1.1, consists of two cams, called the master and the slave cam.

<sup>13</sup>The pressure angle is a measure for the force transmission in a cam-follower mechanism: the closer it is to zero, the better the force transmission.

<sup>14</sup>For an external cam, convex and concave cam portions respectively have positive and negative (pitch profile) radius of curvature  $\rho$  [m], see Appendix G.

<sup>15</sup>Geometrical problems that are associated with the radius of curvature of a cam's pitch profile, that is, *undercutting* and *feasibility problems*, are discussed in detail in Appendix G. In Fig.3.5, the cam profile associated with  $\delta = 0.1$  exhibits undercutting.

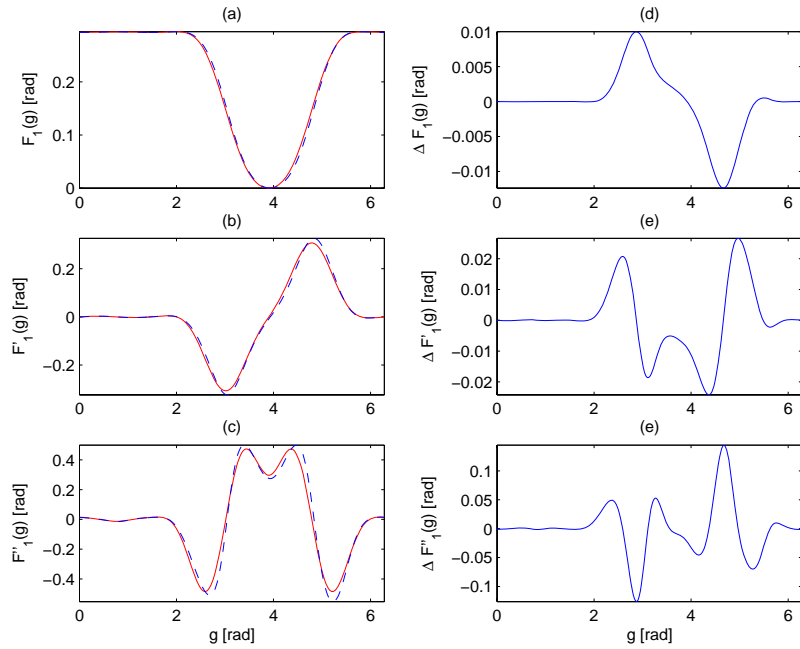


FIGURE 3.3: (a)-(b)-(c) Cam motion law (and its derivatives w.r.t.  $g$ ) of the first cam-follower mechanism ( $i = 1$ ), for the CON-system (solid line) and the VAR-system ( $\delta = 0.90$ , dashed line); (d – e – f) corresponding difference and its derivatives.

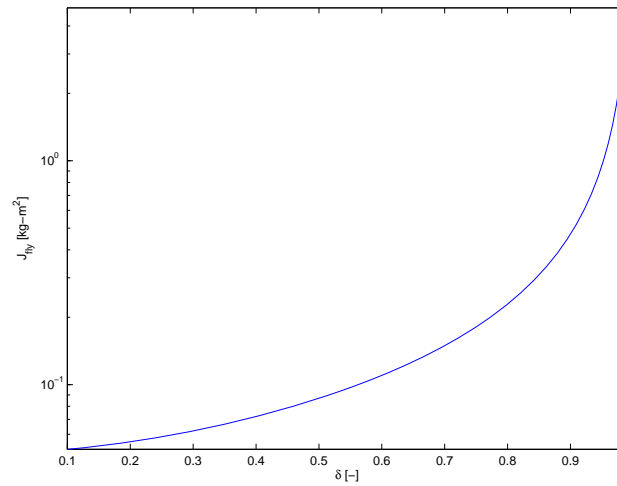


FIGURE 3.4:  $J_{fly}$  as a function of  $\delta$ .

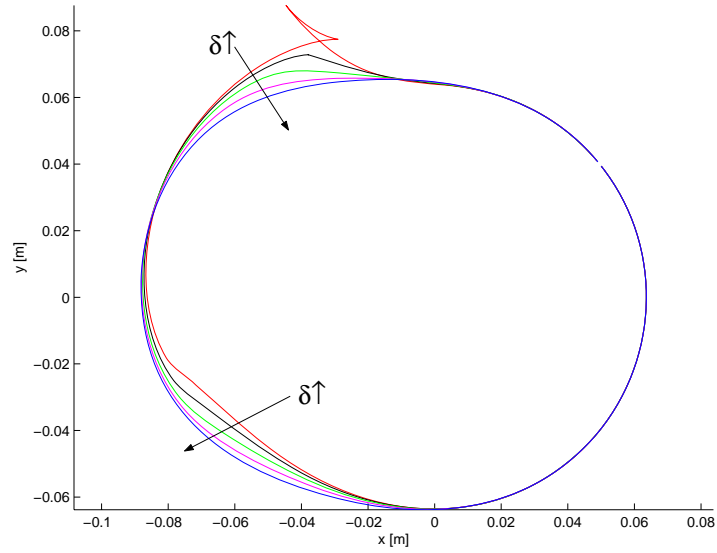


FIGURE 3.5: Cam profile of the master cam of the first cam-follower mechanism ( $i = 1$ ) for  $\delta = \{0.1, 0.3, 0.5, 0.7, 0.9\}$ . The arrows indicate increasing  $\delta$ -values. For  $\delta = 0.1$ , the upper part of the cam profile exhibits undercutting.

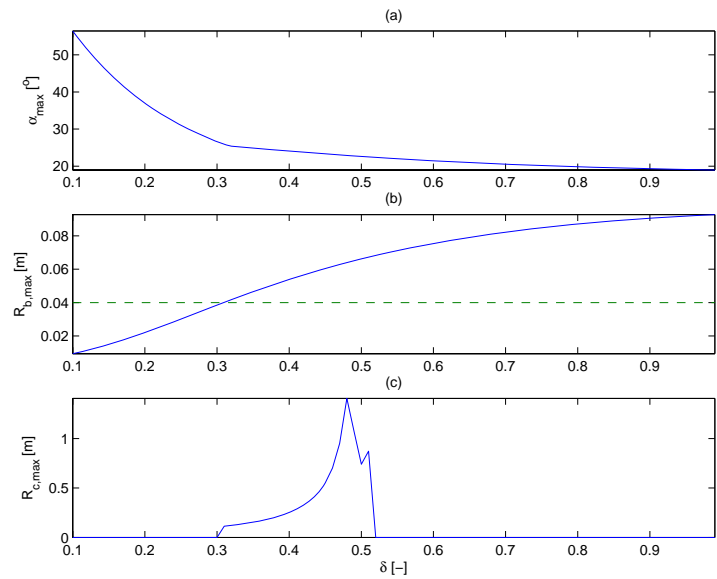


FIGURE 3.6: Properties of the master cam of the first cam-follower mechanism ( $i = 1$ ) as a function of  $\delta$ : (a) maximum pressure angle; (b) maximum roller follower radius (the dashed line indicates  $R_b = 0.04$  m); (c) maximum cutter radius.

Concave portions of an external cam profile cannot exhibit undercutting, but may give rise to *feasibility problems*. Fig.3.6(c) shows the maximum value of the cutter (used to mill or grind the profile) radius  $R_{C,\max}$  in order to avoid these problems. In Appendix G, it is shown that

$$R_{C,\max} = R_b + \rho_{\min,-},$$

where  $\rho_{\min,-}$  denotes the minimum absolute value (over of all concave cam portions) of the radius of curvature  $\rho$  of the cam's pitch profile. For  $\delta \geq 0.52$ , no values of  $R_{C,\max}$  are shown, since there are no concave cam portions for these values of  $\delta$ . For  $\delta \leq 0.31$  it makes no sense to plot a value of  $R_{C,\max}$  as the cam profile is infeasible due to undercutting.

Briefly, the value of  $\delta$  is a compromise between obtaining a small  $J_{\text{fly}}$  (a small flywheel) and maintaining good cam properties. For this design example, a value of  $\delta \approx 0.9$  seems to be a good compromise:  $J_{\text{fly}}$  remains reasonably small, the pressure angle is limited ( $19^\circ$ ), there is no limitation on the cutter radius (the cam has no concave parts), and no undercutting.

### 3.3.3 Sensitivity w.r.t. Energy Dissipation

The design procedure outlined in Section 3.3.1 assumes a conservative system. This section investigates the sensitivity of inertially compensated cams to the presence of energy dissipation. To this end, the previously introduced VAR and CON-system are compared by calculating their respective eigenmotion ( $\eta = 0$ ) and damped eigenmotion ( $\eta = \{0.05, 0.10, 0.20\}$ ). Three aspects of the dynamic behavior are compared: the resulting drive speed fluctuation, the time-domain distortion of the acceleration of the first follower and the corresponding undesired acceleration harmonics. Table 3.1 tabulates, as a function of  $\eta$ , the follower Coulomb friction torque  $M_{\text{coul}}$ , required constant motor torque  $M_{\text{mot}}$  and the resulting coefficient of drive speed fluctuation  $\kappa$ <sup>16</sup>.

Figure 3.7(a–b) compares the difference  $\Delta\dot{g}(t)$  [rad/s] between the desired and actually realized trajectory of  $\dot{g}(t)$  in the VAR and CON-system. The CON-system's *desired* drive speed is *constant* and equal to  $2\pi/0.06 = 104.7$  rad/s. The VAR-system's *desired* drive speed is *fluctuating*, and shown in Fig.3.2. During eigenmotion ( $\eta = 0$ ),  $\Delta\dot{g}(t)$  is zero in the VAR-system: the actually realized and desired drive speed are identical, due to the fact that eigenmotion is assumed in the design of inertially compensated cams. In the presence of energy dissipation (damped eigenmotion),  $\Delta\dot{g}(t)$  is no longer zero, and increases as a function of  $\eta$ . It remains however much smaller than in the CON-system, even for  $\eta = 0.20$ . As opposed to the VAR-system,  $\Delta\dot{g}(t)$  is roughly independent of  $\eta$  in the CON-system: it is mainly the exchange of kinetic energy between the flywheel and the follower inertias, and not the amount of friction, that affects it.

---

<sup>16</sup>Remember that  $\kappa$  [%] is the classical coefficient of drive speed fluctuation, as defined by (2.17), whereas  $\delta$  [-] is the coefficient of drive speed fluctuation, introduced here by (3.13).

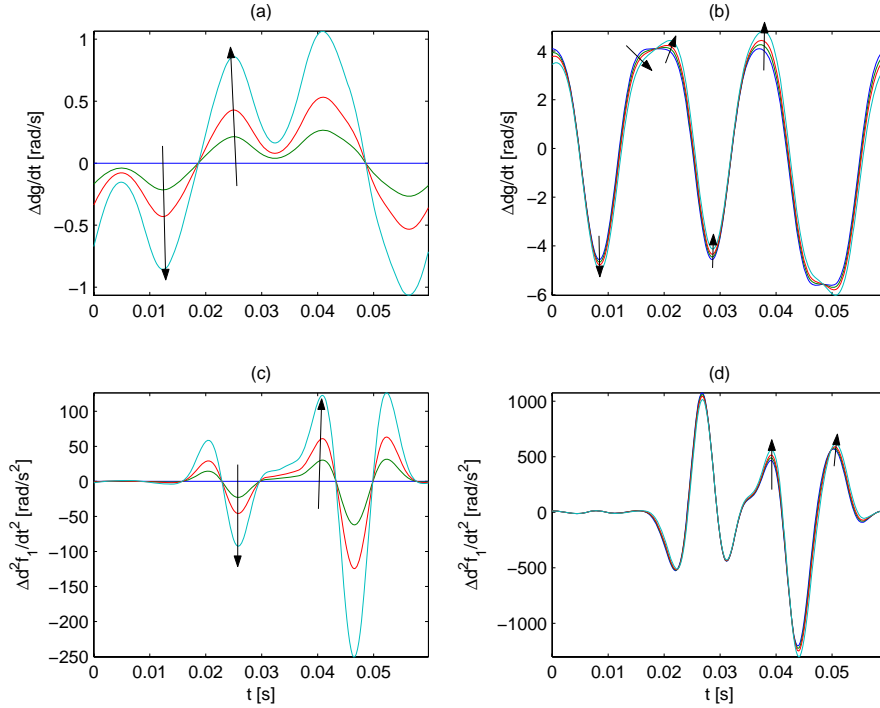


FIGURE 3.7: Comparison of VAR and CON-system for  $\eta = \{0, 0.05, 0.10, 0.20\}$ : difference  $\Delta\dot{g}(t)$  [rad/s], between the desired and actually realized drive speed in the VAR-system (a) and the CON-system (b); difference  $\Delta\ddot{f}_1(t)$  [rad/s<sup>2</sup>] between the desired and actually realized first follower acceleration in the VAR-system (c) and the CON-system (d). The arrows indicate increasing values of  $\eta$ .

The smaller difference between the actually realized and the desired drive speed, results in more accurately realized follower motions in the VAR-system. Figure 3.7(c – d) illustrates this by comparing the difference  $\Delta\ddot{f}_1(t)$  [rad/s<sup>2</sup>] between the desired and actually realized trajectory of the first follower acceleration in the VAR and the CON-system. The deviation is zero for  $\eta = 0$  in the VAR-system. If friction is present, it remains much smaller than in the CON-system, even for  $\eta = 0.20$ .

The corresponding effect on the undesired acceleration harmonics is assessed in Fig.3.8, by showing  $\Delta A_k = A_{k, \text{CON}}/A_{k, \text{VAR}}$  on a dB-scale. Focussing on the undesired harmonics  $k = \{6, 7, \dots\}$ , the following is observed. For  $\eta = 0$ ,  $\Delta A_k, \forall k \geq 7$  is infinite (indicated using a value of 50 dB):  $A_{k, \text{VAR}} = 0$  because of the perfect follower motion realization. For nonzero values of  $\eta$ , the

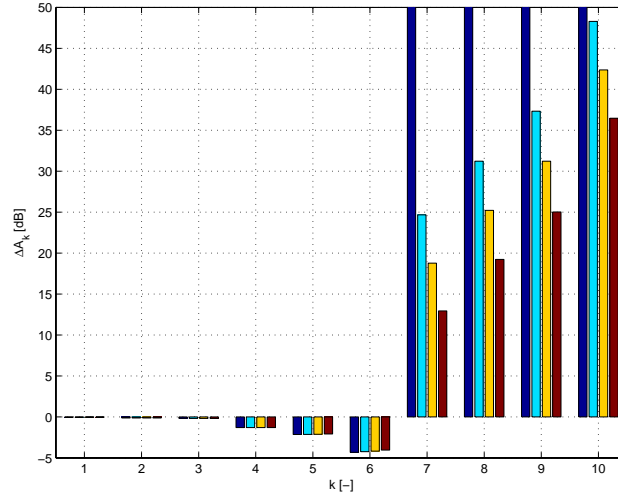


FIGURE 3.8: Comparison of VAR and CON-system for  $\eta = \{0, 0.05, 0.10, 0.20\}$ : difference  $\Delta A_k = A_{k,\text{CON}}/A_{k,\text{VAR}}$  [dB] between the harmonics of the actually realized acceleration of the first follower. For each harmonic  $k$ , the values of  $\Delta A_k$  for  $\eta = \{0, 0.05, 0.10, 0.20\}$  are given from the left to the right. Values of 50 dB indicate  $\Delta A_k = \infty$ .

VAR-system still performs significantly better, although the difference with the CON-system gets smaller as friction increases. The results of this figure are summarized as follows: inertially compensated cams yield undesired harmonics that are *a lot* (at least 25 dB, that is, a factor 18) smaller if a small amount of friction is present ( $\eta = 0.05$ ), and *significantly* (at least 13 dB, that is, a factor 4.5) smaller if a moderate amount of friction is present ( $\eta = 0.20$ ). Inertially compensated cams are hence quite robust for the presence of (Coulomb) friction.

### 3.4 Application to an Airjet Weaving Machine

Inertially compensated cams can be used for reducing the undesired shed follower acceleration harmonics, discussed in Section 2.5. This is done by synthesizing the shed cams as inertially compensated cams. It makes no sense to do so for the sley cam: all inertially compensated cams of a system must turn at the same average drive speed  $\Omega$ , according to the global system's periodicity  $T$ . In the case of an airjet weaving machine, this implies that the sley cam would turn at half its current speed, imposing two back-and-forth sley motions per complete revolution. This is no feasible solution. Furthermore,

		VAR-system			
		$\eta = 0$	$\eta = 0.05$	$\eta = 0.10$	$\eta = 0.20$
$M_{\text{coul}}$ [N-m]	-	117	235	469	
$\kappa$ [%]	10.4	10.7	10.9	11.5	
$M_{\text{mot}}$ [N-m]	-	22.2	44.4	88.8	
		CON-system			
		$\eta = 0$	$\eta = 0.05$	$\eta = 0.10$	$\eta = 0.20$
$M_{\text{coul}}$ [N-m]	-	117	234	469	
$\kappa$ [%]	9.3	9.5	9.8	10.3	
$M_{\text{mot}}$ [N-m]	-	22.2	44.3	88.7	

TABLE 3.1: Comparison of VAR and CON-system: numerical values of some drive system characteristics.

the main problems are associated with the shed cam-follower mechanism. Therefore, only the shed cams are redesigned.

### 3.4.1 Design Procedure

The fact that the sley cams are not redesigned, necessitates adaptations of the previously developed design procedure. The design procedure again starts from the kinetic energy equation (see Section 2.4.1):

$$\frac{J_{\text{fly}} \cdot \dot{g}_{\text{sley}}^2}{2} + \frac{J_{\text{sley}} \cdot \dot{f}_{\text{sley}}^2}{2} + \frac{J_{\text{shed}} \cdot \dot{f}_{\text{shed}}^2}{2} = \frac{J_{\text{fly}} \cdot \dot{g}_{\text{sley},0}^2}{2} + \frac{J_{\text{sley}} \cdot \dot{f}_{\text{sley},0}^2}{2} + \frac{J_{\text{shed}} \cdot \dot{f}_{\text{shed},0}^2}{2}.$$

In order to derive the equation that governs the design of inertially compensated shed cams, the following substitutions are made, based on the idea that the sley cams are conventional (motion law  $F_{\text{sley}}$  hence already known), while the shed cams are inertially compensated (motion law  $F_{\text{shed}}$  to be determined):

$$\begin{aligned} \dot{f}_{\text{sley}} &= F'_{\text{sley}}(g_{\text{sley}}) \cdot \dot{g}_{\text{sley}}; \text{ (see (2.2b))} \\ \dot{f}_{\text{shed}} &= \dot{f}_{\text{shed}}^*, \end{aligned}$$

and hence:

$$\begin{aligned} \frac{J_{\text{fly}} \cdot \dot{g}_{\text{sley}}^2}{2} + \frac{J_{\text{sley}} \cdot \left( F'_{\text{sley}}(g_{\text{sley}}) \cdot \dot{g}_{\text{sley}} \right)^2}{2} + \frac{J_{\text{shed}} \cdot \dot{f}_{\text{shed}}^{*,2}}{2} = \\ \frac{J_{\text{fly}} \cdot \dot{g}_{\text{sley},0}^2}{2} + \frac{J_{\text{sley}} \cdot \left( F'_{\text{sley}}(g_{\text{sley},0}) \cdot \dot{g}_{\text{sley},0} \right)^2}{2} + \frac{J_{\text{shed}} \cdot \dot{f}_{\text{shed},0}^{*,2}}{2}. \end{aligned} \quad (3.20)$$

As opposed to (3.2), this is not an algebraic but a first-order, *differential* equation in  $g_{\text{sley}}(t)$ . Without loss of generality,  $g(0) = 0$  is imposed. In order to obtain a solution with the correct machine period  $T$ , a boundary condition  $g_{\text{sley}}(T) = g_{\text{sley}}(0) + 4\pi$  has to be added (see Section 2.4.1), such that a boundary value problem (BVP) is obtained:

$$\begin{cases} (3.20) & , \quad \forall t \in [0, T]; \\ g_{\text{sley}}(0) & = 0; \\ g_{\text{sley}}(T) & = g_{\text{sley}}(0) + 4\pi. \end{cases} \quad (3.21)$$

Given the desired motions  $f_i^*$  and inertias  $J_i$  of the  $N$  followers, the algebraic equation (3.2) is solved based on one design decision, that is  $\delta$  (which in turn fixes  $J_{\text{fly}}$ ). Given the sley and shed follower inertias  $J_{\text{sley}}$  and  $J_{\text{shed}}$ , the shed follower's desired motion  $f_{\text{shed}}^*$  and the sley's motion law  $F_{\text{sley}}(g_{\text{sley}})$ , the BVP (3.21) is again solved based on one design decision, that is  $J_{\text{fly}}$  (which in turn fixes  $\kappa$ ). In this particular case,  $J_{\text{fly}}$  is taken equal to  $0.7385 \text{ kg}\cdot\text{m}^2$ , that is, no changes are made to the flywheel originally present in the airjet weaving machine.

Solving (3.21) is done using the nonlinear least-squares techniques developed in Section 2.4.2. After that, the motion law of the inertially compensated shed cams is determined as in Section 3.2.4. During the design stage, it is assumed that  $g_{\text{cross}} = 320^\circ$  and that  $N_{\text{shed}} = 10$  frames are moving.

### 3.4.2 Sensitivity w.r.t. Energy Dissipation

This section investigates the sensitivity of the inertially compensated shed cams to the presence of energy dissipation. To this end, an airjet machine with conventional cams (CON-machine) and an airjet machine with inertially compensated shed cams (VAR-machine) are compared by calculating their respective (true or damped) eigenmotion for  $\eta = \{0, 0.05, 0.10, 0.20\}$ .

For reasons of brevity, and as we are mainly concerned with the undesired harmonics of the shed motion, only a figure similar to Fig.3.8 is included, that is, Fig.3.9. This figure assesses the shed follower's acceleration harmonics  $A_k$  [ $\text{m}/\text{s}^2$ ] in the VAR and CON-machine by showing  $\Delta A_k = A_{k,\text{CON}}/A_{k,\text{VAR}}$  on a dB-scale. Concerning the undesired harmonics  $k = \{7, 9, \dots\}$ , similar conclusions as in Section 3.3.3 are drawn: inertially compensated shed cams yield undesired harmonics that are *a lot* (at least 28 dB, that is, a factor 25)

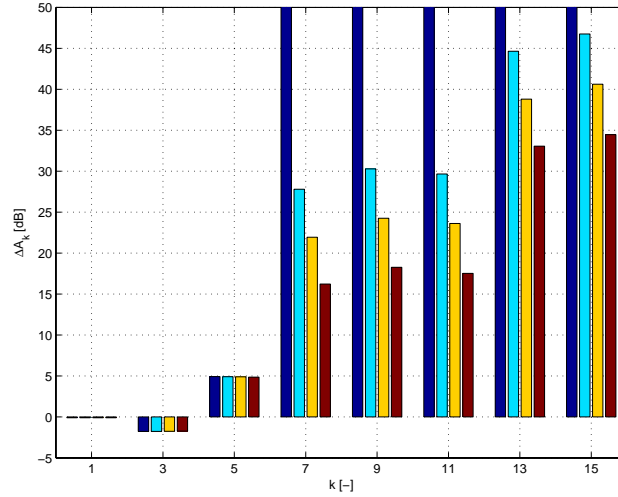


FIGURE 3.9: Comparison of VAR and CON-machine for  $\eta = \{0, 0.05, 0.10, 0.20\}$ : difference  $\Delta A_k = A_{k,\text{CON}}/A_{k,\text{VAR}}$  [dB] between the harmonics of the actually realized shed follower acceleration. For each harmonic  $k$ , the values of  $\Delta A_k$  for  $\eta = \{0, 0.05, 0.10, 0.20\}$  are given from the left to the right. Values of 50 dB indicate  $\Delta A_k = \infty$ . Only the uneven harmonics are relevant; the even harmonics have therefore been omitted from the figure.

smaller if a small amount of friction is present ( $\eta = 0.05$ ), and *significantly* (at least 16 dB, that is, a factor 6) smaller if a moderate amount of friction is present ( $\eta = 0.20$ ).

### 3.4.3 Sensitivity w.r.t. Variable Machine Settings

As indicated in Section 2.2, weaving machines are characterized by variable machine settings, depending on the fabric to be woven. This section investigates the sensitivity of inertially compensated shed cams for variations in the crossing angle  $g_{\text{cross}}$  and the number of moving frames  $N_{\text{shed}}$ . As these settings affect the resulting drive speed fluctuation during (damped) eigenmotion, they result in distortion of the motion imposed by the inertially compensated shed cams. It is assumed that  $g_{\text{cross}}$  ranges from  $280^\circ$  (extremely early crossing) to  $360^\circ$  (extremely late crossing).  $N_{\text{shed}}$  ranges from 4 to 16. The inertially compensated shed cams have been designed in Section 3.4.1 for a setting just in between, that is,  $\{g_{\text{cross}} = 320^\circ, N_{\text{shed}} = 10\}$ .

The effect of the variable synchronization is assessed via the difference, during damped eigenmotion ( $\eta = 0.05$ ), between the undesired 7-th and 9-th harmonic of the shed follower acceleration in the VAR and the CON-machine.

That is,  $\Delta A_7 = A_{7,\text{CON}}/A_{7,\text{VAR}}$  and  $\Delta A_9 = A_{9,\text{CON}}/A_{9,\text{VAR}}$  are determined for the aforementioned range of  $g_{\text{cross}}$  and  $N_{\text{shed}}$ . Figure 3.10(a – b) shows  $\Delta A_7$  and  $\Delta A_9$  on a dB-scale<sup>17</sup>. Positive  $\Delta A_k$  dB-values indicate  $(N_{\text{shed}}, g_{\text{cross}})$  combinations for which the undesired harmonic  $k$  is smaller in the VAR than in the CON-machine.

These figures show that the results are much more sensitive for  $g_{\text{cross}}$  than for  $N_{\text{shed}}$ , since the contour lines are mainly oriented horizontally. In a small zone around the design crossing angle of  $320^\circ$ , the VAR-machine outperforms the CON-machine, more or less independent of the number of moving frames. However,  $g_{\text{cross}}$  deviating more than about  $5^\circ$  from its design value, causes the VAR-machine's undesired shed follower harmonics to be in fact greater than in the CON-machine. Hence, it must be concluded that, if significant synchronization changes are present in an airjet machine, inertially compensated shed cams are no solution for reducing the undesired shed follower acceleration harmonics.

### 3.5 Conclusion

Inertially compensated cams have a cam profile that is designed so as to impose some desired follower motion, despite the (eigenmotion-associated) drive speed fluctuation in a dominantly inertial machine. They are an example of integrated mechanism design, in which kinematic and dynamic design aspects are simultaneously considered. The literature survey concerning integrated design distinguishes between three classes of methods: (i) fully integrated kinematic-dynamic design, (ii) kinematic design with dynamic considerations and (iii) drive speed fluctuation design. Inertially compensated cams belong to the first class. Being based on a single synthesis step, they take a distinct position, as all other such methods require iterative kinematic synthesis-dynamic analysis steps. Furthermore, inertially compensated cams are superior to the (numerical optimization based) cam design methods belonging to the third class.

The developed, nondimensionalized design procedure starts from the assumption that the multi-follower cam-follower system is purely inertial. Distinction must be made between two cases. If all cams are inertially compensated (as with the academic example), the design procedure is based on an algebraic equation and the chosen  $\delta$ , which is given a value so as to obtain a compromise between a small flywheel size and reasonable cam profile properties. If, on the other hand, some of the cams are conventional, while others are inertially compensated (as with the airjet weaving machine), the design procedure is based on a nonlinear differential equation (resulting in a boundary value problem), and the chosen flywheel size.

---

<sup>17</sup>The values for  $k = \{7, 9\}$  and  $\eta = 0.05$  (that is, the second bar in each of the groups of four bars), given in Fig.3.9, can also be obtained from Fig.{3.10(a),3.10(b)} by reading the value at the point  $(N_{\text{shed}} = 10; g_{\text{cross}} = 320)$ .

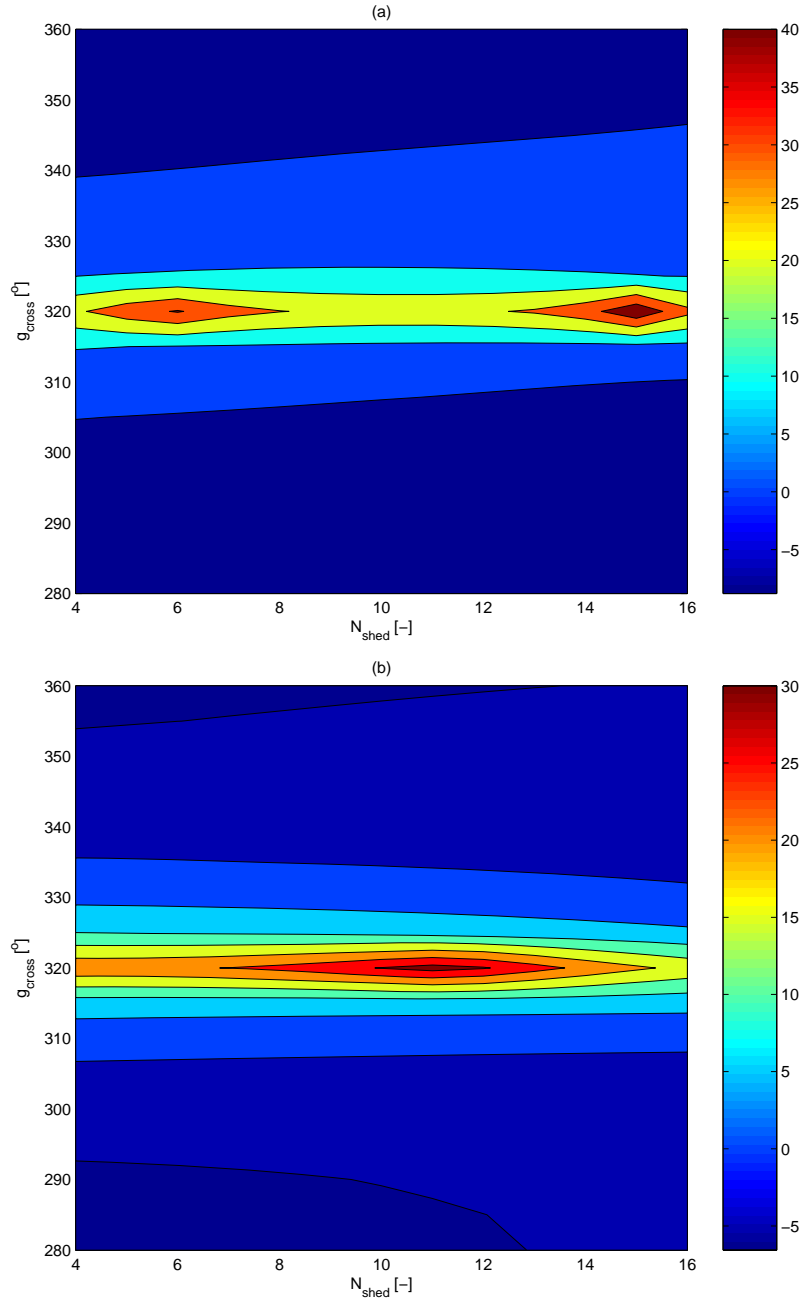


FIGURE 3.10: Comparison of damped eigenmotion ( $\eta = 0.05$ ) of VAR and CON airjet weaving machine:  $\Delta A_7$  [dB] (a) and  $\Delta A_9$  [dB] (b) as a function of the actually applied  $g_{\text{cross}}$  and  $N_{\text{shed}}$ .

Despite that conservativity is a basic assumption during the design process, inertially compensated cams are quite robust for the presence of (Coulomb) friction. That is, the undesired follower acceleration harmonics are reduced a lot if a small amount of friction is present ( $\eta = 0.05$ ) and significantly if the amount of friction is moderate ( $\eta = 0.20$ ). Unfortunately, the opposite is true for synchronization changes, for which the cams are very sensitive. As a result, they provide no solution for the undesired shed follower acceleration harmonics, encountered in weaving machines.

**General Applicability of Inertially Compensated Cams** Consider a general, reciprocating machine containing cam-follower mechanisms. What requirements should be fulfilled for inertially compensated cams to function properly? The design procedure of inertially compensated cams being based on the assumption of eigenmotion, proper functioning results if the reciprocating machine exhibits a regime motion similar to its eigenmotion. This is the case if two requirements are met.

First of all, as explained in Section 2.3, the machine must be driven by a motor with a low-bandwidth controller, such that its regime motion is similar to its damped eigenmotion. In this respect, a novel type of low-bandwidth control system is developed in Section 7.2, that is, *Average Speed Control* (ASC). As opposed to conventional low-bandwidth control systems, which always result in a remaining small fluctuation of the applied motor torque, ASC is theoretically capable of driving a motor such that it exerts a perfectly constant torque. Consequently and by definition, the resulting regime motion *is* the damped eigenmotion.

Secondly, friction losses should be limited, such that the damped eigenmotion resembles the eigenmotion. The simulations of Section 3.3.3 and Section 3.4.2 suggest that imposing  $\eta \leq 0.20$  is reasonable.

The design procedure of inertially compensated cams assumes that inertial forces are dominating in the reciprocating machine. It can however easily be adapted to take into account other types of conservative forces, such as gravity or spring forces (without however dropping the requirement that all bodies be rigid). The price to be paid is that the resulting compensated cams only operate perfectly for one design drive speed. The term *eigenmotion cams* is proposed here as a general name for cams that take into account the drive system dynamics of machines in which *conservative* forces are dominating.

Combining a low-bandwidth controller, such as ASC, with eigenmotion cams embodies one of the basic ideas of the *mechatronics* design paradigm: by highly integrating mechanical and control system design, it is possible to obtain superior overall system performance (that is, accurately realized follower motions in combination with a small flywheel and a minimum of energy losses in the motor), despite a very simple controller structure. This integration is an example of the so-called *concurrent-engineering* viewpoint, a typical feature of the mechatronics paradigm (Van Brussel, 1996).

## Chapter 4

# Input Torque Balancing: State-of-the-Art

*There are no answers, only cross references.*

Wiener's Law of Libraries

**A**S opposed to Wiener's Law of Libraries, this chapter does give an answer, that is, to the following question: 'What kind of input torque balancing method is suitable for reducing the drive speed fluctuation in airjet weaving machines?' In order to answer this question, an attempt to classify ITB methods, rather than an encyclopedic enumeration of all possible methods, is presented here.

Section 4.1 first gives a general overview of input torque balancing methods. As we are mainly concerned with conjugate cam-follower mechanisms in weaving machines, the following requirements are imposed:

- R1** the machine's energy consumption may not be raised substantially;
- R2** the machine's start/stop behavior may not be compromised;
- R3** the method must be valid for any average drive speed of the machine;
- R4** the method must be robust for changing machine settings, that is, variable synchronization between the sley and shed cam-follower mechanisms, and variable shed follower inertia;
- R5** the method must be easy to integrate with the present machine and not substantially raise its cost.

Section 4.1 concludes that the only input torque balancing (ITB) method, complying with these requirements, is the addition of an auxiliary, purely inertial, input torque balancing device. Section 4.2 therefore gives an overview and classification of such devices. After that, two important examples are discussed in detail, that is, the *centrifugal pendulum vibration absorber* (Section 4.3) and the ordinary cam-follower mechanism, used as an ITB mechanism (Section 4.4). The reason for doing so is twofold: (i) these ITB devices are the industrially most relevant ones and (ii) both ITB mechanisms designed in this work, that is, the inverted cam mechanism (Chapter 5), and the cam-based centrifugal pendulum (Chapter 6) are variants of them. Finally, Section 4.5 gives an overview of the benefits of input torque balancing.

## 4.1 Survey of Input Torque Balancing Methods

Koster (1975) distinguishes three causes for drive speed fluctuations in industrial machinery: (i) variations in the angular velocity of the driving actuator, due to load variations, (ii) backlash in the reduction gear between the actuator and the camshaft and (iii) wind-up of the camshaft. Here, an overview is given of methods to reduce drive speed fluctuations due to *load variations*. These methods (except for imposing a steady drive speed through the driving actuator) aim at smoothing or eliminating the input torque, required from the driving actuator. They are hence termed *input torque balancing methods*.

All methods discussed in this chapter assume the kinematics of the mechanism to be fixed, that is, the desired motion of the follower of a cam-follower mechanism or the link lengths and ground point locations of a linkage. Integrated methods that optimize the kinematics of a mechanism for improving its dynamic behavior have been considered in Section 3.1.

Given the kinematics of a mechanism, drive speed fluctuations due to load variations can be reduced *actively* or *passively*. A first active method consists of driving the mechanism with a powerful (and hence large) motor equipped with an adequate, high-bandwidth control algorithm, see e.g. (Tao and Sadler, 1995). This is no ITB method in the true sense of the word. Some actively controlled torsional vibration absorbers are introduced in Section 4.2.1 and 4.3. These devices reduce the drive speed fluctuation by eliminating a (real-time tunable) harmonic of the torque acting on the drive shaft. While offering more flexibility than passive solutions, active methods have the disadvantage of increased system complexity and energy consumption.

*Passive* measures for reducing drive speed fluctuations include the addition of energy dissipating elements or energy storing elements. Energy dissipating elements include torsional friction dampers, see e.g. (Ker Wilson, 1968a), mounted on the drive shaft or dashpots between the links. They come at the cost of an increased energy consumption of the driving motor.

Adding energy storing elements can be done through mass or spring addition, or a combination of both. It is well-known, see e.g. p.49 in (VDI2149, 1999), that spring addition for input torque balancing of dominantly inertial mechanisms, yields results that are optimal for a *single* mean drive speed  $\Omega$  [rad/s] only. For the same class of mechanisms, mass addition results are *independent* of  $\Omega$ . Therefore, mass addition is generally more suitable for weaving machines. A survey of input torque smoothing methods based on springs is given in (Berkof, 1979; VDI2149, 1999). A survey of mass addition methods is given below.

Mounting a flywheel is the simplest and most classical way of adding mass for reducing drive speed fluctuations. However, a large flywheel compromises a mechanism's start/stop behavior. Other mass addition measures include adding mass to the existing mechanism links, or adding extra links, that is, an auxiliary input torque balancing (ITB) device. In general, these measures require much less mass than mere flywheel addition<sup>1</sup>. Adding mass to the existing links generally succeeds at reducing instead of eliminating the input torque. While in e.g. (Hockey, 1971, 1972), only the input torque is considered, present state-of-the-art methods aim at simultaneously reducing the input torque, the shaking force and the shaking moment. These methods are the subject of the literature survey of Chapter 8. Adding mass to the existing links is mainly concerned with linkages, while adding an ITB device is applicable to both linkages and cam-follower mechanisms.

Based on the above survey of methods, and the specific requirements of weaving machines, it is obvious that adding a mass-based ITB device is the only solution complying with {R1,R2,R3}. In order to comply with R4, both the sley and shed mechanism of an airjet weaving machine should be equipped with an ITB device that changes its synchronization together with its corresponding mechanism. R5 imposes that the ITB device be simple and compact. With this in mind, several ITB devices are compared in the following section.

## 4.2 Auxiliary Input Torque Balancing Devices

Auxiliary input torque balancing devices come in two kinds: input torque balancing *mechanisms* and *torsional vibration absorbers*. Torsional vibration absorbers are rotary variants of the well-known *translational undamped dynamic vibration absorber* (TUVVA). They fundamentally differ from input torque balancing mechanisms because they are not kinematically determined. That is, they can adapt their motion amplitude to the amplitude of the torque acting on the drive shaft. Torsional vibration absorbers are *always* tuned in order to eliminate some harmonic component of the torque acting on the drive shaft, while most ITB mechanisms aim at eliminating the *full* torque.

<sup>1</sup>While mounting a flywheel can be considered to be a mechanical feedback system (there must be a drive speed fluctuation for the flywheel to exert a torque), mounting an auxiliary ITB device can be thought of as a mechanical feedforward approach.

ITB mechanisms have mainly been applied to linkages and cam-follower mechanisms appearing in industrial machinery, such as weaving and packaging machines. In this kind of machinery, inertial forces are often dominating. Torsional vibration absorbers are mostly found in crankshaft and transmission systems of aero, automobile and marine propulsion engines and in engine-driven electrical generator systems. Borowski et al. (1991) for instance established the feasibility of crankshaft-mounted centrifugal pendulum vibration absorbers for reducing crankshaft torsional vibration in four-cylinder automobile engines. They also report on application of pendulum-type vibration absorbers to reduce the fuselage shake in helicopters, produced by rotor-associated fluctuating aerodynamic forces. In these systems, there is an important contribution of both inertial and other forces, such as gas or aerodynamic forces.

With respect to input torque balancing *mechanisms*, a distinction is made here between mechanisms providing *full*, *partial* and *harmonic* input torque balance. Full balance is only possible if the added links can perfectly realize a prescribed motion. Methods based on the use of cams or noncircular gear pairs can do this and hence provide full balance. On the contrary, methods based on adding two-link mechanisms (*dyads*) cannot and therefore provide only partial balance. Harmonic balance, such as provided by unbalanced planetary gear systems, implies that one or several harmonics of the input torque are balanced. It constitutes a special case of partial input balance.

Torsional vibration absorbers are discussed in general in Section 4.2.1. Section 4.2.2 discusses cam-based ITB mechanisms, whereas Section 4.2.3 gives an overview of methods based on noncircular gear pairs. Mechanisms providing partial balance are the subject of Section 4.2.4. For a survey of various either fluid-based or mechanical, more exotic ITB mechanisms, the reader is referred to (Ullman and Velkoff, 1979).

### 4.2.1 Torsional Vibration Absorbers

Torsional vibration absorbers are all rotary variants of the translational undamped dynamic vibration absorber (TUVA). They are tuned in order to eliminate some harmonic component of the torque acting on the drive shaft. In general, the frequency of this harmonic component is considered to be an integer multiple  $m\Omega$  of the average drive speed  $\Omega$ .  $m$  is referred to as the *order* of the torque harmonic.

For a torsional system, Den Hartog (1956) suggests two types of undamped dynamic vibration absorbers. The *torsional pendulum vibration absorber* (TPVA), conceptually shown in Fig.4.1(a), takes the shape of a flywheel  $J_c$  [kg-m<sup>2</sup>] attached to the original mechanism through a spring  $k_c$  [N-m/rad]. Being a system containing a spring, the TPVA is tuned for a single  $\Omega$  only, that is, the speed for which the frequency  $m\Omega$  of the disturbing harmonic torque coincides with the natural frequency  $\sqrt{k_c/J_c}$  of the attached absorber.

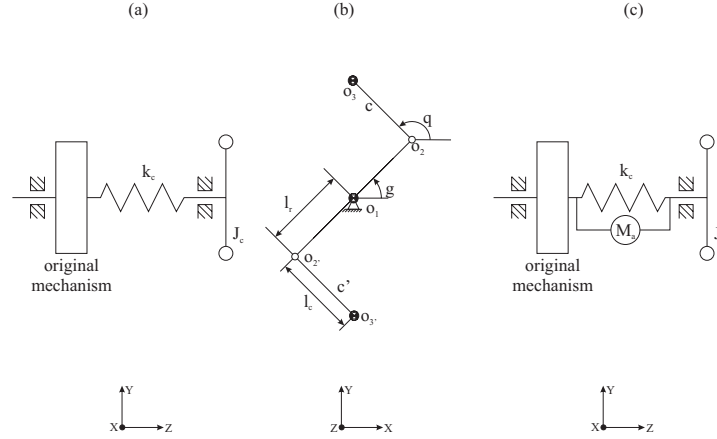


FIGURE 4.1: (a) Torsional pendulum vibration absorber (TPVA); (b) Centrifugal pendulum vibration absorber (CPVA) and (c) Delayed resonator. The Z-axis is defined to be parallel to the drive shaft. Mind its different orientation in (b).

This shortcoming is overcome by the *centrifugal pendulum vibration absorber*<sup>2</sup> (CPVA), conceptually shown in Fig.4.1(b). The rotor of length  $l_r$  [m] revolves around the ground point  $o_1$ , and is connected to the coupler (pendulum)  $c$  of length  $l_c$  [m] by a revolute joint. It is easily shown, see e.g. (Den Hartog, 1956), based on the *linearized* equations of motion, that the natural frequency of the pendulum in the centrifugal field equals  $\Omega\sqrt{l_r/l_c}$ . For any  $\Omega$ , this frequency coincides with the frequency  $m\Omega$  of the disturbing torque, provided that

$$m = \sqrt{\frac{l_r}{l_c}}. \quad (4.1)$$

Being a purely inertial system, a CPVA is a torsional undamped dynamic vibration absorber that is tuned correctly for all  $\Omega$ , provided that (4.1) is satisfied. In that case, the rotor has no oscillatory motion (that is, it rotates at a perfectly steady speed), while the coupler (pendulum) has a finite oscillatory amplitude. The CPVA is discussed in greater detail in Section 4.3.

Recently, some new, adaptive variants of the TPVA have been devised, so as to obtain a TPVA with a tunable eigenfrequency. Some of these devices are actively controlled. The delayed resonator (Filipovič and Olgac, 2002) of Fig.4.1(c) is a conventional TPVA which is turned into a real-time tunable

<sup>2</sup>The CPVA dates from 1929 (Carter, 1929). For a thorough account of the history of the CPVA and examples of its practical implementation, the reader is referred to the treatise by Ker Wilson (Ker Wilson, 1968b).

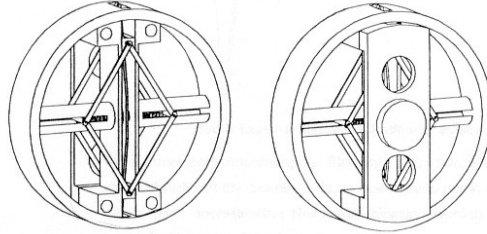


FIGURE 4.2: Passively controlled, tunable TPVA: overall system. Reproduced from (Baron and Poll, 2003).

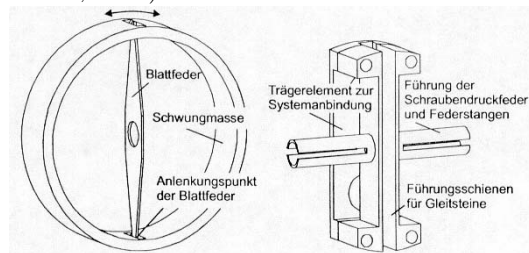


FIGURE 4.3: Passively controlled, tunable TPVA: mass-(leaf)spring system and carrying structure. Reproduced from (Baron and Poll, 2003).

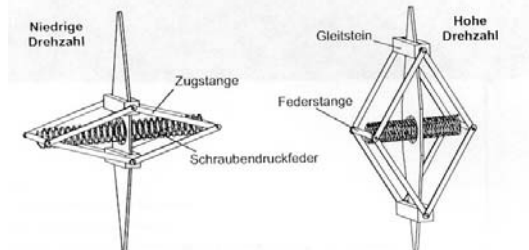


FIGURE 4.4: Passively controlled, tunable TPVA: extreme positions of control system for lowest (left) and highest (right) drive speed. Reproduced from (Baron and Poll, 2003).

TPVA, by application of a control torque  $M_a$  in the form of a proportional position feedback with time delay. Its applicability is however limited to cases in which the frequency of the disturbing torque fluctuates within a certain range around the natural frequency of the passive TPVA used. Real-time tunable, *semi-active* TPVA's are obtained by adapting the spring stiffness with an electromagnetic actuator (Arras, 1996) or by implementing the spring as a controllable magnetic field (Weltin and Hermann, 1997).

An interesting, *passively* controlled, tunable TPVA is proposed by (Baron and Poll, 2003). The overall system, shown in Fig.4.2, consists of three main parts: a mass-(leaf)spring system (Fig.4.3), a carrying structure (Fig.4.3) and a mechanical control system (Fig.4.4). The free length (and hence the stiffness) of the leaf spring is passively controlled through the mechanical control system, under influence of the centrifugal force. The geometry (width) of the leaf spring is optimized so as to approximate the desired stiffness-drive speed characteristic as much as possible. Application of the system to a four-cylinder Diesel motor with direct injection, experimentally proves the ability of the tunable TPVA to compensate, in a broad speed range, for the first-order torque harmonic, caused by the injection pump.

### 4.2.2 Cam-Based Mechanisms

The simplest, cam-based mechanism is an ordinary cam-follower mechanism, with either the follower inertia or a spring working against the follower as accumulator of energy. The main disadvantage of using the follower kinetic energy is the fact that the resulting cam displacement is generally not periodic, such that not an ordinary disk cam, but e.g. an expensive indexing cam must be used. As already mentioned, the main disadvantage of using the spring potential energy is that perfect compensation of a dominantly inertial system is only possible at one design speed. Although only the inertia-based variant is relevant for this work, for the sake of completeness, both the inertia-based and spring-based variant are discussed in detail in Section 4.4.

Figure 4.5 shows another simple, cam-based mechanism, which is a kinematic inversion of an ordinary cam-follower mechanism, hence the name coined here: *inverted cam mechanism* (ICM). A prismatic joint connects the carriage 3 to the rotor 2, which revolves around  $A$ . A groove cam determines the position of the carriage on the rotor.

To the best of our knowledge, the ICM was firstly proposed by Artobolewski (1958) and Dizioğlu (1966), yet without a method to synthesize the internal cam profiles. Artobolewski (1958) mentions, however without any motivation, that the ICM often has more favorable properties than the ordinary, inertia-based cam-follower mechanism.

Meyer zur Capellen (1964) seems to be the first and only one in the open literature to have developed a method to synthesize the internal cam profiles. His method however is not correct, as it is based on a wrong application of the principle of angular momentum (see Section 5.3.2).

The ICM reappears in a European patent by Michelin (1979), who proposes a synthesis method, which is not correct either, as it is based on an algebraic equation, obtained by simplifying the differential equation which governs the cam design (see Section 5.3.2). Finally, the ICM is mentioned in the survey of torque balancing mechanisms given in (Funk and Han, 1996), but again without any reference to a method to synthesize the cam profile.

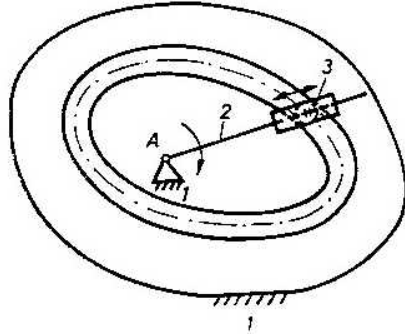


FIGURE 4.5: Inverted cam mechanism. Reproduced from (Dizioğlu, 1966).

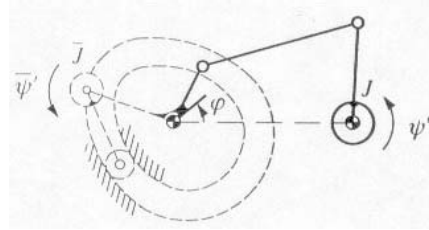


FIGURE 4.6: Cam based centrifugal pendulum, connected to the input crank of a four-bar mechanism. Reproduced from (Dresig, 2001).

A mechanism, comparable to the ICM, is shown in Fig.4.6. This is a centrifugal pendulum, of which the pendulum motion is imposed by a groove cam, hence the name proposed here: *cam-based centrifugal pendulum* (CBCP). This mechanism is described in (VDI2149, 1999) and (Dresig, 2001) but without a method to synthesize the cam profile, and without additional references. To the best of our knowledge, a design procedure for designing this mechanism is not available in open literature.

A first variant of more complicated, cam-based mechanisms, is the mechanism proposed by Funk and Han (1996), shown in Figure 4.7. It consists of a gear pair, an additional link AE and a groove cam that determines the variable angular velocity of the additional link. AE revolves around A and is statically balanced. It turns together with the crank of the crank-rocker four-bar mechanism it balances, but with a variable angular velocity controlled by the groove cam. The cam is rigidly connected to a gear which rolls over a gear fixed to the machine frame. Both gears are spur gears with the same number of teeth. The design of the cam is governed by an algebraic equation, and results in full input torque balance.

Figure 4.8 shows a second variant, a five-bar cam-linkage mechanism proposed by Teng et al. (1999). Link 1 is fixed to the drive shaft of the original mechanism, an indexing cam-follower mechanism, while link 4 is attached to an auxiliary flywheel. A roller follower, of which the motion is imposed by a groove cam, is attached to the point  $\hat{o}_3$ . By imposing that the sum of the kinetic energy of the auxiliary flywheel and the original mechanism be constant (the kinetic energy of the links 2 and 3 is supposed to be negligible), an algebraic equation in the cam pitch radius, for given design parameters (link lengths, flywheel inertia, . . . ) is obtained.

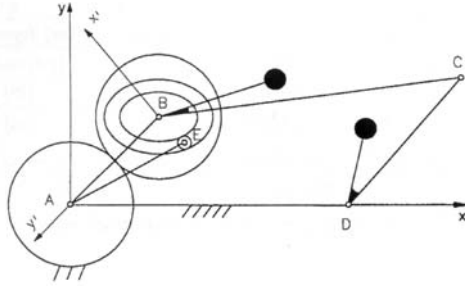


FIGURE 4.7: ITB mechanism connected to the crank AB of a crank-rocker four-bar mechanism. The circles represent two spur gears, the lower of which is fixed to the mechanism frame. Reproduced from (Funk and Han, 1996).

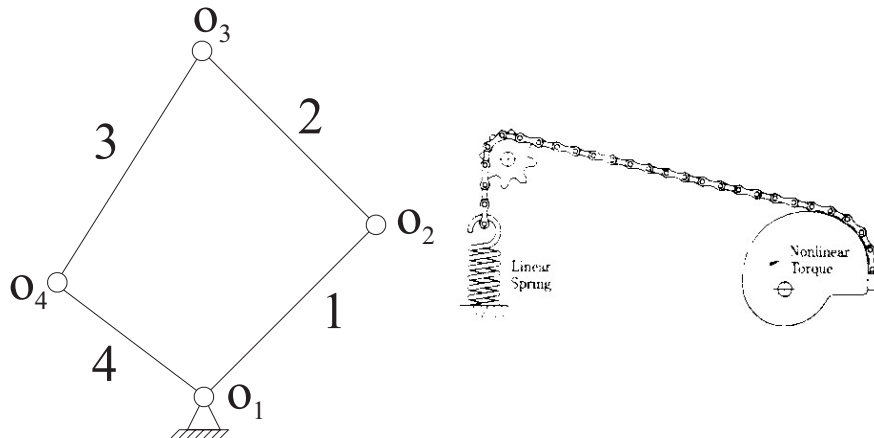


FIGURE 4.8: ITB mechanism proposed by Teng et al. (1999): kinematic scheme.

FIGURE 4.9: Nonlinear torsion spring mechanism. Reproduced from (Tidwell et al., 1994).

The design parameters themselves are obtained based on an optimization problem, which aims at minimizing a weighted combination of the flywheel inertia, the mechanism's transmission angle and the cam pressure angle. The optimization constraints include bound constraints on the design parameters, size constraints for the groove cam, and the requirement that the cam profile be convex. The optimization results in a compact mechanism. However, though theoretical full torque balance is claimed, in simulation it is not obtained, and no justification is given for that.

Tidwell et al. (1994) suggest that a linear spring could be used in conjunction with a wrapping cam (a cam wrapped by a belt or chain) to produce a nonlinear torsional spring. This nonlinear spring, of which the torque-displacement relation is perfectly controlled by the shape of the cam, can be used to balance the input torque of e.g. a crank-rocker four-bar linkage, as shown in Fig.4.9. The mechanism to be balanced must have at least one rocking link, as a wrapping cam generally oscillates back and forth, typically through less than one revolution. The presence of a spring makes the balancing result speed-dependent.

### 4.2.3 Noncircular Gear Pair Based Mechanisms

Both (Kochev, 1990)<sup>3</sup> and (Dooner, 1997) develop, apparently independently from each other, a general design procedure for an auxiliary flywheel, driven by a noncircular gear pair, as a mechanism providing full torque balance. The same principle is also suggested in (VDI2149, 1999).

Application, in (Kochev, 1990), of the method to a force-balanced four-bar linkage shows that this technique demands moderate moment of inertia of the crank and the auxiliary flywheel, and leads to realistic configurations of the noncircular gears. Similar conclusions follow from (Dooner, 1997), in which a crank-slider mechanism, driving a stamping operation, is considered.

(Kochev, 1990) observes that any suitable mechanism could be driving the auxiliary flywheel, but identifies an external, noncircular gear set as the simplest method. In fact, the already discussed mechanisms, proposed by Funk and Han (1996) and Teng et al. (1999) are other variants, in which respectively link AE (Fig.4.7) and link 4 (Fig.4.8) are connected to the auxiliary flywheel.

Noncircular gears provide a much more compact alternative, but are non-standard machine elements, as pointed out by Dooner (1997): '...very few gear manufacturers are capable of fabricating such toothed bodies. Also, the limited success of applying noncircular gears in practice can be attributed to the large amount of computations necessary for the accurate design and manufacture.' Another disadvantage, not mentioned by neither Kochev nor Dooner, is that sign changes of the fluctuating torque, transmitted by the gear pair, cause the gear pair to run through its backlash.

By considering the noncircular gear set as a variator (that is, a transmission having a continuously variable ratio and no steps), an interesting analogy with the work of Liniecki (1969) appears. He considers a slider-crank mechanism, driven by an electric motor via a variator. It is shown that, given the slider-crank data and the torque-speed characteristic of the driving motor, it is possible to keep the crank speed constant, through an appropriately designed variable transmission ratio. If one considers the motor inertia to be a flywheel, the analogy with the work on noncircular gear pair driven flywheels

---

<sup>3</sup>Kochev credits (Hunag and Shi, 1987) to be the original developers of the method.

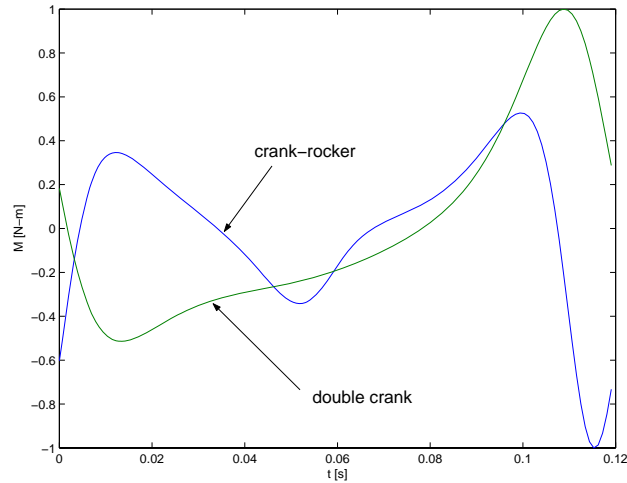


FIGURE 4.10: Typical input torque trajectories for a crank-rocker and a double crank four-bar mechanism.

emerges. In fact, if no energy dissipation nor external work were present, the crank speed would be constant, the motor turning with a fluctuating speed and delivering no torque at all.

#### 4.2.4 Mechanisms Providing Partial Balance

Probably the most simple of ITB mechanisms is the two-link mechanism (*dyad*), which yields *partial* input torque balance. Addition of a dyad to a link (often the crank) of a mechanism is suggested as an ITB measure in several papers. Using conventional kinematic synthesis methods, Ogawa and Funabashi (1969) manage to halve the (maximum of the) input torque required to drive a spatial crank-rocker four-bar, by adding a dyad to the rocker link. Kulitzscher (1970) adds a dyad to the crank of an externally loaded planar crank-rocker four-bar. As a result,  $\kappa$ , determined by assuming that an AC motor drives the mechanism, reduces from 10% to 3.3%. Both papers adopt a synthesis, rather than an optimization approach.

Adding a dyad to the crank of a mechanism, as done in (Kulitzscher, 1970), creates a parallel, input torque balancing four-bar mechanism. A useful observation by Kulitzscher is that the type of parallel four-bar immediately follows from the shape of the torque to be balanced, as shown in Fig.4.10: a crank-rocker four-bar has an input torque with two maxima and two minima, while a double crank four-bar has a single maximum and a single minimum. This result might be useful when optimizing a four-bar for input torque balancing, by constraining the link lengths (using the Grashoff criteria) such that either

a double crank or a crank-rocker is obtained.

Bagci (1978) applies a four-bar mechanism for partial input torque balancing of the top brush of an automatic car washing and waxing line. Through optimization, a satisfactory design is obtained, which results in almost a four-fold mass reduction with respect to the original torque balancing mechanism (a chain-sprocket mechanism).

Yong and Zhen (1989) design a dyad for torque balancing a slowly turning (40-90 rpm), heavy seven-bar linkage, in which, due to the slow drive speed, inertia forces, friction forces and gravitational forces are equally important. Again, the dyad is added to the crank of the original mechanism, such that a parallel (double crank) four-bar mechanism is obtained. Adopting a synthesis<sup>4</sup>, rather than an optimization approach, a 50% reduction of the (maximum of the) input torque is obtained.

While dyads yield partial input torque balance, the unbalanced planetary mechanism suggested by Ogawa and Funabashi (1969), provides harmonic balance. It is a planetary mechanism with unbalanced planets, driven by timing belts and toothed pulleys (instead of gears). Despite that this mechanism aims at eliminating a specified torque harmonic, it is *not* a torsional vibration absorber as it is not capable of adapting its amplitude of motion to the amplitude of the disturbing torque. Experimental results show that this mechanism is effective in removing the torque harmonic it is tuned to.

### 4.3 Centrifugal Pendulum Vibration Absorber

In Section 4.2.1, it was shown that a CPVA is able to eliminate an  $m$ -th order harmonic torque, provided that

$$m = \sqrt{\frac{l_r}{l_c}}. \quad (4.2)$$

The above result is based on the linearized equations of motions of the CPVA, which are valid for small coupler amplitudes only. However, large amplitudes are sometimes unavoidable if e.g. the CPVA's end point mass (located in point  $\hat{o}_3$  in Fig.4.1(b)) is to be limited. In that case, nonlinear effects come into play, which cause the torque balancing properties of a CPVA to become fundamentally different from the torque balancing properties of a TUVA. Nonlinear effects are also present in TUVA's. However, as opposed to the CPVA, of which the nonlinear range is inherent from its design, nonlinearities are much more device dependent for TUVA's.

As a first difference, a TUVA is effective for a large range of amplitudes of the disturbing harmonic force. On the contrary, CPVA's designed based on the linearized equations of motion, so-called *linear* CPVA's, are effective for

---

<sup>4</sup>This synthesis approach seems to be rather sloppy as it contains some redundancy, as shown in (Funk and Han, 1996).

low torque amplitudes only. For higher torque levels, nonlinear effects due to large coupler amplitudes cause the CPVA's frequency to shift. This *detuning* may result in destructive failure of the CPVA (Newland, 1964). A solution for this is to design CPVA's in which the end point mass moves on a noncircular<sup>5</sup> path, such as a kind of epicycloidal path, the *tautochrone*, (Borowski et al., 1991; Denman, 1992). The frequency of these so-called *tautochronic* CPVA's is independent of the coupler (and hence torque) amplitude. In this way, the disastrous detuning is completely avoided. Unfortunately, new dynamic problems then show up, resulting in smaller allowable torque levels than those initially foreshadowed by the tautochronic CPVA's: it has been observed (Chao et al., 1997b,a) that, if CPVA's are divided into a number of identical masses (e.g. due to spatial restrictions), they do not always move in unison: bifurcations may occur in which a single absorber moves out of step with its partners and which limit the allowable torque level.

As a second difference, a TUVA is capable of perfectly balancing a purely harmonic force, as opposed to a (linear or tautochronic) CPVA which induces higher torque harmonics, again due to nonlinear effects. It has however been shown (Lee and Shaw, 1996; Lee et al., 1997) that subharmonic absorber pairs can provide a solution. These tautochronic absorber pairs that are tuned to one-half of the frequency of the disturbing torque, are theoretically effective in the fully nonlinear operating range, and are capable of perfectly eliminating a purely harmonic torque of frequency  $m\Omega$ . The price to be paid is a double number of absorbers. Furthermore, some questions remain (Lee et al., 1997), such as the dynamic stability. Recent results concerning these subharmonic absorber pairs are found in (Chao and Shaw, 2000).

As for the TPVA, an active variant has also been proposed for the CPVA, called the *centrifugal delayed resonator*, in which a control torque is applied to actively control the torque balancing properties (Hosek et al., 1997).

## 4.4 Cam-Follower Mechanism as ITB Device

### 4.4.1 A Historical Note

Kirchhof (1972) points out that the spring-based variant of the cam-follower ITB mechanism, is probably the oldest ITB mechanism, as it was used as such in the knitting machine devised by William Cotton<sup>6</sup> in 1864. This machine had heavy, lead cams mounted on a camshaft of about 20 meters. The follow-

<sup>5</sup>For the conceptual simple pendulum construction of Fig.4.1(b), the CPVA is essentially a point mass which moves along a circular path relative to the rotor. Most currently employed variants of the CPVA are however of the bifilar type, see e.g. (Borowski et al., 1991; Denman, 1992; Eckel and Kunkel, 1997). Bifilar arrangements allow imposing arbitrary, noncircular paths.

<sup>6</sup>In 1864, William Cotton of Loughborough, Leicestershire (England) devised a method of machine-knitting fabric whereby it could be shaped or fashioned automatically. This method is known as 'Cotton's Patent'. Source: <http://www.silk-stockings.co.uk>.

ers were assured to have contact with the cams by heavy springs. However, in order to turn the camshaft by hand (which was required every now and then), Cotton provided balancing cams, also working against a spring.

These cams were designed in a rather heuristic way (Kirchhof, 1972), such that the statical input torque (that is, the input torque to overcome the spring forces) was zero. This was however not the only advantage. It was observed experimentally that the dynamic performance also improved substantially, since the fluctuation of the driving torque substantially decreased at the nominal speed. Consequently, a smaller motor could be selected.

Sarring (1962) develops a method to synthesize the cam for the spring-based variant. This method is valid for systems with or without external work. He suggests that, if a system does work, torque balancing cams can be used to redistribute the work over the cycle, so as to present a constant torque demand to the power source (this is exactly the way a motor is supposed to behave during damped eigenmotion).

Benedict and Tesar (1970) and Benedict et al. (1971) describe input torque balancing of a complex stamping and indexing machine, supposed to operate at 100 rpm (the Mazzoni soap stamp). A collection of measures<sup>7</sup> leads to a spectacular decrease of the drive speed fluctuation from 85–115 rpm to 98–102 rpm. Some generally interesting ideas are developed in this work. Firstly, for the inertia-based variant, it is suggested to take additional measures<sup>8</sup> for shaping the input torque so as to make it reasonably balanceable by a cam with a *periodical* cam displacement. Secondly, for the spring-based variant, an iterative<sup>9</sup> procedure is presented in order to obtain perfect balance, despite the nonzero inertia of the follower (most other methods for the spring-based variant neglect this inertia).

Kirchhof (1972) reports on dynamic problems (heavily increased link accelerations, excessive vibration) due to drive speed fluctuations ( $\kappa = 115\%$  (!) at a nominal speed of 480 rpm) of a conjugate cam-follower mechanism, part of a mechanical data processing machine. Using the spring-based variant,  $\kappa$  is reduced to 85%. An interesting theoretical result developed in this paper is a table, giving in nondimensionalized form, the shape and maximum value of the inertial part of the input torque, for a series of commonly used cam motion laws. The idea is that the lower this maximum value, the easier the cam-follower mechanism can be input torque balanced. This table illustrates that minimizing the maximum follower acceleration and the maximum inertial input torque of a cam-follower mechanism are conflicting demands.

---

<sup>7</sup>These measures include: spring addition, replacement of a Geneva cross by a cam-follower mechanism, change of link mass parameters, and adaptation of the already present cam-follower mechanisms to make them compensate part of the input torque required for the other mechanisms.

<sup>8</sup>In this particular case, the input torque is shaped by attaching an additional spring somewhere in the mechanism.

<sup>9</sup>In this case, the 'second try' cam already provides quasi perfect balancing after two iterations.

Furthermore, general examples are given that illustrate that the inertia-based variant gives rise to nonperiodical compensating cam displacements, while the spring-based variant gives rise to periodical cam displacements. In addition, these general examples illustrate that for a rise (or a return) of a purely inertial, original cam-follower mechanism, a spring-based compensating cam-follower mechanism must have a rise *and* a return. This explains why the compensating mechanism must be bigger in size in order to avoid bad pressure angles or undercutting.

#### 4.4.2 Recent Work

In his survey paper (Nishioka, 1995), Nishioka distinguishes between the so-called *direct* and *indirect* method. In the (original) indirect method, the compensating cam is attached to the input shaft of the original mechanism. In the direct method, the compensating cam is attached to the output shaft, that is, the follower shaft of the original mechanism. Nishioka suspects that the (spring-based) direct method could have the advantage of compactness, but often exhibits undercutting and requires one compensating system per cam-follower mechanism.

Concerning the inertia-based variant of the indirect method, Nishioka does not bother about the nonperiodicity of the displacement function, as the cam-follower mechanism to be balanced consists of a rotary table driven by an indexing cam, which allows for nonperiodical displacement functions. Using such a system also as a compensating system however substantially increases the economical cost of the compensation: Nishioka estimates the cost of the inertia-based, indirect method to be a factor 5 to 10 higher than the cost of the spring-based, indirect method, which, moreover, is more compact.

For these reasons, Nishioka argues that indirect compensation based on spring energy seems industrially more realistic. In that case the remaining problem is the fact that the compensation is only complete for one design speed. In order to overcome this problem, two measures are proposed. First of all, for each machine speed, the preload of the spring is adjusted in order to minimize the torque residual. Secondly, in (Arakawa et al., 1997a), an *air spring* is used instead of a (cheap and compact) coil spring. An air spring, that is, a pneumatic piston-cylinder system, has the advantage that its spring constant is adjustable through the air pressure. A design procedure, minimizing the distortion energy of the air in the cylinder, is proposed, together with a strategy for controlling the air pressure at different drive speeds. Still however, both proposed measures (adjustable preload or air spring) are not capable of yielding complete input torque balance for any drive speed.

Various other developments concerning the (coil) spring-type, indirect method include: corrections for the nonzero inertia of the compensating follower (Nishioka and Yoshizawa, 1994); inclusion of nonconservative terms, such as friction (Arakawa et al., 1997b); design based on measured instead of analytically predicted input torques (Nishioka, 1999); suppression of the *sec-*

*ondary vibration* of the mass-spring system, constituted by the compensating cam's follower mass and the spring against which the compensating cam is working (Nishioka et al., 1999).

In (Wu and Angeles, 2001), the spring-based variant is designed and optimized, so as to (i) avoid excitation of the secondary vibration and (ii) obtain a (helical) spring of minimum mass.

Research concerning the spring-based variant has also been conducted under the supervision of Norton. In his master thesis, Aviza (1997) designs a spring-based variant under the assumption that its follower is massless, as his cam synthesis method fails to converge in the presence of follower mass (Norton, 2002). When a realistic follower mass is applied, a 10% torque residual remains. Experimental work reveals only a 68% reduction in torsional oscillation (much of the residual torque is attributed to resonance in the test setup).

In a subsequent master thesis, Tuxbury (2002) attempts to solve the convergence problems, identified by Aviza. Apparently not aware of the pragmatic, iterative method proposed by Benedict et al. (1971) and the perturbation method proposed by Nishioka and Yoshizawa (1994)<sup>10</sup>, Tuxbury devises his own method for obtaining convergence of the nonlinear differential equation governing the cam design. The rise and return segments of the compensating cam are determined separately, based on iterative application of numerical (Runge-Kutta) integration techniques.

## 4.5 Benefits of Input Torque Balancing

**Reduced Drive Speed Fluctuation** Input torque balancing results in reduced drive speed fluctuation in the presence of a motor, equipped with a low-bandwidth controller. This in turn has several important advantages. The increased link accelerations (and corresponding joint and link loads) due to excessive drive speed fluctuations are avoided. As a consequence, vibration excitation is lower, and '...reduced noise and increased life for certain components will probably result.' (Berkof, 1979).

Moreover, cam profiles compensating for the dynamics of the follower are sensitive to drive speed fluctuations and are useless if these are too big (Saring, 1962).

Improvement of the dynamic behavior is not confined to the driving mechanism alone. Borowski et al. (1991) reports on improvements in NVH (Noise, Vibration and Harshness) performance in a car by equipping its four-cylinder engine with CPVAs: 'During road testing, improvements in NVH performance were subjectively confirmed by experienced development engineers.'

---

<sup>10</sup>This paper being in Japanese, except for the abstract, the effectiveness of this method could not be traced back.

**Reduced Peak Torques** If the driving motor is equipped with a high-bandwidth controller, in order to impose a constant drive speed, input torque balancing results in lower peak torques. 'Since a motor is generally sized for peak operating conditions, it follows that smoothing of input torque requirements is economically rewarding.' (Berkof, 1979). If no friction or external work are present, a perfectly input torque balanced system can run (after start-up) at constant speed, even without a motor. 'Ignoring the effect of friction and start-up problems, a perfectly balanced soap stamp could be driven by a motor in size similar to that used in many household appliances.' (Benedict and Tesar, 1970). 'Neben der Verbesserung der gesamten Dynamik kommt man dadurch u.U. auch mit einem schwächeren Antriebsmotor aus.' (Kirchhof, 1972). Lowering the peak torques, and the associated peak currents also reduces the motor's thermal load and energy losses.

**Reduction of Torsional Stress and Deflection** 'If the motivation is simply to hide the cyclic torque fluctuations from the driving motor (as with a flywheel), then only one torque compensation cam is needed to counteract the sum of the torques of all the driving cams on a given camshaft. If on the other hand, one wishes to reduce the torsional stresses and deflections in the camshaft, then it may be necessary to add a compensating cam adjacent to each driving cam, thus cancelling the torque locally before it has an effect on the relative angular positions between driving cams.' (Norton, 2002).

## 4.6 Conclusion

In Section 4.1, it has been shown that the only measure for reducing drive speed fluctuations, complying with all specific requirements of a weaving machine, is addition of a purely inertial, input torque balancing device. Moreover, this device must be simple and compact.

Although being purely inertial, the CPVA is not suitable for application in a weaving machine. Firstly, the input torque of e.g. the sley motion has seven significant harmonics, necessitating the use of, in principle, seven CPVAs, tuned for the different orders. Furthermore, the nonlinear dynamic behavior of CPVAs is still a problematic issue.

Mechanisms providing full torque balance are preferred here. Despite the compactness and elegance of ITB mechanisms based on noncircular gearing, preference is given to cam-based mechanisms: noncircular gears are difficult to fabricate and exhibit backlash. The ordinary cam-follower mechanism is simple, but its basic spring-based variant is automatically ruled out because of its speed dependency. The more advanced variant using air springs partially overcomes this problem, but is rejected because of the added complexity of the required control system. Moreover, it is still not capable of yielding complete input torque balance for any drive speed. The inertia-based variant on the other hand is unsuitable due to its nonperiodic displacement program.

The ICM and CBCP on the other hand have promising futures, as they are compact and constructively simpler than other cam-based mechanisms. Moreover, design procedures for them are either erroneous, too rough an approximation or simply nonexistent. Therefore, it was decided to choose these mechanisms as candidate ITB mechanisms for weaving machines. The following two chapters point out that the main reason for the problems with the existing design procedures, is that the cam design is governed by a nonlinear differential equation. Although this differential equation is easy to derive, solving it is not trivial. The nonlinear least-squares techniques, developed in Chapter 5–6 for solving this differential equation, in fact also apply to the nonlinear differential equation arising in the work of Aviza (1997).

## Chapter 5

# Input Torque Balancing: Inverted Cam Mechanism

*A scientist is a mimosa,  
when he himself has made a mistake,  
and a roaring lion,  
when he discovers a mistake of others.*

Albert Einstein (1879-1955)

**I**N the literature survey of the previous chapter, the inverted cam mechanism (ICM) of Fig.5.1 has been identified as an interesting candidate ITB mechanism, for which at the moment, only erroneous design procedures seem to exist. This chapter shows how the ICM is designed and optimized.

Section 5.1 derives the nonlinear differential equation that governs the cam design, called the *describing equation* for short, whereas Section 5.2 shows how to solve it, for given values of the design parameters. After that, an ICM is designed in order to input torque balance the sley cam-follower mechanism of an airjet weaving machine (Section 5.3). The ICM's design parameters are determined based on an optimization problem, proposed in Section 5.4. In order to solve this optimization problem efficiently, a nondimensionalization, similar to the one of Chapter 3, is carried out in Section 5.5.

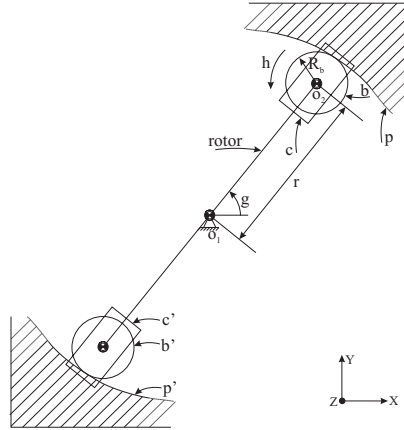


FIGURE 5.1: Inverted cam mechanism (ICM): kinematic scheme.

## 5.1 Derivation of the Describing Equation

### 5.1.1 Nomenclature

The kinematic and dynamic ICM parameters are defined based on Fig.5.1. The rotor, with mass  $m_r$  [kg] and centroidal moment of inertia  $J_r$  [kg-m<sup>2</sup>], revolves around the ground point  $\hat{o}_1$ . A prismatic joint connects the carriages  $c$  and  $c'$ , each having mass  $m_c$  [kg] and centroidal moment of inertia  $J_c$  [kg-m<sup>2</sup>], with the rotor. The roller followers  $b$  and  $b'$ , both having mass  $m_b$  [kg], centroidal moment of inertia  $J_b$  [kg-m<sup>2</sup>] and radius  $R_b$  [m], are connected to the corresponding carriages by a revolute joint. These revolute joints are bearings, of which the inner ring is part of the carriage, and of which the outer ring constitutes the roller follower.

Rotation of the rotor generates centrifugal forces that push  $b$  and  $b'$  against the internal cams  $p$  and  $p'$  respectively.  $p$  and  $p'$  are fixed to the mechanism frame and identical, but rotated 180° with respect to each other. The cams are designed in such a way that the input torque  $M_c(t)$  [N-m] required for driving the ICM, is opposite to the input torque  $M_o(t)$  [N-m] to drive the original system, such that the net input torque to drive the combined system<sup>1</sup> equals zero.

The rotor is assumed to be symmetrical w.r.t.  $\hat{o}_1$ . Hence, its center of gravity (COG) coincides with  $\hat{o}_1$ . Because of the mechanism symmetry w.r.t.  $\hat{o}_1$ , the ICM is completely force-balanced. However, the contact forces between the cams and the roller followers exert a nonzero shaking moment (about the

<sup>1</sup>The *original* system is the mechanism to be input torque balanced; the *combined* system is the combination of the original system and the ICM.

$Z$ -axis) on the mechanism frame. Furthermore, due to the fact that the cams lie in different planes, the contact forces also exert bending moments (about the  $X$  and  $Y$ -axis) on the drive shaft and the mechanism frame. Due to symmetry, the shaking and bending moments are pure couples. The bending moments can be cancelled by using  $n_{\text{ICM}} = 2, 4, \dots$  identical ICMs in an antisymmetrical arrangement.

The distance between  $\hat{o}_1$  and the coinciding carriage and roller follower centers of gravity, located in  $\hat{o}_2$ , is given by the cam pitch radius  $r(t)$  [m].  $g(t)$  [rad] denotes the rotor's rotation angle w.r.t. the positive  $X$ -axis, whereas  $h(t)$  is the rotation angle of the roller follower. As opposed to the rotor angle  $g(t)$ ,  $h(t)$  needs no definition w.r.t. the  $X$ -axis because of the axisymmetry of the roller follower.

### 5.1.2 Describing Equation: General Form

The derivation of the describing equation assumes that the ICM is a purely inertial mechanism with one degree of freedom. More specifically, this implies the following: (i) there is no friction in the revolute joints, (ii) the roller followers roll<sup>2</sup> over the internal cams without sliding, (iii) all bodies are rigid and (iv) the roller followers are always in contact with the cams. (i) and (ii) imply that there is no energy dissipation in the ICM, which, in combination with (iii) allows us to consider the ICM as being purely inertial. (ii) and (iv) cause the ICM to be a kinematically determined mechanism with one degree of freedom, that is, the rotor angle  $g$ . Consequently, (1.3) applies, such that the ICM's input torque  $M_c$  [N-m] is given by:

$$M_c = \frac{1}{\dot{g}} \cdot \frac{dT_c}{dt}, \quad (5.1)$$

where  $T_c$  [J] denotes the kinetic energy of the ICM. The describing equation is derived by imposing the following double condition,  $\forall t \in [0, T]$ :

$$M_o(t) + M_c(t) = 0; \quad (5.2a)$$

$$\dot{g}(t) \equiv \frac{2\pi}{T}, \quad (5.2b)$$

where  $M_o(t)$  [N-m] denotes the original system's input torque. This set of equations expresses that, in the combined system, the net input torque to impose a perfectly constant drive speed  $\dot{g}$  must be zero. It is assumed that the original system is also a mechanism with one degree of freedom (the rotor angle  $g$ ). However, no assumption is made concerning the nature of  $M_o(t)$ : for instance, the original system may be not purely inertial.

---

<sup>2</sup>In fact, friction is necessary to avoid slipping of the roller followers. However, as no slipping occurs, these friction forces are not dissipative.

Multiplying (5.2a) with  $\dot{g}(t) \equiv 2\pi/T$ , and integrating between 0 and  $t$  yields:

$$\frac{2\pi}{T} \cdot \int_0^t M_o(\tau) \cdot d\tau + \frac{2\pi}{T} \cdot \int_0^t M_c(\tau) \cdot d\tau = 0.$$

Since (5.1) shows that

$$T_c(\tau) = \int M_c(\tau) \cdot \dot{g}(\tau) \cdot d\tau = \int M_c(\tau) \cdot \frac{2\pi}{T} \cdot d\tau,$$

and defining

$$E_o(\tau) = \int M_o(\tau) \cdot \dot{g}(\tau) \cdot d\tau = \int M_o(\tau) \cdot \frac{2\pi}{T} \cdot d\tau,$$

the previous equation is restated as:

$$E_o(t) - E_o(0) + T_c(t) - T_c(0) = 0,$$

or

$$E_o(t) + T_c(t) = E_o(0) + T_c(0). \quad (5.3)$$

The energy function  $E_o(t)$  [J] is interpreted as follows. If the original system is not conservative,  $E_o(t)$  represents the sum of the kinetic energy, the potential energy and the integral of the dissipated power as a function of time. If the original system is conservative,  $E_o(t)$  equals the sum of kinetic and potential energy. If it is purely inertial,  $E_o(t)$  is equivalent to the kinetic energy  $T_o(t)$ .

### 5.1.3 Describing Equation: Differential Equation Form

(5.2a) and (5.3) are transformed into differential equations in the cam pitch radius  $r(t)$  by developing expressions for  $T_c(t)$  and  $M_c(t)$ . Due to mechanism symmetry, only<sup>3</sup> the rotor, the carriage  $c$  and the roller follower  $b$  need to be considered. This results in the following expression for  $T_c(t)$ :

$$n_{\text{ICM}} \cdot \left[ \frac{J_r \cdot \dot{g}^2}{2} + 2 \cdot \left( \frac{J_c \cdot \dot{g}^2}{2} + \frac{m_c \cdot \|\vec{v}_2\|^2}{2} \right) + 2 \cdot \left( \frac{J_b \cdot \dot{h}^2}{2} + \frac{m_b \cdot \|\vec{v}_2\|^2}{2} \right) \right]. \quad (5.4)$$

$\|\vec{v}_2\|$  [m/s] denotes the absolute velocity of  $\hat{o}_2$ . Kinematic analysis of the mechanism yields (see Appendix A):

$$\|\vec{v}_2\|^2 = \dot{r}^2 + r^2 \cdot \dot{g}^2.$$

<sup>3</sup>The dynamic effects due to the mass and moment of inertia of the intermediate bodies between the inner and the outer bearing ring (such as the balls in a ball bearing) are neglected.

Due to the fourth design assumption,  $\dot{h}^2(t)$  equals  $\|\vec{v}_2\|^2/R_b^2$ . Based on this observation and (5.2b), (5.4) is transformed into:

$$T_c(t) = \frac{J^* \cdot \left(\frac{2\pi}{T}\right)^2}{2} + \frac{m^* \cdot \left(\dot{r}^2 + r^2 \cdot \left(\frac{2\pi}{T}\right)^2\right)}{2}, \quad (5.5)$$

where

$$J^* = n_{\text{ICM}} \cdot [J_r + 2 \cdot J_c]; \quad (5.6)$$

$$m^* = 2 \cdot n_{\text{ICM}} \cdot \left[ m_c + m_b + \frac{J_b}{R_b^2} \right]. \quad (5.7)$$

The first term in (5.5) is constant and therefore represents the flywheel effect of the ICM, that is, the added 'dumb' rotary inertia. Henceforth,  $J^*$  should be kept as small as possible, in order not to compromise the start/stop behavior of the combined system.

Applying (5.5) to (5.1), taking into account (5.2b), yields the following expression for the ICM's input torque:

$$M_c = \frac{1}{\frac{2\pi}{T}} \cdot m^* \cdot \left( \dot{r} \cdot \ddot{r} + \left(\frac{2\pi}{T}\right)^2 \cdot r \cdot \dot{r} \right). \quad (5.8)$$

Substituting (5.8) in (5.2a) yields:

$$M_o(t) + \frac{1}{\frac{2\pi}{T}} \cdot m^* \cdot \left( \dot{r} \cdot \ddot{r} + \left(\frac{2\pi}{T}\right)^2 \cdot r \cdot \dot{r} \right) = 0. \quad (5.9)$$

For a given  $M_o(t)$ , (5.9) constitutes a second-order, nonlinear, ordinary differential equation (ODE) in  $r(t)$ . However, this second-order differential equation has only one independent initial condition (that is,  $r(0) = r_0$ ) as it is obtained by taking the time-derivative of the following first-order, nonlinear ODE:

$$E_o(t) + \frac{m^* \cdot \left(\dot{r}^2 + r^2 \cdot \left(\frac{2\pi}{T}\right)^2\right)}{2} = \dots$$

$$E_{o,0} + \frac{m^* \cdot \left(\dot{r}_0^2 + r_0^2 \cdot \left(\frac{2\pi}{T}\right)^2\right)}{2}, \quad (5.10)$$

where the subscript 0 indicates values at time instant  $t = 0$  s. This ODE is obtained by substituting in (5.3) the expression (5.5) for  $T_c(t)$  and eliminating common terms on the left and right hand-side. From an analytical point of view, solving  $r$  from either (5.9) or (5.10) is equivalent. However, from a numerical point of view, it is not, as shown in Section 5.2.

## 5.2 Solution of the Describing Equation

In order for the internal cam profile to be closed, it is imperative that  $r(T) = r(0)$ . Combining this requirement with either (5.9) or (5.10) results in a *boundary value problem* that is solved using the nonlinear least-squares approach proposed in Section 2.4.2.

### 5.2.1 Parameterization of the Solution

The requirement that  $r(T) = r(0)$ , is met automatically if  $r(t)$  is parameterized as a Fourier series with period  $T$ :

$$r(t) = a_0 + \sum_{k=1}^{\infty} a_k \cdot \cos(k\Omega t) + b_k \cdot \sin(k\Omega t),$$

where  $\Omega = 2\pi/T$ . Solving (5.9) now is equivalent to determining the unknown amplitudes  $a_k$  and  $b_k$ ,  $k = 1 \dots \infty$ . In order to limit the number of unknown parameters, the Fourier series is truncated after  $K$  harmonics:

$$\hat{r}(t) = a_0 + \sum_{k=1}^K a_k \cdot \cos(k\Omega t) + b_k \cdot \sin(k\Omega t). \quad (5.11)$$

Hence:

$$\dot{\hat{r}}(t) = \sum_{k=1}^K (k\Omega) \cdot \left( a_k \cdot \cos\left(k\Omega t + \frac{\pi}{2}\right) + b_k \cdot \sin\left(k\Omega t + \frac{\pi}{2}\right) \right); \quad (5.12)$$

$$\ddot{\hat{r}}(t) = \sum_{k=1}^K (k\Omega)^2 \cdot \left( a_k \cdot \cos(k\Omega t + \pi) + b_k \cdot \sin(k\Omega t + \pi) \right). \quad (5.13)$$

The hats ( $\hat{\cdot}$ ) are introduced since, due to the truncation of the Fourier series, not the exact solution  $r$  is calculated but an approximation  $\hat{r}$  of it. This approximation is different if it is obtained based on (5.9) or on (5.10).

The value of  $K$  is a compromise between obtaining an accurate solution and limiting the number ( $2K$ ) of unknown parameters. For the design example outlined hereafter,  $K = 20$  is a reasonable choice. The  $2K$  unknown parameters are grouped into the parameter vector  $\mathbf{z} \in \mathbb{R}^{2K}$ :

$$\mathbf{z} = [ a_1 \quad b_1 \quad \cdots \quad a_K \quad b_K ].$$

The average value  $a_0$  is not part of  $\mathbf{z}$  since its value is determined by the initial condition  $\hat{r}(0) = r_0$ . Because of the parameterization,  $\hat{r}$  and its derivatives are denoted as  $\hat{r}(t, \mathbf{z})$ ,  $\dot{\hat{r}}(t, \mathbf{z})$  and  $\ddot{\hat{r}}(t, \mathbf{z})$ .

$R_b$ [m]	$m_c$ [kg]	$m_b$ [kg]	$J_b$ [kg-m <sup>2</sup> ]	$r_0$ [m]
0.050	3.822	1.841	0.00257	0.1174

TABLE 5.1: Design example: numerical values of the five ICM design parameters.

### 5.2.2 Nonlinear Least Squares Problem

Determination of the unknown parameter vector  $\mathbf{z}$  is done by solving a nonlinear least-squares problem. To this end, the torque residual function  $d_M(t)$  is defined, based on (5.9), as:

$$d_M(t, \mathbf{z}) = M_o + M_c = M_o(t) + \frac{1}{\frac{2\pi}{T}} \cdot m^* \cdot \left( \dot{r} \cdot \ddot{r} + \left( \frac{2\pi}{T} \right)^2 \cdot r \cdot \dot{r} \right). \quad (5.14)$$

Since  $\hat{r}$  and its derivatives depend on  $\mathbf{z}$ , also  $d_M$  depends on  $\mathbf{z}$  and is therefore denoted as  $d_M(t, \mathbf{z})$ . The unknown parameter vector  $\mathbf{z}_M$  (and hence the approximate solution  $\hat{r}_M$  of the ODE) is determined based on the following unconstrained optimization problem:

$$\mathbf{z}_M = \min_{\mathbf{z} \in \mathbb{R}^{2K}} \int_0^T d_M^2(t, \mathbf{z}) dt. \quad (5.15)$$

This is a nonlinear least-squares problem that is solved in a similar fashion as outlined in Section 2.4.2. Once  $\mathbf{z}_M$  is calculated,  $\hat{r}_M$  and its time-derivatives result from (5.11), (5.12) and (5.13).

$\hat{r}$  can also be determined using an energy residual  $d_E(t, \mathbf{z})$ , defined based on (5.10). Because of the analytical equivalence of (5.9) and (5.10),  $\mathbf{z}_E \approx \mathbf{z}_M$ . However, as  $\mathbf{z}_M$  minimizes the rms value of the torque residual, the latter is smaller for  $\mathbf{z}_M$  than for  $\mathbf{z}_E$ . Hence,  $\hat{r}_M(t, \mathbf{z}_M)$  is preferred over  $\hat{r}_E(t, \mathbf{z}_E)$  for the compensating mechanism's ultimate goal is to provide the smallest possible torque residual.

## 5.3 Design Example

Here, the theory developed in the previous section is applied to design a double ICM, that is, two identical, parallel ICMs ( $n_{ICM} = 2$ ), for input torque balancing the sley cam-follower mechanism of an airjet weaving machine. Inspection of the describing equation (5.9) reveals that, given  $T$  and the torque  $M_o(t)$  to be balanced,  $r$  depends on two fundamental parameters:  $m^*$  and the initial condition  $r_0$ .

Since (5.7) shows  $m^*$  to depend on  $R_b$ ,  $m_c$ ,  $m_b$  and  $J_b$ , the following five parameters affect  $r$  and hence the shape and the technological properties of

the ICM: the kinematic design parameter  $R_b$ , the dynamic design parameters  $m_c$ ,  $m_b$  and  $J_b$  and the initial condition  $r_0$ . These design parameters must be chosen in such a way that the resulting mechanism is technologically feasible. The design parameters for the design example at hand are given in Table 5.1 and give rise to  $m^* = 26.76$  kg. They are the result of a design optimization which is the subject of Section 5.4 and 5.5.

Section 5.3.1 discusses the cam-follower mechanism to be balanced and gives the solution of the describing equation (5.9). Since the technological feasibility analysis requires a full kinematic and inverse dynamic analysis, this is discussed in Section 5.3.2. Lastly, Section 5.3.3 focuses on the technological analysis of the ICM.

### 5.3.1 Mechanism to be Balanced

The mechanism to be balanced is the sley cam-follower mechanism of an airjet weaving machine, introduced in Section 2.2 and purely inertial, such that (1.3) applies. Taking into account (5.2b), the torque  $M_o$  to be balanced hence equals:

$$M_o = M_{\text{sley}} = \frac{1}{2\pi} \cdot \frac{dT_{\text{sley}}}{dt} = \frac{1}{2\pi} \cdot J_{\text{sley}} \cdot \dot{f}_{\text{sley}} \cdot \ddot{f}_{\text{sley}}, \quad (5.16)$$

which is obtained based on the following expression for the sley follower's kinetic energy:

$$T_o = T_{\text{sley}} = \frac{J_{\text{sley}} \cdot \dot{f}_{\text{sley}}^2}{2}. \quad (5.17)$$

$J_{\text{sley}}$  [kg-m<sup>2</sup>] denotes the centroidal moment of inertia of the statically balanced sley follower, whereas  $\dot{f}_{\text{sley}}$  denotes its angular speed. The dashed line in Fig.5.2 shows  $M_o(t)$ , for a period of motion equal to  $T=0.0667$  s ( $\Omega = 900$  rpm).

Figure 5.3 shows  $\hat{r}_M(t)$  and its derivatives, calculated using the nonlinear least-squares approach, with  $K = 20$  and  $r(0) = r_0$  as initial condition. The solid line in Fig.5.2(a) shows the resulting ICM input torque  $M_c(t)$ , whereas Fig.5.2(b) shows the torque residual  $d_M(t)$ . Due to the Fourier series truncation, the torque residual is not perfectly zero: a dominant 21st harmonic is present, originating from the fact that  $K = 20$  harmonics are used. However, the maximum torque residual (21 N-m) is a negligible percentage (2.5%) of the maximum value of  $M_o$  (856 N-m).

An important property of the combined system is its equivalent inertia  $J_{\text{eq}}$  [kg-m<sup>2</sup>]. If the original system is conservative (as is the case here), the combined system has constant energy such that it can be considered as an equivalent flywheel  $J_{\text{eq}}$ , turning at  $2\pi/T$  [rad/s]. The numerical value of  $J_{\text{eq}}$  is determined by equating the kinetic energy of the equivalent flywheel and

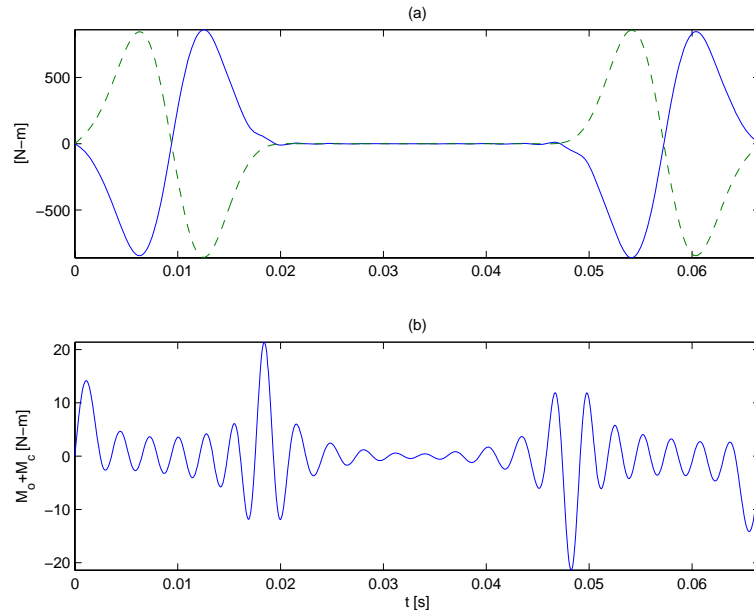


FIGURE 5.2: Design example: (a) original (dashed line) and compensating (solid line) input torque and (b) torque residual.

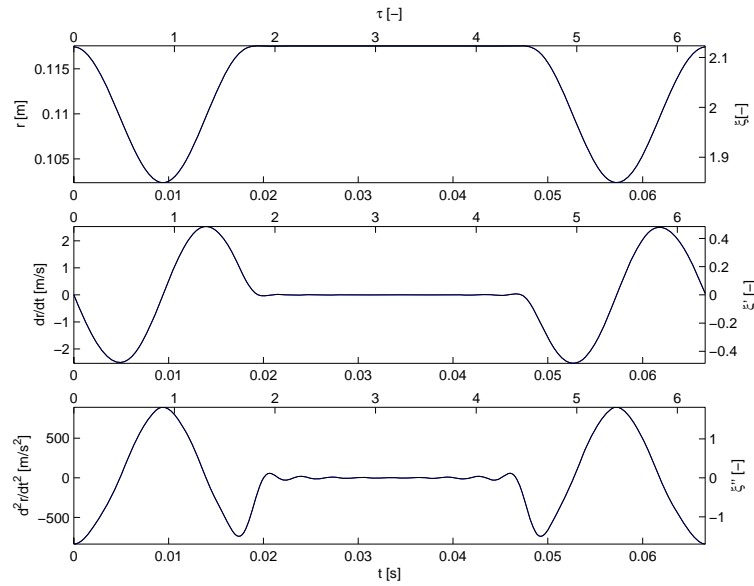
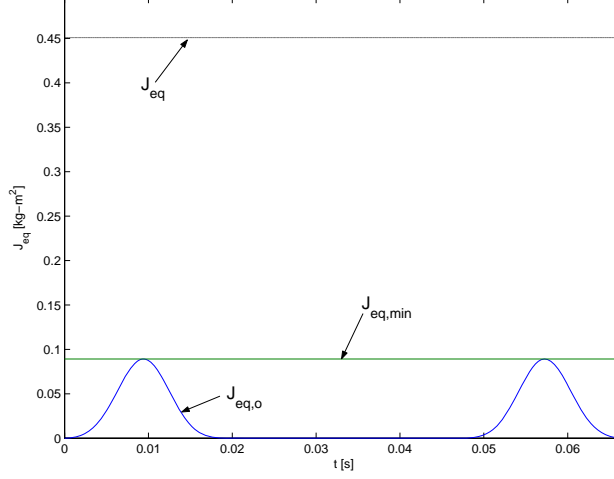


FIGURE 5.3: Design example:  $\hat{r}_M$  and its first two derivatives.

FIGURE 5.4: Design example:  $J_{\text{eq}}$ ,  $J_{\text{eq},\min}$  and  $J_{\text{eq},o}$ .

the constant energy of the combined system:

$$\frac{J_{\text{eq}} \cdot \left(\frac{2\pi}{T}\right)^2}{2} = E_o(t) + T_c(t) = E_{o,0} + T_{c,0}. \quad (5.18)$$

The lower the equivalent inertia, the better the start/stop behavior of the combined system.

The sley cam-follower mechanism is purely inertial, hence  $E_o(t)$  equals  $T_o(t)$ , given by (5.17). The ICM kinetic energy  $T_c(t)$  is calculated using (5.5–5.7), where it is assumed that  $J_r = 0.0321 \text{ kg}\cdot\text{m}^2$  and  $J_c = 0.00427 \text{ kg}\cdot\text{m}^2$ . This results in  $J_{\text{eq}} = 0.4508 \text{ kg}\cdot\text{m}^2$ . In order to assess this value, the original system's equivalent inertia  $J_{\text{eq},o} [\text{kg}\cdot\text{m}^2]$  is introduced in a similar way as  $J_{\text{eq}}$ :

$$\frac{J_{\text{eq},o} \cdot \left(\frac{2\pi}{T}\right)^2}{2} = T_o(t). \quad (5.19)$$

As  $T_o$  is a function of time, so is  $J_{\text{eq},o}$ . Figure 5.4 shows (the constant value of)  $J_{\text{eq}}$  and (the time varying value of)  $J_{\text{eq},o}$  as a function of time for the design example. The constant kinetic energy  $T_o(t) + T_c(t)$  of the combined system has a physical lower limit that equals the maximum of  $T_o(t)$ , since  $T_c(t) \geq 0, \forall t$ . Consequently, the physical lower limit  $J_{\text{eq},\min}$  of  $J_{\text{eq}}$  equals the maximum of  $J_{\text{eq},o}(t)$  over  $[0, T]$ :  $0.0891 \text{ kg}\cdot\text{m}^2$ . Hence,  $J_{\text{eq}}$  is approximately five times greater than its physical lower limit.

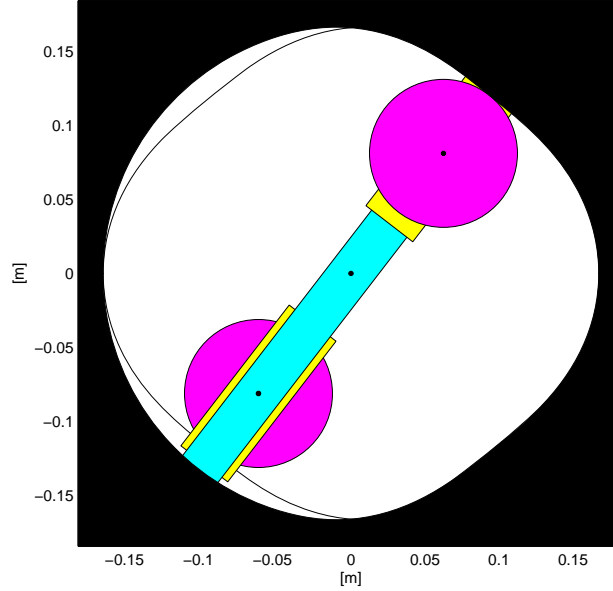


FIGURE 5.5: Design example: resulting ICM configuration. Both the X and the Y-axis are expressed in [m]. The solid boundary indicates the cam against which the upper rolling body rolls. The thin boundary, shown in the left part, and hidden behind the solid boundary in the right part, indicates the cam against which the lower rolling body rolls.

### 5.3.2 Kinematic and Inverse Dynamic Analysis

Determining the technological properties requires a full kinematic and inverse dynamic analysis. The purpose of the kinematic analysis is to determine the position, velocity and acceleration of the points  $\hat{o}_i, i = \{1, 2\}$  in Fig.5.6(a), the kinematics  $(\dot{h}, \ddot{h})$  of the roller follower, and the cam profile. The kinematic analysis is discussed in detail in Appendix A.

As a result of the kinematic analysis, Fig.5.5 shows<sup>4</sup> the ICM with the rotor and the carriages in their positions at time instant  $t = 0.0097s$ . The minimum and maximum of the cam radius are:  $r_{p,\min} = 152$  mm and  $r_{p,\max} = 168$  mm, so the stroke of the mechanism is 16 mm. The limited value of  $r_{p,\max}$  illustrates that the resulting mechanism is quite compact. In the ICM, the rotor and carriages on the one hand and the cams on the other hand do not lie in the same plane, such that they do not interfere (as they do in Fig.5.5).

The purpose of the inverse dynamic analysis is to determine all forces

<sup>4</sup>The shape of the rotor and the carriage are determined based on the mass parameterization of Section 5.4.

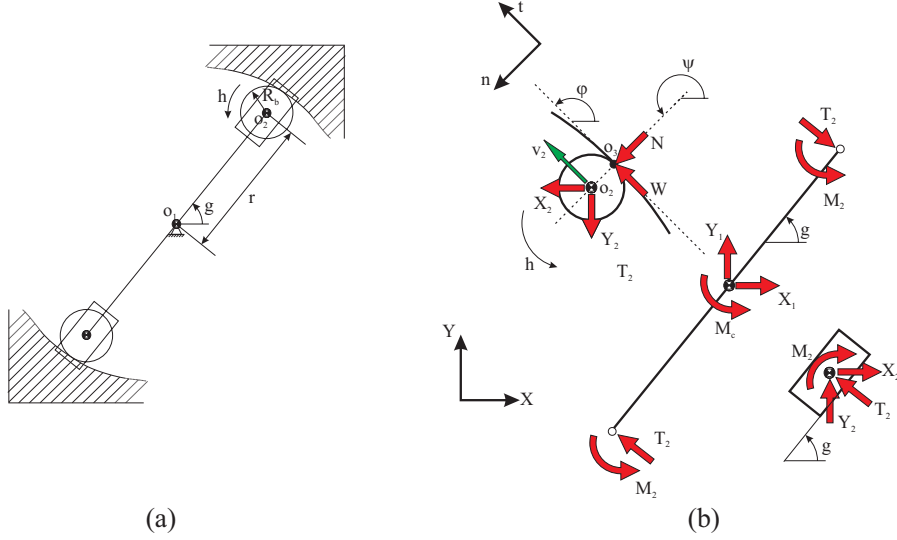


FIGURE 5.6: (a) ICM kinematic scheme and (b) free-body diagram.

and moments based on the kinematics determined in the kinematic analysis. Figure 5.6(b) shows the free-body diagram of the ICM.  $M_c$  is the driving torque;  $X_i$  and  $Y_i$ ,  $i = \{1, 2\}$  are the reaction forces due to the revolute joints in  $\hat{o}_1$  and  $\hat{o}_2$ .  $N$  and  $W$  respectively are the contact force and the friction force exerted by the cam on the roller follower.  $T_2$  and  $M_2$  are the reaction force and torque due to the prismatic joint between the carriage and the rotor. Following the convention of Fig.5.6(b), it is clear that  $N$  should be greater than zero in order to ensure contact between the roller follower and the cam. Figure 5.7 shows that for the design example,  $N$  is well above 0 N: its minimum equals 100 N. The inverse dynamic analysis is discussed in detail in Appendix B.

### Shaking Moment

An interesting side result of the inverse dynamic analysis is the shaking moment  $M_{\text{shak}}$ , which is obtained based on the principle of angular momentum:

$$dA/dt = -M_{\text{shak}}. \quad (5.20)$$

This expression is derived in Section 8.1. The sley mechanism's angular momentum  $A_o(t)$  w.r.t. the pivot of the cam, equals:

$$A_o(t) = J_{\text{cam}} \cdot \dot{g} + J_{\text{sley}} \cdot \dot{f}_{\text{sley}}. \quad (5.21)$$

$J_{\text{cam}}$  [kg-m<sup>2</sup>] denotes the centroidal moment of inertia of the sley cam. This equation is valid provided that (i) the angular momentum of the roller follower is neglected and (ii) the cam and the follower are statically balanced. Combining (5.20) with (5.21), yields the following expression for the shaking moment exerted by the original system:

$$M_{\text{shak,o}}(t) = -J_{\text{cam}} \cdot \ddot{g} - J_{\text{sley}} \cdot \ddot{f}_{\text{sley}}.$$

Due to the static balancing of the cam and the follower, the shaking moment is independent of the chosen reference point and hence a pure couple. The combined system's angular momentum w.r.t.  $\hat{o}_1$  (Fig.5.6(a)), which coincides with the pivot of the cam, equals:

$$A(t) = A_o(t) + A_c(t),$$

where  $A_c(t)$ , the ICM's angular momentum w.r.t.  $\hat{o}_1$ , is given by:

$$A_c(t) = n_{\text{ICM}} \cdot [J_r \cdot \dot{g} + 2 \cdot (J_c \cdot \dot{g} + o_{2x} \cdot m_c \cdot v_{2y} - o_{2y} \cdot m_c \cdot v_{2x}) + 2 \cdot (J_b \cdot \dot{h} + o_{2x} \cdot m_b \cdot v_{2y} - o_{2y} \cdot m_b \cdot v_{2x})]. \quad (5.22)$$

$o_{2x}$  and  $o_{2y}$  denote the  $X$  and  $Y$ -coordinate of  $\hat{o}_2$  (see Fig.5.6(a)), whereas  $v_{2x}$  and  $v_{2y}$  denote the  $X$  and  $Y$ -component of the speed of  $\hat{o}_2$ . As a consequence, the shaking moment in the combined system equals:

$$M_{\text{shak}} = M_{\text{shak,o}} + M_{\text{shak,c}},$$

where  $M_{\text{shak,c}} = -dA_c/dt$ , the shaking moment due to the ICM, is given by:

$$M_{\text{shak,c}}(t) = -n_{\text{ICM}} \cdot [J_r \cdot \ddot{g} + 2 \cdot (J_c \cdot \ddot{g} + o_{2x} \cdot m_c \cdot a_{2y} - o_{2y} \cdot m_c \cdot a_{2x}) + 2 \cdot (J_b \cdot \ddot{h} + o_{2x} \cdot m_b \cdot a_{2y} - o_{2y} \cdot m_b \cdot a_{2x})]. \quad (5.23)$$

$a_{2x}$  and  $a_{2y}$  denote the  $X$  and  $Y$ -component of the acceleration of  $\hat{o}_2$ . Figure 5.8 compares the shaking moment in both the original and the combined system, if  $\dot{g} \equiv 2\pi/T$ . Addition of the ICM results in a 31% increase of the maximum shaking moment from 3662 to 4800 N-m. As foreshadowed in Section 1.2.4, the shaking moment is huge.

### Design Errors From the Past

Here, it is illustrated that previously developed methodologies for designing the ICM are either erroneous (Meyer zur Capellen, 1964), or based on assumptions that are too rough an approximation (Michelin, 1979).

The describing equation derived by Meyer zur Capellen (1964) is based on an erroneous application of the principle of angular momentum: it is stated that the time-derivative of the ICM's angular momentum  $A_c(t)$  w.r.t.  $\hat{o}_1$

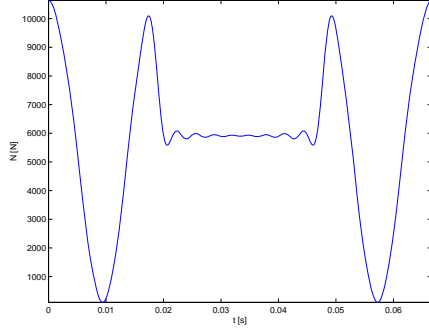


FIGURE 5.7: Design example: contact force  $N$  [N].

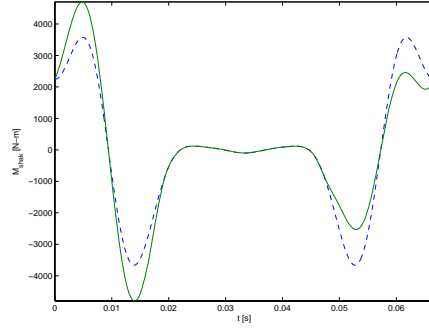


FIGURE 5.8: Design example: shaking moment  $M_{\text{shak}}$  [N-m] in the original system (dashed line) and the combined system (solid line).

equals the input torque  $M_c$ . This is however not true: it equals the sum of *all* externally applied moments, that is:

$$dA_c/dt = M_c - M_{\text{shak,NW}} = -M_{\text{shak,c}}. \quad (5.24)$$

$M_{\text{shak,NW}}$  is defined as the shaking moment component due to the contact forces  $N$  and the friction forces  $W$  between the roller followers and the internal cams. Because of symmetry, this shaking moment is a pure couple and hence independent of the chosen reference point.

Figure 5.9(a – b) graphically proves the correctness of the application of the principle of angular momentum, as expressed by (5.24). This is done by (a) comparing  $dA_c/dt$ ,  $M_c$  and  $-M_{\text{shak,NW}}$  and (b) showing  $dA_c/dt - M_c + M_{\text{shak,NW}}$ . Except for numerical rounding,  $dA_c/dt - M_c + M_{\text{shak,NW}} \equiv 0$ .

In his patent application, Michelin (1979) suggests a design methodology, based on the correct ICM input torque expression (5.1). However, after having obtained the differential equation (5.10), this differential equation is transformed into an algebraic equation by neglecting (i)  $\dot{r}^2$  and (ii) the rotational kinetic energy of the roller followers. This however results in unacceptable errors.

First of all, neglecting the contribution of  $\dot{r}^2$  in (5.10), is equivalent to neglecting  $\dot{r} \cdot \ddot{r}$  in (5.9). This is too rough an approximation, as illustrated by Fig.5.10, which splits up the input torque  $M_c$  (line c) in its two components: the component due to  $r \cdot \dot{r}$  (line a) and the component due to  $\dot{r} \cdot \ddot{r}$  (line b). Obviously, both components are of the same order of magnitude. Hence, neglecting the component due to  $\dot{r} \cdot \ddot{r}$  results in significant errors.

Secondly, (5.7) shows that the contribution to the input torque of the roller follower rotation, expressed by the term  $2 \cdot n_{\text{ICM}} \cdot J_b/R_b^2 = 2 \times 2 \times J_b/R_b^2 = 4 \times$

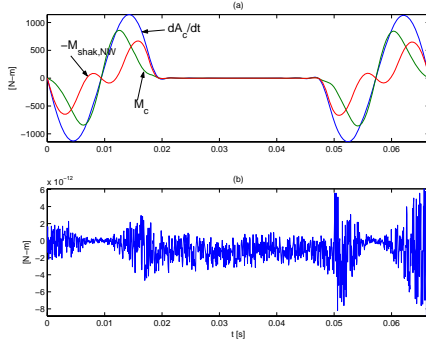


FIGURE 5.9: Design example: (a)  $dA_c/dt$ ,  $M_c$  [N-m] and  $-M_{shak,NW}$  (b)  $dA_c/dt - M_c + M_{shak,NW}$  [N-m].

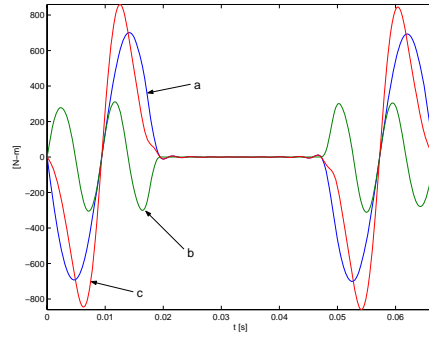


FIGURE 5.10: Design example: comparison of input torque contributions.

$0.002568/0.05^2 = 4.11$  kg, is substantial, as it constitutes 15% of  $m^* = 26.76$  kg. Neglecting the rotational kinetic energy of the rolling bodies hence gives rise to an error of 15% on the predicted ICM input torque.

### 5.3.3 Technological Analysis

A first part of the technological analysis is concerned with the radius of curvature  $\rho$  [m] of the cam pitch profile, that is, the trajectory of the point  $\hat{o}_2$ . How to calculate  $\rho$  is the subject of Appendix G. Figure 5.11(a) shows the resulting curvature  $1/\rho$  [m $^{-1}$ ]. It is positive over the entire internal cam profile, and has a maximum value of  $15.3$  m $^{-1}$ , corresponding to a minimum  $\rho$ -value of 65 mm.

The radius of curvature of the pitch profile is of concern for determining whether or not the following geometric problems occur: *undercutting*, *under-rolling* and *feasibility problems*. These geometric problems are discussed in detail in Appendix G, and do not occur in the case of the internal ICM cam profile, provided that:

$$-\rho > R_b, \forall \rho \leq 0; \quad (5.25)$$

$$\rho + R_b > R_C, \forall \rho \geq 0, \quad (5.26)$$

where  $R_C$  [m] denotes the radius of the cutter or grinding stone used to mill or grind the cam profile. For the design example at hand,  $\rho$  is positive anywhere, so condition (5.25) is of no concern. As the minimum value of  $\rho$  equals 65 mm, condition (5.26) is met provided that  $R_C$  is smaller than  $65 + 50 = 115$  mm.

A second part of the technological analysis is concerned with the Hertzian stresses in the point contact between the crowned roller follower and the cam

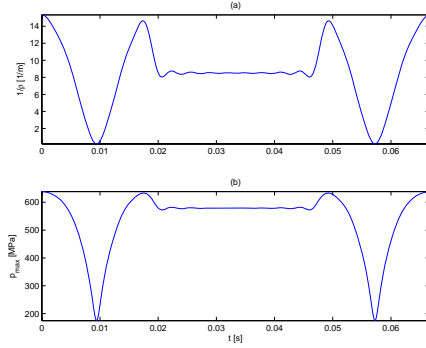


FIGURE 5.11: Design example: (a) curvature  $1/\rho$  [ $\text{m}^{-1}$ ] of cam pitch profile; (b) maximum Hertzian pressure  $p_{\max}$  [MPa].

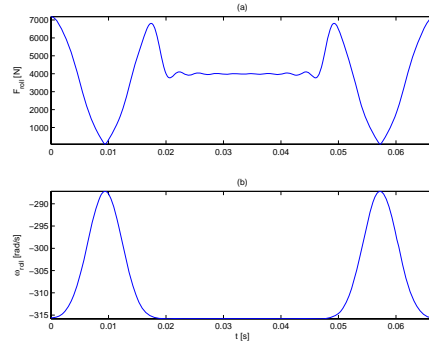


FIGURE 5.12: Design example: (a) force  $F_{\text{roller}}$  [N] transmitted by roller follower bearing; (b) angular speed  $\omega_{\text{roller}}$  [rad/s] of roller follower bearing.

profile. Appendix H shows how the maximum Hertzian stress  $p_{\max}$  in a point contact is calculated, based on the cam profile curvature  $\rho_p = \rho + R_b$  [m], the roller follower radius  $R_b$  and its crown radius  $R_{bc} = 2.5$  m, the contact force  $N$  and the Young's modulus and Poisson's ratio of the cam and roller follower material. Figure<sup>5</sup> 5.11(b) shows the maximum Hertzian pressure  $p_{\max}$  [MPa]. Its largest value is 638 MPa.

$p_{\max}$  should be limited in order to avoid premature failure of the cam due to either *yield* of the cam material or *surface fatigue*. In appendix H it is shown that for the cam material used here (*IMPAX Hi Hard*, a prehardened mould steel with a hardness of 360-400 HB and a yield strength  $R_{p0,2}$  of 1090 MPa), the following upper limits on  $p_{\max}$  should be observed:

$$p_{\max} < 1.47 \cdot R_{p0,2} \Rightarrow p_{\max} < 1600 \text{ MPa (yield avoidance);} \quad (5.27)$$

$$p_{\max} < 1071 \text{ MPa, (fatigue life of 50000h at 900 rpm).} \quad (5.28)$$

The 638 MPa maximum value of  $p_{\max}$  is far below the 1600 MPa limit, so yield does not occur. The upper limit for obtaining a fatigue life of 50000h at 900 rpm is only indicative, as surface fatigue calculations are based on a lot of assumptions (see Appendix H.4) and need experimental verification. However, as 638 MPa is well below 1071 MPa, the cam material has a probable fatigue life of over 50000 h.

A third part of the technological analysis is concerned with the lifetime of the roller follower bearing. Appendix I elaborates the classical bearing lifetime formulae and shows how the equivalent dynamic load on the bearings is

<sup>5</sup>The fact that  $\rho$  and  $p_{\max}$  are given as a function of time  $t$  in Fig.5.11 must be interpreted as follows: the values of  $\rho$  and  $p_{\max}$  at time instant  $t$  are the ones for the contact point between the cam and the roller follower at that same time instant.

calculated, based on the force transmitted by the bearing, its angular speed and its load-carrying capacity  $C$  [N]. Figure 5.12(a) shows the force  $F_{\text{roll}}$  [N] transmitted by the roller follower bearing ( $C = 137$  kN), whereas Fig.5.12(b) shows the angular speed  $\omega_{\text{roll}}$  [rad/s] of the roller follower bearing. The corresponding equivalent dynamic load  $P_{\text{roll}}$  equals 4649 N, yielding a lifetime of 446000h at 900 rpm.

## 5.4 Design Optimization

The design example of the previous section is based on the design parameter values of Table 5.1. These five design parameters result from a design optimization which is the subject of this (and the following) section. The purpose of the design optimization is to obtain a technologically feasible ICM with minimum equivalent inertia. This section firstly discusses the choice of the optimization variables, goal function and constraints. Furthermore, it points out a design procedure for numerically determining the goal function and constraint values. Lastly, the idea of a design chart for solving the optimization problem is introduced.

### 5.4.1 Optimization Variables

It is obvious to use the design parameters  $m_c$ ,  $m_b$ ,  $J_b$ ,  $R_b$  and  $r_0$  directly as the optimization variables. This is however not the approach adopted here. First of all, it is assumed that some given bearing, chosen from a catalogue, implements the revolute joint between the roller follower and the carriage. This determines  $m_b$ ,  $J_b$  and  $R_b$ , since these are properties of the outer bearing ring. These parameters are grouped into the parameter vector  $\mathbf{p}_b \in \mathbb{R}^3$ :

$$\mathbf{p}_b = [ m_b \quad J_b \quad R_b ] .$$

The idea is that the designer selects the bearing, then performs the design optimization and afterwards makes a check whether the bearing is strong enough. If not, another bearing has to be chosen, and a new design optimization has to be performed.

Secondly, the design parameter  $m_c$  is replaced by an optimization variable  $t^*$ , by parameterizing the shape of the carriage as shown in Fig.5.13(c – d): the carriage is a rectangular prism of length  $l_c$ , width  $d_c$  and thickness  $t^*$ , carrying the inner ring of the roller follower, which constitutes a cylinder of radius  $R_c$  and thickness  $t_c$ . The centers of gravity of both the rectangular prism and the cylinder coincide with  $\hat{o}_2$ . Based on this figure, it is obvious that:

$$m_c = \rho_c \cdot (l_c \cdot d_c \cdot t^* + \pi \cdot R_c^2 \cdot t_c) , \quad (5.29)$$

where  $\rho_c$  [kg/m<sup>3</sup>] denotes the carriage mass density of 7800 kg/m<sup>3</sup> (steel).

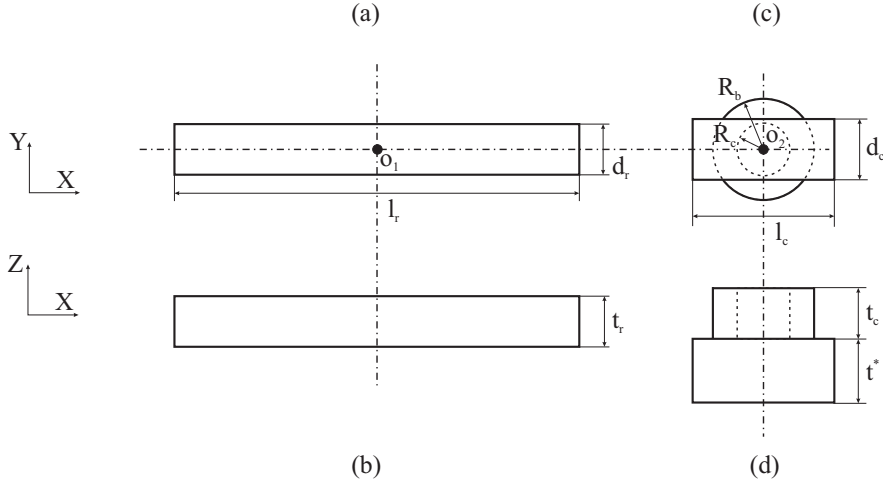


FIGURE 5.13: Shape parameterization: front (a) and top (b) view of the rotor and front (c) and top (d) view of the carriage (with the outer bearing ring of diameter  $R_b$  present).

Defining the parameter vector  $\mathbf{p}_c \in \mathbb{R}^4$  as:

$$\mathbf{p}_c = [ l_c \quad d_c \quad t_c \quad R_c ],$$

$m_c$  is written as:

$$m_c = m_c(t^*, \mathbf{p}_c).$$

Only  $t^*$  is considered to be an optimization variable, whereas  $\mathbf{p}_c$  is assigned a reasonable, fixed value that has to be checked after the design optimization. If the resulting carriage does not have sufficient structural strength,  $\mathbf{p}_c$  has to be modified and a new optimization has to be done.

### 5.4.2 Goal Function

Several optimization criteria can be chosen: minimum size of the cams, maximum bearing lifetime, . . . The goal function chosen here is minimum equivalent inertia  $J_{\text{eq}}$  [kg-m<sup>2</sup>]. The rationale for doing so is that inertia minimization for improved start/stop behavior was exactly the reason for using a torque balancing mechanism instead of a large flywheel.

A practical consequence of this choice of goal function is that  $J^*$  becomes a third fundamental parameter (besides  $m^*$  and  $r_0$ ), as it affects  $T_c$ . Hence, as shown by (5.6),  $J_r$  and  $J_c$  are also design parameters. These additional design parameters however do not introduce additional optimization variables.

Firstly,  $J_c$  is determined by the optimization variable  $t^*$  and the secondary parameters  $\mathbf{p}_c$  (see Fig.5.13):

$$J_c = \frac{1}{12} \cdot (\rho_c \cdot l_c \cdot d_c \cdot t^*) \cdot (l_c^2 + d_c^2) + \frac{1}{2} \cdot (\rho_c \cdot \pi \cdot R_c^2 \cdot t_c) \cdot R_c^2. \quad (5.30)$$

Secondly,  $J_r$  is calculated based on a parameterization of the rotor's shape shown in Fig.5.13(a – b). It is a rectangular prism of length  $l_r$ , width  $d_r$  and thickness  $t_r$ . Consequently,

$$J_r = \frac{1}{12} \cdot (\rho_r \cdot l_r \cdot d_r \cdot t_r) \cdot (l_r^2 + d_r^2), \quad (5.31)$$

where  $\rho_r$  [kg/m<sup>3</sup>] denotes the rotor mass density of 7800 kg/m<sup>3</sup> (steel). As the carriage must be entirely carried by the rotor,  $l_r$  must satisfy (compare Fig.5.13 with Fig.5.5):

$$\frac{l_r}{2} \geq \frac{l_c}{2} + \max_{t \in [0, T]} r(t).$$

Therefore,  $l_r$  is calculated as

$$l_r = 2 \cdot \left[ a \cdot \frac{l_c}{2} + r_{\max} \right], \quad (5.32)$$

where  $a$  is a safety factor greater than one. Defining the vector  $\mathbf{p}_r \in \mathbb{R}^3$  as:

$$\mathbf{p}_r = [ a \quad d_r \quad t_r ],$$

$J_r$  is written as

$$J_r = J_r(\mathbf{p}_r). \quad (5.33)$$

$\mathbf{p}_r$  is not considered as an optimization variable, but is assigned a reasonable, fixed value. Again, this fixed value has to be checked after the design optimization. If the resulting rotor does not have sufficient structural strength,  $\mathbf{p}_r$  has to be modified and a new optimization has to be done.

## Discussion

From the above discussion,  $r_0$  and  $t^*$  emerge as the optimization variables. The ten secondary parameters to which fixed values are assigned and which have to be validated after the design optimization, are contained in the parameter vectors  $\mathbf{p}_b$ ,  $\mathbf{p}_c$  and  $\mathbf{p}_r$ . The values chosen for the secondary parameters are given in Table 5.2.

Replacing the five design parameters by two optimization variables and ten secondary parameters has the following advantages: (i) the link shapes are automatically determined, such that shape and collision constraints are easily implementable (as shown hereafter), (ii) it reflects that the bearing

$\mathbf{P}_b$			$\mathbf{P}_r$		
$m_b$ [kg]	$J_b$ [kg-m <sup>2</sup> ]	$R_b$ [m]	$a$ [-]	$d_r$ [m]	$t_r$ [m]
1.8407	0.002568	0.050	1.2	0.030	0.030
$\mathbf{P}_c$					
$l_c$ [m]	$d_c$ [m]	$t_c$ [m]	$R_c$ [m]		
0.120	0.040	0.050	0.026		

TABLE 5.2: Design example: numerical values chosen for the secondary parameters.

parameters  $m_b$ ,  $J_b$ ,  $R_b$  can only assume a discrete set of values, chosen from a catalogue and (iii) this nonconvex optimization problem is much better tractable.

As the number of optimization variables is one less than the number of fundamental parameters, some degree of suboptimality, introduced by choosing fixed values for the secondary parameters, can be expected. However, it was chosen not to define an additional optimization variable (by transferring one of the secondary parameters to the set of optimization variables), in order to have the same number of fundamental parameters and optimization variables.

### 5.4.3 Constraints

There are three kinds of constraints: (i) bound constraints on the optimization variables, (ii) constraints in order to obtain a technologically feasible mechanism and (iii) constraints in order to avoid collisions between moving parts. The optimization variables are bounded as follows:

$$0 \leq t^* \leq t^{*,M}; \quad (5.34)$$

$$0 \leq r_0. \quad (5.35)$$

Both  $r_0$  and  $t^*$  should be positive. Furthermore, an upper bound on  $t^*$  is imposed in order to avoid excessive carriage mass.

As for technological constraints, first of all, there must always be contact between the roller followers and the cams. This is mathematically expressed by imposing that the contact force  $N(t)$  [N] between the cams and the roller followers should have a minimum  $N_{\min}$  over  $[0, T]$  which is greater than zero, or for robustness reasons, greater than some positive lower bound  $N^m$ :

$$N_{\min} \geq N^m. \quad (5.36)$$

When determining  $N_{\min}$ , only the mechanism regime behavior is considered, and not the transient behavior during the startup or braking phase.

Secondly, in order to avoid cam yield and surface fatigue problems, the maximum  $(p_{\max})_{\max}$  (over the cam profile), of all maximum Hertzian stresses  $p_{\max}$ , should be less than some upper bound  $p_{\max}^M$ :

$$(p_{\max})_{\max} \leq p_{\max}^M. \quad (5.37)$$

Thirdly, the lifetime  $L_{\text{roll}}$  [h] of the roller follower bearing should be greater than some minimum lifetime:

$$L_{\text{roll}} \geq L_{\text{roll}}^m. \quad (5.38)$$

Fourthly, for avoiding cam profile geometrical problems (undercutting, under-rolling and feasibility problems.), (5.25) and (5.26) should be fulfilled, which gives rise to the following constraints:

$$\rho_{\min,-} \geq R_b; \quad (5.39)$$

$$\rho_{\min,+} \geq R_C - R_b, \quad (5.40)$$

where  $\rho_{\min,-}$  and  $\rho_{\min,+}$  are defined as

$$\rho_{\min,-} = \min_{\rho(t) \leq 0, t \in [0, T]} -\rho; \quad (5.41)$$

$$\rho_{\min,+} = \min_{\rho(t) \geq 0, t \in [0, T]} \rho. \quad (5.42)$$

Figure 5.5 shows that collisions can only occur between the drive shaft (not shown in the picture) and either the carriage or the roller follower. Representing the drive shaft's radius by  $R$  [m], collisions do not occur provided that:

$$\min_{t \in [0, T]} r(t) \geq R + \Delta + \max \left( R_b, \frac{l_c}{2} \right),$$

where  $\Delta$  [m] represents a safety tolerance. Defining the collision flag  $i_1$  [m] as

$$i_1 = R + \Delta + \max \left( R_b, \frac{l_c}{2} \right) - r_{\min}, \quad (5.43)$$

collisions are avoided if:

$$i_1 \leq 0. \quad (5.44)$$

#### 5.4.4 Design Procedure

The consecutive steps required for computing the goal function and constraints constitute a design procedure, which starts from the following data: (i) *variable* values of the optimization variables  $r_0$  and  $t^*$ , (ii) *fixed* values of the secondary parameters  $\mathbf{p}_b$ ,  $\mathbf{p}_c$  and  $\mathbf{p}_r$ , (iii)  $T_o(t)$  and  $M_o(t)$  (and their period  $T$ ) and (iv) the number of ICM's  $n_{\text{ICM}}$ . The design procedure consists of eight steps:

1. determine  $m_c$  from (5.29) and  $m^*$  from (5.7);
2. solve (5.9) with  $r(0) = r_0$  and compute  $\hat{r}_{M,\max} = \max_{t \in [0, T]} \hat{r}_M(t)$ ;
3. determine  $l_r$  from (5.32);
4. determine  $J_r$  from (5.31),  $J_c$  from (5.30) and  $J^*$  from (5.6);
5. determine  $J_{\text{eq}}$  from (5.18), (5.17) and (5.5);
6. compute  $N_{\min}$  based on the kinematic and dynamic analysis of Section 5.3.2;
7. compute  $(p_{\max})_{\max}$ ,  $L_{\text{roll}}$ ,  $\rho_{\min,-}$  and  $\rho_{\min,+}$  using the technological analysis of Section 5.3.3 and (5.41–5.42);
8. compute  $\hat{r}_{M,\min} = \min_{t \in [0, T]} \hat{r}(t)$  and determine  $i_1$  from (5.43).

### 5.4.5 Design Chart

The optimization problem is solved by performing an exhaustive search, for it has only two optimization variables  $t^*$  and  $r_0$ . The exhaustive search is done by choosing a number of discrete values for  $t^*$  and  $r_0$  and evaluating the goal function  $J_{\text{eq}}$  and the constraints (5.34–5.44) for all possible combinations of these discrete values. If for example 40 values for  $t^*$  and 30 values for  $r_0$  are chosen, this results in 1200 evaluations of both the goal function and the constraints. Graphically depicting these values in an  $(r_0, t^*)$  design chart then allows to visually determine the optimal  $(r_0, t^*)$  combination complying with all constraints.

The main computational burden results from solving the differential equation (5.9) for each  $(r_0, t^*)$  combination. The next section however shows that, through nondimensionalization, the differential equation needs only to be solved 30 instead of 1200 times for the above example. This results in a dramatic reduction of the time required to compute the  $(r_0, t^*)$  design chart.

## 5.5 Nondimensionalized Analysis

### 5.5.1 Nondimensionalized Trajectories

The nondimensionalization adopted here is very similar to the one introduced in Section 3.2.1. Both the sleigh follower trajectory  $f_{\text{sley}}$  and the pitch radius trajectory  $r$  are nondimensionalized:

$$f_{\text{sley}}(t) = |\Theta| \cdot \theta(t \cdot \Omega) = |\Theta| \cdot \theta(\tau); \quad (5.45)$$

$$r(t) = |\Theta| \cdot \sqrt{\frac{J_{\text{sley}}}{m^*}} \cdot \xi(t \cdot \Omega) = |\Theta| \cdot \sqrt{\frac{J_{\text{sley}}}{m^*}} \cdot \xi(\tau). \quad (5.46)$$

$\Theta$  [rad] represents the sley follower's amplitude of motion.  $\Omega$  [rad/s] is used as a shorthand notation for  $\Omega_{\text{sley}}$  [rad/s]. Applying the chain rule for differentiation to (5.45) and (5.46) yields the following proportional relations between the time-derivatives of  $f_{\text{sley}}(t)$  and  $r(t)$ , and the  $\tau$ -derivatives of  $\theta(\tau)$  and  $\xi(\tau)$  respectively:

$$\frac{d^n f_{\text{sley}}(t)}{dt^n} = |\Theta| \cdot \Omega^n \cdot \theta^{(n)}(\tau); \quad (5.47)$$

$$\frac{d^n r(t)}{dt^n} = |\Theta| \cdot \sqrt{\frac{J_{\text{sley}}}{m^*}} \cdot \Omega^n \cdot \xi^{(n)}(\tau). \quad (5.48)$$

Now substituting (5.45–5.48) and (5.16) in (5.9) yields:

$$J_{\text{sley}} \cdot \Theta^2 \cdot \Omega^2 \cdot (\xi'' \cdot \xi' + \xi \cdot \xi' + \theta' \cdot \theta'') = 0. \quad (5.49)$$

Since  $J_{\text{sley}} \cdot \Theta^2 \cdot \Omega^2$  has the dimension  $[\text{kg}\cdot\text{m}^2/\text{s}^2]=[\text{N}\cdot\text{m}]$  of torque, the describing equation (5.9) can be written in the following nondimensionalized form:

$$\xi'' \cdot \xi' + \xi \cdot \xi' + \theta' \cdot \theta'' = 0. \quad (5.50)$$

This nondimensionalized differential equation shows that  $\xi(\tau)$ , that is, the *shape* of  $r(t)$  (and hence the *shape* of the internal cam), does not depend on  $m^*$ . (5.46) shows that  $m^*$  however does affect the amplitude of  $r(t)$  (and hence the *size* of the internal cam). As both the sley mechanism and the ICM are purely inertial mechanisms, the torque balancing result is independent of  $T$ . This is confirmed by the nondimensionalized analysis, since both  $\xi(\tau)$  and  $r(t)$  are independent of  $T$ , as shown by (5.50) and (5.46) respectively.

Numerically solving (5.50) is done using a nonlinear least-squares approach similar to the one described in Section 5.2. Due to the truncation of the Fourier series, the resulting solution of (5.50) is an approximation of the 'true' solution, and it therefore denoted as  $\hat{\xi}_{\text{M}}$ .

### 5.5.2 Nondimensionalized Design Procedure

Using nondimensionalized variables necessitates some additional steps for the design procedure of Section 5.4.4. The adjusted design procedure starts from the same data as the original design procedure, except that  $\xi_0$  and  $r_{\text{max}} = \max r(t), t \in [0, T]$  are now considered to be the variable parameters instead of  $r_0$  and  $t^*$ . This gives rise to the following:

1. calculate  $\Theta$ ,  $\theta(\tau)$ ,  $\theta'(\tau)$  and  $\theta''(\tau)$  based on (5.45) and (5.47);
2. solve (5.50) with  $\xi(0) = \xi_0$  and compute  $\hat{\xi}_{\text{M},\text{max}} = \max_{\tau \in [0, 2\pi]} \hat{\xi}_{\text{M}}(\tau)$ ;
3. calculate  $m^*$  based on  $r_{\text{max}}$  and (5.46):  $m^* = J_{\text{sley}} \cdot \left( \Theta \cdot \frac{\hat{\xi}_{\text{M},\text{max}}}{r_{\text{max}}} \right)^2$ ;

4. determine  $m_c$  based on (5.7):

$$m_c = \frac{m^*}{2 \cdot n_{\text{ICM}}} - m_b - \frac{J_b}{R_b^2};$$

5. determine the corresponding value of  $t^*$  based on (5.29):

$$t^* = \frac{1}{l_c \cdot d_c} \cdot \left( \frac{m_c}{\rho} - \pi \cdot R_c^2 \cdot t_c \right);$$

6. determine  $r_0$  from  $\xi_0$  and (5.46):

$$r_0 = |\Theta| \cdot \sqrt{\frac{J_{\text{sley}}}{m^*}} \cdot \xi_0.$$

For determining the goal function and constraint values, one can now proceed from step 3 on in the dimensionalized design procedure of Section 5.4.4, since  $r(t)$  and  $t^*$  are known now.

Comparing both design procedures reveals their main difference w.r.t. computational efficiency. The dimensionalized design procedure requires knowledge of  $r_0$  and  $t^*$  before (5.9) can be solved. On the other hand, the nondimensionalized design procedure only requires knowledge of  $\xi_0$  for solving (5.50). Consequently, when computing a dimensionalized design chart, (5.9) has to be solved for each  $(r_0, t^*)$  combination. On the other hand, when computing a nondimensionalized design chart, all  $(\xi_0, r_{\text{max}})$  combinations having the same value of  $\xi_0$  have the same solution for (5.50), so (5.50) has to be solved for all different  $\xi_0$  values, but *not* for all  $(\xi_0, r_{\text{max}})$  combinations.

### 5.5.3 Nondimensionalized Design Chart

For constructing the design chart, 21 equally spaced values between 2 and 3 are chosen for  $\xi_0$ , and 31 equally spaced values between 100 and 250 mm for  $r_{\text{max}}$ , yielding a total of 651  $(\xi_0, r_{\text{max}})$  combinations. Using these 651 combinations, the design chart of Fig.5.14 is drawn, based on 21 solutions of the differential equation (5.50).

The value of  $J_{\text{eq}}$  follows from the colored bar next to the figure. Furthermore, contour lines giving the  $(\xi_0, r_{\text{max}})$  combinations for which  $N_{\text{min}} = \{100, 500, 1000\}$  N are present, as well as contour lines giving the  $(\xi_0, r_{\text{max}})$  combinations for which  $t^* = \{0, 0.08\}$  m.

The various symbols (crosses, circles, ...) mark  $(\xi_0, r_{\text{max}})$  combinations at which constraints are active, and which are hence infeasible. The parameters which define the constraints (5.34–5.44) are:  $t^{*,M} = 0.080$  m,  $N^m = 100$  N,  $p_{\text{max}}^M = 900$  MPa,  $L_{\text{roll}}^m = 50000$  h,  $R_C = 0.05$  m,  $R = 0.035$  m,  $\Delta = 0.002$  m. Clearly, the area of  $(\xi_0, r_{\text{max}})$  combinations complying with all constraints

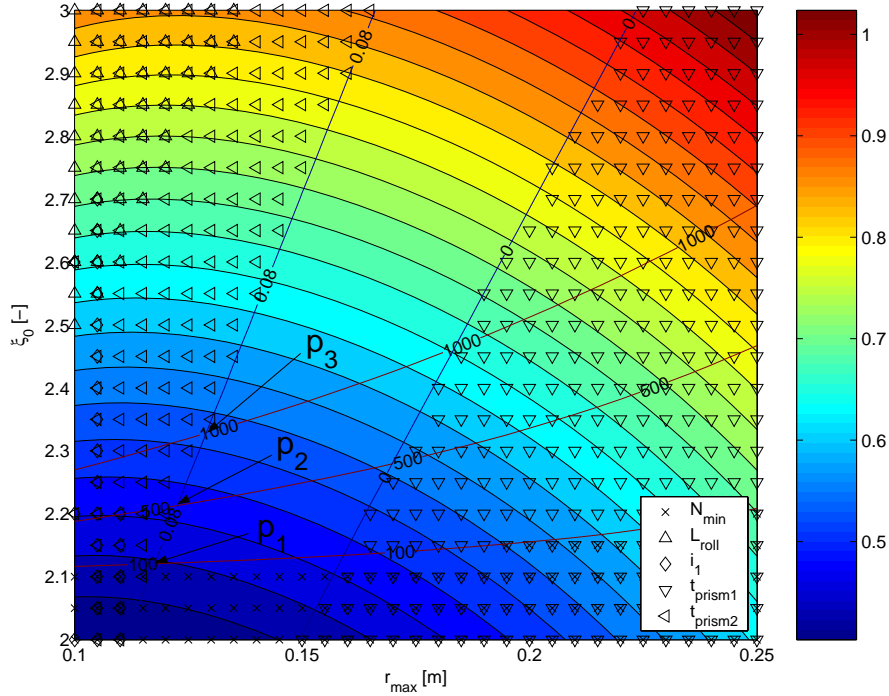


FIGURE 5.14: Design chart using  $J_{eq}$  [kg-m<sup>2</sup>] as goal function. The contour lines {100, 500, 1000} indicate  $N_{min}$ -values [N]. The contour lines {0, 0.08} indicate  $t^*$ -values [m].

(the *feasible area*) is delimited by the  $N_{min} = 100$  N and the  $t^* = \{0, 0.08\}$  m contour lines.

The lowest value of the goal function  $J_{eq}$  is found at

$$\mathbf{p}_1(\xi_0 = 2.1211, r_{max} = 0.11755\text{m}),$$

where the constraints (5.36) and (5.34) are active. Besides providing a simple graphical tool for optimizing the ICM design, the design chart also illustrates the sensitivity of the optimum w.r.t. the constraints. For example, when tightening the constraint on  $N_{min}$  to  $N^m = 500$  or 1000 N, the new design is found at the crossing of the contour lines  $N_{min} = 500$  N and  $N_{min} = 1000$  N with the contour line  $t^* = 0.080$  m (points  $\mathbf{p}_2(2.2133, 0.1225)$  and  $\mathbf{p}_3(2.3281, 0.1289)$ ). This yields only a moderate increase of the goal function to respectively 0.4882 (8% increase) and 0.5377 kg-m<sup>2</sup> (19% increase) (see Table 5.3). Hence the price paid for the additional contact force robustness is rather low.

In order to determine the  $(r_0, t^*)$  combination, corresponding to  $\mathbf{p}_1$ , the design procedure of Section 5.4.4 is followed:

1.  $\Theta = -0.32722$  m;
2.  $\hat{\xi}_M(\tau)$  and its derivatives are shown in Fig.5.3.  $\hat{\xi}_{M,\max} = 2.1233$ ;
3.  $m^* = 0.766 \times \left( 0.32722 \times \frac{2.1233}{0.11755} \right)^2 = 26.76$  kg;
4.  $m_c = \frac{26.76}{2 \times 2} - 1.8407 - \frac{0.002568}{0.05^2} = 3.822$  kg;
5.  $t^* = \frac{1}{0.12 \times 0.04} \cdot \left( \frac{3.822}{7800} - \pi \times 0.026^2 \times 0.05 \right) = 0.080$  m;
6.  $r_0 = |-0.32722| \times \sqrt{\frac{0.766}{26.76}} \times 2.1211 = 0.1174$  m.

$\mathbf{p}_1$  gives rise to the  $(r_0, t^*)$  combination that defines the design example of Section 5.3. All technological properties of this design are summarized in Table 5.3.

### 5.5.4 Prismatic Joint Implementation

An important constructive consideration is the implementation of the prismatic joint between the carriage and the rotor. A simple 'off-the-shelf' solution is implementing it using a standard roller guideway. Calculation of the guideway lifetime, following the guidelines given by guideway manufacturers (such as Schneeberger<sup>6</sup>), shows that a 50000 h lifetime is easily achievable. So at first sight, using a roller guideway seems to be a practical solution.

A complication is however presented by the nature of the carriage movement: its motion combines a rather small amplitude with high velocities and accelerations, as indicated by Fig.5.15(a-c), respectively showing contour plots of  $r_{\max} - r_{\min}$  [m],  $\dot{r}_{\max}$  [m/s] and  $\ddot{r}_{\max}$  [m/s<sup>2</sup>] as a function of  $\xi_0$  and  $r_{\max}$ . This is problematic, as e.g. Schneeberger advises to have  $\ddot{r}_{\max}$  below 100 m/s<sup>2</sup>. From Fig.5.15(c) it is clear that it is not possible to meet this constraint, hence it is not possible to use a standard roller guideway.

A sliding guideway provides an alternative solution to implement the prismatic joint. In this case, restrictions are imposed by the wear in the contact zone between the two contacting elements. As this is not an 'off-the-shelf' solution, further research must be carried out in order to come to a practical solution.

---

<sup>6</sup>[www.schneeberger.com](http://www.schneeberger.com)

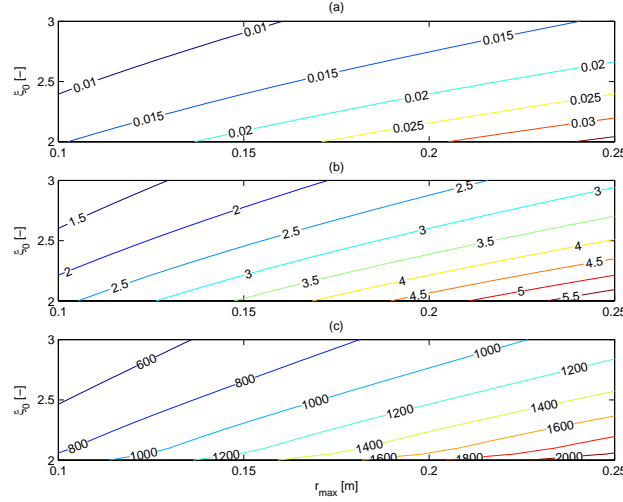


FIGURE 5.15: Design example: contour plots of (a)  $r_{\max} - r_{\min}$  [m], (b)  $\dot{r}_{\max}$  [m/s] and (c)  $\ddot{r}_{\max}$  [m/s<sup>2</sup>] as a function of  $\xi_0$  and  $r_{\max}$ .

### 5.5.5 Peak Phenomenon

If (5.50) is solved with an increasing number of harmonics  $K$ , it is expected that  $\hat{\xi}_M$  becomes an increasingly better approximation of the 'true' solution. Hence it is expected that the nondimensionalized torque residual  $\mu(\tau)$  defined as

$$\mu(\tau) = \xi'' \cdot \xi' + \xi \cdot \xi'' + \theta' \cdot \theta'',$$

gets smaller and smaller. For the design example at hand, this is illustrated by Fig.5.16(d – f), which shows  $\mu(\tau)$  for  $K = \{20, 50, 80\}$ , with  $\xi_0 = 2.5$ : increasing  $K$  makes the torque balancing quasi complete. This is however not the case for  $\xi_0 = 1.3$ , as  $\mu(\tau)$  exhibits a peak that does not disappear by increasing  $K$ , as shown in Fig.5.16(a – c).

This *peak phenomenon* is further illustrated, in dimensionalized form, by Fig.5.17, showing the maximum value of the torque residual  $d_M(t)$ ,  $t \in [0, T]$  as a function of  $\xi_0$ <sup>(7)</sup> for  $K = 20$ . Limiting the maximum torque residual to e.g. 5.5% of the maximum torque (856 N-m), imposes a lower bound of 1.99 to  $\xi_0$ . Therefore, no results for  $\xi_0$  smaller than 1.99 are given in the design chart of Fig.5.14.

<sup>7</sup>(5.49) shows that  $d_M(t) = J_{\text{sley}} \cdot \Theta^2 \cdot \Omega^2 \cdot \mu(\tau)$ . Hence  $d_M(t)$  is independent of the chosen value of  $r_{\max}$ . Therefore, a value of  $r_{\max}$  is not needed to dimensionalize the torque residual.

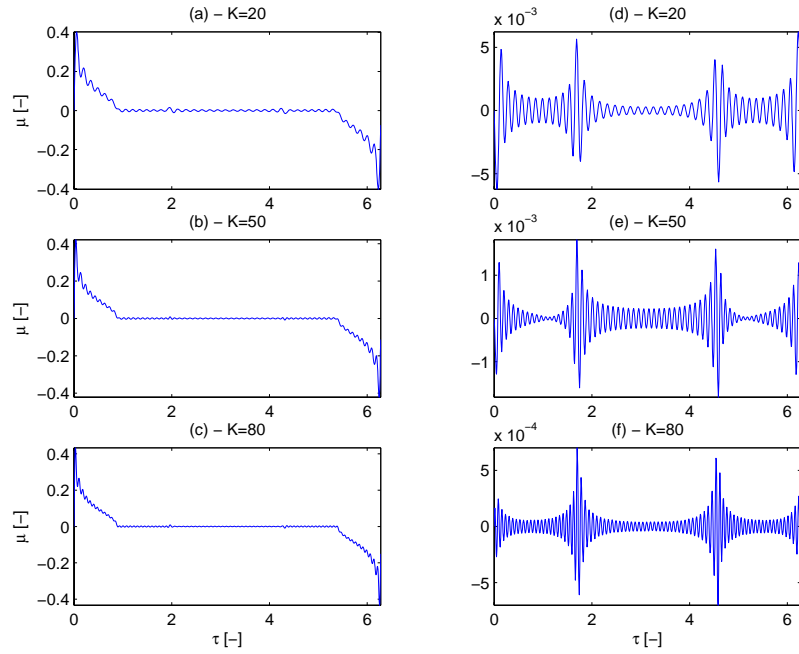


FIGURE 5.16: Design example: nondimensionalized torque residual  $\mu$  as a function of the number of harmonics  $K$  for  $\xi_0 = 1.3$  (a – c) and  $\xi_0 = 2.5$  (d – f).

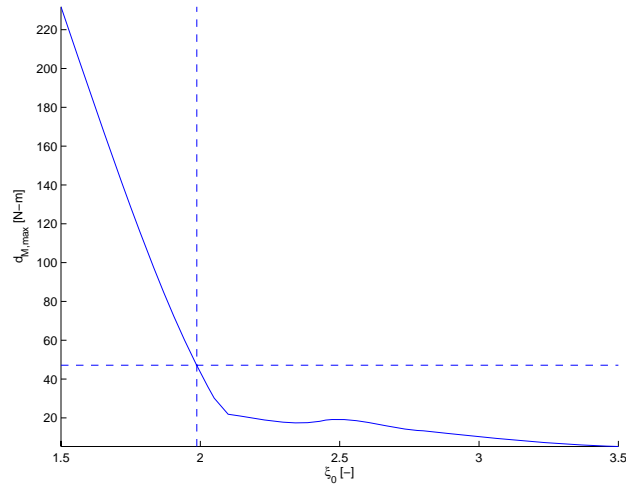


FIGURE 5.17: Design example: maximum torque residual as a function of  $\xi_0$ .

	goal	optimization variables				constraints						sec. constr.	
	$J_{\text{eq}}$ [kg-m <sup>2</sup> ]	$\xi_0$ [-]	$r_{\text{max}}$ [mm]	$r_0$ [mm]	$t^*$ [mm]	$N_{\text{min}}$ [N]	$(p_{\text{max}})_{\text{max}}$ [MPa]	$L_{\text{roll}}$ [1000h]	$\rho_{\text{min,-}}$ [mm]	$\rho_{\text{min,+}}$ [mm]	$i_1$ [mm]	$\dot{r}_{\text{max}}$ [m/s]	$\ddot{r}_{\text{max}}$ [m/s <sup>2</sup> ]
$m$	-	0	0	0	0	100	-	50	50	0	-	-	-
$\mathbf{p}_1$	0.4508	2.1211	118	117	80.0	100	638	446	-	65	-5.4	2.5	891
$\mathbf{p}_2$	0.4882	2.2133	123	122	80.0	500	646	399	-	73	-11.0	2.4	871
$\mathbf{p}_3$	0.5377	2.3281	129	129	80.0	1000	658	348	-	79	-18.2	2.4	846
$M$	-	-	-	-	80	-	900	-	-	-	0	5	100

TABLE 5.3: Properties of the proposed designs  $\mathbf{p}_1$ ,  $\mathbf{p}_2$  and  $\mathbf{p}_3$ . The  $m$  and  $M$  rows respectively give the lower and the upper bound for the corresponding quantity. None of the designs yields negative values of  $\rho$ , hence the empty  $\rho_{\text{min,-}}$  column.

The design chart illustrates that the peak phenomenon is more a theoretical than a practical problem as the area of feasible  $(\xi_0, r_{\max})$  combinations is delimited by the technological constraints, and not by the lower bound on  $\xi_0$  due to the peak phenomenon. At present, the nature of this peak phenomenon is not clear yet: it might be a numerical problem when solving (5.50), or a physical problem.

## 5.6 Conclusion

A methodology has been developed for designing the inverted cam mechanism (ICM). For given design parameters, and based on the assumption that the ICM is purely inertial, it is shown that the internal cam design is governed by a nonlinear, second-order, ordinary differential equation (ODE) in the cam pitch radius  $r$ . The requirement of periodicity turns this ODE into a boundary value problem, which is again solved using a nonlinear least-squares approach, based on parameterizing  $r$  as a finite Fourier series. The resulting solution constitutes the input for a complete kinematic, dynamic and technological analysis of the ICM. Application of this methodology to torque balance the sley mechanism of an airjet weaving machine illustrates the ICM's technological feasibility, as well as the design errors from the past.

The design parameters themselves are determined based on an optimization problem, aiming at minimizing the combined system's equivalent inertia, taking into account technological and collision constraints. Based on a parameterization of the rotor and carriage shape, two optimization variables are identified. As a consequence, the optimization problem can be solved exhaustively using a design chart.

A nondimensionalized analysis of the mechanism reveals the possibility to significantly reduce the computational time for calculating the design chart. This results from the fact that the solution of the boundary value problem is independent of one (namely  $r_{\max}$ ) of the two nondimensionalized optimization variables  $\xi_0$  and  $r_{\max}$ . Furthermore, the nondimensionalized analysis reveals the existence of a so-called peak phenomenon, that is, the fact that the boundary value problem seems to have no exact solution for too low a value of  $\xi_0$ . This is however more a theoretical than practical problem, as technological feasibility imposes tighter constraints on  $\xi_0$  and  $r_{\max}$  than does the lower bound on  $\xi_0$ , imposed by the peak phenomenon.

Finally, and most importantly,  $(\xi_0, r_{\max})$  contour plots of the carriage's amplitude of motion, velocity and acceleration show that the carriage motion combines a rather small amplitude with high velocities and accelerations. As a result, a standard roller guideway cannot be used for implementing the prismatic joint between the rotor and the carriage. Since the alternative of a sliding guideway is not a simple 'off-the-shelf' solution, it was therefore decided to develop the same kind of design methodology for the 'prismatic-joint-free' cam-based centrifugal pendulum mechanism.

## Chapter 6

# Input Torque Balancing: Cam-Based Centrifugal Pendulum

*What is the difference between method and device?  
A method is a device which you used twice.*

George Pólya (1887-1985),  
Hungarian-American mathematician

IN the literature survey of Chapter 4, both the inverted cam mechanism (ICM) and the cam-based centrifugal pendulum (CBCP) have been identified as interesting candidate ITB mechanisms. For the ICM, technological uncertainty is associated with the prismatic joint implementation. Since all joints in the CBCP are revolute, it was decided to develop a methodology for designing and optimizing the CBCP as well. To the best of our knowledge, there seems to be no such methodology available in the open literature.

The methodologies for the ICM and CBCP being very similar<sup>1</sup>, the structure of this chapter has been kept very similar to that of Chapter 5, such that some redundancy is unavoidable. An attempt has been done however to limit it to the strict minimum.

Section 6.1 derives the nonlinear differential equation that governs the cam design, called the *describing equation* for short. Its solution, for given design parameters, is the subject of Section 6.2. After that, a CBCP is designed in order to input torque balance the sley cam-follower mechanism of an airjet weaving machine (Section 6.3). The design parameters of this design example

---

<sup>1</sup>These methodologies hence constitute a *method* in Pólya's sense.

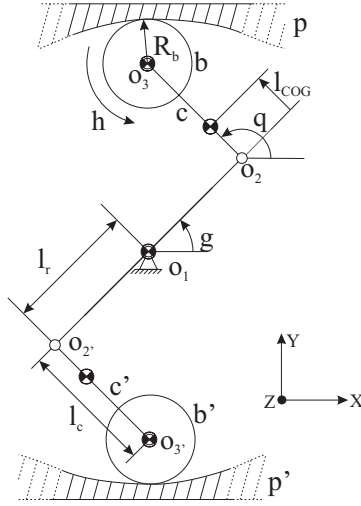


FIGURE 6.1: Cam-based centrifugal pendulum (CBCP): kinematic scheme.

are the result of a design optimization proposed in Section 6.4. Section 6.5 introduces a design chart for finding a quick, *approximate* solution of this optimization problem. Finally, simulation of the eigenmotion of an airjet weaving machine illustrates the beneficial effect of input torque balancing the sleigh mechanism, using the CBCP (Section 6.6).

## 6.1 Derivation of the Describing Equation

### 6.1.1 Nomenclature

The kinematic and dynamic CBCP parameters are defined based on Fig.6.1. The rotor, with mass  $m_r$  [kg], centroidal moment of inertia  $J_r$  [kg-m<sup>2</sup>] and length  $2 \cdot l_r$  [m], revolves around the ground point  $\hat{o}_1$ . Revolute joints connect the couplers  $c$  and  $c'$ , which each have mass  $m_c$  [kg], centroidal moment of inertia  $J_c$  [kg-m<sup>2</sup>] and length  $l_c$  [m], with the rotor. The roller followers  $b$  and  $b'$ , both having mass  $m_b$  [kg], centroidal moment of inertia  $J_b$  [kg-m<sup>2</sup>] and radius  $R_b$  [m], are connected to the corresponding couplers by a revolute joint. These revolute joints are bearings, of which the inner ring is part of the coupler, and of which the outer ring constitutes the roller follower.  $g(t)$  [rad] and  $q(t)$  [rad] respectively denote the rotor's and the coupler's rotation angle w.r.t. the positive  $X$ -axis, whereas  $h(t)$  is the rotation angle of the roller follower. As opposed to the rotor angle  $g(t)$  and the coupler angle  $q(t)$ ,  $h(t)$  needs no definition w.r.t. the  $X$ -axis because of the axisymmetry of the roller

follower.

Rotation of the rotor generates centrifugal forces that push  $b$  and  $b'$  against the internal cams  $p$  and  $p'$  respectively.  $p$  and  $p'$  are fixed to the mechanism frame and are identical, but rotated  $180^\circ$  with respect to each other. The cams are designed in such a way that the input torque  $M_c(t)$  [N-m] required to drive the CBCP is opposite to the input torque  $M_o(t)$  [N-m] for driving the original system, such that the net input torque to drive the combined system<sup>2</sup> equals zero.

The rotor is assumed to be symmetrical w.r.t.  $\hat{o}_1$ . Hence, its center of gravity (COG) coincides with  $\hat{o}_1$ . The coupler  $c$  is assumed to be symmetrical w.r.t. the line  $\hat{o}_2 - \hat{o}_3$ . Consequently, its COG lies along this line. Because of the axisymmetry of the roller follower  $b$ , its COG coincides with the point  $\hat{o}_3$ .

Because of the mechanism symmetry w.r.t.  $\hat{o}_1$ , the CBCP is completely force-balanced. However, the contact forces between the cams and the roller followers exert a nonzero shaking moment (about the  $Z$ -axis) on the mechanism frame. Furthermore, due to the fact that the cams lie in different planes, the contact forces also exert bending moments (about the  $X$  and  $Y$ -axis) on the drive shaft and the mechanism frame. Due to symmetry, the shaking and bending moments are pure couples.

### 6.1.2 Describing Equation: General Form

The derivation of the describing equation assumes that the CBCP is a purely inertial mechanism with one degree of freedom. This implies the same design assumptions as given in Section 5.1.2. Consequently, (1.3) applies, such that the CBCP's input torque  $M_c$  [N-m] is given by:

$$M_c = \frac{1}{\dot{g}} \cdot \frac{dT_c}{dt}, \quad (6.1)$$

where  $T_c$  [J] denotes the kinetic energy of the CBCP. The describing equation is derived by imposing,  $\forall t \in [0, T]$  that,

$$M_o(t) + M_c(t) = 0; \quad (6.2a)$$

$$\dot{g}(t) \equiv \frac{2\pi}{T}, \quad (6.2b)$$

where  $M_o(t)$  [N-m] denotes the original system's input torque. This set of equations expresses that the net input torque to impose a perfectly constant input angular velocity  $\dot{g}$  to the combined system, must be zero.

It is assumed that the original system is also a mechanism with one degree of freedom (the rotor angle  $g$ ). However, no assumption is made concerning

---

<sup>2</sup>The *original* system is the mechanism to be input torque balanced; the *compensated* system is the combination of the original system and the CBCP.

the nature of  $M_o(t)$ : for instance, the original system may be not purely inertial.

The integral form of (6.2a) is (see Section 5.1.2):

$$E_o(t) + T_c(t) = E_o(0) + T_c(0). \quad (6.3)$$

If the original system is not conservative, the energy function  $E_o(t)$  represents the sum of its kinetic, potential and dissipated energy as a function of time. If the original system is conservative,  $E_o(t)$  equals the sum of kinetic and potential energy. If it is purely inertial,  $E_o(t)$  is equivalent to the kinetic energy  $T_o(t)$ .

### 6.1.3 Describing Equation: Differential Equation Form

(6.2a) and (6.3) are transformed into differential equations in the coupler angle  $q(t)$  by developing expressions for  $T_c(t)$  and  $M_c(t)$ . Due to mechanism symmetry, only<sup>3</sup> the rotor and the bodies  $c$  and  $b$  need to be considered for determining  $T_c(t)$ :

$$T_c(t) = \frac{J_r \cdot \dot{q}^2}{2} + 2 \cdot \left( \frac{J_c \cdot \dot{q}^2}{2} + \frac{m_c \cdot \|\vec{v}_c\|^2}{2} \right) + n_b \cdot \left( \frac{J_b \cdot \dot{h}^2}{2} + \frac{m_b \cdot \|\vec{v}_3\|^2}{2} \right), \quad (6.4)$$

where  $\|\vec{v}_c\|$  and  $\|\vec{v}_3\|$  [m/s] denote the absolute velocity of the centers of gravity of the coupler and the roller follower respectively.  $n_b$  denotes the number of roller followers. For the conceptual CBCP of Fig.6.1,  $n_b$  equals two. By using four roller followers however, the CBCP bending moment on the drive shaft is cancelled (Section 6.4.1). Kinematic analysis of the mechanism yields (see Appendix C.1):

$$\|\vec{v}_c\|^2 = l_r^2 \cdot \dot{q}^2 + l_{COG}^2 \cdot \dot{q}^2 + 2 \cdot l_r \cdot l_{COG} \cdot \dot{q} \cdot \dot{q} \cdot \cos(g - q); \quad (6.5)$$

$$\|\vec{v}_3\|^2 = l_r^2 \cdot \dot{q}^2 + l_c^2 \cdot \dot{q}^2 + 2 \cdot l_r \cdot l_c \cdot \dot{q} \cdot \dot{q} \cdot \cos(g - q), \quad (6.6)$$

where  $l_{COG}$  determines the location of the COG of the coupler along the line  $\hat{o}_2 - \hat{o}_3$  (see Fig.6.1). Due to the fourth design assumption,  $\dot{h}^2(t)$  equals  $\|\vec{v}_3\|^2/R_b^2$ . Based on this observation and (6.2b), (6.5) and (6.6), (6.4) is transformed<sup>4</sup> into:

$$T_c(t) = \frac{J_1^* \cdot \left(\frac{2\pi}{T}\right)^2}{2} + \frac{J_2^* \cdot \dot{q}^2}{2} + J_3^* \cdot \left(\frac{2\pi}{T}\right) \cdot \dot{q} \cdot \cos\left(\frac{2\pi}{T} \cdot t - q\right), \quad (6.7)$$

<sup>3</sup>The dynamic effects due to the mass and moment of inertia of the intermediate bodies between the inner and the outer bearing ring (such as the balls in a ball bearing) are neglected.

<sup>4</sup>Because of (6.2b),  $g(t)$  equals  $2\pi/t \cdot t + g(0)$ , where  $g(0)$  is assumed to be zero. This does not compromise the generality of the equations.

where

$$J_1^* = J_r + 2 \cdot m_c \cdot l_r^2 + n_b \cdot m^* \cdot l_r^2; \quad (6.8)$$

$$J_2^* = 2 \cdot (J_c + m_c \cdot l_{\text{COG}}^2) + n_b \cdot m^* \cdot l_c^2; \quad (6.9)$$

$$J_3^* = 2 \cdot m_c \cdot l_{\text{COG}} \cdot l_r + n_b \cdot m^* \cdot l_c \cdot l_r; \quad (6.10)$$

$$m^* = \frac{J_b}{R_b^2} + m_b. \quad (6.11)$$

The first term in (6.7) is constant and therefore represents the flywheel effect of the CBCP, that is, the added 'dumb' rotary inertia. Henceforth,  $J_1^*$  should be kept as small as possible, in order not to compromise the start/stop behavior of the mechanism to be torque balanced.

Applying (6.7) to (6.1), taking into account (6.2b), yields:

$$M_c = \frac{1}{\frac{2\pi}{T}} \cdot J_2^* \cdot \dot{q} \cdot \ddot{q} + J_3^* \cdot s, \quad (6.12)$$

where

$$s(t) = \ddot{q} \cdot \cos\left(\frac{2\pi}{T} \cdot t - q\right) - \dot{q} \cdot \sin\left(\frac{2\pi}{T} \cdot t - q\right) \cdot \left(\frac{2\pi}{T} - \dot{q}\right). \quad (6.13)$$

Substituting (6.12) in (6.2a) yields:

$$M_o(t) + \frac{1}{\frac{2\pi}{T}} \cdot J_2^* \cdot \dot{q} \cdot \ddot{q} + J_3^* \cdot s = 0. \quad (6.14)$$

The structure of (6.13) reveals that, for a given  $M_o(t)$ , (6.14) constitutes a second-order, nonlinear, ordinary differential equation (ODE) in  $q(t)$ . However, this second-order ODE has only one independent initial condition (that is,  $q(0) = q_0$ ) as it is obtained by taking the time-derivative of the following first-order, nonlinear ODE:

$$\begin{aligned} \frac{J_2^* \cdot \dot{q}^2}{2} + J_3^* \cdot \frac{2\pi}{T} \cdot \dot{q} \cdot \cos\left(\frac{2\pi}{T} \cdot t - q\right) + E_o(t) = \dots \\ \dots \frac{J_2^* \cdot \dot{q}_0^2}{2} + J_3^* \cdot \frac{2\pi}{T} \cdot \dot{q}_0 \cdot \cos(q_0) + E_{o,0}, \end{aligned} \quad (6.15)$$

where the subscript 0 indicates values at time instant  $t = 0$  s. This ODE is obtained by substituting in (6.3) the expression (6.7) for  $T_c(t)$  and eliminating common terms on the left and the right hand-side. From an analytical point of view, solving  $q$  from either (6.14) or (6.15) is equivalent. (6.14) however yields more accurate numerical results (see Section 5.2).

$l_r$ [m]	0.072	$m_c$ [kg]	13.825	$m_b$ [kg]	1.841
$l_c$ [m]	0.079	$J_c$ [kg-m <sup>2</sup> ]	0.03148	$J_b$ [kg-m <sup>2</sup> ]	0.00257
$R_b$ [m]	0.050	$l_{\text{COG}}$ [m]	0.0390	$q_0$ [rad]	$\pi/2$

TABLE 6.1: Design example: numerical values of the nine CBCP design parameters.

## 6.2 Solution of the Describing Equation

In order for the internal cam profile to be closed, it is imperative that  $q(T) = q(0) + 2\pi$ . Combining this requirement with (6.14) results in a boundary value problem that is solved using a nonlinear least-squares approach that is quasi identical to the one proposed in Section 5.2, and therefore is not elaborated here. The only difference is the adopted parameterization of  $q(t)$ : the requirement that  $q(T) = q(0) + 2\pi$ , is met automatically if  $\dot{q}(t)$  is parameterized as a Fourier series with period  $T$  and average value  $2\pi/T$ :

$$\dot{q}(t) = \frac{2\pi}{T} + \sum_{k=1}^K a_k \cdot \cos(k\Omega t) + b_k \cdot \sin(k\Omega t). \quad (6.16)$$

Hence:

$$\hat{q}(t) = C + \frac{2\pi t}{T} + \sum_{k=1}^K \frac{1}{k\Omega} \cdot \left( a_k \cdot \cos\left(k\Omega t - \frac{\pi}{2}\right) + b_k \cdot \sin\left(k\Omega t - \frac{\pi}{2}\right) \right); \quad (6.17)$$

$$\ddot{\hat{q}}(t) = \sum_{k=1}^K k\Omega \cdot \left( a_k \cdot \cos\left(k\Omega t + \frac{\pi}{2}\right) + b_k \cdot \sin\left(k\Omega t + \frac{\pi}{2}\right) \right). \quad (6.18)$$

$C$  is an integration constant, determined by imposing that  $\hat{q}(0)$  be equal to some desired value  $q_0$ . The hats ( $\hat{\cdot}$ ) are introduced since, due to the truncation of the Fourier series, not the exact solution  $q$  is calculated but an approximation  $\hat{q}$  of it. Again,  $K = 20$  provides good compromise between obtaining an accurate solution and limiting the number ( $2K$ ) of unknown parameters.

## 6.3 Design Example

In this section, the developed theory is applied to design a CBCP with  $n_b = 4$  roller followers for input torque balancing the sley cam-follower mechanism of an airjet weaving machine. Inspection of the describing equation (6.14)

reveals that, given  $T$  and the torque  $M_o(t)$  to be balanced,  $q$  depends on three fundamental parameters:  $J_2^*$ ,  $J_3^*$  and the initial condition  $q_0$ .

Since (6.9–6.11) show  $J_2^*$  and  $J_3^*$  to depend on  $l_r$ ,  $l_c$ ,  $l_{\text{COG}}$ ,  $m_c$ ,  $J_c$ ,  $R_b$ ,  $m_b$ ,  $J_b$ , the following nine parameters affect  $q$  and hence the shape and the technological properties of the CBCP: the kinematic design parameters  $l_c$ ,  $l_r$  and  $R_b$ , the dynamic design parameters  $m_c$ ,  $m_b$ ,  $J_c$ ,  $J_b$  and  $l_{\text{COG}}$  and the initial condition  $q_0$ . These design parameters must be chosen in such a way that the resulting mechanism is technologically feasible. The design parameters for the design example at hand are found in Table 6.1 and give rise to  $J_2^* = 0.177 \text{ kg}\cdot\text{m}^2$  and  $J_3^* = 0.143 \text{ kg}\cdot\text{m}^2$ . They are the result of a design optimization which is the subject of Section 6.4 and 6.5.

Section 6.3.1 introduces the cam-follower mechanism to be balanced and gives the solution of the describing equation (6.14). Since the technological feasibility analysis requires a full kinematic and inverse dynamic analysis, this is discussed in Section 6.3.2. Lastly, Section 6.3.3 focuses on the technological analysis of the CBCP.

### 6.3.1 Mechanism to be Balanced

The cam-follower mechanism to be balanced is the sley cam-follower mechanism of an airjet weaving machine. This mechanism has been introduced in Section 2.2. Expressions for its input torque and kinetic energy are given in Section 5.3.1 and are repeated here for reference:

$$M_o = M_{\text{sley}} = \frac{1}{\frac{2\pi}{T}} \cdot J_{\text{sley}} \cdot \dot{f}_{\text{sley}} \cdot \ddot{f}_{\text{sley}}; \quad (6.19)$$

$$T_o = T_{\text{sley}} = \frac{J_{\text{sley}} \cdot \dot{f}_{\text{sley}}^2}{2}. \quad (6.20)$$

The dashed line in Fig.6.2 shows  $M_o(t)$ , for a period of motion equal to  $T=0.0667 \text{ s}$ . This corresponds to an average drive speed  $\Omega$  of 900 rpm.

Figure 6.3 shows  $\dot{q}(t)$  and its derivatives, calculated using  $K = 20$  harmonics and  $q(0) = \pi/2$  as an initial condition. Quite remarkably,  $\dot{q}(t)$  is not constant in the zone where  $M_o(t)$  is zero (roughly between  $t = 0.020$  and  $t = 0.045 \text{ s}$ ). This may be attributed to the fact that the solution which has a constant  $\dot{q}(t)$  in this zone, might not comply with the boundary conditions at the boundaries of this zone.

The solution of (6.14) is checked via the torque residual  $M_o + M_c$ . Due to the truncation of the Fourier series when solving the differential equation, it is not perfectly zero. Figure 6.2(a) shows  $M_c$  and  $M_o$ , whereas Fig.6.2(b) shows the torque residual, which is negligible w.r.t. the maximum value of  $M_o$ , equal to 856 N·m. Furthermore, a dominant 21st harmonic is present, originating from the fact that  $K = 20$  harmonics are used.

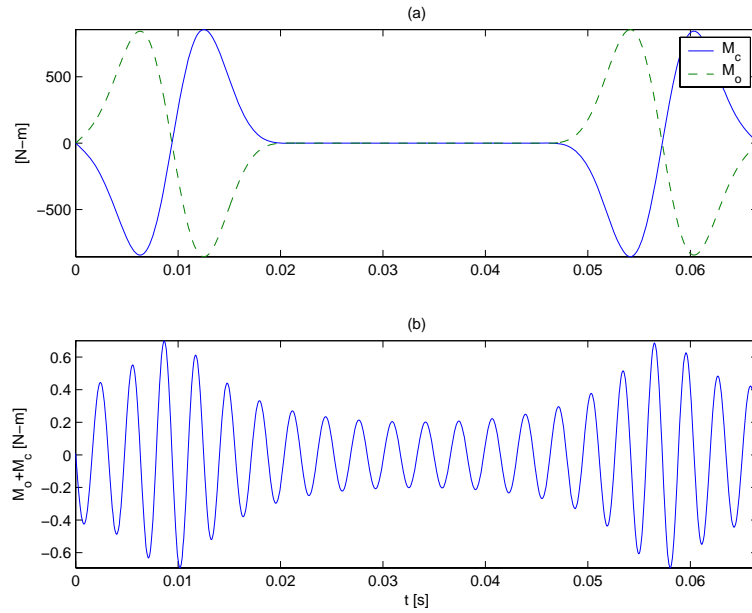


FIGURE 6.2: Design example: (a) original (dashed line) and compensating input torque (solid line) and (b) torque residual.

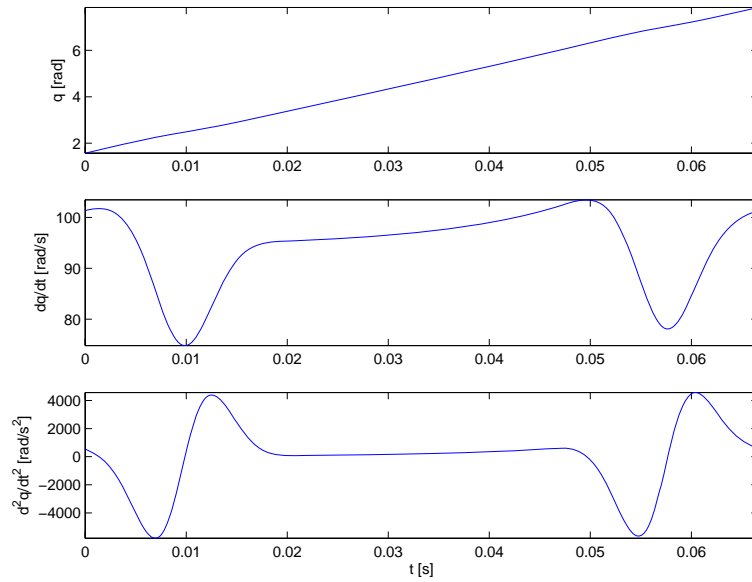


FIGURE 6.3: Design example:  $\hat{q}$  and its first two derivatives.

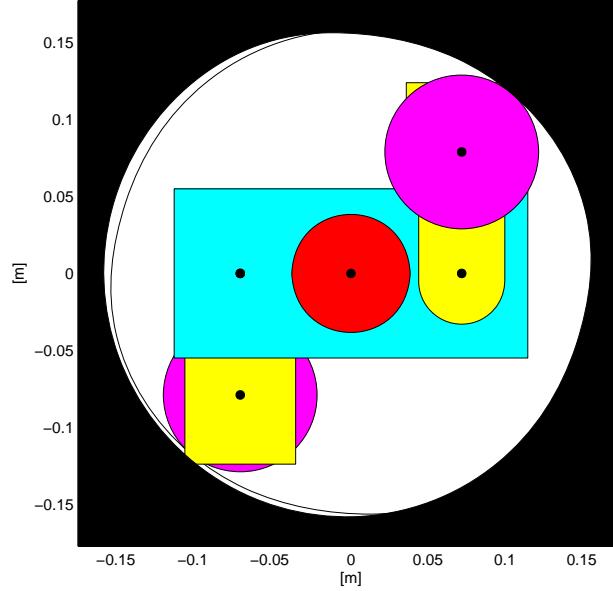


FIGURE 6.4: Design example: resulting CBCP configuration. Both the X and the Y-axis are expressed in [m]. The solid boundary indicates the cam against which the upper rolling body rolls. The thin boundary, shown in the left part, and hidden behind the solid boundary in the right part, indicates the cam against which the lower rolling body rolls.

The equivalent inertia was introduced in Section 5.3.1 as an important property of the combined system:

$$\frac{J_{\text{eq}} \cdot \left(\frac{2\pi}{T}\right)^2}{2} = E_o(t) + T_c(t) = E_{o,0} + T_{c,0}. \quad (6.21)$$

The CBCP kinetic energy is calculated using (6.7–6.11).  $E_o \equiv T_o$  is given by (6.20). With  $J_r = 0.0723 \text{ kg}\cdot\text{m}^2$ ,  $J_{\text{eq}} = 0.4791 \text{ kg}\cdot\text{m}^2$  is obtained. Hence,  $J_{\text{eq}}$  is approximately five times greater than its physical lower limit of  $0.0891 \text{ kg}\cdot\text{m}^2$ , derived in Section 5.3.1.

### 6.3.2 Kinematic and Inverse Dynamic Analysis

Determining the technological properties requires a full kinematic and inverse dynamic analysis. The purpose of the kinematic analysis is to determine the position, velocity and acceleration of the points  $\hat{o}_i$ ,  $i = \{1, 2, c, 3\}$  in Fig.6.5(a),

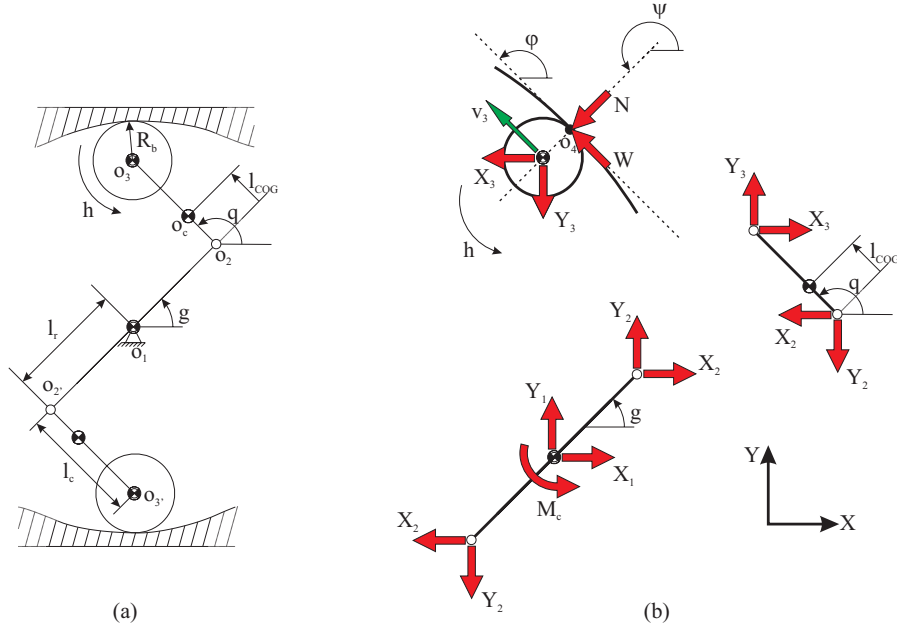


FIGURE 6.5: (a) CBCP kinematic scheme and (b) free-body diagram.

the kinematics ( $\dot{h}$ ,  $\ddot{h}$ ) of the roller follower, and the cam profile. The kinematic analysis is discussed in detail in Appendix C.

As a result of the kinematic analysis, Fig.6.4 shows<sup>5</sup> the CBCP with the rotor and the couplers in their positions at time instant  $t = 0s$  (note that  $q(0)$  effectively equals  $\pi/2$  rad since the coupler starts under an angle of 90 degrees). The minimum and maximum of the cam radius are:  $r_{p,\min} = 153.6$  mm and  $r_{p,\max} = 161.2$  mm, so the stroke of the mechanism is 7.6 mm. The limited value of  $r_{p,\max}$  illustrates that the resulting mechanism is quite compact.

The purpose of the inverse dynamic analysis is to determine all forces and moments based on the kinematics determined in the kinematic analysis. Figure 6.5(b) shows the free-body diagram of the CBCP.  $M_c$  is the driving torque;  $X_i$  and  $Y_i, i = \{1, 2, 3\}$  are the reaction forces due to the revolute joints in  $\hat{o}_1, \hat{o}_2$  and  $\hat{o}_3$  respectively.  $N$  and  $W$  respectively are the contact force and the friction force exerted by the cam on the roller follower. Following the convention of Fig.6.5(b), it is clear that  $N$  should be greater than zero in order to ensure contact between the roller follower and the cam. Figure 6.6

<sup>5</sup>The shape of the rotor and the coupler are determined based on the mass parameterization of Section 6.4.

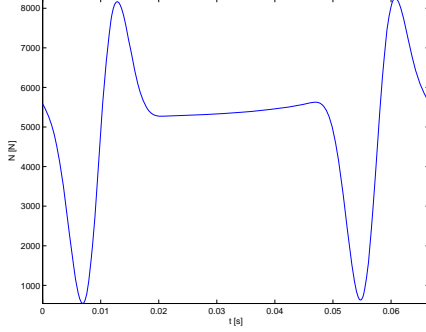


FIGURE 6.6: Design example: contact force  $N$  [N].

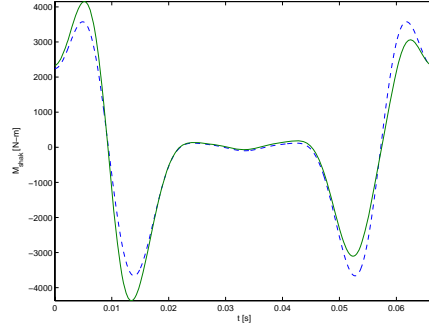


FIGURE 6.7: Design example: shaking moment  $M_{\text{shak}}$  [N-m] in the original system (dashed line) and the combined system (solid line).

shows that for the design example,  $N$  is well above 0 N: its minimum equals 542 N. The inverse dynamic analysis is discussed in detail in Appendix D.

### Shaking Moment

A complete discussion of the shaking moment in the original and the combined system has been given in Section 5.3.2. Only the expressions for the CBCP's angular momentum and its shaking moment  $M_{\text{shak,c}}$  w.r.t.  $\hat{o}_1$  are therefore given here:

$$A_c(t) = J_r \cdot \dot{g} + 2 \cdot (J_c \cdot \dot{q} + o_{cx} \cdot m_c \cdot v_{cy} - o_{cy} \cdot m_c \cdot v_{cx}) + n_b \cdot (J_b \cdot \dot{h} + o_{3x} \cdot m_b \cdot v_{3y} - o_{3y} \cdot m_b \cdot v_{3x}); \quad (6.22)$$

$$M_{\text{shak,c}}(t) = -J_r \cdot \ddot{g} - 2 \cdot (J_c \cdot \ddot{q} + o_{cx} \cdot m_c \cdot a_{cy} - o_{cy} \cdot m_c \cdot a_{cx}) - n_b \cdot (J_b \cdot \ddot{h} + o_{3x} \cdot m_b \cdot a_{3y} - o_{3y} \cdot m_b \cdot a_{3x}), \quad (6.23)$$

where  $o_{cx}$ ,  $o_{cy}$ ,  $o_{3x}$  and  $o_{3y}$  denote the  $X$  and  $Y$ -coordinates of  $\hat{o}_c$  and  $\hat{o}_3$  respectively (see Fig.6.5(a)).  $v_{cx}$ ,  $v_{cy}$ ,  $v_{3x}$  and  $v_{3y}$  denote the  $X$  and  $Y$ -components of the speed of  $\hat{o}_c$  and  $\hat{o}_3$ , while  $a_{cx}$ ,  $a_{cy}$ ,  $a_{3x}$  and  $a_{3y}$  are the  $X$  and  $Y$ -components of the acceleration of  $\hat{o}_c$  and  $\hat{o}_3$ .

Figure 6.7 compares the shaking moment in both the original and the combined system, if  $\dot{g} \equiv 2\pi/T$ . Addition of the CBCP results in a 19% increase of the maximum shaking moment from 3662 to 4370 N-m.

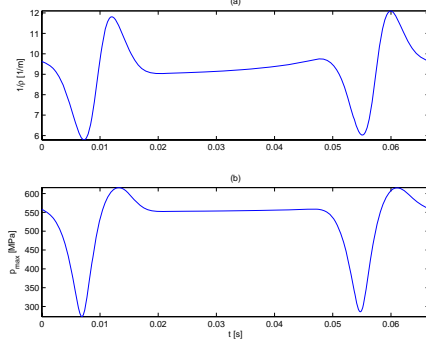


FIGURE 6.8: Design example: (a) curvature  $1/\rho$  [ $\text{m}^{-1}$ ] of cam pitch profile; (b) maximum Hertzian pressure  $p_{\max}$  [MPa].

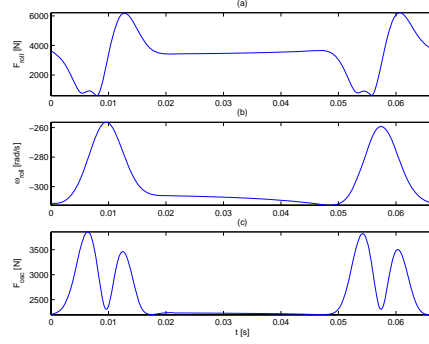


FIGURE 6.9: Design example: (a) force  $F_{\text{roller}}$  [N] transmitted by roller follower bearing; (b) angular speed  $\omega_{\text{roller}}$  [rad/s] of roller follower bearing; (c) force  $F_{\text{osc}}$  [N] transmitted by oscillating bearing.

### 6.3.3 Technological Analysis

A first part of the technological analysis is concerned with the radius of curvature  $\rho$  [m] of the cam pitch profile, that is, the trajectory of the point  $\hat{o}_3$ . How to calculate  $\rho$  is the subject of Appendix G. Figure 6.8(a) shows the resulting curvature  $1/\rho$  [ $\text{m}^{-1}$ ] for the design example. It is positive over the entire internal cam profile, and has a maximum value of  $12.1 \text{ m}^{-1}$ , corresponding to a minimum  $\rho$ -value of 82.6 mm.

The radius of curvature of the pitch profile is of concern for determining whether or not the following geometric problems occur: *undercutting*, *under-rolling* and *feasibility problems*. These geometric problems are discussed in detail in Appendix G, and do not occur in the case of the internal CBCP cam profile, provided that:

$$-\rho > R_b, \forall \rho \leq 0; \quad (6.24)$$

$$\rho + R_b > R_C, \forall \rho \geq 0, \quad (6.25)$$

where  $R_C$  [m] denotes the radius of the cutter or grinding stone used to mill or grind the cam profile. For the design example at hand,  $\rho$  is positive anywhere, so condition (6.24) is of no concern. As the minimum value of  $\rho$  equals 82.6 mm, condition (6.25) is met provided that  $R_C$  is smaller than  $82.6 + 50 = 132.6$  mm.

A second part of the technological analysis is concerned with the Hertzian stresses in the point contact between the crowned roller follower and the cam profile. Appendix H shows how the maximum Hertzian stress  $p_{\max}$  in a point

contact is calculated, based on the cam profile curvature  $\rho_p = \rho + R_b$  [m], the roller follower radius  $R_b$  and its crown radius  $R_{bc} = 2.5$  m, the contact force  $N$  and the Young's modulus and Poisson's ratio of the cam and roller follower material. Figure<sup>6</sup> 6.8(b) shows the maximum Hertzian pressure  $p_{\max}$  [MPa]. Its largest value is 616 MPa.

$p_{\max}$  should be limited in order to avoid premature failure of the cam due to either *yield* of the cam material or *surface fatigue*. In appendix H it is shown that for the cam material used here (*IMPAX Hi Hard*, a prehardened mould steel with a hardness of 360-400 HB and a yield strength  $R_{p0,2}$  of 1090 MPa), the following upper limits on  $p_{\max}$  should be observed:

$$p_{\max} < 1.47 \cdot R_{p0,2} \Rightarrow p_{\max} < 1600 \text{ MPa (yield avoidance);} \quad (6.26)$$

$$p_{\max} < 1071 \text{ MPa, (fatigue life of 50000h at 900 rpm).} \quad (6.27)$$

The 616 MPa maximum value of  $p_{\max}$  is far below the 1600 MPa limit, so yield does not occur. The upper limit for obtaining a fatigue life of 50000h at 900 rpm is only indicative, as surface fatigue calculations are based on a lot of assumptions (see Appendix H.4) and need experimental verification. However, as 616 MPa is well below 1071 MPa, the cam material has a probable fatigue life of over 50000 h.

A third part of the technological analysis is concerned with the lifetimes of the bearings in the CBCP, that is, the roller follower bearing and the oscillating bearing that implements the revolute joint between the rotor and the coupler. Appendix I elaborates the classical bearing lifetime formulae and shows how the equivalent dynamic load on the bearings is calculated, based on the force transmitted by the bearing, its angular speed and its load-carrying capacity  $C$  [N]. Special attention is paid to the oscillating bearing, of which the lifetime is calculated as if it was a statically loaded bearing, as recommended in (Beitz and Küttner, 1986).

Figure 6.9(a) shows the force  $F_{\text{roll}}$  [N] transmitted by the roller follower bearing ( $C = 137$  kN), whereas Fig.6.9(b) shows the angular speed  $\omega_{\text{roll}}$  [rad/s] of the roller follower. The corresponding equivalent dynamic load  $P_{\text{roll}}$  equals 3905 N, yielding a lifetime of 828000h at 900 rpm. Figure 6.9(c) shows the force  $F_{\text{osc}}$  [N] transmitted by the oscillating bearing ( $C_0 = 32$  kN). The corresponding equivalent static load  $P_{\text{osc}}$  equals 2682 N, yielding a lifetime of 72000 h at 900 rpm.

## 6.4 Design Optimization

The design example of the previous section is based on the design parameter values of Table 6.1. These nine design parameters result from a design

<sup>6</sup>The fact that  $\rho$  and  $p_{\max}$  are given as a function of time  $t$  in Fig.6.8 must be interpreted as follows: the values of  $\rho$  and  $p_{\max}$  at time instant  $t$  are the ones for the contact point between the cam and the roller follower at that same time instant.

optimization which is the subject of this (and the following) section. The purpose of the design optimization is to obtain a technologically feasible CBCP with minimum equivalent inertia. This section discusses the choice of the optimization variables, goal function, constraints and optimization algorithm, and finally gives numerical results for the CBCP design optimization in the case of the sley cam-follower mechanism of Section 6.3.1.

### 6.4.1 Optimization Variables

It is obvious to use the nine design parameters as the optimization variables. Here, however, the number of optimization variables is reduced to four, in order to keep this nonconvex optimization problem tractable.

First of all, it is assumed that some given bearing, chosen from a catalogue, implements the revolute joint between the roller follower and the carriage. This determines  $m_b$ ,  $J_b$  and  $R_b$ , since these are properties of the outer bearing ring. These parameters are grouped into the parameter vector  $\mathbf{p}_b \in \mathbb{R}^3$ :

$$\mathbf{p}_b = [ m_b \quad J_b \quad R_b ] .$$

The idea is that the designer selects the bearing, then performs the design optimization and afterwards makes a check whether the bearing is strong enough. If not, another bearing has to be chosen, and a new design optimization has to be performed.

A second reduction in the number of optimization variables is obtained by parameterizing the shape of the coupler. Figure 6.10(c – d) defines the coupler mass parameterization: it is a fork supporting the inner bearing rings (of diameter  $R_7$ ) of the roller follower and two additional masses. These are cylinders of radius  $R^*$  [m] and length  $t^*$  [m]. The second coupler, not shown in Fig.6.10, is identical, except that the inner bearing rings and the additional masses have switched place. Therefore, both couplers have identical values of  $m_c$ ,  $l_{\text{COG}}$  and  $J_c$ . The reason for switching the place of the inner bearing rings and the additional masses is that it results in cancellation of the CBCP bending moment on the drive shaft and the mechanism frame. The number  $n_b$  of roller followers in this CBCP variant is four.

The coupler's shape, and hence its mass parameters  $m_c$ ,  $J_c$  and  $l_{\text{COG}}$  are completely determined by the geometric parameters  $l_c$ ,  $R^*$ ,  $t^*$ ,  $R_3$ ,  $t_3$ ,  $l_4$ ,  $l_{4x}$ ,  $d_4$ ,  $l_5$ ,  $t_{51}$ ,  $t_{52}$ ,  $t_{53}$ ,  $l_6$ ,  $l_{6x}$ ,  $d_6$ ,  $R_7$  and  $t_7$ . Defining the parameter vector  $\mathbf{p}_c \in \mathbb{R}^{15}$  as:

$$\mathbf{p}_c = [ t^* \quad R_3 \quad t_3 \quad l_4 \quad l_{4x} \quad d_4 \quad l_5 \quad t_{51} \quad t_{52} \quad t_{53} \quad l_6 \quad l_{6x} \quad d_6 \quad R_7 \quad t_7 ] ,$$

$m_c$ ,  $l_{\text{COG}}$  and  $J_c$  are written as:

$$m_c = m_c(l_c, R^*, \mathbf{p}_c); \quad (6.28)$$

$$l_{\text{COG}} = l_{\text{COG}}(l_c, R^*, \mathbf{p}_c); \quad (6.29)$$

$$J_c = J_c(l_c, R^*, \mathbf{p}_c). \quad (6.30)$$

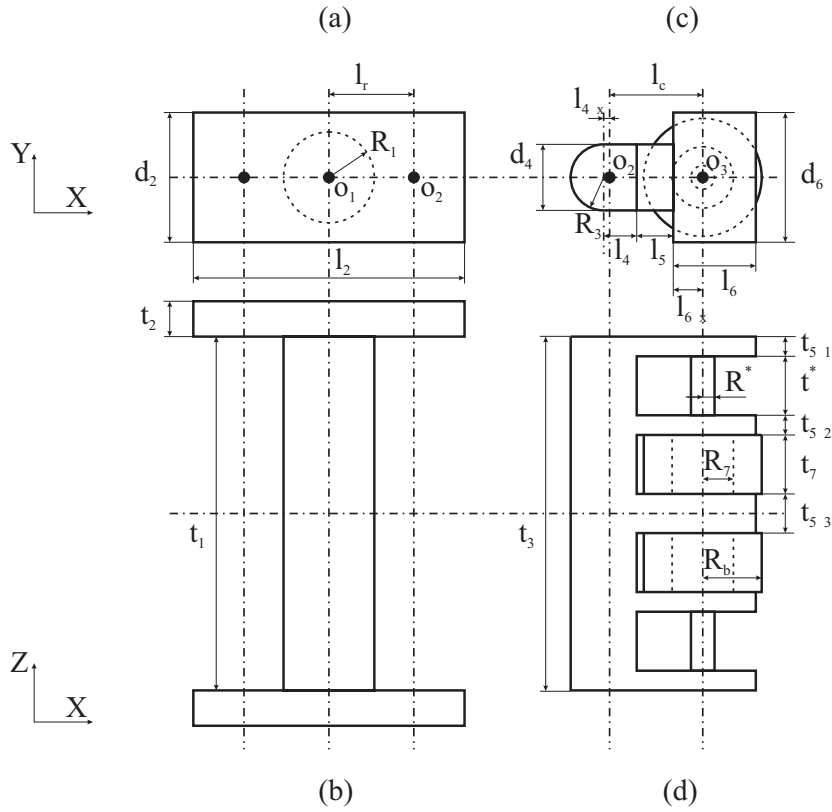


FIGURE 6.10: Shape parameterization: front (a) and top (b) view of the rotor and front (c) and top (d) view of the coupler (with the outer bearing ring of diameter  $R_b$  present).

Only  $l_c$  and  $R^*$  are considered for optimization, whereas  $\mathbf{p}_c$  is assigned a reasonable, fixed value that has to be checked after the design optimization. If the resulting coupler does not have sufficient structural strength,  $\mathbf{p}_c$  has to be modified and a new optimization has to be done.

### 6.4.2 Goal Function

The goal function is minimum equivalent inertia  $J_{eq}$  [kg-m<sup>2</sup>]. The rationale for doing so is that inertia minimization for improved start/stop behavior was exactly the reason for using a torque balancing mechanism instead of a large flywheel.

A practical consequence of this choice of goal function is that  $J_1^*$  becomes a fourth fundamental parameter, as it affects  $T_c$ . Hence, as shown by (6.8),  $J_r$  is also a design variable.  $J_r$  is however not considered as an optimization variable, as it is calculated based on a parameterization of the rotor's shape shown in Fig.6.10(a – b). The rotor's shape, and hence  $J_r$  are completely determined by the geometric parameters  $l_r, R_1, t_1, l_2, d_2$  and  $t_2$ . The parameter vector  $\mathbf{p}_r \in \mathbb{R}^5$  is defined as:

$$\mathbf{p}_r = [ R_1 \quad t_1 \quad l_2 \quad d_2 \quad t_2 ] .$$

Hence

$$J_r = J_r(l_r, \mathbf{p}_r) . \quad (6.31)$$

Only  $l_r$  is considered for optimization, whereas  $\mathbf{p}_r$  is assigned a reasonable, fixed value. Again, this fixed value has to be checked after the design optimization. If the resulting rotor does not have sufficient structural strength,  $\mathbf{p}_r$  has to be modified and a new optimization has to be done.

### Discussion

From the above discussion  $l_r, l_c, R^*$  and  $q_0$  emerge as the optimization variables. The secondary parameters to which fixed values are assigned and which have to be validated after the design optimization are contained in the parameter vectors  $\mathbf{p}_b, \mathbf{p}_c$  and  $\mathbf{p}_r$ . The values chosen for the secondary parameters are given in Table E.4.

Replacing the nine design parameters by four optimization variables and twenty-three secondary parameters has the following advantages: (i) the link shapes are automatically determined, such that shape and collision constraints are easily implementable (as shown hereafter), (ii) it reflects that the bearing parameters  $m_b, J_b, R_b$  can only assume a discrete set of values, chosen from a catalogue and (iii) this nonconvex optimization problem is much better tractable.

As the number of optimization variables and fundamental parameters are equal, it is to be expected that the degree of suboptimality, introduced by choosing fixed values for the secondary parameters, is a minimum.

### 6.4.3 Constraints

There are three kinds of constraints: (i) bound constraints on the optimization variables, (ii) constraints in order to obtain a technologically feasible mechanism and (iii) constraints in order to avoid collisions between moving mechanism parts.

### Bound Constraints

The optimization variables are bound as follows:

$$l_r^m \leq l_r; \quad (6.32)$$

$$l_c^m \leq l_c; \quad (6.33)$$

$$0 \leq R^* \leq R^{*,M}; \quad (6.34)$$

$$0 \leq q_0 \leq \pi. \quad (6.35)$$

The first two constraints express that  $l_r$  and  $l_c$  should have a minimum length, in order to avoid construction problems. The third constraint imposes a positivity constraint and an upper bound on  $R^*$  in order to avoid excessive additional masses. The fourth constraint makes sure that only values of  $q_0 \in [0, \pi]$  are considered since values of  $q_0 \in [-\pi, 0]$  yield an identical dynamic behavior of the mechanism. Therefore, it makes sense to tighten the search space using this positivity<sup>7</sup> constraint.

### Technological Constraints

The following technological constraints are taken into account. First of all, there must always be contact between the roller followers and the cams. This is mathematically expressed by imposing that the contact force  $N(t)$  [N] between the cams and the roller followers should have a minimum  $N_{\min}$  over  $[0, T]$  which is greater than zero, or for robustness reasons, greater than some positive lower bound  $N^m$ :

$$N_{\min} \geq N^m. \quad (6.36)$$

When determining  $N_{\min}$ , only the mechanism regime behavior is considered, and not the transient behavior during the startup or braking phase.

Secondly, in order to avoid cam yield and surface fatigue problems, the maximum  $(p_{\max})_{\max}$  (over the cam profile), of all maximum Hertzian stresses  $p_{\max}$ , should be less than some upper bound  $p_{\max}^M$ :

$$(p_{\max})_{\max} \leq p_{\max}^M. \quad (6.37)$$

Thirdly, the lifetime  $L_{\text{roll}}$  [h] of the roller follower bearing and the lifetime  $L_{\text{osc}}$  [h] of the oscillating bearing should be greater than some minimum lifetime:

$$L_{\text{roll}} \geq L_{\text{roll}}^m; \quad (6.38)$$

$$L_{\text{osc}} \geq L_{\text{osc}}^m. \quad (6.39)$$

Fourthly, for avoiding cam profile geometrical problems (undercutting, under-rolling and feasibility problems.), (6.24) and (6.25) should be fulfilled, which

<sup>7</sup>Imposing a negativity constraint yields identical optimization results, except for the sign of  $q_0$  of course.

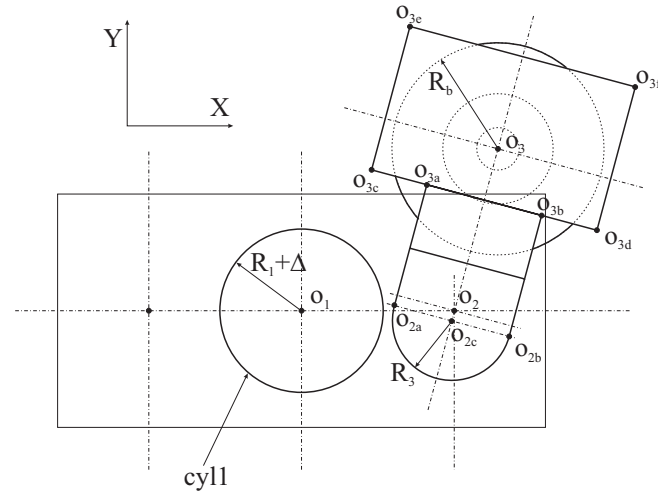


FIGURE 6.11: Front view of the assembled rotor, coupler and roller follower.

gives rise to the following constraints:

$$\rho_{\min,-} \geq R_b; \quad (6.40)$$

$$\rho_{\min,+} \geq R_C - R_b, \quad (6.41)$$

where  $\rho_{\min,-}$  and  $\rho_{\min,+}$  are defined as

$$\rho_{\min,-} = \min_{\rho(t) \leq 0, t \in [0, T]} -\rho;$$

$$\rho_{\min,+} = \min_{\rho(t) \geq 0, t \in [0, T]} \rho.$$

### Collision Constraints

Figure 6.11 shows the assembly of the rotor  $r$ , coupler  $c$  and roller follower  $b$ . For reasons of clarity, the rotor flanges of length  $l_2$  and width  $d_2$  are drawn as a thin, solid line. When the coupler moves w.r.t. the rotor, two collisions may occur: (i) a collision between the roller follower of radius  $R_b$  and the cylinder  $\text{cyl1}$  of radius  $R_1 + \Delta$ , belonging to the rotor and (ii) a collision between the coupler and  $\text{cyl1}$ .

Avoiding the collision between the roller follower and cyll is mathematically expressed by imposing that circle  $(\hat{o}_3, R_b)$  and circle  $(\hat{o}_1, R_1 + \Delta)$  do not intersect. In other words: the distance  $d(\hat{o}_1, \hat{o}_3)$  between  $\hat{o}_1$  and  $\hat{o}_3$  must be greater than  $R_1 + \Delta + R_b$ :

$$\left[ (o_{1x} - o_{3x})^2 + (o_{1y} - o_{3y})^2 \right]^{\frac{1}{2}} \geq R_1 + \Delta + R_b, \quad (6.42)$$

where  $\Delta$  [m] represents a safety tolerance.  $o_{1x}$ ,  $o_{3x}$ ,  $o_{1y}$  and  $o_{3y}$  are given by (C.1a–C.1h) in Appendix C.

If sometime during the motion cycle, condition (6.42) is violated, the collision flag  $i_1$  is set to one. If, on the other hand, (6.42) is valid during the whole motion cycle,  $i_1$  is set to  $-d_1$ , where  $d_1$  represents the minimum distance, over the motion cycle, between circle  $(\hat{o}_1, R_1 + \Delta)$  and circle  $(\hat{o}_3, R_b)$ :

$$d_1 = \min_{t \in [0, T]} \left[ (o_{1x} - o_{3x})^2 + (o_{1y} - o_{3y})^2 \right]^{\frac{1}{2}} - (R_1 + \Delta + R_b).$$

Avoiding the collision between the coupler and cyll is mathematically expressed by the following conditions:

- There must be no intersection between circle  $(\hat{o}_1, R_1 + \Delta)$ , and the following line segments:  $[\hat{o}_{2a} \hat{o}_{3a}]$ ,  $[\hat{o}_{3a} \hat{o}_{3c}]$ ,  $[\hat{o}_{3c} \hat{o}_{3e}]$ ,  $[\hat{o}_{2b} \hat{o}_{3b}]$ ,  $[\hat{o}_{3b} \hat{o}_{3d}]$  and  $[\hat{o}_{3d} \hat{o}_{3f}]$ . A detailed discussion of these conditions is given in Appendix F.1.
- Circle  $(\hat{o}_{2c}, R_3)$  and circle  $(\hat{o}_1, R_1 + \Delta)$  must not intersect. In other words: the distance  $d(\hat{o}_1, \hat{o}_{2c})$  between  $\hat{o}_1$  and  $\hat{o}_{2c}$  must be greater than  $R_1 + \Delta + R_3$ :

$$\left[ (o_{1x} - o_{2cx})^2 + (o_{1y} - o_{2cy})^2 \right]^{\frac{1}{2}} \geq R_1 + \Delta + R_3, \quad (6.43)$$

where  $\Delta$  [m] represents a safety tolerance.  $o_{2cx}$  and  $o_{2cy}$  are determined in Appendix F.2.

If sometime during the motion cycle, an intersection is detected, the collision flag  $i_2$  is set to one. In the other case,  $i_2$  is set to  $-\min(d_{2a}, d_{2b})$ .  $d_{2a}$  represents the minimum distance, over the motion cycle, between any of the line segments (see Appendix F.1) and circle  $(\hat{o}_1, R_1 + \Delta)$ .  $d_{2b}$  on the other hand represents the minimum distance, over the motion cycle, between circle  $(\hat{o}_{2c}, R_3)$  and circle  $(\hat{o}_1, R_1 + \Delta)$ :

$$d_{2b} = \min_{t \in [0, T]} \left[ (o_{1x} - o_{2cx})^2 + (o_{1y} - o_{2cy})^2 \right]^{\frac{1}{2}} - (R_1 + \Delta + R_3).$$

Based on the above definitions of  $i_1$  and  $i_2$ , avoiding collisions in the CBCP is mathematically expressed by the following constraints:

$$i_1 \leq 0; \quad (6.44)$$

$$i_2 \leq 0. \quad (6.45)$$

#### 6.4.4 Optimization Algorithm

The optimization problem is solved using the `fmincon` algorithm of the MATLAB OPTIMIZATION TOOLBOX. This algorithm implements a Sequential Quadratic Programming (SQP) technique.

As the optimization problem is nonconvex, the algorithm gets stuck in local optima and is therefore started from a lot of different starting points. Afterwards, the most optimal local optimum is chosen. Due to the optimization problem's nonconvex nature, there is no guarantee that this optimum in fact is the global minimum. However, for this particular optimization problem, the SQP technique with multiple starting points converge quite robustly to a single optimum, which is therefore probably the global optimum.

#### 6.4.5 Optimization Results

In order to optimize the design parameters  $l_r$ ,  $l_c$ ,  $R^*$  and  $q_0$ , knowledge is required of (i)  $M_o(t)$ , (ii) the secondary parameters  $\mathbf{p}_b \in \mathbb{R}^3$ ,  $\mathbf{p}_c \in \mathbb{R}^{15}$  and  $\mathbf{p}_r \in \mathbb{R}^5$  and (iii) the parameters that define the bound, technological and collision constraints.

$M_o(t)$  is calculated based on (6.19), and is shown in Fig.6.2(a). The numerical values of  $m_b$ ,  $J_b$  and  $R_b$  are given in Table 6.1. The numerical values of  $\mathbf{p}_r \in \mathbb{R}^5$  and  $\mathbf{p}_c \in \mathbb{R}^{15}$  are given in Table E.4. Furthermore, the following numerical values quantify the constraints:  $l_r^m = 0.072$  m,  $l_c^m = 0.079$  m,  $R^{*,M} = 0.035$  m,  $N^m = 100$  N,  $p_{\max}^M = 900$  MPa,  $L_{\text{roll}}^m = L_{\text{osc}}^m = 50000$  h,  $R_C = 0.1$  m and  $\Delta = 0.002$  m.

The starting points for the optimization are all possible combinations of the following values:

$$\begin{aligned} l_r &: \{0.08, 0.11, 0.14\} \text{ m;} \\ l_c &: \{0.08, 0.11, 0.14\} \text{ m;} \\ q_0 &: \{5.7, 27.5, 49.3, 71.0, 92.8, 114.6\} \text{ degrees;} \\ R^* &: \{0, 0.012, 0.023, 0.035\} \text{ m,} \end{aligned}$$

resulting in  $3 \cdot 3 \cdot 6 \cdot 4 = 216$  different starting points for the optimization. 72 of the 216 optimizations converged to a local optimum. For the best local optimum, labelled  $\mathbf{p}_1$ , the first row of Table 6.2 gives the values of the optimization variables, the goal function and the constraints. There is a fairly good chance that this local optimum is in fact the global optimum for it is attained in 38 out of the 72 converged optimizations. In  $\mathbf{p}_1$ , the lower bound constraint on  $l_r$  is active, together with the constraints (6.36) and (6.45) on  $N_{\min}$  and  $i_2$ .

The value of the goal function at  $\mathbf{p}_1$  is  $J_{\text{eq}} = 0.4499$  kg-m<sup>2</sup>. In Section 6.3.1 it was derived that the physical lower limit for  $J_{\text{eq}}$  equals 0.0891 kg-m<sup>2</sup>. Hence,  $J_{\text{eq}}$  is approximately five times greater than its physical lower limit. This is due to the fact that the mechanism must comply with the

	goal		optimization variables				constraints							
	$J_{\text{eq}}$ [kg-m <sup>2</sup> ]		$l_r$ [mm]	$l_c$ [mm]	$q_0$ [°]	$R^*$ [mm]	$N_{\text{min}}$ [N]	$(p_{\text{max}})_{\text{max}}$ [MPa]	$L_{\text{roll}}$ [1000h]	$L_{\text{osc}}$ [1000h]	$\rho_{\text{min,-}}$ [mm]	$\rho_{\text{min,+}}$ [mm]	$i_1$ [mm]	$i_2$ [mm]
$m$	-		72	79	0	0	100	-	50	50	50	50	-	-
$\mathbf{p}_1$	0.4499		72.0	84.8	104.5	22.9	100	603	742	68	-	69.6	-2.3	0
$\mathbf{p}_2$	0.4512		72.0	79.0	100.3	23.6	107	604	733	72	-	70.0	-2.7	-1.4
$\mathbf{p}_3$	0.4791		72.0	79.0	90.0	10.0	542	616	828	72	-	82.6	-13.1	-3.3
$\mathbf{p}_4$	0.4698		72.0	79.0	102.8	35.0	500	617	482	72	-	69.2	-0.4	-0.7
$\mathbf{p}_5$	0.4956		72.0	79.0	98.4	35.0	1000	630	424	72	-	75.6	-5.1	-2.0
$M$	-		-	-	180	35	-	900	-	-	-	-	0	0

TABLE 6.2: Properties of the proposed designs  $\mathbf{p}_1$ ,  $\mathbf{p}_2$ ,  $\mathbf{p}_3$ ,  $\mathbf{p}_4$  and  $\mathbf{p}_5$ . The  $m$  and  $M$  rows respectively give the lower and the upper bound for the corresponding quantity. None of the designs yields negative values of  $\rho$ , hence the empty  $\rho_{\text{min,-}}$  column.

bound, collision and technological constraints. Any lower value of  $J_{\text{eq}}$  would result in a mechanism which does not comply with one of the aforementioned constraints.

## 6.5 Design Chart

The design optimization of the previous section is computationally quite costly. Each optimization run takes 20–30 minutes of CPU-time on a Pentium III@600 MHz processor. Hence, the full multi-start (216 starting points) SQP process takes about 70–110 hours of CPU time. The design optimization must possibly be repeated several times if the values of the secondary parameters do not yield a rotor or coupler with sufficient structural strength, and hence need to be updated. In that case, repeating the full multi-start SQP process over and over again is cumbersome. Therefore, the design process is accelerated by constructing a two-dimensional design chart, as in the case of the ICM.

Making a two-dimensional design chart requires setting two out of the four optimization variables  $l_r$ ,  $l_c$ ,  $R^*$  and  $q_0$  to fixed values. It is chosen to set  $l_r$  and  $l_c$  to their respective lower bounds:

$$l_r = 0.072 \text{ mm}; \quad (6.46)$$

$$l_c = 0.079 \text{ mm}. \quad (6.47)$$

The choice of  $l_r = 0.072$  is motivated by the fact that 68 of the 72 converged optimizations have an active lower bound on  $l_r$ . The choice of  $l_c = 0.079$  is motivated by the fact that in other design examples, such as the one discussed in (Demeulenaere and De Schutter, 2004), the lower bound on  $l_c$  is often active.

For drawing up the design chart, 40 equally spaced values between  $57^\circ$  and  $115^\circ$  are chosen for  $q_0$ , and 40 equally spaced values between 0 and 35 mm for  $R^*$ . Using these 1600 combinations of  $(q_0, R^*)$ , the design chart of Fig.6.12 is drawn. This takes about four hours of CPU time. The value of  $J_{\text{eq}}$  follows from the colored bar next to the figure. The various symbols (crosses, circles, ...) mark  $(q_0, R^*)$  combinations at which constraints are active, and which are hence infeasible. Furthermore, contour lines mark  $(q_0, R^*)$  combinations for which  $N_{\min} = \{100, 500, 1000\}$  N.

In Fig.6.12, the best  $(q_0, R^*)$  combination  $\mathbf{p}_2$ , denoted with a hexagram, is located near the  $N_{\min} = 100$  N line. Table 6.2 shows that  $\mathbf{p}_2$  ( $J_{\text{eq}} = 0.4512$  kg-m<sup>2</sup>) is only marginally less optimal than  $\mathbf{p}_1$  ( $J_{\text{eq}} = 0.4499$  kg-m<sup>2</sup>), the global optimum. The design chart thus generates a very good approximation of  $\mathbf{p}_1$ .

Furthermore, the design chart illustrates the sensitivity of the optimum w.r.t. the constraints. For example, when tightening the constraint on  $N_{\min}$  to  $N^m = 500$  or 1000 N, the new design is found at the crossing of the contour lines  $N_{\min} = 500$  N and  $N_{\min} = 1000$  N with the vertical line  $R^* = 35$  mm

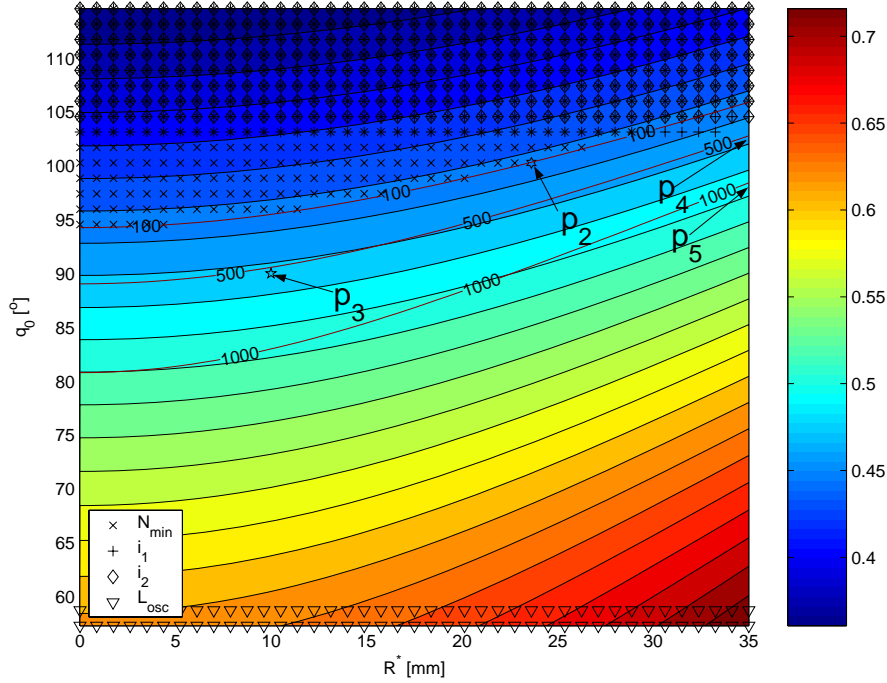


FIGURE 6.12: Design chart using  $J_{eq}$  [kg-m<sup>2</sup>] as goal function. The contour lines {100, 500, 1000} indicate  $N_{min}$ -values [N].

(points  $\mathbf{p}_4$  and  $\mathbf{p}_5$ ). This yields only a minor increase of the goal function to respectively 0.4698 and 0.4956 kg-m<sup>2</sup>. Hence the price paid for the additional contact force robustness is rather low: respectively a 4.4% or a 10.2%  $J_{eq}$ -increase.

### 6.5.1 Parameter Choice for Design Example and Prototype

This section motivates the choice of  $\mathbf{p}_3$  ( $q_0 = 90^\circ$ ,  $R^* = 10$  mm) as the combination of optimization variables that gives rise (in conjunction with  $l_r = 0.072$  mm and  $l_c = 0.079$  mm) to the design parameters of Table 6.1. These design parameters in turn determine both the design example of Section 6.3 and the CBCP prototype construction, discussed in Chapter 7.

The reason for choosing  $\mathbf{p}_3$  is that the optimum  $\mathbf{p}_1$  was not yet found at the time of the prototype construction: only the design chart was available. Some robustness concerning  $N_{min}$  was wanted, so it was decided that  $N_{min}$  needed to be at least 500 N. The best point along the  $N_{min} = 500$  N line being  $\mathbf{p}_4$ ,

this would have been the logical choice. However, due to a misunderstanding with the prototype manufacturer,  $R^*$  turned out to be 10 mm instead of 35 mm, so  $\mathbf{p}_3$  *de facto* became the optimization variable combination defining the CBCP prototype.

As the variation of  $J_{\text{eq}}$  along the  $N_{\text{min}} = 500$  N line is very limited,  $\mathbf{p}_3$  ( $J_{\text{eq}} = 0.4791$  kg-m<sup>2</sup>) is only 2% less optimal than  $\mathbf{p}_4$  ( $J_{\text{eq}} = 0.4698$  kg-m<sup>2</sup>). Furthermore,  $\mathbf{p}_3$  is only 6% less optimal than the global optimum  $\mathbf{p}_1$  ( $J_{\text{eq}} = 0.4499$  kg-m<sup>2</sup>).

## 6.6 Application to an Airjet Weaving Machine

*Perfect* realization of the shed follower motion could theoretically be obtained by balancing the combined input torque of the shed and the sley mechanism, as this would result in a perfectly constant drive speed. It is however chosen to input torque balance solely the sley mechanism, based on a double motivation.

First of all, the variable synchronization between the sley and the shed mechanism necessitates the use of separate CBCPs for both mechanisms: if a single CBCP was used, different cams would have to be mounted for every possible synchronization. Mounting two separate CBCPs, however, is not economically feasible. Secondly, the main problem is the effect of the sley on the shed motion. Therefore, it makes sense to assume that merely input torque balancing the sley, suffices for obtaining a substantial reduction of the undesired shed follower acceleration harmonics. The simulation results presented here, show that this indeed is a valid approach.

**Derivation of Boundary Value Problem** The effect of the CBCP addition is assessed by determining the eigenmotion of the previously introduced simplified airjet weaving machine model ( $g_{\text{cross}} = 360^\circ$ ;  $N_{\text{shed}} = 4$ ), in the presence of a sley balancing CBCP. The CBCP is mounted on the sley axis, as shown in Fig.6.13. The total kinetic energy  $T_{\text{tot}}(t)$  equals the sum of the kinetic energies of the flywheel, sley, shed follower and CBCP:

$$T_{\text{tot}}(t) = \underbrace{\frac{J_{\text{fly}} \cdot \dot{g}_{\text{sley}}^2}{2}}_{T_{\text{fly}}(t)} + \underbrace{\frac{J_{\text{sley}} \cdot \dot{f}_{\text{sley}}^2}{2}}_{T_{\text{sley}}(t)} + \underbrace{\frac{J_{\text{shed}} \cdot \dot{f}_{\text{shed}}^2}{2}}_{T_{\text{shed}}(t)} + T_{\text{c}}(t),$$

where

$$T_{\text{c}}(t) = \frac{J_1^* \cdot \dot{g}_{\text{sley}}^2}{2} + \frac{J_2^* \cdot \dot{q}^2}{2} + J_3^* \cdot \dot{g}_{\text{sley}} \cdot \dot{q} \cdot \cos(g_{\text{sley}} - q).$$

Based on (2.2b), (2.5b) and (2.7), it is easily shown that imposing

$$T_{\text{tot}}(t) = T_{\text{tot}}(0), \forall t \in [0, T]$$

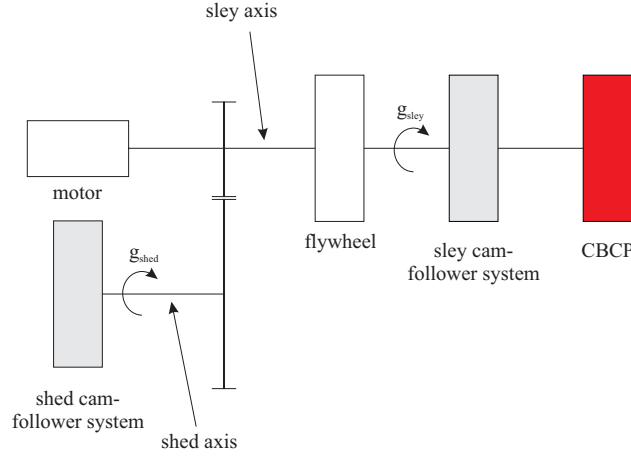


FIGURE 6.13: Simplified airjet weaving machine model after addition of the CBCP to the sley axis.

constitutes a first-order differential equation in  $g_{sley}$ . Without loss of generality,  $g(0) = 0$  is imposed. However, in order to obtain a solution with the correct machine period  $T = 2\pi/\Omega_{shed}$ , a boundary condition  $g_{sley}(T) = g_{sley}(0) + 4\pi$  has to be added (see Section 2.4.1), such that a boundary value problem is obtained:

$$\begin{cases} T_{tot}(t) &= T_{tot}(0), \forall t \in [0, T]; \\ g_{sley}(0) &= 0; \\ g_{sley}(T) &= g_{sley}(0) + 4\pi. \end{cases} \quad (6.48)$$

Solving (6.48) proceeds using the nonlinear least-squares techniques developed in Section 2.4.2. In order to assess the torque balancing effect, three different situations are compared:

- (S1) original weaving machine;
- (S2) original weaving machine with enlarged flywheel;
- (S3) original weaving machine with CBCP.

The CBCP added in situation S3 is the double CBCP corresponding to the optimum  $\mathbf{p}_3$ . The amount of additional flywheel inertia in situation S2 equals

$$J_{eq} - 0.0891 = 0.4791 - 0.0891 = 0.3900 \text{ kg-m}^2.$$

The inertia of  $0.0891 \text{ kg-m}^2$  is the physical lower limit of  $J_{eq}$ , determined in Section 5.3.1, based on the maximum of  $T_{sley}(t)$ . The additional flywheel

inertia hence physically implements the excess (w.r.t its physical lower limit), 'pure flywheel' part of the equivalent flywheel. In this manner, distinction can be made between the *flywheel effect* of the CBCP (due to the *constant* part of its kinetic energy, expressed as an equivalent flywheel of  $0.3900 \text{ kg}\cdot\text{m}^2$ ) and the *torque balancing effect* of the CBCP (due to the *fluctuating* part of its kinetic energy), by comparing situation *S2* and situation *S3*.

**Kinetic Energy** In order to assess the difference between a machine with and without CBCP, Fig.6.14 and Fig.6.15 show, for *S1* and *S3*, one shed period  $2\pi/\Omega_{\text{shed}}$  of the kinetic energy components. In the original machine, the sum of the sley and shed kinetic energy attains its minimum, zero, when both the sley and the shed follower stand still. As a consequence,  $T_{\text{fly}}(t)$ , shown in Fig.6.14(b), attains its maximum of 3462 J in these portions of the motion cycle.

When the sley and the shed follower move, they pull kinetic energy from the flywheel, resulting in a slowdown of the latter, popping up as  $T_{\text{fly}}(t)$  dips in Fig.6.14(b). Four<sup>8</sup> sharp dips are present, which are due to the sley movement and are superimposed on two broader dips, due to the shed follower movement. As a check of the solution, Fig.6.14(c) shows the sum of the flywheel, sley and shed follower kinetic energy, which is constant, apart from some remaining jitter, due to the fact that the Fourier series, parameterizing  $\dot{g}_{\text{sley}}(t)$ , is truncated after  $K = 20$  harmonics.

The purpose of the CBCP is to cancel the effect of the sley motion. It is designed in such a way that the sum of  $T_{\text{sley}}(t)$  and  $T_c(t)$  is constant, under the assumption of a perfectly constant  $\dot{g}_{\text{sley}}(t)$ . However, as the shed motion is not taken into account during the CBCP design, the weaving machine with CBCP does not have a perfectly constant  $\dot{g}_{\text{sley}}(t)$ . Consequently, the sum of  $T_{\text{sley}}(t)$  and  $T_c(t)$  is not constant, as shown in Fig.6.15(a). Still, the effect of the CBCP is clearly visible, as the sum of  $T_{\text{sley}}(t)$ ,  $T_{\text{shed}}(t)$  and  $T_c(t)$  no longer exhibits four, but two peaks: the effect of the sley is almost completely compensated for by the CBCP. As a result,  $T_{\text{fly}}(t)$  still has two broad dips due to the (non-compensated) shed motion, whereas the sharp sley-dips have disappeared.

**Drive Speed Fluctuation** Based on the above discussion, an intuitive interpretation of Fig.6.16, showing  $\dot{g}_{\text{sley}}$  and  $\ddot{g}_{\text{sley}}$  for *S1*, *S2* and *S3* is straightforward. Since

$$T_{\text{fly}} = \frac{J_{\text{fly}} \cdot \dot{g}_{\text{sley}}^2}{2},$$

the same qualitative behavior is expected in Fig.6.16(a) as in Fig.6.14(b) and Fig.6.15(b): in the non-compensated situations *S1* and *S2*,  $\dot{g}$  exhibits four

---

<sup>8</sup>During one shed period, the sley moves back and forth two times, as the sley axis has twice the speed of the shed axis.

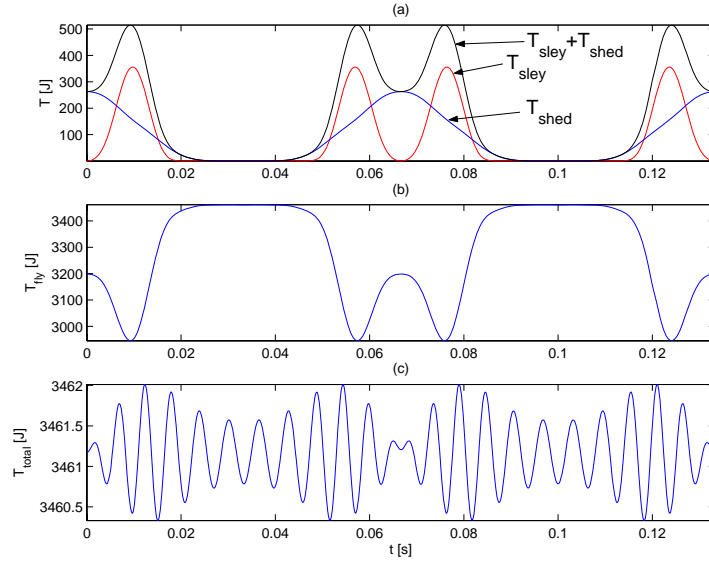


FIGURE 6.14: Eigenmotion results for  $S1$ : (a)  $T_{sley}$ ,  $T_{shed}$  and their sum; (b)  $T_{fly}$ ; (c) total kinetic energy.

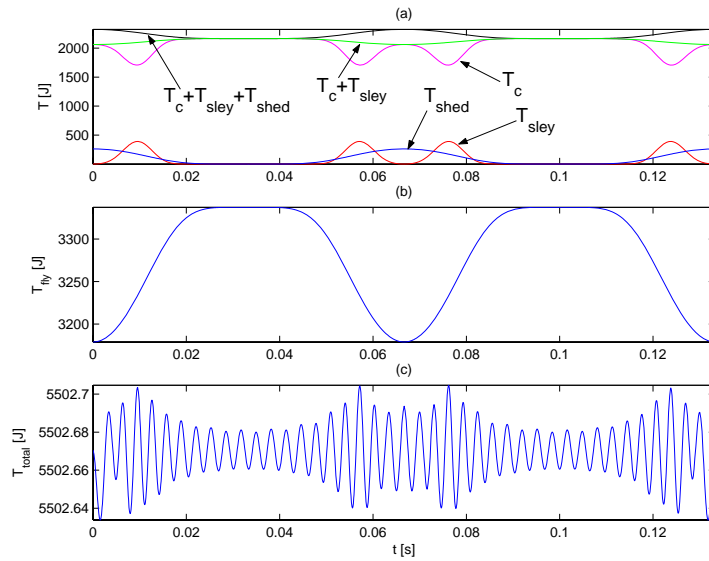


FIGURE 6.15: Eigenmotion results for  $S3$ : (a)  $T_{sley}$ ,  $T_{shed}$ ,  $T_c$ ,  $T_c + T_{sley}$  and  $T_c + T_{sley} + T_{shed}$ ; (b)  $T_{fly}$ ; (c) total kinetic energy.

sharp sley and two broad shed dips (which are of course less deep in  $S2$  due to the larger flywheel), while it exhibits only two broad shed dips if the CBCP is present. As a consequence, the combined system has a much smoother  $\ddot{g}_{\text{sley}}$  time trajectory.

**Follower Motion Distortion (time domain)** A smoother drive shaft speed fluctuation results in smoother sley and shed follower acceleration trajectories, as shown in Fig.6.17. For  $S1$ ,  $S2$  and  $S3$ , Fig.6.17(a) and (c) respectively show the actually realized sley and shed follower acceleration, whereas Fig.6.17(b) and (d) show the difference  $\Delta\ddot{f}_{\text{sley}}$  and  $\Delta\ddot{f}_{\text{shed}}$  with the desired acceleration.

For the sley motion, the CBCP roughly seems to have a similar effect as flywheel addition:  $\Delta\ddot{f}_{\text{sley}}$  exhibits the same qualitative behavior for  $S1$ ,  $S2$  and  $S3$ , that is, the same peaks, but with smaller amplitudes. On the other hand, the shed follower acceleration is much more affected by the CBCP addition (which is logical: the CBCP is designed to cancel the effect of the sley on the shed motion): also the qualitative behavior changes, since the double peaks, labelled  $p_i, i = \{1, 2, 3, 4\}$ , in Fig.6.17(d) almost disappear if the CBCP is present. An intuitive explanation for this is that the CBCP removes the four sharp double peaks, labelled  $p_i, i = \{1, 2, 3, 4\}$ , from  $\ddot{g}_{\text{sley}}$  (see Fig.6.16(b)). These double peaks correspond to the four dips in  $\dot{g}_{\text{sley}}$  shown in Fig.6.16(a).

**Follower Motion Distortion (frequency domain)** Figure 6.19 shows the shed follower's acceleration spectrum. The beneficial effect of the CBCP is clearly present: all undesired harmonics  $k = \{7, 9, 11, \dots\}$  are at least 28 dB (that is, a factor 25) smaller as compared to the situation with enlarged flywheel ( $S2$ ).

The beneficial CBCP effect is however not confined to the shed motion alone. Figure 6.18 indicates that, while the CBCP cannot do much about the undesired seventh sley harmonic, the eight and ninth harmonic are 30 dB (that is, a factor 32) lower than in situation  $S2$ . Hence, although the time-domain acceleration results suggest that the CBCP roughly has the effect of a flywheel for the sley motion, the frequency-domain results prove that this is not quite true.

**Conclusions** Some important conclusions follow from the presented simulations. First of all, it has been demonstrated that mere flywheel addition cannot change the qualitative behavior of the drive speed fluctuation, as can ITB.

Secondly, it has been shown ( $S1, S2$ ) that drive speed fluctuations have a dramatic effect on the follower acceleration. In this respect, the shape rather than the amount of drive speed fluctuation is important: in  $S1$ ,  $\kappa$  equals 8.0%, whereas it respectively equals 5.4% and 2.4% for  $S2$  and  $S3$ . Despite that the difference between  $\kappa(S2)$  and  $\kappa(S3)$  is not much bigger than the difference

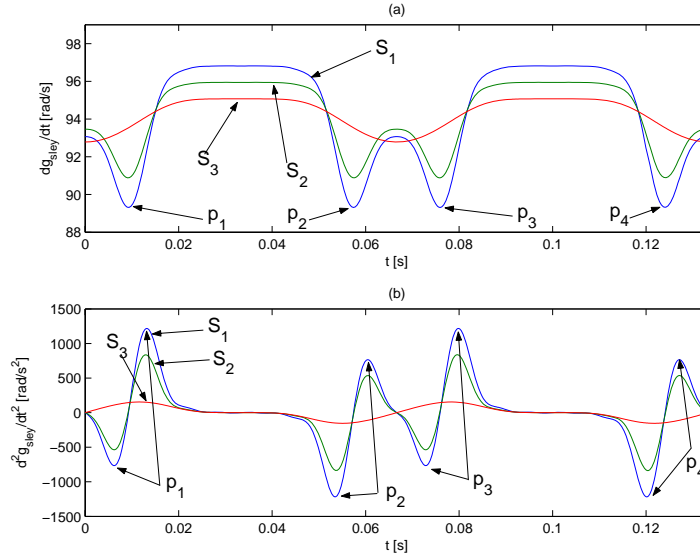


FIGURE 6.16: Drive shaft speed and acceleration for situation  $S_1, S_2$  and  $S_3$ .

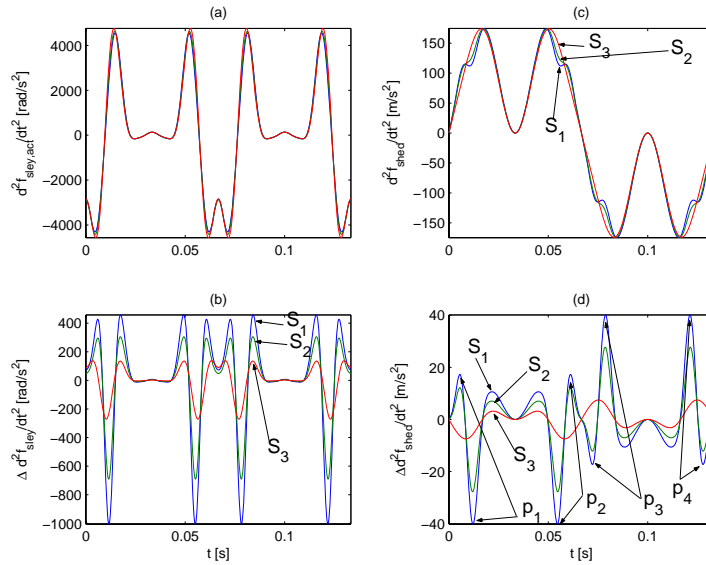


FIGURE 6.17: Actually realized sley (a) and shed follower (c) acceleration and difference with the desired sley (b) and shed follower (d) acceleration for situation  $S_1, S_2$  and  $S_3$ .

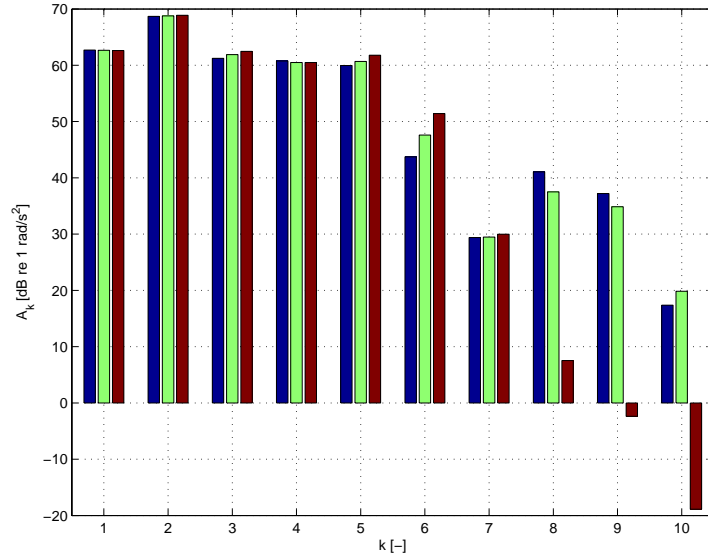


FIGURE 6.18: Sley acceleration spectrum [dB re 1 rad/s<sup>2</sup>] for situation  $S1$ ,  $S2$  and  $S3$  (in that order).  $k$  denotes the harmonic order.

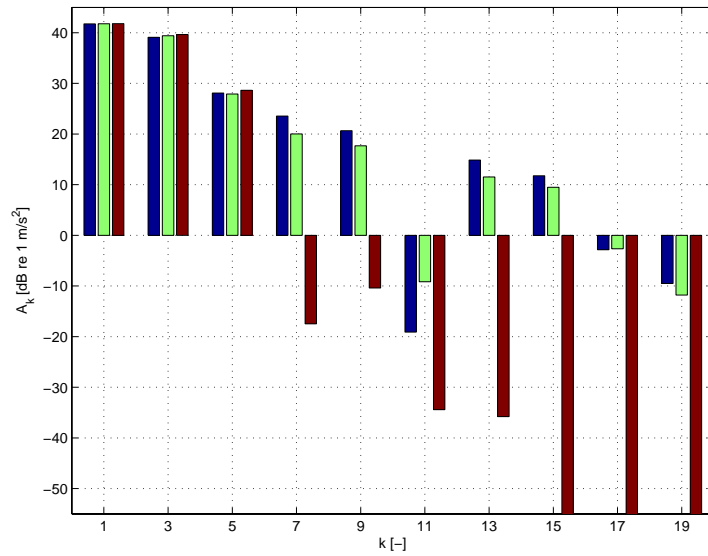


FIGURE 6.19: Shed acceleration spectrum [dB re 1 m/s<sup>2</sup>] for situation  $S1$ ,  $S2$  and  $S3$  (in that order).  $k$  denotes the harmonic order.

between  $\kappa(S1)$  and  $\kappa(S2)$ , the difference in acceleration distortion is much more significant, which illustrates the importance of the shape of the drive speed fluctuation.

Thirdly, it has been shown that ITB is capable of yielding a dramatic decrease of the undesired acceleration harmonics. Fourthly, it is able to do so quite robustly, as the decrease of the undesired acceleration harmonics is realized despite the presence of the shed mechanism, which is not taken into consideration during the CBCP design.

## 6.7 Conclusion

For the CBCP, the same design methodology as for the ICM has been applied: (i) the internal cam design is governed by a nonlinear, second-order, ordinary differential equation in the coupler angle  $q$ ; (ii) the resulting boundary value problem is solved using a nonlinear least-squares approach; (iii) a complete kinematic/dynamic/technological analysis is developed and (iv) in order to optimize the design parameters, an optimization problem with a similar goal function and constraints is formulated, based on a parameterization of the rotor and coupler shape.

The main difference with the ICM methodology is the presence of four instead of two optimization variables. Exhaustively solving the optimization problem is therefore not an option: a multi-start SQP approach is applied instead. Still a design chart based on two optimization variables can be constructed: since the lower bound constraints on the two other variables (the rotor and coupler length) are often active, these variables are fixed to their respective lower bounds. The design chart generates a good approximation of the 'true', SQP-determined optimum, and gives insight in the sensitivity of the optimum for the used constraints.

Speeding up the design chart calculation through nondimensionalization is not possible, due to the presence of the nonlinear trigonometric term in the describing equation. The peak phenomenon is present in the CBCP as well, but has not been discussed explicitly, since technological feasibility again imposes tighter constraints on the optimization variables than does the peak phenomenon.

Four conclusions emerge from simulation of the developed CBCP on an airjet weaving machine. (i) Mere flywheel addition cannot change the qualitative behavior of the drive speed fluctuation, as can input torque balancing. (ii) Drive speed fluctuations have a dramatic effect on the follower acceleration, in which respect more the shape than the amount of drive speed fluctuation is important. (iii) Input torque balancing is capable of yielding a dramatic decrease of the undesired acceleration harmonics, (iv) even if part of the input torque is not balanced.



## Chapter 7

# Input Torque Balancing: Experimental Validation

*The doctoral student Ilse Rosenthal-Schneider asked Einstein in 1919 how he would have reacted if his general theory of relativity had not been confirmed experimentally that year by Arthur Eddington and Frank Dyson. His answer was: "Then I would feel sorry for the good Lord. The theory is correct anyway."*

**T**HIS chapter discusses the experimental validation of the CBCP on an airjet weaving machine. This experimental validation serves a double purpose: (i) to check whether the CBCP functions properly, that is, whether it delivers the designed torque and (ii) to check whether the CBCP is capable of enhancing the dynamic behavior of an airjet weaving machine.

Firstly, the experimental setup is introduced (Section 7.1). In order to drive the setup, not its industrial, but a new type of control system, *Average Speed Control* (ASC), is used. ASC is designed such that a motor, operated in torque mode, acts as a constant torque source, and hence forces the machine to move according to its damped eigenmotion. An intuitive discussion of ASC, as well as simulation results, are the subject of Section 7.2, whereas Section 7.3.1 provides experimental ASC results.

The experimental results themselves are discussed in Section 7.3, and show that the CBCP delivers the designed torque, and improves the dynamic machine behavior, provided that the average drive speed  $\Omega_{\text{shed}}$  is below 350 rpm. Above that speed, an unexpected resonance phenomenon dominates the dynamic behavior. This resonance phenomenon is explained by extending the rigid-body setup model with torsional flexibility (Section 7.4).

## 7.1 Experimental Setup

The experimental setup consists of a Picanol airjet weaving machine to which a CBCP prototype is added. Figure 7.1 shows the setup from its back side. Section 7.1.1 firstly discusses the airjet weaving machine itself. After that, Section 7.1.2 gives some details concerning the construction of the CBCP prototype. The control and measurement systems are the subject of Section 7.1.3. Finally, the measurement sensors and signal processing are reviewed in Section 7.1.4 and 7.1.5 respectively.

### 7.1.1 Airjet Weaving Machine

The airjet weaving machine is a *machine à blanc*<sup>1</sup>, that is, a stripped version of a complete machine. This implies that the machine is reduced to its essential parts: (i) the driving motor, (ii) the conjugate cam-follower mechanisms that drive the sley and (iii) the cam-linkage mechanisms that impose the motion of the frames. All other parts associated with the air insertion of the insertion threads, the handling of the yarn threads, and the transport of the woven fabric are removed. Testing a machine à blanc is a typical stage (before proceeding to testing a complete machine) in the characterization of a weaving machine's dynamic behavior.

The frames perform an up-and-down movement, while the sley moves back-and-forth, as indicated in Fig.7.2. Four frames are present in the setup. The CBCP is contained in the steel barrel mounted on the right side<sup>2</sup>. To the right side of this steel barrel, an aluminium measurement extension is attached.

### Overall Setup Structure

The overall structure of the setup is clarified in Fig.7.3, showing a schematic top view. The motor drives the sley axis via a spur gear set imposing a 2:1 reduction (not shown in the figure). In view of the considerable machine width (the sley width is 190 cm), two conjugate cam-follower pairs drive the sley, which oscillates w.r.t. the sley follower axis. Both pairs are mounted on the sley axis, one in the left, and one in the right carter. The CBCP is also mounted on the sley axis. The motion law of the sley cams and the sley inertia are those given in Section 2.2.1.

The motor drives the shed axis via a spur gear set imposing a 2:1 reduction and a conical gear set imposing a 4:1 reduction (not shown in the figure), such

---

<sup>1</sup>This French term can be translated as *a machine in white*, by analogy with the term *body in white*. A body in white is a car body from which the trim panels, seats, motor, suspension ... are stripped in order to characterize its dynamic behavior.

<sup>2</sup>Left (L), right (R), front (F) and back (B) are defined by the arrows in Fig.7.1 and Fig.7.3.

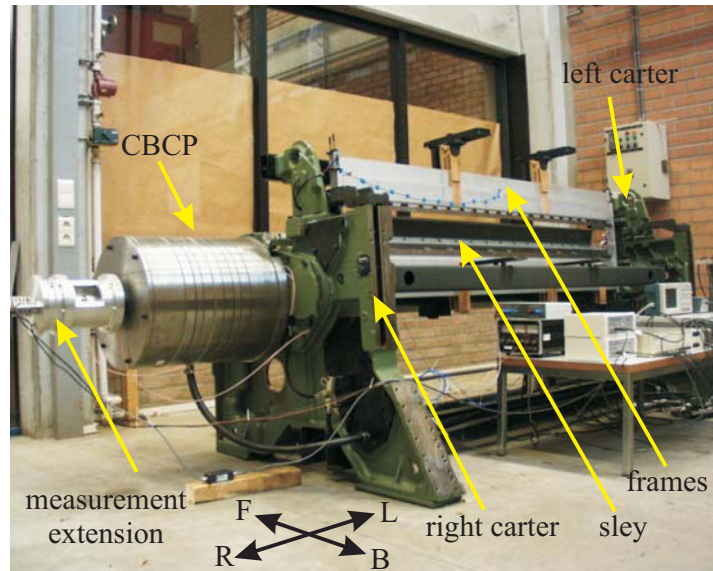


FIGURE 7.1: Back view of the setup. The steel barrel on the right side contains the CBCP. Left (L), right (R), front (F) and back (B) are defined by the arrows.

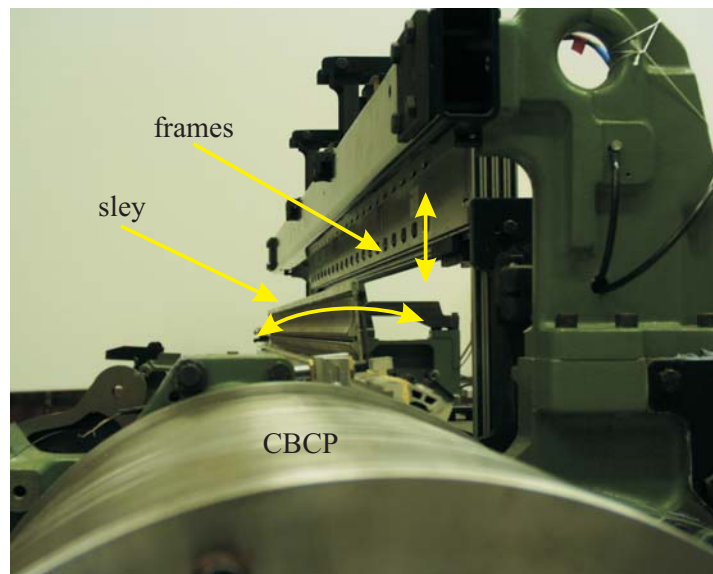


FIGURE 7.2: Right side view of the setup. The arrows indicate the back-and-forth sley movement and the up-and-down frame movement.

that the shed axis turns at one fourth of the speed of the sley axis:

$$\dot{g}_{\text{shed}} = \frac{\dot{g}_{\text{sley}}}{4}.$$

The shed axis is the input axis for the cam-box system, which drives the frames via the linkage shown in Fig.7.4. The main parts of the cam-box are (i) the four rotating, conjugate, *shed cams*, mounted on the shed axis and (ii) their oscillating followers (denoted as the *swords*), oscillating w.r.t. the axis  $p$  (indicated in Fig.7.3 and Fig.7.4) with a point-to-point amplitude of  $17.2^\circ$  (0.30 rad). The motion law  $F_{\text{sword}}(g_{\text{shed}})$  imposed by the shed cams is:

$$F_{\text{sword}}(g_{\text{shed}}) = 0.15 \cdot \sin(2 \cdot g_{\text{shed}}),$$

which implies that the swords perform a pure sine motion twice per complete shed axis revolution. As a consequence, the shed axis can conceptually be considered to turn at *half* the speed of the sley axis:

$$\dot{g}_{\text{shed}} = \frac{\dot{g}_{\text{sley}}}{2}, \quad (7.1)$$

while imposing the motion law:

$$F_{\text{sword}}(g_{\text{shed}}) = 0.15 \cdot \sin(g_{\text{shed}}), \quad (7.2)$$

where  $g_{\text{shed}}$  is determined by the crossing angle  $g_{\text{cross}}$ , as defined in Section 2.2.3:

$$g_{\text{shed}} = \frac{g_{\text{sley}} - g_{\text{cross}}}{2}. \quad (7.3)$$

In the setup, the crossing angle equals 360 degrees. (7.1) and (7.3) are in agreement with the simplified airjet weaving machine model derived in Section 2.2, in which the shed axis is assumed to turn at half the speed of the sley axis.

Each of the four frames is driven by a separate linkage, of which a conceptual image is given in Fig.2.2 and a kinematic scheme in Fig.7.4. The links I (the sword), II, IVa, Va and VI (the frame) constitute a six-bar mechanism, with one degree of freedom: the angle  $f_{\text{sword}}$  [rad], imposed by the shed cam<sup>3</sup>. The links IVa and IVb perform identical motions, as the polygon  $stxw$  constitutes a parallelogram (hence link III moves in perfect translation). The same goes for the links Va and Vb, as the polygons  $suyw$  and  $uyzv$  also constitute parallelograms. For reasons of confidentiality, the link lengths are not given here. The proportions in the figure are however correct and thus give an idea of the relative link lengths. The sword I length is adjustable and determines the amplitude of motion of the frame VI. The amplitude of motion  $\Theta_i, i = \{1, 2, 3, 4\}$  [m] of the frames is given in Table J.1. Frame 1 is the front frame, while frame 4 is the rear frame.

<sup>3</sup> $f_{\text{sword}}(t)$  is determined by (7.2) and the chosen time trajectory for the shed axis angle  $g_{\text{shed}}$ .

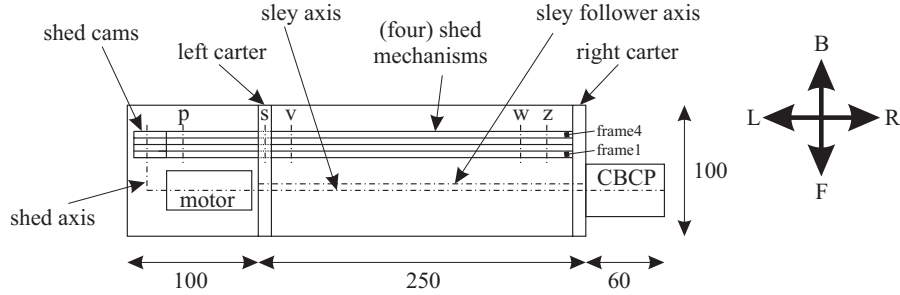


FIGURE 7.3: Schematic top view of the experimental setup. All measures are indicative and expressed in [cm]. Left (L), right (R), front (F) and back (B) are defined by the arrows.

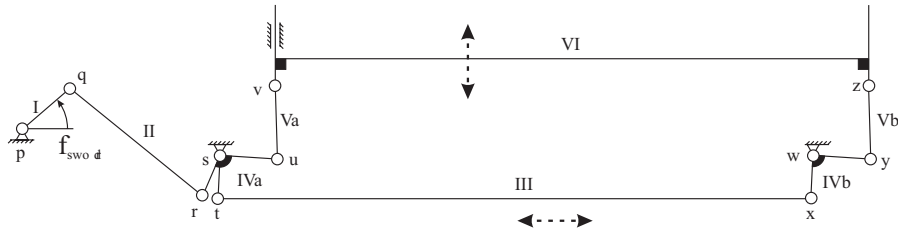


FIGURE 7.4: Kinematic scheme of (one instance of) the linkage that drives the frames (front view).

### Simplified Setup Model

In order to model the setup, the simplified airjet weaving machine model of Fig.2.4 is used. This implies that the four cam-linkage mechanisms for driving the frames are simplified to a single cam-follower mechanism with a rotating, conjugate cam and a translating follower. The translating follower has a mass  $m_{\text{shed}}$  of 43.1 kg and moves with a (point-to-point) amplitude of 90 mm. Its motion law  $F_{\text{shed}}(g_{\text{shed}})$  is given by:

$$F_{\text{shed}}(g_{\text{shed}}) = 0.045 \cdot \sin(g_{\text{shed}}). \quad (7.4)$$

This simplification is justified, from a kinematic and a dynamic point of view, in Appendix J. While in the previous chapters, the shed motion law was assumed to have a first, third and fifth harmonic (typical for a machine equipped with a dobby system), it is purely sinusoidal (typical for a machine with a cam-box system) in the experimental setup.

	CAD	theory	$\epsilon$ [%]
$m_c$ [kg]	14.4	13.8	4.3
$l_{\text{COG}}$ [m]	0.0361	0.0390	7.4
$J_c$ [kg-m <sup>2</sup> ]	0.0302	0.0315	4.1
$J_r$ [kg-m <sup>2</sup> ]	0.0624	0.0723	13.7

TABLE 7.1: Comparison of theoretical and CAD-based coupler and rotor mass parameters and their relative difference  $\epsilon$ .

For reference, the properties of the other model parts are reviewed here. Firstly, although the shed axis physically turns at one fourth of the speed of the sley axis, for modelling purposes, it can be considered to turn at half the speed of the sley axis:  $\dot{g}_{\text{shed}} = \dot{g}_{\text{sley}}/2$ , with  $g_{\text{shed}} = (g_{\text{sley}} - g_{\text{cross}})/2$ . In the setup, the crossing angle  $g_{\text{cross}}$  is 360 degrees. Secondly, the sley mechanism is a cam-follower mechanism with a rotating, conjugate cam and an oscillating follower (that is, the sley). Its motion law and follower inertia are given in Section 2.2.1. Thirdly, the flywheel represents the rotational inertia, reduced to the sley axis, of all rotating parts (motor inertia, cams, gears, . . .) that are attached to the sley, shed or motor axis. In the setup, its inertia  $J_{\text{fly}}$  equals 0.816 kg-m<sup>2</sup>.

### 7.1.2 CBCP Design and Construction

The CBCP design is based on the optimum design  $\mathbf{p}_3$  (Section 6.5.1), in conjunction with the secondary parameter variables tabulated in Table E.4. Based on the shape parameterization of Fig.6.10, these values determine the shape of the CBCP parts, and hence also their mass properties. In order to calculate the internal CBCP cams however, not these theoretical coupler mass properties are used, but the ones obtained from the CAD-package Pro/ENGINEER<sup>4</sup>, in which the CBCP prototype is designed, as these values are more accurate<sup>5</sup>. Table 7.1 compares the theoretical and CAD-based coupler mass parameters, and shows that the theoretical parameters approximate the CAD-based ones quite well.

In order to mount the CBCP, the original camshaft, connected to the (hollow) sley axis via a clamping joint, is extended outside the right carter, as shown in Fig.7.5. The CBCP rotor is clamped on the extended camshaft by a conical pressed fit. Clamping of the conical pressed fit is achieved by

<sup>4</sup>[www.ptc.com](http://www.ptc.com)

<sup>5</sup>This stems from the fact that the shape parameterization is a simplified representation of the true coupler shape.

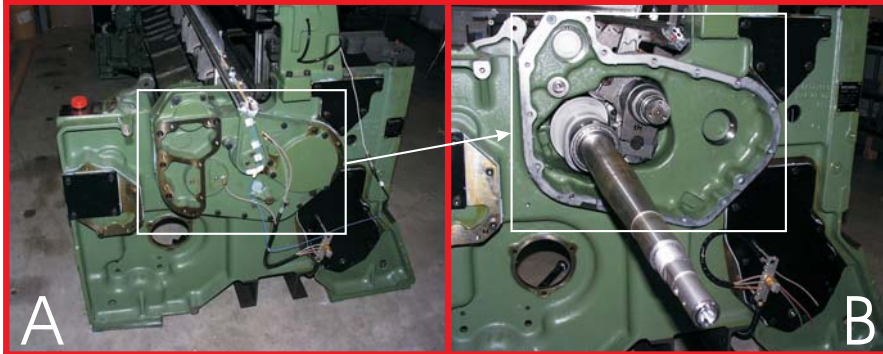


FIGURE 7.5: Extension of right-carter camshaft: (a) right machine carter before rebuilding. (b) right machine carter after rebuilding: the sley conjugate cams and the sley follower are clearly visible.

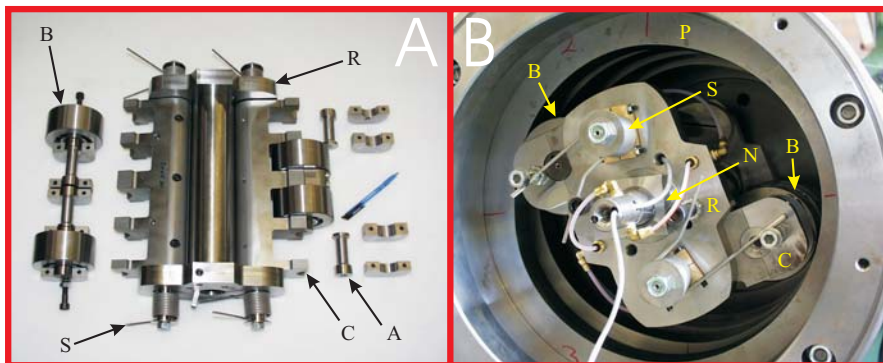


FIGURE 7.6: CBCP construction: (a) exploded view of the CBCP parts; (b) CBCP after mounting on the extended camshaft, and addition of the internal cams. (A) additional mass; (B) roller follower; (C) coupler; (N) nut; (P) internal cam; (R) rotor; (S) spring.

tightening a nut (Fig.7.6(b) and Fig.7.7), screwed on the extended camshaft. Dimensioning of the cone and the required screw moment constitutes a classical machine design problem, see e.g. (Matek et al., 2000).

Figure 7.5 shows the right machine carter before and after mounting of the extended camshaft. With the cover (indicated with the rectangle in Fig.7.5(a)) removed in Fig.7.5(b), the sley conjugate cams and their oscillating follower (to which the sley is attached) become visible.

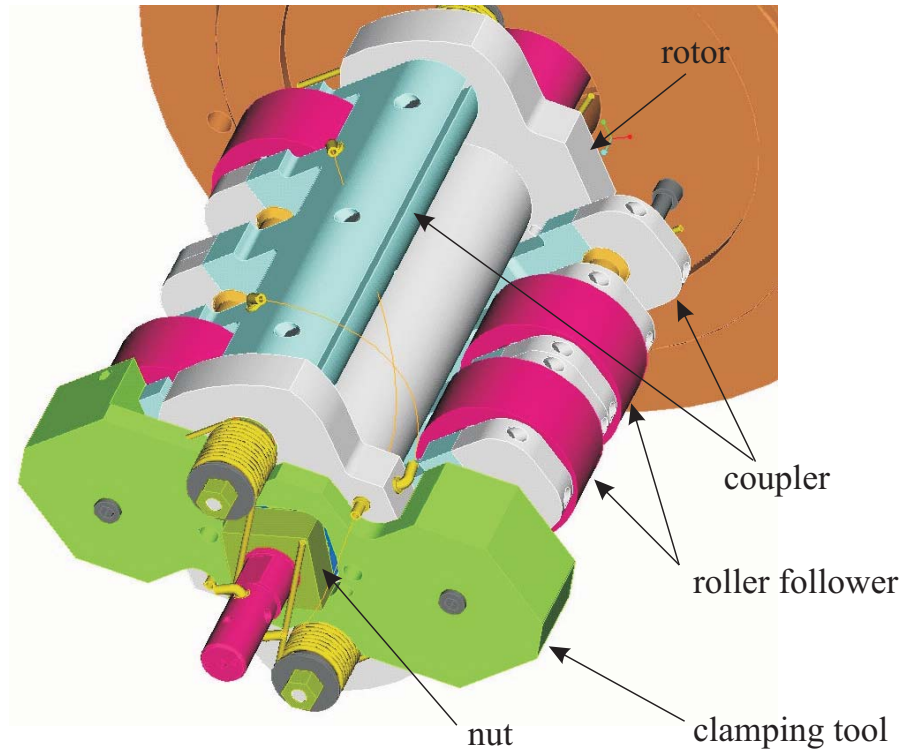


FIGURE 7.7: CBCP construction: CAD-assembly without internal cams and with clamping tool.

Figure 7.6 shows the CBCP itself, before and after mounting on the extended camshaft. The (torsional) springs are required for guaranteeing contact between the roller followers and the internal cams during standstill. In regime, the contact is guaranteed by the centrifugal force, as imposed by design constraint (6.36).

Lubrication of the internal cam-roller follower contact is done by transporting oil, via flexible tubes, to the inner ring of the bearing that constitutes the roller follower. From that point on, the oil seeks its way outside the bearing, which results in satisfactory lubrication of the contact.

In order to drive the setup without the CBCP being active ('active' means 'with the couplers free to move'), a clamping tool is used. Figure 7.7 shows a CAD-assembly of the CBCP, with the internal cams removed and the clamping tool mounted. In clamped condition, the CBCP acts as a pure flywheel with a CAD-based inertia  $J_{\text{CBCP}} = 0.330 \text{ kg}\cdot\text{m}^2$ .

### 7.1.3 Measurement and Control Systems

The setup is controlled using a dSpace DS1103 PPC Controller Board, directly installed into the measurement/control PC. The board and its associated software are intended for *rapid control prototyping*: the user is offered a Matlab/Simulink environment in which he develops a controller, which is subsequently translated (by the dSpace software) to a C-program that is compiled and downloaded to the board's real-time processor. In order to read the measurement signal(s), which the developed controller requires for calculating the control signal(s), the board offers (amongst other things) 16 A/D channels (16 bits) and 7 incremental encoder interfaces. In order to output control signal(s), 8 D/A channels (14 bits) are available. The ASC control scheme runs on the board with a sample period of  $T_s = 0.001$  s.

Besides the dSpace board, also an LMS Pimento measurement system is used, of which the specifications are given in Appendix K. It is a 'real' measurement system, in that it provides internal anti-alias filters (cut-off frequency 10 kHz) and ICP<sup>6</sup> power supplies, as opposed to the dSpace system (a control system 'that can measure as well'). The external anti-alias filters and ICP power supplies, required for the signals captured with the dSpace system, are respectively provided by an Alligator Technologies<sup>7</sup> AAF-3 16-channel low-pass filter card and a PCB Piezotronics 481A02 16-channel signal conditioner. The AAF-3 provides standard 8-pole elliptic filters (cut-off frequency 3 kHz).

Averaging is an essential signal processing step (see Section 7.1.5) and requires synchronization between the measurement and the control system, if it is done in the time domain. Since the Pimento system cannot be synchronized with the dSpace system, the dSpace system is preferred for capturing (at 10 kHz) the measurements. The Pimento system is however necessary for capturing the microphone signals, due to the fact that the required sample rate of 25 kHz is too high for the dSpace board.

### 7.1.4 Measurement Sensors

Below, an overview of the measurement sensors is given. Additional specifications, as well as calibration data are given in Appendix K.

**Sley Axis Rotation Angle** A resolver, mounted on the sley axis, close to the motor, measures  $g_{\text{sley}}$ . A resolver-to-encoder electronic circuit uses this signal to emulate a 1024-line (4096 count/turn) quadrature encoder. The resolver and the electronic circuit are standard accessories of the airjet weaving machine. The emulated encoder signal is read using the incremental encoder interface of the dSpace system.

<sup>6</sup>The meaning of ICP is clarified in Appendix K. ICP power supply is required for accelerometer and microphone measurements.

<sup>7</sup>[www.alligatortech.com](http://www.alligatortech.com)

**Sley and Sword Angular Acceleration** The sley and rear sword (that is, the sword driving the rear frame) angular accelerations  $\ddot{f}_{\text{sley}}$  and  $\ddot{f}_{\text{sword}}$  [rad/s<sup>2</sup>] are measured using piezoelectric ICP accelerometers. In case of the sley, the accelerometer is mounted using a support piece, designed such that the accelerometer's measurement direction coincides with the direction of the tangential acceleration in the measurement point. Hence, the measured acceleration is directly proportional to  $\ddot{f}_{\text{sley}}$ .

In case of the sword however, it is not possible to use a support piece, resulting in the impossibility to obtain perfect alignment of the measurement and tangential acceleration direction. As the angle between both directions is however only 7.7°, the measurement error due to the misalignment is negligible. Hence, the measured acceleration can again be considered to be directly proportional to  $\ddot{f}_{\text{sword}}$ .

**Frame Acceleration** The acceleration of (the right side of) the rear frame is measured using a triaxial ICP accelerometer which measures the up-and-down acceleration  $\ddot{f}_{\text{frame}}$  [m/s<sup>2</sup>] (channel Y), as well as the out-of-plane acceleration  $\ddot{h}_{\text{frame}}$  [m/s<sup>2</sup>] (channel Z).

**Radiated Noise** The radiated noise is measured at three spots, indicated in Fig.K.1: microphone 1 (MIC1) is located behind the frames; microphone 2 (MIC2) is located near the motor and microphone 3 (MIC3) is located near the CBCP. They are all at a height of about 125 cm.

**CBCP Torque** The torque delivered by the CBCP, is measured using a strain gauge bridge with four active (metal) strain gauges, glued on the extended camshaft. As a signal conditioning element, a BLH<sup>8</sup> BA 660 strain gauge amplifier is used. This is a miniature (40 × 30 × 12 mm) amplifier, which supplies the excitation voltage for the bridge, and outputs an analogue signal. The amplifier turns with the extended camshaft. Hence collector rings are required for providing the amplifier's supply voltage, and reading its analogue output. The collector rings are contained within the measurement extension, shown in Fig.7.1.

### 7.1.5 Signal Processing

**Time-Domain Averaging** In dealing with periodical signals, time-domain averaging is a natural, simple and very efficient way for improving the signal-to-noise ratio: averaging a signal with noise variance  $\sigma^2$  over  $S$  periods yields an averaged signal with noise variance  $\sigma^2/S$ , and therefore constitutes the first measurement processing step.

---

<sup>8</sup>[www.blh.de](http://www.blh.de)

A basic prerequisite for time-domain averaging in a reliable way (without needing cumbersome subsampling and data interpolation steps) is that the combination of the sample frequency and the period of motion is such that a period exactly contains an integer number of samples. For reciprocating machinery, accurately imposing some desired period of motion is not a trivial task, as the period of motion is determined by the average speed of the slowest turning axis to which a mechanism is attached. Consequently, in the present setup,  $\Omega_{\text{shed}}$  must be controlled very accurately, which is possible using ASC.

For practical purposes (limitations imposed by the writing of data to the hard disk of the measurement PC), the measurement time is limited to 10 seconds. When the setup is driven at its lowest speed ( $\Omega_{\text{shed}} = 125$  rpm), the period is  $60/125 = 0.48$  s. The time window hence contains 20 periods. When the setup is driven at its highest speed ( $\Omega_{\text{shed}} = 437.5$  rpm), the period is 0.130 s, resulting in 76 periods in the time window.

The fact that ASC imposes a nearly, but not perfectly constant average drive speed introduces leakage<sup>9</sup> during the averaging process. This means that the energy, which is supposed to be exclusively concentrated in the *harmonic* frequencies of the signal spectrum, is leaked over the neighboring frequencies. Leakage errors are discussed in a detailed way in Appendix L, in which two quality indices for measuring the periodicity, or conversely, the leakage are introduced. These indices show that for the present setup, ASC performs (more than) good enough for time-domain averaging in a reliable way.

**Frequency-Domain Filtering and Differentiation** After averaging, a second signal processing step is to filter, and if necessary differentiate, the averaged signal in the frequency domain. In order to do so, the averaged signal is first approximated in the least-squares sense, as a finite Fourier series, of which the number of harmonics determines the bandwidth of the frequency-domain filtering. This off-line filtering technique does not introduce any amplitude nor phase distortion.

If the amplitudes  $a_k$  and  $b_k$  of the frequency-domain filtered signal are known, it is straightforward to determine the amplitudes of the differentiated signal, using results similar to (2.12–2.14). This differentiation technique is termed *analytic* differentiation and has for instance been applied in the area of experimental robot identification (Swevers et al., 1997). It is simple, efficient, and more accurate than numeric differentiation. Its main application in the present setup is obtaining reliable estimates of the sley axis speed and acceleration, despite the limited resolution of the encoder reading.

**Microphone Signals** The three sound pressure measurements are converted to A-weighted sound pressure levels (SPL) [dB(A) re 2e-5 Pa] as follows.

<sup>9</sup>Leakage is a term frequently used to describe errors due to nonperiodicity when the Discrete Fourier Transform is applied. Here, it is used in a less inclusive sense to describe nonperiodicity errors when averaging signals.

The total measurement sequence of length 30 s is split into sequences of 0.6 s. For each of these sequences, the autopower spectrum is determined. All of these autopower spectra are averaged<sup>10</sup> to obtain an average autopower spectrum, to which the A-weighting is applied. From this weighted spectrum, the SPL-value is obtained. From here on, dB(A) is used as a shorthand notion for [dB(A) re 2e-5 Pa].

## 7.2 Average Speed Control

In Section 3.5, it was shown that a basic requirement for correct functioning of inertially compensated cams, is that the driving motor is equipped with a low-bandwidth controller, such that the machine's regime motion is similar to its damped eigenmotion. As opposed to conventional low-bandwidth control systems (which result in a remaining small fluctuation of the applied motor torque), Average Speed Control (ASC), developed in this section, is theoretically capable of driving a motor, such that it exerts a perfectly constant torque. Consequently and by definition, the resulting regime motion *is* the damped eigenmotion. Section 7.2.1 firstly gives the basic intuition behind ASC. After that, Section 7.2.2 illustrates, in simulation, its behavior when applied to an airjet weaving machine. Experimental ASC results are discussed in Section 7.3.1.

### 7.2.1 Basic Idea

A general feedback control system can be represented as:

$$U(s) = C(s) \cdot E(s), \quad (7.5)$$

where  $s$  denotes the Laplace variable,  $C(s)$  the Laplace transform of the control law, and  $U(s)$  the Laplace transform of the control signal  $u(t)$  [V].  $E(s)$  is the Laplace transform of the error  $e(t)$  on which the control action is based. Classical feedback control systems are based on measuring the *instantaneous* drive speed. That is,  $e$  [rad/s] is calculated as the difference between some desired drive speed  $\dot{g}_{\text{des}}$  and the measured, actually realized drive speed  $\dot{g}$  [rad/s]:

$$e_{\text{inst}}(t) = \dot{g}_{\text{des}}(t) - \dot{g}(t). \quad (7.6)$$

ASC is different in that it calculates  $e$  as the difference between the desired *average* speed  $\Omega = 2\pi/T$  and the measured, actually realized *average* drive speed  $\dot{g}_{\text{avg}}(t)$  [rad/s]:

$$e_{\text{avg}}(t) = \frac{2\pi}{T} - \dot{g}_{\text{avg}}(t). \quad (7.7)$$

---

<sup>10</sup>This frequency-domain averaging process does not suffer from the lack of synchronization between the Pimento and the dSpace system.

$\dot{g}_{\text{avg}}(t)$  is calculated as a moving average<sup>11</sup> over the time window  $T_w$  [s]:

$$\dot{g}_{\text{avg}}(t) = \frac{g(t) - g(t - T_w)}{T_w}. \quad (7.8)$$

The use of  $\dot{g}_{\text{avg}}(t)$  for generating the feedback error signal is the key element of ASC. Hereafter, the intuition behind ASC is explained by studying its behavior for machines without and with friction.

**ASC in a machine without friction** Assume a frictionless machine, moving according to its eigenmotion, with period  $T$ . The instantaneous drive speed  $\dot{g}(t)$  is then a periodical function, with period  $T$  and average value  $\Omega = 2\pi/T$ . In that case,  $\dot{g}_{\text{avg}}(t)$  is constant as a function of time, and equal to  $2\pi/T$ , provided that  $T_w$  equals an integer  $L$  times  $T$ . Subsequently,  $e_{\text{avg}} \equiv 0$ , hence  $u \equiv 0$ , and, if it is assumed that the motor is operated in torque mode<sup>12</sup>, no torque is demanded from the motor: the fluctuation of the instantaneous drive speed is 'hidden' for the controller.

On the other hand, if  $e_{\text{inst}}$  is used to generate the control signal, two cases are possible. The classical approach is to assign a constant value  $\dot{g}_{\text{des}}(t) \equiv 2\pi/T$  to the desired drive speed. Hence, if the machine moves (with period  $T$ ) according to its eigenmotion,  $e_{\text{inst}}(t)$  is a periodical function with period  $T$  and zero mean value. Consequently, the torque demand  $u$  is also a periodical function with period  $T$  and zero mean value<sup>13</sup>, and significant eigenmotion distortion results. In fact, accurate eigenmotion realization is not the purpose of approaches that combine (7.6) with  $\dot{g}_{\text{des}}(t) \equiv 2\pi/T$ : these approaches aim at a drive speed that is as constant as possible, and focus on designing a high-bandwidth controller  $C(s)$  (Tao and Sadler, 1995; Dulger and Uyan, 1997; Fung and Chen, 1997). The performance of these feedback-based approaches can be improved using either model-based or learning feedforward, as applied in e.g. (Demeulenaere and Swevers, 2002).

A more integrated  $e_{\text{inst}}$ -based approach uses an accurate, inertial machine model for generating the desired drive speed<sup>14</sup> trajectory  $\dot{g}_{\text{des}}(t)$ . That is, based on the model, the eigenmotion's drive speed trajectory is calculated a priori, and  $\dot{g}_{\text{des}}(t)$  is set equal to it. In that case, as with ASC, during eigenmotion, the control signal is zero as  $e_{\text{inst}} = 0$ .

In (VDI2149, 1999; Dresig, 2001) reference is made to a German patent<sup>15</sup> in the area of pilgrim rolling mills as an example of such a model-based ap-

<sup>11</sup>Some theoretical properties of this moving average are discussed in Appendix M.

<sup>12</sup>That is, the control signal is interpreted by the motor as a desired torque.

<sup>13</sup>A nonzero mean torque value would result in the drive speed going to infinity due to the absence of friction.

<sup>14</sup>A more conventional use of a machine model is to determine an adequate feedforward action.

<sup>15</sup>Patent no. DE 41 16 307 C1: *Verfahren zum Drehmomentenausgleich an einer Antriebsrichtung eines Pilgerschrittwalzwerkes*, allowed 29.10.1992 (method for input torque balancing the drive system of a pilgrim rolling mill).

proach. Energy efficiency is mentioned as the motivation to adopt it. The same approach is developed independently in (Demeulenaere and De Schutter, 2001) for simulating the behavior of inertially compensated cams, driven by a DC-motor in the presence of friction. This control approach has in common with ASC that it results in a zero torque demand in the absence of friction. However, ASC, being a model-free approach, does not require a good a priori knowledge of the inertial machine dynamics, and can therefore be considered to be more robust.

**ASC in a machine with friction** If energy dissipation is present, the error  $e$ <sup>(16)</sup> is nonzero, such that the controller structure  $C(s)$  is relevant. If  $e(t = \infty)$  is to be zero, the controller should contain at least one free integrator. Practically, this means that  $C(s)$  equals:

$$C(s) = \left( K_p + \frac{K_i}{s} \right) \cdot C_2(s),$$

that is, a PI-controller connected in series with some other controller  $C_2(s)$ . Assuming that  $C_2(s) \equiv 1$ , the following controller behavior results: if the machine starts from standstill, setting the desired average speed to  $2\pi/T$  results in an initial error  $e(t = 0) = 2\pi/T$ , hence  $u(t = 0) = K_p \cdot 2\pi/T$ . The machine starts up, and, due to the presence of the integrator, eventually reaches its desired average speed, that is,  $e(t = \infty) = 0$ , with a constant torque demand  $u(t = \infty)$  equal to

$$u(t = \infty) = K_i \cdot \int_0^\infty e(t) \cdot dt.$$

Due to the presence of the integrator, also zero error is obtained in the presence of step-type torque disturbances. If other, nonperiodical disturbances are present,  $e(t)$  remains nonzero. In that case, performance (in terms of disturbance suppression) can be improved by adequately designing  $C_2(s)$ .

## 7.2.2 Simulation Results

**Simulation Model** Simulation of ASC is based on the *discrete*<sup>17</sup> control scheme of Fig.7.8, of which the sample period is  $T_s = 0.001$  s. The control law is a discrete PI-controller, tuned by trial-and-error to obtain satisfactory system performance. The torque demand  $u(k)$  is transformed into the motor torque  $M_{SR}(k)$ , based on the following motor model, experimentally identified

---

<sup>16</sup>From now on, only ASC is considered, that is  $e = e_{avg}$ , and hence the subscript  $(\cdot)_{avg}$  is dropped in the remainder of this chapter.

<sup>17</sup>Simulation of this discrete model is based on a sixth-order Adams-Bashforth integration scheme.

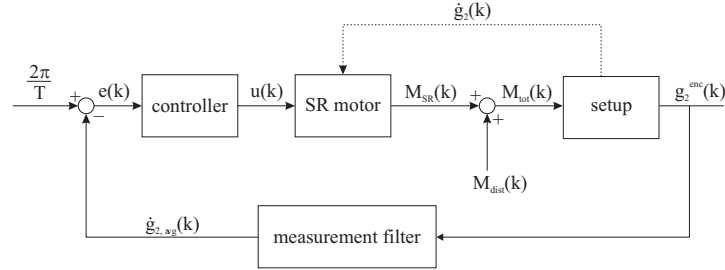


FIGURE 7.8: ASC Simulation: simulation model.

for the switched-reluctance (SR) motor of the setup:

$$M_{SR}(k) = \frac{u(k-1)}{u_{\max}} \cdot M_{SR,\max}(\dot{g}_1(k)).$$

That is, the SR motor delivers, with a one-sample delay, a fraction  $u/u_{\max}$  of the maximum motor torque  $M_{SR,\max}$ .  $u_{\max}$  equals 10 V, while  $M_{SR,\max}$  depends on the instantaneous sley axis speed  $\dot{g}_1(k)$ <sup>18</sup>. For reasons of confidentiality, the  $M_{SR,\max}$  vs.  $\dot{g}_1(k)$  relation is not given here. The total torque  $M_{tot}$  [N-m] that is applied to the setup, is the sum of  $M_{SR}$  and the disturbance torque  $M_{dist}$ .

The setup model is the simplified setup model of Section 7.1.1, with the adaptation that the sley and shed follower inertias respectively operate against a Coulomb friction torque  $M_{coul}$  [N-m] and Coulomb friction force  $M_{coul}$  [N], in order to introduce energy dissipation. The simplified model results in the following differential equation:

$$M_{tot} = J_{fly} \cdot \ddot{g}_1 + F'_1(g_1) \cdot \left( J_1 \cdot \ddot{f}_1 + M_{coul,1} \cdot \text{sign}(\dot{f}_1) \right) + \frac{F'_2(g_2)}{2} \cdot \left( J_2 \cdot \ddot{f}_2 + M_{coul,2} \cdot \text{sign}(\dot{f}_2) \right). \quad (7.9)$$

Given that ( $i = \{1, 2\}$ ):

$$\begin{aligned} \dot{f}_i &= F'_i(g_i) \cdot \dot{g}_i; \\ \ddot{f}_i &= F''_i(g_i) \cdot \dot{g}_i^2 + F'_i(g_i) \cdot \ddot{g}_i; \\ g_2 &= (g_1 - g_{\text{cross}})/2, \end{aligned}$$

(7.9) constitutes a second-order, nonlinear differential equation in  $g_1$ . As the shed axis is the slowest turning axis, the time window  $T_w$  equals  $T = 2\pi/\Omega_{\text{shed}}$

<sup>18</sup>For ease of notation, the subscripts  $(\cdot)_{\text{sley}}$  and  $(\cdot)_{\text{shed}}$  are replaced by subscripts  $(\cdot)_1$  and  $(\cdot)_2$  respectively

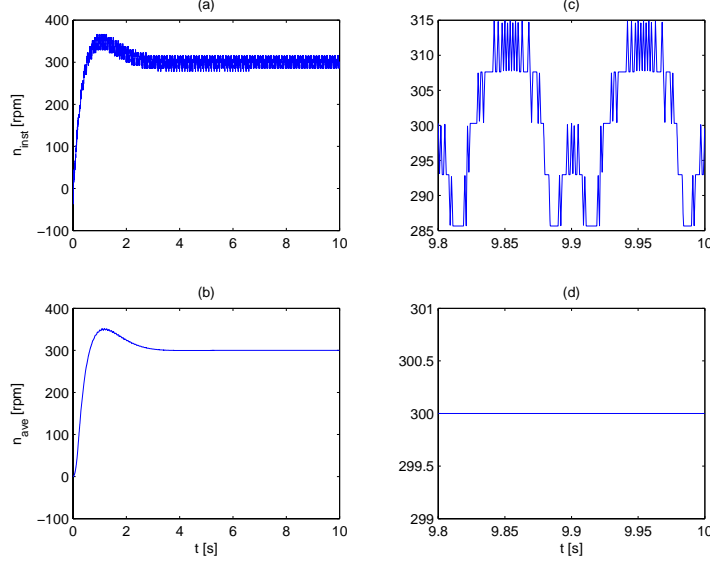


FIGURE 7.9: ASC Simulation: complete time trajectory ( $a - b$ ) and final period ( $c - d$ ) of instantaneous shed axis speed  $n_{\text{inst}}$  [rpm] and average shed axis speed  $n_{\text{avg}}$  [rpm].

( $L = 1$ ).  $g_2^{\text{enc}}(k)$  [rad], that is,  $g_2$  with the finite resolution of the encoder, is used as the input for the measurement filter. The discrete form of (7.8) is:

$$\dot{g}_{\text{avg}}(k) = \frac{g(k) - g(k - P)}{P \cdot T_s},$$

where  $T_s$  [s] is the sample period of the discrete control system and  $P = T_w/T_s$ , where  $P$  must be an integer. Keeping in mind that  $T_w = L \cdot T$ ,  $L \in \mathbb{Z}$ , the following drive speeds  $\Omega_{\text{shed}} = 2\pi/T$  [rad/s] can be imposed:

$$\Omega_{\text{shed}} = 2\pi \cdot \frac{L}{P \cdot T_s}, \quad (7.10)$$

where  $L, P \in \mathbb{Z}$ .

**Numerical Results** Numerical results are generated with both the shed and sley follower working against a Coulomb friction torque of 103 N-m, which corresponds to a nondimensionalized coefficient of energy dissipation  $\eta = 0.10$ . The desired  $\Omega_{\text{shed}}$  equals 300 rpm, which corresponds to a machine period of 0.20 s. With  $T_s = 0.001$  s and  $L = 1$ , this gives rise to  $P = 200$ . The disturbance torque  $M_{\text{dist}}$  is zero.

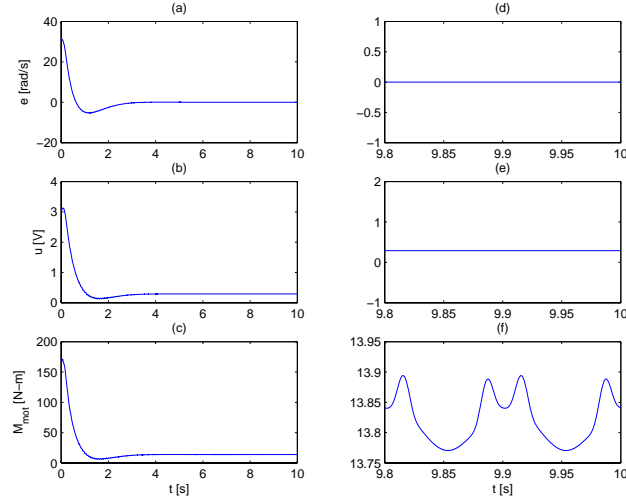


FIGURE 7.10: ASC Simulation: complete time trajectory ( $a - b - c$ ) and final period ( $d - e - f$ ) of error signal  $e$  [rad/s], torque demand  $u$  [V] and motor torque  $M_{SR}$  [N-m].

Figure 7.9 shows the complete time trajectory  $t \in [0, 10]$  and the final period  $t \in [9.80, 10]$  of the instantaneous shed axis speed  $n_{inst} = \dot{g}_2 \cdot 60 / (2\pi)$  [rpm] and the average shed axis speed  $n_{avg} = \dot{g}_{2,avg} \cdot 60 / (2\pi)$  [rpm]. The machine starts from standstill and reaches its nominal speed within approximately 4 s. As the nominal speed is by far not reached after at the end of the first machine cycle, this transient behavior is not satisfactory (see Section 2.1.4). However, ASC is not meant to be a controller for transient behavior<sup>19</sup> but for steady-state behavior. As such, it does perform well, as shown by Fig.7.9(d): in the final period,  $n_{avg}$  perfectly equals the desired 300 rpm, while  $n_{inst}$  fluctuates around 300 rpm (Fig.7.9(c)). The resolution of  $n_{inst}$  is rough, as it is derived from the encoder signal  $g_2^{enc}$ .

Figure 7.10 focuses on the controller itself, by showing the complete time trajectory and the final period of the error signal  $e$  [rad/s], torque demand  $u$  [V] and motor torque  $M_{SR}$  [N-m]. Since  $n_{avg} \equiv 300$  rpm in the final period,  $e \equiv 0$ . In that period, the torque demand has converged to a perfectly constant value of 0.29 V. Despite the constant torque demand, the motor torque is not, due to the dependency of  $M_{SR,max}$  on the instantaneous sley axis speed. The motor torque fluctuation is however very limited: its peak-to-peak amplitude equals 0.12 N-m, which is 0.9% of its average value of 13.8219 N-m.

<sup>19</sup>Fast transient behavior can e.g. be obtained by adding feedforward action to the control structure.

As a result of the small motor torque fluctuation, the resulting motion is very close, but not perfectly equal to the damped eigenmotion. This is illustrated by Fig.7.11, which compares the final period of the sley axis motion, resulting from the ASC simulation, with damped eigenmotion results ( $\eta = 0.10$ ), calculated using the frequency-domain technique of Section 2.6. For both the sley axis speed and acceleration, the differences are very small. Furthermore, the constant motor torque, determined during damped eigenmotion calculation, equals 13.8175 N-m, which differs only 0.03% from the average value of the torque in the ASC simulation (13.8219 N-m). If the dependency of  $M_{SR,max}$  on  $\dot{g}_1$  was removed from the simulation model and if the setup simulation model was continuous instead of discrete, the ASC simulation and damped eigenmotion results would be identical.

Figure 7.12 illustrates the ASC behavior if the disturbance torque shown in Fig.7.12(a) is applied. This is a random torque with a normal distribution, mean value 0.24 N-m and standard deviation 9.98 N-m. The figures show the regime behavior for  $t \in [5, 10]$  s. The PI-controller is not capable of suppressing the disturbance (but it has not been tuned to do so: it is the same controller as used for the simulations without disturbance). Still however, the behavior is quite satisfactory, as the mean value of  $n_{avg}$  over  $t \in [5, 10]$  s is 300.02 rpm. Furthermore,  $u$ , and hence  $M_{SR}$  do not overreact to the disturbance. Their mean values over  $t \in [5, 10]$  s (0.296 V and 14.1 N-m) are slightly higher than in the simulation without disturbance, due to the nonzero mean value of the disturbance torque.

### 7.2.3 Conclusion

As no stability or any other thorough theoretical analysis of its properties have been carried out, tuning of ASC is done by trial-and-error. Nevertheless, its performance is satisfactory: it results in a constant torque demand and does not overreact to the presence of disturbances.

## 7.3 Experimental Measurement Campaign

The experimental measurement campaign has a twofold goal: (i) to check whether the CBCP functions properly, that is, whether it delivers the designed torque and (ii) to check whether the CBCP is capable of enhancing the dynamic behavior of the weaving machine setup. Answering the first question is done by measuring the torque delivered by the CBCP, for a range of speeds ( $\Omega_{shed}$  ranging from 125 to 437.5 rpm with an interval of about<sup>20</sup> 12.5 rpm), and comparing it to the theoretical torque.

In order to answer the second question, the dynamic behavior of two setup configurations is compared (for the aforementioned speed range of  $\Omega_{shed}$ ):

---

<sup>20</sup>Some of the drive speeds are not multiples of 12.5 rpm. This is due to the discrete implementation of ASC, which only allows for drive speeds that comply with (7.10).

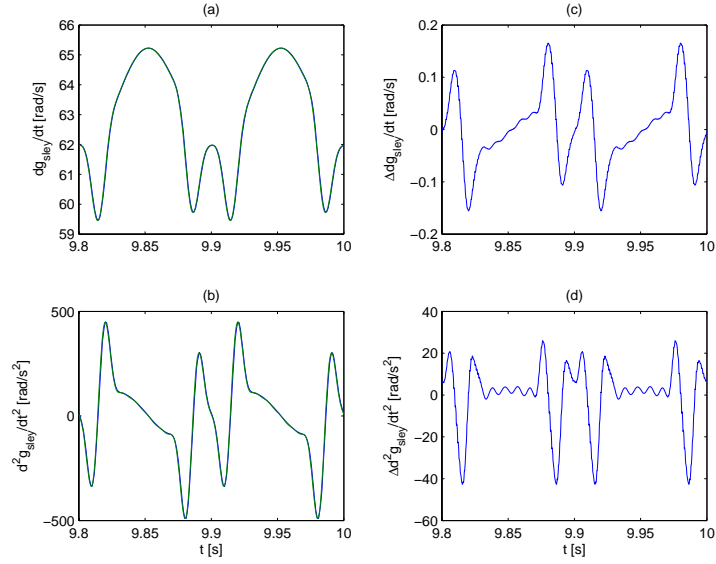


FIGURE 7.11: Comparison of ASC simulation and damped eigenmotion ( $\eta = 0.10$ ): (a)  $\dot{g}_{\text{sley}}$  for both cases; (c) difference  $\Delta\dot{g}_{\text{sley}}$  between both cases; (b)  $\ddot{g}_{\text{sley}}$  for both cases; (d) difference  $\Delta\ddot{g}_{\text{sley}}$  between both cases.

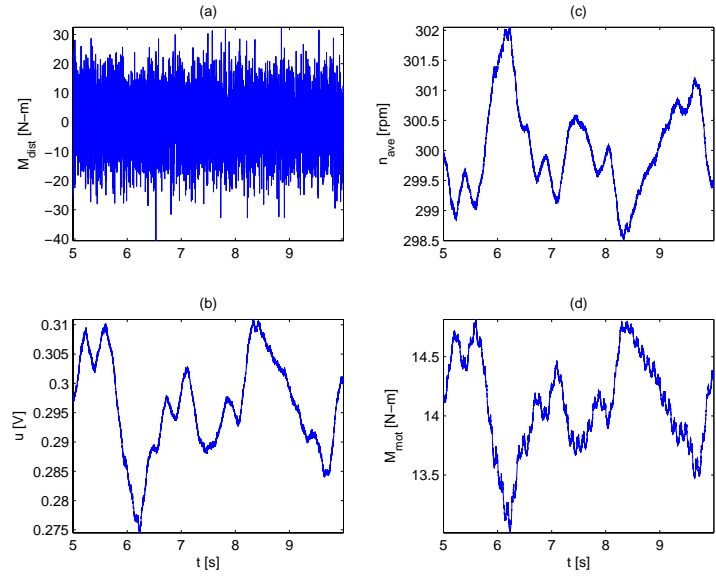


FIGURE 7.12: ASC simulation in the presence of disturbances: results for  $t \in [5, 10]$  s. (a) disturbance torque  $M_{\text{dist}}$ ; (b) torque demand  $u$ ; (c) average shed axis speed  $n_{\text{avg}}$ ; (d) motor torque  $M_{\text{SR}}$ .

the FLY and the CBCP-configuration. In both configurations, the CBCP is present, but it is clamped (and hence behaves like a pure flywheel) in the FLY-configuration and is active in the CBCP-configuration.

Comparing these two configurations is required to distinguish between the *flywheel effect* of the CBCP and its *torque balancing effect*. The flywheel effect is due to the *constant* part of the CBCP's kinetic energy, that is, its dumb equivalent inertia of  $0.39 \text{ kg}\cdot\text{m}^2$  (see Section 6.6), which is significant compared to the original flywheel inertia of  $0.816 \text{ kg}\cdot\text{m}^2$ . The torque balancing effect is due to the *fluctuating* part of the CBCP's kinetic energy. The flywheel effect is quasi equally present in both configurations, as the  $0.33 \text{ kg}\cdot\text{m}^2$  pure flywheel inertia, constituted by the clamped CBCP, comes quite close to the  $0.39 \text{ kg}\cdot\text{m}^2$  dumb equivalent inertia of the moving CBCP. On the other hand, the torque balancing effect is only present in the CBCP-configuration, and its effect on the dynamic behavior can therefore be honestly assessed by comparing the FLY and the CBCP-configuration. Experimentally comparing both configurations is very similar to what was done when comparing situation *S2* (original machine, with enlarged flywheel of  $0.39 \text{ kg}\cdot\text{m}^2$ ) and *S3* (original machine, with CBCP active) in the simulations of Section 6.6.

The steel barrel in which the internal cams are fixed, adds 286 kg to the right carter and would have significant dynamic influence if the CBCP-configuration was compared to the original setup, that is, the setup before the CBCP was added. This constitutes another advantage of comparing the CBCP and the FLY-configuration: as the barrel is present in both setups, its 286 kg does not favor one configuration over the other.

This section is organized as follows. As time-domain averaging is an important signal processing step, requiring accurate control of the average drive speed, first the ASC performance is quantified (Section 7.3.1). Section 7.3.2 gives an answer to the first question. The second question is answered step-by-step, by first investigating the CBCP effect on the shed axis speed and acceleration (Section 7.3.3) and the low-frequency sword and frame acceleration spectrum (Section 7.3.4). After that, the vibration and sound pressure level are evaluated in Section 7.3.5 and 7.3.6 respectively.

### 7.3.1 ASC Performance

The setup is controlled using ASC. The discrete controller  $C(z)$  (sample period  $T_s = 0.001 \text{ s}$ ) is the product of a PI-controller and a lead-type controller. Its parameters are tuned by trial-and-error for the FLY-configuration, with  $\Omega_{\text{shed}} = 300 \text{ rpm}$ . The same controller settings are stable for the whole speed range (125 to 437.5 rpm) and for both the FLY and the CBCP-configuration, thus nicely illustrating the robustness of ASC.

A straightforward check of the ASC performance is to evaluate the error  $e(k) = 2\pi/T - \dot{g}_{2,\text{avg}}(k)$ , which is nonzero due to the presence of nonperiodical disturbances. Figure 7.13 shows, for both the CBCP and the FLY-configuration, the (absolute value of the) average value and the standard

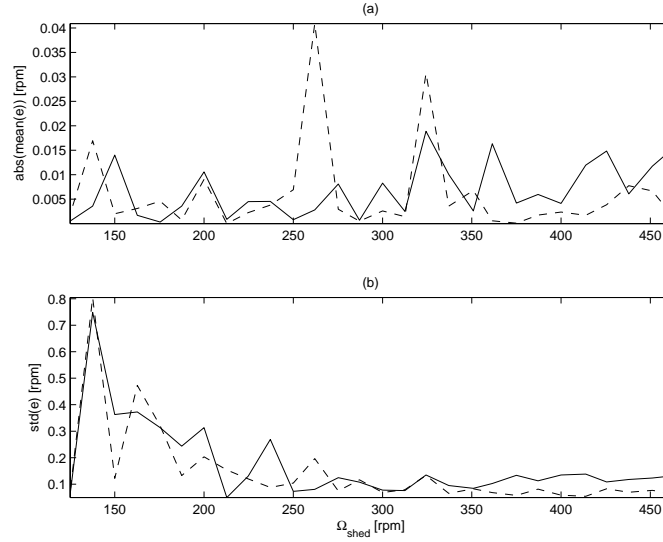


FIGURE 7.13: (a) Average value and (b) standard deviation (over the complete time window of 10 s) of  $e$  [rpm] as a function of  $\Omega_{shed}$  [rpm] for the CBCP (solid line) and the FLY-configuration (dashed line).

deviation (over the complete measurement window of 10 s) of  $e$  (expressed in [rpm]) as a function of  $\Omega_{shed}$ . The mean of  $e$  is very close to zero, and almost independent of  $\Omega_{shed}$ . The fact that the error on the mean of  $e$  is very close to zero, is due to the presence of the PI-controller and is essential for the averaging process. If this error was large, the associated substantial drift of the average drive speed would render time-domain averaging useless. A simple but effective check of the drift is to plot the first, last and some intermediate periods of a measurement signal on top of each other. If drift is negligible, these periods overlap well, as shown in Fig.L.4 for the measured CBCP torque.

The standard deviation of  $e$  increases if  $\Omega_{shed}$  decreases. These somewhat worse results for lower drive speeds can intuitively be explained by the fact that the time delay of  $T_w/2$  s, introduced by the average speed calculation (see Appendix M), increases with low drive speeds. The correspondingly greater phase lag reduces the phase margin and hence the damping of the closed loop. Recently developed measures for overcoming this and for improving the transient ASC behavior, are the subject of the internal report (Smolders et al., 2004).

The fact that  $e$  fluctuates with some limited standard deviation around a (practically) zero mean value causes the system response to be nearly, but

not perfectly periodical. As a result, leakage occurs. Appendix L gives a detailed discussion of the resulting leakage errors and introduces two quality indices for measuring the periodicity, or conversely, the leakage. The main conclusion is that for the present setup, ASC performs (more than) good enough for time-domain averaging in a reliable way.

### 7.3.2 CBCP Torque

Figure 7.14 gives a first indication that the CBCP delivers the designed torque. It shows one period of the measured<sup>21</sup> torque  $M_{c,\text{exp}}$  (solid line) and the theoretical torque  $M_{c,\text{the}}$  (dashed line) for  $\Omega_{\text{shed}} = \{200, 250, 300, 413.5\}$  rpm. For  $\Omega_{\text{shed}} = \{200, 250\}$  rpm, the experimental and theoretical results agree quite well, except during the phase where the CBCP is supposed to deliver no torque. This deviation is attributed to a combination of drive speed fluctuation, friction and/or imperfections of the mechanism. It cannot be attributed to the torsional springs that ensure the contact between the roller followers and the internal cams during standstill of the mechanism: numerical simulation shows that these springs have a negligible effect on  $M_c$  ( $< 3$  N-m, independently of  $\Omega_{\text{shed}}$ ).

At 413.5 rpm, the response is heavily dominated (peak amplitude of 2280 N-m!) by a resonance phenomenon, which is attributed to torsional flexibility of the sley axis. This hypothesis is justified by simulations in Section 7.4. Analysis of the spectrum of the CBCP torque reveals that the torsional resonance frequency is situated around 96-97 Hz, and that it is excited by the fourteenth torque harmonic of  $413.5/60=6.9$  Hz for  $\Omega_{\text{shed}} = 413.5$  rpm. As a result, the CBCP response explodes and completely dominates the setup's dynamic behavior. At 300 rpm, the onset of this resonance is already visible in a dual manner: (i) during the zero-torque phase, there is a remaining fluctuation and (ii) the positive and negative torque peaks are respectively higher and lower than for the predicted torque.

The results of Fig.7.14 are generalized for the entire speed range by Fig.7.15. Figure 7.15(a) shows the maximum absolute value of  $M_{c,\text{exp}}$  and  $M_{c,\text{the}}$  as a function of  $\Omega_{\text{shed}}$ . There is good agreement (relative error smaller than 10%) between the theoretical and experimental results for  $\Omega_{\text{shed}} < 275$  rpm. From then on, the resonance phenomenon sets on and reaches its peak value of 2280 N-m at 413.5 rpm. These results are confirmed by 7.15(b), which shows the relative rms difference  $\epsilon$  [%], defined as

$$\epsilon = 100 \cdot \frac{\text{rms}(M_{c,\text{exp}} - M_{c,\text{the}})}{\max(|M_{c,\text{the}}|)}.$$

$\epsilon$  is less than 10% for  $\Omega_{\text{shed}} \leq 300$  rpm and less than 25% for  $\Omega_{\text{shed}} \leq 350$  rpm. It is therefore concluded that the CBCP delivers the expected torque for

<sup>21</sup>The measured torque is obtained by time-domain averaging the raw torque results, followed by frequency-domain filtering of the averaged signal, that is, selecting the first twenty spectral lines.

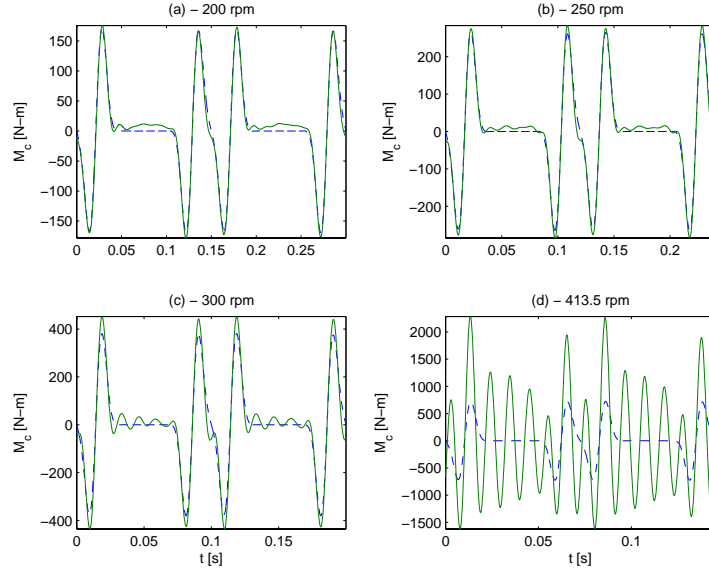


FIGURE 7.14: One period of measured torque  $M_{c,exp}$  (solid line) and theoretical torque  $M_{c,the}$  (dashed line) for  $\Omega_{shed} = \{200, 250, 300, 413.5\}$  rpm.

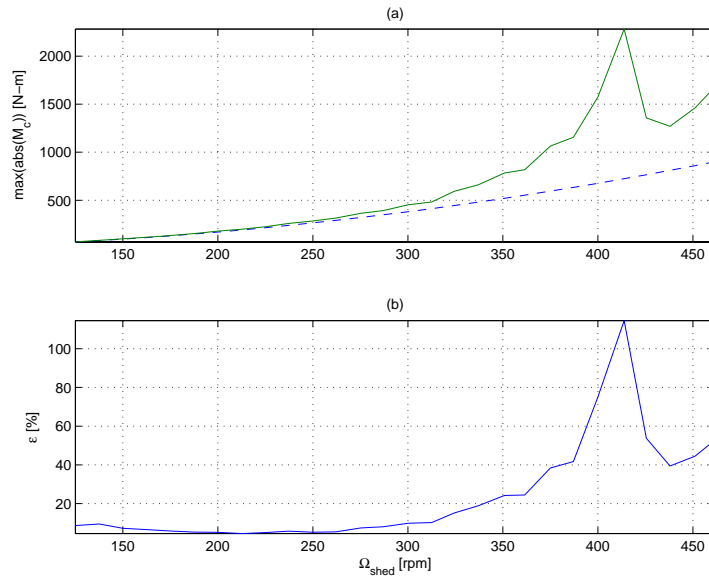


FIGURE 7.15: Overview of measured CBCP torque results as a function of  $\Omega_{shed}$  [rpm]: (a)  $\max(|M_{c,exp}|)$  [N-m] (solid line) and  $\max(|M_{c,the}|)$  [N-m] (dashed line); (b) relative rms difference  $\epsilon$  [%].

drive speeds below 300 rpm, and deviates more significantly, but still functions 'properly', between 300 and 350 rpm.

### 7.3.3 Shed Axis Speed and Acceleration

Figure 7.16 shows one period of the measured<sup>22</sup> shed axis speed  $\dot{g}_{\text{shed}}$  [rad/s] in the CBCP-configuration and the FLY-configuration for  $\Omega_{\text{shed}} = \{200, 250, 300, 413.5\}$  rpm. For  $\Omega_{\text{shed}} = 413.5$  rpm, the CBCP-configuration's torsional resonance phenomenon is clearly present under the form of a heavily fluctuating drive speed. For  $\Omega_{\text{shed}} = \{200, 250, 300\}$  rpm on the other hand, the drive speed fluctuation is much smaller in the CBCP-configuration than in the FLY-configuration.

Moreover, for these speeds, the results for the CBCP-configuration are qualitatively in agreement with the simulation results of Section 6.6, that is, the sharp dips in the drive speed, as they occur in the FLY-configuration, are much smaller in the CBCP-configuration. Theoretically, the sharp dips should disappear completely, but they do not, for two reasons. Firstly, the CBCP does not perfectly deliver the desired torque. Secondly, the CBCP internal cam design is based on a CAD-based sley inertia of limited accuracy, so if the CBCP perfectly delivered the designed torque, compensation would still not be complete.

Figure 7.17 shows one period of  $\ddot{g}_{\text{sley}}$  [rad/s<sup>2</sup>] in the CBCP-configuration and the FLY-configuration for  $\Omega_{\text{shed}} = \{200, 250, 300, 413.5\}$  rpm. The reduction of the sharp dips in the drive speed for  $\Omega_{\text{shed}} = \{200, 250, 300\}$  rpm gives rise to a much smoother acceleration profile. Furthermore, for  $\Omega_{\text{shed}} = 413.5$  rpm, the resonance phenomenon is again dominating.

Figure 7.18 gives an overview of the behavior of  $\dot{g}_{\text{sley}}$  over the entire speed range by showing the coefficient of drive speed fluctuation  $\kappa$  [%] in the FLY and CBCP-configuration as a function of  $\Omega_{\text{shed}}$ . For the FLY-configuration,  $\kappa$  is almost independent of  $\Omega_{\text{shed}}$ , which illustrates that the FLY-configuration behaves like a purely inertial system. For the CBCP-configuration, the same is true for  $\Omega_{\text{shed}} < 300$  rpm. In this speed range,  $\kappa$  is a factor 2.5 smaller ( $\kappa \approx 2\%$  vs.  $\kappa \approx 5\%$ ) than for the FLY-configuration. On the other hand, the CBCP-configuration does not behave like a purely inertial system for  $\Omega_{\text{shed}} > 350$  rpm, since  $\kappa$  rapidly mounts as a function of  $\Omega_{\text{shed}}$  and reaches a peak at 413.5 rpm.

### Verification of Simplified Setup Model

In order to verify the validity of the simplified setup model of Section 7.1.1, Fig.7.19 and Fig.7.20 show one period of respectively  $\dot{g}_{\text{shed}}$  and  $\ddot{g}_{\text{shed}}$  for

<sup>22</sup>The measured speed and acceleration are obtained by time-domain averaging the raw encoder results, followed by (i) frequency-domain filtering of the averaged signal, that is, selecting the first sixteen spectral lines and (ii) analytical differentiation.

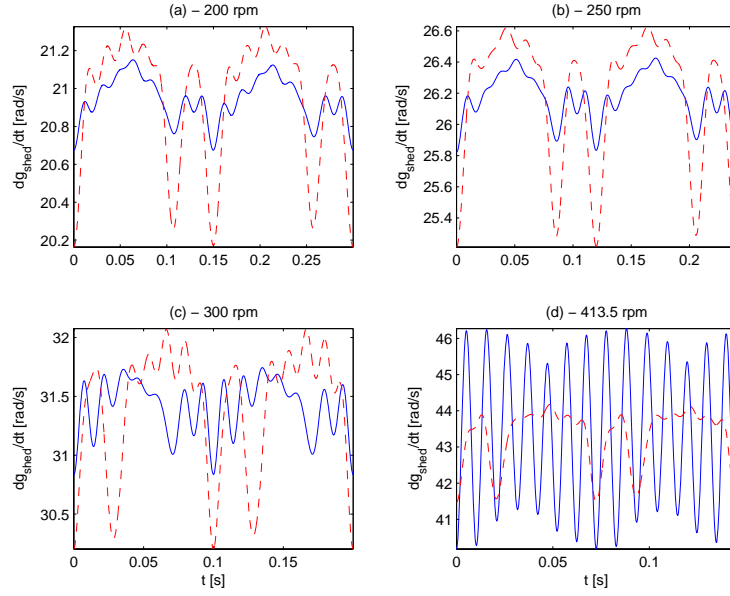


FIGURE 7.16: One period of  $\dot{g}_{\text{shed}}$  [rad/s] in the CBCP-configuration (solid line) and the FLY-configuration (dashed line) for  $\Omega_{\text{shed}} = \{200, 250, 300, 413.5\}$  rpm.

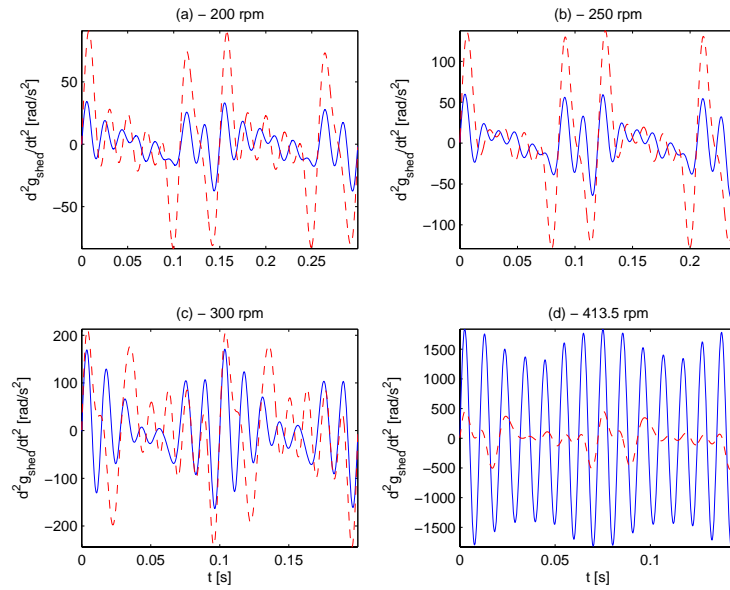


FIGURE 7.17: One period of  $\ddot{g}_{\text{shed}}$  [rad/s<sup>2</sup>] in the CBCP-configuration (solid line) and the FLY-configuration (dashed line) for  $\Omega_{\text{shed}} = \{200, 250, 300, 413.5\}$  rpm.

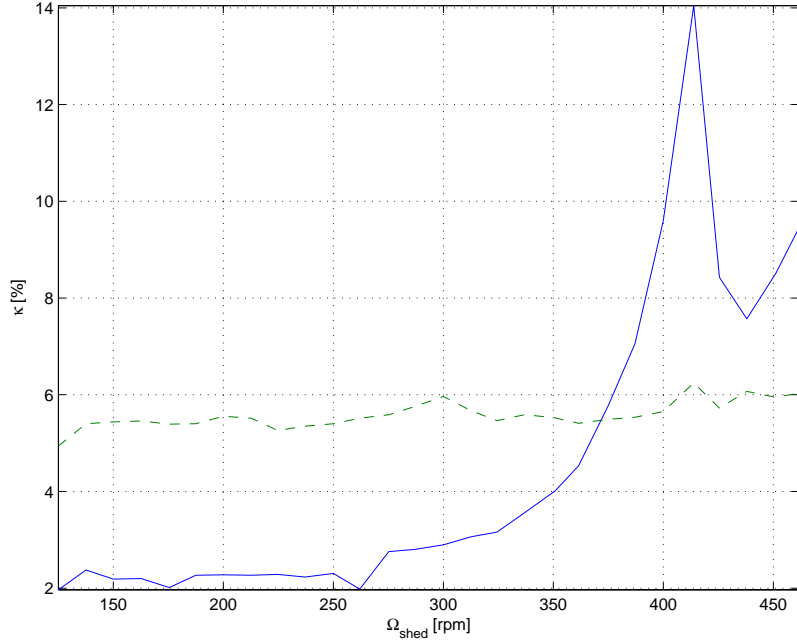


FIGURE 7.18:  $\kappa$  [%] as a function of  $\Omega_{\text{shed}}$  [rpm] in the FLY-configuration (dashed line) and the CBCP-configuration (solid line).

$\Omega_{\text{shed}} = \{150, 250, 350.8, 451.1\}$  rpm. Compared are the time trajectories measured in the FLY-configuration, and the time trajectories based on the damped eigenmotion ( $\eta = 0.10$ ) of the simplified setup model (with  $J_{\text{CBCP}} = 0.33 \text{ kg}\cdot\text{m}^2$  added to  $J_{\text{fly}}$ ). In view of the simplicity of the model, and the complexity of the setup, the agreement is quite good.

The experimental results show deeper dips in the speed trajectory (and consequently greater acceleration extrema), which suggests that in the model, the sley and/or shed inertia are underestimated or the flywheel inertia is overestimated. The values of these inertias are CAD-based and have a limited accuracy. More accurate values can be obtained by experimental identification, using the robot identification based techniques outlined in (Demeulenaere et al., 2000).

Furthermore, in both the experimental velocity and acceleration results, a residual vibration is present, which is attributed to the same torsional resonance that is dominating the response of the CBCP-configuration. In the FLY-configuration however, the resonance is not so heavily excited, such that its effect is visible, but not dominating.

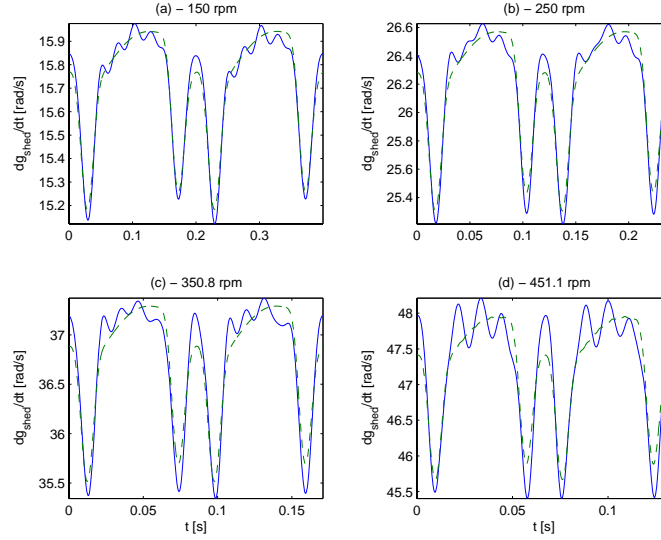


FIGURE 7.19: One period of  $\dot{g}_{\text{shed}}$ , measured in the FLY-configuration (solid line) and based on the damped eigenmotion ( $\eta = 0.10$ ) of the simplified setup model (dashed line) for  $\Omega_{\text{shed}} = \{150, 250, 350.8, 451.1\}$  rpm.

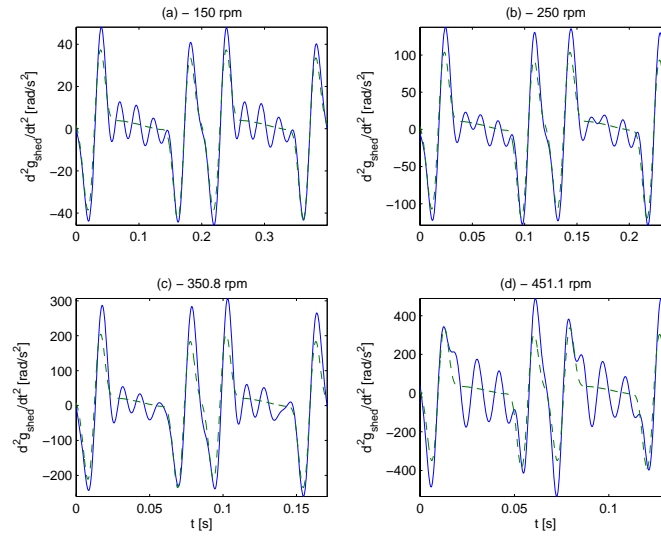


FIGURE 7.20: One period of  $\ddot{g}_{\text{shed}}$ , measured in the FLY-configuration (solid line) and based on the damped eigenmotion ( $\eta = 0.10$ ) of the simplified setup model (dashed line) for  $\Omega_{\text{shed}} = \{150, 250, 350.8, 451.1\}$  rpm.

### 7.3.4 Low-Frequency Sword and Frame Acceleration Spectrum

The simulation results of Section 6.6 predict that the drive speed fluctuation reduction due to the CBCP, results in lower undesired harmonics  $A_k$ <sup>23</sup> in the sword/frame acceleration. Figure 7.21 and 7.22 compare the low-frequency (that is, the first ten) harmonics (of  $\Omega_{\text{sley}}$ ) of the averaged sword and frame acceleration signals  $\dot{f}_{\text{sword}}$  and  $\dot{f}_{\text{frame}}$ . This is done for  $\Omega_{\text{shed}} \leq 350$  rpm, that is, the in Section 7.3.2 delimited speed range of 'proper' CBCP functioning. For both figures, the subplots ( $a - c - e$ ) give the results in the FLY-configuration, while the subplots ( $b - d - f$ ) give the difference  $\Delta A_k$  with the CBCP-configuration.  $\Delta A_k \geq 0$  implies that the corresponding harmonics are smaller in the CBCP than in the FLY-configuration. Since we are only interested in undesired harmonics, the first harmonic is not shown.

The ( $a - c - e$ ) subplots show that for both the sword and the frame acceleration, on average (over the observed speed range), the three largest undesired harmonics in the FLY-configuration are the harmonics  $k = \{7, 9, 10\}$ . As shown by the ( $b - d - f$ ) subplots, these are also the harmonics that are on average reduced most. The average reduction over the observed speed range equals:

**Sword acceleration** 14.0 dB ( $k = 7$ ); 14.1 dB ( $k = 9$ ); 5.0 dB ( $k = 10$ );

**Frame acceleration** 13.2 dB ( $k = 7$ ); 12.5 dB ( $k = 9$ ); 6.0 dB ( $k = 10$ ).

The average reduction is hence significant. These results confirm qualitatively the simulation results of Section 6.6.

### 7.3.5 Vibration Level

The vibration level VL [dB re  $b$ ] of an acceleration signal  $\ddot{y}$  is defined here as

$$VL = 20 \cdot \log_{10} \left( \frac{\text{rms}(\ddot{y} - \ddot{y}_{\text{des}})}{b} \right), \quad (7.11)$$

where  $\ddot{y}_{\text{des}}$  denotes the desired acceleration of the considered machine part, such as the pure sine motion of the frames and the swords, or the finite Fourier series in case of the sley. The vibration level represents the rms value of the undesired vibration  $\ddot{y} - \ddot{y}_{\text{des}}$ .

Practically, the vibration level is determined as follows.  $\ddot{y}$  represents the raw acceleration signal, containing  $S$  periods.  $\ddot{y}_{\text{des}}$  is obtained from the averaged acceleration signal by removing (through frequency-domain filtering) all but the desired harmonics and repeating the resulting signal over  $S$  periods. After that (7.11) is applied.

<sup>23</sup>The symbols  $A_k$ ,  $\Delta A_k$  and the notation [dB re  $b$ ] are introduced in Section 2.5.

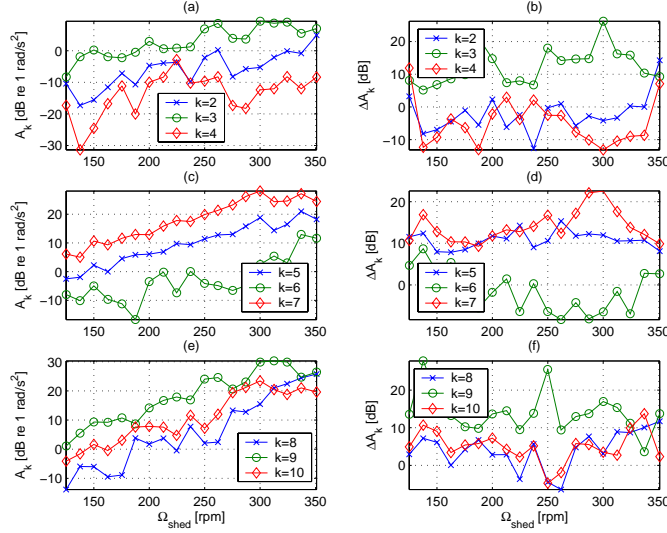


FIGURE 7.21: (a – c – e) Sword acceleration harmonics  $A_k$ ,  $k = 2, \dots, 10$  in the FLY-configuration, as a function of  $\Omega_{\text{shed}}$ ; (b – d – f) Difference  $\Delta A_k$  with the sword acceleration harmonics in the CBCP-configuration, as a function of  $\Omega_{\text{shed}}$ : a positive value indicates a smaller value in the CBCP-configuration.

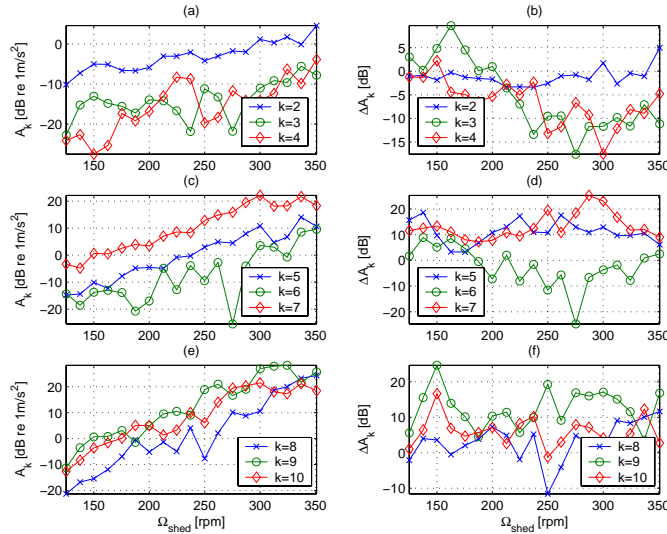


FIGURE 7.22: (a – c – e) Frame (up-and-down) acceleration harmonics  $A_k$ ,  $k = 2, \dots, 10$  in the FLY-configuration, as a function of  $\Omega_{\text{shed}}$ ; (b – d – f) Difference  $\Delta A_k$  with the sword acceleration harmonics in the CBCP-configuration, as a function of  $\Omega_{\text{shed}}$ : a positive value indicates a smaller value in the CBCP-configuration.

Figure 7.23 compares the vibration level of the up-and-down frame acceleration  $\ddot{f}_{\text{frame}}$  as a function of  $\Omega_{\text{shed}}$  [rpm] in the FLY-configuration and the CBCP-configuration. The values of  $\Delta VL = VL_{\text{FLY}} - VL_{\text{CBCP}}$  indicate that the vibration level is up to 10 dB lower in the CBCP-configuration, except around  $\Omega_{\text{shed}} = 413.5$  rpm, where the torsional resonance is dominant. For the out-of-plane frame acceleration,  $\ddot{h}_{\text{frame}}$ , the same conclusion applies (Fig.7.24). In the speed range of proper CBCP functioning (below 350 rpm), a significant frame vibration reduction is obtained: on average 5.2 dB for  $\ddot{f}_{\text{frame}}$  and 5.7 dB for  $\ddot{h}_{\text{frame}}$ .

Figure 7.25 focuses on the vibration level of the sley. Results here are somewhat, but not significantly, better in the functional drive speed range of the CBCP (which is logical: the CBCP was exactly added with improving the *frame* dynamic behavior in mind), and considerably worse in the torsional resonance speed range.

### 7.3.6 Noise Level

The main goal of the noise measurements is to quantify numerically two qualitative impressions concerning the noise production of the setup's FLY and CBCP-configuration. These impressions are: (i) for speeds above 250 rpm, the dominating, more irritating noise is the chattering noise of the frames. For drive speeds below 350 rpm, this noise is however 'much' smaller in the CBCP-configuration, which runs 'much' more quietly for these speeds; (ii) for speeds below 200 rpm, the rolling noise, caused by the rolling of the roller followers against the internal cams, can clearly be heard.

The numerical quantification of these impressions is obtained by comparing, for both setup configurations, the A-weighted sound pressure level SPL [dB(A)] resulting from three microphone measurements. Given the limited number of microphones and accelerometers, no attempt is done to correlate the vibration and sound measurements.

Figure 7.26 compares the SPL measured by MIC1 (located behind the frames, see Fig.K.1) in the FLY and CBCP-configuration. For  $\Omega_{\text{shed}}$  between 250 and 375 rpm, one observes a sound pressure level reduction in the CBCP-machine (that is,  $\Delta SPL = SPL_{\text{FLY}} - SPL_{\text{CBCP}} \geq 0$ ) that is significant (that is, greater than 3 dB(A)). Based on the impression that the frames dominate the noise production, this is attributed to the previously discussed frame vibration level reduction.

For  $\Omega_{\text{shed}} < 187.5$  rpm, the sound pressure level is higher in the CBCP-configuration, which is attributed to the rolling noise, caused by the CBCP's roller followers. For  $\Omega_{\text{shed}} > 375$  rpm, sound pressure levels are much higher in the CBCP-configuration, due to the torsional resonance.

Figure 7.27 shows the sound pressure level measured by MIC2, located near the motor. No noise level increase is observed for low drive speeds, which suggests that the distance (in terms of wavelengths) between this microphone and the CBCP is high enough for the microphone not to pick up the rolling

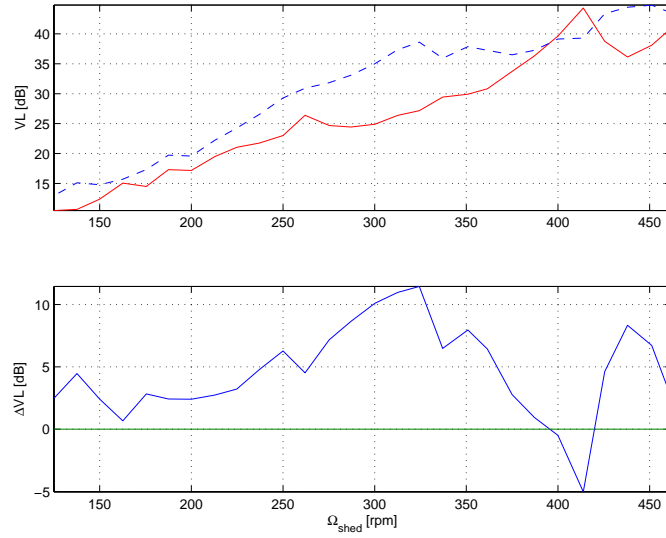


FIGURE 7.23: (a) Vibration level [dB re  $1 \text{ m/s}^2$ ] of the up-and-down frame acceleration  $\ddot{j}_{frame}$  as a function of  $\Omega_{shed}$  [rpm] in the FLY-configuration (dashed line) and the CBCP-configuration (solid line); (b)  $\Delta VL = VL_{FLY} - VL_{CBCP}$  [dB] as a function of  $\Omega_{shed}$ .

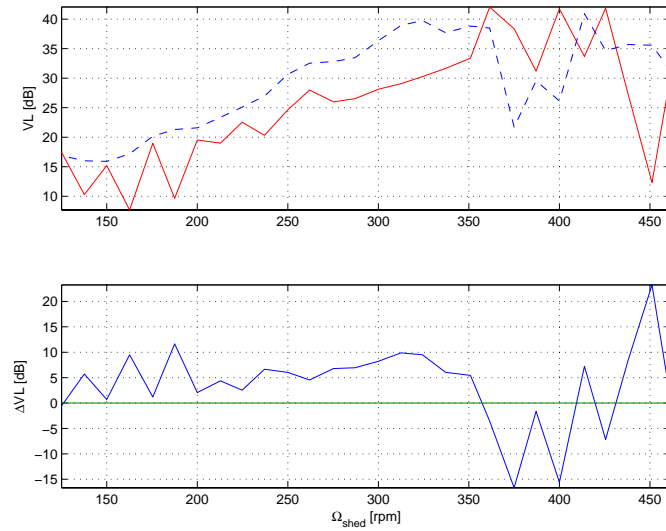


FIGURE 7.24: (a) Vibration level [dB re  $1 \text{ m/s}^2$ ] of the out-of-plane frame acceleration  $\ddot{h}_{frame}$  as a function of  $\Omega_{shed}$  [rpm] in the FLY-configuration (dashed line) and the CBCP-configuration (solid line); (b)  $\Delta VL = VL_{FLY} - VL_{CBCP}$  [dB] as a function of  $\Omega_{shed}$ .

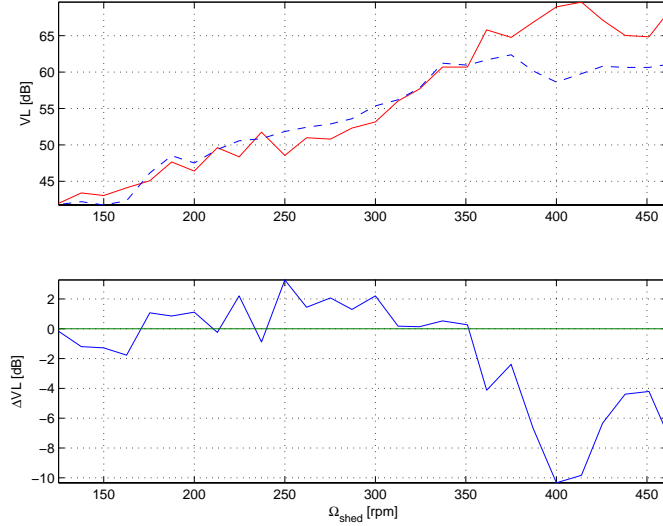


FIGURE 7.25: (a) Vibration level [dB re 1 m/s<sup>2</sup>] of the sley acceleration  $\ddot{f}_{sley}$  as a function of  $\Omega_{shed}$  [rpm] in the FLY-configuration (dashed line) and the CBCP-configuration (solid line); (b)  $\Delta VL = VL_{FLY} - VL_{CBCP}$  [dB] as a function of  $\Omega_{shed}$ .

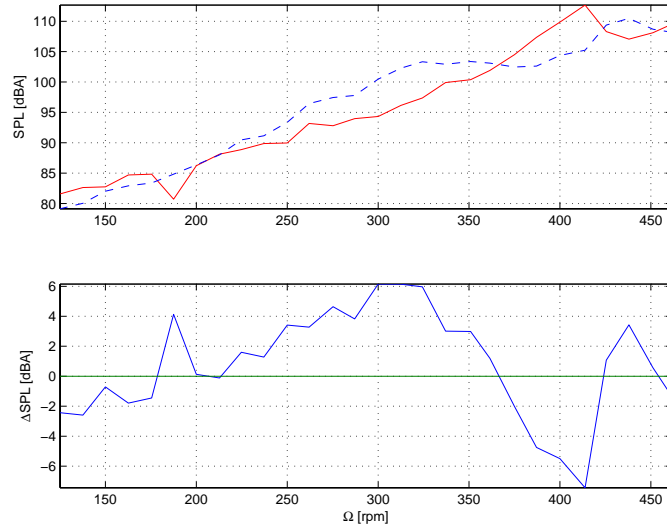


FIGURE 7.26: (a) A-weighted sound pressure level [dB(A)] in MIC1 as a function of  $\Omega_{shed}$  [rpm] in the FLY-configuration (dashed line) and the CBCP-configuration (solid line); (b)  $\Delta SPL = SPL_{FLY} - SPL_{CBCP}$  [dB(A)] as a function of  $\Omega_{shed}$ .

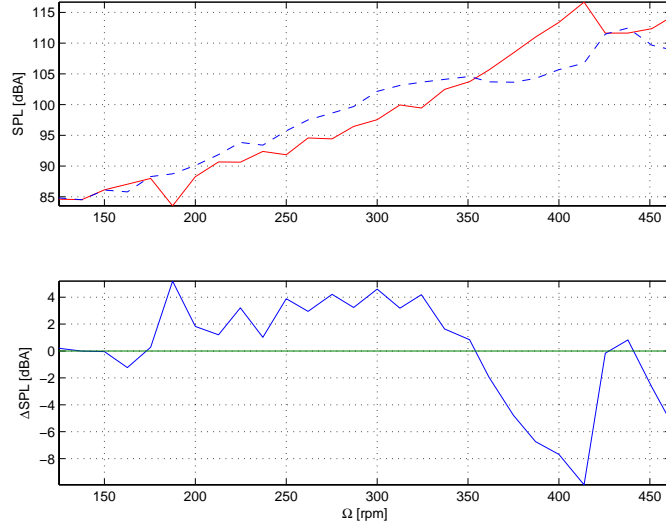


FIGURE 7.27: (a) A-weighted sound pressure level [dB(A)] in MIC2 as a function of  $\Omega_{shed}$  [rpm] in the FLY-configuration (dashed line) and the CBCP-configuration (solid line); (b)  $\Delta SPL = SPL_{FLY} - SPL_{CBCP}$  [dB(A)] as a function of  $\Omega_{shed}$ .

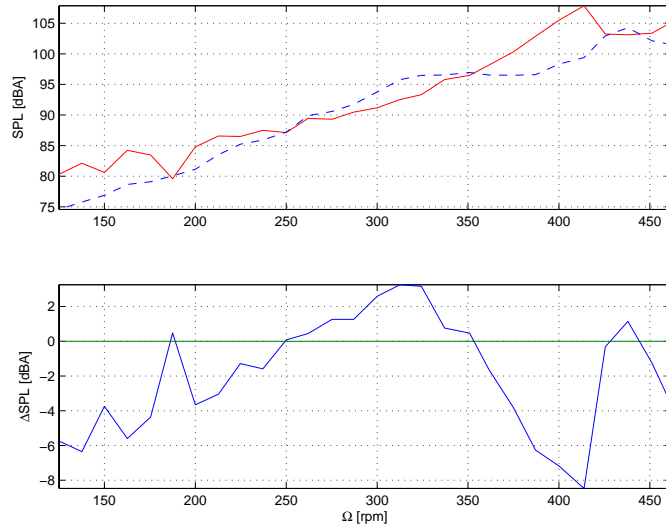


FIGURE 7.28: (a) A-weighted sound pressure level [dB(A)] in MIC3 as a function of  $\Omega_{shed}$  [rpm] in the FLY-configuration (dashed line) and the CBCP-configuration (solid line); (b)  $\Delta SPL = SPL_{FLY} - SPL_{CBCP}$  [dB(A)] as a function of  $\Omega_{shed}$ .

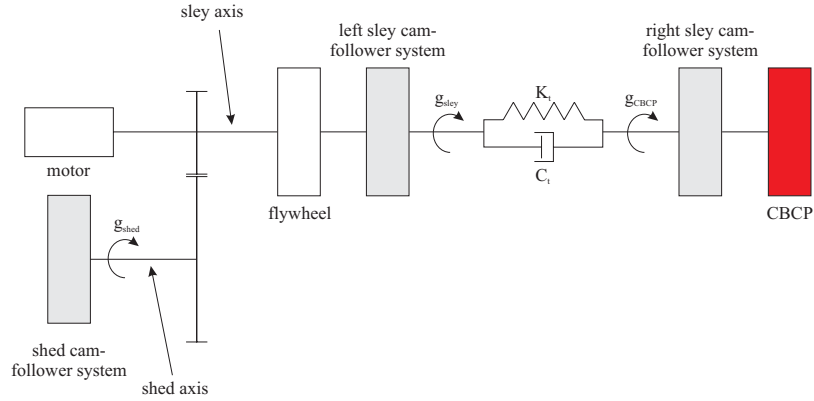


FIGURE 7.29: Simplified setup model, including CBCP and torsional sley axis flexibility  $K_t$  [N-m/rad] and damping  $C_t$  [N-m-s/rad].

noise. Between 200 and 350 rpm, the average noise level reduction is around 3 dB(A) and hence significant. Again, the effect of the torsional resonance can be observed.

The effect of the CBCP rolling noise is quite pronounced in the sound pressure level measured by MIC3 near the CBCP, shown in Fig.7.28: the higher sound pressure levels in the CBCP-configuration for low drive speeds, already observed in Fig.7.26, are much more significant here.

## 7.4 Torsional Vibration

In the previous section, the experimentally observed resonance phenomenon has been attributed to torsional resonance. The purpose of the present section is to show that this hypothesis is plausible, by simulating a torsional setup model, obtained by extending the rigid-body, simplified setup model of Section 7.1.1, with a torsional degree of freedom. Section 7.4.1 introduces the torsional degree of freedom, while Section 7.4.2 develops the corresponding mathematical model. The simulation results are the subject of Section 7.4.3

### 7.4.1 Derivation of Torsional Setup Model

As the sley axis is a long ( $L = 1.721$  m), hollow axis (outer diameter  $D = 101.0$  mm, inner diameter  $d = 86.8$  mm), it is a premier candidate for introducing torsional flexibility. Its torsional stiffness  $K_t$  [N-m/rad] equals, see e.g. (Den Hartog, 1956):

$$K_t = \frac{\pi}{32} \cdot \frac{G \cdot (D^4 - d^4)}{L},$$

where  $G$  denotes the shear modulus of steel, equal to 80.8 GPa. This results in  $K_t = 220$  kN-m/rad. Figure 7.29 shows the resulting torsional setup model. The sley cam-follower mechanism is split up into two parts: one in the left and one in the right machine carter, each with half of the inertia  $J_{\text{sley}}$ . The rotation angle of the left and right sley axis part are denoted as  $g_{\text{sley}}$  and  $g_{\text{CBCP}}$  respectively. For reasons of simplicity, no stiffness is assigned to the sley itself, which implies that the left and right sley follower parts move freely w.r.t. each other.

Due to the addition of the torsional degree of freedom, the rotational inertia of the sley axis ( $0.114$  kg-m<sup>2</sup>) is split into two halves. As a consequence,  $J_{\text{fly}}$  decreases from  $0.816$  to  $0.759$  kg-m<sup>2</sup>, while the CBCP rotor inertia increases from  $0.0624$  (see Table 7.1) to  $0.1194$  kg-m<sup>2</sup>. Hence, the *constant* part of the CBCP's kinetic energy, that is, its dumb equivalent inertia, increases from  $0.390$  to  $0.447$  kg-m<sup>2</sup>, while the clamped inertia  $J_{\text{CBCP}}$  increases from  $0.330$  to  $0.387$  kg-m<sup>2</sup>.

The one-degree-of-freedom system (left sley axis side clamped, right sley axis side free to move) with torsional stiffness  $220$  kN/rad and (equivalent) inertia  $0.447$  kg-m<sup>2</sup> has an eigenfrequency of  $111$  Hz. This 'quick and dirty' approximation comes quite close to the experimentally observed resonance frequency of  $96$ - $97$  Hz, so it was decided to do a full nonlinear simulation of the model of Fig.7.29, again for a CBCP-configuration (CBCP free to move) and a FLY-configuration (CBCP clamped). Coulomb friction torques  $M_{\text{coul}} = 383$  N and  $M_{\text{coul}}/2 = 191.5$  N-m are assigned to the shed follower and each of the sley follower halves respectively, resulting in  $\eta = 0.10$ <sup>(24)</sup>. As the sley axis damping is hard to assess, three damping values  $C_t$  are simulated:  $C_t = \{2.2, 11.1, 22.3\}$  N-m-s/rad. For the aforementioned one-degree-of-system, this would give rise to the following damping ratio  $\zeta$  [%]:

$$\zeta = 100 \cdot \frac{C_t}{2\sqrt{220000 \times 0.447}} = \{0.4, 1.8, 3.6\}\%.$$

#### 7.4.2 Simulation of Torsional Setup Model

Simulation of the damped eigenmotion ( $\eta = 0.10$ ) of the torsional setup model is based on the following two equations, which express torsional balance of the left and the right side of the setup. The right side includes the right sley cam-follower mechanism and the CBCP, whereas the left side includes the shed and the left sley cam-follower mechanism, the flywheel and the motor:

$$M_{\text{mot}} - M_{\text{tors}} = \frac{1}{\dot{g}_{\text{sley}}} \cdot \left( \frac{dT_{\text{tot,l}}}{dt} + P_{\text{loss,l}} \right); \quad (7.12a)$$

$$M_{\text{tors}} = \frac{1}{\dot{g}_{\text{CBCP}}} \cdot \left( \frac{dT_{\text{tot,r}}}{dt} + P_{\text{loss,r}} \right). \quad (7.12b)$$

<sup>24</sup>As simulation results turned out to depend only in a very limited way on  $\eta$ , only results for  $\eta = 0.10$  are presented here.

The motor torque  $M_{\text{mot}}$  [N-m] is constant (damped eigenmotion).  $M_{\text{tors}}$  [N-m] is the torque transmitted by the sleigh axis.  $T_{\text{tot,l}}$  and  $T_{\text{tot,r}}$  [J] denote the kinetic energy of the left and right setup side.  $P_{\text{loss,l}}$  and  $P_{\text{loss,r}}$  [W] represent the power dissipated by Coulomb friction in the left and right setup side. The following expressions are easily derived for these quantities:

$$M_{\text{tors}}(t) = K_t \cdot (g_{\text{sley}} - g_{\text{CBCP}}) + C_t \cdot (\dot{g}_{\text{sley}} - \dot{g}_{\text{CBCP}}); \quad (7.13a)$$

$$T_{\text{tot,l}}(t) = \frac{J_{\text{fly}} \cdot \dot{g}_{\text{sley}}^2}{2} + \frac{\frac{1}{2} \cdot J_{\text{sley}} \cdot \dot{f}_{\text{sley,l}}^2}{2} + \frac{J_{\text{shed}} \cdot \dot{f}_{\text{shed}}^2}{2}; \quad (7.13b)$$

$$T_{\text{tot,r}}(t) = \frac{\frac{1}{2} \cdot J_{\text{sley}} \cdot \dot{f}_{\text{sley,r}}^2}{2} + T_c(t); \quad (7.13c)$$

$$P_{\text{loss,l}}(t) = M_{\text{coul}} \cdot \left( \frac{1}{2} \cdot |\dot{f}_{\text{sley,l}}| + |\dot{f}_{\text{shed}}| \right); \quad (7.13d)$$

$$P_{\text{loss,r}}(t) = \frac{1}{2} \cdot M_{\text{coul}} \cdot |\dot{f}_{\text{sley,r}}|. \quad (7.13e)$$

The CBCP kinetic energy  $T_c$  [J] depends on the setup configuration:

$$T_c(t) = \begin{cases} \frac{J_{\text{CBCP}} \cdot \dot{g}_{\text{CBCP}}^2}{2} & (\text{FLY}); \\ \frac{J_1^* \cdot \dot{g}_{\text{CBCP}}^2}{2} + \frac{J_2^* \cdot \dot{q}^2}{2} + J_3^* \cdot \dot{g}_{\text{CBCP}} \cdot \dot{q} \cdot \cos(g_{\text{CBCP}} - q) & (\text{CBCP}). \end{cases}$$

$J_1^*$ ,  $J_2^*$  and  $J_3^*$  are given by (6.8–6.11).  $\dot{f}_{\text{sley,r}}$  is determined based on the sleigh motion law, with input angle  $g_{\text{CBCP}}$ , whereas  $\dot{f}_{\text{sley,l}}$  and  $\dot{f}_{\text{shed}}$  are determined based on the sleigh and shed motion law, with input angle  $g_{\text{sley}}$ . (7.12a–7.12b) constitutes a set of two second-order, nonlinear differential equations in  $g_{\text{sley}}$  and  $g_{\text{CBCP}}$ .

Without loss of generality, the initial condition  $g_{\text{sley}}(0) = 0$  is imposed<sup>25</sup>. This set of differential equations turns into a boundary value problem by imposing that  $g_{\text{sley}}(T) = g_{\text{sley}}(0) + 4\pi$ , and  $g_{\text{CBCP}}(T) = g_{\text{CBCP}}(0) + 4\pi$ , in order to guarantee the correct periodicity. This boundary value problem is again solved using a nonlinear least-squares approach, based on parameterizing  $\dot{g}_{\text{sley}}(t)$  and  $\dot{g}_{\text{CBCP}}(t)$  as a finite Fourier series with period  $T$  and average value  $4\pi/T$ .  $K = 50$  harmonics are used. The residual for the nonlinear least-squares problem is based on (7.12a–7.12b).

### 7.4.3 Simulation Results

Figure 7.30(a) shows, as a function of  $\Omega_{\text{shed}}$ , the maximum (over  $[0, T]$ ) of the CBCP torque  $M_c$ , for  $C_t = \{2.2, 11.1, 22.3\}$  N-m-s/rad. Results are given for both the CBCP and the FLY-configuration. In the latter case,  $M_c =$

<sup>25</sup> $g_{\text{CBCP}}(0) = 0$  can *not* be imposed.

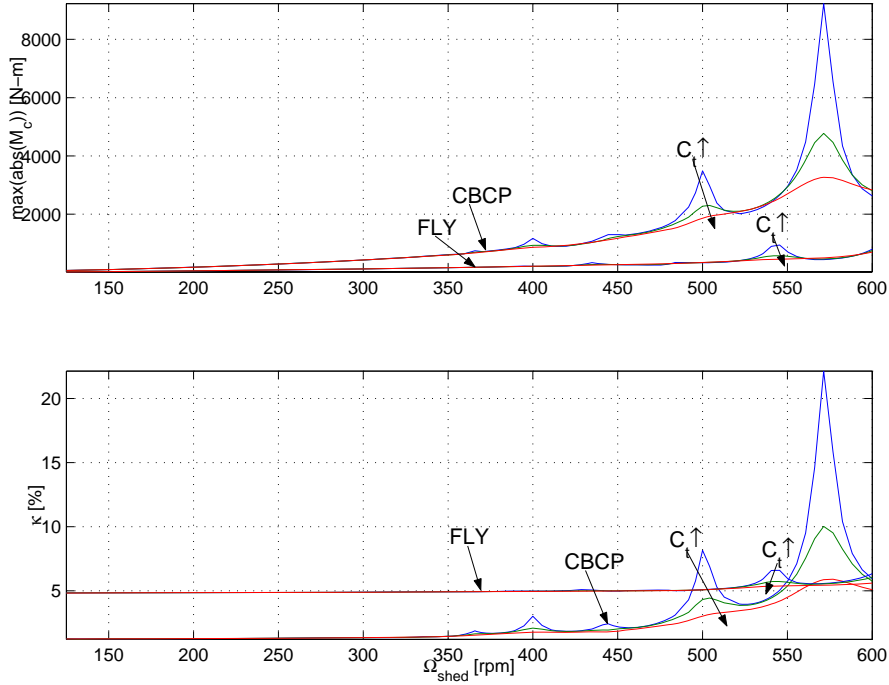


FIGURE 7.30: Simulation of torsional setup model in the FLY and the CBCP-configuration ( $C_t = \{2.2, 11.1, 22.3\}$  N-m-s/rad): (a)  $\max(|M_c|)$  [N-m] and (b)  $\kappa$  [%] as a function of  $\Omega_{shed}$ .

$J_{CBCP} \cdot \ddot{g}_{CBCP}$ . Resonance phenomena are present in both configurations, (with, quite obviously, higher peaks if damping is lower), but are much more pronounced in the CBCP-configuration.

The resonance frequency lies somewhere between 115 and 120 Hz (which is in the same order of magnitude as the resonance frequency predicted based on the one-degree-of-freedom model), and is excited in the CBCP-configuration by the harmonics of the CBCP torque. For instance, for  $C_t = 2.2$  N-m-s/rad, resonances occur at  $\{366, 400, 444, 500, 571\}$  rpm. These are excited by respectively the harmonics  $k = \{20, 18, 16, 14, 12\}$ . This is easily shown by multiplying the base frequencies corresponding to these drive speeds with the corresponding harmonic orders  $k$ , yielding frequencies  $\{122, 120, 118, 117, 114\}$  Hz, situated around the resonance frequency. In the FLY-configuration, the (small) resonance around 545 rpm is associated with the thirteenth harmonic of  $\ddot{g}_{CBCP}$ :  $13 \cdot 545/60 = 118$  Hz.

$C_t = 11.1$  N-m-s/rad seems to model quite realistically the sley axis damp-

ing, as it results in a first resonance peak in the CBCP-configuration at 500 rpm. This implies that the resonance is excited by the 14th CBCP torque harmonic, as is the case in the experimental setup. The resonance occurring at 500 instead of 413.5 rpm implies that  $K_t$  is overrated by a factor of about  $(500/413.5)^2 = 1.5$ , if it is assumed that the used inertia values are accurate. In the actual setup, additional torsional flexibility is possibly introduced by the clamping joints and the conical pressed fit discussed in Section 7.1.2.

Figure 7.30(b) shows  $\kappa$  [%] (determined based on  $\dot{g}_{\text{sley}}$ ) as a function of  $\Omega_{\text{shed}}$  for both the FLY and CBCP-configuration. This figure confirms that the CBCP torque harmonics excite the torsional resonance, as only small resonance peaks are present in the FLY-configuration with its clamped CBCP. This figure is also in good qualitative agreement with the experimentally observed  $\kappa$  shown in Fig.7.18.

The fact that the simulation results show (i) a first resonance phenomenon around 500 rpm for  $C_t = 11.1$  N-m-s/rad and (ii) almost no resonance if the CBCP is clamped, supports the hypothesis that the experimentally observed resonance phenomenon is due to the torsional flexibility of the sley axis, and that it is excited by the fourteenth harmonic of the CBCP torque.

## 7.5 Conclusion

**Average Speed Control** Average Speed Control has been developed as a novel control system technique for reciprocating machinery. As no stability or any other thorough theoretical analysis of its properties have been carried out, tuning of ASC is done by trial-and-error. Nevertheless, its performance is satisfactory, both in simulation as experimentally.

Applying ASC in simulation to the simplified setup model of Section 7.1.1, shows that a constant torque demand is obtained in regime. Nevertheless, the motor torque is slightly fluctuating, due to the instantaneous drive speed dependency of the motor model that converts the torque demand into the actual motor torque. However, since the motor torque fluctuation is small, a regime behavior is obtained that comes very close to the damped eigenmotion.

Experimentally, ASC illustrates its robustness by being stable, using the same controller settings, for both the FLY and the CBCP-configuration, and despite the presence of the torsional resonance phenomenon. Moreover, the average speed is controlled so accurately that reliable time-domain averaging of measurement signals is possible, with a minimum of leakage. As a result, frequency-domain filtering and differentiation of the measurement signals becomes possible.

**CBCP Torque** The experimental measurement campaign firstly shows that the CBCP delivers the designed torque ( $\epsilon \leq 10\%$ ) for  $\Omega_{\text{shed}} \leq 300$  rpm. Due to a torsional resonance, the CBCP torque starts to deviate significantly above that speed, although the CBCP still functions properly ( $\epsilon \leq 25\%$ ) below

350 rpm. From then on, the CBCP torque gradually 'explodes' and reaches a maximum of 2280 N-m (i.e. three times its predicted amplitude) at 413.5 rpm.

**Effect of CBCP on Dynamic Setup Behavior** A second goal of the measurement campaign is to assess the CBCP's effect on the setup's dynamic behavior. In order to distinguish between the flywheel effect and the torque balancing effect of the CBCP, the FLY and the CBCP-configuration are compared.

In the speed range of proper CBCP functioning (below 350 rpm), a significant improvement of the dynamic behavior is obtained: (i) the drive speed fluctuation  $\kappa$  is a factor 2.5 lower; (ii) the more significant, low-frequency sword and frame acceleration harmonics are on average reduced by between 5 and 14 dB; (iii) the frame vibration level is on average reduced by 5.2 dB (up-and-down motion) and 5.7 dB (out-of-plane motion); (iv) the sound pressure level in the microphone near the frames is reduced by more than 3 dB(A) in the speed range between 250 and 337 rpm, where the lower limit is due to the CBCP's rolling noise and the upper limit is again due to the torsional resonance.

The reduction of the frame vibration level brings us back to the primary goal of this work, that is, reducing vibration in reciprocating machinery. In a vulgarizing manner, this 'dB' result is restated as follows: *input torque balancing using the CBCP, results in halving the vibration level of the frames.*

The reduction of  $\kappa$  and the low-frequency sword and frame acceleration harmonics are in qualitative agreement with the simulation results of Section 6.6. Furthermore, the experimentally measured drive speed and acceleration in the FLY-configuration match quantitatively quite well with the ones determined in simulation, using the simplified, rigid-body setup model of Section 7.1.1. In order to explain the torsional resonance phenomenon however, this simple model needs extension with a torsional degree of freedom, which models the torsional flexibility, introduced by the long and hollow sley axis.

**Torsional Setup Model** The fact that the simulation results show (i) a first resonance phenomenon around 500 rpm for  $C_t = 11.1$  N-m-s/rad and (ii) almost no resonance if the CBCP is clamped, supports the hypothesis that the experimentally observed resonance phenomenon is due to the torsional flexibility of the sley axis, and that it is excited by a harmonic of the CBCP torque. Nevertheless, only an experimental campaign, focussing on the torsional resonance, can provide the ultimate proof of this hypothesis. Based on the formulated hypothesis, the logical solution for solving the resonance problems is augmenting the resonance frequency, through division of the CBCP over the left and right machine carter and stiffening of the sley axis.

**A Critical Note** Although the obtained experimental vibration and noise results are promising, care must be taken when evaluating them: the measured vibration and noise reduction levels are only valid for the machine present at PMA, that is, a machine à blanc. The heddles, tissue, . . . present in a complete industrial weaving machine may dramatically change its dynamic behavior. Hence, based on the present measurements, no conclusions can be drawn concerning the vibration, and, even more, the noise level reduction obtainable in an industrial machine. On the other hand, the torsional resonance inhibits revealing the full potential of the CBCP. Therefore, the next step in the evaluation of the CBCP should be its testing on a complete industrial weaving machine, after taking measures to obtain a sufficiently high torsional resonance frequency.

## Chapter 8

# Counterweight Balancing: State-of-the-Art

Westheimer's Discovery  
*A couple of months  
in the laboratory can save  
a couple of hours  
in the library.*

Frank H. Westheimer, chemistry professor (1912- )

**C**OMplete balance of any mechanism can be obtained by creating a second *mirror* mechanism connected to it, so as to cancel all dynamic forces and moments. Certain configurations of multicylinder internal combustion engines do this. The pistons and cranks of some cylinders cancel the inertial effects of others. However, this approach is expensive and is only justified if the added mechanism serves some second purpose such as increasing power, as in the case of additional cylinders in an engine (Norton, 2001).

This chapter gives an overview of the state-of-the-art of a more realistic balancing scheme: *counterweight balancing*, that is, dynamic balancing of linkages through the redistribution of link mass (by counterweight addition or link shape modification), given the kinematics of the mechanism.

**Scope** Dynamic balancing methods involving adaptations of the kinematic topology (such as dyad addition and addition of geared inertia counterweights) are quite related to counterweight balancing and are therefore also briefly addressed here. A more elaborate overview is for instance given in Section 1.4.2 of (VDI2149, 1999). Methods involving optimization of kinematic parameters have already been dealt with in Section 3.1.2.

Only planar mechanisms are considered here. For a survey of the rather limited number of papers on balancing of *spatial* mechanisms, the reader is referred to (Gill and Freudenstein, 1983; Chen, 1984; Kochev, 1987; Arakelian and Dahan, 2001). These papers focus on spatial one-degree-of-freedom linkages. Gosselin and Wu (2002) provide additional references, and develop interesting results concerning complete shaking force and shaking moment balancing of multi-degree-of-freedom parallel manipulators.

Several aspects of counterweight balancing of planar mechanisms are excluded here. They are listed below, together with 'entrance points' in literature: (i) the use of counterweights for reducing dynamic problems due to joint clearance [(Li and Bai, 1992), Section 3 of (VDI2149, 1999)]; (ii) the influence of link elasticity on dynamic balancing, either from a simulation point of view (Xi and Sinatra, 1997) or a design point of view (Zobairi et al., 1986a,b); (iii) the dedicated methods for shaking force, shaking moment and input torque balancing of slider-crank mechanisms in multicylinder engines [Chapter 14 of (Norton, 2001)]; (iv) methods based on redundant actuation (Thuemmel, 1995); (v) harmonic shaking force and shaking moment balancing, aiming at the reduction of certain dangerous harmonics [Section 1.3 of (VDI2149, 1999)].

**Aim** The survey by Lowen et al. (1983) constitutes the absolute literature reference concerning dynamic balancing up to 1983. An overview of German<sup>1</sup> literature until 1999, with a lot of interesting application examples, is given in (VDI2149, 1999). The completeness of the former literature survey, which covers Anglo-Saxon, German and Eastern-European literature by means of 156 references, is not claimed here. In the present survey, three aims are pursued. It is firstly meant as a gentle introduction to the subject for the newcomer in the field. Hence the presence of a section with basic definitions<sup>2</sup> (Section 8.1) and a section with basic theoretical results (Section 8.3).

Secondly, since linearly independent vector (LIV) expressions are a basic ingredient of the convex optimization framework of Chapter 9, Section 8.2 is entirely devoted to them and reveals the resemblance between LIV expressions and the minimal, linear models used in experimental robot identification. This bridging of the gap between the counterweight balancing community and the robotics community is considered to be a contribution of this thesis.

The focus of Chapter 9 lies on *formulating* the CWB optimization problem, not on numerical optimization results. Therefore, the third goal of the present survey, is to provide an overview of how the CWB optimization problem was *formulated* in the past. No detailed comparison of numerical results, resulting from these methods, is given.

---

<sup>1</sup>In German literature, the following terms are used: *Massenausgleich* for shaking force and shaking moment balancing; *Leistungsausgleich* for input torque balancing and *Gelenkkraftausgleich* for measures that aim at reducing bearing (or joint) forces.

<sup>2</sup>The only other gentle, but less complete introduction known to the author, is Chapter 13 in (Norton, 2001).

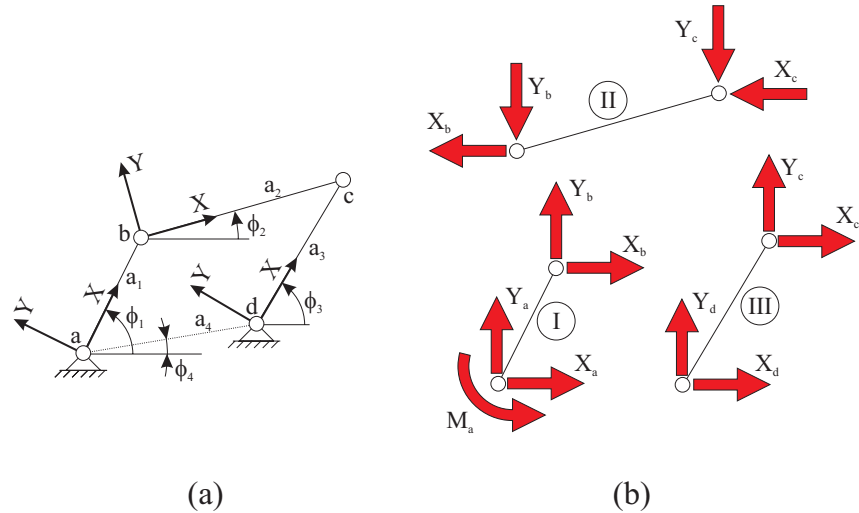


FIGURE 8.1: Kinematic scheme (a) and free-body diagram of a crank-rocker four-bar mechanism.

**Conventions** Unless stated otherwise, it is assumed in this, and the following chapter that (i) all linkages are planar and purely inertial and (ii) all four-bar mechanisms are  $4R$  four-bars, that is, they have four rotational joints (see Fig.8.1).  $m_i$  [kg] and  $J_i$  [kg-m<sup>2</sup>] denote link  $i$ 's mass and centroidal moment of inertia, while  $X_i$  [m] and  $Y_i$  [m] are the COG's coordinates w.r.t. some local coordinate system, fixed to the link. When counterweights are added, the counterweight mass parameters are indicated with a superscript  $(\cdot)^*$ , the original link mass parameters with a superscript  $(\cdot)^\circ$  and the link mass parameters after counterweight addition without superscript. Link numbers refer to the links in Fig.8.1.

## 8.1 Basic Definitions

This section gives some basic definitions related to dynamic balancing, and reviews some frequently used alternative formulations of Newton's laws.

**Shaking Force and Linear Momentum** The shaking force  $F_{\text{shak}}$  [N] exerted by a mechanism, is defined as the total force, transmitted to the machine frame, by the mechanism. It equals minus the sum of all ground bearing forces, where a ground bearing force is defined as a force, acting on a mechanism link through a ground bearing. In Fig.8.1,  $X_a$ ,  $X_d$ ,  $Y_a$  and  $Y_d$  are ground bearing

forces and the shaking force components equal:

$$\begin{aligned} F_{\text{shak},x} &= -(X_a + X_d); \\ F_{\text{shak},y} &= -(Y_a + Y_d). \end{aligned}$$

The linear momentum  $\vec{L}$  [kg-m/s] of a planar  $N$ -bar linkage (the ground link is denoted as link 0) equals

$$\vec{L} = \sum_{i=1}^{N-1} m_i \cdot \vec{v}_i,$$

where  $m_i$  [kg] and  $\vec{v}_i$  [m/s] respectively denote the link's mass and center of gravity's (vectorial) velocity.

The principle of linear momentum states that the time rate of change of linear momentum equals the sum of externally applied forces. If no external *work* forces are present, the only external forces are the ground bearing forces, and the following result is obtained:

$$F_{\text{shak},x} = -\frac{dL_x}{dt}; \quad (8.1)$$

$$F_{\text{shak},y} = -\frac{dL_y}{dt}. \quad (8.2)$$

An alternative (and time-integrated) formulation of the principle of linear momentum states that the shaking force is zero, provided that the linkage's overall<sup>3</sup> center of gravity  $S$  is stationary.

**Shaking Moment and Angular Momentum** The shaking moment  $M_{\text{shak}}$  [N] (taken w.r.t. some arbitrary point  $\hat{o}$ ) exerted by a mechanism, is defined as the total moment, transmitted to the machine frame, by the mechanism (w.r.t. the same point  $\hat{o}$ ). It is composed of the ground reaction  $-M_{\text{drv}}$  of the motor, as well as minus the moment due to the ground bearing forces<sup>4</sup>. In Fig.8.1,  $M_{\text{shak}}$  w.r.t.  $\hat{a}$  equals:

$$M_{\text{shak}} = -(M_a + Y_d \cdot a_4 \cdot \cos \phi_4 - X_d \cdot a_4 \cdot \sin \phi_4).$$

The angular momentum  $A$  [kg-m<sup>2</sup>/s] of a planar  $N$ -bar linkage (w.r.t. the reference point  $\hat{o}$ ) equals

$$A = \sum_{i=1}^{N-1} \vec{r}_i \times m_i \cdot \vec{v}_i + J_i \cdot \dot{\phi}_i,$$

<sup>3</sup>How  $S$  is determined is shown in Section 8.2.2.

<sup>4</sup>This is true provided that (i) the mechanism and the motor are mounted on the same frame and (ii) the motor actually delivers the required input torque, which is for instance not the case if Average Speed Control is applied (in that case, only a small constant torque acts on the motor stator).

where  $\vec{r}_i$  denotes the position vector of the  $i$ -th link's center of gravity w.r.t.  $\hat{o}$ .  $\dot{\phi}_i$  [rad/s] denotes the link's angular velocity.

The principle of angular momentum states that the time rate of change of angular momentum equals the sum of externally applied moments, both taken w.r.t. the same point  $\hat{o}$ . If no external *work* moments are present, the only external moments are the moment of the ground bearing forces and the driving torque  $M_{\text{drv}}$ , and the following result is obtained:

$$M_{\text{shak}} = -\frac{dA}{dt}.$$

**Driving Torque and Kinetic Energy** As already derived in Section 1.2.2, the driving torque  $M_{\text{drv}}$  [N-m] and the total kinetic energy  $T_{\text{tot}}$  [J] of a purely inertial, single-degree-of-freedom (input angle  $\phi_1$ ) mechanism are related by:

$$M_{\text{drv}} = \frac{1}{\dot{\phi}_1} \cdot \frac{dT_{\text{tot}}}{dt},$$

where the total kinetic energy  $T_{\text{tot}}$  of a planar  $N$ -bar linkage equals:

$$\sum_{i=1}^{N-1} \frac{m_i \cdot \|\vec{v}_i\|^2}{2} + \frac{J_i \cdot \dot{\phi}_i^2}{2}.$$

## 8.2 Linearly Independent Vectors

A fundamental concept in 'modern' dynamic balancing, and also in the developed convex optimization framework, is the *Linearly Independent Vector* (LIV) formalism, introduced by Berkof and Lowen (1969). This formalism expresses a dynamic reaction<sup>5</sup>  $d(t)$  as:

$$d(t) = \mathbf{e}^T(t) \cdot \mathbf{p} = \sum_{i=1}^n e_i(t) \cdot p_i. \quad (8.3)$$

$\mathbf{e} \in \mathbb{R}^n$  is a vector containing  $n$  linearly independent time functions  $e_i(t)$ , fixed by the mechanism's kinematics.  $\mathbf{p} \in \mathbb{R}^n$  is a vector of  $n$  constants  $p_i$  depending on the mass parameters and the kinematic parameters. Expressions like (8.3) are here generally referred to as LIV expressions.

Firstly, the different ways in which LIV expressions are used, is discussed in Section 8.2.1. How Berkof and Lowen (1969) determined these expressions is the subject of Section 8.2.2, while generalizations of the latter work are given in Section 8.2.3.

<sup>5</sup>LIV expressions have also been developed for the overall center of gravity (this was in fact their first use), the linear/angular momentum and the kinetic energy of a mechanism.

### 8.2.1 Purpose of LIV Expressions

#### Elimination of Dynamic Reactions

Firstly, because of the linear independence, eliminating a dynamic reaction  $d(t)$ , that is, imposing that  $d(t) \equiv 0, \forall t$  implies that

$$p_i = 0, \quad i = 1, \dots, n. \quad (8.4)$$

This is the basic idea proposed in (Berkof and Lowen, 1969), in which the coefficients of the non-stationary terms of  $\vec{r}_S$ , the position vector pointing to  $S$  (the mechanism's overall center of gravity), are required to be zero for obtaining a stationary  $S$  and hence complete shaking force balance.

In case of a four-bar with constant input crank speed, (8.4) respectively leads to  $n = 4$ ,  $n = 5$  and  $n = 3$  conditions for obtaining shaking force, shaking moment or input torque balance. Only the shaking force balance conditions lead to physically realizable counterweight mass parameters (that is,  $m_i^* \geq 0$  and  $J_i^* \geq 0$ ). The shaking moment balance conditions lead to the requirement of negative counterweight inertia (Section 8.3.2), while the input torque balance conditions impose the mechanism to be in fact massless (Elliott and Tesar, 1977).

#### Specification of Dynamic Reaction Values

If a vector  $\mathbf{d} \in \mathbb{R}^K$  of desired values  $d(t_k)$  at the time instances  $t_k, k = 1 \dots K$  is constructed<sup>6</sup>:

$$\mathbf{d} = [d(t_1) \quad \dots \quad d(t_K)]^T, \quad (8.5)$$

as well as a corresponding matrix  $\mathbf{E} \in \mathbb{R}^{K \times n}$ , defined as

$$\mathbf{E} = [e(t_1) \quad \dots \quad e(t_K)]^T, \quad (8.6)$$

then, because of the linear independence,  $\mathbf{E}$  is of full rank and the linear set of equations

$$\mathbf{E} \cdot \mathbf{p} = \mathbf{d} \quad (8.7)$$

can be solved exactly for  $K = n$  and in the least-squares sense for  $K > n$ . This use of LIV expressions is proposed in (Elliott and Tesar, 1977, 1982), however without a method for determining the actual link mass parameters from the calculated  $p_i$  values. In fact, if feasibility constraints on the mass parameters are to be taken into account, (8.7) must be integrated in an optimization problem formulation.

<sup>6</sup> $K$  denotes the number of considered time instances. It hence has a different meaning than in Chapter 2–7, in which  $K$  denotes the number of harmonics in a Fourier series.

### Calculation of the RMS Value of Dynamic Reactions

The rms value  $d_{\text{rms}}$  of a dynamic reaction  $d(t)$  is defined as:

$$d_{\text{rms}} = \sqrt{\frac{1}{T} \cdot \int_0^T d(t)^2 dt},$$

where  $T$  [s] determines the mechanism's period of motion. Numerically evaluating this integral is done based on:

$$d_{\text{rms}} = \sqrt{\frac{1}{K} \cdot \sum_{k=1}^K d^2(t_k)}, \quad (8.8)$$

where  $K \in \mathbb{Z}$  denotes the (sufficiently big) number of samples in one period and  $t_k = (k-1) \cdot T_s$ . The sample period  $T_s$  [s] equals  $T/K$ . Based on (8.5–8.7), (8.8) is converted into:

$$d_{\text{rms}} = \sqrt{\frac{\mathbf{d}^T \cdot \mathbf{d}}{K}} = \sqrt{\frac{\mathbf{p}^T \cdot \mathbf{E}^T \cdot \mathbf{E} \cdot \mathbf{p}}{K}}. \quad (8.9)$$

$\mathbf{E}^T \cdot \mathbf{E}$  is symmetric and positive definite, and only depends on the mechanism kinematics. Hence, (8.9) yields an efficient way of calculating  $d_{\text{rms}}$  if the kinematics of a mechanism are fixed, and the effect of changing mass parameters is under study.

### Experimental Identification Based on Dynamic Reactions

If the kinematics of a mechanism are measured experimentally, as well as a particular dynamic reaction, (8.3) provides a basis for estimating<sup>7</sup> the constants  $p_i$  of an open or closed kinematic chain of rigid bodies. *Experimental identification* based on (8.3) is well-known in the robotics community, which requires accurate estimates of the  $p_i$  for simulation and control purposes.

Quite remarkably, not a single cross-reference exists between the papers using (8.3) for experimental identification (denoted as experimental robot identification (ERI) literature) and those using (8.3) in the area of counterweight balancing (denoted as counterweight balancing (CWB) literature). As a result, methodologies for developing LIV expressions have been developed independently in both communities. Where these methodologies are symbolical and only intended for planar, closed-loop kinematic chains (mechanisms) in the area of CWB, both symbolical and numerical approaches, both for 3D,

<sup>7</sup>Depending on the noise properties of the measured quantities, an unbiased estimate of the 'true' parameters  $\mathbf{p}$  is obtained based on a least-squares problem, a weighted least-squares problem, . . . . A comprehensive overview is given in (Swevers et al., 1997) and (Ganseman, 1998).

open loop (serial robots) and closed-loop (parallel robots) kinematic chains have been developed in ERI. The flavor of symbolical CWB methods is clarified in Section 8.2.2 and 8.2.3. Numerical methods are based on eliminating linear dependency (rank deficiency) through application of the singular value decomposition (SVD) or other matrix factorizations. The development of such a novel method is the subject of Section 9.5.

CWB literature focuses on all dynamic reactions, whereas the main focus of ERI literature is on the driving torque(s). That is, the  $p_i$  factors are in general experimentally identified using driving torque measurements. An exception to this is the work of Raucet et al. (1992), who (i) show that the set of  $p_i$  factors for the actuator torques of a serial robot, is a subset of the set of  $p_i$  factors for the ground reaction forces and torques<sup>8</sup> and (ii) experimentally identify this set of parameters, based on the measured ground reaction forces and torques. The cost of a force-torque sensor capable of carrying a robot is however high, which reduces the industrial applicability of this approach.

Briefly reviewing ERI literature here, it can be said that its foundation was laid by the work of Atkeson et al. (1986). They introduced a numerical, SVD based procedure for determining LIV expressions for the driving torques of a serial robot. Symbolical methods were first introduced for serial robots (Mayeda et al., 1990; Gautier and Khalil, 1990), and later on for robots with closed kinematic chains (Bennis et al., 1992). Symbolic methods have the advantage of providing more analytical insight than numerical methods. However, they are very complicated and do not guarantee to eliminate all linear dependency, although most of the times, they do (Khalil and Bennis, 1995; Chen et al., 2002).

## 8.2.2 Basic Berkof-Lowen Method

'Modern' literature on dynamic balancing starts with the seminal paper of Berkof and Lowen (1969), which develops the so-called *Method of Linearly Independent Vectors* (LIV) for complete *force balancing*<sup>9</sup> of simple, planar linkages (four-bars and six-bars are considered). Given the importance of this paper, and the relevance of LIV expressions for the developed convex optimization framework, its methodology and main results are reviewed here for the case of a four-bar linkage.

Imposing complete force balance is equivalent to requesting a stationary center of gravity (COG)  $S$  of the total linkage. The vector  $\vec{r}_s$ , giving the

---

<sup>8</sup>Ground reaction forces and torques are the equivalent of shaking forces and shaking moments in CWB literature.

<sup>9</sup>A mechanism is shaking force balanced, or force-balanced for short, if it exerts no shaking force on its supporting frame.

position of  $S$  w.r.t.  $\hat{a}$  (see Fig.8.1) equals:

$$\vec{r}_s = \frac{1}{m} \cdot \sum_{i=1}^3 m_i \cdot \vec{r}_i, \quad (8.10a)$$

where  $m$  [kg] denotes the total mechanism mass and  $\vec{r}_i$  the position vector of the  $i$ -th link's center of gravity w.r.t.  $\hat{a}$ . Using complex notation, the following expressions for  $\vec{r}_i$  are obtained, based on Fig.8.1:

$$\vec{r}_1 = r_1 \cdot \exp(j \cdot (\phi_1 + \theta_1)); \quad (8.10b)$$

$$\vec{r}_2 = a_1 \cdot \exp(j \cdot \phi_1) + r_2 \cdot \exp(j \cdot (\phi_2 + \theta_2)); \quad (8.10c)$$

$$\vec{r}_3 = a_4 \cdot \exp(j \cdot \phi_4) + r_3 \cdot \exp(j \cdot (\phi_3 + \theta_3)), \quad (8.10d)$$

where  $j$  is the imaginary unit, while  $(r_i, \theta_i)$  denotes the polar coordinates of the COG of link  $i$  w.r.t. the local coordinate system (LCS) attached to that link.  $a_i$  [m] and  $\phi_i$  [rad] respectively denote the link lengths and the link angles.  $\phi_4$  is constant as a function of time. The basic idea of the method of LIV is to apply the loop closure equation

$$a_1 \cdot \exp(j \cdot \phi_1) + a_2 \cdot \exp(j \cdot \phi_2) - a_3 \cdot \exp(j \cdot \phi_3) - a_4 \cdot \exp(j \cdot \phi_4) = 0,$$

such that (8.10a–8.10d) is rewritten as a linear combination of linearly independent vectors  $\vec{e}_i$ , by eliminating  $\phi_2$ :

$$m \cdot \vec{r}_s = p_1 \cdot \vec{e}_1 + p_2 \cdot \vec{e}_2 + p_3 \cdot \vec{e}_3, \quad (8.11)$$

where

$$\vec{e}_1(t) = \exp(j \cdot \phi_1);$$

$$\vec{e}_2(t) = \exp(j \cdot \phi_3);$$

$$\vec{e}_3 = \exp(j \cdot \phi_4),$$

and

$$p_1 = m_1 \cdot r_1 \exp(j \cdot \theta_1) + m_2 \cdot a_1 - m_2 \cdot \frac{a_1}{a_2} \cdot r_2 \cdot \exp(j \cdot \theta_2);$$

$$p_2 = m_3 \cdot r_3 \exp(j \cdot \theta_3) + m_2 \cdot \frac{a_3}{a_2} \cdot r_2 \cdot \exp(j \cdot \theta_2);$$

$$p_3 = m_3 \cdot a_4 + m_2 \cdot \frac{a_4}{a_2} \cdot r_2 \cdot \exp(j \cdot \theta_2).$$

Hence  $S$  can be made stationary if the time-independent, complex-valued coefficients  $p_1$  and  $p_2$  of the time-dependent terms  $\vec{e}_1(t)$  and  $\vec{e}_2(t)$  vanish.

Employing Cartesian COG coordinates  $X_i = r_i \cdot \cos(\theta_i)$  and  $Y_i = r_i \cdot \sin(\theta_i)$ , this gives rise to the following four scalar equations:

$$m_1 \cdot X_1 + a_1 \cdot m_2 - \frac{a_1}{a_2} \cdot m_2 \cdot X_2 = 0; \quad (8.14)$$

$$m_1 \cdot Y_1 - \frac{a_1}{a_2} \cdot m_2 \cdot Y_2 = 0; \quad (8.15)$$

$$m_3 \cdot X_3 + \frac{a_3}{a_2} \cdot m_2 \cdot X_2 = 0; \quad (8.16)$$

$$m_3 \cdot Y_3 + \frac{a_3}{a_2} \cdot m_2 \cdot Y_2 = 0. \quad (8.17)$$

These equations imply that, if the mass properties of one link are given, the mass properties of the remaining links can be rearranged for full force balance (through link shape modification or counterweight addition). Full force balance is maintained regardless of the input crank speed trajectory.

### 8.2.3 Extensions of Berkof-Lowen Method

#### Four-Bar Mechanisms

Berkof and Lowen (1971) show that the shaking moment of a *force-balanced* four-bar linkage is a pure couple, for which the following LIV expression with  $n = 4$  terms is valid:

$$M_{\text{shak}} = \sum_{i=1}^4 K_i \cdot \ddot{\phi}_i. \quad (8.18)$$

The first term of the summation drops if the input crank speed  $\dot{\phi}_1$  is constant.  $\ddot{\phi}_4$  is a composite time function depending on the mechanism's kinematics. The constants  $K_i$  are given by:

$$\begin{aligned} K_i &= -J_i - m_i \cdot (X_i^2 + Y_i^2) + a_i \cdot m_i \cdot X_i \quad (i = 1, 2, 3); \\ K_4 &= -2 \cdot a_1 \cdot m_2 \cdot Y_2. \end{aligned}$$

A comparable result for the driving torque of a force-balanced four-bar, with the additional restriction that it be *inline*<sup>10</sup> is given in (Berkof, 1979).

Elliott and Tesar (1977) provide complete results for four-bar mechanisms, in two senses. Firstly the force balance conditions are given for all of the four-bar mechanisms, that is, the  $4R$  four-bar, the slider-crank, the inverted slider-crank, and the oscillating block mechanism. Secondly, and without requiring force balance, LIV expressions are developed for the shaking moment<sup>11</sup> and driving torque. These LIV expressions consist of  $n = 6$  and  $n = 4$  terms for

<sup>10</sup>A mechanism is inline if all of its links are inline. An inline link is a link of which the COG lies on the line connecting the pivots. This line may extend beyond the pivots.

<sup>11</sup>With respect to the input crank pivot, denoted by  $\hat{a}$  in Fig.8.1

the shaking moment<sup>12</sup> and the driving torque of a  $4R$  four-bar respectively. In both cases, one term drops if the input crank speed is constant.

In (Tepper and Lowen, 1975), LDV expressions are developed for the ground bearing forces of a four-bar mechanism. LDV, or linearly *dependent* vector expressions, are of the general form (8.3), but with linearly dependent time functions  $e_i(t)$ . The ground bearing force LDV expressions are developed by rearranging the force equations, which are obtained through application of the principle of superposition<sup>13</sup> in (Lowen et al., 1974). By application of the loop closure equations, these LDV expressions could be turned into LIV expressions.

A 'boot-strap' method for obtaining LDV expressions for the joint forces in a four-bar is proposed in (Lee and Cheng, 1984). This method is based on successive and combined applications of Newtonian and Lagrangian mechanics.

Both aforementioned papers are the only examples in which LDV expressions for joint forces are developed. A new, general method for automated generation of LIV expressions for joint forces, is developed in Section 9.5.3.

### **$N$ -bar Mechanisms**

Tepper and Lowen (1972) extend the LIV formalism of (Berkof and Lowen, 1969) to determine force-balance relations for planar, one-degree-of-freedom  $N$ -bar mechanisms. As a result, force balancing rules for such mechanisms are derived (see Section 8.3.1). A reformulation of this formalism in terms of vector algebra, as well as some additional theoretical developments, are presented in (Kochev, 1988).

Elliott and Tesar (1982) develop a general method for determining LIV expressions for the shaking force, shaking moment and driving torque of planar  $N$ -bar mechanisms. Since using the loop closure equations for elimination of linear dependency is burdensome for an  $N$ -bar linkage with  $N > 4$ , a different approach, based on applying systematic elimination rules, is proposed. These rules, though rather complicated, are easily implementable in a computer program. As a side result of the procedure, also expressions for the number

---

<sup>12</sup>Note: Elliott and Tesar (1982) indicate that the result for the shaking moment of the slider-crank mechanism is erroneous.

<sup>13</sup>For the case of a four-bar mechanism, application of this principle proceeds as follows. Six different mechanisms are derived from the original mechanism, by considering in turn two out of its three links to be massless and the third link to have either zero mass or inertia. For each of these mechanisms, application of Newton's laws is very simple due to the presence of two massless links and the absence of mass or inertia in the third link. Afterwards, each force/moment in the original mechanism is determined as the sum of the corresponding forces/moments in the six 'help' mechanisms.

$n$  of linearly independent vectors are given:

$$\begin{aligned} n_{\text{msh}} &= s - j - h; && \text{(angular momentum and shaking moment)} \\ n_{\text{fsh}} &= s - 2 \cdot j; && \text{(linear momentum and shaking force)} \\ n_{\text{drv}} &= s - j - 2 \cdot f, && \text{(kinetic energy and driving torque)} \end{aligned}$$

where  $s = 4 \cdot (N - 1)$  is the number of available mass parameters,  $j$  is the number of lower-pair connectors (revolute joints and prismatic joints),  $f$  is the number of lower-pair connectors attached to ground and  $h = 2$  if the angular momentum/shaking moment is measured about a revolute fixed pivot and zero otherwise. The authors however have to indicate that  $n$  is an overestimation<sup>14</sup>, as special geometries, such as parallelograms, introduce additional dependencies.  $n_{\text{msh}}$  and  $n_{\text{drv}}$  reduce by one if a constant drive speed is applied, since the mechanism dynamics is then independent of the moment of inertia of the driving crank.

Kochev (1991) builds upon this work and shows that the methodology significantly simplifies if an alternative formalism is adopted. His formalism also leads to particular invariant forms of the angular momentum, leading to some interesting and intuitive balancing options for  $N$ -bar mechanisms.

## 8.3 Main Theoretical Results

### 8.3.1 Shaking Force Balancing of Planar Linkages

**Balancing of  $N$ -bar Mechanisms** Tepper and Lowen (1972) develop a contour theorem to differentiate between mechanisms which can be fully force-balanced and those which cannot: *A planar mechanism without axisymmetric link groupings can be fully force-balanced by internal mass redistribution if, and only if, from each link there is a contour (a path) to the ground by way of revolute joints only.* Hence, if a link (or a group of links) is entirely surrounded by prismatic joints, the mechanism cannot be fully force-balanced. Furthermore, this implies that all linkages that contain only revolute joints, are fully force balanceable.

Bagci (1979) coins the term *irregular force transmission mechanism* for mechanisms that do not comply with the contour theorem. The contour theorem is generalized to spatial mechanisms by stating that a force transmission irregularity is generated 'by a link or a group of links which have connections to the frame through pairs all permitting linear freedoms'<sup>(15)</sup>. In order to make such a mechanism force balanceable, it is suggested to connect

---

<sup>14</sup>This is exactly the same problem as with the symbolical methods from ERI literature

<sup>15</sup>In planar mechanisms, such pairs are the prismatic and revolute-prismatic pairs. In a spatial mechanism these are cylinder pairs, prismatic pairs and other pairs permitting linear pair freedoms.

the problematic link (or group of links) to the frame using a two-link mechanism (a 'force-balancing idler loop'), containing only revolute (or revolute and spherical joints in a spatial mechanism) joints.

For single-degree-of-freedom, planar  $N$ -bar mechanisms that comply with the contour theorem, the *apparent* minimum number of counterweights, resulting in full force balance, equals  $N/2$  (Tepper and Lowen, 1972). The term *apparent* is coined because, although it seems theoretically possible to obtain full force balance with fewer than  $N/2$  counterweights, it is found impossible for practical examples to obtain physically realizable solutions (that is, with positive mass counterweights) with fewer than  $N/2$  counterweights.

Based on the complex mass method (see further), Walker and Oldham (1979) derive an expression<sup>16</sup> for the minimum number of counterweights for a *multi*-degree-of-freedom, planar  $N$ -bar mechanism. Furthermore, advisory guidelines are given for selecting the links to which counterweights are attached, so as to obtain the best results w.r.t. joint forces, shaking moment and driving torque. These guidelines are in agreement with the advice (without formal justification) given in (VDI2149, 1999): 'Balancing actions should preferably be carried out at links that a) are connected with the frame by a revolute joint or b) are connected with a link that belongs to a).'

**Complex Mass Formalism** Besides the formalism based on LIV expressions, a second formalism (not requiring the determination of the mechanism's kinematics) has been developed (Smith, 1975; Oldham and Walker, 1978; Walker and Oldham, 1978, 1979) for force balancing  $N$ -bar planar linkages. Lowen et al. (1983) term it the *Complex Mass Method*. Both formalisms are comprehensively reviewed, with indication of their benefits and disadvantages, by Yao and Smith (1993), who propose a simplification of the complex mass method.

**Sensitivity and Robustness** Due to unavoidable manufacturing tolerances and the unpredictable nonhomogeneity of the materials used, the shaking force of an actual mechanism, built to be theoretically force-balanced, generally does not vanish completely. In a set of two papers (Tricamo and Lowen, 1981a,b), Tricamo and Lowen address this problem. The former paper shows, based on the results of Tepper and Lowen (1972), that it is theoretically possible to find  $N/2$  correction masses (based on the experimentally measured residual shaking forces as well as the link velocities) to remove the residual shaking forces of all types of fully force balanceable, single-degree-of-freedom, planar  $N$ -bar mechanisms.

---

<sup>16</sup>This expression confirms the contour theorem. It however overestimates the required number of counterweights for linkages with either special geometries (such as parallelograms) or special mass distributions, of which they give an illustrative example in the discussion of their results.

This technique is experimentally validated, using a developed fine-balancing machine, in the latter paper and shown to reduce the magnitudes of the residual shaking force components by more than 50 percent. This work in fact shows a lot of similarities with the work of Raucent et al. (1992) on experimental robot identification.

Li (1998) investigates, from a theoretical point of view, the sensitivity to manufacturing tolerances of the shaking force (as well as the shaking moment) and applies the developed formulae to a planar four-bar mechanism. In order to obtain robust balancing results, an optimization approach is suggested, in which the goal function is a weighted combination of the dynamic reactions and their sensitivity functions w.r.t. to the uncertain mass parameters.

**Partial Force Balancing of Four-Bars** In a set of two papers (Tricamo and Lowen, 1983a,b), Tricamo and Lowen develop analytical *partial* force balancing results for four-bars running at constant speed. It is shown that imposing a specified reduction of the maximum shaking force gives rise to a quadratic equality constraint (the *equipollent circle constraint equation*) in the mass-distance products  $m_i \cdot X_i$  and  $m_i \cdot Y_i$  of link II and link III. These mass-distance products subsequently fix the link I mass-distance products, based on a general, nonlinear equation.

### 8.3.2 Shaking Moment Balancing of Planar Linkages

**Isomomental Ellipses** Berkof and Lowen (1971) show that the shaking moment of a *force-balanced* four-bar linkage is a pure couple, i.e., it does not depend on the chosen reference point. This follows from the fact that it is the sum of two pure couples: (i) the motor torque and (ii) the moment of the ground bearing forces. The latter moment is a pure couple due to the fact that the two ground bearing forces are equal in magnitude and opposite in direction, because of the force-balance.

If a planar mechanism is not fully force-balanced, its shaking moment is dependent on the chosen reference point. For this case, Tepper and Lowen (1973) show that the rms shaking moment is constant<sup>17</sup> with respect to all points which lie on certain (concentric and proportional) ellipses. The center<sup>18</sup> of these *isomomental* ellipses represents the point of minimum rms shaking moment. Points lying on larger ellipses are points w.r.t. which the rms shaking moment is bigger. This theory is extended in (Kochev and Gurdev, 1989) to the case of external forces acting on the linkage.

---

<sup>17</sup>Even though the derivation assumes constant input angular velocity and identical density for all links, the results may be extended to cases in which these conditions are not fulfilled.

<sup>18</sup>The location of this minimum point depends only on the kinematic parameters.

**Shaking Force and Shaking Moment Balance Using Inertia Counterweights** In (Berkof and Lowen, 1971), the LIV expression (8.18) is derived, based on which it is shown that, except for special cases<sup>19</sup>, internal mass redistribution (no additional links) cannot yield full shaking moment balance of a force-balanced four-bar linkage, since it requires negative moment of inertia.

Negative moment of inertia can be obtained by addition of *inertia counterweights*, that is, rotary inertias rotating or oscillating with the opposite angular velocity of the corresponding links. An inertia counterweight is driven by its corresponding link, for instance through gears or a figure-eight timing belt or chain. A *geared* inertia counterweight is shown in Fig.8.2. Its properties are comprehensively discussed in (Berkof, 1973), where it is recognized that the backlash and the loads on the gear teeth may be large and pose serious design problems. As a way to overcome this, Elliott et al. (1979) suggest to drive the counterweight using a dyad, which is not a perfect angular inverter, but comes quite close to it (less than 1% error in the presented design example).

Berkof (1973) shows, based on (8.18), that complete shaking force and shaking moment balance of a four-bar linkage (regardless of any variation of the input speed) is possible, provided that (i) the mass of link II is redistributed such that it becomes inline, as well as a physical pendulum<sup>20</sup>; (ii) counterweights are added to the input link I and the output link III so as to comply with (8.10a–8.10d); (iii) an inertia counterweight of inertia  $-K_1$  [kg-m<sup>2</sup>] is added to the input link I; (iv) an inertia counterweight with inertia  $-K_3$  is added to the output link III.

The cost of achieving full shaking force and shaking moment balance is a larger motor to supply the increased motor torque, shorter life due to greater joint forces, and the extra counterweight masses. Figure 8.3 shows a force and shaking moment balanced four-bar, illustrating the significant additional masses. If this particular example is driven with constant drive speed (in that case, the input link's inertia counterweight drops), the required input torque quadruples, while the joint forces on average double.

The more general LIV expressions developed in (Elliott and Tesar, 1977) confirm (Berkof, 1973), and complement them by proving that not only the coupler, but in fact all mechanism links must be inline for simultaneous shaking force and shaking moment balance. A general methodology, not based on LIV expressions, for achieving complete shaking force and shaking moment balance of  $N$ -bar planar linkages, through the use of counterweights and inertia counterweights, is presented in (Yang and Zhang, 1995).

**Other Approaches for Obtaining Shaking Force and Shaking Moment Balance** Another approach towards complete force and shaking mo-

<sup>19</sup>Such as a parallelogram ( $\ddot{\phi}_2 \equiv 0$ ) running at constant velocity ( $\dot{\phi}_1 = \dot{\phi}_3 \equiv 0$ ) with an inline coupler.

<sup>20</sup>An inline link of length  $a$  is a physical pendulum if its moment of inertia is precisely related to the location of its COG by:  $J = m \cdot X \cdot (a - X)$ . A comprehensive discussion of this concept and how to construct physical pendula is given in (Berkof, 1973).

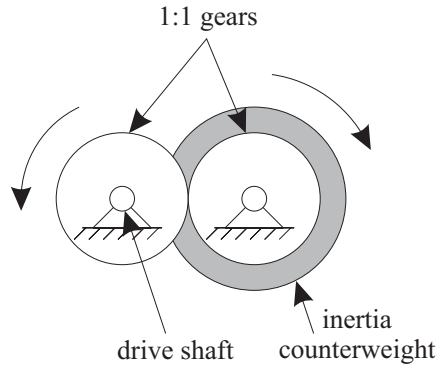


FIGURE 8.2: Geared inertia counterweight.

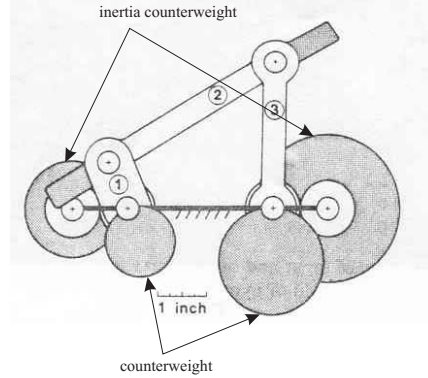


FIGURE 8.3: Shaking force and moment balanced four-bar. Reproduced from (Berkof, 1973).

ment balancing of  $N$ -bar linkages, introduced in (Bagci, 1982), is the addition of moment balancing idler parallelogram loops (in conjunction with inertia counterweights), which provides an extension of the force balancing idler loops discussed in Section 8.3.1. Although the method is conceptually simple, the resulting mechanism configurations are quite complex, even in the case of a four-bar, therefore compromising its practical applicability.

Further concepts for achieving complete shaking force and shaking moment balance in planar linkages are discussed in (Arakelian and Smith, 1999) and the survey by Kochev (2000). All of these methods result in very complex configurations however, such that Kochev has to decide: 'The price paid for shaking force and shaking moment balancing is discouraging. It ranges from a four times increase in added complexity and masses in the case of duplicate linkages, up to a seven times rise for methods employing parallelograms to transfer the rotations of floating members to the ground revolutes.'

## 8.4 Optimization Approaches

In a reaction<sup>21</sup> on (Berkof and Lowen, 1969), Ku made the following remarks concerning the developed shaking force balancing method. These remarks are reproduced here, since they give the basic motivation for formulating counterweight balancing as an optimization problem:

'Firstly, although this method ensures that the vector sum of the forces acting on the mechanism frame vanish at all times, the individual force com-

<sup>21</sup>This reaction, as well as the author's closure are found on p.26 of (Berkof and Lowen, 1969).

ponents in the horizontal and vertical directions are nevertheless finite and time varying. Hence, each of the linkage supports at the frame is individually still being subjected to a cyclic shaking force. The magnitude of these forces may actually be greater than the magnitude before balancing, due to the added counterweights. (...) Secondly, this method of balancing, in common with many other linkage balancing methods, does not eliminate the cyclic rocking moment acting on the frame due to the equal but opposite vertical force components acting on the linkage supports. Again, this shaking moment may actually be greater than that of the 'unbalanced' case.'

These qualitative remarks are quantified in (Lowen et al., 1974), which reports on the influence of *full force balancing* on the joint forces, the input torque and the shaking moment of 39 families of crank-rocker four-bar linkages of standard inline configuration, running at constant input speed. The main conclusions drawn by the authors are twofold. (i) With very few exceptions (with up to fivefold increases), the (rms and maximum values of the) joint forces, the input torque, as well as the shaking moment increase by no more than 50%. (ii) The counterweight<sup>22</sup> diameters vary between slightly less than the crank length to more than three times the crank length. *These rather large counterweight dimensions represent the most pronounced drawback of full force balancing.* The use of thicker counterweights or a denser counterweight material may offer some solution in such cases.

The above discussion shows that, 'as with any design endeavor, there are trade-offs' (Norton, 2001) and 'a compromise between the effect on the frame, the effect to the input and the joint loads is to be searched for' (VDI2149, 1999). A typical engineering way of handling these trade-offs is to incorporate them into an optimization problem.

This section surveys the optimization approaches that have been proposed for obtaining the aforementioned compromise. Two groups of approaches are distinguished: those combining full force balance with minimization of the shaking moment or driving torque (Section 8.4.1) and those giving up the requirement of full force balance, and aiming at a simultaneous minimization of (some or) all dynamic reactions. (Section 8.4.2) Focus lies on how the optimization problem is formulated, not on the obtained results.

### 8.4.1 Full Force Balance Approaches

Approaches requiring full force balance have the advantage that the shaking moment is independent of the reference point. On the other hand, for a planar  $N$ -bar mechanism, imposing full force balance already imposes  $N$  conditions<sup>23</sup> on the  $4 \cdot (N - 1)$  available mass parameters.

<sup>22</sup>The counterweights are made of the same material as the links and have a thickness equal to 2.5 times the link thickness.

<sup>23</sup> $N/2$  counterweights are required for balancing an  $N$ -bar mechanism. Per counterweight, two conditions are imposed on the mass parameters. For instance: a four-bar can be balanced using two counterweights, satisfying four conditions, that is (8.14–8.17).

**Berkof/Lowen Approach** Berkof and Lowen (1971) minimize, in the root-mean-square sense, the shaking moment of an inline, force-balanced four-bar mechanism, based on (8.18). It is analytically shown that, if the value of one  $K_i$  is chosen, the optimal values of the remaining  $K_i$  are proportional to it, with a proportionality factor purely dependent on the link lengths. However, the fact that one  $K_i$  needs to be chosen beforehand introduces suboptimality, as indicated by (Haines, 1981).

The problem of determining the link mass properties in order to obtain the desired (suboptimal)  $K_i$  values in the case of constant input crank speed, is considered in (Lowen and Berkof, 1971) and in (Carson and Stephens, 1978). Slightly oversimplifying, it can be said that the former paper is based upon a shape parameterization of the links, such that the link mass properties are fully determined by the shape parameters (amongst which are the link lengths  $a_i$ ). Then, nomograms are developed in which lines of the desired<sup>24</sup> and actually realized  $K_i$  are plotted as a function of the shape parameters. Intersections of these lines give shape parameter values, and hence link shapes, that realize in practice the desired (suboptimal)  $K_i$  values.

The approach in Carson and Stephens (1978) is not based on a mass parameterization, and starts from the premise that the link lengths are fixed beforehand by the kinematic mechanism synthesis. Again, dedicated nomograms are developed, as well as an iterative procedure for applying them, so as to obtain link mass parameters that are physically meaningful (no negative moment of inertia). The problem of determining the link shapes from the desired mass parameters is not addressed. In this respect, (Lowen and Berkof, 1971) is superior, as it automatically generates the link shapes. However, it is not clear if this approach yields satisfactory results if the link lengths are fixed beforehand: the only shape parameters allowed to vary in the presented results are the link lengths and one additional shape parameter. It is not clear if there actually are intersections of the desired and actually realized  $K_i$ -lines, if the link lengths are kept fixed.

In (Berkof, 1979), LIV expressions for the driving torque of an inline, force-balanced four-bar mechanism are derived, and shown to have the same structure as (8.18). As a result, the same suboptimal optimization technique as in (Berkof and Lowen, 1971; Lowen and Berkof, 1971) is applied to minimize in the root-mean-square sense, the mechanism's driving torque.

**Wiederrich/Roth Approach** Wiederrich and Roth (1976) consider force-balanced, purely inertial four-bars with constant input crank speed and develop analytical design rules for reducing the shaking moment. They work directly with the angular momentum instead of the shaking moment, and use a formalism, based on representing the four mass parameters of a link by

---

<sup>24</sup>Remember that the desired  $K_i$  themselves are a function of the kinematic parameters, and hence depend also on the shape parameters, since the kinematic parameters are a subset of the shape parameters.

two equivalent point masses. The design rules are developed by reducing the dominating, time-dependent terms of the angular momentum expression. The resulting rules are approximate (the authors speak about 'good balance'), but very simple and do not require knowledge of the linkage kinematics. They are therefore useful if numeric optimization tools are not available, or for providing a good initial guess for numeric optimization.

**Haines Approach** Haines (1981) considers the same problem as in (Berkof and Lowen, 1971; Lowen and Berkof, 1971), that is, minimization in the root-mean-square sense of the shaking moment of a force-balanced four-bar mechanism, however without inline restrictions. The significance of this paper is somewhat underestimated: it appears only as a supplementary reference in the survey (Lowen et al., 1983), and except for Kochev, most authors in the area of dynamic balancing do not incorporate this paper in their literature surveys. Nevertheless, it makes a double contribution: (i) it stresses the beneficial superposition properties of an alternative mass parameterization, termed the  $\mu$ -parameters in this thesis, and (ii) it generalizes and interprets all of the approaches described in this section, within a common framework.

The  $\mu$ -parameters are defined as follows:

$$\mu_{1i} = m_i; \quad (8.20a)$$

$$\mu_{2i} = m_i \cdot X_i; \quad (8.20b)$$

$$\mu_{3i} = m_i \cdot Y_i; \quad (8.20c)$$

$$\mu_{4i} = J_i + m_i \cdot (X_i^2 + Y_i^2). \quad (8.20d)$$

That is:  $\mu_{2i}$  [kg-m] and  $\mu_{3i}$  [kg-m] are the  $X$  and  $Y$ -components of the mass-distance product, while  $\mu_{4i}$  [kg-m<sup>2</sup>] is the moment of inertia w.r.t. the local coordinate system (attached to the link) in which  $X_i$  and  $Y_i$  are measured. These mass parameters are not new, but Haines is the first to stress their superposition property (see Section 9.3.1), which is the basis of the developed convex optimization framework.

Using this mass parameterization and LIV expressions, an optimization framework is developed, in which two kinds of constraints are considered: ultimate constraints and practical constraints. The *ultimate* constraints on the counterweight  $\mu$ -parameters involve physical feasibility and impose:

$$\mu_{1i}^* \geq 0;$$

$$\mu_{4i}^* \geq 0.$$

It has to be noted, however, that imposing the latter constraint does not yield physically realizable mass parameters, since  $\mu_{4i}^* \geq 0$  does not imply that  $J_i^* \geq 0$ . The *practical* constraints are involved with practical feasibility. For this purpose, it is assumed that the counterweights are circular, of a given maximum thickness and density  $\rho$ , and that their radius and COG

coordinates are the optimization variables. Without assuming one of the  $K_i$ -factors to be fixed, as done by (Berkof and Lowen, 1971), and hence obtaining truly optimal results, the following is shown: (i) minimizing the rms shaking moment subject to ultimate constraints has an analytical solution; (ii) minimizing the rms shaking moment, subject to practical constraints, is equivalent to an unconstrained optimization problem with two variables. These results are equally applicable if the rms input torque is to be minimized.

**Shchepetil'nikov Approach** For the sake of completeness, also (Arakelian and Dahan, 2001) and (Arakelian et al., 2001) are mentioned here. These papers minimize, using an analytical method, the rms shaking moment of fully force-balanced linkages through application of counterweights, of which the axis of rotation is displaced w.r.t. the link they are 'attached' to, an idea firstly proposed by Shchepetil'nikov (1974). That is, the counterweight is attached to an auxiliary link, which revolves around a different point than the original link, and which is driven by the original link through e.g. a toothed belt.

#### 8.4.2 Partial Force Balance Approaches

Methods giving up full force balance, and aiming at a simultaneous minimization of (some or) all dynamic reactions, are classified here into three groups. The first group realizes the trade-off through minimization of a goal function that is a weighted combination of some measure (e.g. the rms values or the maximum absolute value) of the dynamic reactions. A second group minimizes some measure of a single dynamic reaction, while keeping the increase of the other dynamic reactions under control through constraints. The third group handles the trade-off by considering the dynamic model of the frame that supports the mechanism.

**Weighted Goal Function Approach** Porter and Sanger (1972) are seemingly the first ones to formulate CWB as a nonlinear optimization problem with the typical goal function, consisting of a weighted combination of the rms values of all dynamic reactions (including the joint forces). They confine themselves to four-bars and optimize solely the radius and off-pivot distance of an inline, circular counterweight on link III. Having only two optimization variables, they present design charts similar to Fig.5.14 and Fig.6.12, with contour lines of the goal function (for various weighting factors), and indication of the constraints (bound constraints on the optimization variables and the requirement that link III be statically balanced).

Dresig and Schönfeld (1976) develop a classical weighted goal function approach in which the input torque, shaking force and shaking moment are considered. Two particular aspects of this work are noteworthy. Firstly, LDV expressions are used for efficient calculation of the goal function. The authors

claim that this results in a speedup of a factor of 100 to 1000, compared to the situation in which the kinematics are calculated over and over again. Secondly, in order to obtain a better optimum, the number of optimization variables is increased, by adding a *dyad* to the original mechanism. Both the dyad's kinematic and mass parameters are considered for optimization. The idea of adding a dyad had already been suggested in (Dresig and Jacobi, 1974), but solely for having more flexibility for force balancing. This method is again called to attention in (VDI2149, 1999).

In order to overcome the problem of having to choose an arbitrary shaking moment reference point in the absence of full force balance, Lee and Cheng (1984) suggest the following goal function, which combines the ground bearing forces and the input torque:

$$\frac{1}{2\pi} \int_0^{2\pi} \left[ W_1 \cdot \sqrt{F_a^2 + F_d^2} + W_2 \cdot \sqrt{M_{\text{drv}}^2} \right] d\phi_1. \quad (8.21)$$

The underlying reasoning is that (i) minimizing the input torque and the ground bearing forces minimizes the shaking moment, as it is the sum of the input torque and the moment of the ground bearing forces and (ii) minimizing the ground bearing forces minimizes the shaking force as it is the sum of the ground bearing forces. This goal function is again efficiently evaluated using LDV expressions.

Guo et al. (2000) develop a classical weighted goal function method in which the input torque, shaking force and shaking moment are considered. They adopt a 'brute force' approach: no LDV nor LIV expressions are used, and the set of optimization variables is redundant, in order to 'enhance the convergence' of the genetic algorithm, used for solving the problem.

**Constraint Approach** Sadler and Mayne (1973) introduce the idea of handling the trade-off via constraints. Four-bar mechanisms are considered, of which the COG location and the mass of *point-mass* counterweights, attached to link I and link III are optimized. The goal function of this optimization problem, involving six optimization variables, is the maximum value of the shaking force. The following constraints are considered: (i) an upper bound on the maximum of the shaking moment and/or the largest joint force and (ii) an upper bound on the total counterweight mass. Using different upper bounds on the shaking moment, trade-off curves are determined that plot the maximum shaking force as a function of the imposed upper bound on the maximum shaking moment. Basically the same approach is applied to six-bar linkages in (Sadler, 1975).

Tepper and Lowen (1975) consider a four-bar with constant input crank speed. The rms shaking force is minimized subject to an upper bound on the rms ground bearing forces. No effort is made to control the driving torque, shaking moment or the other joint forces. The optimization variables are the

polar COG coordinates of *minimum inertia* counterweights, that is counterweights that are circular and tangent to the pivots<sup>25</sup>. The counterweights are attached to link I and link III.

Based on LDV expressions for the ground bearing forces and the shaking force, a semi-analytic approach (using the  $\mu$ -parameters) is developed for solving the problem. This approach requires numerical solution of a set of equations, obtained by analytical determination of the so-called Karush-Kuhn-Tucker conditions. This results in eight local optima, of which the best one is chosen, which is hence the global<sup>26</sup> optimum. The cost for obtaining a global optimum is however a very complicated formalism, which is therefore difficult to extend to  $N$ -bar linkages.

Again, a purely numerical approach is adopted by Tricamo and Lowen (1983b), who develop an optimization formalism that covers all dynamic reactions of a four-bar mechanism with constant input crank speed. Minimum inertia counterweights, attached to each of the three links are optimized. The following constraint-based problem formulation is adopted:

$$\min z,$$

subject to (i) the already introduced quadratic equipollent circle equality constraint in the mass-distance products  $m_i \cdot X_i$  and  $m_i \cdot Y_i$  of link II and link III (in order to keep the maximum shaking force to a specified fraction of the original maximum shaking force), (ii) a nonlinear equality constraint in order to determine the mass-distance products of link I and (iii)  $6K$  inequality constraints

$$W_j \cdot \left[ \frac{(d_{j,k})^2 - (d_{j,\max}^o)^2}{(d_{j,\max}^o)^2} \right] \leq z, \quad \begin{cases} j = 1 \dots 6 \\ k = 1 \dots K \end{cases}$$

$d_j, j = 1 \dots 6$  denotes the magnitude of each of the six considered reactions, that is, the shaking moment, driving torque and the four joint forces. The index  $k$  denotes the  $k$ -th sample, with  $K$  the total number of samples. The superscript ( $^o$ ) denotes the value of  $d_j$  in the original mechanism. LDV expressions, similar to the ones used by Tepper and Lowen (1975), are used for efficiently computing all forces and moments, without requiring recalculation of the mechanism kinematics.

<sup>25</sup>Do not confuse 'minimum inertia counterweights' with 'inertia counterweights': the former are masses (of a particular shape), rigidly attached to their corresponding link, while the latter rotate w.r.t. their corresponding link, and are driven by it through for instance a gear pair.

<sup>26</sup>It must be noted however that the whole procedure starts from an arbitrarily chosen total moment of inertia of link III. Hence the obtained 'global' optimum depends on this initial choice. The authors remark that 'the best results were obtained when the total moment of inertia of link III was assumed to be 2.5 to 3.0 times that of the unbalanced link.'

The dynamic reactions to be optimized appear in multiple inequality constraints, which are themselves subject to minimization, rather than as part of a composite objective function. The authors claim that this is beneficial for the efficiency of the optimization algorithm (an augmented Lagrangian penalty function code). Reference is made to works on linear programming as previous examples (e.g. Chebyshev approximation problems involving linear inequalities or inconsistent linear equations) of such problem formulations.

**Dynamic Model Approach** In handling the trade-off between dynamic reactions, the dynamic model approach is the more integrated approach, since it considers a dynamic model of the supporting frame and aims at reducing the vibrational response of the overall system, including the frame. Additionally, it overcomes the problems of (i) the choice of a shaking moment reference point in the absence of full force balance and (ii) the lack of physical grounds in choosing weighting factors in goal functions that combine the shaking force and the shaking moment.

Kochev and Gurdev (1988) consider a three-degree-of-freedom (two translational and one rotational degree of freedom), planar frame model, attached to the foundation by springs and dampers with linear characteristics. This frame supports a four-bar mechanism, assumed to have the standard configuration of (Lowen et al., 1974). The criteria chosen to measure the frame response are generalizations of the original ideas of Johnson and Schenectady (1935), which are the average frame kinetic energy (measuring the frame vibration level) and the average mounting potential energy (measuring the transmission of the vibration to the foundation).

It is shown that (if some approximations are made) all of the considered criteria are quadratic forms of the link mass parameters. The procedure, used for minimizing these quadratic forms, is however iterative, as the coefficients of the quadratic forms depend on the optimization variables as well.

Zhang and Chen (1995) also develop a dynamic model approach, seemingly unaware of (Kochev and Gurdev, 1988), despite publishing in the same journal. Again, a frame model with three degrees of freedom, carrying a four-bar mechanism, is considered. The developed methodology however requires weighting factors in order to combine the translational and rotational response of the frame into one goal function. The energy-based approaches (Johnson and Schenectady, 1935; Kochev and Gurdev, 1988) do not suffer from this problem. Experimental results on a dedicated setup are presented. The obtained frame vibration reduction is less spectacular than in simulation, which is attributed to modelling errors and joint wear and clearance.

## 8.5 Conclusion

This literature survey should serve as a gentle introduction to counterweight balancing for the newcomer in the field. Therefore, the basic definitions involved, as well as the main theoretical results are reviewed: (i) if an  $N$ -bar mechanism is force balanceable, it generally requires  $N/2$  counterweights; (ii) the shaking moment of a force-balanced mechanism is a pure couple; otherwise it depends on the chosen reference point; (iii) full shaking moment balance requires the addition of negative inertia, e.g. via inertia counterweights.

The use and derivation of LIV expressions has been reviewed in a comprehensive way, and the relation with experimental robot identification has been established. It is believed that bridging this gap has the potential of revealing some interesting new research results. For instance, mass transfer concepts for mechanisms are used both in ERI literature (Beale and Chen, 2002), in which they are applied to the driving torque, and in the Complex Mass Method of CWB literature (Walker and Oldham, 1979; Yao and Smith, 1993), in which they are applied to the shaking force. A thorough comparison and unification of these formalisms may result in a novel method, well suited for both communities.

Furthermore, a classification has been given of the various optimization approaches that deal with the trade-off of dynamic reactions. The approach that combines full force balance with minimization of the shaking moment or driving torque, has the advantage that the shaking moment is independent of the reference point. On the other hand, for a planar  $N$ -bar mechanism, imposing full force balance already imposes  $N$  conditions on the  $4 \cdot (N - 1)$  available mass parameters. In this approach, the underestimated work of (Haines, 1981) is the most general, and makes the important contribution of stressing the superposition properties of the  $\mu$ -parameters.

The second approach gives up the requirement of full force balance, and aims at a simultaneous minimization of (some or) all dynamic reactions. Three variants are distinguished: the use of a weighted goal function, the use of constraints and the use of a dynamic model. The latter, more integrated method is attractive, for the ultimate goal of dynamic balancing is reducing the vibrational response of the overall mechanical system, including the frame. Additionally, it overcomes the problems of (i) the choice of a shaking moment reference point in the absence of full force balance and (ii) the lack of physical grounds in choosing weighting factors in goal functions that combine the shaking force and the shaking moment.

In light of these advantages, this third variant should be the primary designer's choice if a dynamic frame model is available, which, unfortunately is often not the case. Furthermore, the present results still lack robustness. Firstly, due to the presence of springs in the frame model, the obtained results inherently depend on the mean drive speed of the mechanism. Secondly, obtaining a reliable frame model is not a trivial task, and subject to modelling errors. For both reasons, measures for making the results of (Kochev

and Gurdev, 1988) more robust are required. In this respect, it is noteworthy that the aforementioned problems are quite similar to the problems, discussed in Section 3.1.1, of dynamically compensated cams that compensate for follower dynamics. It can therefore be expected that the methods, developed for making dynamically compensated cams more robust, provide a good starting point for robustifying dynamic-model-based balancing methods.

A final note is that, in the area of the balancing of *rotating* machinery, dynamic balancing has a more inclusive meaning than the one considered here. That is, it is considered to be an extension of *static balancing*, which itself is defined to be the addition or removal of mass from a rotating link so as to force its center of gravity to its fixed pivot. Static balancing cancels out the shaking force, but does not eliminate the bending moment acting on the drive shaft, if the masses that generate the inertia forces, are not in the same plane. In that case, that is, if the device is long in the axial direction compared to the radial direction, 'dynamic balancing' is required, which is defined (Norton, 2001) as the addition or removal of mass in *two* correction planes separated by some distance along the shaft, in order to provide a counter couple to cancel the unbalanced shaft bending moment. A well-known example is the addition of counterweights to the inner and outer edges of an automobile wheel rim.



## Chapter 9

# Counterweight Balancing: A Convex Optimization Framework

*Developing a working knowledge of convex optimization can be mathematically demanding, especially for the reader interested primarily in applications. In our experience (mostly with graduate students in electrical engineering and computer science), the investment often pays off well, and sometimes very well.*

Boyd and Vandenberghe (2004)

**T**HIS chapter develops a convex optimization framework for counterweight balancing. This framework is general in nature: it is applicable to planar, purely inertial four-bar or  $N$ -bar mechanisms, and can be extended to spatial mechanisms. In order to illustrate its basic flavor, it is first applied to a purely inertial,  $4R$  four-bar mechanism, for which the trade-off between the dynamic reactions is handled via a constraint-based optimization approach, similar to the ones discussed in Section 8.4.2. After that, the results are generalized to planar, purely inertial  $N$ -bar mechanisms.

This results in the following structure of this chapter. First, a brief introduction to convex optimization is given in Section 9.1. Section 9.2 develops the constraint-based optimization problem formulation for the  $4R$  four-bar. This optimization problem is nonconvex, but is reformulated as a convex problem in Section 9.3. Numerical results and benchmarks are presented in Section 9.4. Finally, the convex optimization framework is extended to planar, purely inertial  $N$ -bar mechanisms in Section 9.5.

This chapter adopts an inverse dynamic approach, whereby the input crank speed of the linkage is assumed to be perfectly constant.

## 9.1 A Convex Optimization Primer

The following section is essentially a summary of the initial chapters of (Boyd and Vandenberghe, 2004). Firstly, the standard form of an optimization problem is defined. After giving the definition of convex sets and convex functions, convex programs are formally defined. Two specific subclasses of convex programs are of particular interest here, and are therefore shortly discussed: second-order cone programs and semidefinite programs. Finally, some remarks concerning numerical solving convex programs are given.

**Standard Optimization Problem Form** Adopting the notation<sup>1</sup> of (Boyd and Vandenberghe, 2004), the standard mathematical form of an optimization problem (or *mathematical program*) is:

$$\begin{aligned} & \text{minimize} && f_0(x), \\ & \text{subject to} && f_i(x) \leq 0, \quad i = 1, \dots, m \\ & && h_i(x) = 0, \quad i = 1, \dots, p \end{aligned} \tag{9.1}$$

where  $x \in \mathbb{R}^n$  is the optimization variable and the function  $f_0 : \mathbb{R}^n \rightarrow \mathbb{R}$  is the objective or cost function.  $f_i(x) : \mathbb{R}^n \rightarrow \mathbb{R}$  and  $h_i(x) : \mathbb{R}^n \rightarrow \mathbb{R}$  are respectively called the inequality and equality constraint functions.

**Convex Sets and Convex Functions** A set  $S \subseteq \mathbb{R}^n$  is convex if the line segment between any two points in  $S$  lies in  $S$ , i.e., if for any  $x, y \in S$  and  $\theta \in [0, 1]$ , we have

$$\theta x + (1 - \theta)y \in S. \tag{9.2}$$

Figure 9.1 gives a number of examples of two-dimensional ( $n = 2$ ) convex and nonconvex sets. A function  $f : \mathbb{R}^n \rightarrow \mathbb{R}$  is convex if its domain  $\mathbf{dom} f$  is a convex set and if for all  $x, y \in \mathbf{dom} f$  and  $\theta \in [0, 1]$ , we have

$$f(\theta x + (1 - \theta)y) \leq \theta f(x) + (1 - \theta)f(y). \tag{9.3}$$

This is geometrically interpreted for a scalar ( $n = 1$ ) function  $f$  in Fig.9.2: the line segment between  $(x, f(x))$  and  $(y, f(y))$  lies above the graph of  $f$ . A function  $f$  is concave if  $-f$  is convex. Some examples (on  $\mathbb{R}$ ) include: (i)  $f(x) = x^2$  is convex; (ii)  $f(x) = \log x$  is concave ( $\mathbf{dom} f = \{x | x > 0\}$ );  $f(x) = 1/x$  is convex ( $\mathbf{dom} f = \{x | x > 0\}$ ).

---

<sup>1</sup>In the notation of (Boyd and Vandenberghe, 2004), vectors and matrices are indicated with lower case and upper case characters respectively. In Section 9.1, this overrules the standard notation used in this thesis, that is, lower case and upper case *bold* characters for vectors and matrices.

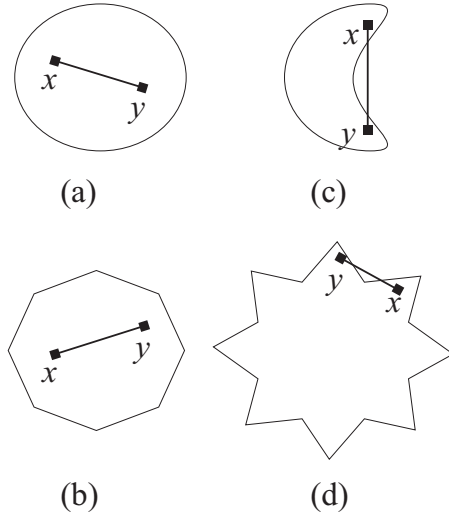


FIGURE 9.1: Convex ( $a - b$ ) and nonconvex ( $c - d$ ) subsets of  $\mathbb{R}^2$ .

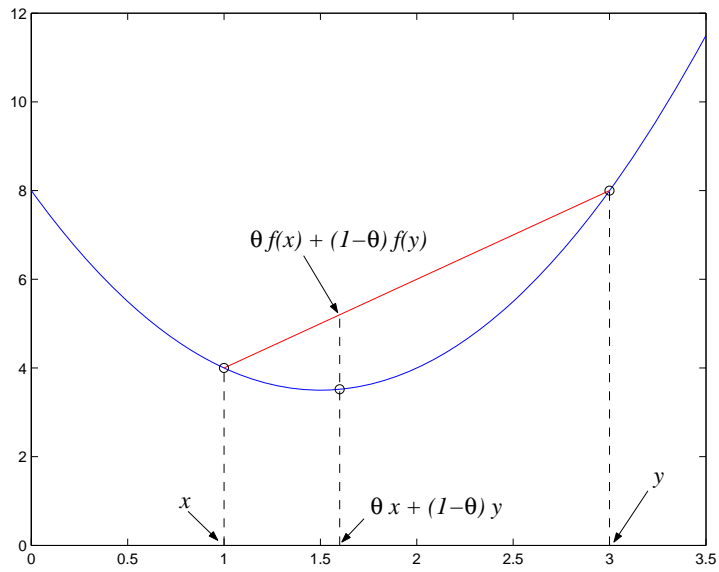


FIGURE 9.2: Geometrical interpretation of (9.3) for a convex function  $f$ .

**Convex Programs** A convex optimization problem, or convex program (CP), is an optimization problem of the form:

$$\begin{aligned} & \text{minimize} && f_0(x), \\ & \text{subject to} && f_i(x) \leq 0, \quad i = 1, \dots, m \\ & && a_i^T x = b_i, \quad i = 1, \dots, p \end{aligned} \tag{9.4}$$

where  $f_0, \dots, f_m$  are convex functions,  $a_i \in \mathbb{R}^n$  and  $b_i$  is a scalar. Comparing (9.4) with the standard form (9.1), the convex problem has three additional requirements: (i) the objective function must be convex, (ii) the inequality constraint functions must be convex; (iii) the equality constraint functions  $h_i(x) = a_i^T x - b_i$  must be affine, that is, linear plus a translation.

Two important and easily provable properties of convex programs are: (i) the feasible set of a convex program is convex; thus, in a convex optimization problem, a convex objective function is minimized over a convex set; (ii) any locally optimal point of a convex program is also *globally* optimal.

Several classes of CPs exist, each of which are a subclass of a more general type of problems. Starting with the smallest class, we have: linear programs (LPs), convex quadratic programs (QPs), *second-order cone programs* (SOCPs) and *semidefinite programs* (SDPs):

$$\text{LP} \subset \text{QP} \subset \text{SOCP} \subset \text{SDP} \subset \text{CP}.$$

SOCPs and SDPs are of particular interest here.

**Second-Order Cone Programs** SOCPs are closely related to quadratic programs and are of the general form:

$$\begin{aligned} & \text{minimize} && f^T x, \\ & \text{subject to} && \|A_i \cdot x + b_i\| \leq c_i^T x + d_i, \quad i = 1, \dots, m \\ & && Fx = g, \end{aligned} \tag{9.5}$$

where  $x \in \mathbb{R}^n$  is the optimization variable,  $A_i \in \mathbb{R}^{n_i \times n}$ ,  $b_i \in \mathbb{R}^{n_i}$ ,  $c_i, f \in \mathbb{R}^n$ ,  $d_i \in \mathbb{R}$ ,  $F \in \mathbb{R}^{p \times n}$  and  $g \in \mathbb{R}^p$ .  $\|\cdot\|$  denotes the *L2*-norm:  $\|x\| = \sqrt{x^T \cdot x}$ . A constraint of the general form

$$\|A \cdot x + b\| \leq c^T x + d, \tag{9.6}$$

is called a *second-order cone constraint*. In an SOCP, one hence minimizes a linear goal function, subject to linear equality constraints, linear inequality constraints (if the corresponding  $A_i = 0$ ) and second-order cone constraints. If  $A_i = 0, i = 1, \dots, m$ , the SOCP reduces to a linear program.

**Semidefinite Programs** SDPs are of the general form:

$$\begin{aligned} & \text{minimize} && f^T x, \\ & \text{subject to} && A(x) \succeq 0, \\ & && Fx = g, \end{aligned} \tag{9.7}$$

where

$$A(x) = A_0 + x_1 A_1 + \dots + x_n A_n,$$

and  $A_i \in \mathbb{R}^{n \times n}$  are symmetric matrices. The inequality sign in  $A(x) \succeq 0$  means that  $A(x)$  is positive definite, i.e.,  $z^T A(x) z \geq 0$  for all  $z \in \mathbb{R}^n$ .  $A(x) \succeq 0$  is called a *linear matrix inequality* (LMI) in  $x$ . The solution set of a linear matrix inequality,  $\{x | A(x) \succeq 0\}$ , is convex. If the matrices  $A_i$  are all diagonal, then the corresponding LMI is equivalent to a set of  $n$  linear inequalities, and the SDP reduces to a linear program.

SDPs constitute a generalization of SOCPs, since a second-order cone constraint can be written as an LMI (Lobo et al., 1998):

$$\|A \cdot x + b\| \leq c^T x + d \Leftrightarrow \begin{bmatrix} (c^T x + d)I_n & A \cdot x + b \\ (A \cdot x + b)^T & c^T x + d \end{bmatrix} \succeq 0, \tag{9.8}$$

where  $I_n$  denotes the  $n \times n$  unity matrix. A mathematical program in which one minimizes a linear goal function, subject to linear equality constraints, linear inequality constraints, second-order cone constraints and LMIs, is hence an SDP.

**Solving Convex Programs** With respect to numerically solving convex programs, Boyd and Vandenberghe (2004) state: '(...) interior-point methods can solve the problem (9.4) in a number of steps or iterations that is almost always in the range between 10 and 100. Ignoring any structure in the problem (such as sparsity), each step requires on the order of

$$\max\{n^3; n^2 m; F\}$$

operations, where  $F$  is the cost of evaluating the first and second derivatives of the objective and constraint functions  $f_0, \dots, f_m$ . Like methods for solving linear programs, these interior-point methods are quite reliable. We can easily solve problems with hundreds of variables and thousands of constraints on a current desktop computer, in at most a few tens of seconds. By exploiting problem structure (such as sparsity), we can solve far larger problems, with many thousands of variables and constraints. We cannot yet claim that solving general convex optimization problems is a mature technology, like solving least-squares or linear programming problems. Research on interior-point methods for general nonlinear convex optimization is still a very active research area, and no consensus has emerged yet as to what the best method or methods are. But it is reasonable to expect that solving

general convex optimization problems will become a technology within a few years. And for some subclasses of convex optimization problems, for example second-order cone programming or geometric programming, it is fair to say that interior-point methods are approaching a technology.<sup>7</sup>

Lobo et al. (1998) stress that, although SDPs constitute a generalization of SOCPs, solving an SOCP as an SDP, based on (9.8), is not a good idea. Firstly, interior-point methods for SOCPs have a much better worst-case complexity. Moreover, and more importantly in practice, each iteration is also much faster, especially if the dimensions of the second-order constraints are large.

## 9.2 4R Four-Bar: Constraint-Based Optimization Approach

This section develops a constraint-based optimization approach for handling the trade-off between the shaking force, shaking moment and driving torque of a purely inertial, 4R four-bar mechanism. The motivation for adopting this approach is the following. If a trade-off is to be sought, it is obvious not to impose *full* force balance. Of the *partial* force balance approaches, the approach based on a dynamic frame model is not chosen, since an accurate dynamic model is often not available, and the method still lacks robustness. A choice needs therefore to be made between the weighted goal function approach and the constraint based approach. The latter approach is preferred due to the inherent possibilities it offers for creating trade-off curves.

### 9.2.1 Optimization Variables

The unbalanced mechanism has the geometry of Fig.8.1. It is assumed that no material is allowed to be removed. This corresponds to the industrial practice of making links as lightweight as possible, especially the links that are subject to high accelerations. Counterweights are added to each of the links. Their mass parameters, indicated with an asterisk (\*), constitute the optimization variables, and are grouped into the optimization variable vector  $\mathbf{x} \in \mathbb{R}^{12}$ :

$$\mathbf{x} = [ m_1^* \quad X_1^* \quad Y_1^* \quad J_1^* \quad m_2^* \quad X_2^* \quad Y_2^* \quad J_2^* \quad m_3^* \quad X_3^* \quad Y_3^* \quad J_3^* ]^T.$$

### 9.2.2 Goal Function—Handling the Trade-Off

The *balancing effect index*  $\alpha$  [-] is introduced in (Lowen et al., 1974) as the rms of the optimized dynamic reaction  $d(t)$  w.r.t. the rms of the original dynamic reaction  $d^o(t)$ :

$$\alpha = \frac{d_{\text{rms}}}{d_{\text{rms}}^o}. \quad (9.9)$$

In order to numerically determine  $\alpha$ , a vector  $\mathbf{d} \in \mathbb{R}^K$  of  $d(t_k)$ -values at the time instances  $t_k = (k-1) \cdot T_s$  is constructed, as in equation (8.5). The sample period  $T_s$  [s] equals  $T/K$  and  $k$  ranges from 1 to  $K$ . As a result, following the reasoning expressed by (8.8–8.9), the following is obtained:

$$\alpha = \frac{\sqrt{\mathbf{d}^T \cdot \mathbf{d}}}{\sqrt{(\mathbf{d}^o)^T \cdot \mathbf{d}^o}} = \frac{\|\mathbf{d}\|}{\|\mathbf{d}^o\|}, \quad (9.10)$$

where  $\|\cdot\|$  denotes the  $L2$ -norm. Balancing indices are defined for all of the considered dynamic reactions:

- $\alpha_a, \alpha_b, \alpha_c$  and  $\alpha_d$  for the joint forces  $F_a, F_b, F_c$  and  $F_d$ ;
- $\alpha_{\text{fsh}}$  for the shaking force;
- $\alpha_{\text{drv}}$  and  $\alpha_{\text{msh}}$  for the driving torque and the shaking moment.

For the moment, joint forces are not considered. The trade-off between the remaining dynamic reactions is handled as follows (Sadler and Mayne, 1973):

$$\text{minimize} \quad \alpha_{\text{msh}}, \quad (9.11a)$$

$$\text{subject to} \quad \alpha_{\text{fsh}} \leq \alpha_{\text{fsh}}^{\text{M}}, \quad (9.11b)$$

$$\alpha_{\text{drv}} \leq \alpha_{\text{drv}}^{\text{M}}, \quad (9.11c)$$

that is, the shaking moment is minimized, while keeping the shaking force and driving torque under control, using constraints on  $\alpha_{\text{fsh}}$  and  $\alpha_{\text{drv}}$ .  $\alpha_{\text{fsh}}^{\text{M}}$  and  $\alpha_{\text{drv}}^{\text{M}}$  represent upper bounds, chosen by the designer. Choosing either  $\alpha_{\text{fsh}}$  or  $\alpha_{\text{msh}}$  as a goal function is arbitrary. Contrary to that, it is better to keep  $\alpha_{\text{drv}}$  as a constraint, since most optimization results from the past indicate that  $\alpha_{\text{drv}}$  is hard to reduce through counterweight addition. It therefore makes sense to constrain it, in order to keep it under control, instead of minimizing it.

### 9.2.3 Constraints–Counterweight Implementation

Besides the constraints (9.11b–9.11c) that keep  $\alpha_{\text{fsh}}$  and  $\alpha_{\text{drv}}$  under control, constraints are also required to ensure feasibility of the counterweights. These constraints are expressed in their most general form, that is, as a function of the counterweight parameters  $m_i^*$ ,  $X_i^*$ ,  $Y_i^*$  and  $J_i^*$ : no assumptions concerning the actual counterweight shape are made. As such, these constraints (except for the ultimate constraints) are novel in literature. Distinction is made here between *ultimate*, *practical* and *practical*<sup>+</sup> feasibility.

### 9.2.3.1 Ultimate Constraints

Ultimate constraints imply that the counterweights be physically realizable, that is, that they have positive mass and moment of inertia:

$$m_i^* \geq 0; \quad (9.12a)$$

$$J_i^* \geq 0. \quad (9.12b)$$

These ultimate constraints deviate from the ones proposed in (Haines, 1981):

$$\mu_{1i}^* \geq 0; \quad (9.13a)$$

$$\mu_{4i}^* \geq 0. \quad (9.13b)$$

The definition (8.20d) of  $\mu_{4i}$  reveals that (9.13b) is too loose a constraint, since it may result in negative  $J_i^*$  values if either  $X_i^*$  or  $Y_i^*$  deviate from zero (with  $m_i^* > 0$ ). Hence, (9.12a–9.12b) represent the true ultimate constraints. These constraints allow adding a nonzero mass with a zero inertia. Such a counterweight, in fact, is a point mass, which is theoretically, but not practically implementable.

### 9.2.3.2 Practical Constraints

In practice, for a given mass density  $\rho$  [kg/m<sup>3</sup>], counterweights with a very small surface and a very large thickness approximate point masses. However, for practical reasons, the counterweight thickness needs to be constrained to an upper bound  $t^M$  [m]. This gives rise to practical constraints on the counterweight mass parameters, derived as follows.

Suppose a given counterweight mass  $m_i^*$  [kg] is to be implemented in a plate of thickness  $t_i^*$  and density  $\rho$ . Using the calculus of variations, it is straightforward to show that the minimum obtainable centroidal moment of inertia  $J^*$  [kg-m<sup>2</sup>] is that of a cylinder of thickness (length)  $t_i^*$  and radius

$$R_i^* = \sqrt{\frac{m_i^*}{\pi \cdot t_i^* \cdot \rho}}.$$

The corresponding centroidal moment of inertia equals:

$$J^* = \frac{m_i^* \cdot (R_i^*)^2}{2} = \frac{(m_i^*)^2}{2 \cdot \pi \cdot t_i^* \cdot \rho},$$

which formally confirms the intuition that a greater counterweight thickness  $t_i^*$  results in a smaller  $J_i^*$ . The absolute lower limit on  $J_i^*$  is attained if  $t_i^* = t^M$ . As a result, *any* counterweight to be implemented in a plate of maximum thickness  $t^M$  must satisfy:

$$J^* \geq \frac{(m_i^*)^2}{2 \cdot \pi \cdot t^M \cdot \rho}, \quad (9.14a)$$

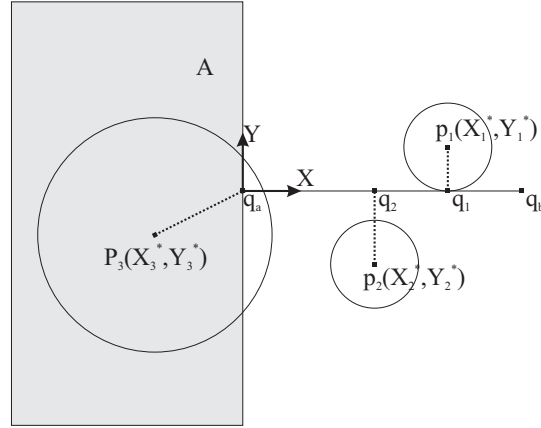


FIGURE 9.3: Definition of contact between a binary link  $[\hat{q}_a, \hat{q}_b]$  and a counterweight. Counterweights 1 and 3 are in contact; counterweight 2 is loose.

in conjunction with the mass positivity constraint

$$m_i^* \geq 0. \quad (9.14b)$$

Equations (9.14a–9.14b) constitute the *practical* constraints.

### 9.2.3.3 Practical<sup>+</sup> Constraints

Although the practical constraints (9.14a–9.14b) assure that the counterweight can be fabricated from a plate with maximum thickness  $t^M$ , they do not guarantee that the counterweight is in contact with the link to which it is attached. For a *binary* link, that is, a link with two pivot points  $\hat{q}_a$  and  $\hat{q}_b$  (see Fig.9.3), the following (strict) definition of contact between a link and its counterweight is adopted. A counterweight is *in contact* with its corresponding link if it contains  $\hat{q}_i$ , that is, the point on the line segment  $[\hat{q}_a, \hat{q}_b]$  that is the closest to the center of gravity  $\hat{p}_i$  of the counterweight.  $\hat{q}_i$  is denoted as the *contact point*. Figure 9.3 illustrates these definitions. This definition of 'contact' is a simplification of reality, since it considers a link to be a line and hence makes abstraction of the actual link shape.

It is possible to derive constraints that guarantee contact for a binary link, provided that the counterweight has a center of gravity  $\hat{p}_i$  lying in the shaded left half plane  $A$  (Fig.9.3). This constraint may seem rather restrictive at this point, but is justified in the discussion at the end of this section. For such a left-half-plane counterweight, the closest point on the line segment is  $\hat{q}_a$ . A constraint that guarantees that the counterweight contains  $\hat{q}_a$  hence guarantees that it is in contact.

In deriving this constraint, the notion of *minimum inertia counterweight* is essential. First, general properties of such counterweights are discussed. After that, these properties are exploited for deriving the constraint that guarantees a left-half-plane counterweight to be in contact.

**Minimum Inertia Counterweights** Consider the following problem: given the mass-distance products  $m_i^* \cdot X_i^*$  and  $m_i^* \cdot Y_i^*$  [kg-m], and given the thickness-density product  $t_i^* \cdot \rho$  [kg/m<sup>2</sup>], determine the shape of the counterweight, to be attached to a link, revolving around a fixed pivot point  $\hat{o}^{(2)}$ , that has a minimum moment of inertia  $J_{o,i}^*$  w.r.t.  $\hat{o}$ .

The solution for this problem is well-known in CWB literature: the counterweight should be circular and tangent to the fixed pivot  $\hat{o}$ . A derivation of this result, based on the calculus of variations, can for instance be found in (Hertrich, 1963), and shows that the parameterization of the variational problem is such that  $\hat{o}$  always belongs to the counterweight.

A second observation is that, for given mass-distance products  $m_i^* \cdot X_i^* = a$  and  $m_i^* \cdot Y_i^* = b$  [kg-m], there is a one-to-one relation between the minimum inertia counterweight's mass  $m_i^*$  and the thickness-density product  $t_i^* \cdot \rho$ :

$$m_i^* = [(t_i^* \cdot \rho) \cdot \pi \cdot (a^2 + b^2)]^{\frac{1}{3}}. \quad (9.15)$$

This implies that specifying in the aforementioned problem either  $t_i^* \cdot \rho$  or  $m_i^*$  is equivalent: in the former case, the counterweight's mass adapts itself to yield the specified  $t_i^* \cdot \rho$ , whereas in the latter case, the counterweight's thickness adapts itself to yield the specified  $m_i^*$ . Therefore, circular counterweights, tangent to  $\hat{o}$ , also yield minimum inertia if  $m_i^*$ ,  $m_i^* \cdot X_i^*$  and  $m_i^* \cdot Y_i^*$  are specified, which, in turn, is equivalent to specifying  $m_i^*$ ,  $X_i^*$  and  $Y_i^*$ .

The above discussion results in the following conclusion: if  $m_i^*$ ,  $X_i^*$  and  $Y_i^*$  are specified (with  $X_i^*$  and  $Y_i^*$  expressed in an LCS with  $\hat{o}$  as origin), the lowest possible inertia  $J_{o,i}^*$  w.r.t.  $\hat{o}$ , of all counterweights that contain  $\hat{o}$ , is realized by a circular counterweight, tangent to  $\hat{o}$ .

Before proceeding to the derivation of the contact constraint, an expression is derived for the minimum inertia  $J_{o,i,\min}^*$  w.r.t.  $\hat{o}$ , realized by a minimum inertia counterweight. Being circular, a minimum inertia counterweight has a centroidal moment of inertia  $J_i^*$  equal to:

$$J_i^* = \frac{m_i^* \cdot (R_i^*)^2}{2}, \quad (9.16)$$

and a radius given by

$$(R_i^*)^2 = (X_i^*)^2 + (Y_i^*)^2,$$

---

<sup>2</sup> $X_i^*$  and  $Y_i^*$  are measured in a local coordinate system, attached to the link, with its origin coinciding with  $\hat{o}$ .

due to the fact that it is tangent to  $\widehat{c}$ , that also serves as the origin of the LCS in which  $X_i^*$  and  $Y_i^*$  are defined. Combining the above results with Steiner's theorem yields:

$$J_{o,i,\min}^* = J_i^* + m_i^* \cdot [(X_i^*)^2 + (Y_i^*)^2] = \frac{3}{2} \cdot m_i^* \cdot [(X_i^*)^2 + (Y_i^*)^2].$$

**Derivation of Contact Constraint** Consider Fig.9.3 and suppose that the LCS, in which  $X_i^*$  and  $Y_i^*$  are measured, is attached to  $\widehat{q}_a$ , with its  $X$ -axis lying along the line  $\widehat{q}_a - \widehat{q}_b$ . The above discussion shows that any counterweight, which contains  $\widehat{q}_a$ , satisfies:

$$J_{a,i}^* \geq J_{a,i,\min} = \frac{3}{2} \cdot m_i^* \cdot [(X_i^*)^2 + (Y_i^*)^2], \quad (9.17)$$

where  $J_{a,i}^*$  is the counterweight's inertia w.r.t.  $\widehat{q}_a$ . By application of Steiner's theorem:

$$J_{a,i}^* = J_i^* + m_i^* \cdot [(X_i^*)^2 + (Y_i^*)^2]. \quad (9.18)$$

Combining (9.17) and (9.18) yields, for any counterweight that contains  $\widehat{q}_a$ :

$$J_i^* \geq \frac{1}{2} \cdot m_i^* \cdot [(X_i^*)^2 + (Y_i^*)^2]. \quad (9.19)$$

Now consider counterweights that lie in the left half plane  $A$ . Such counterweights satisfy

$$X_i^* \leq 0. \quad (9.20)$$

If such a left-half-plane counterweight also satisfies (9.19), it contains  $\widehat{q}_a$ , and hence is in contact with the link. Therefore, (9.19–9.20) constitute a necessary and sufficient set of constraints for contact between the link and the counterweight, *with  $\widehat{q}_a$  as the contact point*.

**Resulting Practical<sup>+</sup> Constraints** Besides guaranteeing contact, also the maximum counterweight thickness should be taken into account, by imposing (9.14a–9.14b). All of these constraints together constitute the so-called practical<sup>+</sup> constraints:

$$J_i^* \geq \frac{1}{2} \cdot m_i^* \cdot [(X_i^*)^2 + (Y_i^*)^2]; \quad (9.21a)$$

$$X_i^* \leq 0; \quad (9.21b)$$

$$J_i^* \geq \frac{(m_i^*)^2}{2 \cdot \pi \cdot t^M \cdot \rho}; \quad (9.21c)$$

$$m_i^* \geq 0. \quad (9.21d)$$

**Discussion** (9.21a–9.21b) constitute a necessary and sufficient set of constraints for contact between the link and the counterweight, *with the LCS origin  $\hat{q}_a$  as the contact point*. If for the *true practical<sup>+</sup> optimum*<sup>3</sup>, the LCS origin *is* the contact point between each counterweight and its corresponding link, then the global optimum of the optimization problem with the practical<sup>+</sup> constraints *is* the true practical<sup>+</sup> optimum. If not, the latter optimum cannot be found. In that case, the obtained global optimum has an active constraint (9.21b), i.e.,  $X_i^* = 0$ . Conversely, if the obtained global optimum has  $X_i^* < 0$  for each counterweight, it is the true practical<sup>+</sup> optimum.

In the case of a  $4R$  crank-rocker four-bar, we are 'pretty sure' to obtain a solution where  $X_i^* < 0$ , provided that the LCSs are chosen as in Fig.8.1. This 'suspicion' is induced by known balancing results from literature and is confirmed by the numerical results of Section 9.4.2.

### 9.2.3.4 Additional constraints

Besides the ultimate, practical or practical<sup>+</sup> constraints, additional constraints are required: (i) in order to avoid excessive link loading, the total counterweight mass is constrained to a maximum  $m_{\text{tot}}^M$ , as done in (Sadler and Mayne, 1973) and (ii) bound constraints are imposed on the counterweight COG coordinates:

$$X_i^m \leq X_i^* \leq X_i^M; \quad (9.22a)$$

$$Y_i^m \leq Y_i^* \leq Y_i^M; \quad (9.22b)$$

$$m_1^* + m_2^* + m_3^* \leq m_{\text{tot}}^M. \quad (9.22c)$$

## 9.2.4 Resulting Optimization Problems

The optimization problems with the optimization variable  $\mathbf{x}$ , (9.11a) as a goal function and the ultimate set of constraints (9.11b–9.11c, 9.12a–9.12b, 9.22a–9.22c), the practical set of constraints (9.11b–9.11c, 9.14a–9.14b, 9.22a–9.22c) or the practical<sup>+</sup> set of constraints (9.11b–9.11c, 9.21a–9.21d, 9.22a–9.22c) are nonconvex. For instance, the balancing effect indices  $\alpha_{\text{fsh}}$ ,  $\alpha_{\text{msh}}$  and  $\alpha_{\text{drv}}$  are complicated, implicit, nonconvex functions of the optimization variable  $\mathbf{x}$ . In the following section, it is shown how to reformulate these nonconvex problems as convex programs.

## 9.3 $4R$ Four-Bar: Convex Reformulation

Two 'tricks' are required for convexly reformulating the optimization problems of the previous section. Firstly, the  $\mu$ -parameters are adopted as optimization

<sup>3</sup>That is, the counterweight configuration that minimizes (9.11a), complies with (9.11b–9.11c), (9.14a–9.14b) and (9.22a–9.22c) and that has every counterweight in contact with the corresponding link.

variables, instead of the conventional mass parameters. The key element of this parameterization is that it has the property of superposition, as shown in Section 9.3.1. Secondly, LIV expressions are used to express the balancing effect indices as an *explicit* function of the optimization variables (Section 9.3.2). Application of both tricks finally results in the convex programs proposed in Section 9.3.3.

### 9.3.1 Mass Parameterization

For reference, the definition of the  $\mu$ -parameters is repeated here:

$$\mu_{1i} = m_i; \tag{9.23a}$$

$$\mu_{2i} = m_i \cdot X_i; \tag{9.23b}$$

$$\mu_{3i} = m_i \cdot Y_i; \tag{9.23c}$$

$$\mu_{4i} = J_i + m_i \cdot (X_i^2 + Y_i^2). \tag{9.23d}$$

Although these parameters had already been used by other authors, Haines (1981) is the first one in CWB literature to point out their remarkable superposition property: 'Although it is conventional to regard  $X_i$ ,  $Y_i$  and  $J_i$  as fundamental properties and  $\mu_{2i}$ ,  $\mu_{3i}$  and  $\mu_{4i}$  as derived properties, the boot could as well be regarded as being on the other foot, especially since, for an arbitrary body,  $X_i$ ,  $Y_i$  and  $J_i$  are in practice calculated from the  $\mu$ -terms rather than vice versa. What is more,  $\mu$  has an important quality lacking in its rival: it obeys the principal of superposition, that is to say that  $\mu$  for a whole body is equal to the sum of the  $\mu$ 's for its constituent parts.'

The proof of these superposition properties is not given in (Haines, 1981) and is therefore developed in Appendix N. Grouping the  $\mu$ -parameters of the original mechanism in  $\mu^o \in \mathbb{R}^{12}$ , the counterweight  $\mu$ -parameters in  $\mu^* \in \mathbb{R}^{12}$  and the  $\mu$ -parameters after counterweight addition in  $\mu \in \mathbb{R}^{12}$ , results in the following concise formulation of the superposition property:

$$\mu = \mu^o + \mu^*. \tag{9.24}$$

Using the  $\mu$ -parameters as optimization variables requires reformulation of the mass constraints of Section 9.2.3. Furthermore, a redundant constraint  $\mu_{4i}^* \geq 0$  is added to each set of equations, for reasons that are explained hereafter. As a result, the following sets of constraints are obtained:

#### Ultimate constraints

$$\mu_{1i}^* \geq 0; \tag{9.25a}$$

$$\mu_{1i}^* \cdot \mu_{4i}^* \geq (\mu_{2i}^*)^2 + (\mu_{3i}^*)^2; \tag{9.25b}$$

$$\mu_{4i}^* \geq 0; \tag{9.25c}$$

**Practical constraints**

$$\mu_{4i}^* \geq \frac{(\mu_{1i}^*)^2}{2 \cdot \pi \cdot t^M \cdot \rho} + \frac{(\mu_{2i}^*)^2}{\mu_{1i}^*} + \frac{(\mu_{3i}^*)^2}{\mu_{1i}^*}; \quad (9.26a)$$

$$\mu_{1i}^* \geq 0; \quad (9.26b)$$

$$\mu_{4i}^* \geq 0; \quad (9.26c)$$

**Practical<sup>+</sup> constraints**

$$\mu_{1i}^* \cdot \mu_{4i}^* \geq \frac{3}{2} \cdot [(\mu_{2i}^*)^2 + (\mu_{3i}^*)^2]; \quad (9.27a)$$

$$\mu_{2i}^* \leq 0; \quad (9.27b)$$

$$\mu_{4i}^* \geq \frac{(\mu_{1i}^*)^2}{2 \cdot \pi \cdot t^M \cdot \rho} + \frac{(\mu_{2i}^*)^2}{\mu_{1i}^*} + \frac{(\mu_{3i}^*)^2}{\mu_{1i}^*}; \quad (9.27c)$$

$$\mu_{1i}^* \geq 0; \quad (9.27d)$$

$$\mu_{4i}^* \geq 0; \quad (9.27e)$$

**Additional constraints**

$$\mu_{1i}^* \cdot X_i^m \leq \mu_{2i}^* \leq \mu_{1i}^* \cdot X_i^M; \quad (9.28a)$$

$$\mu_{1i}^* \cdot Y_i^m \leq \mu_{3i}^* \leq \mu_{1i}^* \cdot Y_i^M; \quad (9.28b)$$

$$\mu_{11}^* + \mu_{12}^* + \mu_{13}^* \leq m_{\text{tot}}^M. \quad (9.28c)$$

All of these constraints are linear in the  $\mu$ -parameters, except for (9.25b), (9.26a/9.27c) and (9.27a). These nonlinear constraints are however convex: it is shown hereafter that (9.25b) and (9.27a) are second-order cone constraints of the general form (9.6) and that (9.26a/9.27c) is a linear matrix inequality.

**Convexity of (9.25b) and (9.27a)** The sets of equations (9.25a–9.25c) on the one hand and (9.27a,9.27d–9.27e) are known as hyperbolic constraints, as they describe a half hyperboloid. Using the fact (Lobo et al., 1998):

$$\mathbf{w}^T \mathbf{w} \leq xy, x \geq 0, y \geq 0 \iff \left\| \begin{bmatrix} 2\mathbf{w} \\ x - y \end{bmatrix} \right\| \leq x + y, \quad (9.29)$$

where  $\mathbf{w}$  is a vector and  $x$  and  $y$  are scalars<sup>4</sup>, (9.25a–9.25c) can be replaced by the following second-order cone constraint:

$$\left\| \begin{bmatrix} 2\mu_{2i}^* \\ 2\mu_{3i}^* \\ \mu_{1i}^* - \mu_{4i}^* \end{bmatrix} \right\| \leq \mu_{1i}^* + \mu_{4i}^*. \quad (9.30)$$

---

<sup>4</sup>(9.29) clarifies the addition of the redundant constraint  $\mu_{4i}^* \geq 0$ : it is required for application of (9.29) to be allowed.

Similarly, (9.27a,9.27d–9.27e) are equivalent to the following second-order cone constraint:

$$\left\| \begin{bmatrix} \sqrt{6} \cdot \mu_{2i}^* \\ \sqrt{6} \cdot \mu_{3i}^* \\ \mu_{1i}^* - \mu_{4i}^* \end{bmatrix} \right\| \leq \mu_{1i}^* + \mu_{4i}^*. \quad (9.31)$$

**Convexity of (9.26a/9.27c)** Appendix P reformulates this constraint as a linear matrix inequality, which implies that it is convex. A more intuitive proof of convexity is given here, and is based on rewriting the constraint as:

$$(-\mu_{4i}^*) + \frac{(\mu_{1i}^*)^2}{2 \cdot \pi \cdot t^M \cdot \rho} + \frac{(\mu_{2i}^*)^2}{\mu_{1i}^*} + \frac{(\mu_{3i}^*)^2}{\mu_{1i}^*} \leq 0.$$

The constraint is convex if the left part of the above inequality is a convex function. To prove this, it suffices to show that each of the constituting terms is convex, since the sum of convex functions is again a convex function (Boyd and Vandenberghe, 2004).

The proof that the first two terms are convex is trivial: a scalar function  $f$  is convex if and only if its domain is convex (that is, an interval) and its second derivative  $f'' \geq 0$ . The second derivatives of the first two terms respectively equal zero and  $1/(\pi \cdot t^M \cdot \rho)$  and hence comply with the convexity constraint. The third and the fourth term are examples of so-called *quadratic-over-linear* functions  $y^2/x$ . In (Boyd and Vandenberghe, 2004), it is proven that these functions are convex for  $x > 0$ . Hence  $\mu_{1i}^* > 0$  must be used instead of  $\mu_{1i}^* \geq 0$ , imposed by (9.26b/9.27d).

### 9.3.2 LIV Expressions

This section shows that LIV expressions provide a way of expressing the balancing effect indices explicitly as a function of the  $\mu$ -parameters. This is first illustrated for a general dynamic reaction  $d(t)$ . After that, results are given for the shaking force, shaking moment and input torque of the considered 4R four-bar.

**General Dynamic Reaction** Consider a general dynamic reaction  $d(t)$  and its LIV expression

$$d(t) = \mathbf{e}^T(t) \cdot \mathbf{p} = \sum_{i=1}^n e_i(t) \cdot p_i. \quad (9.32)$$

The corresponding balancing index  $\alpha$  is given by (9.10). It is generally known in experimental robot identification literature (Atkeson et al., 1986; Raucant et al., 1992) that, if the  $\mu$ -parameters are used instead of the conventional mass

parameters, the elements of  $\mathbf{p}$  are linear combinations of the  $\mu$ -parameters, with the coefficients depending on the kinematic parameters:

$$\mathbf{p} = \mathbf{C} \cdot \boldsymbol{\mu}, \quad (9.33)$$

where  $\mathbf{p} \in \mathbb{R}^n$ , and  $\mathbf{C} \in \mathbb{R}^{n \times 12}$  only depends on the mechanism's kinematics. Hence, for establishing an explicit relation between the  $\mu$ -parameters and  $\alpha$ , it suffices to establish a relation between  $\mathbf{p}$  and  $\alpha$ .

First, construct a vector  $\mathbf{d} \in \mathbb{R}^K$  of  $d(t_k)$ -values at equidistant time instances  $t_k = (k - 1) \cdot T_s$ . Based on (9.32), the following result is obtained:

$$\mathbf{d} = \mathbf{E} \cdot \mathbf{p}, \quad (9.34)$$

where the (regular) matrix  $\mathbf{E} \in \mathbb{R}^{K \times n}$  is defined as:

$$\mathbf{E} = [\mathbf{e}(t_1) \quad \dots \quad \mathbf{e}(t_K)]^T.$$

As a result, the balancing index expression (9.10) transforms into:

$$\alpha = \frac{\|\mathbf{d}\|}{\|\mathbf{d}^\circ\|} = \frac{(\mathbf{p}^T \cdot \mathbf{E}^T \cdot \mathbf{E} \cdot \mathbf{p})^{\frac{1}{2}}}{\|\mathbf{d}^\circ\|},$$

where  $\mathbf{E}^T \cdot \mathbf{E}$  is symmetric and positive definite. Hence, its singular value decomposition (SVD) equals

$$\mathbf{E}^T \cdot \mathbf{E} = \mathbf{U} \cdot \text{diag}(\sigma_1, \dots, \sigma_n) \cdot \mathbf{U}^T, \quad (9.35)$$

where all singular values  $\sigma_i \geq 0$ .  $\mathbf{U} \in \mathbb{R}^{n \times n}$  contains the  $n$  singular vectors. Now define the vector  $\mathbf{z} \in \mathbb{R}^n$  as:

$$\mathbf{z} = \frac{\text{diag}(\sqrt{\sigma_1}, \dots, \sqrt{\sigma_n}) \cdot \mathbf{U}^T}{\|\mathbf{d}^\circ\|} \cdot \mathbf{p} = \boldsymbol{\Psi} \cdot \mathbf{p}, \quad (9.36)$$

then it is easily verified that

$$\alpha = \|\mathbf{z}\|. \quad (9.37)$$

(9.36) and (9.37) constitute the desired explicit relation between  $\mathbf{p}$  and  $\alpha$ .  $\boldsymbol{\Psi} \in \mathbb{R}^{n \times n}$  is of full rank, and only depending on the mechanism kinematics and the mass properties of the unbalanced mechanism (through  $\|\mathbf{d}^\circ\|$ ).

**Dynamic Reactions in 4R Four-Bar** Given the kinematics of the 4R four-bar, that is, the link lengths  $a_i, i = \{1, 2, 3, 4\}$ , the fixed angle  $\phi_4$  and the input crank angle's time trajectory  $\phi_1(t)$ , the following LIV expressions for

the considered dynamic reactions are obtained:

$$F_{\text{shak},x}(t) = \mathbf{e}_{\text{fshx}}^T(t) \cdot \mathbf{p}_{\text{fsh}} = \sum_{i=1}^4 e_{\text{fshx},i}(t) \cdot p_{\text{fsh},i}; \quad (9.38a)$$

$$F_{\text{shak},y}(t) = \mathbf{e}_{\text{fshy}}^T(t) \cdot \mathbf{p}_{\text{fsh}} = \sum_{i=1}^4 e_{\text{fshy},i}(t) \cdot p_{\text{fsh},i}; \quad (9.38b)$$

$$M_{\text{shak}}(t) = \mathbf{e}_{\text{msh}}^T(t) \cdot \mathbf{p}_{\text{msh}} = \sum_{i=1}^6 e_{\text{msh},i}(t) \cdot p_{\text{msh},i}; \quad (9.38c)$$

$$M_{\text{drv}}(t) = \mathbf{e}_{\text{drv}}^T(t) \cdot \mathbf{p}_{\text{drv}} = \sum_{i=1}^4 e_{\text{drv},i}(t) \cdot p_{\text{drv},i}. \quad (9.38d)$$

The functions  $e_{\text{fshx},i}(t)$ ,  $e_{\text{fshy},i}(t)$ ,  $e_{\text{msh},i}(t)$  and  $e_{\text{drv},i}(t)$  are determined by the mechanism's kinematics and are linearly independent. Expressions for these functions are derived using the classical method of Berkof and Lowen (1969), and are given in Appendix O. Since  $e_{\text{msh},1}(t) = e_{\text{drv},1}(t) = \ddot{\phi}_1(t)$ , the first element of  $\mathbf{e}_{\text{drv}}(t)$  and  $\mathbf{e}_{\text{msh}}(t)$  is zero if the mechanism is driven with a constant input crank speed. In that case, the expressions for  $M_{\text{shak}}(t)$  and  $M_{\text{drv}}(t)$  respectively contain five (instead of six) and three (instead of four) nonzero terms, and hence the first element of  $\mathbf{p}_{\text{msh}}$  and  $\mathbf{p}_{\text{drv}}$  is dropped. Therefore, the notation  $\mathbf{p}_i \in \mathbb{R}^{n_i}$ ,  $i = \{\text{fsh}, \text{msh}, \text{drv}\}$  is introduced, where

$$\begin{aligned} \{n_{\text{fsh}}, n_{\text{msh}}, n_{\text{drv}}\} &= \{4, 5, 3\} \quad (\text{constant input crank speed}); \\ \{n_{\text{fsh}}, n_{\text{msh}}, n_{\text{drv}}\} &= \{4, 6, 4\} \quad (\text{fluctuating input crank speed}). \end{aligned} \quad (9.39)$$

Expressions for the time-independent elements of  $\mathbf{p}_i$ ,  $i = \{\text{fsh}, \text{msh}, \text{drv}\}$  are also derived in Appendix O and are given below. They illustrate that these elements are linear combinations of the  $\mu$ -parameters, with the coefficients depending on the kinematic parameters. Setting the expressions for the elements of  $\mathbf{p}_{\text{fsh}}$  equal to zero, results in the force-balance conditions (8.14–8.17) derived in Section 8.2.2.

$$p_{\text{fsh},1} = \mu_{21} + a_1 \cdot \mu_{12} - \frac{a_1}{a_2} \cdot \mu_{22}; \quad (9.40a)$$

$$p_{\text{fsh},2} = \mu_{31} - \frac{a_1}{a_2} \cdot \mu_{32}; \quad (9.40b)$$

$$p_{\text{fsh},3} = \mu_{23} + \frac{a_3}{a_2} \cdot \mu_{22}; \quad (9.40c)$$

$$p_{\text{fsh},4} = \mu_{33} + \frac{a_3}{a_2} \cdot \mu_{32}; \quad (9.40d)$$

$$p_{\text{msh},1} = p_{\text{drv},1} = \mu_{41} - \frac{2 \cdot a_1^2}{a_2} \cdot \mu_{22} + \mu_{12} \cdot a_1^2 + \frac{a_1^2}{a_2^2} \cdot \mu_{42}; \quad (9.41a)$$

$$p_{\text{msh},2} = p_{\text{drv},2} = \mu_{43} + \frac{a_3^2}{a_2^2} \cdot \mu_{42}; \quad (9.41b)$$

$$p_{\text{msh},3} = p_{\text{drv},3} = -\mu_{42} + a_2 \cdot \mu_{22}; \quad (9.41c)$$

$$p_{\text{msh},4} = p_{\text{drv},4} = \mu_{32}; \quad (9.41d)$$

$$p_{\text{msh},5} = \mu_{23} + \frac{a_3}{a_2^2} \cdot \mu_{42}; \quad (9.41e)$$

$$p_{\text{msh},6} = \mu_{33}. \quad (9.41f)$$

Based on (9.36) and (9.37), we have:

$$\alpha_{\text{fsh}} = \|\mathbf{z}_{\text{fsh}}\|; \quad (9.42a)$$

$$\alpha_{\text{msh}} = \|\mathbf{z}_{\text{msh}}\|; \quad (9.42b)$$

$$\alpha_{\text{drv}} = \|\mathbf{z}_{\text{drv}}\|, \quad (9.42c)$$

where  $\mathbf{z}_i \in \mathbb{R}^{n_i}$ ,  $i = \{\text{fsh}, \text{msh}, \text{drv}\}$  and

$$\mathbf{z}_{\text{fsh}} = \frac{\text{diag}(\sqrt{\sigma_{\text{fsh},1}}, \dots, \sqrt{\sigma_{\text{fsh},n_{\text{fsh}}}}) \cdot \mathbf{U}_{\text{fsh}}^T}{\|\mathbf{F}_{\text{shak}}^{\text{o}}\|} \cdot \mathbf{p}_{\text{fsh}} = \mathbf{\Psi}_{\text{fsh}} \cdot \mathbf{p}_{\text{fsh}}; \quad (9.43a)$$

$$\mathbf{z}_{\text{msh}} = \frac{\text{diag}(\sqrt{\sigma_{\text{msh},1}}, \dots, \sqrt{\sigma_{\text{msh},n_{\text{msh}}}}) \cdot \mathbf{U}_{\text{msh}}^T}{\|\mathbf{M}_{\text{shak}}^{\text{o}}\|} \cdot \mathbf{p}_{\text{msh}} = \mathbf{\Psi}_{\text{msh}} \cdot \mathbf{p}_{\text{msh}}; \quad (9.43b)$$

$$\mathbf{z}_{\text{drv}} = \frac{\text{diag}(\sqrt{\sigma_{\text{drv},1}}, \dots, \sqrt{\sigma_{\text{drv},n_{\text{drv}}}}) \cdot \mathbf{U}_{\text{drv}}^T}{\|\mathbf{M}_{\text{drv}}^{\text{o}}\|} \cdot \mathbf{p}_{\text{drv}} = \mathbf{\Psi}_{\text{drv}} \cdot \mathbf{p}_{\text{drv}}. \quad (9.43c)$$

$\mathbf{\Psi}_i \in \mathbb{R}^{n_i \times n_i}$ ,  $i = \{\text{fsh}, \text{msh}, \text{drv}\}$ , while the singular values  $\sigma_i$  and the matrices  $\mathbf{U}_i \in \mathbb{R}^{n_i \times n_i}$  of singular vectors are obtained from:

$$\mathbf{E}_{\text{fshx}}^T \cdot \mathbf{E}_{\text{fshx}} + \mathbf{E}_{\text{fshy}}^T \cdot \mathbf{E}_{\text{fshy}} = \mathbf{U}_{\text{fsh}} \cdot \text{diag}(\sigma_{\text{fsh},1}, \dots, \sigma_{\text{fsh},n_{\text{fsh}}}) \cdot \mathbf{U}_{\text{fsh}}^T; \quad (9.44a)$$

$$\mathbf{E}_{\text{msh}}^T \cdot \mathbf{E}_{\text{msh}} = \mathbf{U}_{\text{msh}} \cdot \text{diag}(\sigma_{\text{msh},1}, \dots, \sigma_{\text{msh},n_{\text{msh}}}) \cdot \mathbf{U}_{\text{msh}}^T; \quad (9.44b)$$

$$\mathbf{E}_{\text{drv}}^T \cdot \mathbf{E}_{\text{drv}} = \mathbf{U}_{\text{drv}} \cdot \text{diag}(\sigma_{\text{drv},1}, \dots, \sigma_{\text{drv},n_{\text{drv}}}) \cdot \mathbf{U}_{\text{drv}}^T. \quad (9.44c)$$

### 9.3.3 Resulting Convex Programs

The optimization vector is defined as:

$$\mathbf{x} = [(\mu^*)^T \quad \mu^T \quad \mathbf{p}_{\text{fsh}}^T \quad \mathbf{p}_{\text{msh}}^T \quad \mathbf{p}_{\text{drv}}^T \quad \mathbf{z}_{\text{fsh}}^T \quad \mathbf{z}_{\text{msh}}^T \quad \mathbf{z}_{\text{drv}}^T \quad q]^T,$$

where  $q$  is a scalar, auxiliary variable, the introduction of which is justified below.  $\mathbf{x} \in \mathbb{R}^{49}$  if the input crank speed  $\dot{\phi}_1$  is constant and  $\mathbf{x} \in \mathbb{R}^{53}$  if it is fluctuating. The goal function to be minimized is:

$$f_{\text{optim}} = q.$$

Minimizing  $\alpha_{\text{msh}}$  (or equivalently  $\|\mathbf{z}_{\text{msh}}\|$ ) directly or minimizing  $q$  subject to  $\|\mathbf{z}_{\text{msh}}\| \leq q$  is equivalent. The auxiliary variable  $q$  has to be introduced in order to obtain a goal function, linear in the optimization variables. The minimum is to be sought subject to the following constraints:

- linear equality constraints  $\mu = \mu^{\circ} + \mu^*$ , due to the superposition of the original and counterweight  $\mu$ -parameters;
- linear equality constraints, due to the linear conversion (9.40a–9.40d, 9.41a–9.41f) from  $\mu$  to  $\mathbf{p}_i, i = \{\text{fsh}, \text{msh}, \text{drv}\}$ ;
- linear equality constraints, due to the linear conversion (9.43a–9.43c) from  $\mathbf{p}_i$  to  $\mathbf{z}_i, i = \{\text{fsh}, \text{msh}, \text{drv}\}$ ;
- feasibility constraints on counterweight  $\mu$ -parameters:
  - ultimate constraints: second-order cone constraint (9.30);
  - practical constraints: linear inequality constraints (9.26b–9.26c) and LMI (9.26a);
  - practical<sup>+</sup> constraints: linear inequality constraint (9.27b), second-order cone constraint (9.27a) and LMI (9.27c).
- additional linear inequality constraints (9.28a–9.28c) on  $\mu^*$ -parameters;
- upper bounds (9.11b–9.11c) on the balancing indices. Based on (9.42a, 9.42c), this is equivalent to imposing upper bounds on the norms of  $\mathbf{z}_i, i = \{\text{fsh}, \text{drv}\}$ , which gives rise to the following second-order cone constraints:

$$\begin{aligned}\|\mathbf{z}_{\text{fsh}}\| &\leq \alpha_{\text{fsh}}^{\text{M}}; \\ \|\mathbf{z}_{\text{drv}}\| &\leq \alpha_{\text{drv}}^{\text{M}}.\end{aligned}$$

- an additional second-order cone constraint, due to the introduction of the auxiliary variable  $q$ :

$$\|\mathbf{z}_{\text{msh}}\| \leq q.$$

If the ultimate constraints are used, this optimization problem has a linear goal function that is minimized subject to linear equality constraints, linear inequality constraints and second-order cone constraints. It is hence a second-order cone program. If the practical or practical<sup>+</sup> constraints are used, an LMI is present and an SDP is obtained. These convex programs are equivalent to the original, nonconvex optimization problems, defined in Section 9.2.

	$i = 1$	$i = 2$	$i = 3$
$a_i$ [m]	0.0508	0.1524	0.0762
$m_i$ [kg]	0.0894	0.2394	0.1215
$X_i$ [m]	0.0254	0.0762	0.0381
$Y_i$ [m]	0	0.102	0
$J_i$ [ $10^{-3}$ kg-m <sup>2</sup> ]	0.0198	0.6792	0.2198

TABLE 9.1: Crank-rocker four-bar: numerical parameters of link 1, link 2 and link 3.  $a_4 = 0.1397$  m and  $\phi_4 = 0$ .

### 9.3.4 Discussion

Although the  $\mu$ -parameters are used by some authors (Tepper and Lowen, 1975; Haines, 1981; Kochev and Gurdev, 1988), and the LIV expressions are frequently applied in CWB literature, the present convex formulation is new. The main reason for this is that, in order to obtain practical counterweights, all of the previous studies, even if they (such as Haines and Kochev) do use  $\mu$ -parameters and LIV expressions at the same time, do not impose general constraints, expressed as a function of the  $\mu^*$ -parameters, as done here.

Instead, they assume the counterweights to be circular (and very often tangent to the pivots in order to obtain minimum inertia). The circular counterweight radius, COG location, . . . , are then used as optimization variables, instead of the  $\mu^*$ -parameters. This inherently results in nonconvexity, due to the introduction of nonlinear equality constraints, such as (9.16).

The approach proposed here does not assume a particular counterweight shape, but is still guaranteed, by imposing the practical<sup>+</sup> constraints, to converge to a practically implementable solution.

## 9.4 Numerical Results

Numerical results are generated for a 4R (crank-rocker) four-bar linkage, considered in (Tricamo and Lowen, 1983b; Lee and Cheng, 1984), of which the kinematic and mass parameters are tabulated in Table 9.1. The mechanism runs at a constant input crank speed of 500 rpm. As a result, the inertia of the counterweight attached to the input crank I, does not affect the optimization process.

The following upper and lower bounds on the COG coordinates of the

counterweights are adopted ( $i = \{1, 2, 3\}$ ) throughout this section:

$$\begin{aligned} X_i^m &= -a_i/2; & X_i^M &= 3a_i/2; \\ Y_i^m &= -a_i/2; & Y_i^M &= a_i/2. \end{aligned}$$

Firstly, Section 9.4.1 discusses the optimization results in case the practical<sup>+</sup> constraints are used. After that, Section 9.4.2 compares these results to those obtained if the ultimate or practical constraints are used.

### 9.4.1 Practical<sup>+</sup> Constraints

In order to quantify the various trade-offs, 41 equidistant values of  $\alpha_{\text{fish}}^M$  between 0 and 1 are considered, and 25 equidistant values of  $\alpha_{\text{drv}}^M$  between 0.5 and 1.7. This means that the SDP needs to be solved 1025 times. Moreover, and in order to check the sensitivity of the results for the added mass, these 1025 optimization runs need to be done four times, as four values of  $m_{\text{tot}}^M$  are considered ( $m_{\text{tot}}^M = \{0.225, 0.338, 0.450, 0.675\}$  kg), which respectively represent  $\{50, 75, 100, 150\}\%$  of the original, total mechanism mass (0.45 kg). As in (Tricamo and Lowen, 1983b; Lee and Cheng, 1984), the maximum link thickness  $t^M$  equals 15.9 mm<sup>(5)</sup>.

**Numerically Solving the SDP** In this particular example, it is observed that the second-order cone constraint (9.31) is always active in the optimum. This fact is exploited, as shown in Appendix P, to convert the LMI (9.27c) into a second-order cone constraint, such that the SDP reduces to an SOCP, which can be solved faster.

The resulting SOCP is solved using **SeDuMi**, a dedicated package for solving optimization problems over symmetric cones (Sturm, 1999). Over the whole range of  $(\alpha_{\text{fish}}, \alpha_{\text{drv}}, m_{\text{tot}})$  values, **SeDuMi** reports on numerical problems. Therefore, the SOCP is also solved using the general-purpose matlab routine `fmincon`, which implements a sequential quadratic programming algorithm. Both packages yield quasi identical results, which shows that **SeDuMi**'s numerical results are reliable, despite the numerical problems.

Besides (9.31), also the inequality constraint (9.22c) is always active. Both constraints being active implies that the maximum amount of mass is added, under the form of counterweights that are tangent to the origin of the chosen LCS (that is  $\hat{a}$  for link I,  $\hat{b}$  for link II and  $\hat{d}$  for link III).

Moreover, the counterweights always have a negative  $X_i^*$  coordinate, implying that the addition of the constraint  $X_i^* \leq 0$ , which was needed in the derivation of the practical<sup>+</sup> constraints, does not constrain the found optimum. In other words: the LCSs have been chosen adequately and the *true* practical<sup>+</sup> optimum has been found.

<sup>5</sup>That is, 2.5 times the thickness of the unbalanced links.

**Assessing the Trade-off** Figure 9.4 shows contour plots of  $\alpha_{\text{msh}}$  as a function of  $\alpha_{\text{fsh}}^{\text{M}}$  and  $\alpha_{\text{drv}}^{\text{M}}$ , for the four selected values of  $m_{\text{tot}}^{\text{M}}$ . The crosses 'x' indicate infeasible points, which indicates that the required values of  $\alpha_{\text{fsh}}^{\text{M}}$  and  $\alpha_{\text{drv}}^{\text{M}}$  are too tight. Quite logically, the feasible area grows if the constraint on the total counterweight mass is relaxed (by increasing  $m_{\text{tot}}^{\text{M}}$ ). The contour lines behave rather 'shaky' at the boundary of the feasible area: in this region, SeDuMi runs into more severe numerical problems, and does not deliver reliable results.

Clearly, total shaking force balance ( $\alpha_{\text{fsh}} = 0$ ) is not possible with the given mass constraints. It is however possible if the total added mass is allowed to be 200% of the original mass. Zero driving torque is not possible either, but allowing for more added mass does not yield zero driving torque: only a massless four-bar can have zero input torque, as shown in (Elliott and Tesar, 1977).

Figure 9.4 provides a useful tool for assessing the trade-off between shaking force, shaking moment and driving torque. It shows for instance that there indeed are zones in which all of the three dynamic reactions are smaller than in the original mechanism ( $\alpha_i \leq 1, i = \{\text{fsh}, \text{msh}, \text{drv}\}$ ). However, if the rms driving torque is allowed to be greater than in the original mechanism, possibilities for reducing the other dynamic reactions are greater.

Another way of assessing the trade-off is provided by Fig.9.5, which shows  $\alpha_{\text{msh}}$  as a function of  $\alpha_{\text{fsh}}^{\text{M}}$  if a 20% increase of the driving torque is allowed ( $\alpha_{\text{drv}}^{\text{M}} = 1.2$ ). The four lines in this figure are the result of cutting the four  $\alpha_{\text{msh}}$ -surfaces, the contour lines of which are shown in Fig.9.4(a-d), with a vertical plane along the line  $\alpha_{\text{drv}}^{\text{M}} = 1.2$ .

The resulting curves for instance show that for  $m_{\text{tot}}^{\text{M}} = \{0.225, 0.338, 0.450, 0.675\}$  kg, both the shaking force and the shaking moment can be reduced simultaneously to respectively  $\{0.76, 0.71, 0.68, 0.63\}$  times their original values. These results indicate that counterweight addition is no magical solution: it is capable of decreasing the dynamic reactions, but the obtained reductions are moderate and come at the cost of significant mass addition.

**Effect on Joint Forces** In order to assess the effect of counterweight balancing on the joint forces, Fig.9.6 shows contour plots of  $\alpha_i, i = \{a, b, c, d\}$  as a function of  $\alpha_{\text{fsh}}^{\text{M}}$  [-] and  $\alpha_{\text{drv}}^{\text{M}}$  [-], for one of the four  $m_{\text{tot}}^{\text{M}}$  values, that is,  $m_{\text{tot}}^{\text{M}} = 0.450$  kg. These figures show that in general, counterweight balancing results in an increase of the joint forces ( $\alpha_i \geq 1$ ).

The best way of keeping this increase under control is to limit  $\alpha_{\text{drv}}^{\text{M}}$ , since the joint forces are more sensitive to  $\alpha_{\text{drv}}^{\text{M}}$  than to  $\alpha_{\text{fsh}}^{\text{M}}$ . This is derived from the fact that the contour lines are mainly oriented horizontally. Choosing  $\alpha_{\text{drv}}^{\text{M}} = 1.20$ , as done previously, seems reasonable, as it allows for a substantial decrease of the shaking force and shaking moment (illustrated by the line for  $m_{\text{tot}}^{\text{M}} = 0.450$  kg in Fig.9.5), while the joint force increase is maximally around 30%.

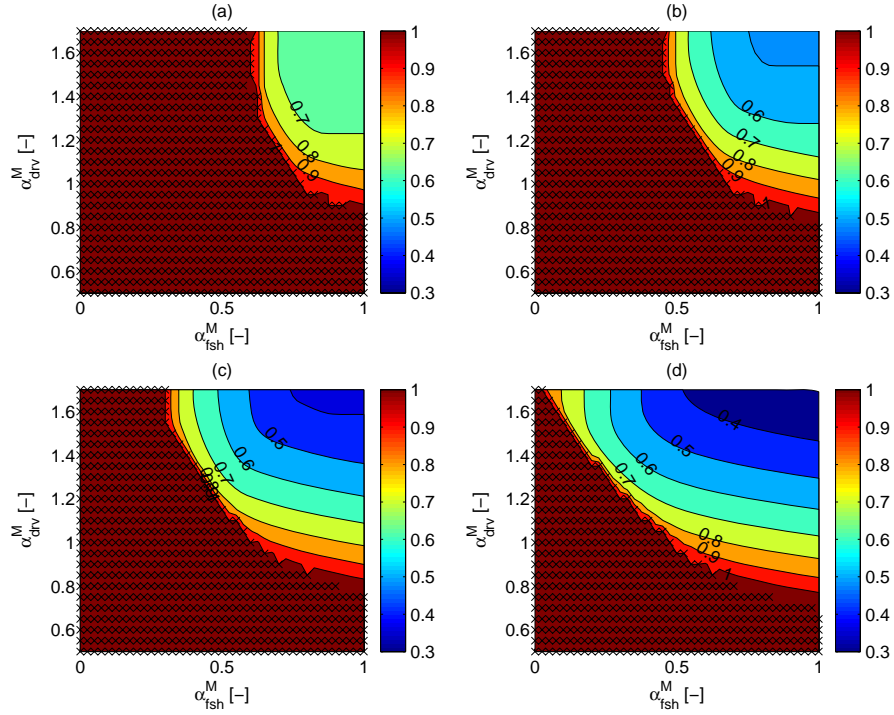


FIGURE 9.4: Contour plots of  $\alpha_{\text{msh}} [-]$  as a function of  $\alpha_{\text{fsh}}^{\text{M}} [-]$  and  $\alpha_{\text{drv}}^{\text{M}} [-]$  for  $m_{\text{tot}}^{\text{M}} = \{0.225(a), 0.338(b), 0.450(c), 0.675(d)\}$  kg. The crosses 'x' indicate infeasible points.

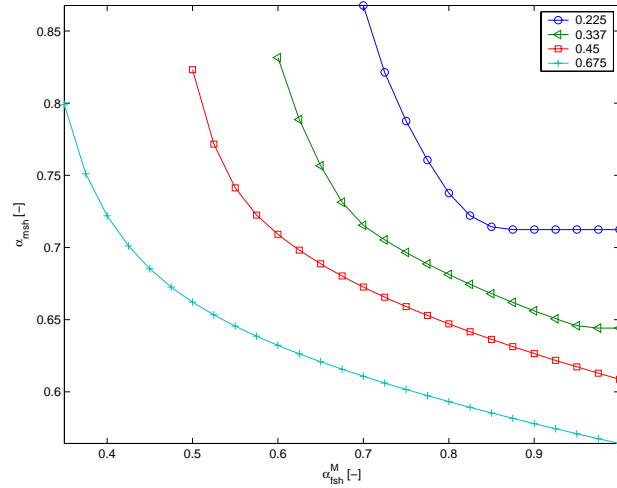


FIGURE 9.5:  $\alpha_{\text{msh}} [-]$  as a function of  $\alpha_{\text{fsh}}^{\text{M}} [-]$  for  $\alpha_{\text{drv}}^{\text{M}} = 1.2 [-]$  and  $m_{\text{tot}}^{\text{M}} = \{0.225, 0.338, 0.450, 0.675\}$  kg.

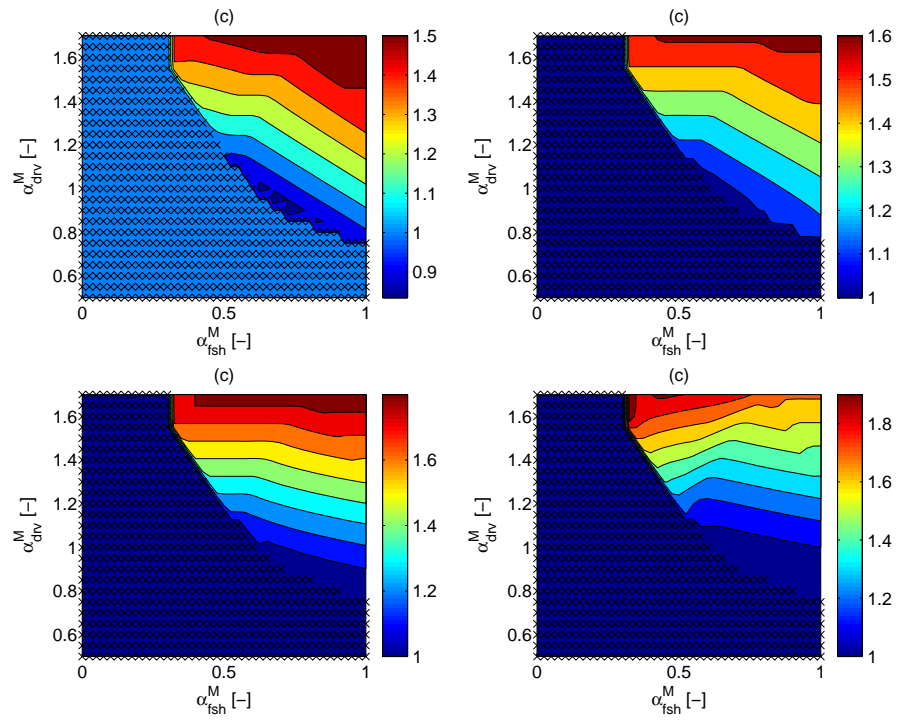


FIGURE 9.6: Contour plots of  $\alpha_a$  [-] (a),  $\alpha_b$  [-] (b),  $\alpha_c$  [-] (c) and  $\alpha_d$  [-] (d) as a function of  $\alpha_{\text{fsh}}^M$  [-] and  $\alpha_{\text{drv}}^M$  [-] for  $m_{\text{tot}}^M = 0.450$  kg. The crosses 'x' indicate infeasible points.

### 9.4.2 Relation with Ultimate and Practical Constraints

While the previous section has solely focussed on the practical<sup>+</sup> constraints, this section investigates the effect of using the more relaxed practical and ultimate constraints. Here, it is assumed that the values of  $\{\alpha_{\text{fsh}}^{\text{M}}, \alpha_{\text{drv}}^{\text{M}}, m_{\text{tot}}^{\text{M}}\}$  are fixed and given by  $\{0.6, 1.2, 0.450\}$ . On the other hand, the maximum thickness  $t^{\text{M}}$ , which was kept fixed to 15.9 mm in the previous section, is varied now by choosing different values for the link thickness ratio  $\gamma$  [-], defined as:

$$\gamma = \frac{t^{\text{M}}}{0.0159},$$

that is, the ratio of  $t^{\text{M}}$  w.r.t. the maximum link thickness, used throughout the previous section. Numerical results are generated for  $\gamma$  ranging between 0.1 and 100. Firstly, the effect of  $\gamma$  on the counterweight parameters is quantified. This is useful for the analysis of the effect of  $\gamma$  on the goal function value  $\alpha_{\text{msh}}$ . Lastly, numerical results are presented for  $\gamma = 2$ .

**Effect on Counterweight Parameters** For the practical and practical<sup>+</sup> constraints, the variation of the counterweight parameters as a function of  $\gamma$  is shown in Fig.9.7 and Fig.9.8. The ultimate constraints, on the other hand, are independent of  $\gamma$ , and so is hence the corresponding optimum. The resulting, ultimate counterweight parameters are tabulated in Table 9.2. No counterweight is added to link II, whereas the counterweight on link III is a point mass, as it combines nonzero mass with zero centroidal moment of inertia. No  $J_1^*$  value is given, since it is not an optimization variable, due to the assumption of constant input crank speed.

In case of the practical constraints, numerical evaluation of the maximum thickness constraint (9.14a) shows that it is active for any value of  $\gamma$ . As a consequence, the counterweights are always realized as cylinders of maximum thickness. Moreover, comparing the radius of these cylinders with their COG distance to the LCS origin, shows that they are never in contact with their corresponding link.

In case of the practical<sup>+</sup> constraints, numerical evaluation of the contact constraint (9.21a) shows that it is active for any value of  $\gamma$ . Hence, all counterweights are cylinders that are tangent to the LCS origin. These counterweights are of maximum thickness for  $\gamma \leq 1.9$ , but not for higher  $\gamma$ -values. Figure 9.8(a-c) confirms that  $X_i^*$  is always strictly negative, which implies that the obtained global optimum is the 'true practical<sup>+</sup> optimum', as explained in Section 9.2.3. Note also that the counterweight on link II has zero mass, and thus disappears, for  $\gamma \geq 1.45$ .

**Effect on Goal Function Value** The fact that the practical and the practical<sup>+</sup> constraints are more stringent than the ultimate constraints, results in a less optimal, that is, higher goal function value  $\alpha_{\text{msh}}$ . In order to

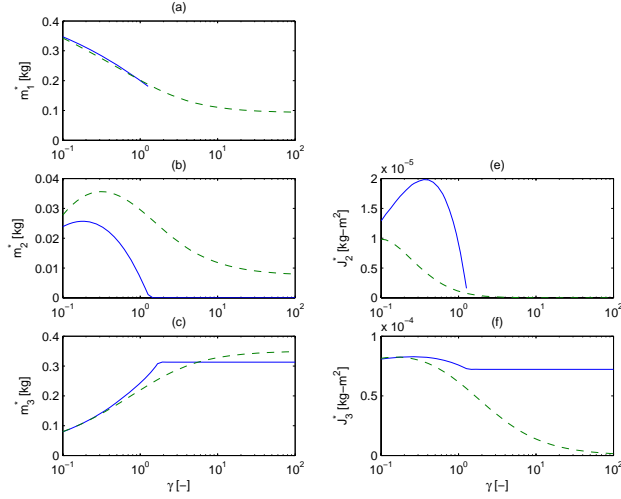


FIGURE 9.7: Counterweight mass and centroidal moment of inertia as a function of  $\gamma [-]$  for the practical (dashed line) and the practical<sup>+</sup> constraints (solid line) [ $\alpha_{\text{fsh}}^M = 0.6$ ,  $\alpha_{\text{drv}}^M = 1.2$ ,  $m_{\text{tot}}^M = 0.450$  kg]. No results for  $J_1^*$  are given, since it is not an optimization variable

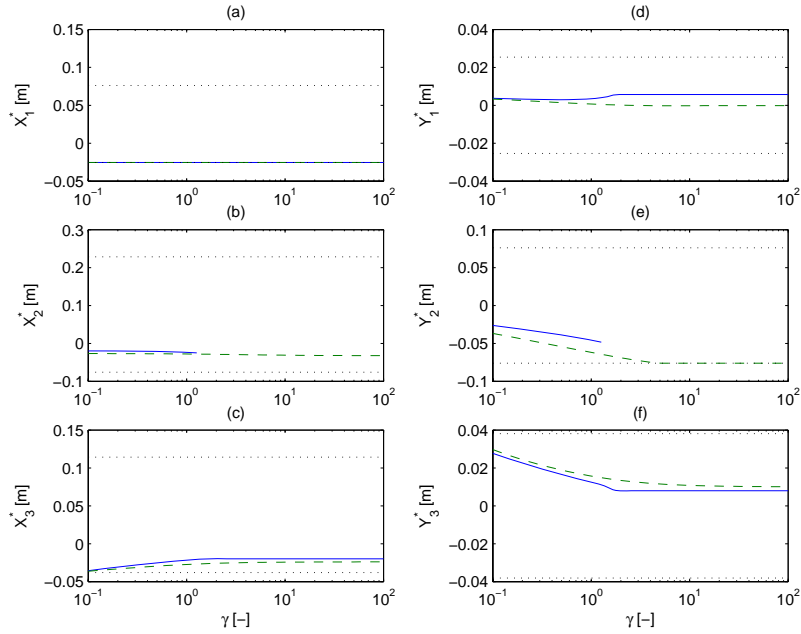


FIGURE 9.8: Counterweight coordinates as a function of  $\gamma [-]$  for the practical (dashed line) and the practical<sup>+</sup> constraints (solid line) [ $\alpha_{\text{fsh}}^M = 0.6$ ,  $\alpha_{\text{drv}}^M = 1.2$ ,  $m_{\text{tot}}^M = 0.450$  kg]. The dotted horizontal lines indicate the upper and lower bounds imposed by (9.22a–9.22b).

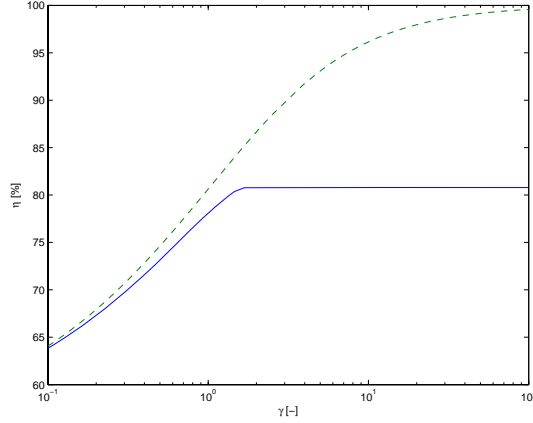


FIGURE 9.9:  $\eta$  [%] as a function of  $\gamma$  [-] for the practical (dashed line) and the practical<sup>+</sup> constraints (solid line) [ $\alpha_{\text{fish}}^{\text{M}} = 0.6$ ,  $\alpha_{\text{drv}}^{\text{M}} = 1.2$ ,  $m_{\text{tot}}^{\text{M}} = 0.450$  kg].

quantify this effect, a *balancing efficiency index*  $\eta$  [%] is introduced as follows:

$$\eta_{\text{prac}} = 100 \cdot \frac{\alpha_{\text{msh,ult}}}{\alpha_{\text{msh,prac}}}; \quad (9.45a)$$

$$\eta_{\text{prac}^+} = 100 \cdot \frac{\alpha_{\text{msh,ult}}}{\alpha_{\text{msh,prac}^+}}. \quad (9.45b)$$

As opposed to  $\alpha_{\text{msh,ult}}$ ,  $\alpha_{\text{msh,prac}}$  and  $\alpha_{\text{msh,prac}^+}$  do depend on  $\gamma$  and hence the efficiency indices do so too. Figure 9.9 illustrates this dependency for  $\gamma$  ranging between 0.1 and 100. As could be expected,  $\eta_{\text{prac}^+}$  is always smaller than  $\eta_{\text{prac}}$  since the practical<sup>+</sup> constraints are more restrictive than the practical constraints. Furthermore, for very large values of  $\gamma$ ,  $\eta_{\text{prac}}$  tends to 100%, whereas  $\eta_{\text{prac}^+}$  saturates at a value of 81%.  $\eta_{\text{prac}^+}$  is independent of  $\gamma$  for  $\gamma \geq 1.9$ , which is due to the already mentioned fact that the maximum thickness constraint is then no longer active.

In case of the practical constraints, the efficiency  $\eta_{\text{prac}}$  reaches 100% for infinitely high values of  $\gamma$ , which is explained as follows. Using the ultimate constraints results in point-mass counterweights. For any value of  $\gamma$ , the practical constraints yield counterweights that are cylindrical and of maximum thickness. Increasing values of  $\gamma$  therefore result in counterweights that get thicker and of a smaller radius. Hence, they come closer and closer to point masses. Numerical experiments with very large  $\gamma$ -values ( $\gamma > 1\text{e}6$ ) show that in that case, an efficiency of 100% is obtained, as well as counterweight parameters that are identical to the ultimate ones<sup>6</sup>. On the other hand, the

<sup>6</sup>Table 9.2 show that there is no link II counterweight in case of the ultimate constraints.

practical<sup>+</sup> constraints impose that the counterweights contain the LCS origin. Therefore, these counterweights can never approximate a point mass that does not coincide with the LCS origin.

The use of an efficiency plot like Fig.9.9 is twofold: (i) it provides a simple, graphical tool for choosing a suitable link thickness and (ii) it reveals that from a certain point on, the maximum link thickness is not a limiting factor for obtaining a better practical<sup>+</sup> balancing result.

**Results for  $\gamma = 2$**  As a further illustration of the difference between the different kinds of constraints, Table 9.2 tabulates<sup>7</sup> the optimized counterweight mass properties corresponding to  $\gamma = 2$ . In that case,  $t^M = 2 \cdot 15.9 = 31.8$  mm. Furthermore, for the practical and practical<sup>+</sup> constraints, the radius  $R_i^*$  and thickness  $t_i^*$  of the resulting cylindrical counterweights are given. Since  $J_1^*$  is no optimization variable,  $t_1^*$  can be chosen freely. Using (9.15),  $t_1^*$  is chosen such that a minimum inertia counterweight, tangent to  $\hat{a}$ , results.

Concerning the counterweights 2 and 3, the following is observed. The practical<sup>+</sup> counterweight 3 is tangent to the LCS origin:  $(R_3^*)^2 = (X_3^*)^2 + (Y_3^*)^2$ , while the maximum thickness constraint is no longer active ( $\gamma = 2 > 1.9$ ):  $t_3^* < 31.8$  mm. On the other hand, the practical counterweights 2 and 3 are of maximum thickness, and not in contact with the link, since they have  $X_i^* < 0$ , but also  $(R_i^*)^2 < (X_i^*)^2 + (Y_i^*)^2, i = \{1, 2\}$ .

Table 9.3 gives an overview of the balancing effect indices  $\alpha_i$  and  $\beta_i, i = \{\text{fsh, msh, drv}\}$ , where the balancing effect index  $\beta$  is defined as the maximum absolute value of the optimized dynamic reaction  $d(t)$  w.r.t. the maximum absolute value of the original dynamic reaction  $d^o(t)$ :

$$\beta = \frac{\max |d(t)|}{\max |d^o(t)|}. \quad (9.46)$$

This table reveals that  $\beta_i$  and  $\alpha_i$  are very similar to each other. Hence, in this case, using either  $\alpha_i$  or  $\beta_i$  in the optimization problem formulation, will yield very similar balancing results.

Figure 9.10 and Fig.9.11 respectively show the dynamic reactions (compared to the original dynamic reactions) and the resulting mechanism configuration, if the practical<sup>+</sup> counterweights of Table 9.2 are implemented. The mechanism remains quite compact, at the cost however of a counterweight thickness, five times that of the unbalanced links. Since all counterweights that have the same product  $t_i^* \cdot \rho$ , yield the same balancing result, smaller thicknesses are obtained by using a material with a greater mass density, such as lead.

---

This implies that counterweight 2 also eventually disappears for the practical constraints: for very large  $\gamma$ -values ( $\gamma > 1e6$ ), the dashed line in Fig.9.7(b) does not saturate on a nonzero value, but goes down to zero.

<sup>7</sup>The values for the practical and the practical<sup>+</sup> constraints can be read for  $\gamma = 2$  from Fig.9.7–9.8.

	ultimate		practical			practical <sup>+</sup>	
	$i = 1$	$i = 3$	$i = 1$	$i = 2$	$i = 3$	$i = 1$	$i = 3$
$m_i^*$ [kg]	0.089	0.361	0.162	0.023	0.265	0.137	0.313
$X_i^*$ [mm]	-25.4	-22.6	-25.4	-28.8	-25.8	-25.4	-19.9
$Y_i^*$ [mm]	1.8	9.5	0.1	-69.0	13.4	5.7	8.0
$J_i^*$ [kg-mm <sup>2</sup> ]	-	0	-	0.3	45.0	-	72.2
$R_i^*$ [mm]	-	-	25.4	5.4	18.4	26.0	21.5
$t_i^*$ [mm]	-	-	10.2	31.8	31.8	8.2	27.6

TABLE 9.2: Counterweight parameters of optimized mechanism, using ultimate, practical and practical<sup>+</sup> constraints [ $\alpha_{\text{fsh}}^{\text{M}} = 0.6$ ,  $\alpha_{\text{drv}}^{\text{M}} = 1.2$ ,  $m_{\text{tot}}^{\text{M}} = 0.450$  kg,  $\gamma = 2$ ]. No counterweight is attached to link II in case of the ultimate and the practical<sup>+</sup> constraints. The results for the ultimate constraints are independent of  $\gamma$ .

ultimate			practical			practical <sup>+</sup>		
$\alpha_{\text{fsh}}$	$\alpha_{\text{msh}}$	$\alpha_{\text{drv}}$	$\alpha_{\text{fsh}}$	$\alpha_{\text{msh}}$	$\alpha_{\text{drv}}$	$\alpha_{\text{fsh}}$	$\alpha_{\text{msh}}$	$\alpha_{\text{drv}}$
0.60	0.56	1.20	0.60	0.64	1.20	0.60	0.69	1.20
$\beta_{\text{fsh}}$	$\beta_{\text{msh}}$	$\beta_{\text{drv}}$	$\beta_{\text{fsh}}$	$\beta_{\text{msh}}$	$\beta_{\text{drv}}$	$\beta_{\text{fsh}}$	$\beta_{\text{msh}}$	$\beta_{\text{drv}}$
0.58	0.58	1.21	0.59	0.66	1.23	0.61	0.71	1.21

TABLE 9.3: Balancing effect indices  $\alpha_i$  and  $\beta_i$  [-] of optimized mechanism, using ultimate, practical and practical<sup>+</sup> constraints [ $\alpha_{\text{fsh}}^{\text{M}} = 0.6$ ,  $\alpha_{\text{drv}}^{\text{M}} = 1.2$ ,  $m_{\text{tot}}^{\text{M}} = 0.450$  kg,  $\gamma = 2$ ].

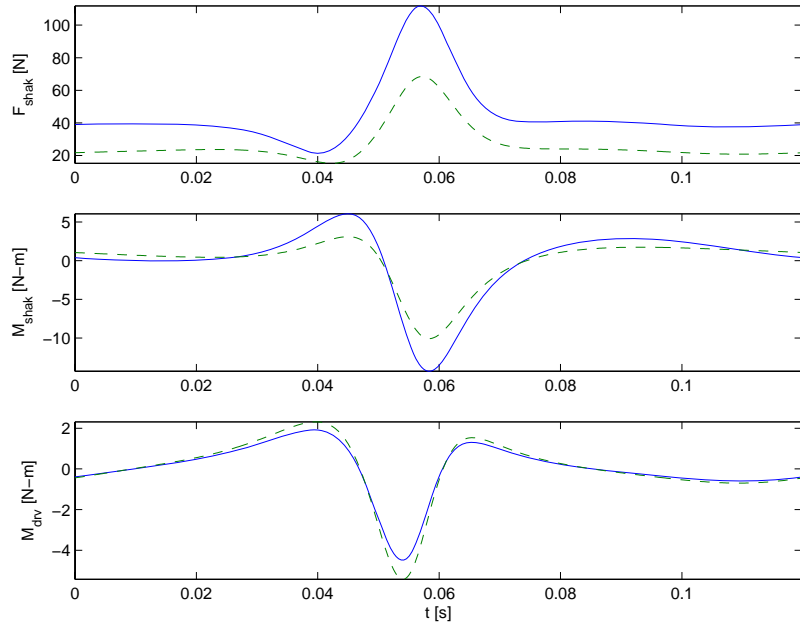


FIGURE 9.10: One period of the dynamic reactions of the original (solid line) and optimized (dashed line) mechanism, using practical<sup>+</sup> constraints [ $\alpha_{\text{fsh}}^{\text{M}} = 0.6$ ,  $\alpha_{\text{drv}}^{\text{M}} = 1.2$ ,  $m_{\text{tot}}^{\text{M}} = 0.450$  kg,  $\gamma = 2$ ].

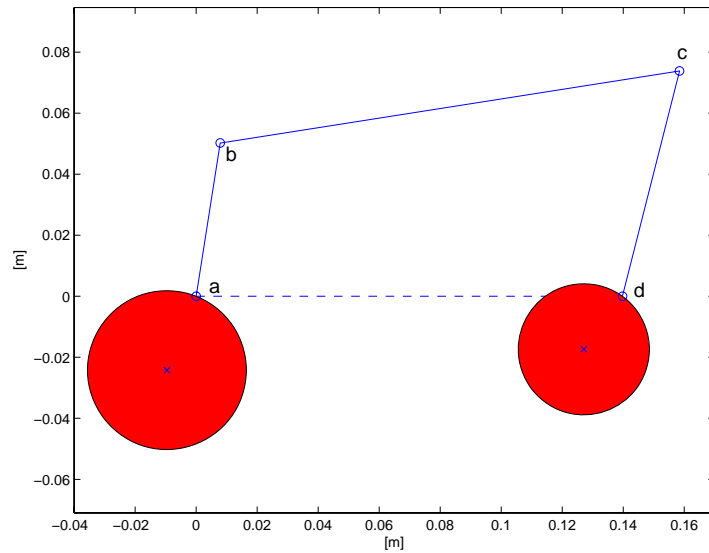


FIGURE 9.11: Front view of optimized mechanism, using practical<sup>+</sup> constraints [ $\alpha_{\text{fsh}}^{\text{M}} = 0.6$ ,  $\alpha_{\text{drv}}^{\text{M}} = 1.2$ ,  $m_{\text{tot}}^{\text{M}} = 0.450$  kg,  $\gamma = 2$ ].

## 9.5 Extension to $N$ -bar planar mechanisms

### 9.5.1 Problem Statement

Although the convex optimization framework has been developed for a planar, purely inertial four-bar mechanism, it is in principle valid for planar, purely inertial mechanisms with an arbitrary number of links  $N$ . A practical complication however arises from the basic prerequisite that, for any considered dynamic reaction  $d(t)$ , the vector  $\mathbf{d} \in \mathbb{R}^K$  of  $d(t_k)$ -values at equidistant time instances  $t_k = (k - 1) \cdot T_s$  must be written as in (9.34):

$$\mathbf{d} = \mathbf{E} \cdot \mathbf{p}, \quad (9.47)$$

where  $\mathbf{E} \in \mathbb{R}^{K \times n}$  is a regular matrix. In the four-bar case of Section 9.3.2,  $\mathbf{E}$  is constructed as

$$\mathbf{E} = [\mathbf{e}(t_1) \quad \dots \quad \mathbf{e}(t_K)]^T,$$

where the  $n$  functions  $e_i(t)$ , which constitute the elements of the  $n$ -vector  $\mathbf{e}(t)$ , are determined analytically in Appendix O. This same derivation also yields the linear relations

$$\mathbf{p} = \mathbf{C} \cdot \boldsymbol{\mu}, \quad (9.48)$$

between the elements of the  $n$ -vector  $\mathbf{p}$  and the  $\mu$ -parameters, where  $\mathbf{C} \in \mathbb{R}^{n \times 12}$ . The analytical derivation of Appendix O is based on symbolic manipulation and elimination of the expressions (O.2a–O.2d) and is already burdensome for a four-bar mechanism. For mechanisms of higher complexity, it is practically impossible to do the derivation by hand, and therefore an automated procedure is required.

This section develops such an automated procedure. Its basic goal is to develop expressions (9.47) and (9.48) that are valid for any planar  $N$ -bar mechanism, that do not require symbolic manipulation and that have a full-rank matrix  $\mathbf{E}$ . Here,  $\boldsymbol{\mu} \in \mathbb{R}^s$  and  $\mathbf{C} \in \mathbb{R}^{n \times s}$ , where  $s = 4 \cdot (N - 1)$  denotes the number of link mass parameters in an  $N$ -bar (planar) mechanism. The development of this procedure is the subject of Section 9.5.3. It is based on the force superposition principle that is developed in Section 9.5.2.

### 9.5.2 Force Superposition Principle

Consider an arbitrary link  $i$  of a planar, purely inertial mechanism, driven with a known input crank speed. Consider three different mass distributions for this link:

$$\begin{aligned} \mathbf{p} \boldsymbol{\mu}_i^T &= [{}^p \mu_{1i} \quad {}^p \mu_{2i} \quad {}^p \mu_{3i} \quad {}^p \mu_{4i}]; \\ \mathbf{q} \boldsymbol{\mu}_i^T &= [{}^q \mu_{1i} \quad {}^q \mu_{2i} \quad {}^q \mu_{3i} \quad {}^q \mu_{4i}]; \\ \mathbf{r} \boldsymbol{\mu}_i^T &= [{}^r \mu_{1i} \quad {}^r \mu_{2i} \quad {}^r \mu_{3i} \quad {}^r \mu_{4i}]. \end{aligned}$$

Furthermore, let  $\{^p d_j(t)\}$ ,  $\{^q d_j(t)\}$  and  $\{^r d_j(t)\}$ ,  $j = 1 \dots J$  be the set of  $J$  forces and moments that act on the link, corresponding to the mass distributions  $^p \mu_i^T$ ,  $^q \mu_i^T$  and  $^r \mu_i^T \in \mathbb{R}^4$ . If now

$$^r \mu_i = v \cdot (^p \mu_i) + w \cdot (^q \mu_i), \quad (9.49)$$

where  $v, w \in \mathbb{R}$ , then the following result is valid:

$$^r d_j(t) = v \cdot (^p d_j(t)) + w \cdot (^q d_j(t)), j = 1 \dots J. \quad (9.50)$$

The proof of this superposition principle is rather involved and is therefore deferred to Appendix Q. Note the notation used: the scalar  $\mu_{il}$  is a link  $i$  mass parameter ( $l = 1 \dots 4$ ), whereas  $\mu_i \in \mathbb{R}^4$  is a link  $i$  mass distribution. Furthermore,  $\mu \in \mathbb{R}^s$ , where  $s = 4 \cdot (N - 1)$ , is used in the remainder of this chapter to denote a linkage mass distribution. It is constructed as follows:

$$\mu = [\mu_1^T \quad \mu_2^T \quad \dots \quad \mu_{N-1}^T]^T,$$

where  $N$  denotes the number of links (link 0 is the fixed ground). A leading superscript  $^i(\cdot)$  is used to distinguish between mechanisms (or mechanism links) that have the same kinematic parameters, but different mass distributions.

### 9.5.3 Automated LIV Procedure

The superposition principle of the previous section is now used to develop an automated procedure for deriving (9.47–9.48). It is assumed that the kinematic parameters and the input crank speed are given. The procedure is applied to some dynamic reaction<sup>8</sup>  $d(t)$  and consists of four steps, given below.

**Step 1** Construct the matrix  $\mathbf{M} \in \mathbb{R}^{s \times s}$ :

$$\mathbf{M} = \begin{bmatrix} \mathbf{1} & \mu & \mathbf{2} & \mu & \dots & \mathbf{s} & \mu \end{bmatrix}.$$

Each vector  $^i \mu \in \mathbb{R}^s$  represents a possible mass distribution of the mechanism. These vectors are chosen such that they are linearly independent. Hence  $\mathbf{M}$  is of full rank  $s$ , and constitutes a basis for representing any mass distribution of the linkage. The coordinates  $\mathbf{s} \in \mathbb{R}^s$  of any linkage mass distribution  $\mu$  can therefore be determined based on a simple matrix inversion:

$$\mathbf{M} \cdot \mathbf{s} = \mu \quad \Rightarrow \quad \mathbf{s} = \mathbf{M}^{-1} \cdot \mu. \quad (9.51)$$

---

<sup>8</sup>This dynamic reaction can be any force component, moment or linear combination of them, such as the shaking moment. It must be stressed that the developed procedure is only applicable to force *components*, not to force magnitudes. This does not imply that force magnitudes cannot be considered in the developed convex optimization framework. In this respect, the four-bar example of Section 9.3.2 is illuminating: LIV expressions (9.38a–9.38b) are for instance given for the *X* and *Y*-*component* of the shaking force, and it is these expressions that are subsequently used to develop (9.42a), (9.43a) and (9.44a), which apply to the shaking force *magnitude*.

**Step 2** Construct the corresponding matrix  $\mathbf{D} \in \mathbb{R}^{K \times s}$ :

$$\mathbf{D} = [\mathbf{}^1\mathbf{d} \ \mathbf{}^2\mathbf{d} \ \dots \ \mathbf{}^s\mathbf{d}].$$

Each vector  $\mathbf{}^i\mathbf{d} \in \mathbb{R}^K$  is the vector of  ${}^i d(t_k)$ -values, corresponding to the mass distribution  $\mathbf{}^i\boldsymbol{\mu}$ .  $\mathbf{D}$  is not necessarily of full rank.

**Step 3** Apply the force superposition principle of the previous section:

$$\mathbf{d} = \mathbf{D} \cdot \mathbf{s}, \quad (9.52)$$

where  $\mathbf{d} \in \mathbb{R}^K$  is the vector of  $d(t_k)$ -values, corresponding to the arbitrary mass distribution  $\boldsymbol{\mu}$ . This result can be understood as follows. Since the force superposition principle is valid for any link, it is also valid for the complete mass distribution of the mechanism: if  $\mathbf{}^r\boldsymbol{\mu} = v \cdot (\mathbf{}^P\boldsymbol{\mu}) + w \cdot (\mathbf{}^Q\boldsymbol{\mu})$  then  ${}^r d(t) = v \cdot ({}^P d(t)) + w \cdot ({}^Q d(t))$ . Equation (9.52) expresses this equation for the  $K$  considered time instances and the superposition of  $s$  considered mass distributions  $\mathbf{}^i\boldsymbol{\mu}$ .

**Step 4** Remove the rank deficiency of  $\mathbf{D}$  using the singular value decomposition (SVD):

$$\mathbf{D} = \mathbf{U} \cdot \begin{bmatrix} \text{diag}(\sigma_1, \dots, \sigma_r) & \mathbf{0}_{r \times (s-r)} \\ \mathbf{0}_{(K-r) \times r} & \mathbf{0}_{(K-r) \times (s-r)} \end{bmatrix} \cdot \mathbf{V}^T, \quad (9.53)$$

where  $\mathbf{U} \in \mathbb{R}^{K \times K}$  and  $\mathbf{V} \in \mathbb{R}^{s \times s}$ . Only the singular values  $\sigma_i, i = 1 \dots r$  are (numerically) nonzero, with  $r \leq s$  the rank of  $\mathbf{D}$ . (9.53) can therefore be rewritten as:

$$\mathbf{D} = \mathbf{U}_r \cdot \text{diag}(\sigma_1, \dots, \sigma_r) \cdot \mathbf{V}_r^T, \quad (9.54)$$

where  $\mathbf{U} \in \mathbb{R}^{K \times r}$  and  $\mathbf{V} \in \mathbb{R}^{s \times r}$  are obtained by selecting the first  $r$  columns of  $\mathbf{U}$  and  $\mathbf{V}$  respectively. Using this equation, (9.52) is rewritten as:

$$\mathbf{d} = \underbrace{\mathbf{U}_r \cdot \text{diag}(\sigma_1, \dots, \sigma_r)}_{\mathbf{E}} \cdot \underbrace{\mathbf{V}_r^T \cdot \mathbf{s}}_{\mathbf{p}}. \quad (9.55)$$

Hence,

$$\mathbf{d} = \mathbf{E} \cdot \mathbf{p},$$

where  $\mathbf{E} \in \mathbb{R}^{K \times r}$  is the product of full-rank matrices and hence of full rank. Furthermore, by application of (9.51) to (9.54):

$$\mathbf{p} = \mathbf{V}_r^T \cdot \mathbf{s} = \mathbf{V}_r^T \cdot \mathbf{M}^{-1} \cdot \boldsymbol{\mu} = \mathbf{C} \cdot \boldsymbol{\mu},$$

where  $\mathbf{C} \in \mathbb{R}^{r \times s}$  and  $\mathbf{p} \in \mathbb{R}^r$ . We have therefore obtained, in an automated way (that is, without symbolical manipulation of the equations of motion) the desired expressions (9.47–9.48). The rank  $r$  of  $\mathbf{D}$  is equivalent to the number  $n$  of linearly independent vectors for the dynamic reaction  $d(t)$ .

### 9.5.4 Discussion

The force superposition principle of Section 9.5.2 has been developed based on a hint in the appendix of (Haines, 1981) but is, in the present form, novel in literature. The same goes for the procedure that results in (9.52). Application of the SVD for eliminating the rank deficiency of  $\mathbf{D}$  is a well-known principle in robot literature, but is now introduced for the first time in the area of counterweight balancing. Furthermore, the procedure has several significant advantages over existing procedures:

- Generating  $\mathbf{D}$  does not require symbolic manipulation of the equations of motion: it suffices to model and simulate the mechanism in a standard multi-body simulation package, in order to generate the  ${}^i\mathbf{d}$  vectors, corresponding to the  $s$  mass distributions  ${}^i\mu$ <sup>(9)</sup>. As a result, complexity of the mechanism is no longer an issue in deriving LIV expressions.
- The procedure is equally applicable to all dynamic reactions, including the joint forces. To the best of our knowledge, no methodologies exist that generate LIV expressions for joint forces in an automated way, and for mechanisms of arbitrary complexity. For instance, in the area of robotics, dedicated packages (Maes et al., 1989; Khalil et al., 1994) exist for generating LIV expressions in an automated way, but they only do so for the driving torques or the ground reaction forces. Also the symbolical methods (Elliott and Tesar, 1982; Kochev, 1991), developed in the area of counterweight balancing, are only concerned with the driving torque and the shaking force and shaking moment. Only for four-bars, results (in the form of LDV instead of LIV expressions) are available (Tepper and Lowen, 1975; Lee and Cheng, 1984).
- Appendix N shows that the definition of the  $\mu$ -parameters can be extended in such a way that the mass superposition property (9.24) remains valid for the ten link mass parameters of a link in 3D-motion. As a result, the here developed procedure is also useful for generating LIV expressions for spatial mechanisms, for which the fact that no symbolical manipulation of the equations of motion is required, is particularly important.

## 9.6 Conclusion

This chapter has developed a convex optimization framework for counterweight balancing of purely inertial, planar four-bar and  $N$ -bar linkages. Two basic ingredients of the convex reformulation are (i) the use of the  $\mu$ -parameters, because of their superposition properties and (ii) the use of LIV

---

<sup>9</sup>The  $\mu$ -parameters must of course first be converted to standard mass parameters in order to be used in the simulation package.

expressions for establishing an explicit relation between the  $\mu$ -parameters and the balancing indices  $\alpha_i$ .

These ingredients are not new and even appear together in the work of Haines and Kochev. However, none of the previous work in the area of CWB has resulted in convex programs. Besides unawareness of convex optimization in general, the main reason for this is that until now, the  $\mu$ -parameters have not been used directly as the optimization variables. All present methods obtain practically feasible counterweights by direct optimization of the radius, COG location and thickness of circular counterweights, and convert these variables, somewhere during the optimization process, into the  $\mu$ -parameters.

Here, on the other hand, the  $\mu$ -parameters are used directly, and novel (practical and practical<sup>+</sup>) constraints are developed that assure practical feasibility of the counterweights. It is therefore concluded that the development of these general constraints constitutes the third, equally necessary ingredient of the convex framework.

Although generating numerical results was not the primary goal of this chapter, still some interesting conclusions follow from the numerical, four-bar experiments: (i) joint forces can primarily be kept under control by keeping the driving torque under control; (ii) counterweight balancing is no magical solution: it is capable of decreasing the dynamic reactions, but the obtained reductions are moderate and come at the cost of significant mass addition; (iii) using either  $\alpha_i$  (rms) or  $\beta_i$  (max) as balancing indices in the optimization problem formulation, will yield very similar balancing results.

## Generalization to Planar/Spatial $N$ -bar Mechanisms

In order to generalize the convex framework to mechanisms of arbitrary complexity, an automated procedure for generating LIV expressions has been devised. This procedure is based on a force superposition principle that was initiated by an idea of Haines, but is novel in literature in its present form. The procedure does not require symbolic manipulation of the equations of motion, and is based on (i) simulation of the inverse dynamics of the mechanism, for which a multi-body simulation package can be used and (ii) application of the singular value decomposition. As opposed to all existing methods, it also generates LIV expressions for the joint forces.

The fact that the LIV formalism can easily be extended to complex, planar, as well as spatial mechanisms, implies that the whole convex optimization framework is so too. This is certainly true if the ultimate and practical constraints are used. For the practical<sup>+</sup> constraints, things are different however, due to the critical choice of the LCS locations. For a  $4R$  four-bar, this choice is easy, as it is practically known beforehand where the COGs of the counterweights will lie. This is however not the case for more complex mechanisms. In that case, the practical constraints are very helpful: if it is assumed that the counterweight COG locations do not move much when switching from the practical to the practical<sup>+</sup> constraints, the results of the practical constraints

give a very good indication on how to place the LCSs. This will work fine, unless the practical constraints indicate a counterweight that is not in contact and somewhere in the middle of the link (such as counterweight 2 in Fig.9.3). In that case an iterative procedure, or new kinds of practical<sup>+</sup> constraints are needed.

In fact, before using the practical or practical<sup>+</sup> constraints, a first step in counterweight balancing a complex linkage should be application of the ultimate constraints. This reveals if counterweight balancing has reasonable potential for the example at hand, and can save the designer the trouble of proceeding to the practical or practical<sup>+</sup> constraints if this is not the case. Moreover, the ultimate results also provide a basis for choosing the link thickness, based on efficiency plots like 9.9. Hence, although the practical<sup>+</sup> constraints are the ones that should eventually be applied, both the ultimate and practical constraints are quite useful.

### Relation with ICM and CBCP Design Optimization

The reader may wonder whether it is possible to reformulate the design optimization of the ICM and the CBCP, discussed in Chapter 5 and 6, as convex optimization problems. The main complication for developing such a reformulation is that also kinematic parameters are involved in the optimization. As a result, LIV expressions no longer give an explicit relation between the forces and moments on the one hand and the optimization variables on the other hand. Developing a convex reformulation therefore requires other 'ingredients' (tricks) than the ones developed in this chapter.

Since no convex reformulation was found, another approach was developed to keep these optimization problems tractable, by selecting a limited number of 'main design parameters' as optimization variables: two in case of the ICM ( $\xi_0, r_{\max}$ ); four in case of the CBCP ( $q_0, R^*, L_r, L_c$ ).

In the case of the ICM, exhaustively checking a large number of combinations is feasible and results in the design chart of Fig.5.14, based on which the optimization problem is graphically 'solved'. In the case of the CBCP, the optimization problem is solved using a sequential quadratic programming algorithm, starting from 216 starting points, for a third of which the algorithm converges to a local optimum. The best of these local optima yields a satisfactory design. In order to reduce the computational time (70–110 hours), the design chart of Fig.6.12 is developed, based on fixing two of the four optimization variables ( $l_r$  and  $l_c$ ).

## Convex Optimization in Engineering

A final remark concerns application of convex optimization in engineering in general, and elaborates on the citation at the beginning of this chapter. The methodology developed in this chapter is based on a 'working knowledge' of convex optimization, that is, a basic understanding of its fundamentals. These fundamentals include a list of known convex functions, basic rules for combining them, standard tricks for converting nonconvex problems into convex ones and a lot of examples of such convex reformulations.

It is our conviction that the simplicity and mathematical elegance of the aforementioned fundamentals constitute the real power of convex optimization. In that respect, convex optimization can be compared with integral calculus: using a limited list of known analytical solutions, and a few standard tricks like partial integration, it is possible, though not always straightforward, and sometimes only after studying a lot of example problems, to solve analytically a much broader class of integration problems.



## Chapter 10

# Conclusions and Future Work

*If you knew everything beforehand,  
you'd be rich with just one coin.*

Old saying from West-Flanders<sup>1</sup>

### 10.1 Conclusions

**Simulation of Reciprocating Machinery** Two novel concepts concerning the *forward* dynamic analysis of reciprocating machinery have been developed. Firstly, *damped eigenmotion* has been proposed for generalizing eigenmotion to mechanisms in which energy is dissipated. The basic idea is to overcome energy losses by applying a *constant* motor torque. Simulating the damped eigenmotion of a simplified model of an airjet weaving machine, confirms the claim that, if friction losses are small ( $\eta \leq 0.10$ ), or even moderate ( $\eta \leq 0.20$ , as in an airjet weaving machine), damped eigenmotion is very similar to 'true' eigenmotion.

Secondly, instead of directly integrating the governing differential equation, the forward dynamic analysis problem is solved by formulating it as a boundary value problem and applying (well-known) nonlinear least-squares techniques to it. This frequency-domain approach is introduced in mechanism literature for the first time. It is applicable to any (that is, with an arbitrary number of degrees of freedom) model of a reciprocating machine, using any type of motor model. The price to be paid is the number of unknown pa-

---

<sup>1</sup>West-Flanders is the Flemish region near the North Sea coast. In the Dutch dialect of this region, this saying goes more or less like 'Moest j'oaalles van tevor'n weet'n, ge zoe rikke zin mè ne soe'.

rameters, which increases linearly with the number of states in the model and hence negatively affects the required computational time.

**Dynamically Compensated Cam Design** Dynamically compensated cams are designed so as to impose some desired motion, despite the machine dynamics. Classically, only *follower* system dynamics are taken into account, assuming a constant drive speed. The present work, by contrast, integrates *drive* system dynamics into cam design. This results in so-called *inertially compensated cams*. Such cams allow accurate realization of follower motions in the presence of significant (eigenmotion-associated) drive speed fluctuation, provided that the machine in which they are mounted, behaves dominantly inertially. As such, they provide a solution for the undesired follower acceleration harmonics, which result from drive speed fluctuations in cam-follower mechanisms with classically designed cams.

The academic and industrial relevance of employing inertially compensated cams, stems from the fact that this method is cheap (as opposed to mounting an auxiliary input torque balancing mechanism), energy efficient (as opposed to imposing a constant drive speed through the motor) and does not compromise a machine's start/stop behavior (as opposed to a large fly-wheel).

Despite that conservativity is a basic premise during the design process, inertially compensated cams are quite robust for the presence of friction, provided that the friction losses are overcome by applying a constant motor torque<sup>2</sup>. Unfortunately, the opposite is true for synchronization changes, for which the cams are very sensitive. As a result, they provide no solution for the follower motion distortion encountered in weaving machines.

Inertially compensated cams are generally applicable to reciprocating machines provided that (i) the driving actuator is equipped with a low-bandwidth controller, and (ii) friction losses are moderate (for instance,  $\eta \leq 0.20$ ).

While the design procedure assumes dominating inertial forces, it can easily be extended to other types of conservative forces. *Eigenmotion cams* is the general term proposed here for cams that compensate for the drive system dynamics of reciprocating machines, in which conservative forces are dominating. Combining a low-bandwidth controller, such as Average Speed Control (ASC), with eigenmotion cams embodies the concurrent engineering viewpoint of the *mechatronics* design paradigm

**Input Torque Balancing** Based on a survey of literature (bridging the gap between the literature on input torque balancing (ITB) mechanisms and that on torsional vibration absorbers), it is concluded that addition of a purely inertial, simple and compact ITB device, provides a solution for reducing the

---

<sup>2</sup>The resulting damped eigenmotion is characterized by a drive speed fluctuation that is very similar to the eigenmotion's drive speed fluctuation, based on which the cams are designed.

follower motion distortion in weaving machines. The *inverted cam mechanism* (ICM) and cam-based centrifugal pendulum (CBCP) are interesting candidate ITB devices, since they are compact and constructively simpler than other cam-based mechanisms.

For neither of both mechanisms, a (correct) design methodology exists in literature. Therefore, a methodology has been devised, with following features: (i) formulation of nonlinear boundary value problems for determining the internal cams in the ICM and the CBCP, and the application of nonlinear least-squares techniques for solving them; (ii) integration of collision and technological constraints into the ICM and CBCP design optimization; (iii) development of design charts to speed up the design optimization.

The CBCP is preferred over the ICM, due to the technological problems associated with the prismatic joint implementation in the ICM. Simulation of the CBCP on an airjet weaving machine shows that (i) mere flywheel addition cannot change the qualitative behavior of the drive speed fluctuation, as can input torque balancing; (ii) drive speed fluctuations have a dramatic effect on the follower acceleration, in which respect more the shape than the amount of drive speed fluctuation is important; (iii) input torque balancing is capable of yielding a dramatic decrease of the undesired acceleration harmonics, (iv) even if part of the input torque is not balanced.

In order to validate these simulation results, a CBCP prototype has been built and tested on an airjet weaving machine à blanc. The experimental measurement campaign firstly shows that the CBCP indeed delivers the designed torque for  $\Omega_{\text{shed}} \leq 300$  rpm. Due to a torsional resonance, the CBCP torque starts to deviate significantly above that speed, and 'explodes' at 413.5 rpm where it reaches a maximum of 2280 N-m (i.e. three times its predicted amplitude). The torsional resonance phenomenon can be qualitatively simulated, and its excitation attributed to the 14th CBCP torque harmonic, by extending the rigid-body, simplified airjet weaving machine model with a torsional degree of freedom. This torsional degree of freedom models the torsional flexibility, introduced by the long and hollow sley axis.

The measurement campaign furthermore reveals that, in the speed range of proper CBCP functioning (below 350 rpm), a significant improvement of the dynamic behavior is obtained: (i) the drive speed fluctuation  $\kappa$  is a factor 2.5 lower; (ii) the more significant, low-frequency sword and frame acceleration harmonics are on average reduced by between 5 and 14 dB; (iii) the frame vibration level is on average reduced by 5.2 dB (up-and-down motion) and 5.7 dB (out-of-plane motion); (iv) the sound pressure level in the microphone near the frames is reduced by more than 3 dB(A) in the speed range between 250 and 337 rpm, where the lower limit is due to the CBCP's rolling noise and the upper limit is again due to the torsional resonance.

The reduction of the frame vibration level brings us back to the primary goal of this work, that is, reducing vibration in reciprocating machinery. In a vulgarizing manner, this 'dB' result is restated as follows: *input torque balancing using the CBCP, results in halving the vibration level of the frames.*

**Control of Reciprocating Machinery** The idea of Average Speed Control as a way to practically impose damped eigenmotion, is new. As no stability or any other thorough theoretical analysis of its properties have been carried out, tuning of ASC is done by trial-and-error. Nevertheless, its performance is satisfactory, both in simulation as experimentally.

Applying ASC in simulation to a simplified setup model, shows that a constant torque demand is obtained in regime. Nevertheless, the motor torque is slightly fluctuating, due to the instantaneous drive speed dependency of the motor model that converts the torque demand into the actual motor torque. However, since the motor torque fluctuation is small, a regime behavior is obtained that comes very close to the damped eigenmotion.

Experimentally, ASC illustrates its robustness by being stable, using the same controller settings, for both the FLY and the CBCP-configuration, and despite the presence of the torsional resonance phenomenon. Moreover, the average speed is controlled so accurately that reliable time-domain averaging of measurement signals is possible, with a minimum of leakage. As a result, frequency-domain filtering and differentiation of the measurement signals becomes possible.

**Counterweight Balancing** First of all, a literature survey has been given, which, as opposed to existing, more encyclopedic literature surveys on the topic, can serve as a gentle introduction for the newcomer in the field. Furthermore, it reveals the resemblance between the linearly independent vector expressions, common in counterweight balancing literature, and the minimal, linear models used in experimental robot identification.

Secondly, a convex optimization framework has been developed for counterweight balancing of purely inertial, planar four-bar and  $N$ -bar linkages. The three basic ingredients of the convex reformulation are (i) the use of the  $\mu$ -parameters, because of their superposition properties, (ii) the use of LIV expressions for establishing an explicit relation between the  $\mu$ -parameters and the balancing indices  $\alpha_i$  and (iii) the development of novel practical and practical<sup>+</sup> constraints, which express practical feasibility of the counterweights directly as a function of the  $\mu^*$ -parameters.

In order to generalize the convex framework to mechanisms of arbitrary complexity, an automated procedure for generating LIV expressions has been devised. This procedure is based on a force superposition principle that is novel in literature in its present form. The procedure does not require symbolic manipulation of the equations of motion, and is based on (i) simulation of the inverse dynamics of the mechanism, for which a multi-body simulation package can be used and (ii) application of the singular value decomposition. As opposed to all existing methods, it also generates LIV expressions for the joint forces.

The fact that the LIV formalism can easily be extended to complex planar, as well as spatial mechanisms, implies that the whole convex optimiza-

tion framework is so too. This is certainly true if the ultimate and practical constraints are used. In that respect, results provided by the ultimate constraints are valuable, since they reveal if counterweight balancing *überhaupt* has reasonable potential for the example at hand. Generalization to  $N$ -bars is however less obvious if the practical<sup>+</sup> constraints are used. The applicability of the hints, given in Section 9.6, can only be assessed by doing balancing experiments with complicated mechanisms.

Although generating numerical results was not the primary goal, still some interesting conclusions follow from the numerical experiments with the  $4R$  four-bar mechanism: (i) joint forces can primarily be kept under control by keeping the driving torque under control; (ii) counterweight balancing is no magical solution: it is capable of decreasing the dynamic reactions, but the obtained reductions are moderate and come at the cost of significant mass addition; (iii) using either  $\alpha_i$  (rms) or  $\beta_i$  (max) as balancing indices in the optimization problem formulation, will yield very similar balancing results.

## 10.2 Limitations and Future Work

**Simulation of Reciprocating Machinery** As already mentioned, the developed frequency-domain approach is applicable to any (that is, with an arbitrary number of degrees of freedom) model of a reciprocating machine, using any type of motor model. The limiting factor is however the required computational time, which grows exponentially with the number of degrees of freedom. This is already observed in this work: simulation of the torsional setup model takes much longer than simulation of the rigid-body setup model. Hence, measures should be taken for augmenting the computational efficiency.

**Dynamically Compensated Cams** The design of inertially compensated cams can be integrated with methods that compensate for follower dynamics. This results in cams that (i) compensate for follower dynamics and (ii) are no longer sensitive to drive speed fluctuations.

Experimental work concerning inertially compensated cams has been carried out within the framework of the Picanol project, by mounting inertially compensated shed cams in a gripper weaving machine, equipped with a dobbie mechanism. Results were disappointing, even if the machine synchronization was exactly the same as the synchronization assumed during the cam design. However, in the subsequent evaluation of this experimental campaign, questions arose concerning (i) the accuracy of the dynamic model of the gripper machine, based on which the cams were designed and (ii) the accuracy of the cams, which had been manufactured by a third party. Hence, no definitive conclusion concerning the industrial relevance of inertially compensated cams can be drawn, based on this measurement campaign.

Therefore, a new experimental campaign is planned, but now on the airjet weaving machine à blanc. Since this machine is equipped with a cam-box

mechanism, inertially compensated shed cams are much easier to manufacture. Moreover, the simplified dynamic model of this machine has already proven its value in the design of the CBCP mechanism, and can be enhanced by applying the experimental identification techniques proposed in (Demeulenaere et al., 2000).

**Input Torque Balancing** One of the aspects that has not been covered yet in the study of the CBCP, is its transient behavior. For the prototype developed in this work, contact between the roller followers and the internal cams is guaranteed during start-up, but not during braking: if the machine slows down to fast, contact is lost. Groove cams, as shown in Fig.4.5, do not exhibit this problem, but are more difficult to manufacture than internal cams. Another, brute force, solution is to mount additional springs. The ideal solution (if no groove cams are used) is a system that is active during transient phases, but not during regime, such that the regime torque of the CBCP is not affected. Comparing the technological and economical feasibility of these different alternatives is a topic of future work.

Although the experimentally obtained vibration and noise reductions are promising, care must be taken when evaluating them: the measured vibration and noise reduction levels are only valid for the machine present at PMA, that is, a machine à blanc. The heddles, tissue, . . . present in a complete industrial weaving machine, may dramatically change its dynamic behavior. Hence, based on the present measurements, no conclusions can be drawn concerning the vibration, and, even more, the noise level reduction obtainable in an industrial machine.

On the other hand, the torsional resonance inhibits revealing the full potential of the CBCP. Therefore, the next step in the evaluation of the CBCP is its testing on a complete industrial weaving machine, after taking measures to obtain a sufficiently high torsional resonance frequency. These measures include stiffening the sley axis, and distributing the mechanism over the left and the right machine carter. If the then obtained experimental results reveal sufficient technological potential, an economic study must finally decide whether the CBCP will be introduced or not in a standard weaving machine.

**Control of Reciprocating Machinery** Although ASC performs satisfactorily for a (weaving) machine in steady state, its transient behavior is rather poor. Recent research concerning ASC has shown (both in simulation and experimentally) that adding a feedforward part, only active during transient phases, already spectacularly improves the transient behavior. Further such investigations as well as experimental validation of them, should result in a control system structure that can handle both the transient and the steady-state regime adequately.

**Counterweight Balancing** As already mentioned, the main issue in extending the developed framework to  $N$ -bar planar and spatial mechanisms, is whether or not the practical<sup>+</sup> constraints yield satisfactory results. This can however only be assessed by actually *applying* the developed methodology to a number of complicated mechanisms. Other short-term action points include (i) looking for solutions for the encountered numerical problems and (ii) extending the framework to mechanisms that are not purely inertial.

In this thesis, the kinematic parameters of the mechanism are assumed to be fixed. However, in the work of (Conte et al., 1975), discussed in Section 3.1.2, spectacular dynamic reaction improvements are obtained by optimizing the four kinematic parameters of a four-bar linkage, and assuming the link mass parameters to be dependent on the link lengths. The present convex optimization framework can be used to optimize the sixteen (four kinematic and twelve mass) parameters simultaneously, with an outer, nonconvex optimization loop for the kinematic parameters, and an inner, extremely fast, convex optimization loop for the link mass parameters.

Inclusion of the dynamic frame model approach in the convex framework seems feasible if the frame model dynamics are governed by a linear differential equation. Provided that a convex formulation be found, one can start to think of robustifying the method by, for instance, optimizing the dynamic behavior over a range of input crank speeds, or considering uncertainty on the dynamic frame model parameters.

**Application of Convex Optimization in Mechanical Engineering** It has been found in the present work that the application of superposition principles is one of the key factors in reformulating convex programs. As a result, since mechanics is ruled by Newton's laws, one of which actually *is* a superposition principle, it is our conviction that many convex optimization applications in mechanical engineering are waiting to be found.

One such example for instance concerns *overactuated* systems. The developed automated method for generating LIV expressions, has already been transformed into a method for generating LIV-like expressions for the dynamic reactions in an overactuated system. In that case, the parameters  $\mathbf{p}$  are not linear combinations of the  $\mu$ -parameters but of the redundant driving forces/torques that are to be optimized. Overactuated parallel robots are an important example of overactuated systems. Here, the LIV-like expressions can be used for developing a convex optimization framework that minimizes for instance the thermal load of the driving actuators.

Also the human body is an overactuated system: we have much more muscles than actually required for driving all of our degrees of freedom. At the moment, research is being carried out (and has already yielded promising results), concerning application of convex optimization techniques to *dynamic musculo-skeletal analysis* of the human body, based on the aforementioned LIV-like expressions. The musculo-skeletal analysis problem is that of deter-

mining the muscle forces that result in an experimentally observed human motion, taking into account the muscle excitation and activation dynamics. At the moment, this is considered to be a *very* difficult optimization problem. The aim of the present research is to find a convex *approximation* of this problem, so as to generate a good starting point for the exact, nonconvex optimization problem.

A final candidate for application of convex optimization techniques is kinematic linkage synthesis. This is a problem in which superposition is inherently ruled out. A reformulation of the classical precision point synthesis problem has however already been developed, in which the goal function and all but one constraints are convex. The remaining nonconvex constraint is a quadratic equality constraint. For such constraints however, techniques are available for approximating the exact problem by an approximate problem that, again, at least generates a good starting point for the exact, nonconvex optimization problem.

# Bibliography

- J. Angeles and C. López-Cajún. *Optimization of Cam Mechanisms*. Kluwer Academic Publishers, 1991.
- M. Arakawa, M. Nishioka, and N. Morita. Torque compensation cam mechanism. *Proc. Joint International Conf. on Advanced Science and Technology*, pages 302–305, Zhejiang University, Hangzhou, China, 1997a.
- M. Arakawa, M. Takamura, and M. Nishioka. Compensation of input shaft torque on indexing cam mechanisms (5th report, peak torque cutoff considering nonconservative terms). *Transactions of the JSME*, 63(611-C): 289–293, 1997b. (in Japanese).
- V. Arakelian and M. Dahan. Partial shaking moment balancing of fully force balanced linkages. *Mechanism and Machine Theory*, 36:1241–1252, 2001.
- V. Arakelian, M. Dahan, and M.R. Smith. Complete shaking force and partial shaking moment balancing of planar four-bar linkages. *Proceedings of the Institution of Mechanical Engineers: Part K—Journal of Multi-Body Dynamics*, 215:31–34, 2001.
- V. Arakelian and M.R. Smith. Complete shaking force and shaking moment balancing of linkages. *Mechanism and Machine Theory*, 34:1141–1153, 1999.
- B. Arras. Entwicklung eines adaptiven zusatzsystems zur minderung von torsionsschwingungen in antriebsträngen (development of an adaptive additional system for torsional vibration reduction in drive trains), dissertation th darmstadt. *Fortschritt-Berichte VDI Reihe 11 Nr. 233*, 1996.
- I.I. Artobolewski. Das dynamische laufkriterium bei getrieben. *Maschinenbautechnik*, 7(12):663–667, 1958.
- U.M. Ascher, R.M.M. Mattheij, and R.D. Russell. *Numerical Solution of Boundary Value Problems for Ordinary Differential Equations*. Prentice Hall Englewood Cliffs (N.J.), 1988.

- C.G. Atkeson, C.H. An, and J.M. Hollerbach. Estimation of inertial parameters of manipulator loads and links. *The International Journal of Robotics Research*, 5(3):101–119, 1986.
- G.D. Aviza. An experimental investigation of torque balancing to reduce the torsional vibration of camshafts. Master's thesis, Worcester Polytechnic Institute, 1997.
- C. Bagci. Synthesis of the plane four-bar mechanism for torque generation, and application to a case study for the design of a new balancing mechanism for rotary top brush in power wax car washing machines. *ASME Mechanisms Conference*, Paper No. 78-DET-71, 1978.
- C. Bagci. Shaking force balancing of planar linkages with force transmission irregularities using balancing idler loops. *Mechanism and Machine Theory*, 14:267–284, 1979.
- C. Bagci. Complete shaking force and shaking moment balancing of link mechanisms using balancing idler loops. *Transactions of the ASME, Journal of Mechanical Design*, 104:482–493, 1982.
- J. Baron and G. Poll. Schwingungskompensation durch einen fliehkraftgesteuerten drehschwingungstilger (vibration compensation by a centrifugally controlled torsional vibration absorber). In *VDI Berichte 1749 (Proceedings of Schwingungen in Antrieben 2003)*, 2003.
- D. Beale and K. Chen. A new symbolic method to determine base inertia parameters for general spatial mechanisms. *Proc. ASME 2002 Design Engineering Technical Conferences and Computers and Information in Engineering Conference*, Paper No. DETC2002/DAC-34111, Montréal, Canada, 2002.
- W. Beitz and K.-H. (Eds.) Küttner. *Taschenbuch für den Maschinenbau*. Springer-Verlag, 15th edition, 1986.
- C.E. Benedict, G.K. Matthew, and D. Tesar. Torque balancing of machines by sub-unit cam systems. *2nd Applied Mechanism Conference*, Paper No. 15, Oklahoma State University, Stillwater, Oklahoma, 1971.
- C.E. Benedict and D. Tesar. Optimal torque balance for a complex stamping and indexing machine. *Mechanisms Conference*, Paper No. 70-Mech-82, Columbus, Ohio, 1970.
- F. Bennis, W. Khalil, and M. Gautier. Calculation of the base inertial parameters of closed-loop robots. *Proc. of the IEEE International Conference on Robotics and Automation*, pages 370–375, Nice, France, 1992.
- J.P. Bentley. *Principles of Measurement Systems, 3rd Edition*. Longman, 1995.

- R.S. Berkof. Complete force and moment balancing of inline four-bar linkages. *Mechanism and Machine Theory*, 8:397–410, 1973.
- R.S. Berkof. The input torque in linkages. *Mechanism and Machine Theory*, 14:61–73, 1979.
- R.S. Berkof and G.G. Lowen. A new method for completely force balancing simple linkages. *Transactions of the ASME, Journal of Engineering for Industry*, pages 21–26, 1969.
- R.S. Berkof and G.G. Lowen. Theory of shaking moment optimization of force-balanced four-bar linkages. *Transactions of the ASME, Journal of Engineering for Industry*, pages 53–60, 1971.
- V.J. Borowski, H.H. Denman, D.L. Cronin, S.W. Shaw, J.P. Hanisko, L.T. Brooks, D.A. Mikulec, W.B. Crum, and M.P. Anderson. Reducing vibration of reciprocating engines with crankshaft pendulum absorbers. *SAE Technical Paper Series, Paper No. 911,876*, 1991.
- S. Boyd and L. Vandenberghe. *Convex Optimization*. Cambridge University Press, 2004.
- J. Brändlein, P. Eschmann, L. Hasbargen, and K. Weigand. *Ball and Roller Bearings*. John Wiley and Sons, 3rd edition, 1999.
- W.L. Carson and J.M. Stephens. Feasible parameter design spaces for force and root-mean-square moment balancing an in-line 4r 4-bar synthesized for kinematic criteria. *Mechanism and Machine Theory*, 13:649–658, 1978.
- B.C. Carter. Rotating pendulum absorbers with partly solid and partly liquid inertia members with mechanical or fluid damping. *British Patent No. 337,466*, 1929.
- C.-P. Chao, C.-T. Lee, and S.W. Shaw. Non-unison dynamics of multiple centrifugal pendulum vibration absorbers. *Journal of Sound and Vibration*, 204(5):769–794, 1997a.
- C.-P. Chao and S.W. Shaw. The dynamic response of multiple pairs of sub-harmonic torsional vibration absorbers. *Journal of Sound and Vibration*, 231(2):411–431, 2000.
- C.-P. Chao, S.W. Shaw, and C.-T. Lee. Stability of the unison response for a rotating system with multiple tautochronic pendulum vibration absorbers. *Transactions of the ASME, Journal of Applied Mechanics*, 64: 149–156, 1997b.
- F. Y. Chen. *Mechanics and Design of Cam Mechanisms*. Pergamon Press, 1982.

- F.Y. Chen. An analytical method for synthesizing the four-bar crank-rocker mechanism. *Transactions of the ASME, Journal of Engineering for Industry*, 1:45–54, 1969.
- K. Chen, D.G. Beale, and D. Wang. A new method to determine the base inertial parameters of planar mechanisms. *Mechanism and Machine Theory*, 37:971–984, 2002.
- N.-X. Chen. The complete shaking force balancing of a spatial linkage. *Mechanism and Machine Theory*, 19(2):243–255, 1984.
- F.L. Conte, G.R. George, R.W. Mayne, and J.P. Sadler. Optimum mechanism design combining kinematic and dynamic force considerations. *Transactions of the ASME, Journal of Engineering for Industry*, 2:662–670, 1975.
- B. Demeulenaere and J. De Schutter. Dynamically compensated cams for rigid cam-follower systems with fluctuating cam speed and dominating inertial forces. *Proc. IEEE/ASME Int. Conf. on Advanced Intelligent Mechatronics*, pages 763–768, Como, Italy, 2001.
- B. Demeulenaere and J. De Schutter. Input torque balancing using an inverted cam mechanism. *Transactions of the ASME, Journal of Mechanical Design*, 2004. Accepted for Publication.
- B. Demeulenaere, V. Lampaert, J. Swevers, and J. De Schutter. Optimal excitation for identification of a cam set-up. *Proc. of Int. Conf. on Noise and Vibration Engineering, ISMA 2000*, III:1209–1216, Leuven, Belgium, 2000.
- B. Demeulenaere and J. Swevers. Application of learning feed-forward control to cam-follower systems. *Book of Abstracts of 21st Benelux Meeting on Systems and Control*, page 79, Veldhoven, The Netherlands, 2002.
- J.P. Den Hartog. *Mechanical Vibrations*. McGraw-Hill, 4th edition, 1956.
- H.H. Denman. Tautochronic bifilar pendulum torsion absorbers for reciprocating engines. *Journal of Sound and Vibration*, 159(2):251–277, 1992.
- B. Dizioğlu. Synthese der periodischen getriebe mit vorgeschriebener dynamischer wirkung. *Maschinenbautechnik*, 5(11):565–574, 1956.
- B. Dizioğlu. *Getriebelehre, Band 3: Dynamik*. Vieweg und Sohn, Braunschweig, 1966.
- D. B. Dooner. Use of noncircular gears to reduce torque and speed fluctuations in rotating shafts. *Transactions of the ASME, Journal of Mechanical Design*, 119:299–306, 1997.

- H. Dresig. *Schwingungen Mechanischer Antriebssysteme: Modellbildung, Berechnung, Analyse, Synthese (Vibrations of Mechanical Drive Systems: Modelling, Calculation, Analysis, Synthesis)*. Springer-Verlag, 2001.
- H. Dresig and P. Jacobi. Vollständiger trägheitskraftausgleich von ebenen koppelgetrieben durch anbringen eines zweischlages. *Maschinenbautechnik*, 23(1):5–8, 1974.
- H. Dresig and S. Schönfeld. Rechnergestützte optimierung der antriebs- und gestellkraftgrößen ebener koppelgetriebe. *Mechanism and Machine Theory*, 11(6):363–379, 1976.
- L.C.T. Dulger and S. Uyan. Modelling, simulation and control of a four-bar mechanism with a brushless servo motor. *Mechatronics*, 7(4):369–383, 1997.
- H.-G. Eckel and A. Kunkel. Drehzahladaptiver tilger. *Deutsches Patentamt, DE 196 04 160 C1*, 1997.
- J.L. Elliott and D. Tesar. The theory of torque, shaking force and shaking moment balancing of four link mechanisms. *Transactions of the ASME, Journal of Engineering for Industry*, pages 715–722, 1977.
- J.L. Elliott and D. Tesar. A general mass balancing method for complex planar mechanisms. *Mechanism and Machine Theory*, 17(2):153–172, 1982.
- J.L. Elliott, D. Tesar, and G.K. Matthew. Partial dynamic state synthesis by use of mass parameters in a system coupler link. *Transactions of the ASME, Journal of Mechanical Design*, 101:246–249, 1979.
- D. Filipović and N. Olgac. Delayed resonator with speed feedback – design and performance analysis. *Mechatronics*, 12:393–413, 2002.
- R.F. Fung and K.W. Chen. Constant speed control of the quick return mechanism driven by a dc motor. *JSME International Journal, Series C: Mechanical Systems, Machine Elements and Manufacturing*, 40(3):454–461, 1997.
- W. Funk and J. Han. On the complete balancing of the inertia-caused input torque for plane mechanisms. *Proc. ASME 1996 Design Engineering Technical Conferences and Computers in Engineering Conference*, Paper No. 96-DETC/MECH-1570, Irvine, California, 1996.
- C. Ganseman. *Dynamic Modeling and Identification of Mechanisms with Application to Industrial Robots*. PhD thesis, Dept. of Mech. Eng., K.U.Leuven, Leuven, Belgium, 1998.
- M. Gautier and W. Khalil. Direct calculation of minimum set of inertial parameters for robots. *IEEE Transactions on Robotics and Automation*, 6(3):368–373, 1990.

- G.S. Gill and F. Freudenstein. Minimization of inertia-induced forces in spherical four-bar mechanisms. part 1: The general spherical four-bar linkage. *Transactions of the ASME, Journal of Mechanical Design*, 105:471–475, 1983.
- C.M. Gosselin and Y. Wu. On the development of reactionless spatial 3-dof parallel-piped mechanisms. *Proc. ASME 2002 Design Engineering Technical Conferences and Computers and Information in Engineering Conference*, Paper No. DETC2002/MECH-34310, Montréal, Canada, 2002.
- G. Guo, N. Morita, and T. Torii. Optimum dynamic design of planar linkage using genetic algorithms. *JSME International Journal, Series C: Mechanical Systems, Machine Elements and Manufacturing*, 43(2):372–377, 2000.
- R.S. Haines. Minimum rms shaking moment or driving torque of a force-balanced 4-bar linkage using feasible counterweights. *Mechanism and Machine Theory*, 16:185–190, 1981.
- S. Hanachi and F. Freudenstein. The development of a predictive model for the optimization of high-speed cam-follower systems with coulomb damping, internal friction and elastic and fluidic elements. *Transactions of the ASME, Journal of Mechanisms, Transmissions, and Automation in Design*, 108:506–515, 1986.
- T.A. Harris. *Rolling Bearing Analysis*. John Wiley & Sons, Inc., 1966. pp.409–411.
- F.R. Hertrich. How to balance high-speed mechanisms with minimum inertia counterweights. *Machine Design*, 35(6):160–164, 1963.
- B.A. Hockey. An improved technique for reducing the fluctuation of kinetic energy in plane mechanisms. *Jnl. Mechanisms*, 6:405–418, 1971.
- B.A. Hockey. The minimization of the fluctuation of input-shaft torque in plane mechanisms. *Mechanism and Machine Theory*, 7:335–346, 1972.
- M. Hosek, H. Elmali, and N. Olgac. A tunable torsional vibration absorber: The centrifugal delayed resonator. *Journal of Sound and Vibration*, 205(2):151–165, 1997.
- M.H. Hsu and W.R. Chen. On the design of speed function for improving torque characteristics of cam-follower systems. *Proc. 10th World Congress on the Theory of Machines and Mechanisms*, pages 272–277, Oulu, Finland, 1999.
- Z. Hunag and Z.D. Shi. In *Proc. 7th World Congress on the Theory of Machines and Mechanisms*, pages 473–476, 1987.
- K.L. Johnson. *Contact Mechanics*. Cambridge University Press, 1985. p.85.

- W.E. Johnson and N.Y. Schenectady. A method of balancing reciprocating machines. *Transactions of the ASME, Journal of Applied Mechanics*, 57: A81–A86, 1935.
- K. Kanzaki and K. Itao. Polydyne cam mechanisms for typehead positioning. *Transactions of the ASME, Journal of Engineering for Industry*, 94:250–254, 1972.
- W. Ker Wilson. *Practical Solution of Torsional Vibration Problems*, volume IV: Devices for controlling vibration, Chapter XXIX: Special Devices for Controlling Torsional Vibration: Friction Dampers. Chapman and Hall Ltd, London, 3rd edition, 1968a.
- W. Ker Wilson. *Practical Solution of Torsional Vibration Problems*, volume IV. Devices for controlling vibration. Chapman and Hall Ltd, London, 3rd edition, 1968b.
- W. Khalil and F. Bennis. Symbolic calculation of the base inertial parameters of closed-loop robots. *The International Journal of Robotics Research*, 14 (2):112–128, 1995.
- W. Khalil, D. Creusot, C Chevallerau, and F. Bennis. Symoro+, symbolic modelling of robots. *User Guide, Nantes*, 1994.
- M. Kirchhof. Ausgleichsgetriebe zur erhöhung der leistungsfähigkeit und betriebssicherheit von maschinen und geräten. *Wiss. Zeitschrift der Tech. Hochschule Karl-Marx-Stadt*, 14(1):51–59, 1972.
- I.S. Kochev. General method for full force balancing of spatial and planar linkages by internal mass redistribution. *Mechanism and Machine Theory*, 22(4):333–341, 1987.
- I.S. Kochev. A new general method for full force balancing of planar linkages. *Mechanism and Machine Theory*, 23(6):475–480, 1988.
- I.S. Kochev. General method for active balancing of combined shaking moment and torque fluctuations in planar linkages. *Mechanism and Machine Theory*, 25(6):679–687, 1990.
- I.S. Kochev. Contribution to the theory of torque, shaking force and shaking moment balancing of planar linkages. *Mechanism and Machine Theory*, 26 (3):275–284, 1991.
- I.S. Kochev. General theory of complete shaking moment balancing of planar linkages: a critical review. *Mechanism and Machine Theory*, 35:1501–1514, 2000.

- I.S. Kochev and G.H. Gurdev. General criteria for optimum balancing of combined shaking force and shaking moment in planar linkages. *Mechanism and Machine Theory*, 23(6):481–489, 1988.
- I.S. Kochev and G.H. Gurdev. Balancing of linkages under the combined action of inertia and external forces. *Mechanism and Machine Theory*, 24(2):93–98, 1989.
- M. P. Koster. Effect of flexibility of driving shaft on the dynamic behavior of a cam mechanism. *Transactions of the ASME, Journal of Engineering for Industry*, 97:595–602, 1975.
- P. Kulitzscher. Leistungsausgleich von koppelgetrieben durch veränderung der massenverteilung oder zusatzkoppelgetriebe. *Maschinenbautechnik*, 19(11):562–568, 1970.
- C.-T. Lee and S.W. Shaw. On the counteraction of periodic torques for rotating systems using centrifugally driven vibration absorbers. *Journal of Sound and Vibration*, 191(5):695–719, 1996.
- C.-T. Lee, S.W. Shaw, and V.T. Coppola. A subharmonic vibration absorber for rotating machinery. *Transactions of the ASME, Journal of Vibration and Acoustics*, 119:590–595, 1997.
- T.W. Lee and C. Cheng. Optimum balancing of combined shaking force, shaking moment, and torque fluctuations in high-speed linkages. *Transactions of the ASME, Journal of Mechanisms, Transmissions, and Automation in Design*, 106:242–251, 1984.
- Z. Li. Sensitivity and robustness of mechanism balancing. *Mechanism and Machine Theory*, 33(7):1045–1054, 1998.
- Z. Li and S. Bai. Optimum balancing of linkages with clearances. *Mechanism and Machine Theory*, 27(5):535–541, 1992.
- A. Liniecki. The equation of a variable transmission ratio for a mechanical system with fluctuating load. *Journal of Mechanisms*, 4:139–144, 1969.
- A. Liniecki. Synthesis of a slider-crank mechanism with consideration of dynamic effects. *Journal of Mechanisms*, 5(3):337–349, 1970.
- F.W. Liou, A.G. Erdman, and C.S. Lin. Dynamic analysis of a motor-gear-mechanism system. *Mechanism and Machine Theory*, 26(3):239–252, 1991.
- H.T.J. Liu. Synthesis and steady-state analysis of high-speed elastic cam-actuated linkages with fluctuated speeds by a finite element method. *Transactions of the ASME, Journal of Mechanical Design*, 119:395–402, 1997.

- M.S. Lobo, L. Vandenberghe, S. Boyd, and H. Le Bret. Applications of second-order cone programming. *Linear Algebra and its Applications*, 284(1–3): 193–228, 1998.
- G.G. Lowen and R.S. Berkof. Survey of investigations into the balancing of linkages. *Journal of Mechanisms*, 3:221–231, 1968.
- G.G. Lowen and R.S. Berkof. Determination of force-balanced four-bar linkages with optimum shaking moment characteristics. *Transactions of the ASME, Journal of Engineering for Industry*, pages 39–46, 1971.
- G.G. Lowen, F.R. Tepper, and R.S. Berkof. The quantitative influence of complete force balancing on the forces and moments of certain families of four-bar linkages. *Mechanism and Machine Theory*, 9:299–323, 1974.
- G.G. Lowen, F.R. Tepper, and R.S. Berkof. Balancing of linkages—an update. *Mechanism and Machine Theory*, 18(3):213–220, 1983.
- H. H. Mabie and C. F. Reinholtz. *Mechanisms and Dynamics of Machinery*. Wiley, 4th edition, 1987.
- P. Maes, J.C. Samin, and P.Y. Willems. Robotran. *Multibody System Handbook*, W. Schiehlen (ed.), pages 246–264, 1989.
- W. Matek, D. Muhs, H. Wittel, M. Becker, and D. Janasch. *Roloff/Matek Maschineonderdelen: Normering, Berekening, Vormgeving*. Academic Service, 2000. Dutch translation of Roloff/Matek Maschinenelemente, 14. vollständig überarbeitete und erweiterte Auflage.
- H. Mayeda, K. Yoshida, and K. Osuka. Base parameters of manipulator dynamic model. *IEEE Transactions on Robotics and Automation*, 6(3): 312–321, 1990.
- R.W. Mayne, J.P. Sadler, and K.C. Fan. Generalized study of crank-rocker mechanisms driven by a d.c. motor part ii. applications. *Mechanism and Machine Theory*, 15:447–461, 1980.
- K.T. McDonald. The rolling motion of a half-full beer can. <http://puhep1.princeton.edu/mcdonald/examples/beercan.pdf>, 1996.
- W. Meyer zur Capellen. Die bewegung periodischer getriebe unter einfluß von kraft-und massenwirkungen. *Industrie-Anzeiger*, 86(9):135–140, (17):282–289, 1964.
- V. Michelin. European patent no. 0,010,267. *European Patent Office*, pages 1–16, 1979.
- A. Myklebust. Dynamic response of an electric motor-linkage system during startup. *Transactions of the ASME, Journal of Mechanical Design*, 104: 137–142, 1982.

- D.E. Newland. Nonlinear aspects of the performance of centrifugal pendulum vibration absorbers. *Transactions of the ASME, Journal of Engineering for Industry*, pages 257–263, 1964.
- M. Nishioka. State of the art of torque compensation cam mechanisms. *Proc. 9th World Congress on the Theory of Machines and Mechanisms*, pages 713–717, Milan, Italy, 1995.
- M. Nishioka. Design of torque compensation cam using measured torque distribution. *Proc. 10th World Congress on the Theory of Machines and Mechanisms*, pages 1471–1476, Oulu, Finland, 1999.
- M. Nishioka, M. Takamura, and S. Suzuki. Compensation of input shaft torque on indexing cam mechanisms (7th report, development of the vibration free twin type mechanism). *Transactions of the JSME*, 65(630-C):313–318, 1999. (in Japanese).
- M. Nishioka and M. Yoshizawa. Compensation of input shaft torque on indexing cam mechanisms (3rd report, correction by inertia term for compensating system with dominant spring force). *Transactions of the JSME*, 60(576-C):340–346, 1994. (in Japanese).
- J. Nocedal and S.J. Wright. *Numerical Optimization*. Springer-Verlag, 1999.
- R.L. Norton. *Design of Machinery: An Introduction to the Synthesis and Analysis of Mechanisms and Machines (2nd Edition)*. McGraw-Hill, 2001.
- R.L. Norton. *Cam Design and Manufacturing Handbook*. Industrial Press, Inc., 2002.
- K. Ogawa and H. Funabashi. On the balancing of the fluctuating input torques caused by inertia forces in the crank-and-rocker mechanisms. *Transactions of the ASME, Journal of Engineering for Industry*, pages 97–102, 1969.
- K. Oldham and M.J. Walker. A procedure for force-balancing planar linkages using counterweights. *Proceedings of the Institution of Mechanical Engineers: Part C—Journal of Mechanical Engineering Science*, 20(4):177–182, 1978.
- A. P. Pisano. Coulomb friction in high-speed cam systems. *Transactions of the ASME, Journal of Mechanisms, Transmissions, and Automation in Design*, 106:470–474, 1984.
- A. P. Pisano and F. Freudenstein. An experimental and analytical investigation of the dynamic response of a high-speed cam-follower system. part 1: Experimental investigation. *Transactions of the ASME, Journal of Mechanisms, Transmissions, and Automation in Design*, 105:692–698, 1983.

- B. Porter and D.J. Sanger. Synthesis of dynamically optimal four-bar linkages. *Proc. Conf. Mechanisms 1972*, Paper No. C69/72:24–28, Institution of Mechanical Engineers, 1972.
- B. Raucent, G. Champion, G. Bastin, J.C. Samin, and P.Y. Willems. Identification of the barycentric parameters of robot manipulators from external measurements. *Automatica*, 28(5):1011–1016, 1992.
- R.T. Rockafellar. Lagrange multipliers and duality. *SIAM Review*, 35:183–283, 1993.
- J.P. Sadler. Balancing of six-bar linkages by nonlinear programming. In *Proc. 4th World Congress on the Theory of Machines and Mechanisms*, pages 139–144, Newcastle-upon-Tyne, U.K., 1975.
- J.P. Sadler and R.W. Mayne. Balancing of mechanisms by nonlinear programming. *3rd Applied Mechanism Conference*, Paper No. 29, Oklahoma State University, Stillwater, Oklahoma, 1973.
- J.P. Sadler, R.W. Mayne, and K.C. Fan. Generalized study of crank-rocker mechanisms driven by a d.c. motor part i. mathematical model. *Mechanism and Machine Theory*, 15:435–445, 1980.
- E.J. Sarring. Torque compensation for cam systems. *Trans. 7th Conference on Mechanisms*, pages 179–185, Purdue University, 1962.
- V.A. Shchepetil'nikov. The balancing of bar mechanisms with unsymmetrical links). *Mechanism and Machine Theory*, 10:461–466, 1974.
- A.A. Sherwood. The dynamic synthesis of a mechanism with time-dependent output. *Journal of Mechanisms*, 3(1):35–40, 1968.
- M.R. Smith. Optimal balancing of planar multi-bar linkages. In *Proc. 4th World Congress on the Theory of Machines and Mechanisms*, pages 145–149, Newcastle-upon-Tyne, U.K., 1975.
- K. Smolders, B. Demeulenaere, J. Swevers, and J. De Schutter. Average speed control: Analysis, tuning and enhancements for transient behavior. Internal Report 2004RP002, Mech. Eng. Dept., Katholieke Universiteit Leuven, 2004.
- L. N. Srinivasan and Q. Jeffrey Ge. Designing dynamically compensated and robust cam profiles with bernstein-bézier harmonic curves. *Transactions of the ASME, Journal of Mechanical Design*, 120:40–45, 1998.
- D. A. Stoddart. Polydyne cam design. *Machine Design*, pages January, 121–135; February, 146–154; March, 149–164, 1953.

- J.F. Sturm. Using sedumi 1.02, a matlab toolbox for optimization over symmetric cones. *Optimization Methods and Software*, 11–12:625–653, 1999. Special issue on Interior Point Methods (CD supplement with software).
- J. Swevers, C. Ganseman, D. Tükel, J. De Schutter, and H. Van Brussel. Optimal robot excitation and identification. *IEEE Transactions on Robotics and Automation*, 13:730–739, 1997.
- S. Taşcan. The minimization of the fluctuations of input shaft speed in cam mechanisms. *Mechanism and Machine Theory*, 20(2):135–138, 1985.
- S. Taşcan. Effect of eccentricity on the speed fluctuation of cam mechanisms with translating followers. *Transactions of the ASME, Journal of Mechanisms, Transmissions, and Automation in Design*, 110:11–15, 1988.
- J. Tao and J.P. Sadler. Constant speed control of a motor driven mechanism system. *Mechanism and Machine Theory*, 30(5):737–748, 1995.
- G. Teng, H. Fu, and W. Zhou. A new method of torque compensation for high speed indexing cam mechanism. *Transactions of the ASME, Journal of Mechanical Design*, 121:319–323, 1999.
- F.R. Tepper and G.G. Lowen. General theorems concerning full force balancing of planar linkages by internal mass redistribution. *Transactions of the ASME, Journal of Engineering for Industry*, pages 789–796, 1972.
- F.R. Tepper and G.G. Lowen. On the distribution of the rms shaking moment of unbalanced planar mechanisms: Theory of isomomental ellipses. *Transactions of the ASME, Journal of Engineering for Industry*, pages 665–671, 1973.
- F.R. Tepper and G.G. Lowen. Shaking force optimization of four-bar linkage with adjustable constraints on ground bearing forces. *Transactions of the ASME, Journal of Engineering for Industry*, pages 643–651, 1975.
- T. Thuemmel. Dynamic balancing of linkages by active control with redundant drives. *Proc. 9th World Congress on the Theory of Machines and Mechanisms*, pages 970–974, Milan, Italy, 1995.
- P.H. Tidwell, N. Bandukwala, S.G. Dhande, C.F. Reinholtz, and G. Webb. Synthesis of wrapping cams. *Transactions of the ASME, Journal of Mechanical Design*, 116:634–638, 1994.
- S.J. Tricamo and G.G. Lowen. A new concept for force balancing machines for planar linkages. part 1: Theory. *Transactions of the ASME, Journal of Mechanical Design*, 103:637–642, 1981a.

- S.J. Tricamo and G.G. Lowen. A new concept for force balancing machines for planar linkages. part 2: Application to four-bar linkage and experiment. *Transactions of the ASME, Journal of Mechanical Design*, 103:784–792, 1981b.
- S.J. Tricamo and G.G. Lowen. A novel method for prescribing the maximum shaking force of a four-bar linkage with flexibility in counterweight design. *Transactions of the ASME, Journal of Mechanisms, Transmissions, and Automation in Design*, 105:511–519, 1983a.
- S.J. Tricamo and G.G. Lowen. Simultaneous optimization of dynamic reactions of a four-bar linkage with prescribed maximum shaking force. *Transactions of the ASME, Journal of Mechanisms, Transmissions, and Automation in Design*, 105:520–525, 1983b.
- M. Tuxbury. Analytical modeling and design of torque compensation cams. Master's thesis, Worcester Polytechnic Institute, 2002.
- D. Ullman and H. Velkoff. An introduction to the variable inertia flywheel (vif). *Transactions of the ASME, Journal of Applied Mechanics*, 46:186–190, 1979.
- Y. S. Ünlüsoy and S. T. Tümer. Non-linear dynamic model and its solution for a high-speed cam mechanism with coulomb friction. *Journal of Sound and Vibration*, 169:395–407, 1994.
- H.M.J. Van Brussel. Mechatronics—a powerful concurrent engineering framework. *IEEE/ASME Transactions on Mechatronics*, 1(2):127–136, 1996.
- H. J. Van de Straete and J. De Schutter. Optimal variable transmission ratio and trajectory for an inertial load with respect to servo motor size. *Transactions of the ASME, Journal of Mechanical Design*, 121:544–551, 1999.
- VDI2142. Blatt 1: Auslegung ebener kurvengetriebe: Grundlagen, profilberechnung und konstruktion (construction of planar cam mechanisms: Fundamentals, profile calculation and design). Verein Deutscher Ingenieure – Richtlinien, 1994.
- VDI2149. Blatt 1: Getriebedynamik–starrkörper mechanismen (dynamics of mechanisms–rigid body mechanisms). Verein Deutscher Ingenieure – Richtlinien, 1999.
- M.J. Walker and K. Oldham. A general theory of force balancing using counterweights. *Mechanism and Machine Theory*, 13:175–185, 1978.
- M.J. Walker and K. Oldham. Extensions to the theory of balancing frame forces in planar linkages. *Mechanism and Machine Theory*, 14:201–207, 1979.

- U. Weltin and D. Hermann. Schwingungsdämpfer. *Deutsches Patentamt, DE 41 38 405 C1*, 1997.
- J.L. Wiederrich. Analysis of drive shaft speed variations in a scotch yoke mechanism. *Transactions of the ASME, Journal of Mechanical Design*, 104:239–246, 1982.
- J.L. Wiederrich and B. Roth. Momentum balancing of four-bar linkages. *Transactions of the ASME, Journal of Engineering for Industry*, pages 1289–1295, 1976.
- C.-J. Wu and J. Angeles. The optimum synthesis of an elastic torque-compensating cam mechanism. *Mechanism and Machine Theory*, 36:245–259, 2001.
- F. Xi and R. Sinatra. Effect of dynamic balancing on four-bar linkage vibrations. *Mechanism and Machine Theory*, 32(6):715–728, 1997.
- H.S. Yan and R.C. Soong. Kinematic and dynamic design of four-bar linkages by links counterweighting with variable input speed. *Mechanism and Machine Theory*, 36:1051–1071, 2001.
- H.S. Yan, M.C. Tsai, and M.H. Hsu. An experimental study of the effects of cam speeds on cam-follower systems. *Mechanism and Machine Theory*, 31(4):397–412, 1996a.
- H.S. Yan, M.C. Tsai, and M.H. Hsu. A variable-speed method for improving motion characteristics of cam-follower systems. *Transactions of the ASME, Journal of Mechanical Design*, 118:250–258, 1996b.
- T.-L. Yang and M. Zhang. A general theory for complete balancing of shaking force and shaking moment of planar linkages using counterweights and inertia-counterweights. *Proc. 9th World Congress on the Theory of Machines and Mechanisms*, pages 875–880, Milan, Italy, 1995.
- J. Yao and M.R. Smith. An improved complex mass method for force balancing of planar linkages. *Mechanism and Machine Theory*, 28(3):417–425, 1993.
- L.D. Yong and H. Zhen. Input torque balancing of linkages. *Mechanism and Machine Theory*, 24(2):99–103, 1989.
- L. Yuan and J. Rastegar. A new method for determining the steady-state response of mechanical systems with structural flexibility. *Proc. ASME 2002 Design Engineering Technical Conferences and Computers and Information in Engineering Conference*, Paper No. DETC2002/MECH-34360, Montréal, Canada, 2002.

- S. Zhang and J. Chen. The optimum balance of shaking force and shaking moment of linkage. *Mechanism and Machine Theory*, 30:589–597, 1995.
- M.A.K. Zobairi, S.S. Rao, and B. Sahay. Kineto-elastodynamic balancing of 4r four-bar mechanisms by internal mass redistribution. *Mechanism and Machine Theory*, 21(4):317–323, 1986a.
- M.A.K. Zobairi, S.S. Rao, and B. Sahay. Kineto-elastodynamic balancing of 4r four-bar mechanisms combining kinematic and dynamic stress considerations. *Mechanism and Machine Theory*, 21(4):317–323, 1986b.



# Curriculum Vitae

Demeulenaere, Bram Eugène Georges

°April 28, 1976, Kortrijk (Belgium)  
Belgian, male

Katholieke Universiteit Leuven  
Department of Mechanical Engineering  
Celestijnenlaan 300B  
B-3001 Leuven (Heverlee), Belgium  
Tel: (+32) 16 32 25 51  
Fax: (+32) 16 32 29 87

bram.demeulenaere@mech.kuleuven.ac.be  
<http://www.mech.kuleuven.ac.be/~bdemeule/>

## Education

- **1999-2004:** Ph.D. student at the Department of Mechanical Engineering, Katholieke Universiteit Leuven (Belgium); funded (1999–2003) by the Fund for Scientific Research-Flanders (F.W.O.) and K. U. Leuven's Concerted Research Action GOA/99/04 (2003–2004).
- **July 1999:** degree in Mechanical Engineering (with the greatest distinction and congratulations of the examination board, 89.6%), specialization Machine Design and Mechatronics, Katholieke Universiteit Leuven.  
My master thesis was entitled: 'Optimal Excitation for Identification of a Cam Set-Up'. It tackled the problem of determining optimal excitation trajectories for experimental identification of a setup, consisting of a DC-motor and an industrial cam mechanism with a flexible follower. This thesis won the 1999 Scientific Prize Barco N.V. for 'an original contribution in the domain of automatization applicable to the textile sector'.
- **1994-1999:** Mechanical Engineering Student at the Faculty of Applied Sciences, Katholieke Universiteit Leuven.
- **1988-1994:** Secondary School (Latijn-Wiskunde) at the Sint-Vincentius College, Ieper (Belgium). Final year laureate (90.5%).



# List of Publications

## Articles in International Journals (peer reviewed)

- [1] B. Demeulenaere and J. De Schutter. Synthesis of Inertially Compensated Variable-Speed Cams. *Transactions of the ASME, Journal of Mechanical Design*, Vol.125:593–601, 2003.
- [2] B. Demeulenaere, P. Spaepen and J. De Schutter. Input Torque Balancing Using a Cam-Based Centrifugal Pendulum: Design Procedure and Example. *Journal of Sound and Vibration*, Accepted for Publication.
- [3] B. Demeulenaere, P. Spaepen and J. De Schutter. Input Torque Balancing Using a Cam-Based Centrifugal Pendulum: Design Optimization and Robustness. *Journal of Sound and Vibration*, Accepted for Publication.
- [4] B. Demeulenaere and J. De Schutter. Input Torque Balancing Using an Inverted Cam Mechanism. *Transactions of the ASME, Journal of Mechanical Design*, Accepted for Publication.

## Full Papers in International Conference Proceedings (peer reviewed)

- [1] B. Demeulenaere, J. Swevers and J. De Schutter. Dynamic Balancing of Four-Bar Linkages: A Convex Optimization Framework for Efficiently Obtaining Globally Optimal Counterweights. *Proceedings of ASME 2004 Design Engineering Technical Conferences and Computers and Information in Engineering Conference*, Paper No. DETC2004-57092, Salt Lake City, USA, 2004 (Accepted for Publication).
- [2] B. Demeulenaere, J. Swevers and J. De Schutter. Dynamic Balancing of Linkages: A Convex Optimization Framework for Efficiently Obtaining Globally Optimal Counterweights. *Proceedings of VDI-Getriebetagung 2004*, Fulda, Germany, 2004 (Accepted for Publication).

- [3] B. Demeulenaere, J. Swevers and J. De Schutter. A Convex Optimization Framework for Dynamic Balancing of Planar Linkages. *Proceedings of International Conference on Noise and Vibration Engineering (ISMA2004)*, Leuven, Belgium, 2004 (Accepted for Publication).
- [4] B. Demeulenaere, F. Al-Bender and J. De Schutter. Input Torque Balancing Using an Inverted Cam Mechanism. *Proceedings of ASME 2002 Design Engineering Technical Conferences and Computers and Information in Engineering Conference*, Paper No. DETC2002/MECH-34313, Montréal, Canada, 2002.
- [5] B. Demeulenaere and J. De Schutter. Accurate Realization of Follower Motions in High-Speed Cam-Follower Mechanisms. *Proceedings of International Conference on Noise and Vibration Engineering (ISMA2002)*, 1107–1116, Leuven, Belgium, 2002.
- [6] B. Demeulenaere and J. De Schutter. Dynamically Compensated Cams for Rigid Cam-Follower Systems with Fluctuating Cam Speed and Dominating Inertial Forces. *Proceedings of IEEE/ASME International Conference on Advanced Intelligent Mechatronics (AIM01)*, 763–768, Como, Italy, 2001.
- [7] B. Koninckx, H. Van Brussel, B. Demeulenaere and J. Swevers. Closed-Loop, Fieldbus-Based Clock Synchronisation for Decentralised Motion Control Systems. *Proceedings of CIRP, 1st International Conference on Agile, Reconfigurable Manufacturing*, Keynote Lecture, Michigan, USA, 2001.
- [8] B. Demeulenaere, V. Lampaert, J. Swevers and J. De Schutter. Optimal Excitation for Identification of a Cam Set-Up. *Proceedings of International Conference on Noise and Vibration Engineering (ISMA2000)*, Vol.III:1209–1216, Leuven, Belgium, 2000.

### **Full Papers in National Conference Proceedings (peer reviewed)**

- [1] B. Demeulenaere, P. Spaepen and J. De Schutter. Input Torque Balancing Using a Cam-Based Centrifugal Pendulum. *Proceedings of 6th National Congress on Theoretical and Applied Mechanics*, Paper No. 37, Gent, Belgium, 2003.
- [2] B. Demeulenaere and V. Lampaert. Optimal Excitation for Identification of a Cam Set-Up. *Proceedings of 5th National Congress on Theoretical and Applied Mechanics*, 263–266, Louvain-la-Neuve, Belgium, 2000.

# Appendix A

## ICM: Kinematic Analysis

In this appendix, expressions are derived for the kinematics of the ICM, based on the kinematic scheme given in Fig.A.1(a). The purpose of the kinematic analysis is to determine the position, velocity and acceleration of the points  $\hat{o}_i, i = \{1, 2\}$ , the kinematics of  $(\hat{h}, \check{h})$  the roller follower and the cam profile. It requires the following data:

- the pitch radius  $r$  and its derivatives;
- the rotor angle  $g$  and its derivatives;
- the kinematic design parameter  $R_b$ .

The following conventions are observed:

- coordinates are expressed in the  $(X, Y)$  frame indicated in Fig.A.1, of which the origin coincides with the point  $\hat{o}_1$ , the center of the drive shaft;
- $\vec{o}_i$  denotes the vector with begin point  $\hat{o}_1$  and end point  $\hat{o}_i$ ;  $\vec{0}$  denotes the zero-vector;
- angles are defined w.r.t. the positive  $X$ -axis<sup>1</sup> and are positive counter-clockwise;
- $o_{ix}$  and  $o_{iy}$  denote the  $X$  and  $Y$ -component of  $\vec{o}_i$ ;
- $v_{ix}$  and  $v_{iy}$  denote the  $X$  and  $Y$ -component of  $\vec{v}_i = d\vec{o}_i/dt$ ;
- $a_{ix}$  and  $a_{iy}$  denote the  $X$  and  $Y$ -component of  $\vec{a}_i = d^2\vec{o}_i/dt^2$ ;
- $\|\cdot\|$  denotes the  $L2$ -norm;

---

<sup>1</sup>except for  $h$  that has no absolute reference because of the axisymmetry of the roller follower.

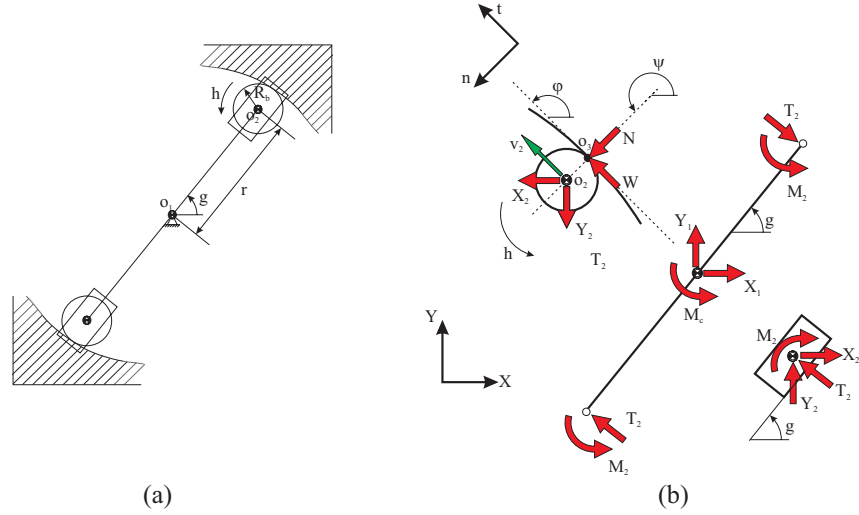


FIGURE A.1: (a) ICM kinematic scheme and (b) free-body diagram.

- $j$  denotes the imaginary unit:  $j = \sqrt{-1}$ .

### A.1 Position, Velocity and Acceleration of the Points $\hat{o}_i, i = \{1, 2\}$

Using complex notation,  $\vec{o}_1$  and  $\vec{o}_2$  are given by:

$$\begin{aligned}\vec{o}_1 &= \vec{0}; \\ \vec{o}_2 &= r \cdot \exp(j \cdot g).\end{aligned}$$

Projecting these equations on the  $X$  and  $Y$ -axis gives the following expressions for the corresponding  $X$  and  $Y$ -components:

$$o_{1x} = 0; \tag{A.1a}$$

$$o_{1y} = 0; \tag{A.1b}$$

$$o_{2x} = r \cdot \cos g; \tag{A.1c}$$

$$o_{2y} = r \cdot \sin g. \tag{A.1d}$$

Deriving (A.1a–A.1d) w.r.t. time  $t$ , yields the  $X$  and  $Y$ -components of the velocity vectors  $\vec{v}_i, i = \{1, 2\}$ :

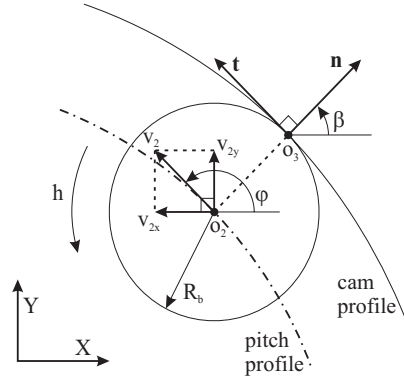


FIGURE A.2: Cam profile determination.

$$v_{1x} = 0; \quad (\text{A.2a})$$

$$v_{1y} = 0; \quad (\text{A.2b})$$

$$v_{2x} = -r \cdot \sin g \cdot \dot{g} + \dot{r} \cdot \cos g; \quad (\text{A.2c})$$

$$v_{2y} = r \cdot \cos g \cdot \dot{g} + \dot{r} \cdot \sin g. \quad (\text{A.2d})$$

Consequently, the  $L2$ -norm of the vector  $\vec{v}_2$  is given by:

$$\|\vec{v}_2\|^2 = v_{2x}^2 + v_{2y}^2 = r^2 \cdot \dot{g}^2 + \dot{r}^2. \quad (\text{A.3a})$$

Deriving (A.1a–A.1d) twice w.r.t. time  $t$ , yields the  $X$  and  $Y$ -components of the acceleration vectors  $\vec{a}_i, i = \{1, 2\}$ :

$$a_{1x} = 0; \quad (\text{A.4a})$$

$$a_{1y} = 0; \quad (\text{A.4b})$$

$$a_{2x} = -r \cdot \cos g \cdot \dot{g}^2 - r \cdot \sin g \cdot \ddot{g} - 2 \cdot \dot{r} \cdot \sin g \cdot \dot{g} + \ddot{r} \cdot \cos g; \quad (\text{A.4c})$$

$$a_{2y} = -r \cdot \sin g \cdot \dot{g}^2 + r \cdot \cos g \cdot \ddot{g} + 2 \cdot \dot{r} \cdot \cos g \cdot \dot{g} + \ddot{r} \cdot \sin g. \quad (\text{A.4d})$$

## A.2 Kinematics of the Roller Follower

The assumption that the roller follower rolls over the cam profile without sliding allows determining both the cam profile and the kinematics of the roller follower. Let  $\hat{o}_3$  denote the contact point between the roller follower and the cam profile. From Fig.A.2, it follows that:

$$\vec{o}_3 = \vec{o}_2 + R_b \cdot \exp(j \cdot \beta). \quad (\text{A.5})$$

Determining the speed of  $\hat{o}_3$ , starting from the speed of  $\hat{o}_2$  yields:

$$\vec{v}_3 = d\vec{o}_3/dt = \vec{v}_2 + R_b \cdot \dot{h} \cdot \exp\left(j \cdot \left(\beta + \frac{\pi}{2}\right)\right). \quad (\text{A.6})$$

Based on the rolling without sliding assumption, the contact point  $\hat{o}_3$  must stand still, hence  $\vec{v}_3 = \vec{0}$ . (A.6) shows that this condition can only be satisfied if:

$$\beta = \phi - \frac{\pi}{2}; \quad (\text{A.7})$$

$$\dot{h} = -\frac{\|\vec{v}_2\|}{R_b}, \quad (\text{A.8})$$

where  $\phi$  denotes the angle measured from the positive  $X$ -axis to  $\vec{v}_2$ . In other words, the tangent to the cam profile is parallel to the absolute velocity of the point  $\hat{o}_2$ .  $\phi$  is determined from the previous results as:

$$\phi = \text{atan2}(v_{2y}, v_{2x}), \quad (\text{A.9})$$

where  $\text{atan2}$  denotes the *4-quadrant arc tangent*<sup>2</sup>. Determining the acceleration of  $\hat{o}_3$ , starting from the acceleration of  $\hat{o}_2$  yields:

$$\vec{a}_3 = d^2\vec{o}_3/dt^2 = \vec{a}_2 + R_b \cdot \dot{h}^2 \cdot \exp(j \cdot (\beta - \pi)) + R_b \cdot \ddot{h} \cdot \exp\left(j \cdot \left(\beta + \frac{\pi}{2}\right)\right).$$

The rolling without sliding assumption imposes that the component of  $\vec{a}_3$ , tangent to the cam-profile (direction  $\vec{t}$  in Fig.A.2), should be zero. Projecting this vectorial equation on the tangent direction  $\vec{n}$ , and substituting  $\beta$  by  $\phi - \pi/2$  yields:

$$\cos(\phi) \cdot a_{2x} + \sin(\phi) \cdot a_{2y} + R_b \cdot \ddot{h} = 0 \Rightarrow \ddot{h} = \frac{-\cos(\phi) \cdot a_{2x} - \sin(\phi) \cdot a_{2y}}{R_b}. \quad (\text{A.10})$$

The results of (A.10) are easily verified by comparing them with the estimate for  $\ddot{h}$  obtained by numerically deriving  $\dot{h}$ , calculated from (A.8).

### A.3 Cam Profile

Determining the cam profile is equivalent to determining the path of the contact point  $\hat{o}_3$ . Based on (A.5) and (A.7), the contact point is determined as:

$$\vec{o}_3 = \vec{o}_2 + R_b \cdot \exp\left(j \cdot \left(\phi - \frac{\pi}{2}\right)\right). \quad (\text{A.11})$$

---

<sup>2</sup> $\text{atan2}(y,x)$  computes  $\tan^{-1}(y/x)$  but uses the signs of both  $x$  and  $y$  to determine the quadrant in which the resulting angle lies. For example,  $\text{Atan2}(-2.0,-2.0)=-135^\circ$ ; whereas  $\text{Atan2}(2.0,2.0)=45^\circ$ , a distinction which would be lost with a single argument arc tangent function. The function  $\text{atan2}$  is undefined if both arguments are zero.

## Appendix B

# ICM: Inverse Dynamic Analysis

In this appendix, expressions are derived for the inverse dynamics of the ICM, based on the free-body diagram of Fig.A.1(b). The purpose of the inverse dynamic analysis is to determine all forces and moments based on the kinematics determined in the kinematic analysis. Furthermore, as a side result, the shaking moment is calculated. Lastly, the inverse dynamic analysis is double checked by comparing the resulting driving moment and shaking moment with the driving moment and shaking moment obtained using the kinetic energy and angular momentum formalism respectively.

The inverse dynamic analysis requires the following data:

- from the kinematic analysis:
  - $g, r, \ddot{g}, \ddot{r}$  and  $\ddot{h}$ ;
  - $a_{1x}, a_{1y}, a_{2x}$  and  $a_{2y}$ ;
  - $\phi$  and  $\psi = \phi + \pi/2$  (see Fig.A.1(b));
- the kinematic design parameter  $R_b$ ;
- the dynamic design parameters  $m_i$  and  $J_i, i = \{r, c, b\}$ .

Figure A.1(b) defines all forces and torques:  $M_c$  is the driving torque;  $X_i$  and  $Y_i, i = \{1, 2\}$  are the reaction forces due to the revolute joints in  $\hat{o}_1$  and  $\hat{o}_2$ .  $N$  and  $W$  respectively are the contact force and the friction force exerted by the cam on the roller follower.  $T_2$  and  $M_2$  are the reaction force and torque due to the prismatic joint between the carriage and the rotor. Due to mechanism symmetry, only one half of the mechanism needs to be considered.

Application of Newton's laws yields the following nine equations in these nine unknown forces:

Rotor:

$$X_1 = m_r \cdot a_{1x}; \quad (\text{B.1a})$$

$$Y_1 = m_r \cdot a_{1y}; \quad (\text{B.1b})$$

$$M_c + 2 \cdot M_2 - 2 \cdot r \cdot T_2 = J_r \cdot \ddot{g}. \quad (\text{B.1c})$$

Carriage:

$$X_2 + T_2 \cdot \cos(g + \pi/2) = m_c \cdot a_{2x}; \quad (\text{B.1d})$$

$$Y_2 + T_2 \cdot \sin(g + \pi/2) = m_c \cdot a_{2y}; \quad (\text{B.1e})$$

$$-M_2 = J_c \cdot \ddot{g}. \quad (\text{B.1f})$$

Roller follower:

$$-X_2 + W \cdot \cos \phi + N \cdot \cos \psi = m_b \cdot a_{2x}; \quad (\text{B.1g})$$

$$-Y_2 + W \cdot \sin \phi + N \cdot \sin \psi = m_b \cdot a_{2y}; \quad (\text{B.1h})$$

$$W \cdot R_b = J_b \cdot \ddot{h}. \quad (\text{B.1i})$$

(B.1a), (B.1b), (B.1f) and (B.1i) are solved<sup>1</sup> directly:

$$X_1 \equiv 0 \equiv Y_1; \quad (\text{B.2a})$$

$$M_2 = -J_c \cdot \ddot{g}; \quad (\text{B.2b})$$

$$W = \frac{J_b \cdot \ddot{h}}{R_b}. \quad (\text{B.2c})$$

The remaining forces are solved from the following set of five equations, linear in the five unknown forces, which is solved for each time instance  $t$ :

$$\begin{bmatrix} 1 & 0 & 0 & -2 \cdot r & 0 \\ 0 & 1 & 0 & \cos(g + \pi/2) & 0 \\ 0 & 0 & 1 & \sin(g + \pi/2) & 0 \\ 0 & -1 & 0 & 0 & \cos \psi \\ 0 & 0 & -1 & 0 & \sin \psi \end{bmatrix} \cdot \begin{bmatrix} M_c \\ X_2 \\ Y_2 \\ T_2 \\ N \end{bmatrix} = \begin{bmatrix} J_r \cdot \ddot{g} - 2 \cdot M_2 \\ m_c \cdot a_{2x} \\ m_c \cdot a_{2y} \\ m_b \cdot a_{2x} - W \cdot \cos \phi \\ m_b \cdot a_{2y} - W \cdot \sin \phi \end{bmatrix}. \quad (\text{B.3})$$

## B.1 Validity of the Results: Input Torque

A first test of the validity of the results is comparing  $n_{\text{ICM}} \cdot M_c$ , with  $M_c$  obtained using the above Newtonian analysis, with  $M_c$ , obtained using the

<sup>1</sup>remember from (A.4a–A.4b) that  $a_{1x} = a_{1x} = 0$

kinetic energy formalism, as given by (5.8), which is repeated here for convenience:

$$M_c = \frac{1}{\frac{2\pi}{T}} \cdot m^* \cdot \left( \dot{r} \cdot \ddot{r} + \left( \frac{2\pi}{T} \right)^2 \cdot r \cdot \dot{r} \right).$$

Figure B.1 shows that, except for numerical rounding, both ways of calculating the input torque are equivalent, implying that both formalisms are applied correctly.

## B.2 Validity of the Results: Shaking Moment

A second test of the validity of the results is comparing the ICM's shaking moment  $M_{\text{shak},c}$ , obtained using the above Newton analysis, with the shaking moment obtained using the angular momentum formalism, as given by (5.23).

Calculating  $M_{\text{shak},c}$  using the Newton analysis results is based on the observation<sup>2</sup> that:

$$M_{\text{shak},c} = n_{\text{ICM}} \cdot (M_{\text{shak},\text{NW}} - M_c).$$

$-M_c$  is part of the shaking moment as the reaction torque of  $M_c$  acts on the motor anchor, which is supposed to be fixed to the machine frame.  $M_{\text{shak},\text{NW}}$  is defined as the shaking moment component due to the contact forces  $N$  and the friction forces  $W$  between the roller followers and the cams, fixed to the frame. Because of symmetry, this shaking moment is a pure couple and hence independent of the chosen reference point. Choosing  $\hat{o}_1$  as the reference point is mathematically convenient.  $M_{\text{shak},N}$ , the shaking moment due to  $N$ , equals twice (due to symmetry) minus (reaction force!) the  $Z$ -component of the vectorial product:

$$(o_{3x} \ o_{3y} \ 0) \times (N_X \ N_Y \ 0),$$

where  $N_X = N \cdot \cos \psi$  and  $N_Y = N \cdot \sin \psi$  respectively denote the  $X$  and  $Y$ -component of the contact force  $N$ , and  $\psi = \phi + \pi/2$  (see Fig.A.1).  $M_{\text{shak},W}$ , the shaking moment due to  $W$ , equals twice (due to symmetry) minus (reaction force!) the  $Z$ -component of the vectorial product:

$$(o_{3x} \ o_{3y} \ 0) \times (W_X \ W_Y \ 0),$$

where  $W_X = W \cdot \cos \phi$  and  $W_Y = W \cdot \sin \phi$  respectively denote the  $X$  and  $Y$ -component of the friction force  $W$  (see Fig.C.1). Summing these two expressions for  $M_{\text{shak},N}$  and  $M_{\text{shak},W}$  yields:

$$M_{\text{shak},\text{NW}} = -2 \cdot (o_{3x} \cdot N_Y - o_{3y} \cdot N_X + o_{3x} \cdot W_Y - o_{3y} \cdot W_X). \quad (\text{B.4})$$

Figure B.2 compares both approaches for calculating  $M_{\text{shak},c}$  for the design example of Section 5.3. It shows that, except for numerical rounding, both approaches yield identical results, implying that both are applied correctly.

<sup>2</sup>Note the difference with (5.24) which is due to the fact that here, as opposed to Chapter 5,  $M_c$  and  $M_{\text{shak},\text{NW}}$  are properties of a *single* ICM configuration.

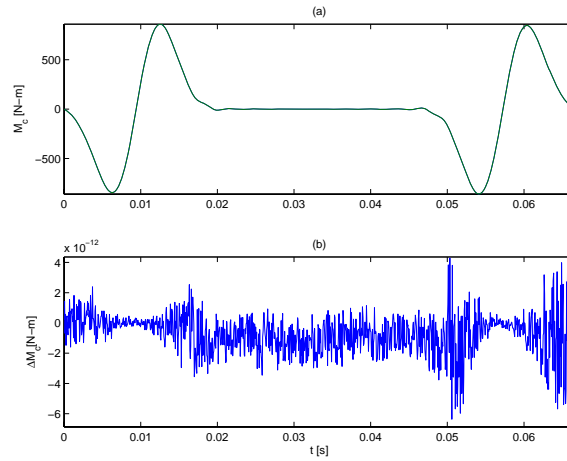


FIGURE B.1: Check of driving torque for the design example of Section 5.3: (a)  $M_c$  obtained using the Newton analysis (solid line) and the kinetic energy formalism (dashed line); (b) difference between both approaches.

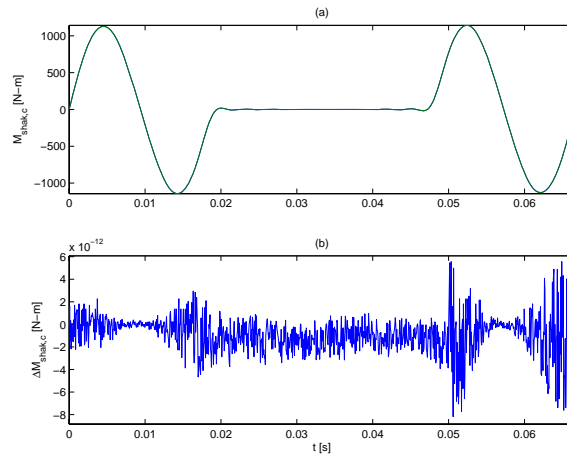


FIGURE B.2: Check of shaking moment for the design example of Section 5.3: (a)  $M_{shak,c}$  obtained using the Newton analysis (solid line) and the angular momentum formalism (dashed line); (b) difference between both approaches.

## Appendix C

# CBCP: Kinematic Analysis

In this appendix, expressions are derived for the kinematics of the CBCP, based on the kinematic scheme given in Fig.C.1(a). The purpose of the kinematic analysis is to determine the position, velocity and acceleration of the points  $\hat{o}_i, i = \{1, 2, c, 3\}$ , the kinematics ( $\dot{h}, \ddot{h}$ ) of the roller follower and the cam profile. It requires the following data:

- the coupler angle  $q$  and its derivatives;
- the rotor angle  $g$  and its derivatives;
- the kinematic design parameters  $l_r, l_c$  and  $R_b$ ;
- the dynamic design parameter  $l_{COG}$ .

The following conventions are observed:

- coordinates are expressed in the  $(X, Y)$  frame indicated in Fig.C.1, of which the origin coincides with the point  $\hat{o}_1$ , the center of the drive shaft;  $\hat{o}_c$  denotes the COG of the coupler;
- $\vec{o}_i$  denotes the vector with begin point  $\hat{o}_1$  and end point  $\hat{o}_i$ ;  $\vec{0}$  denotes the zero-vector;
- angles are defined w.r.t. the positive  $X$ -axis<sup>1</sup> and are positive counter-clockwise;
- $o_{ix}$  and  $o_{iy}$  denote the  $X$  and  $Y$ -component of  $\vec{o}_i$ ;
- $v_{ix}$  and  $v_{iy}$  denote the  $X$  and  $Y$ -component of  $\vec{v}_i = d\vec{o}_i/dt$ ;
- $a_{ix}$  and  $a_{iy}$  denote the  $X$  and  $Y$ -component of  $\vec{a}_i = d^2\vec{o}_i/dt^2$ ;

---

<sup>1</sup>except for  $h$  that has no absolute reference because of the axisymmetry of the roller follower.

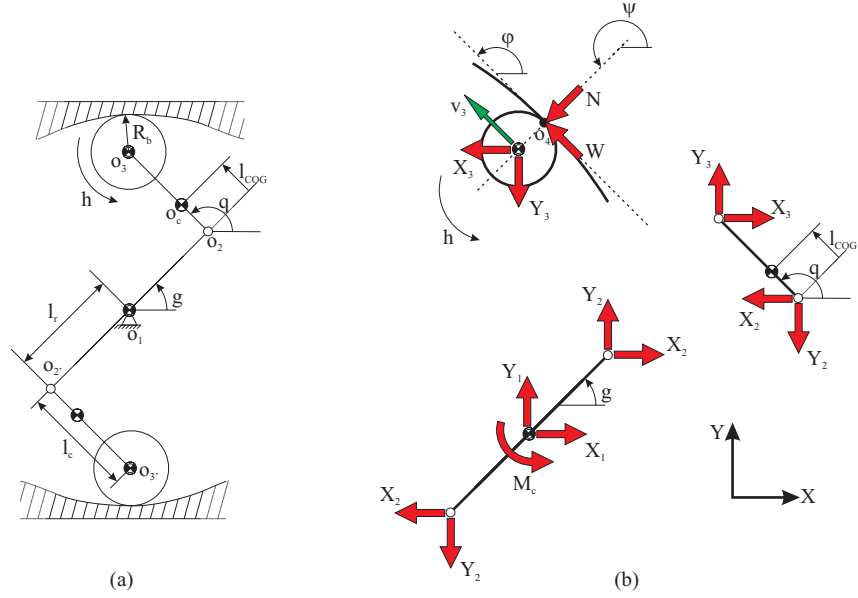


FIGURE C.1: (a) CBCP kinematic scheme and (b) free-body diagram.

- $\|\cdot\|$  denotes the  $L2$ -norm;
- $j$  denotes the imaginary unit:  $j = \sqrt{-1}$ .

### C.1 Position, Velocity and Acceleration of the Points $\hat{o}_i, i = \{1, 2, c, 3\}$

Using complex notation,  $\vec{o}_1, \vec{o}_2, \vec{o}_c$ , and  $\vec{o}_3$  are given by:

$$\begin{aligned} \vec{o}_1 &= \vec{0}; \\ \vec{o}_2 &= l_r \cdot \exp(j \cdot g); \\ \vec{o}_c &= \vec{o}_2 + l_{COG} \cdot \exp(j \cdot q) = l_r \cdot \exp(j \cdot g) + l_{COG} \cdot \exp(j \cdot q); \\ \vec{o}_3 &= \vec{o}_2 + l_c \cdot \exp(j \cdot q) = l_r \cdot \exp(j \cdot g) + l_c \cdot \exp(j \cdot q). \end{aligned}$$

Projecting these equations on the  $X$  and  $Y$ -axis gives the following expressions for the corresponding  $X$  and  $Y$ -components:

$$o_{1x} = 0; \quad (C.1a)$$

$$o_{1y} = 0; \quad (C.1b)$$

$$o_{2x} = l_r \cdot \cos g; \quad (C.1c)$$

$$o_{2y} = l_r \cdot \sin g; \quad (C.1d)$$

$$o_{cx} = l_r \cdot \cos g + l_{COG} \cdot \cos q; \quad (C.1e)$$

$$o_{cy} = l_r \cdot \sin g + l_{COG} \cdot \sin q; \quad (C.1f)$$

$$o_{3x} = l_r \cdot \cos g + l_c \cdot \cos q; \quad (C.1g)$$

$$o_{3y} = l_r \cdot \sin g + l_c \cdot \sin q. \quad (C.1h)$$

Deriving (C.1a–C.1h) w.r.t. time  $t$ , yields the  $X$  and  $Y$ -components of the velocity vectors  $\vec{v}_i, i = \{1, 2, c, 3\}$ :

$$v_{1x} = 0; \quad (C.2a)$$

$$v_{1y} = 0; \quad (C.2b)$$

$$v_{2x} = -l_r \cdot \sin g \cdot \dot{g}; \quad (C.2c)$$

$$v_{2y} = l_r \cdot \cos g \cdot \dot{g}; \quad (C.2d)$$

$$v_{cx} = -l_r \cdot \sin g \cdot \dot{g} - l_{COG} \cdot \sin q \cdot \dot{q}; \quad (C.2e)$$

$$v_{cy} = l_r \cdot \cos g \cdot \dot{g} + l_{COG} \cdot \cos q \cdot \dot{q}; \quad (C.2f)$$

$$v_{3x} = -l_r \cdot \sin g \cdot \dot{g} - l_c \cdot \sin q \cdot \dot{q}; \quad (C.2g)$$

$$v_{3y} = l_r \cdot \cos g \cdot \dot{g} + l_c \cdot \cos q \cdot \dot{q}. \quad (C.2h)$$

Consequently, the  $L2$ -norms of the vectors  $\vec{v}_c$  and  $\vec{v}_3$  are given by:

$$\begin{aligned} \|\vec{v}_c\|^2 &= v_{cx}^2 + v_{cy}^2; \\ &= l_r^2 \cdot \dot{g}^2 + l_{COG}^2 \cdot \dot{q}^2 + 2 \cdot \dot{g} \cdot \dot{q} \cdot l_r \cdot l_{COG} \cdot (\sin q \cdot \sin q + \cos q \cdot \cos g); \\ &= l_r^2 \cdot \dot{g}^2 + l_{COG}^2 \cdot \dot{q}^2 + 2 \cdot \dot{g} \cdot \dot{q} \cdot l_r \cdot l_{COG} \cdot \cos(g - q); \end{aligned} \quad (C.3a)$$

$$\begin{aligned} \|\vec{v}_3\|^2 &= v_{3x}^2 + v_{3y}^2; \\ &= l_r^2 \cdot \dot{g}^2 + l_c^2 \cdot \dot{q}^2 + 2 \cdot \dot{g} \cdot \dot{q} \cdot l_r \cdot l_c \cdot (\sin q \cdot \sin q + \cos q \cdot \cos g); \\ &= l_r^2 \cdot \dot{g}^2 + l_c^2 \cdot \dot{q}^2 + 2 \cdot \dot{g} \cdot \dot{q} \cdot l_r \cdot l_c \cdot \cos(g - q). \end{aligned} \quad (C.3b)$$

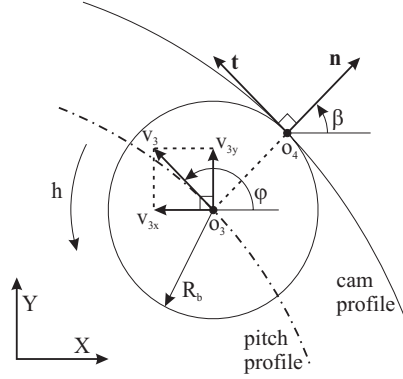


FIGURE C.2: Cam profile determination.

Deriving (C.1a–C.1h) twice w.r.t. time  $t$ , yields the  $X$  and  $Y$ -components of the acceleration vectors  $\vec{a}_i, i = \{1, 2, c, 3\}$ :

$$a_{1x} = 0; \quad (C.4a)$$

$$a_{1y} = 0; \quad (C.4b)$$

$$a_{2x} = -l_r \cdot \cos g \cdot \dot{g}^2 - l_r \cdot \sin g \cdot \ddot{g}; \quad (C.4c)$$

$$a_{2y} = -l_r \cdot \sin g \cdot \dot{g}^2 + l_r \cdot \cos g \cdot \ddot{g}; \quad (C.4d)$$

$$a_{cx} = -l_r \cdot \cos g \cdot \dot{g}^2 - l_r \cdot \sin g \cdot \ddot{g} - l_{\text{COG}} \cdot \cos q \cdot \dot{q}^2 - l_{\text{COG}} \cdot \sin q \cdot \ddot{q}; \quad (C.4e)$$

$$a_{cy} = -l_r \cdot \sin g \cdot \dot{g}^2 + l_r \cdot \cos g \cdot \ddot{g} - l_{\text{COG}} \cdot \sin q \cdot \dot{q}^2 + l_{\text{COG}} \cdot \cos q \cdot \ddot{q}; \quad (C.4f)$$

$$a_{3x} = -l_r \cdot \cos g \cdot \dot{g}^2 - l_r \cdot \sin g \cdot \ddot{g} - l_c \cdot \cos q \cdot \dot{q}^2 - l_c \cdot \sin q \cdot \ddot{q}; \quad (C.4g)$$

$$a_{3y} = -l_r \cdot \sin g \cdot \dot{g}^2 + l_r \cdot \cos g \cdot \ddot{g} - l_c \cdot \sin q \cdot \dot{q}^2 + l_c \cdot \cos q \cdot \ddot{q}. \quad (C.4h)$$

## C.2 Kinematics of the Roller Follower

The assumption that the roller follower rolls over the cam profile without sliding allows determining both the cam profile and the kinematics of the roller follower. Let  $\hat{o}_4$  denote the contact point between the roller follower and the cam profile. From Fig.C.2, it follows that:

$$\vec{o}_4 = \vec{o}_3 + R_b \cdot \exp(j \cdot \beta). \quad (C.5)$$

Determining the speed of  $\hat{o}_4$ , starting from the speed of  $\hat{o}_3$  yields:

$$\vec{v}_4 = d\vec{o}_4/dt = \vec{v}_3 + R_b \cdot \dot{h} \cdot \exp\left(j \cdot \left(\beta + \frac{\pi}{2}\right)\right). \quad (C.6)$$

Based on the rolling without sliding assumption, the contact point  $\widehat{o}_4$  must stand still, hence  $\vec{v}_4 = \vec{0}$ . (C.6) shows that this condition can only be satisfied if:

$$\beta = \phi - \frac{\pi}{2}; \tag{C.7}$$

$$\dot{h} = -\frac{\|\vec{v}_3\|}{R_b}, \tag{C.8}$$

where  $\phi$  denotes the angle measured from the positive  $X$ -axis to  $\vec{v}_3$ . In other words, the tangent to the cam profile is parallel to the absolute velocity of the point  $\widehat{o}_3$ .  $\phi$  is determined from the previous results as:

$$\phi = \text{atan2}(v_{3y}, v_{3x}), \tag{C.9}$$

where  $\text{atan2}$  denotes the *4-quadrant arc tangent*<sup>2</sup>.

Determining the acceleration of  $\widehat{o}_4$ , starting from the acceleration of  $\widehat{o}_3$  yields:

$$\vec{a}_4 = d^2\vec{o}_4/dt^2 = \vec{a}_3 + R_b \cdot \dot{h}^2 \cdot \exp(j \cdot (\beta - \pi)) + R_b \cdot \ddot{h} \cdot \exp\left(j \cdot \left(\beta + \frac{\pi}{2}\right)\right).$$

The rolling without sliding assumption imposes that the component of  $\vec{a}_4$ , tangent to the cam-profile (direction  $\vec{t}$  in Fig.C.2), should be zero. Projecting this vectorial equation on the tangent direction  $\vec{n}$ , and substituting  $\beta$  by  $\phi - \pi/2$  yields:

$$\cos(\phi) \cdot a_{3x} + \sin(\phi) \cdot a_{3y} + R_b \cdot \ddot{h} = 0 \Rightarrow \ddot{h} = \frac{-\cos(\phi) \cdot a_{3x} - \sin(\phi) \cdot a_{3y}}{R_b}. \tag{C.10}$$

The results of (C.10) are easily verified by comparing them with the estimate for  $\ddot{h}$  obtained by numerically deriving  $\dot{h}$ , calculated from (C.8).

### C.3 Cam Profile

Determining the cam profile is equivalent to determining the path of the contact point  $\widehat{o}_4$ . Based on (C.5) and (C.7), the contact point is determined as:

$$\vec{o}_4 = \vec{o}_3 + R_b \cdot \exp\left(j \cdot \left(\phi - \frac{\pi}{2}\right)\right). \tag{C.11}$$

---

<sup>2</sup> $\text{atan2}(y,x)$  computes  $\tan^{-1}(y/x)$  but uses the signs of both  $x$  and  $y$  to determine the quadrant in which the resulting angle lies. For example,  $\text{Atan2}(-2.0,-2.0)=-135^\circ$ ; whereas  $\text{Atan2}(2.0,2.0)=45^\circ$ , a distinction which would be lost with a single argument arc tangent function. The function  $\text{atan2}$  is undefined if both arguments are zero.



## Appendix D

# CBCP: Inverse Dynamic Analysis

In this appendix, expressions are derived for the inverse dynamics of the CBCP, based on the free-body diagram of Fig.C.1(b). The purpose of the inverse dynamic analysis is to determine all forces and moments based on the kinematics determined in the kinematic analysis. Furthermore, as a side result, the shaking moment is calculated. Lastly, the inverse dynamic analysis is double checked by comparing the resulting driving moment and shaking moment with the driving moment and shaking moment obtained using the kinetic energy and angular momentum formalism respectively.

The inverse dynamic analysis requires the following data:

- from the kinematic analysis:
  - $g, q, \ddot{g}, \ddot{q}$  and  $\ddot{h}$ ;
  - $a_{1x}, a_{1y}, a_{cx}, a_{cy}, a_{3x}$  and  $a_{3y}$ ;
  - $\phi$  and  $\psi = \phi + \pi/2$  (see Fig.C.1(b));
- the kinematic design parameters  $l_r, l_c$  and  $R_b$ ;
- the dynamic design parameters  $m_i$  and  $J_i, i = \{r, c, b\}$  and  $l_{\text{COG}}$ .

Figure C.1(b) defines all forces and torques:  $M_c$  is the driving torque;  $X_i$  and  $Y_i, i = \{1, 2, 3\}$  are the reaction forces due to the revolute joints in  $\hat{o}_1, \hat{o}_2$  and  $\hat{o}_3$  respectively.  $N$  and  $W$  respectively are the contact force and the friction force exerted by the cam on the roller follower. Due to mechanism symmetry, only one half of the mechanism needs to be considered. Per coupler, only one roller follower is considered, while in the actual mechanism, two roller followers per coupler are present. Consequently,  $m_b$  and  $J_b$  here represent double the mass and moment of inertia of a single roller follower.

Application of Newton's laws yields the following nine equations in these nine unknown forces:

Rotor:

$$X_1 = m_r \cdot a_{1x}; \quad (\text{D.1a})$$

$$Y_1 = m_r \cdot a_{1y}; \quad (\text{D.1b})$$

$$M_c + 2 \cdot l_r \cdot \cos g \cdot Y_2 - 2 \cdot l_r \cdot \sin g \cdot X_2 = J_r \cdot \ddot{g}. \quad (\text{D.1c})$$

Coupler:

$$-X_2 + X_3 = m_c \cdot a_{cx}; \quad (\text{D.1d})$$

$$-Y_2 + Y_3 = m_c \cdot a_{cy}; \quad (\text{D.1e})$$

$$\begin{aligned} & -X_2 \cdot l_{\text{COG}} \cdot \sin q - X_3 \cdot (l_c - l_{\text{COG}}) \cdot \sin q + \dots \\ & \dots + Y_2 \cdot l_{\text{COG}} \cdot \cos q + Y_3 \cdot (l_c - l_{\text{COG}}) \cdot \cos q = J_c \cdot \ddot{q}. \end{aligned} \quad (\text{D.1f})$$

Roller follower:

$$-X_3 + W \cdot \cos \phi + N \cdot \cos \psi = m_b \cdot a_{3x}; \quad (\text{D.1g})$$

$$-Y_3 + W \cdot \sin \phi + N \cdot \sin \psi = m_b \cdot a_{3y}; \quad (\text{D.1h})$$

$$W \cdot R_b = J_b \cdot \ddot{h}. \quad (\text{D.1i})$$

(D.1a), (D.1b) and (D.1i) are solved<sup>1</sup> directly:

$$X_1 \equiv 0 \equiv Y_1; \quad (\text{D.2a})$$

$$W = \frac{J_b \cdot \ddot{h}}{R_b}. \quad (\text{D.2b})$$

(D.1c–D.1h) form a set of six linear equations in the remaining six unknown forces, which is solved for each time instance  $t$ :

$$\begin{bmatrix} 0 & f_{12} & f_{13} & 0 & 0 & 0 \\ 0 & -1 & 0 & 1 & 0 & 0 \\ 0 & 0 & -1 & 0 & 1 & 0 \\ 0 & f_{42} & f_{43} & f_{44} & f_{45} & 0 \\ 0 & 0 & 0 & -1 & 0 & f_{56} \\ 0 & 0 & 0 & 0 & -1 & f_{66} \end{bmatrix} \cdot \begin{bmatrix} M_c \\ X_2 \\ Y_2 \\ X_3 \\ Y_3 \\ N \end{bmatrix} = \begin{bmatrix} J_r \cdot \ddot{g} \\ m_c \cdot a_{cx} \\ m_c \cdot a_{cy} \\ J_c \cdot \ddot{q} \\ m_b \cdot a_{3x} - W \cdot \cos \phi \\ m_b \cdot a_{3y} - W \cdot \sin \phi \end{bmatrix}, \quad (\text{D.3})$$

---

<sup>1</sup>remember from (C.4a–C.4b) that  $a_{1x} = a_{1x} = 0$

where

$$f_{12} = -2 \cdot l_r \cdot \sin g; \quad (\text{D.4a})$$

$$f_{13} = 2 \cdot l_r \cdot \cos g; \quad (\text{D.4b})$$

$$f_{42} = -l_{\text{COG}} \cdot \sin q; \quad (\text{D.4c})$$

$$f_{43} = l_{\text{COG}} \cdot \cos q; \quad (\text{D.4d})$$

$$f_{44} = -(l_c - l_{\text{COG}}) \cdot \sin q; \quad (\text{D.4e})$$

$$f_{45} = (l_c - l_{\text{COG}}) \cdot \cos q; \quad (\text{D.4f})$$

$$f_{56} = \cos \psi; \quad (\text{D.4g})$$

$$f_{66} = \sin \psi. \quad (\text{D.4h})$$

$$(\text{D.4i})$$

## D.1 Validity of the Results: Input Torque

A first test of the validity of the results is comparing  $M_c$ , obtained using the above Newtonian analysis, with  $M_c$ , obtained using the kinetic energy formalism, as given by (6.12), which is repeated here for convenience:

$$M_c = \frac{1}{\frac{2\pi}{T}} \cdot J_2^* \cdot \dot{q} \cdot \ddot{q} + J_3^* \cdot s,$$

where

$$s(t) = \ddot{q} \cdot \cos\left(\frac{2\pi}{T} \cdot t - q\right) - \dot{q} \cdot \sin\left(\frac{2\pi}{T} \cdot t - q\right) \cdot \left(\frac{2\pi}{T} - \dot{q}\right).$$

Figure D.1 shows that, except for numerical rounding, both ways of calculating the input torque are equivalent, implying that both formalisms are applied correctly.

## D.2 Validity of the Results: Shaking Moment

A second test of the validity of the results is comparing the CBCP's shaking moment  $M_{\text{shak},c}$ , obtained using the above Newton analysis, with the shaking moment obtained using the angular momentum formalism, as given by (6.23).

Calculating  $M_{\text{shak},c}$  using the Newton analysis results is based on the observation that:

$$M_{\text{shak},c} = M_{\text{shak},\text{NW}} - M_c.$$

$-M_c$  is part of the shaking moment as the reaction torque of  $M_c$  acts on the motor anchor, which is supposed to be fixed to the machine frame.  $M_{\text{shak},\text{NW}}$  is defined as the shaking moment component due to the contact forces  $N$  and the friction forces  $W$  between the roller followers and the cams, fixed to

the frame. Because of symmetry, this shaking moment is a pure couple and hence independent of the chosen reference point. Choosing  $\hat{o}_1$  as the reference point is mathematically convenient.  $M_{\text{shak},N}$ , the shaking moment due to  $N$ , equals twice (due to symmetry) minus (reaction force!) the  $Z$ -component of the vectorial product:

$$(o_{4x} \ o_{4y} \ 0) \times (N_X \ N_Y \ 0),$$

where  $N_X = N \cdot \cos \psi$  and  $N_Y = N \cdot \sin \psi$  respectively denote the  $X$  and  $Y$ -component of the contact force  $N$ , and  $\psi = \phi + \pi/2$  (see Fig.C.1).  $M_{\text{shak},W}$ , the shaking moment due to  $W$ , equals twice (due to symmetry) minus (reaction force!) the  $Z$ -component of the vectorial product:

$$(o_{4x} \ o_{4y} \ 0) \times (W_X \ W_Y \ 0),$$

where  $W_X = W \cdot \cos \phi$  and  $W_Y = W \cdot \sin \phi$  respectively denote the  $X$  and  $Y$ -component of the friction force  $W$  (see Fig.C.1). Summing these two expressions for  $M_{\text{shak},N}$  and  $M_{\text{shak},W}$  yields:

$$M_{\text{shak},NW} = -2 \cdot (o_{4x} \cdot N_Y - o_{4y} \cdot N_X + o_{4x} \cdot W_Y - o_{4y} \cdot W_X). \quad (\text{D.5})$$

Figure D.2 compares both approaches for calculating  $M_{\text{shak}}$  for the design example of Section 6.3. It shows that, except for numerical rounding, both approaches yield identical results, implying that both are applied correctly.

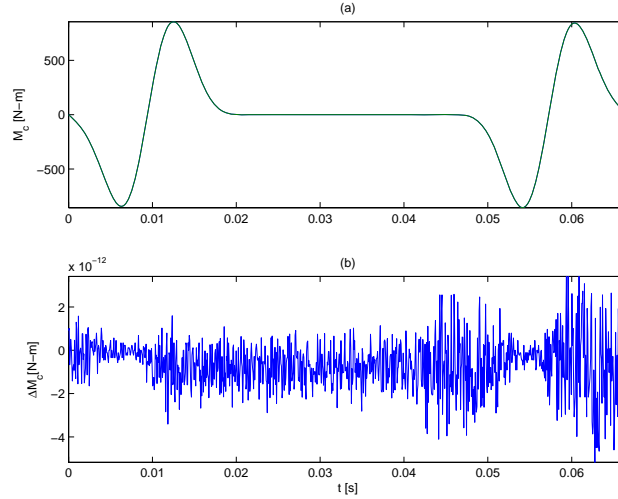


FIGURE D.1: Check of driving torque for the design example of Section 6.3: (a)  $M_c$  obtained using the Newton analysis (solid line) and the kinetic energy formalism (dashed line); (b) difference between both approaches.

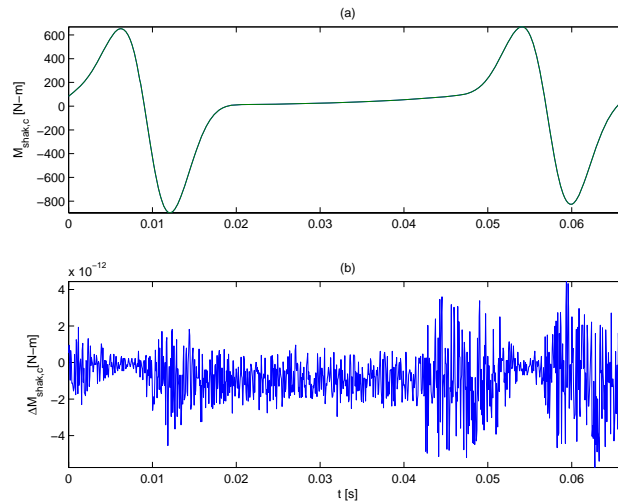


FIGURE D.2: Check of shaking moment for the design example of Section 6.3: (a)  $M_{\text{shak},c}$  obtained using the Newton analysis (solid line) and the angular momentum formalism (dashed line); (b) difference between both approaches.



## Appendix E

# CBCP: Mass Parameterization

### E.1 Parameterization

Figure E.1 defines the parameterization of the rotor and coupler shape. Both the rotor and the coupler are made up of mass primitives, i.e., cylinders, half-cylinders and rectangular prisms: two mass primitives (Primitives 1, 2) for the rotor while six (Primitives 3,...,8) for the coupler. Table E.1 defines these primitives by giving their type (cylinder 'cyl', half-cylinder 'hcyl' or rectangular prism 'prism'), their main dimensions (length  $l$ , width  $d$  and thickness  $t$  for a rectangular prism; radius  $R$  and thickness  $t$  for a cylinder and a half-cylinder) and their number of occurrences  $n_i$ . The main dimensions are defined in Fig.E.1. Some of these dimensions are not independent:

$$\begin{aligned}d_4 &= 2 \cdot R_3; \\l_5 &= l_c + l_{4x} - l_4 - l_{6x}; \\t_5 &= t_{53} + 2 \cdot t_{52} + 2 \cdot t_{51}; \\t^* &= t_7.\end{aligned}$$

The shape parameterization is a compromise between accuracy and simplicity. In this case, the rather simple parameterization of Fig.E.1 is shown to yield rather accurate results in Section E.3.

### E.2 Mass Properties

The mass properties of the rotor and the coupler are calculated based on the mass properties of the constituting mass primitives. Table E.2 gives general

$i$	type	$n_i[-]$	parameters
1	cyl	1	$(R_1, t_1)$
2	prism	2	$(l_2, d_2, t_2)$
3	hcyl	1	$(R_3, t_3)$
4	prism	1	$(l_4, d_4, t_3)$
5	prism	1	$(l_5, d_4, t_5)$
6	prism	1	$(l_6, d_6, t_5)$
7	cyl	2	$(R_7, t_7)$
8	cyl	2	$(R^*, t^*)$

TABLE E.1: Mass primitives constituting the rotor and the coupler: type, number of occurrences  $n_i$  and defining parameters.

expressions for these mass properties<sup>1</sup> (COG, mass, centroidal moment of inertia). Based on the parameters defined in Table E.1 and Fig.E.1, Table E.3 translates these general expressions into specific ones for this case. The origin of the local coordinate system (LCS) for determining the COG  $X$  and  $Y$ -coordinates coincides with  $\hat{o}_1$  for the rotor and  $\hat{o}_2$  for the coupler (see Fig.E.1).

Given the values of the optimization variables  $l_r$ ,  $l_c$  and  $R^*$ , the rotor secondary parameters  $R_1$ ,  $t_1$ ,  $l_2$ ,  $d_2$  and  $t_2$ , and the coupler secondary parameters  $R_3$ ,  $t_3$ ,  $l_4$ ,  $l_{4x}$ ,  $d_4$ ,  $l_5$ ,  $t_{51}$ ,  $t_{52}$ ,  $t_{53}$ ,  $l_6$ ,  $l_{6x}$ ,  $d_6$ ,  $R_7$ ,  $t_7$  and  $t^*$ , the mass properties of the mass primitives are completely determined. Adequate combination of these then yields the rotor and coupler mass properties. This is done by using the previously introduced  $\mu$ -mass parameters, as it is allowed to simply *sum* the  $\mu$ -parameters of the mass primitives in order to obtain the  $\mu$ -parameters of the complete body. For completeness, the definition of the  $\mu$ -parameters is repeated here:

$$\mu_{1i} = m_i; \quad (\text{E.1a})$$

$$\mu_{2i} = m_i \cdot X_i; \quad (\text{E.1b})$$

$$\mu_{3i} = m_i \cdot Y_i; \quad (\text{E.1c})$$

$$\mu_{4i} = J_i + m_i \cdot (X_i^2 + Y_i^2). \quad (\text{E.1d})$$

$\mu_{ji}$  ( $j = 1, \dots, 4, i = 1, \dots, 8$ ) are readily obtained based on these definitions and the results of Table E.3. Subsequently,  $\mu_{j,r}$  ( $j = 1, \dots, 4$ ) and  $\mu_{j,c}$  ( $j =$

<sup>1</sup>The mass properties of a rectangular prism and a cylinder are well-known. The mass properties of half a cylinder are taken from McDonald (1996), and were numerically verified using a CAD-package.

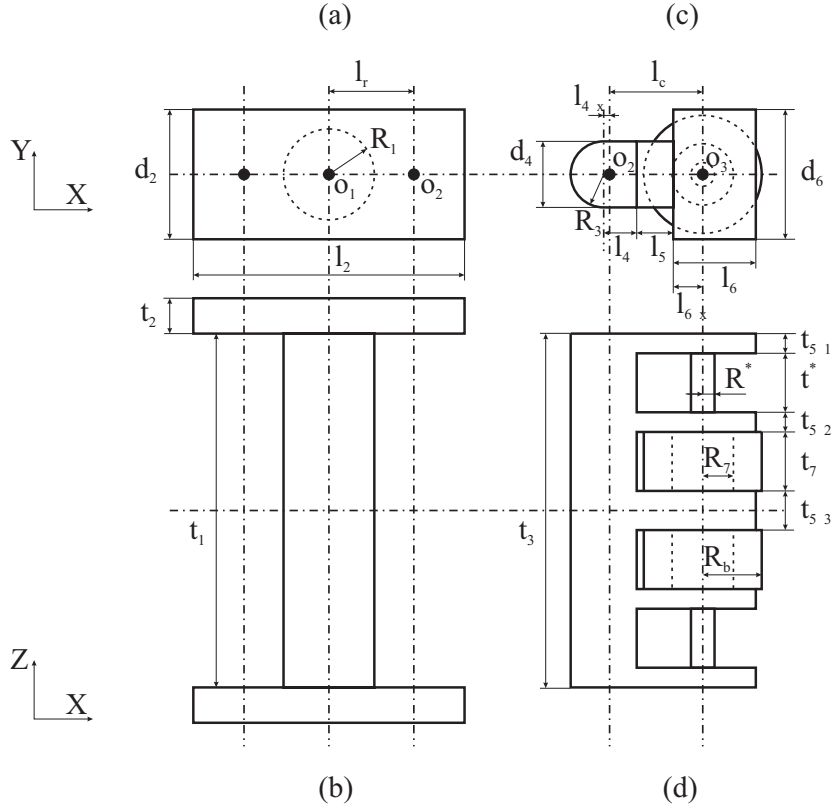


FIGURE E.1: Shape parameterization: front (a) and top (b) view of the rotor and front (c) and top (d) view of the coupler (with the outer bearing ring of diameter  $R_b$  present).

1, ..., 4) are calculated as:

$$\mu_{j,r} = \sum_{i=1}^2 n_i \cdot \mu_{ji} \quad (j = 1 \dots 4); \quad (\text{E.2a})$$

$$\mu_{j,c} = \sum_{i=3}^8 n_i \cdot \mu_{ji} \quad (j = 1 \dots 4). \quad (\text{E.2b})$$

Subsequently,  $m_i$ ,  $X_i$ ,  $Y_i$  and  $J_i$ , ( $j = r, c$ ) are determined based on (E.1a–

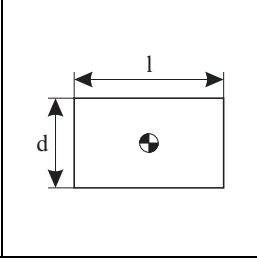
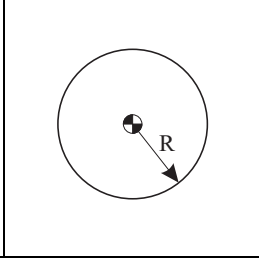
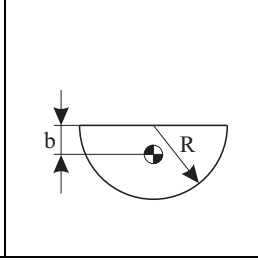
			
COG	trivial	trivial	$b = \frac{4 \cdot R}{3 \cdot \pi}$
$m$ [kg]	$\rho \cdot l \cdot d \cdot t$	$\rho \cdot \pi \cdot R^2 \cdot t$	$\frac{1}{2} \cdot \rho \cdot \pi \cdot R^2 \cdot t$
$J$ [kg-m <sup>2</sup> ]	$\frac{1}{12} \cdot m \cdot (l^2 + d^2)$	$\frac{m \cdot R^2}{2}$	$m \cdot \left( \frac{R^2}{2} - b^2 \right)$

TABLE E.2: Mass properties of the mass primitives used for parameterizing the rotor and coupler shape. All mass primitives are assumed to have thickness  $t$  [m] and mass density  $\rho$  [kg/m<sup>3</sup>].

E.1d) as:

$$m_i = \mu_{1i}; \quad (\text{E.3a})$$

$$X_i = \frac{\mu_{2i}}{\mu_{1i}}; \quad (\text{E.3b})$$

$$Y_i = \frac{\mu_{3i}}{\mu_{1i}}; \quad (\text{E.3c})$$

$$J_i = \mu_{4i} - \frac{1}{\mu_{1i}} \cdot (\mu_{2i}^2 + \mu_{3i}^2). \quad (\text{E.3d})$$

### E.3 Parameter Values

Table E.4 gives an overview of the numerical values of the rotor and coupler secondary parameters for the design example of Section 6.3. Based on these values,  $\rho = 7800$  kg/m<sup>3</sup> and the values of the primary parameters  $l_c$ ,  $l_r$  and  $R^*$  of Table 6.1, the rotor and coupler mass properties are determined. Their values are given in the second column of Table E.5, and compared to the 'true' values generated by a CAD-package (third column). Due to the fact that the mass primitives yield a rotor and coupler shape that is an approximation of the true shape, the relative error  $\epsilon$  is not zero. It is however limited, illustrating that using the mass primitives yields a good approximation of the 'true' values

$i$	$X_i$ [m]	$Y_i$ [m]	$m_i$ [kg]	$J_i$ [kg-m <sup>2</sup> ]
1	0	0	$\rho \cdot \pi \cdot R_1^2 \cdot t_1$	$\frac{m_1 \cdot R_1^2}{2}$
2	0	0	$\rho \cdot l_2 \cdot d_2 \cdot t_2$	$\frac{1}{12} \cdot m_2 \cdot (l_2^2 + d_2^2)$
3	$-l_{4x} - b$	0	$\frac{1}{2} \cdot \rho \cdot \pi \cdot R_3^2 \cdot t_3$	$m_3 \cdot \left( \frac{R_3^2}{2} - b^2 \right)$
4	$-l_{4x} + l_4/2$	0	$\rho \cdot l_4 \cdot d_4 \cdot t_3$	$\frac{1}{12} \cdot m_4 \cdot (l_4^2 + d_4^2)$
5	$-l_{4x} + l_4 + l_5/2$	0	$\rho \cdot l_5 \cdot d_4 \cdot t_5$	$\frac{1}{12} \cdot m_5 \cdot (l_5^2 + d_4^2)$
6	$l_c - l_{6x} + l_6/2$	0	$\rho \cdot l_6 \cdot d_6 \cdot t_5$	$\frac{1}{12} \cdot m_6 \cdot (l_6^2 + d_6^2)$
7	$l_c$	0	$\rho \cdot \pi \cdot R_7^2 \cdot t_7$	$\frac{m_7 \cdot R_7^2}{2}$
8	$l_c$	0	$\rho \cdot \pi \cdot (R^*)^2 \cdot t^*$	$\frac{m^* \cdot (R^*)^2}{2}$

TABLE E.3: Mass properties of the mass primitives constituting the rotor and the follower.  $b$  introduced for Primitive 3 equals  $\frac{4 \cdot R_3}{3 \cdot \pi}$  and is defined in Table E.2

Rotor		Coupler					
$R_1$	38.5 mm	$R_3$	28 mm	$l_5$	30 mm	$l_6$	70 mm
$t_1$	302 mm	$t_3$	300 mm	$t_{51}$	15 mm	$l_{6x}$	25 mm
$l_2$	230 mm	$l_4$	29 mm	$t_{52}$	20 mm	$d_6$	72 mm
$d_2$	110 mm	$l_{4x}$	5 mm	$t_{53}$	30 mm	$R_7$	26 mm
$t_2$	30 mm	$d_4$	56 mm	$t^*$	50 mm	$t_7$	50 mm

TABLE E.4: Numerical values of the rotor and coupler secondary parameters for the design example of Section 6.3.

of the mass properties, or at least an approximation that is 'good enough' for optimization purposes.

	Primitives	CAD	$\epsilon$
$m_r$ [kg]	22.8	20.9	9%
$X_r$ [mm]	0	0	-
$Y_r$ [mm]	0	0	-
$J_r$ [kg-m <sup>2</sup> ]	0.0723	0.0624	14%
$m_c$ [kg]	13.8	14.4	4%
$X_c$ [mm]	39.0	36.1	7 %
$Y_c$ [mm]	0	0	-
$J_c$ [kg-m <sup>2</sup> ]	0.0315	0.0302	4%

TABLE E.5: Comparison (for the design example of Section 6.3) between the rotor and coupler mass properties as determined based on the mass parameterization on the one hand and on a CAD-package on the other hand. The last column gives the relative error  $\epsilon$  in %.

## Appendix F

# CBCP: Collision Constraints

This appendix elaborates two aspects of the detection of collisions in the CBCP, that is (i) intersection of and distance between a circle and a line segment and (ii) the coordinates of the coupler points.

### F.1 Intersection of/Distance Between a Circle and a Line Segment

The problem considered here is determining (i) whether or not a circle  $(\hat{p}_0, R)$  with origin  $\hat{p}_0$  and radius  $R$  intersects with a line segment  $[\hat{p}_1 \hat{p}_2]$  and (ii), if not, the distance between them. It is well-known that the coordinates  $(p_x, p_y)$  of an arbitrary point  $\hat{p}$  on a line segment  $[\hat{p}_1 \hat{p}_2]$  are given by

$$p_x(v) = (1 - v) \cdot p_{1x} + v \cdot p_{2x}; \quad (\text{F.1a})$$

$$p_y(v) = (1 - v) \cdot p_{1y} + v \cdot p_{2y}, \quad (\text{F.1b})$$

where  $v \in [0, 1]$  and  $(p_{1x}, p_{1y})$  and  $(p_{2x}, p_{2y})$  represent the coordinates of  $\hat{p}_1$  and  $\hat{p}_2$  respectively.  $\hat{p}$  now lies on the circle  $(\hat{p}_0, R)$  if its distance to  $\hat{p}_0$  equals  $R$ , or mathematically expressed:

$$(p_x - p_{x0})^2 + (p_y - p_{y0})^2 = R^2. \quad (\text{F.2})$$

Taking into account (F.1a–F.1b), (F.2) represents a quadratic equation in the independent variable  $v$ :

$$A \cdot v^2 + B \cdot v + C = 0, \quad (\text{F.3})$$

where

$$\begin{aligned}
 A &= (p_{1x} - p_{2x})^2 + (p_{1y} - p_{2y})^2; \\
 B &= -2 \cdot p_{x1}^2 - 2 \cdot p_{y1}^2 + 2 \cdot p_{x1} \cdot p_{x2} + 2 \cdot p_{y1} \cdot p_{y2} \\
 &\quad + 2 \cdot p_{x0} \cdot p_{x1} + 2 \cdot p_{y0} \cdot p_{y1} - 2 \cdot p_{x0} \cdot p_{x2} + 2 \cdot p_{y0} \cdot p_{y2}; \\
 C &= (p_{1x} - p_{0x})^2 + (p_{1y} - p_{0y})^2 - R^2.
 \end{aligned}$$

The line segment and the circle intersect if the quadratic equation (F.3) has at least one real solution  $v \in [0, 1]$ . If there is no intersection, the distance between the line segment and the circle is determined as:

$$\min_{v \in [0,1]} \left( (p_x(v) - p_{0x})^2 + (p_y(v) - p_{0y})^2 \right)^{\frac{1}{2}} - R. \quad (\text{F.4})$$

## F.2 Coordinates of Coupler Points

Using complex notation, the coupler points have the following coordinates in the coupler local coordinate system (LCS), fixed to  $\hat{o}_2$  (compare Fig.E.1 with Fig.6.11):

$$\begin{aligned}
 {}^{LCS}\hat{o}_{2a} &= -l_{4x} + j \cdot \frac{d_4}{2}; \\
 {}^{LCS}\hat{o}_{2b} &= -l_{4x} - j \cdot \frac{d_4}{2}; \\
 {}^{LCS}\hat{o}_{2c} &= -l_{4x}; \\
 {}^{LCS}\hat{o}_{3a} &= l_c - l_{6x} + j \cdot \frac{d_6}{2}; \\
 {}^{LCS}\hat{o}_{3b} &= l_c - l_{6x} - j \cdot \frac{d_6}{2}; \\
 {}^{LCS}\hat{o}_{3c} &= l_c - l_{6x} + j \cdot \frac{d_6}{2}; \\
 {}^{LCS}\hat{o}_{3d} &= l_c - l_{6x} - j \cdot \frac{d_6}{2}; \\
 {}^{LCS}\hat{o}_{3e} &= l_c - l_{6x} + l_6 + j \cdot \frac{d_6}{2}; \\
 {}^{LCS}\hat{o}_{3f} &= l_c - l_{6x} + l_6 - j \cdot \frac{d_6}{2}.
 \end{aligned}$$

When determining the values of the collision flags, the coordinates in the world coordinate system (WCS) are required. The world coordinate system is, as in appendix C, the  $(X, Y)$  frame indicated in Fig.6.5, of which the origin coincides with the point  $\hat{o}_1$ . Conversion from the LCS to the

WCS coordinates is done as follows, for each of the coupler points  $\widehat{o}_i, i = \{2a, 2b, 2c, 3a, 3b, 3c, 3d, 3e, 3f\}$  (see Fig.6.5):

$$\widehat{o}_i = l_r \cdot \exp(j \cdot g) + {}^{LCS} \widehat{o}_i \cdot \exp(j \cdot q).$$

Afterwards, the WCS  $X$  and  $Y$ -coordinates ( $o_{ix}, o_{iy}$ ) and are determined by taking the real and imaginary part of the complex number  $\widehat{o}_i$ :

$$\begin{aligned} o_{ix} &= \Re(\widehat{o}_i); \\ o_{iy} &= \Im(\widehat{o}_i). \end{aligned}$$



## Appendix G

# Technological Analysis of Cams: Radius of Curvature

This appendix discusses the radius of curvature of cam pitch profiles: (i) its determination and (ii) its relation with undercutting and other geometrical problems.

### G.1 Determination of the Radius of Curvature

The following formula is generally valid for the radius of curvature  $\rho$  [m] of a planar curve expressed in polar coordinates  $(R, \phi)$ , see e.g. (Mabie and Reinholtz, 1987), p.97:

$$\rho = \frac{\left[ R^2 + (dR/d\phi)^2 \right]^{\frac{3}{2}}}{R^2 + 2 \cdot (dR/d\phi)^2 - R \cdot d^2R/d\phi^2}. \quad (\text{G.1})$$

The value of  $\rho$  at some point on the curve is positive if the corresponding center of curvature lies at the same side of the curve as the origin of the polar coordinate system. Otherwise  $\rho$  is negative.

Table G.1 gives an overview of how the polar coordinates  $(R, \phi)$  of the pitch profile are determined for (a) the internal disk cams of the ICM and (b) the internal disk cams of the CBCP. The atan2-function is the 4-quadrant arc tangent as defined in Appendix C.2.

An alternative way of calculating the radius of curvature at some point on a curve is determining the radius of the tangent circle in that point. The tangent circle is determined by calculating the circle through the point of

	$R$	$\phi$	additional info
(a)	$\sqrt{o_{2x}^2 + o_{2y}^2}$	$\text{atan2}(o_{2y}, o_{2x})$	$o_{2x}$ : Eq.(A.1c) $o_{2y}$ : Eq.(A.1d)
(b)	$\sqrt{o_{3x}^2 + o_{3y}^2}$	$\text{atan2}(o_{3y}, o_{3x})$	$o_{3x}$ : Eq.(C.1g) $o_{3y}$ : Eq.(C.1h)

TABLE G.1: Pitch profile polar coordinates for (a) the internal cams of the ICM and (b) the internal cams of the CBCP.

interest and its immediate left and right neighbor. It is easy to show that the following linear set of equations allows determining the origin  $(x_0, y_0)$  of the circle through three points  $(x_1, y_1)$ ,  $(x_2, y_2)$  and  $(x_3, y_3)$  (it is supposed that  $(x_2, y_2)$  is the point of interest;  $(x_1, y_1)$  and  $(x_3, y_3)$  are the points to its immediate left and right;  $(x_0, y_0)$  is the center of curvature):

$$\underbrace{\begin{bmatrix} -2 \cdot (x_1 - x_2) & -2 \cdot (y_1 - y_2) \\ -2 \cdot (x_1 - x_3) & -2 \cdot (y_1 - y_3) \end{bmatrix}}_{\mathbf{A}} \cdot \begin{bmatrix} x_0 \\ y_0 \end{bmatrix} = \underbrace{\begin{bmatrix} x_2^2 - x_1^2 + y_2^2 - y_1^2 \\ x_3^2 - x_1^2 + y_3^2 - y_1^2 \end{bmatrix}}_{\mathbf{b}}. \quad (\text{G.2})$$

The radius of curvature is then determined as the distance between the point of interest and the center of curvature:

$$\rho = ((x_2 - x_0)^2 + (y_2 - y_0)^2)^{\frac{1}{2}}.$$

This alternative way can be used for checking the calculations based on (G.1). Figure<sup>1</sup> G.1(a–b) compares both approaches for the internal cam of the CBCP prototype of Section H.4 and shows that they are nearly equivalent. The difference can be attributed to the rather poor numerical conditioning of  $\mathbf{A}$  in (G.2): determining a circle through three nearby points is generally known to be a poorly conditioned numerical problem. This is illustrated by Fig.G.1(c) which shows the condition number of  $\mathbf{A}$  as a function of  $g$ : higher values of the condition number and larger differences between the analytical and the tangent-circle approach coincide. Because of these numerical problems, the analytical approach of (G.1) is preferred over the tangent-circle approach.

<sup>1</sup>The fact that  $\rho$  is given as a function of time  $t$  in Fig.G.1 must be interpreted as follows: the value of  $\rho$  at time instant  $t$  is the one for the contact point between the cam and the roller follower at that same time instant.

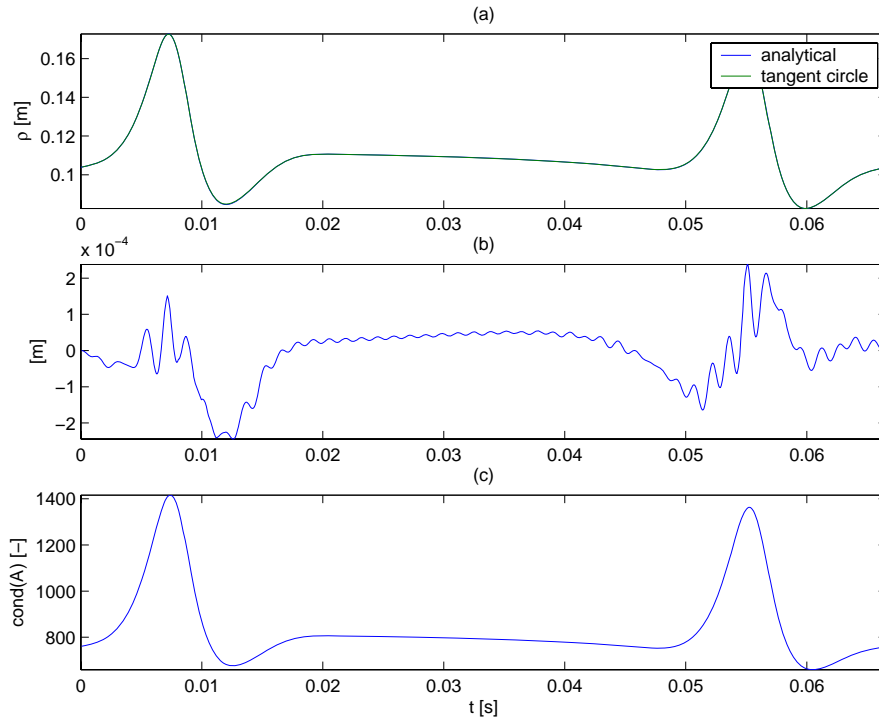


FIGURE G.1: (a) Radius of curvature based on the analytical formula (G.1) and based on the tangent circle; (b) difference between the two approaches; (c) condition of the matrix  $\mathbf{A}$  in (G.2).

## G.2 Undercutting and Other Geometrical Problems

The radius of curvature of the pitch profile is of concern for determining whether or not *undercutting* or other geometrical problems occur. In this context, it is important to make a distinction between convex and concave portions of a cam. (VDI2142, 1994) gives an unambiguous definition of convexity or concavity: a piece of a cam contour is convex if its center of curvature lies towards the material side of the cam; otherwise it is concave. This definition allows a unified discussion of undercutting and other geometrical problems in both internal and external cam profiles.

Figure G.2 shows parts of a cam contour of both an internal (*b*) and an external (*a*) cam. It is assumed that the origin  $\hat{o}_R$  of the polar coordinate system lies inside the closed pitch curve. The thin circles indicate the tangent

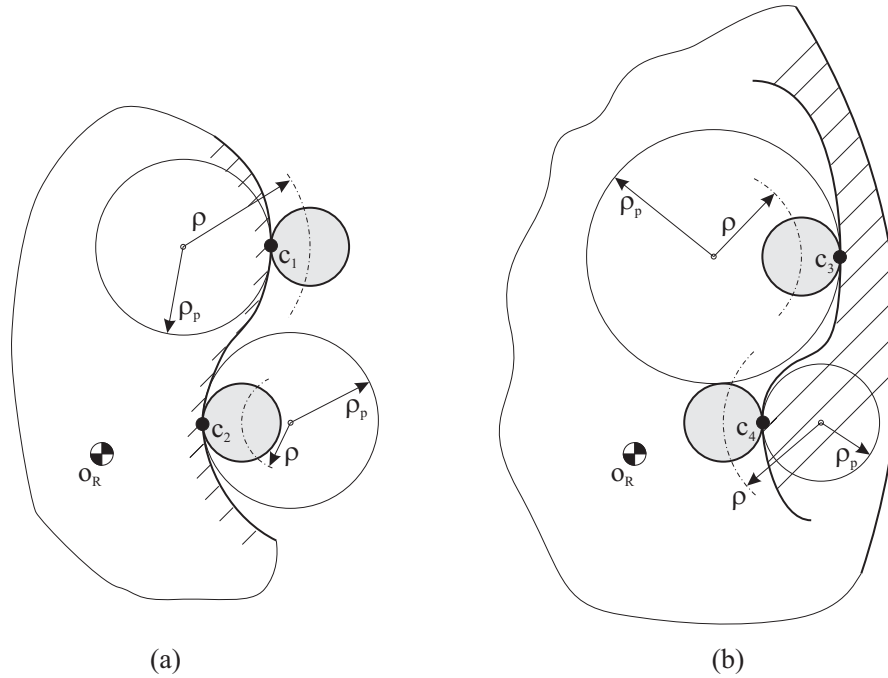


FIGURE G.2: Radius of curvature in external and internal cams with roller follower.

circle (radius  $\rho_p$ ) to the cam profile in the contact points  $\hat{c}_i, i = 1, \dots, 4$ ; the dash-dotted lines show part of the corresponding tangent circles to the pitch profile (radius  $\rho$ ). Based on the aforementioned conventions (sign convention for  $\rho$  and convexity/concavity convention), the table below gives, for these contact points, the sign of  $\rho$  and indicates whether the contour is convex or concave:

$$\begin{aligned} \hat{c}_1 : \rho > 0 & - \text{convex;} \\ \hat{c}_2 : \rho < 0 & - \text{concave;} \\ \hat{c}_3 : \rho > 0 & - \text{concave;} \\ \hat{c}_4 : \rho < 0 & - \text{convex.} \end{aligned}$$

These results are generalized in the first two rows of Table G.2: internal cam profiles are convex if  $\rho < 0$  and concave otherwise; external cam profiles are convex if  $\rho > 0$  and concave otherwise.

Three possible geometric problems can occur in internal and external cam profiles with *roller* followers: *undercutting*, *underrolling* and *feasibility prob-*

*lems*. Undercutting is a problem of convex cam profile segments, while underrolling and feasibility problems are typical for concave profile segments.

### G.2.1 Undercutting

If on a convex profile segment, the absolute value of the radius of curvature  $\rho$  is equal to or smaller than the roller radius  $R_b$ , the cam profile itself respectively exhibits a sharp cusp or undercutting (Norton, 2002), (VDI2142, 1994), (Chen, 1982). A sharp cusp gives rise to infinite contact stress. Undercutting on the other hand means that, during cam manufacture, the cutter undercuts or removes material needed for cam contours in different locations. As a result, a degenerate, useless cam profile is obtained. An example of such a profile is given in Fig.3.5, in which the cam profile associated with  $\delta = 0.1$  exhibits undercutting. The translation of the condition that

$$|\rho| > R_b \tag{G.3}$$

on convex profile segments, for the specific cases of internal and external cam profiles, is found on the fifth row of Table G.2.

It is common to tighten the theoretical bound (G.3) to:

$$\begin{aligned} |\rho| &> 1.4 \cdot R_b && \text{(VDI2142, 1994);} \\ |\rho| &> 1.5 \dots 3 \cdot R_b && \text{(Norton, 2002);} \\ |\rho| &> 3 \cdot R_b && \text{(Chen, 1982).} \end{aligned}$$

In order to limit the contact stress. However, as the contact stress is explicitly calculated, these engineering rules of thumb have not been taken into account, and the theoretical bound (G.3) used throughout this thesis.

### G.2.2 Underrolling

Underrolling occurs in concave profile segments where the radius of curvature  $\rho_p$  of the *cam* (not the pitch) profile is smaller (in absolute value) than the

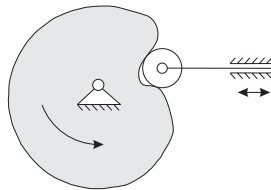


FIGURE G.3: Underrolling in the case of a rotating, external cam with translating roller follower.

	external	internal
convex	$\rho \geq 0$	$\rho \leq 0$
concave	$\rho \leq 0$	$\rho \geq 0$
cam profile	$\rho_p = \rho - R_b$	$\rho_p = \rho + R_b$
no undercutting: $ \rho  > R_b$ (convex)	$\rho > R_b, \forall \rho \geq 0$	$-\rho > R_b, \forall \rho \leq 0$
no underrolling: $ \rho_p  > R_b$ (concave)	$ \rho - R_b  > R_b, \forall \rho \leq 0$ $-\rho + R_b > R_b, \forall \rho \leq 0$ $\rho > 0, \forall \rho \leq 0$	$\rho + R_b > R_b, \forall \rho \geq 0$ $\rho > 0, \forall \rho \geq 0$
feasible profile: $ \rho_p  > R_C$ (concave)	$-\rho + R_b > R_C, \forall \rho \leq 0$	$\rho + R_b > R_C, \forall \rho \geq 0$

TABLE G.2: The relation between the radius of curvature  $\rho$  and possible geometric problems in internal and external cams with roller followers.

roller radius  $R_b$ . Figure G.3 shows an exaggerated case of a rotating, external cam with translating roller follower. Because of the underrolling, the follower does not realize its desired motion.

In order to determine a criterium for avoiding underrolling, first an expression for  $\rho_p$  must be developed. Figure G.2 shows that  $\rho_p = \rho - R_b$  for an external cam, while for an internal cam  $\rho_p = \rho + R_b$ . Based on this observation and the fact that underrolling is avoided if  $|\rho_p| > R_b$  on concave segments, the fifth row of Table G.2 develops criteria for underrolling avoidance in internal and external cams, resulting in trivial criteria, explained as follows: if a cam profile is created, based on the pitch profile, underrolling can never occur; if on the other hand, one starts from the cam profile, and determines the pitch profile afterwards, then underrolling may be a problem. In that case, the pitch profile exhibits cusps similar to an undercut cam profile.

### G.2.3 Feasibility Problems

Concave parts of a cam profile may exhibit feasibility problems. When milling or grinding the profile, the radius  $R_C$  of the cutter or grinding stone must be limited in order to avoid undercut cam profiles or other useless cam profiles. These problems are avoided if (VDI2142, 1994):

$$|\rho_p| > R_C \text{ (concave parts)}. \tag{G.4}$$

This general condition gives rise to the conditions, specific for internal and external cams, given in Table G.2.

## Appendix H

# Technological Analysis of Cams: Allowable Stresses

When two bodies, such as a cam and a roller follower, are in contact, the pressure on the contact patch creates a three-dimensional stress state in the material. These contact stresses are called *Hertzian stresses* in honor of their original discoverer.

This appendix gives formulae for the Hertzian stresses in contacts between cams and roller followers and determines criteria for avoiding premature failure of the cam. Two failure conditions are important. First of all, the Hertzian stresses should be limited in order to avoid *yield* of the cam material. Secondly, the rolling of the roller follower over the cam profile gives rise to a repeated loading of the cam surface, such that a fatigue mechanism called *surface fatigue* comes into play. Again, Hertzian stresses should be limited, such that surface fatigue does not limit the life of the cam profile below some given number of cycles.

For both failure conditions (yield and surface fatigue), criteria are developed (in Section H.2 and H.3 respectively) which are based on the maximum Hertzian stress  $p_{\max}$ , discussed in Section H.1. The developed criteria are illustrated by applying them in Section H.4 to the CBCP prototype of Section 6.3.

### H.1 Contact Pressure in General Contacts

This section gives a brief summary of the theory of contact pressure in general contacts, and is essentially based on (Norton, 2002).

If the geometry of two contacting bodies is allowed to have any general curvature, the contact patch is an ellipse and the pressure distribution is a semi-ellipsoid (see (Norton, 2002), Fig.12-11(a), p.353). The general curvature

of both contacting bodies is represented by two mutually orthogonal radii of curvature (also called principal radii of curvature)  $R_i$  and  $R'_i$  ( $i$  is an index denoting the first or the second body in contact) at the contact point.

The contact pressure is a maximum  $p_{\max}$  [MPa] at the center of the contact patch and zero at the edge.  $p_{\max}$  equals:

$$p_{\max} = \frac{3}{2} \cdot \frac{F}{\pi \cdot a \cdot b},$$

where  $F$  denotes the total applied load on the contact patch.  $a$  and  $b$  respectively denote the half-width of the major and minor axis of the contact patch ellipse. In order to determine  $a$  and  $b$ , the following geometry constants, depending on the principal radii of curvature of the two bodies, are defined:

$$A = \frac{1}{2} \cdot \left[ \frac{1}{R_1} + \frac{1}{R'_1} + \frac{1}{R_2} + \frac{1}{R'_2} \right]; \quad (\text{H.1})$$

$$B = \frac{1}{2} \cdot \left[ \left( \frac{1}{R_1} - \frac{1}{R'_1} \right)^2 + \left( \frac{1}{R_2} - \frac{1}{R'_2} \right)^2 + 2 \left( \frac{1}{R_1} - \frac{1}{R'_1} \right) \cdot \left( \frac{1}{R_2} - \frac{1}{R'_2} \right) \cdot \cos(2\theta) \right]^{\frac{1}{2}}. \quad (\text{H.2})$$

$\theta$  is the angle between the planes containing  $R_1$  and  $R_2$ . The contact-patch dimensions are then found from:

$$a = k_a \cdot \sqrt[3]{\frac{3 \cdot F \cdot \left( \frac{1-\nu_1^2}{E_1} + \frac{1-\nu_2^2}{E_2} \right)}{4 \cdot A}}; \quad (\text{H.3})$$

$$b = k_b \cdot \sqrt[3]{\frac{3 \cdot F \cdot \left( \frac{1-\nu_1^2}{E_1} + \frac{1-\nu_2^2}{E_2} \right)}{4 \cdot A}}. \quad (\text{H.4})$$

$k_a$  and  $k_b$  are determined from Table H.1 and depend on  $\phi$ , defined as:

$$\phi = \cos^{-1} \left( \frac{B}{A} \right).$$

Besides the maximum contact pressure  $p_{\max}$ , also the maximum shear stress  $\tau_{\max}$  is important.  $\tau_{\max}$  occurs slightly below the surface, with that distance dependent on the ratio of the semiaxes of the contact ellipse. For  $b/a = 1.0$ , the largest shear stress occurs at  $z = 0.63 \cdot a$ , and for  $b/a = 0.34$  at  $z = 0.24 \cdot a$ . Its peak magnitude is approximately  $0.34 \cdot p_{\max}$ , roughly independent of  $b/a$ .

The formulae presented here assume that pure rolling occurs between the contacting bodies. If rolling and sliding are both present, the stress field is distorted by the tangential loading. The distortion of the stress field due to sliding has not been considered in this thesis (see e.g. (Norton, 2002)),

$\phi$	0	10	20	30	35	40	45	50
$k_a$	$\infty$	6.612	3.778	2.731	2.397	2.136	1.926	1.754
$k_b$	0	0.319	0.408	0.493	0.530	0.567	0.604	0.641
$\phi$	55	60	65	70	75	80	85	90
$k_a$	1.611	1.486	1.378	1.284	1.202	1.128	1.061	1
$k_b$	0.678	0.717	0.759	0.802	0.846	0.893	0.944	1

TABLE H.1:  $k_a$  and  $k_b$  as a function of  $\phi$  for use in (H.3–H.4).

Section 12.15). The formulae furthermore assume that a convex<sup>1</sup> surface has a positive radius, but apply equally to concave or saddle-shaped surfaces by ascribing a negative sign to the curvatures (Johnson, 1985).

## H.2 Avoiding Yield in Cam Profiles

Based on the theory developed in the previous section, it is possible to determine a critical value of  $p_{\max}$  for avoiding yield. It is common, in dealing with yield in materials, to convert multi-axial stresses to an *equivalent uni-axial* stress  $\sigma_e$ . This equivalent stress must then be smaller than the yield strength  $R_{p0,2}$  [MPa]. In order to predict the yield in a *ductile* material, such as the material used for constructing the CBCP cams, two criteria are commonly used for calculating  $\sigma_e$  (Beitz and Küttner, 1986): the *maximum shear stress criterion*, also known as Tresca’s or Guest’s criterion, and the *von Mises criterion* (1913), also known as the maximum distortion energy criterion, octahedral shear stress theory, or Maxwell-Huber-Hencky-von Mises theory.

According to the maximum shear stress criterion, yield does not occur in a 3-axial (spatial) stress condition provided that

$$\sigma_e = 2 \cdot \tau_{\max} = \sigma_3 - \sigma_1 < R_{p0,2}, \quad (\text{H.5})$$

where  $\sigma_1$ ,  $\sigma_2$  and  $\sigma_3$  denote the principal stresses ( $\sigma_1 > \sigma_2 > \sigma_3$ ).

The maximum shear stress criterion is more conservative than the von Mises criterion, which is generally believed to be more accurate. The von Mises criterion states that failure occurs if the energy of distortion reaches the same energy as for yield/failure in uniaxial tension. Mathematically, this is expressed as:

$$\sigma_e = \frac{1}{\sqrt{2}} \cdot \sqrt{(\sigma_1 - \sigma_2)^2 + (\sigma_2 - \sigma_3)^2 + (\sigma_3 - \sigma_1)^2} < R_{p0,2}. \quad (\text{H.6})$$

---

<sup>1</sup>Recall from Section G.2 that a surface is convex if its center of curvature lies towards the material side of the surface.

Despite that the von Mises criterion is more accurate, the maximum shear stress criterion was used here. The reason to do so is that standard text books on cams, such as (Chen, 1982) and (Norton, 2002), focus on the maximum shear stress.

Since the maximum shear stress  $\tau_{\max}$  was already shown to be approximately equal to  $0.34 \cdot p_{\max}$ , the maximum shear criterion yields the following upper limit on  $p_{\max}$ :

$$\sigma_e = 2\tau_{\max} = 0.68 \cdot p_{\max} < R_{p0,2} \Rightarrow p_{\max} < 1.47 \cdot R_{p0,2}. \quad (\text{H.7})$$

### H.3 Limiting Surface Fatigue in Cam Profiles

When two surfaces are in pure rolling contact, or are primarily rolling in combination with a small percentage of sliding, *surface fatigue* is the main surface failure mechanism. Cams with roller followers are an example of this condition and typically have essentially pure rolling with only about 1% sliding (Norton, 2002).

(Norton, 2002), (Chen, 1982) and (VDI2142, 1994)<sup>2</sup> all base their discussion of surface fatigue on the experimental surface wear tests done at United Shoe Machinery Corporation from 1932 to 1956. The objects under test were two contacting cylinders of dissimilar metal, subject to rolling only and rolling combined with 9% sliding action. The result from the surface wear tests is a least-squares load-life curve, giving  $\log_{10}(K)$  as a function of  $\log_{10}(N)$ .  $N$  denotes the number of stress cycles, whereas  $K$  [MPa] is called the *experimental load-stress factor for cylinders in contact*. For  $\nu_1 = \nu_2 = 0.3$ , a common assumption for metals, the  $K$ -factor [MPa] equals (Chen, 1982):

$$K = \frac{p_{\max}^2}{0.35} \cdot \left( \frac{1}{E_1} + \frac{1}{E_2} \right). \quad (\text{H.8})$$

Representing the slope and intercept of these load-life curves by  $A$  [-] and  $B$  [-], yields the following result:

$$\log_{10} K = \frac{B - \log_{10} N}{A}. \quad (\text{H.9})$$

The values of  $A$  and  $B$  result from the surface wear tests and are tabulated in (Norton, 2002) (Table 12-4), (Chen, 1982) (Table 12-4) and (VDI2142, 1994) (Tabelle 5). Values are given for pure rolling and for rolling with 9 % sliding. The values for rolling are only applicable to cam-follower combinations where sliding is not anticipated. The values listed under 9% sliding are applicable to spur and helical gears, or to cams where a small amount of sliding is

---

<sup>2</sup>The discussion of surface fatigue in this VDI-norm is in fact based on the discussion in (Chen, 1982).

anticipated (Chen, 1982). The use of (H.8) and (H.9) is demonstrated in the forthcoming example.

Concerning the prediction of fatigue life, Chen (1982) remarks: *The load life curve represents probable values. Exact load-life factors, therefore, may be greater or less than those listed. In addition, tests are generally conducted under optimum conditions, which are not normally encountered in the field. Engineering judgement must still be applied in allowing for mounting errors, lubrication deficiencies, thermal effects, and other operating and geometric variables not accounted for in the laboratory tests. Therefore, it is logical that factors of safety should be considered when determining the safe wear load capacity of cams.* Taking this consideration into account, it is clear that predicting the surface fatigue life of a cam mechanism based on the above formulae can only give an indication of the expected fatigue life, and must always be validated experimentally.

## H.4 Example: CBCP Prototype

The developed criteria now are illustrated by applying them to the CBCP prototype of Section 6.3. First, the maximum Hertzian stress is calculated. Secondly, the upper limit on  $p_{\max}$  for avoiding yield is determined. Lastly, the upper limit on  $p_{\max}$  for obtaining a fatigue life of 50000h is calculated.

$p_{\max}$  is determined based on the formulae of Section H.1. The roller follower used in the CBCP is crowned, that is, it has a gentle radius transverse to its rolling direction to eliminate the need for critical alignment of its axis with that of the cam. The roller radius  $R_b$  is 50 mm and the crown radius  $R_{bc}$  at  $90^\circ$  to the roller radius is 2500 mm. The rotational axes of the cam and roller are parallel, which makes the angle  $\theta$  between the two bodies zero. In this case,  $R_1$  is minus<sup>3</sup> the radius of curvature  $\rho_p$  of the cam profile<sup>4</sup>,  $R'_1$  is infinity as the cam profile is flat in the direction perpendicular to the cam plane.  $R_2$  is equal to  $R_b$  and  $R'_2$  equals the crown radius.

The list below summarizes all data required for determining  $p_{\max}$ :

- $R_1 = -\rho_p = -(\rho + R_b)$ .  $\rho_p$  is shown in Fig.H.1(b);
- $R'_1 = \infty$ ;
- $R_2 = R_b = 0.050$  m;
- $R'_2 = R_{bc} = 2.500$  m;
- $F$  is the contact force  $N$  [N] between the cam and the roller follower, shown in Fig.H.1(a);

<sup>3</sup>The internal cam profile is concave, which means that its radius of curvature is positive, if it is determined based on the formulae of Section G. As for a concave profile, the Hertzian pressure formulae are valid provided that the curvature is negative, a minus sign is added.

<sup>4</sup>Remember from Table G.2 that  $\rho_p = \rho + R_b$ .

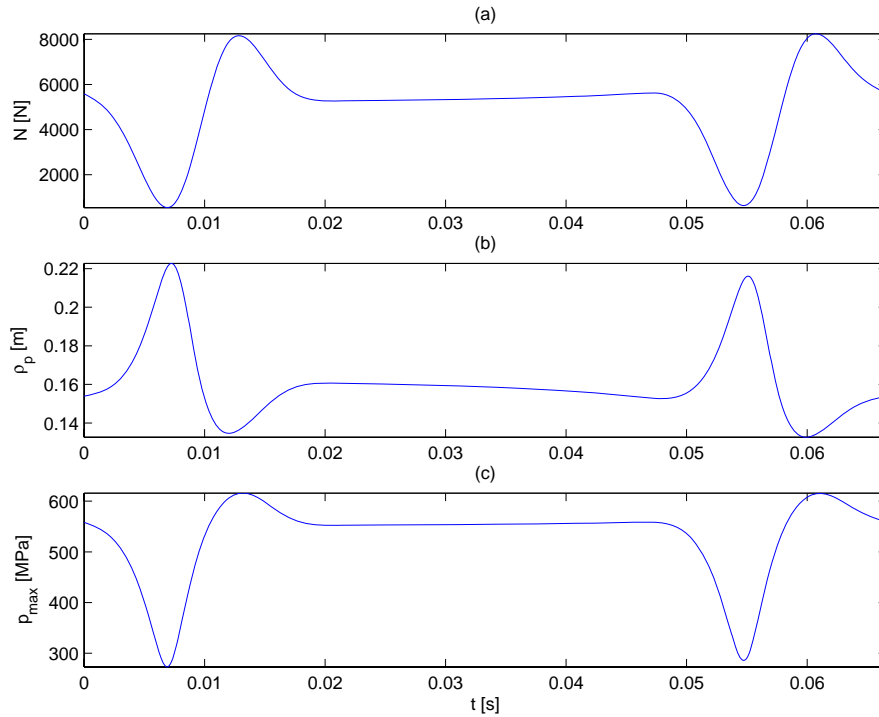


FIGURE H.1: (a) contact force  $N$  [N] between the cam and the roller follower; (b) cam profile radius of curvature  $\rho_p$  [m]; (c) maximum Hertzian pressure  $p_{\max}$  [MPa].

- $E_1 = E_2 = 210 \cdot 10^9$  Pa;
- $\nu_1 = \nu_2 = 0.3$ ;
- $\theta = 0$ .

Figure<sup>5</sup> H.1(c) shows the trajectory of  $p_{\max}$  as a function of the CBCP rotor angle  $g$ . The maximum value of  $p_{\max}$  over the cam profile equals 616 MPa.

The cam material used here is *IMPAX Hi Hard*, a material produced by Uddeholm Tooling AB (<http://www.uddeholm.com>). *IMPAX Hi Hard* is a 100% ultrasonic tested, prehardened mould steel with a hardness of 360-400 HB. Table H.2 gives its main specifications. Table H.3 gives its mechanical

---

<sup>5</sup>The fact that  $N$ ,  $\rho_p$  and  $p_{\max}$  are given as a function of time  $t$  in Fig.H.1 must be interpreted as follows: the values of  $N$ ,  $\rho_p$  and  $p_{\max}$  at time instant  $t$  are the ones for the contact point between the cam and the roller follower at that same time instant.

Approximate analysis %	C	Si	Mn	Cr	Ni	Mo	S
	0.37	0.3	1.4	2.0	1.0	0.2	<0.010
Standard spec.	AISI P20 modified						
Delivery condition	Hardened and tempered to 360-400 HB						
Color code	Brown						

TABLE H.2: IMPAX Hi Hard specifications

<b>Tensile strength</b>	
Testing temperature	20°C
Ultimate tensile strength, $R_m$	1180 N/mm <sup>2</sup>
Yield strength, $R_{p0,2}$	1090 N/mm <sup>2</sup>
Hardness	370 HB
<b>Compressive strength</b>	
Compressive yield strength, $R_{c0,2}$	~1150 N/mm <sup>2</sup>

TABLE H.3: IMPAX Hi Hard (approximate) mechanical properties

properties<sup>6</sup>. Combining (H.7) with the value of  $R_{p0,2}$  in Table H.3 yields that the cam profile does not yield provided that

$$p_{\max} < 1.47 \cdot R_{p0,2} \Rightarrow p_{\max} < 1600 \text{ MPa},$$

a condition which is fulfilled in the CBCP prototype.

Predicting the surface fatigue life of the mechanism is complicated by the fact that (i) the Hi Hard material is not listed in the surface wear tables and (ii) the hardness of the roller follower is not known (in the tests, a HRC 60-62 tool-steel roller was used). In order to circumvent these problems, it is assumed that the roller-follower used here is in fact the same as the test-roller follower. Furthermore, from the aforementioned surface wear tables, two materials are chosen that look like the Hi Hard material (a prehardened mould steel of 370 HB), that is, two heat-treated steels with roughly the same hardness: (i) 4150 steal, heat-treated, HB 270–300, flash-chrome plated (material *I*) and (ii) 4150 steal, heat-treated, HB 270–300, phosphate coated

<sup>6</sup>More material properties, and further information are given at <http://www.uddeholm.com/UTAB/index.asp?id=469>.

Pure Rolling				
	$K$ [MPa]	$p_{\max}^*$ [MPa]	$A$ [-]	$B$ [-]
I	41.8	1220	11.18	26.14
II	83.0	1720	11.40	29.87

TABLE H.4: Surface fatigue properties of material I and II.

(material *II*). The numerical values of  $K$ ,  $A$  and  $B$  are listed in Table H.4, and are taken from the pure rolling part of the tables listed in (Chen, 1982) and (VDI2142, 1994). The same table also lists  $p_{\max}^*$ , the maximum Hertzian pressure giving rise to a lifetime of  $N = 10^8$  cycles. This value is easily verified based on (H.8), with  $E_1 = E_2 = 210 \cdot 10^9$  Pa, and  $N = 10^8$ .

The desired lifetime is 50000h, which is the equivalent of  $N = 2.7 \cdot 10^9$  cycles if the machine turns at 900 rpm. The corresponding  $K$ -factor is determined based on (H.9) and the numerical values in Table H.4:

$$I : \log_{10} K = \frac{26.14 - \log_{10} 2.7 \cdot 10^9}{11.18} \rightarrow K = 31.23 \text{ MPa} \Rightarrow p_{\max} = 1071 \text{ MPa};$$

$$II : \log_{10} K = \frac{29.87 - \log_{10} 2.7 \cdot 10^9}{11.40} \rightarrow K = 62.07 \text{ MPa} \Rightarrow p_{\max} = 4315 \text{ MPa}.$$

The value obtained for material II is not realistic. The value obtained for material I (which is softer than IMPAX Hi Hard) seems more realistic as it is lower than the 1600 MPa bound for avoiding yield of the material. As the largest  $p_{\max}$  is 616 MPa, well below 1071 MPa, it is expected that the CBCP prototype has a fatigue life longer than 50000h.

## Appendix I

# Technological Analysis of Cams: Bearing Lifetime

### I.1 Roller Followers

The roller followers considered in this thesis are in fact special versions of ordinary roller bearings. Two technological properties of these roller bearings are considered here: the maximum allowable speed and the bearing fatigue life. Bearing catalogues give for each bearing the corresponding maximum allowable speed, so this issue needs no further attention. The bearing fatigue life on the other hand is governed by the equation:

$$L = \left(\frac{C}{P}\right)^p [10^6 \text{ revolutions}],$$

where the dynamic load-carrying capacity  $C$  [N] is defined as the load corresponding to a rated life of  $L = 10^6$  revolutions. The life exponent  $p$  is 3 for ball bearings and 10/3 for roller bearings.  $P$  [N] denotes the equivalent dynamic load. In dynamically stressed bearings, the variable load and speed are approximated by a series of individual loads  $F_i$  and speeds  $n_i$  [rpm] of a certain duration  $q_i\%$ . In this case, the equivalent dynamic load  $P$  is obtained as (Brändlein et al., 1999):

$$P = \sqrt[p]{F_1^p \cdot \frac{n_1}{n_m} \cdot \frac{q_1}{100} + F_2^p \cdot \frac{n_2}{n_m} \cdot \frac{q_2}{100} + \dots} \text{ [N]}, \quad (\text{I.1})$$

and the mean rotary speed  $n_m$  [rpm] as:

$$n_m = n_1 \cdot \frac{q_1}{100} + n_2 \cdot \frac{q_2}{100} + \dots \text{ [rpm]}. \quad (\text{I.2})$$

(I.1) and (I.2) are in fact numerical approximations of:

$$P = \sqrt[p]{\frac{1}{T} \int_0^T (F)^p(t) \cdot \frac{n(t)}{n_m} \cdot dt}; \quad (I.3)$$

$$n_m = \frac{1}{T} \int_0^T n(t) dt, \quad (I.4)$$

which are the formulae used in this thesis. For the roller bearings in the CBCP,  $F(t)$  and  $n(t)$  are determined as follows (results for the ICM are obtained in a very similar way). Recall that in the dynamic analysis, only one roller follower per coupler was considered, while in the actual mechanism, two roller followers per coupler are present. Consequently, this roller follower was assumed to have double the mass and moment of inertia of a single roller follower. The magnitude of the force transmitted by the single roller follower of Fig.C.1 equals

$$\sqrt{X_3^2 + Y_3^2}.$$

As two roller followers per coupler are present in the actual mechanism, each of these roller followers transmits a force of magnitude

$$F(t) = \sqrt{X_3^2 + Y_3^2}/2.$$

$n(t)$  on the other hand is the speed difference between the inner and the outer bearing ring and hence equals  $\dot{h} - \dot{q}$  (Fig.C.1). The roller follower itself is a non-standard roller follower with a dynamic load-carrying capacity  $C$  of 137 kN. Its maximum allowable speed is not known.

## I.2 Oscillating bearings

An oscillating bearing does not turn through complete revolutions. In (Harris, 1966), the following formula is derived, which relates the fatigue life  $L_{osc}$  of an oscillating bearing to the life  $L_{rot}$  of the corresponding rotating bearing:

$$L_{oscill} = L_{rot} \cdot \frac{90}{\phi},$$

where  $\phi$  [degrees] is the amplitude of oscillation. Harris however indicates that, if

$$\frac{90}{\phi} < \frac{1}{Z}, \quad (I.5)$$

where  $Z$  is the number of rolling elements per row, then a strong possibility exists that indentation of the raceways occurs. In this situation, surface fatigue may not be a valid criterion of failure in view of the vibration which can develop. For this case, no fatigue life formulae are given in (Harris, 1966).

On the other hand, Beitz and Küttner (1986), pp.418–419, do not take into account (I.5), and recommend to calculate the fatigue life of oscillating bearings based on the static load-carrying capacity  $C_0$ . This is the approach taken in this thesis. The oscillating bearing life is hence calculated as:

$$L = \left(\frac{C_0}{P}\right)^p [10^6 \text{ revolutions}],$$

where the static equivalent load  $P$  is determined as:

$$P = \sqrt[p]{\frac{1}{T} \int_0^T (F)^p(t) dt}. \quad (\text{I.6})$$

In the case of the oscillating bearing in the CBCP,  $F(t)$  equals  $\sqrt{X_2^2 + Y_2^2}/2$  (Fig.C.1) due to the fact that the revolute joint between the rotor and the coupler is implemented as two identical SKF NKIA 59/22 needle roller/angular contact ball bearings. These bearings have a static load-carrying capacity  $C_0$  of 32 kN. As they are oscillating, their maximum allowable speed is not of concern.



## Appendix J

# Modelling of Shed Mechanism

This appendix shows that the four cam-linkage shed mechanisms in the setup can be simplified to a single cam-follower mechanism with a rotating, conjugate cam and a translating follower, moving with a (point-to-point) amplitude of 90 mm. Its motion law  $F_{\text{shed}}(g_{\text{shed}})$  is given by:

$$F_{\text{shed}}(g_{\text{shed}}) = 0.045 \cdot \sin(g_{\text{shed}}). \quad (\text{J.1})$$

The translating follower has a mass  $m_{\text{shed}}$  of 43.1 kg. This simplification is justified from a kinematic point of view in Section J.1 and from a dynamic point of view in Section J.2.

$i$	$\Theta_i$ [mm]	$\Theta_i^u$ [mm]	$\Theta_i^l$ [mm]	$\gamma_i^{(0)}$ [%]	$\gamma_i^{(2)}$ [%]	$m_i$ [kg]
1	70.5	34.7	35.8	-2.9	4.9	13.9
2	77.5	38.5	39.0	-1.1	3.3	13.5
3	84.0	42.1	41.9	0.5	2.4	13.3
4	90.0	45.4	44.6	1.9	3.5	13.1

TABLE J.1: Kinematic properties  $\Theta_i$ ,  $\Theta_i^u$ ,  $\Theta_i^l$ ,  $\gamma_i^{(0)}$  and  $\gamma_i^{(2)}$  and equivalent mass  $m_i$  for the four frames in the setup.

## J.1 Kinematic Modelling

The sword I (see Fig.7.4) length of the shed mechanism is adjustable and determines the amplitude of motion of the frame VI. The amplitude of motion  $\Theta_i, i = \{1, 2, 3, 4\}$  [m] of the frames is given in Table J.1. Frame 1 is the front frame, while frame 4 is the rear frame.

While the swords perform a purely sinusoidal motion, the frames do not, because of the motion distortion due to the linkage. The degree of asymmetry  $\gamma_{\text{pos},i}$  [%] measures this distortion, and is defined as:

$$\gamma_{\text{pos},i} = 100 \cdot \frac{\Theta_i^u - \Theta_i^l}{\Theta_i/2},$$

where  $\Theta_i^u$  [m] and  $\Theta_i^l$  [m] are the amplitudes of the upper and lower part of the  $i$ -th frame motion, formally defined as

$$\begin{aligned} \Theta_i^u &= \max_{t \in [0, T]} f_{\text{frame},i}; \\ \Theta_i^l &= \max_{t \in [0, T]} -f_{\text{frame},i}. \end{aligned}$$

$f_{\text{frame},i}$  [m] is the vertical  $i$ -th frame displacement w.r.t. the zero frame position, which by convention is the frame position in which the lines  $su$  and  $wy$  are horizontal. Note that  $\Theta_i = \Theta_i^l + \Theta_i^u$ .

$\gamma_{\text{pos},i}$  depends on the  $\Theta_i$ : it is a minimum for  $\Theta_i = 80$  to  $85$  mm,  $-7\%$  for the minimum amplitude of  $56$  mm and  $17\%$  for the maximum amplitude of  $144$  mm. With frame amplitudes between  $70$  and  $90$  mm, the motion distortion in the setup is small, as shown by the  $\gamma_{\text{pos},i}$  values tabulated in Table J.1.

These results are confirmed by Fig.J.1, which shows  $f_{\text{frame},i}$  and its derivatives ( $a - b - c$ ) and the difference with a purely sinusoidal motion  $\Delta f_{\text{frame},i}$  and its derivatives ( $d - e - f$ ) for all four frames. The relative acceleration difference  $\gamma_{\text{acc},i}$  [%], defined as,

$$\gamma_{\text{acc},i} = 100 \cdot \frac{\max_{t \in [0, T]} |\Delta \ddot{f}_{\text{frame},i}|}{\max_{t \in [0, T]} |\ddot{f}_{\text{frame},i}|},$$

is small, as shown by Table J.1, and gives the same classification of asymmetry<sup>1</sup> as does  $\gamma_{\text{pos},i}$ . The motion distortion causes undesired harmonics in the frame acceleration spectrum, but these are insignificant: they are all at least a factor 100 smaller than the desired, first harmonic. From a kinematic point of view, therefore, it is reasonable to neglect the motion distortion due to the linkage, and to assume that the frames move in a purely sinusoidal way, with amplitude  $\Theta_i$ , given by Table J.1.

---

<sup>1</sup>That is: frame 1 has the more asymmetrical motion; frame 3 has the more symmetrical motion.

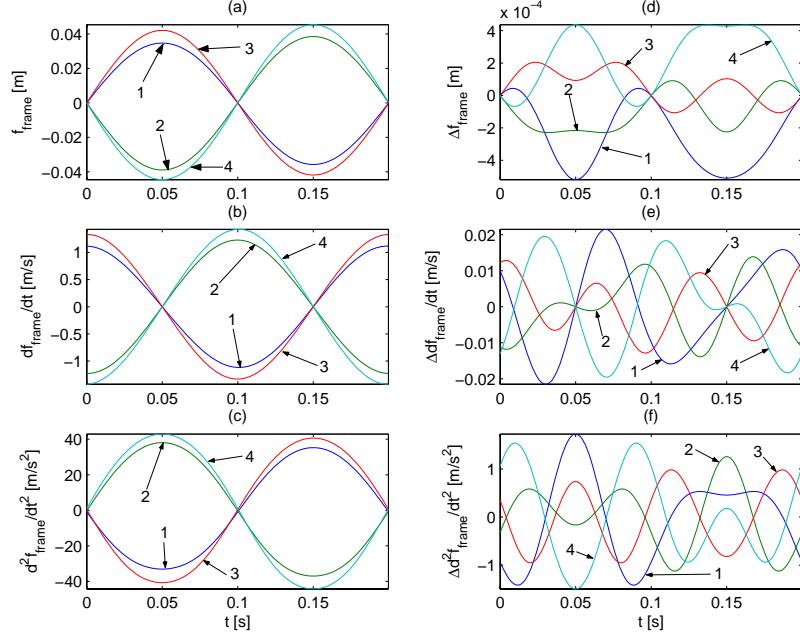


FIGURE J.1: One period ( $T = 0.02$  s) of frame motion  $f_{\text{frame},i}$  [m] and its derivatives (a–b–c), and difference (and its derivatives)  $\Delta f_{\text{frame},i}$  [m] with a purely sinusoidal motion (d–e–f). The numbers indicate the corresponding frame.

## J.2 Dynamic Modelling

Considering the linkage to be purely inertial, its input torque  $M_{\text{shed}}$  [N-m] equals:

$$M_{\text{shed}} = \frac{1}{\dot{g}_{\text{shed}}} \cdot \frac{dT_{\text{shed}}}{dt}, \quad (\text{J.2})$$

where  $T_{\text{shed}}$  [J] denotes the kinetic energy of the shed mechanism. The linkage manufacturer proposes to consider all links, except for the frames, to be massless. Each frame is given an *equivalent* mass  $m_i$ , dependent on  $\Theta_i$  (see Table J.1). The validity of this equivalent-mass approach could not be checked, due to the absence of accurate data on the link mass properties. With all linkage mass concentrated in the frames,  $T_{\text{shed}}$  [J] equals the sum of the kinetic energy of the four frames:

$$T_{\text{shed}} = \sum_{i=1}^4 \frac{m_i \cdot \dot{f}_{\text{frame},i}^2}{2}. \quad (\text{J.3})$$

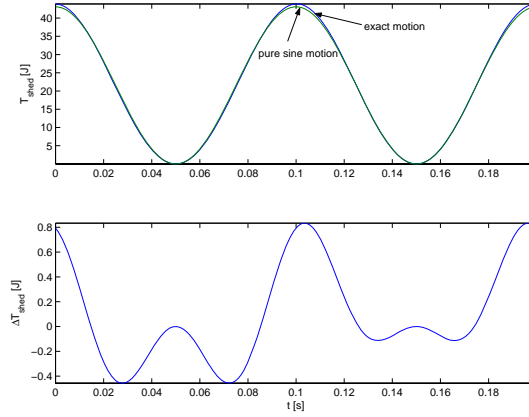


FIGURE J.2: (a) Comparison of (one period of)  $T_{shed}$ , obtained based on (J.3), using the exact frame motions, and  $T_{shed}$ , obtained based on (J.4a–J.4c), using pure sine frame motions; (b) difference  $\Delta T_{shed}$  between both approaches.

If all frames are assumed to perform a purely sinusoidal motion, yet with different amplitude,  $T_{shed}$  can be written as

$$T_{shed} = \frac{m_{shed} \cdot \dot{f}_{shed}^2}{2}, \quad (\text{J.4a})$$

that is, the kinetic energy of a translating cam follower of which the mass  $m_{shed}$  and velocity  $\dot{f}_{shed}$  are given by:

$$\dot{f}_{shed} = \dot{f}_{frame,4}; \quad (\text{J.4b})$$

$$m_{shed} = \sum_{i=1}^4 m_i \cdot \frac{\Theta_i^2}{A_4^2}. \quad (\text{J.4c})$$

The numerical values of Table J.1 give rise to  $m_{shed} = 43.1$  kg. Figure J.2(a) compares  $T_{shed}$ , obtained based on (J.3), using the exact frame motions, and  $T_{shed}$ , obtained based on (J.4a–J.4c), using pure sine frame motions. The difference between them is small, as shown in Fig.J.2(b): the maximum deviation is 0.83 J compared to a maximum value of 43.9 J (that is, 1.9%). In view of the approximation already made (concentrating all linkage mass in the frames), it is therefore justifiable, also from a dynamic point of view, to assume that the frames move in a purely sinusoidal manner, and to determine the input torque based on (J.4a–J.4c).

## Appendix K

# Measurement Equipment Specifications

**LMS Pimento** LMS<sup>1</sup> Pimento is a portable, modular front-end system for multi-channel data acquisition. It uses a high-speed serial IEEE 1394a link to transmit the captured data to the measurement PC. The Pimento system used here is equipped with an eight-channel ASP824 card. Each channel is equipped with (i) a voltage amplifier (input range  $\pm 316$  mV to  $\pm 10$  V), (ii) an ICP power supply and (iii) a 24-bit sigma-delta A/D converter, preceded by a 3-pole analog anti-alias filter.

**Accelerometers** The main characteristics of the used piezoelectric ICP<sup>2</sup> accelerometers are summarized in Table K.1. PCB advises that it is generally acceptable to use an accelerometer over the frequency range where the sensitivity<sup>3</sup> deviates by less than  $\pm 5\%$ . The lower limit of the frequency range is critical here: the lowest frequency to be measured by the accelerometers occurs when the setup is driven at its lowest speed, that is  $\Omega_{\text{shed}} = 125$  rpm. In that case, the period equals  $60/125 = 0.48$  s, which corresponds to a base frequency of 2.1 Hz. As Table K.1 shows, this coincides with the lower limit on the accelerometers' frequency range.

---

<sup>1</sup>[www.lms.be](http://www.lms.be)

<sup>2</sup>ICP is a registered trademark of PCB Piezotronics, Inc. ([www.pcb.com](http://www.pcb.com)), which uniquely identifies PCB sensors that incorporate built-in microelectronics. ICP accelerometers are powered by simple, inexpensive, constant-current signal conditioners and offer several advantages over traditional charge mode sensors. A comprehensive comparison is made in [www.pcb.com/techsupport/techsignal.aspx](http://www.pcb.com/techsupport/techsignal.aspx).

<sup>3</sup>The sensitivity is obtained via a calibration experiment with a PCB 394C06 vibration hand-held shaker, delivering  $1g$  rms at 159.2 Hz.

measurement	sensor type	sensitivity [mV/g]	$\pm 5\%$ range [Hz]
$\ddot{f}_{\text{sley}}$	PCB303A	10.98	1-10000
$\ddot{f}_{\text{sword}}$	PCB303A02	12.20	1-10000
$\ddot{f}_{\text{frame}}$	PCB356A11-Y	7.38	2-7000
$\ddot{h}_{\text{frame}}$	PCB356A11-Z	9.44	2-10000

TABLE K.1: Dynamic accelerometer characteristics.  $g = 9.81 \text{ m/s}^2$  denotes the gravity acceleration.

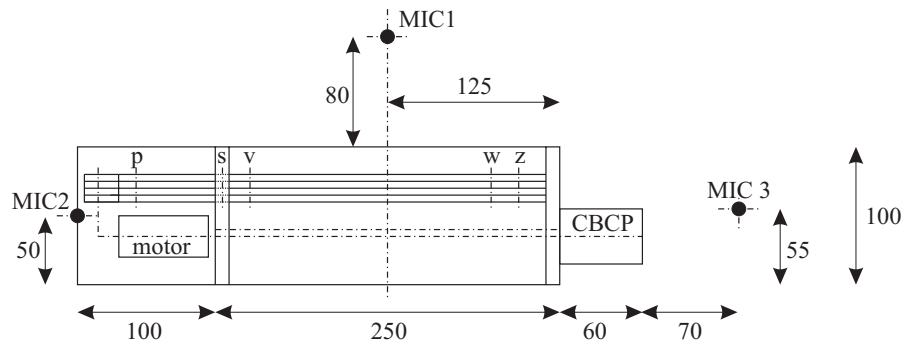


FIGURE K.1: Schematic top view of the measurement setup with indication of the microphone locations. All microphones are oriented towards the setup. The measures are indicative and expressed in [cm].

**Microphones** The microphones are located on the spots indicated in Fig.K.1, all at a height of about 125 cm. Each of the microphones is a Brüel & Kjær<sup>4</sup> Type 4188 prepolarized condenser microphone cartridge, which drives a Brüel & Kjær DeltaTron<sup>5</sup> Type 2671 microphone preamplifier. The microphone sensitivity<sup>6</sup> equals 28.0 mV/Pa (MIC1), 26.0 mV/Pa (MIC2) and 30.4 mV/Pa (MIC3). DeltaTron preamplifiers are ICP compatible, and can therefore be directly plugged in into the Pimento ASP824 card.

<sup>4</sup>[www.bksv.com](http://www.bksv.com)

<sup>5</sup>DeltaTron is a registered trademark of Brüel & Kjær, which identifies Brüel & Kjær accelerometers and signal conditioning products that operate on a constant-current power supply and give output signals in the form of voltage modulation on the power supply line.

<sup>6</sup>The sensitivity is obtained via a calibration experiment with a Brüel & Kjær 4320 hand-held microphone calibrator, delivering 94dB rms at 1000 Hz.

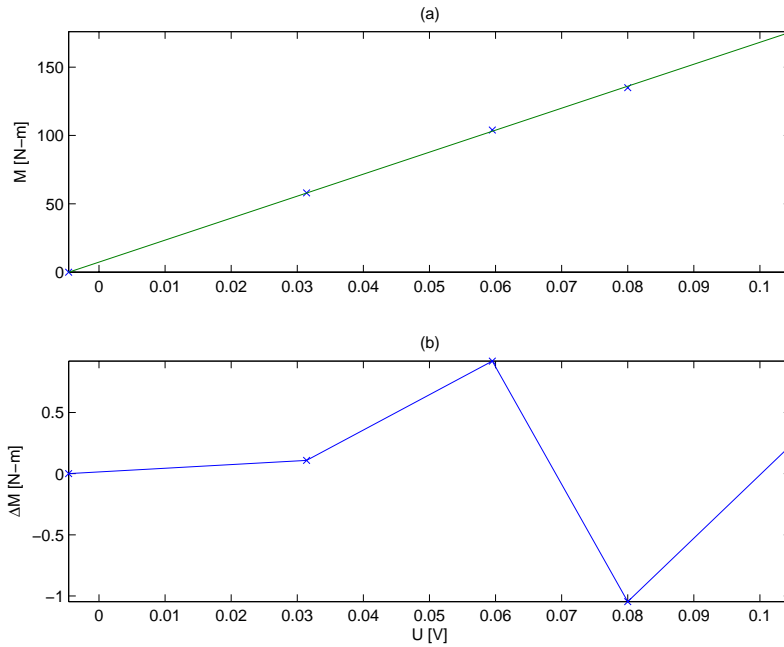


FIGURE K.2: Strain gauge calibration. (a) applied static torque  $M$  [N-m] versus measured voltage  $U$  [V]: measurement points (indicated with the crosses 'x') and linear regression line; (b) difference between the linear regression line and the measurement points.

**Strain Gauges** Calibration of the strain gauges is done by loading the extended camshaft with a known, static torque, applied using a lever on which a known weight is put. Using linear regression, this results in an experimental calibration factor of 1608 N-m/V, which deviates 7.6% of the theoretical calibration factor of 1740 N-m/V, obtained using classical strain gauge formulae as given in e.g. (Bentley, 1995). This, as well as the excellent quality of the linear regression, as shown in Fig.K.2, confirms the correctness of the experimental calibration factor.



## Appendix L

# Measurement Averaging in Reciprocating Machinery

In Section 7.3.1 it is shown that in the present setup, the error  $e = 2\pi/T - \dot{g}_{2,\text{avg}}(k)$  fluctuates (as a function of the imposed period  $T$ ) with some limited standard deviation around a (practically) zero mean value. As a result, the setup's response is nearly, but not perfectly periodical, which introduces leakage when averaging in the time domain. This appendix defines two quality indices  $\lambda_1$  and  $\lambda_2$  for measuring the periodicity, or conversely, the leakage, and applies them to the results of the measurement campaign.

A simple means of assessing the overall nonperiodicity of a signal is to compare the energy in its harmonic frequencies with the energy in its full spectrum. This is equivalent to comparing the rms value of the full signal with the rms value of the averaged signal. If the signal was perfectly periodical, both energies (rms values) would be equal. If not, the former is always smaller than the latter.

This method, though simple, assesses the overall nonperiodicity and does not allow isolating the contribution due to average drive speed variations from other contributions, such as high-frequency, nonperiodical disturbances. Therefore, if the quality of the control algorithm is to be investigated, an alternative method has to be sought. The here proposed method is applicable if the dominant, low-frequency harmonics of a signal are known beforehand. In the setup at hand, this is the case for three signals:

- $\ddot{f}_{\text{sley}}$  has six even harmonics of  $1/T$  [Hz]:  $k = 2, 4, 6, 8, 10, 12$ ;
- $\ddot{f}_{\text{sword}}$  has one harmonic of  $1/T$ :  $k = 1$ ;
- $M_c$  has seven even<sup>1</sup> harmonics of  $1/T$ :  $k = 2, 4, 6, 8, 10, 12, 14$ .

---

<sup>1</sup>In fact,  $M_c$  theoretically has twelve even harmonics. However, the first seven harmonics

These harmonics are present if the drive speed is perfectly constant. A fluctuating drive speed causes additional (undesired) harmonics, but the desired harmonics are always present, and dominating.

In the low-frequency spectrum (that is, the frequency range determined by the known, dominant low-frequency harmonics), leakage can almost exclusively be attributed to average drive speed fluctuations. Therefore, comparing the low-frequency *harmonic* energy (that is, the energy of the harmonic frequencies, indicated with a circle 'o' in Fig.L.5) with the low-frequency *total* energy, yields a way of assessing the quality of the control algorithm. For the three signals, Fig.L.1-L.3(a) shows the energy ratio  $\lambda_1$  [-], defined as the ratio of the harmonic energy to the total energy in the low-frequency spectrum, as a function of  $\Omega_{\text{shed}}$  [rpm], for the CBCP and the FLY-configuration. These figures illustrate that almost<sup>2</sup> all energy is concentrated in the harmonics. This proves that the leakage due to average speed fluctuations is negligible, and that the ASC algorithm hence functions 'good enough'.

A second check, besides  $\lambda_1$ , is provided by comparing the amplitude of the harmonic frequency lines with the amplitude of the neighboring, nonharmonic frequency lines. If no leakage occurs, these nonharmonic frequency lines should be zero. If a limited amount of leakage occurs, the ratio of the amplitude of the harmonic frequency to the amplitude of the neighboring frequencies should be high. Therefore, the following numeric measure is proposed which is termed the *harmonic signal/noise ratio*  $\lambda_2$  [dB] and which is determined based on the following algorithm:

- Suppose that the signal contains 13 periods;
- For each harmonic  $k$  (with amplitude  $A_k$ ) of the low-frequency spectrum, do:
  - Determine the maximum amplitude  $A_{k,\text{left}}$  of the  $\lfloor 13/2 \rfloor = 6$  nonharmonic frequency lines lying to the immediate left of  $k$ ;
  - Determine the maximum amplitude  $A_{k,\text{right}}$  of the six nonharmonic frequency lines lying to the immediate right of  $k$ ;
  - Determine  $\lambda_{2,k}$  as

$$\lambda_{2,k} = 20 \cdot \log_{10} \left( \frac{A_k}{\max(A_{k,\text{left}}, A_{k,\text{right}})} \right);$$

- Determine  $\lambda_2$  as the mean value of all  $\lambda_{2,k}$ 's.

---

yield 99.2% of the rms value, so practically,  $M_c$  has seven harmonics. This statement is of course only true for the CBCP-configuration. In the FLY-configuration, the CBCP acts as a flywheel, so  $M_c$  is expected to have as many harmonics as  $\ddot{g}_{\text{sley}}$ . In this case, also seven harmonics are used, for convenience.

<sup>2</sup>That is, at least 99.2% for  $\ddot{f}_{\text{sley,exp}}$ , at least 99.99% for  $\ddot{f}_{\text{sword,exp}}$  and at least 98.6% for  $M_{c,\text{exp}}$

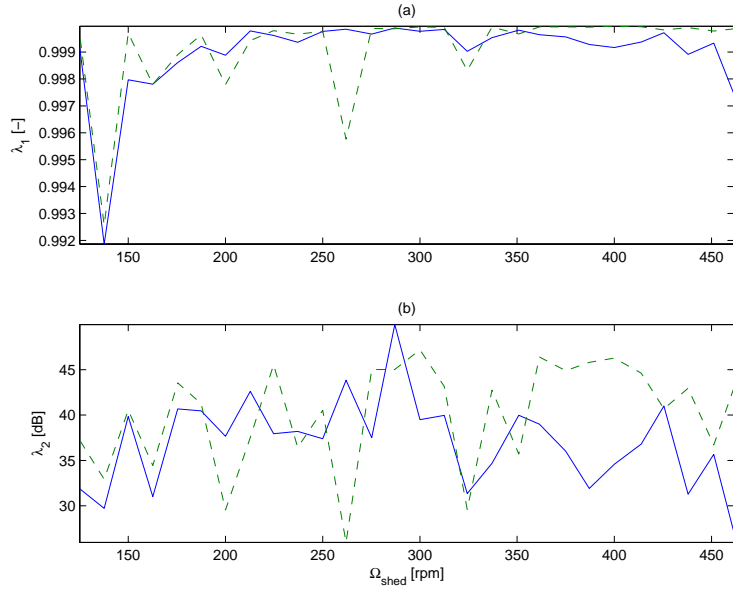


FIGURE L.1: (a) Energy ratio  $\lambda_1$  [-] and (b) harmonic signal/noise ratio  $\lambda_2$  [dB] as a function of  $\Omega_{shed}$  [rpm] for  $\dot{f}_{sley,exp}$ , for the CBCP (solid line) and the FLY-configuration (dashed line).

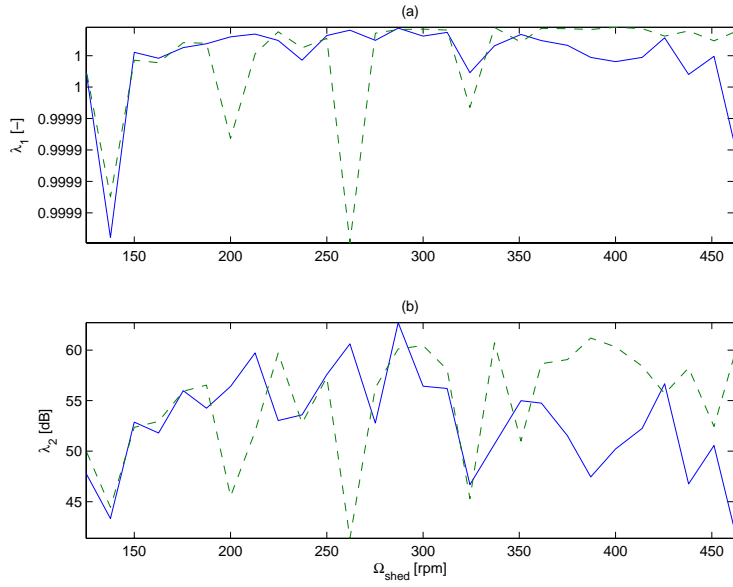


FIGURE L.2: (a) Energy ratio  $\lambda_1$  [-] and (b) harmonic signal/noise ratio  $\lambda_2$  [dB] as a function of  $\Omega_{shed}$  [rpm] for  $\dot{f}_{sword,exp}$ , for the CBCP (solid line) and the FLY-configuration (dashed line).

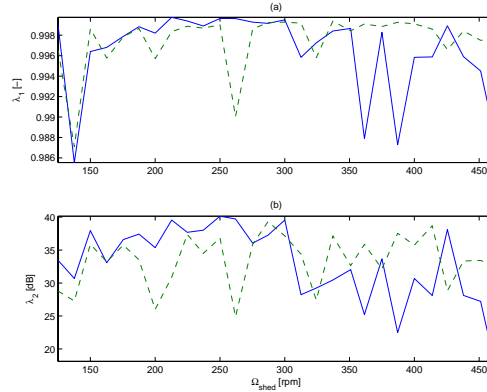


FIGURE L.3: (a) Energy ratio  $\lambda_1$  [-] and (b) harmonic signal/noise ratio  $\lambda_2$  [dB] as a function of  $\Omega_{shed}$  [rpm] for  $M_{c,exp}$ , for the CBCP (solid line) and the FLY-configuration (dashed line).

Fig.L.1-L.3(b) shows  $\lambda_2$  [dB] as a function of the average main shaft speed  $\Omega_{shed}$  [rpm], for the CBCP and the FLY-configuration. These results confirm the results obtained using the energy ratio  $\lambda_1$ : the best results are obtained for  $\dot{f}_{sword,exp}$  ( $\lambda_2$  everywhere at least 41 dB and 54 dB on average), followed by  $\dot{f}_{sley,exp}$  ( $\lambda_2$  everywhere at least 26 dB and 39 dB on average) and  $M_{c,exp}$  ( $\lambda_2$  everywhere at least 18 dB and 33 dB on average). The results for  $\lambda_1$  and  $\lambda_2$ , prove that the leakage errors due to average speed fluctuations are minimal, and that the ASC algorithm hence functions good enough for doing time-domain averaging in a reliable way.

The periodicity of the measurements is illustrated by Fig.L.4 and Fig.L.5 which give time and frequency-domain results for the CBCP torque  $M_{c,exp}$  in the case of the CBCP-configuration turning at 600 rpm. Fig.L.4 shows the 1st, 12th, 25th, 37th and 50th (that is, the last) period of the CBCP torque. The periods overlap quite well, indicating that the signal is highly periodical. This is further illustrated by Fig.L.5, which shows the frequency spectrum (0-100 Hz) of  $M_{c,exp}$  on a linear scale (a) and on a dB-scale. Remember that seven<sup>3</sup> even harmonics of  $1/T = 600/120 = 5$  Hz are to be expected. The circles 'o' indicate harmonic frequencies, while the crosses 'x' indicate the low-frequency spectrum. In the linear spectrum, only the harmonic frequencies (indicated by a circle overlapping with a cross) are visible. A clearer image is given in the dB-spectrum, which illustrates that the harmonic signal/noise ratio is excellent (order of magnitude 40 dB) in this case.

<sup>3</sup>The eighth even harmonic visible in Fig.L.5(a - b) results from the drive speed fluctuation.

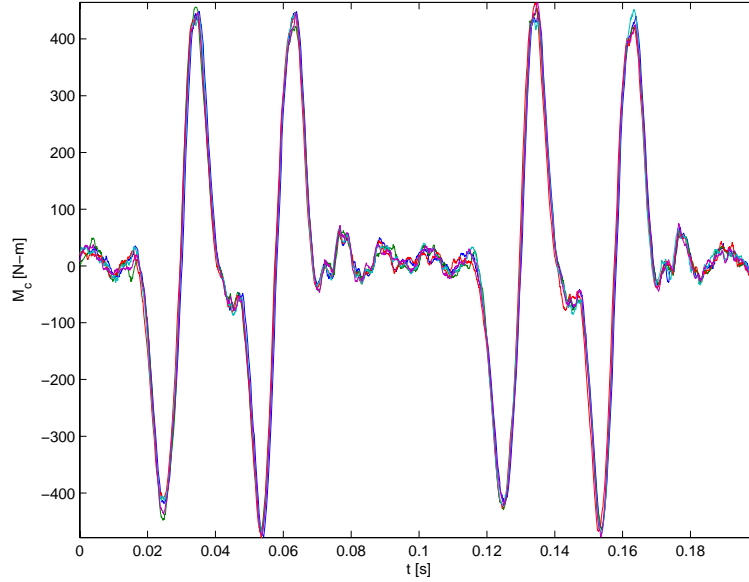


FIGURE L.4: 1st, 12th, 25th, 37th and 50th period of the CBCP torque  $M_{c,\text{exp}}$  (raw measurement signal) in the CBCP-configuration ( $\Omega_{\text{shed}} = 600$  rpm).

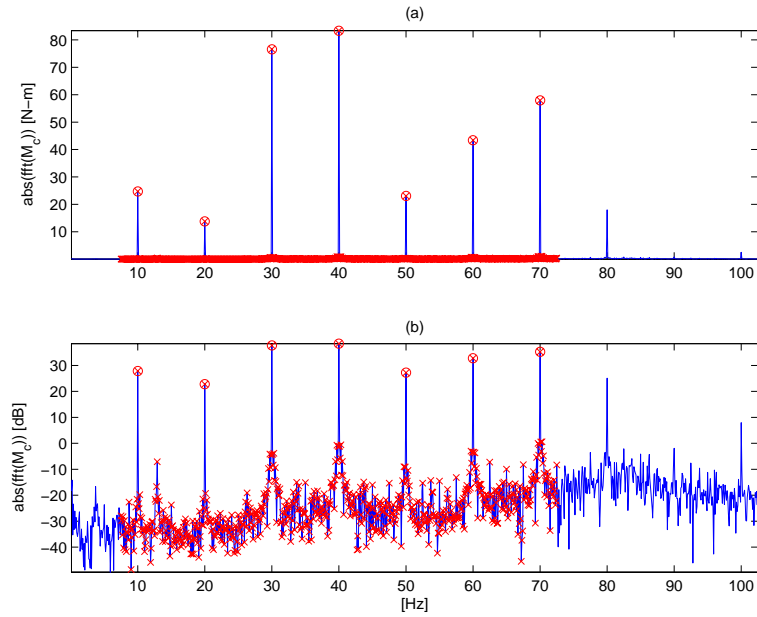


FIGURE L.5: Frequency spectrum from 0 to 100 Hz, for the CBCP torque  $M_{c,\text{exp}}$ , on a linear scale (a) and a dB-scale (b) in the case of the CBCP-configuration ( $\Omega_{\text{shed}} = 600$  rpm). The circles 'o' indicate harmonic frequencies, while the crosses 'x' indicate the low-frequency spectrum.



## Appendix M

# Average Speed Control: Moving Average Properties

This appendix investigates the dynamic properties of the moving average calculation, described by (7.8). Taking into account that a time delay  $T_w$  [s] gives rise to a multiplication with  $\exp(-s \cdot T_w)$  in the Laplace domain, the measurement's filter Laplace transform  $G_m(s)$  equals:

$$G_m(s) = \frac{V_{\text{avg}}(s)}{X(s)} = \frac{1 - \exp(-s \cdot T_w)}{T_w},$$

where  $V_{\text{avg}}(s)$  and  $X(s)$  denote the Laplace transform of  $\dot{g}_{\text{avg}}(t)$  and  $g(t)$  respectively. It is shown here that (i) in the frequency range from 0 to  $0.6/T_w$  [rad/s], the moving average calculation approximately behaves like a pure differentiator, with a time delay equal to  $T_w/2$  s and (ii) the amplitude of  $G_m(s)$  is zero for frequencies  $\omega$  [rad/s] equal to  $k \cdot 2\pi/T_w$ ,  $k \in \mathbb{Z}$ . In order to do so, the Laplace variable  $s$  is replaced by  $j\omega$ , where  $j$  represents the imaginary unit, and  $\omega$  the angular frequency expressed in [rad/s]:

$$G_m(j\omega) = \frac{V_{\text{avg}}(j\omega)}{X(j\omega)} = \frac{1 - \exp(-j\omega \cdot T_w)}{T_w} = \frac{(1 - \cos(\omega T_w)) + j \cdot \sin(\omega T_w)}{T_w}.$$

The properties of the measurement filter are studied by determining the amplitude  $|G_m(j\omega)|$  and phase  $\angle G_m(j\omega)$  characteristic of  $G_m(j\omega)$ .

## M.1 Amplitude and Phase Characteristic

$|G_m(j\omega)|$  equals the square root of the sum of the squares of the real and imaginary parts of  $G_m(j\omega)$ :

$$|G_m(j\omega)| = \frac{1}{T_w} \cdot \left[ (1 - \cos(\omega T_w))^2 + \sin^2(\omega T_w) \right]^{\frac{1}{2}}.$$

Consequently, by application of basic trigonometric identities:

$$|G_m(j\omega)| = \frac{1}{T_w} \cdot [2 \cdot (1 - \cos(\omega T_w))]^{\frac{1}{2}}; \quad (\text{M.1a})$$

$$|G_m(j\omega)| = \frac{2}{T_w} \cdot \left| \sin\left(\frac{\omega \cdot T_w}{2}\right) \right|. \quad (\text{M.1b})$$

$\angle G_m(j\omega)$  is the arc tangent of the ratio of the imaginary and the real part of  $G_m(j\omega)$ :

$$\angle G_m(j\omega) = \arctan\left(\frac{\sin(\omega T_w)}{1 - \cos(\omega T_w)}\right).$$

Now, basic trigonometric manipulation shows:

$$\frac{\sin(\omega T_w)}{1 - \cos(\omega T_w)} = \frac{2 \cdot \sin\left(\frac{\omega \cdot T_w}{2}\right) \cdot \cos\left(\frac{\omega \cdot T_w}{2}\right)}{1 - (1 - 2 \cdot \sin^2\left(\frac{\omega \cdot T_w}{2}\right))} = \cot\left(\frac{\omega \cdot T_w}{2}\right) = \tan\left(\frac{\pi}{2} - \frac{\omega \cdot T_w}{2}\right).$$

Hence

$$\angle G_m(j\omega) = \frac{\pi}{2} - \frac{\omega \cdot T_w}{2}. \quad (\text{M.2})$$

## M.2 Interpretation

(M.1b) shows that  $|G_m(j\omega)|$  is zero provided that

$$\omega = k \cdot 2\pi/T_w, \quad k \in \mathbb{Z}.$$

The measurement filter hence completely suppresses all signals of frequency  $\omega = k \cdot 2\pi/T_w$  [rad/s]. Consequently, any periodic signal, with periodicity equal to  $T_w$ , is completely suppressed.

Secondly, using the observation that  $\sin(\alpha) \approx \alpha, \alpha \leq 0.3$  [rad], (M.1b) leads to:

$$|G_m(j\omega)| \approx \frac{2}{T_w} \cdot \frac{\omega \cdot T_w}{2} \approx \omega, \quad (\text{M.3})$$

for  $\omega T_w \leq 0.6$ . Since (i) (M.2) can be interpreted as the phase of a pure differentiator, in series with a time delay of  $T_w/2$  s, while (ii) (M.3) is the amplitude of a pure differentiator, it follows that for  $\omega T_w \leq 0.6$ , the moving average calculation behaves like a pure differentiator, with a time delay equal to  $T_w/2$  s (remember that a time delay has an amplitude equal to one).

## Appendix N

# Proof of Mass Superposition Principle

This appendix consists of two parts. In Section N.1, a proof is given for the superposition principle of the  $\mu$ -parameters for a link in plane motion. Only a proof for  $\mu_4$  is given, since the fact that  $\mu_1$ ,  $\mu_2$  and  $\mu_3$  obey the superposition principle, is common engineering knowledge. Section N.2 subsequently extends the definition of the  $\mu$ -parameters of a link in plane motion to the  $\nu$  parameters of a link in spatial motion. Also these  $\nu$  parameters are shown to obey the superposition principle.

### N.1 Link in Plane Motion

Consider a link that is fabricated by welding together a link with mass parameters  $(m_a, X_a, Y_a, J_a)$  and a link with mass parameters  $(m_b, X_b, Y_b, J_b)$ . The mass parameters of the compound link are denoted as  $(m, X, Y, J)$ . All COG coordinates are expressed w.r.t. the same local coordinate system, attached to the link.

In order to prove that  $\mu_4 = \mu_{4a} + \mu_{4b}$ , Steiner's theorem is applied to express the centroidal moment of inertia of the compound link as:

$$J = J_a + m_a \cdot [(X - X_a)^2 + (Y - Y_a)^2] + J_b + m_b \cdot [(X - X_b)^2 + (Y - Y_b)^2].$$

Elaborating the right part yields:

$$\begin{aligned} J = & J_a + m_a \cdot (X^2 + Y^2) + m_a \cdot (X_a^2 + Y_a^2) - 2 \cdot m_a \cdot (X \cdot X_a + Y \cdot Y_a) \dots \\ & \dots + J_b + m_b \cdot (X^2 + Y^2) + m_b \cdot (X_b^2 + Y_b^2) - 2 \cdot m_b \cdot (X \cdot X_b + Y \cdot Y_b). \end{aligned}$$

Taking into account that  $\mu_4 = J + m \cdot (X^2 + Y^2)$ , and rearranging some terms:

$$J = \mu_{4a} + \mu_{4b} + (m_a + m_b) \cdot (X^2 + Y^2) \dots \\ \dots - 2 \cdot X \cdot (m_a \cdot X_a + m_b \cdot X_b) - 2 \cdot Y \cdot (m_a \cdot X_a + m_b \cdot X_b).$$

Since  $m_a + m_b = m$ ,  $m_a \cdot X_a + m_b \cdot X_b = m \cdot X$  and  $m_a \cdot Y_a + m_b \cdot Y_b = m \cdot Y$ :

$$J = \mu_{4a} + \mu_{4b} + m \cdot (X^2 + Y^2) - 2 \cdot X \cdot m \cdot X - 2 \cdot Y \cdot m \cdot Y.$$

As a result:

$$J = \mu_{4a} + \mu_{4b} - m \cdot X^2 - m \cdot Y^2 \quad \Rightarrow \quad \mu = \mu_{4a} + \mu_{4b}.$$

□

## N.2 Link in Spatial Motion

A link in spatial motion is characterized by ten mass parameters: its mass  $m$ , COG coordinates  $X$ ,  $Y$  and  $Z$  and the six moments and products of inertia, grouped into the symmetric inertia tensor  $\mathbf{I}$ :

$$\mathbf{I} = \begin{bmatrix} I_{xx} & I_{xy} & I_{xz} \\ I_{xy} & I_{yy} & I_{yz} \\ I_{xz} & I_{yz} & I_{zz} \end{bmatrix}.$$

As a result, ten  $\nu$  parameters are defined:

$$\begin{aligned} \nu_1 &= m; \\ \nu_2 &= m \cdot X; \\ \nu_3 &= m \cdot Y; \\ \nu_4 &= m \cdot Z; \\ \nu_5 &= I_{zz} + m \cdot (X^2 + Y^2); \\ \nu_6 &= I_{yy} + m \cdot (X^2 + Z^2); \\ \nu_7 &= I_{xx} + m \cdot (Y^2 + Z^2); \\ \nu_8 &= I_{xy} + m \cdot X \cdot Y; \\ \nu_9 &= I_{xz} + m \cdot X \cdot Z; \\ \nu_{10} &= I_{yz} + m \cdot Y \cdot Z. \end{aligned}$$

The superposition of  $\nu_i, i = 1 \dots 7$  follows directly from the results of a link in plane motion. A proof is given here for  $\nu_8$ . Those for  $\nu_9$  and  $\nu_{10}$  are of course similar.

Consider a link that is fabricated by welding together a link with mass parameters  $(m_a, X_a, X_a, Z_a, \mathbf{I}_a)$  and a link with mass parameters

$(m_b, X_b, Y_b, Z_b, \mathbf{I}_b)$ . The mass parameters of the compound link are denoted as  $(m, X, Y, Z, \mathbf{I})$ . All COG coordinates are expressed w.r.t. the same local coordinate system, attached to the link.

In order to prove that  $\nu_8 = \nu_{8a} + \nu_{8b}$ , Steiner's theorem is applied to express the centroidal product of inertia of the compound link as:

$$I_{xy} = I_{xy,a} + m_a \cdot (X - X_a) \cdot (Y - Y_a) + I_{xy,b} + m_b \cdot (X - X_b) \cdot (Y - Y_b).$$

Elaborating the right part yields:

$$\begin{aligned} I_{xy} = & I_{xy,a} + m_a \cdot X \cdot Y + m_a \cdot X_a \cdot Y_a - m_a \cdot (X \cdot Y_a + Y \cdot X_a) \dots \\ & \dots + I_{xy,b} + m_b \cdot X \cdot Y + m_b \cdot X_b \cdot Y_b - m_b \cdot (Y \cdot X_b + X \cdot Y_b). \end{aligned}$$

Taking into account that  $\nu_8 = I_{xy} + m \cdot X \cdot Y$ , and rearranging some terms:

$$\begin{aligned} I_{xy} = & \nu_{8a} + \nu_{8b} + (m_a + m_b) \cdot X \cdot Y \dots \\ & \dots - X \cdot (m_a \cdot Y_a + m_b \cdot Y_b) - Y \cdot (m_a \cdot X_a + m_b \cdot X_b). \end{aligned}$$

Since  $m_a + m_b = m$ ,  $m_a \cdot X_a + m_b \cdot X_b = m \cdot X$  and  $m_a \cdot Y_a + m_b \cdot Y_b = m \cdot Y$ :

$$I_{xy} = \nu_{8a} + \nu_{8b} + m \cdot X \cdot Y - X \cdot m \cdot Y - Y \cdot m \cdot X.$$

As a result:

$$J = \nu_{8a} + \nu_{8b} - m \cdot X \cdot Y \quad \Rightarrow \quad \nu_8 = \nu_{8a} + \nu_{8b}.$$

□



## Appendix O

# 4R Four-Bar: Linearly Independent Vector Expressions

(9.38a–9.38d) are obtained based on the following expressions, which have already been derived in Section 8.1 and are repeated here for convenience:

$$F_{\text{shak},x}(t) = -dL_x/dt; \quad (\text{O.1a})$$

$$F_{\text{shak},y}(t) = -dL_y/dt; \quad (\text{O.1b})$$

$$M_{\text{shak}}(t) = -dA/dt; \quad (\text{O.1c})$$

$$M_{\text{drv}}(t) = (dT_{\text{tot}}/dt)/\dot{\phi}_1(t). \quad (\text{O.1d})$$

$L_x(t)$  [N-m/s] and  $L_y(t)$  [N-m/s] denote the  $X$  and  $Y$ -component of the mechanism's linear momentum, whereas  $A(t)$  [N-m-rad/s] is its angular momentum w.r.t. the point  $\hat{a}$  in Fig.8.1.  $T_{\text{tot}}(t)$  [J] is the mechanism's kinetic energy. These quantities are linear in the (classical) mass parameters:

$$L_x = \sum_{i=1}^3 m_i \cdot \dot{r}_{ix}; \quad (\text{O.2a})$$

$$L_y = \sum_{i=1}^3 m_i \cdot \dot{r}_{iy}; \quad (\text{O.2b})$$

$$A = \sum_{i=1}^3 J_i \cdot \dot{\phi}_i + m_i \cdot (r_{ix} \cdot \dot{r}_{iy} - r_{iy} \cdot \dot{r}_{ix}); \quad (\text{O.2c})$$

$$T_{\text{tot}} = \frac{1}{2} \cdot \sum_{i=1}^3 J_i \cdot \dot{\phi}_i^2 + m_i \cdot (\dot{r}_{ix}^2 + \dot{r}_{iy}^2). \quad (\text{O.2d})$$

$r_{ix}$  [m] and  $r_{iy}$  [m] denote the  $X$  and  $Y$ -component of the position (w.r.t to  $\hat{a}$ ) of link  $i$ 's COG. Combining (O.2a–O.2d) with (O.1a–O.1d) yields (9.38a–9.38d) by (i) expressing  $r_{ix}$  and  $r_{iy}$  and their derivatives as a function of the link angles  $\phi_i, i = \{1, 2, 3\}$  and (ii) eliminating  $\phi_2$  and its derivatives<sup>1</sup>, through application of the loop closure equations (see Fig.8.1), and their time-derivatives:

$$\begin{aligned} a_1 \cdot c_1 + a_2 \cdot c_2 - a_3 \cdot c_3 - a_4 \cdot c_4 &= 0; \\ a_1 \cdot s_1 + a_2 \cdot s_2 - a_3 \cdot s_3 - a_4 \cdot s_4 &= 0, \end{aligned}$$

where the shorthand notation  $s_i = \sin \phi_i$ ;  $c_i = \cos \phi_i$  is used. The functions that constitute the time dependent elements of the vectors  $\mathbf{e}_{fshx}(t)$ ,  $\mathbf{e}_{fshy}(t)$ ,  $\mathbf{r}_{drv}(t)$  and  $\mathbf{e}_{msh}(t)$  in (9.38a–9.38d) are given by the following expressions, in which  $s_{ij} = \sin(\phi_i - \phi_j)$  and  $c_{ij} = \cos(\phi_i - \phi_j)$ :

$$\begin{cases} e_{fshx,1} = c_1 \cdot \dot{\phi}_1^2 + s_1 \cdot \ddot{\phi}_1 \\ e_{fshx,2} = -s_1 \cdot \dot{\phi}_1^2 + c_1 \cdot \ddot{\phi}_1 \\ e_{fshx,3} = c_3 \cdot \dot{\phi}_3^2 + s_3 \cdot \ddot{\phi}_3 \\ e_{fshx,4} = -s_3 \cdot \dot{\phi}_3^2 + c_3 \cdot \ddot{\phi}_3 \end{cases} \quad \begin{cases} e_{fshy,1} = s_1 \cdot \dot{\phi}_1^2 - c_1 \cdot \ddot{\phi}_1 \\ e_{fshy,2} = c_1 \cdot \dot{\phi}_1^2 + s_1 \cdot \ddot{\phi}_1 \\ e_{fshy,3} = s_3 \cdot \dot{\phi}_3^2 - c_3 \cdot \ddot{\phi}_3 \\ e_{fshy,4} = c_3 \cdot \dot{\phi}_3^2 + s_3 \cdot \ddot{\phi}_3 \end{cases}$$

$$\begin{cases} \phi_{e,1} = -\ddot{\phi}_1 \\ \phi_{e,2} = -\ddot{\phi}_3 \\ \phi_{e,3} = \frac{a_1}{a_2} \cdot \left\{ a_4 \cdot \left[ s_{14} \cdot \dot{\phi}_1^2 - c_{14} \cdot \ddot{\phi}_1 \right] + \right. \\ \quad \left. a_3 \cdot \left[ s_{13} \cdot \left( \dot{\phi}_1^2 - \dot{\phi}_3^2 \right) - c_{13} \cdot \left( \ddot{\phi}_1 + \ddot{\phi}_3 \right) \right] \right\} \\ \phi_{e,4} = \frac{a_1}{a_2} \cdot \left\{ a_4 \cdot \left[ -c_{14} \cdot \dot{\phi}_1^2 - s_{14} \cdot \ddot{\phi}_1 \right] + \right. \\ \quad \left. a_3 \cdot \left[ -c_{13} \cdot \left( \dot{\phi}_1^2 - \dot{\phi}_3^2 \right) - s_{13} \cdot \left( \ddot{\phi}_1 + \ddot{\phi}_3 \right) \right] \right\} \\ \phi_{e,5} = a_4 \cdot \left[ s_{34} \cdot \dot{\phi}_3^2 - c_{34} \cdot \ddot{\phi}_3 \right] \\ \phi_{e,6} = a_4 \cdot \left[ c_{34} \cdot \dot{\phi}_3^2 + s_{34} \cdot \ddot{\phi}_3 \right] \end{cases}$$

$$\begin{cases} e_{drv,1} = \ddot{\phi}_1 \\ e_{drv,2} = \dot{\phi}_3 \cdot \ddot{\phi}_3 / \dot{\phi}_1 \\ e_{drv,3} = \frac{1}{\dot{\phi}_1} \cdot \frac{a_1 \cdot a_3}{a_2^2} \cdot \left[ -s_{13} \cdot \left( \dot{\phi}_1 - \dot{\phi}_3 \right) \cdot \dot{\phi}_1 \cdot \dot{\phi}_3 + \right. \\ \quad \left. c_{13} \cdot \left( \ddot{\phi}_1 \cdot \dot{\phi}_3 + \dot{\phi}_1 \cdot \ddot{\phi}_3 \right) \right] \\ e_{drv,4} = \frac{1}{\dot{\phi}_1} \cdot \frac{a_1 \cdot a_3}{a_2} \cdot \left[ c_{13} \cdot \left( \dot{\phi}_1 - \dot{\phi}_3 \right) \cdot \dot{\phi}_1 \cdot \dot{\phi}_3 + \right. \\ \quad \left. s_{13} \cdot \left( \ddot{\phi}_1 \cdot \dot{\phi}_3 + \dot{\phi}_1 \cdot \ddot{\phi}_3 \right) \right] \end{cases}$$

<sup>1</sup>In (Elliott and Tesar, 1977),  $\phi_3$  and its derivatives are eliminated instead.

## Appendix P

# LMI Derivation and Conversion

This appendix shows how the constraint (9.26a/9.27c) is written as a linear matrix inequality or LMI (Section P.2), and how it is converted into a second-order cone constraint, based on the assumption that the second-order cone constraint (9.31) is active in the optimum (Section P.3). First however, the so-called Schur-complement is introduced in Section P.1, as its properties lay the theoretical foundation for the results of Section P.2.

### P.1 The Schur Complement

Consider a symmetric  $n \times n$  matrix  $\mathbf{X}$  partitioned as

$$\mathbf{X} = \begin{bmatrix} \mathbf{A} & \mathbf{B} \\ \mathbf{B}^T & \mathbf{C} \end{bmatrix},$$

where  $\mathbf{A}$  is a symmetric  $k \times k$  matrix. If  $\mathbf{A}$  is regular, the matrix

$$\mathbf{S} = \mathbf{C} - \mathbf{B}^T \mathbf{A}^{-1} \mathbf{B}$$

is called the *Schur complement* of  $\mathbf{A}$  in  $\mathbf{X}$ . Schur complements arise in several contexts, and appear in many important formulas and theorems. A property of interest here is that, if  $\mathbf{A}$  is positive definite, then  $\mathbf{X}$  is positive semidefinite if and only if  $\mathbf{S}$  is positive semidefinite, see e.g. (Boyd and Vandenberghe, 2004).

## P.2 LMI Derivation

In order to show that (9.26a/9.27c) constitutes an LMI, it is first rewritten as (the superscript  $(\cdot)^*$  and the subscript  $(\cdot)_i$  are dropped for ease of notation):

$$\mu_4 - a \cdot \mu_1^2 - \frac{\mu_2^2}{\mu_1} - \frac{\mu_3^2}{\mu_1} \geq 0, \quad (\text{P.1})$$

where

$$a = \frac{1}{2 \cdot \pi \cdot t^M \cdot \rho}.$$

This can be further transformed into

$$\mu_4 - [\mu_1 \ \mu_2 \ \mu_3] \cdot \begin{bmatrix} a & 0 & 0 \\ 0 & \frac{1}{\mu_1} & 0 \\ 0 & 0 & \frac{1}{\mu_1} \end{bmatrix} \cdot \begin{bmatrix} \mu_1 \\ \mu_2 \\ \mu_3 \end{bmatrix} \geq 0.$$

The left part of this equation is the Schur complement of the matrix  $\mathbf{A}$

$$\mathbf{A} = \begin{bmatrix} 1/a & 0 & 0 \\ 0 & \mu_1 & 0 \\ 0 & 0 & \mu_1 \end{bmatrix},$$

in the matrix  $\mathbf{X}$ , defined as,

$$\mathbf{X} = \begin{bmatrix} \begin{bmatrix} 1/a & 0 & 0 \\ 0 & \mu_1 & 0 \\ 0 & 0 & \mu_1 \end{bmatrix} & \begin{bmatrix} \mu_1 \\ \mu_2 \\ \mu_3 \end{bmatrix} \\ \begin{bmatrix} \mu_1 & \mu_2 & \mu_3 \end{bmatrix} & \begin{bmatrix} \mu_4 \end{bmatrix} \end{bmatrix}.$$

If  $\mathbf{A}$  is positive definite (which is the case if  $\mu_1 > 0$ ), then imposing (P.1) is equivalent to imposing that  $\mathbf{X}$  be positive semidefinite. Hence, the following set of equations is equivalent to (P.1):

$$\mathbf{X} \succeq 0; \quad (\text{P.2})$$

$$\mu_1 > 0. \quad (\text{P.3})$$

Since all elements of  $\mathbf{X}$  are linear functions of the optimization variables  $\mu_1, \mu_2, \mu_3, \mu_4$ , (P.2) constitutes an LMI. The trivial conversion to the standard form of an LMI (a linear combination of symmetric matrices with  $\mu_1, \mu_2, \mu_3, \mu_4$  as coefficients) is left as an exercise to the reader.

### P.3 LMI Conversion

Instead of explicitly converting (9.26a/9.27c), the maximum thickness constraint is derived all over again, using the additional fact that (9.31) is active, that is, that the counterweight is cylindrical and tangent to the LCS origin. In that case, the following is true (again the superscript  $(\cdot)^*$  and the subscript  $(\cdot)_i$  are dropped for ease of notation):

$$m = \pi \cdot R^2 \cdot t \cdot \rho; \quad (\text{P.4})$$

$$J = \frac{m \cdot R^2}{2}; \quad (\text{P.5})$$

$$R^2 = X^2 + Y^2. \quad (\text{P.6})$$

Based on this, the moment of inertia  $\mu_4$  w.r.t. the LCS origin equals:

$$\mu_4 = J + m \cdot (X^2 + Y^2) = \frac{3}{2} \cdot m \cdot R^2 = \frac{3}{2} \cdot m \cdot \frac{m}{\pi \cdot \rho \cdot t} = \frac{3}{2 \cdot \pi \cdot \rho \cdot t} \cdot m^2.$$

The absolute lower limit on  $\mu_4$  is attained if  $t = t^M$ . As a result, *any* counterweight *tangent to the LCS origin* (that is, any counterweight with (9.31) active), to be implemented in a plate of maximum thickness  $t^M$  must satisfy

$$\mu_4 \geq b^2 \cdot m^2,$$

or

$$\mu_4 \geq b^2 \cdot \mu_1^2, \quad (\text{P.7})$$

where

$$b^2 = \frac{3}{2 \cdot \pi \cdot \rho \cdot t^M}.$$

In order to prove that (P.7) constitutes a second-order cone constraint, it is rewritten as:

$$\mu_4 \cdot 1 \geq (b \cdot \mu_1)^2, \quad (\text{P.8})$$

which, in conjunction with the redundant constraint

$$\mu_4 \geq 0$$

constitutes a set of hyperbolic constraints that can again be written as a second-order cone constraint, using (9.29):

$$\left\| \begin{bmatrix} 2 \cdot b \cdot \mu_1 \\ \mu_4 - 1 \end{bmatrix} \right\| \leq \mu_4 + 1. \quad (\text{P.9})$$



## Appendix Q

# Proof of Force Superposition Principle

Consider an arbitrary link in a purely inertial, planar mechanism. The set of forces and moments acting on this link is denoted as  $\{\mathbf{F}_i, \mathbf{M}_j\}$ ,  $i = 1 \dots I$ ,  $j = 1 \dots J$ . All forces are either joint forces (due to revolute or prismatic joints) or driving forces, whereas all moments are either joint moments (due to prismatic joints) or driving torques. The standard link mass parameters are contained in the vector

$$\mathbf{m} = [m \ X \ Y \ J]^T,$$

whereas the  $\mu$ -parameters are grouped into the vector

$$\boldsymbol{\mu} = [\mu_1 \ \mu_2 \ \mu_3 \ \mu_4]^T.$$

Now consider three different mass distributions for the link, denoted with the leading superscripts  $p$ ,  $q$  and  $r$ , and suppose that

$$({}^r \boldsymbol{\mu}) = v({}^p \boldsymbol{\mu}) + w({}^q \boldsymbol{\mu}), \quad (\text{Q.1})$$

where  $v, w \in \mathbb{R}$ . The force superposition principle to be proven here states that, for an inverse dynamic analysis (prescribed kinematics), the corresponding sets of forces and moments satisfy:

$$\{{}^r \mathbf{F}_i, {}^r \mathbf{M}_j\} = v\{{}^p \mathbf{F}_i, {}^p \mathbf{M}_j\} + w\{{}^q \mathbf{F}_i, {}^q \mathbf{M}_j\}. \quad (\text{Q.2})$$

The proof of this principle is given hereafter. Before proceeding to the proof itself, first some notation and basic facts need to be introduced.

## Q.1 Notation and Basic Facts

The elements of the vectors  ${}^p\mathbf{m}$ ,  ${}^q\mathbf{m}$  and  ${}^r\mathbf{m}$ , corresponding to  ${}^p\mu$ ,  ${}^q\mu$  and  ${}^r\mu$ , are denoted as:

$${}^p\mathbf{m} = [m_p \ X_p \ Y_p \ J_p]^T;$$

$${}^q\mathbf{m} = [m_q \ X_q \ Y_q \ J_q]^T;$$

$${}^r\mathbf{m} = [m_r \ X_r \ Y_r \ J_r]^T,$$

where, because of (Q.1):

$$m_r = v \cdot m_p + w \cdot m_q; \quad (\text{Q.3})$$

$$m_r \cdot X_r = v \cdot m_p \cdot X_p + w \cdot m_q \cdot X_q; \quad (\text{Q.4})$$

$$m_r \cdot Y_r = v \cdot m_p \cdot Y_p + w \cdot m_q \cdot Y_q. \quad (\text{Q.5})$$

All COG coordinates are expressed w.r.t. the same local coordinate system (LCS). Let  $\hat{o}$  be the LCS origin, and let  $a_{ox}$  and  $a_{oy}$  [ $\text{m/s}^2$ ] be its acceleration components. The analysis is supposed to be inverse dynamic, that is, the kinematics of the mechanism are prescribed. In that case,  $a_{ox}$  and  $a_{oy}$ , as well as the link's rotational velocity  $\dot{\phi}$  [ $\text{rad/s}$ ] and acceleration  $\ddot{\phi}$  [ $\text{rad/s}^2$ ] are identical for the three considered situations. Hence, the COG acceleration components  $a_{kx}$  and  $a_{ky}$  [ $\text{m/s}^2$ ],  $k = \{p, q, r\}$  are given by:

$$a_{kx} = a_{ox} - \dot{\phi}^2 \cdot X_k - \ddot{\phi} \cdot Y_k; \quad (\text{Q.6})$$

$$a_{ky} = a_{oy} - \dot{\phi}^2 \cdot Y_k + \ddot{\phi} \cdot X_k. \quad (\text{Q.7})$$

Application of Newton's laws gives the following relations between  $\{{}^k\mathbf{F}_i, {}^k\mathbf{M}_j\}$  and  $\{a_{kx}, a_{ky}, \ddot{\phi}\}$  ( $k = \{p, q, r\}$ ):

$$\sum_{i=1}^I ({}^k F_{ix}) = m_k \cdot a_{kx}; \quad (\text{Q.8})$$

$$\sum_{i=1}^I ({}^k F_{iy}) = m_k \cdot a_{ky}; \quad (\text{Q.9})$$

$$\sum_{i=1}^I [(X_i - X_k) \cdot ({}^k F_{iy}) - (Y_i - Y_k) \cdot ({}^k F_{ix})] + \sum_{j=1}^J ({}^k M_j) = J_k \cdot \ddot{\phi}, \quad (\text{Q.10})$$

where  $(X_i, Y_i)$  denote the LCS coordinates of the point at which the force  $F_i$  acts on the link.

The proof of (Q.2) requires to show that  $v\{{}^p\mathbf{F}_i, {}^p\mathbf{M}_j\} + w\{{}^q\mathbf{F}_i, {}^q\mathbf{M}_j\}$  satisfies (Q.8–Q.10). Section Q.2 shows that this set of forces and moments satisfies (Q.8) for  $k = r$  (the proof that it satisfies (Q.9) is left as an exercise to the reader). After that, Section Q.3 shows that also (Q.10) is satisfied.

## Q.2 Force Superposition

Here, it is proven that  $v\{^p\mathbf{F}_i, ^p\mathbf{M}_j\} + w\{^q\mathbf{F}_i, ^q\mathbf{M}_j\}$  complies with (Q.8) for  $k = r$ . That is:

$$\sum_{i=1}^I [v(^pF_{ix}) + w(^qF_{ix})] = m_r \cdot a_{rx}.$$

The proof proceeds as follows. Rearranging the left part of the equation and applying of (Q.8) for  $k = p$  and  $k = q$ , yields:

$$\sum_{i=1}^I [v(^pF_{ix}) + w(^qF_{ix})] = v \cdot \sum_{i=1}^I (^pF_{ix}) + w \cdot \sum_{i=1}^I (^qF_{ix}) = v \cdot m_p \cdot a_{px} + w \cdot m_q \cdot a_{qx}.$$

Substituting (Q.6) for  $k = p$  and  $k = q$ , we obtain:

$$\begin{aligned} \sum_{i=1}^I [v(^pF_{ix}) + w(^qF_{ix})] &= v \cdot m_p \cdot (a_{ox} - \dot{\phi}^2 \cdot X_p - \ddot{\phi} \cdot Y_p) \dots \\ &\dots + w \cdot m_q \cdot (a_{ox} - \dot{\phi}^2 \cdot X_q - \ddot{\phi} \cdot Y_q), \end{aligned}$$

and hence:

$$\begin{aligned} \sum_{i=1}^I [v(^pF_{ix}) + w(^qF_{ix})] &= (v \cdot m_p + w \cdot m_q) \cdot a_{ox} - \dot{\phi}^2 \cdot (v \cdot m_p \cdot X_p + w \cdot m_q \cdot X_q) \dots \\ &\dots - \ddot{\phi} \cdot (v \cdot m_p \cdot Y_p + w \cdot m_q \cdot Y_q). \end{aligned}$$

Now substitute (Q.3–Q.5):

$$\begin{aligned} \sum_{i=1}^I [v(^pF_{ix}) + w(^qF_{ix})] &= m_r \cdot a_{ox} - \dot{\phi}^2 \cdot m_r \cdot X_r - \ddot{\phi} \cdot m_r \cdot Y_r; \\ &= m_r \cdot (a_{ox} - \dot{\phi}^2 \cdot X_r - \ddot{\phi} \cdot Y_r). \end{aligned}$$

Finally, taking into account (Q.6) for  $k = r$ , we obtain:

$$\sum_{i=1}^I [v(^pF_{ix}) + w(^qF_{ix})] = m_r \cdot a_{rx}.$$

□

### Q.3 Moment Superposition

Here, it is proven that  $v\{^p\mathbf{F}_i, {}^p\mathbf{M}_j\} + w\{^q\mathbf{F}_i, {}^q\mathbf{M}_j\}$  complies with (Q.10) for  $k = r$ , that is:

$$\begin{aligned} & \sum_{i=1}^I \{(X_i - X_r) \cdot [v({}^p F_{iy}) + w({}^q F_{iy})] - (Y_i - Y_r) \cdot [v({}^p F_{ix}) + w({}^q F_{ix})]\} \dots \\ & \dots + \sum_{j=1}^J [v({}^p M_j) + w({}^q M_j)] = J_r \cdot \ddot{\phi}. \end{aligned}$$

The left part of this equation is rewritten as:

$$\begin{aligned} & \sum_{i=1}^I [(X_i - X_p) \cdot v \cdot ({}^p F_{iy}) - (Y_i - Y_p) \cdot v \cdot ({}^p F_{ix})] + \sum_{j=1}^J v({}^p M_j) \dots \\ & \dots + \sum_{i=1}^I [(X_i - X_q) \cdot w \cdot ({}^q F_{iy}) - (Y_i - Y_q) \cdot w \cdot ({}^q F_{ix})] + \sum_{j=1}^J w({}^q M_j) \dots \\ & \dots + \sum_{i=1}^I [(X_p - X_r) \cdot v \cdot ({}^p F_{iy}) - (Y_p - Y_r) \cdot v \cdot ({}^p F_{ix})] \dots \\ & \dots + \sum_{i=1}^I [(X_q - X_r) \cdot w \cdot ({}^q F_{iy}) - (Y_q - Y_r) \cdot w \cdot ({}^q F_{ix})]. \end{aligned}$$

Taking into account (Q.10) for  $k = p$  and  $k = q$ , we obtain:

$$\begin{aligned} & v \cdot J_p \cdot \ddot{\phi} + w \cdot J_q \cdot \ddot{\phi} \dots \\ & \dots + \sum_{i=1}^I [(X_p - X_r) \cdot v \cdot ({}^p F_{iy}) - (Y_p - Y_r) \cdot v \cdot ({}^p F_{ix})] \dots \\ & \dots + \sum_{i=1}^I [(X_q - X_r) \cdot w \cdot ({}^q F_{iy}) - (Y_q - Y_r) \cdot w \cdot ({}^q F_{ix})]. \end{aligned}$$

Rearranging yields:

$$\begin{aligned} & v \cdot J_p \cdot \ddot{\phi} + w \cdot J_q \cdot \ddot{\phi} \dots \\ & \dots + (X_p - X_r) \cdot v \cdot \sum_{i=1}^I ({}^p F_{iy}) - (Y_p - Y_r) \cdot v \cdot \sum_{i=1}^I ({}^p F_{ix}) \dots \\ & \dots + (X_q - X_r) \cdot w \cdot \sum_{i=1}^I ({}^q F_{iy}) - (Y_q - Y_r) \cdot w \cdot \sum_{i=1}^I ({}^q F_{ix}). \end{aligned}$$

Now taking into account (Q.8–Q.9) for  $k = p$  and  $k = q$ :

$$\begin{aligned} & v \cdot J_p \cdot \ddot{\phi} + w \cdot J_q \cdot \ddot{\phi} \dots \\ & \dots + (X_p - X_r) \cdot v \cdot m_p \cdot a_{py} - (Y_p - Y_r) \cdot v \cdot m_p \cdot a_{px} \dots \\ & \dots + (X_q - X_r) \cdot w \cdot m_q \cdot a_{qy} - (Y_q - Y_r) \cdot w \cdot m_q \cdot a_{qx}. \end{aligned}$$

After substituting (Q.6–Q.7) for  $k = p$  and  $k = q$  and rearranging the terms, the following result is obtained:

$$\begin{aligned} & v \cdot J_p \cdot \ddot{\phi} + w \cdot J_q \cdot \ddot{\phi} \dots \\ & \dots + [X_p \cdot (X_p - X_r) \cdot v \cdot m_p + Y_p \cdot (Y_p - Y_r) \cdot v \cdot m_p \dots \\ & \dots + X_q \cdot (X_q - X_r) \cdot w \cdot m_q + Y_q \cdot (Y_q - Y_r) \cdot w \cdot m_q] \cdot \ddot{\phi}. \end{aligned}$$

Rearranging yields:

$$\begin{aligned} & v \cdot J_p \cdot \ddot{\phi} + w \cdot J_q \cdot \ddot{\phi} \dots \\ & \dots + [v \cdot m_p (X_p^2 + Y_p^2) + w \cdot m_q (X_q^2 + Y_q^2) \dots \\ & \dots - X_r \cdot (v \cdot m_p \cdot X_p + w \cdot m_q \cdot X_q) - Y_r \cdot (v \cdot m_p \cdot Y_p + w \cdot m_q \cdot Y_q)] \ddot{\phi}. \end{aligned}$$

Taking into account (Q.4–Q.5), we obtain:

$$v \cdot J_p \cdot \ddot{\phi} + w \cdot J_q \cdot \ddot{\phi} + [v \cdot m_p (X_p^2 + Y_p^2) + w \cdot m_q (X_q^2 + Y_q^2) - m_r (X_r^2 + Y_r^2)] \ddot{\phi}.$$

Now applying the definition of  $\mu_4$  as  $J + m \cdot (X^2 + Y^2)$ :

$$[v \cdot \mu_{4p} + w \cdot \mu_{4q} - m_r (X_r^2 + Y_r^2)] \cdot \ddot{\phi}.$$

Because of (Q.1), we have  $v \cdot \mu_{4p} + w \cdot \mu_{4q} = \mu_{4r}$ , and hence:

$$[\mu_{4r} - m_r (X_r^2 + Y_r^2)] \cdot \ddot{\phi}.$$

Again applying the definition of  $\mu_4$  finally yields:

$$J_r \cdot \ddot{\phi}.$$

□



# Index

- A**
- airjet weaving machine . . . . . liii, 22
    - compensated cams . . . . . 62
    - damped eigenmotion . . . . . 39
    - eigenmotion . . . . . 32
    - experimental setup . . . . . 150
    - input torque balancing . . . . . 140
    - simplified model . . . . . 23
    - specific requirements . . . . . 44
    - torsional setup model . . . . . 182
  - analytic differentiation . . . . . 159
  - Average Speed Control liii, 29, 68, 160, 168
- B**
- balancing
    - counterweight . . . . . liii, 4, 11, 204
    - dynamic . . . . . liv, 9, 11
    - rotating machinery . . . . . 213
    - static . . . . . lvii, 9, 10, 213
  - binary link . . . . . liii, 223
  - blanc, à . . . . . lvii, 150, 188
- C**
- cam-based centrifugal pendulum 76, 118
  - cam-box mechanism . . . . . 21
  - CBCP-configuration . . . . . lii, 168
  - chain yarn . . . . . 20
  - compensated cams
    - dynamically . . . . . liv, 13, 46, 47
    - inertially . . . . . lv, 10, 50, 162
  - Complex Mass Method . . . . . 201
  - CON-system . . . . . lii, 57
  - conjugate . . . . . liii, 7, 8, 21, 25
  - constraint function . . . . . liii, 216
- constraints
  - practical . . . . . 207, 222
  - practical+ . . . . . 223
  - ultimate . . . . . 207, 222
- contour theorem . . . . . 200
  - convex
    - function . . . . . liii, 216
    - functions, sum of . . . . . 229
    - optimization . . . . . 3
    - program . . . . . liii, 5, 218, 232
    - program, properties . . . . . 218
    - programs, classes of . . . . . 218
    - programs, solving . . . . . 219
    - set . . . . . liii, 216
  - counterweight
    - balancing . . . . . liii, 4, 11, 204
    - minimum inertia lvi, 210, 224
  - crank-rocker liii, 11, 48, 49, 79, 234
  - crossing angle . . . . . liii, 26, 65, 152
- D**
- damped eigenmotion . . . . . liv, 28, 68
    - airjet weaving machine . . . . . 39
    - ASC . . . . . 160
    - frequency domain . . . . . 37
    - torsional setup model . . . . . 174
  - degree-of-freedom
    - multi . . . . . 201
    - single . . . . . lvii, 8, 201
  - dobby system . . . . . 21, 153
  - double crank . . . . . liv, 79, 80
  - driving torque . . . . . *see* input torque
  - dyad . . . . . liv, 72, 79, 189, 203, 209
  - dynamic
    - balancing . . . . . liv, 1, 3, 9, 11

reactions . . . . liv, 1, 3, 9, 193

**E**

Eigenbewegung . . . . . 29  
 eigenmotion . . . . . liv, 28, 68  
     airjet weaving machine . . . . 32  
     cams . . . . . 68  
     frequency domain . . . . . 29  
 equipollent circle . . . . . 202  
 experimental identification . . . 195

**F**

FLY-configuration . . . . . lii, 168  
 force-balanced . . . . . liv  
 force-closed . . . . . liv, 7  
 form-closed . . . . . liv, 7  
 forward dynamic approach . . liv, 3,  
     9, 26  
 frame  
     acceleration spectrum . . . 176  
     equivalent mass . . . . . 25  
     resonances . . . . . 34  
     system . . . . . 20

**G**

Gelenkkraftausgleich . . . . . 190  
 Grashoff . . . . . liv, 48, 79  
 ground bearing force . . . . . lv, 191

**H**

heddle . . . . . 21

**I**

inertia counterweight . . . . . lv, 202  
 inline . . . . . lv, 198, 203, 205–208  
 input crank . . . . . lv, 8  
 input torque . . . . . lv, 3, 8, 11, 193  
     balancing . . . . . lv, 70  
     balancing mechanism . . lv, 10  
     balancing, benefits . . . . . 84  
 insertion yarn . . . . . 20  
 inverse dynamic approach . . lv, 3, 9,  
     48, 97, 125, 215, 249  
 inverted cam mechanism . . . 75, 88  
 irregular force transmission . . 200

isomomental ellipse . . . . . 202

**J**

jacquard system . . . . . 20  
 joint  
     force . . . . . lv, 3, 11, 236, 248  
     friction . . . . . 7

**L**

Leistungsausgleich . . . . . 190  
 linear  
     matrix inequality . . . lvi, 219,  
         228, 229, 233  
     program . . . . . lvi, 4, 218, 219  
 linearly independent vector  
     Berkof and Lowen . . . . . 196  
     formalism . . . . . 193  
 low-bandwidth controller . . 28, 29,  
     45, 68, 160

**M**

machine . . . . . lvi  
 Massenausgleich . . . . . 190  
 mechanism . . . . . lvi, 1  
 mechatronics . . . . . 68  
 motion law . . . . . lvi, 24  
     calculation . . . . . 54  
     comparison . . . . . 57, 82  
     shed, setup . . . . . 153  
     shed, simulation . . . . . 25  
     sley . . . . . 24  
     sword . . . . . 152

**N**

Nishioka  
     (in)direct method . . . . . 83  
     air spring . . . . . 83  
     secondary vibration . . . . . 84

**P**

peak phenomenon . . . . . 113, 147  
 polydyne method . . . . . 47  
 program  
     linear . . . . . lvi, 4, 218, 219  
     mathematical . . . . . lvi, 4, 216

- 
- second-order cone ..... lvi,  
218–220, 233, 235
- semidefinite lvi, 218–220, 233,  
235
- Q**
- quadratic-over-linear ..... 229
- R**
- rapier weaving machine ..... 22
- reciprocating machinery ..... lvi, 1
- period of motion ..... 24, 159
- reed ..... 22
- S**
- second-order cone
- constraint .. lvi, 218, 219, 228,  
233, 235
- program lvi, 218–220, 233, 235
- shaking
- force ..... lvi, 3, 10, 11, 191
- moment .... lvi, 3, 10, 11, 192
- shed ..... 20
- follower mass ..... 25, 153
- mechanism ..... lvii, 20, 25
- motion law, setup ..... 153
- motion law, simulation .... 25
- sley
- follower inertia ..... 24
- mechanism ..... lvii, 22, 24
- motion law ..... 24
- switched reluctance .... lii, 23, 163
- sword ..... lvii, 21, 152
- acceleration spectrum .... 176
- T**
- torque mode ..... lvii, 29, 149
- Totlagenkonstruktion ..... 48
- U**
- undercutting lvii, 57, 83, 101, 128,  
315
- V**
- VAR-system ..... lii, 57
- VDI ..... lii, 6
- vibration absorber ..... 71
- centrifugal pendulum ..... 73
- delayed resonator ..... 73, 81
- detuning ..... 81
- tautochrone ..... 81
- torsional pendulum ..... 72